On the Application of Rotating Cylinders to Micro Air Vehicles

By

Carmine Badalamenti

Thesis submitted as part of the requirements for the degree of Doctor of Philosophy

School of Engineering and Mathematical Sciences,
City University London,
Northampton Square, London, EC1V 0HB

July 2010

Contents

List of Tables

List of Figures

Acknowledgements

Many thanks to my brother, whose knowledge of Photoshop, and willingness to share it, was instrumental in getting everything “just right”.

I’d also like to extend my gratitude to Mr Mike Smith, Mr Chris Barber, Mr Tim Barnes, and Mr Jim Ford for their invaluable technical assistance in realising the experimental parts of this project.

Declaration

I grant powers of the discretion to the University Librarian to allow my thesis to be copied in whole or in part without further reference to the author. This permission covers only single copies made for study purposes, subject to normal conditions of acknowledgment.

Abstract

An investigation into the feasibility of using rotating circular cylinders as the primary means of generating lift for the class of very small (0.15 m maximum dimension, 50 g weight) unmanned aircraft known as Micro Air Vehicles (MAV) has been carried out. It is hoped that such a design would be able to exploit the large lift generating properties of the rotating cylinder for the purposes of increasing the available payload weight. This would provide considerable benefits as, at present, the inability to support capable payloads significantly restricts the usefulness of MAV-sized craft.

A preliminary design study was performed to investigate possible configurations for the proposed design, resulting in the selection, for reasons of simplicity, of an arrangement having two rotating cylinders about a central fuselage. Initial assessments of the practical feasibility of such a design, as well as its likely performance (in terms of lift, drag, and power requirements) were then carried out. An examination of the consequences of the presence of the cylinders on the stability and control of such a vehicle was also performed.

Existing understanding of the aerodynamic characteristics of a rotating cylinder in cross-flow was extended through a series of wind tunnel tests examining all aspects of rotating cylinder flow, including force and moment coefficients, behaviour at non-zero yaw angles ($-30^\circ \leq \Psi \leq 10^\circ$), power requirements for spinning the cylinder, and wake phenomena. A particular focus was the use of endplates to improve aerodynamic performance. The tests were conducted with a cylinder of aspect ratio $AR = 5$ across a range of Reynolds numbers ($1.6 \times 10^4 \leq Re \leq 9.5 \times 10^4$, based on cylinder diameter) and velocity ratios ($\Omega \leq 4$) identified as being of interest by the preliminary design study. The results were generally found to be in very good agreement with existing published data, though power requirements for spinning the cylinder were much higher than anticipated, and revealed the influence of tip vortices to be of great significance.

Wind tunnel experiments with a simple prototype aircraft, based on the outcome of the preliminary design study and isolated cylinder tests, examined the overall aerodynamic performance of this type of design for a single Reynolds number of $Re = 1.8 \times 10^4$, across a velocity ratio range of $\Omega \leq 2.5$, and at various angles of attack ($-10^\circ \leq \alpha \leq 25^\circ$) and yaw ($-10^\circ \leq \Psi \leq 30^\circ$). These tests also investigated the interaction between the cylinders and the other components of the aircraft to help determine the most favourable layout. The tests revealed the effect of propeller wash over the rotors, the influence of the cylinder wake on the tail, and the design of the tail, fin, and fuselage to be of considerable importance to the aerodynamic characteristics and performance of the vehicle.

Overall, the study indicated that an aircraft of the proposed configuration and suitable capability was theoretically possible at the MAV scale of flight if an appropriate rotor geometry was chosen. However, the actual construction of a vehicle able to fully provide the desired performance within the constraints placed on platform size and weight was not currently possible using commonly available materials and components. Slightly larger designs (of dimension 0.4 m and weight 250 g) were more realisable, but still lacked in performance. Successful development of this type of design is thus dependent on technological advancement, particularly improvements in power and propulsion systems.

Nomenclature

English Symbols

a	Cylinder radius
A	Model frontal area
AR	Aspect ratio
b	Cylinder span
B	Wind tunnel working section width
c	Chord length
C	Wind tunnel working section cross-sectional area
C_D	Drag coefficient
$C_{D_{\infty_1}}$	Drag coefficient corrected by Maskell's one-step method
C_{D_0}	Profile drag coefficient
C_{D_f}	Skin friction drag coefficient
C_{D_i}	Induced drag coefficient
C_{D_s}	Separated flow drag coefficient
C_f	Skin friction coefficient; Shear stress coefficient
C_l	Rolling moment coefficient
C_L	Lift coefficient
C_m	Pitching moment coefficient
C_n	Yawing moment coefficient
C_p	Pressure coefficient
C_P	Power coefficient
C_Q	Torque coefficient
C_Y	Sideforce coefficient
ΔC_D	Incremental drag correction due to wake distortion

d	Cylinder diameter
d_e	Endplate diameter
D	Drag
e	Oswald efficiency factor
f	Frequency
f_b	Body carried frame of reference fixed to the aircraft
f_c	Body carried frame of reference fixed to the cylinder
f_e	Inertial frame of reference fixed to the Earth
f_s	Vortex shedding frequency
F	Frictional force on cylinder surface
g	Acceleration due to gravity
G	Vector of external moments
H	Vector of angular momentum
H	Wind tunnel working section height; Total pressure
i_t	Tail setting angle
I	Current
I	Moment or product of inertia of aircraft
J	Moment or product of inertia of rotor
k_1	Lift-dependent profile drag factor
k_2	Induced drag factor
K	Circulation; Lift-dependent drag factor
K_v	Motor speed constant
l	Rolling moment
l_1	Distance between $o_i x_i y_i z_i$ and $o_w x_w y_w z_y$
L	Lift; Resultant aerodynamic moment about body fixed x axis

m	Pitching moment; Mass
M	Mach number; Resultant aerodynamic moment about body fixed y axis
n	Yawing moment
N	Rotational rate; Resultant aerodynamic moment about body fixed z axis
p	Static pressure; Rate of roll
P	Total power required for flight; Power requirements for spinning an isolated rotating cylinder
P_H	Power required for hovering flight
P_R	Power required to spin both rotating cylinders
P_S	Power required for onboard systems
P_T	Power required for horizontal translational flight
q	Dynamic pressure; Rate of pitch
Q	Torque
r	Radial coordinate; Rate of yaw
Re	Reynolds number based on cylinder diameter
Re_b	Reynolds number based on body diameter
Re_c	Reynolds number based on chord length
Re_ℓ	Reynolds number based on characteristic length
s	Total length of both rotors
S	Model reference area; Longitudinal spacing between multiple tandem cylinders
$\underline{S}$	Center-to-center spacing between multiple staggered cylinders
S_a	Actuator disc reference area
S_w	Wing reference area
St	Strouhal number
t	Thickness
T	Thrust; Transverse spacing between multiple side-by-side cylinders

u Linear velocity along x axis

U Resultant speed through actuator disc

v Linear velocity along y axis

V Voltage

V Velocity

V_r Peripheral velocity

w Linear velocity along z axis

W Weight

x Cartesian coordinate

X Resultant aerodynamic and thrust force along x axis

y Cartesian coordinate

Y Sideforce; Resultant aerodynamic and thrust force along y axis

z Cartesian coordinate

Z Resultant aerodynamic and thrust force along z axis

Greek Symbols

α Geometric angle of attack

α_s Stall angle

β Sideslip angle; Angular coordinate around cylinder circumference

γ Angle of climb or descent

Γ Rotor angular velocity

δ Boundary layer thickness

ϵ Total correction factor due to solid and wake blockage

ϵ_s Correction factor due to solid blockage

ϵ_w Correction factor due to wake blockage

ε Downwash angle; Maskell's correction factor due to blockage

η Electrical efficiency

θ Euler angle about local y axis; Angular coordinate

Λ Body-shape factor for wind tunnel wall interference

ν Kinematic viscosity of air

ρ Density of air

τ Wind tunnel shape factor for wall interference calculation

ϕ Euler angle about local x axis

ψ Euler angle about local z axis

Ψ Yaw angle

ω Angular velocity

$\boldsymbol{\omega}$ Vector of angular velocity of complete aircraft

Ω Velocity ratio

Ω_c Critical velocity ratio for suppression of vortex shedding

Ω_K Velocity ratio for which $C_L = 0$ during Magnus effect inversion

$\boldsymbol{\Omega}$ Vector of angular velocity of $oxyz$ to $Ox_e y_e z_e$

Subscripts

∞ Associated with freestream conditions

0 Associated with initial conditions

b Associated with frame f_b

$base$ Associated with cylinder base conditions

c Corrected quantity

cyl Cylinder

C Control term

e Associated with frame f_e

g Gyroscopic component

i Associated with the intersection of the model longitudinal axis and the cylinders' axis of rotation

int Associated with interference effects

m Measured quantity

max Maximum

min Minimum

rel Relative to cylinder surface

$strut$ Associated with the model support structure

tot Total

w Associated with the attachment point between the T2 balance and the model

Superscripts

b Relative to or within frame f_b

e Relative to or within frame f_e

1 Introduction

The success of Unmanned Aerial Vehicles (UAV) such as Predator and Global Hawk has led to a recent surge of interest in all aspects of unmanned flight and an examination of the possible military relevance of very small UAVs known as Micro Air Vehicles (MAV). Generally defined as having a maximum linear dimension no greater than 6" (0.15 m) and typically weighing a few hundred grams at most, this type of unmanned platform came to prominence during the mid-1990s through a Defence Advanced Research Projects Agency (DARPA) led investigation into micro-aircraft.

The envisaged role for MAVs is as a provider of local reconnaissance and surveillance for small military units, or individual soldiers, in both traditional battlefield scenarios and more exotic conditions, such as jungle or urban environments. MAV-scale vehicles have only become possible due to recent advances in the miniaturisation of technologies for propulsion, power, sensors, and actuators, but there are still many obstacles to be overcome before MAVs enjoy the same level of acceptance from the defence sector as larger UAVs. Meeting the many stringent technological requirements of MAV-scale flight whilst providing a suitable mission capability has proved particularly difficult.

The majority of existing MAV designs are of a fixed-wing nature, many of which are of the flying-wing type. A number of rotary-wing and flapping-wing designs also exist but are hampered by limited information on the aerodynamics of flapping and rotary flight at the low Reynolds numbers at which MAVs operate (typically $2 \times 10^4 \leq Re_\ell \leq 2 \times 10^5$). This lack of fundamental knowledge is also problematic for current fixed-wing designs, which tend to suffer from low lift coefficients, high drag, and reduced payload weights (as a percentage of total vehicle weight).

Analysis of existing small-UAV and MAV designs reveals a trend of rapidly decreasing payload weight percentage with decreasing size (see Figure 1.1). In fact, empirical data suggests the available payload weight reduces almost five times more rapidly than the vehicle weight.[1] Given the smaller mass of smaller craft, this places a considerable constraint on the size and type of payload that can be realistically carried at these scales. The lack of available space for the storage of propulsive and systems energy, and the resulting short flight durations, further compound the problem. Consequently, current MAV designs are limited to fairly short range, low endurance missions, with restricted sensor capability, and reduced communications. This has led to the focus moving away from 6"-sized craft for the time being whilst solutions to these problems are sought.

The relative simplicity and low cost of very small UAVs and MAVs provides a particularly

good opportunity to explore unconventional solutions to such problems. Additionally, with the need to accommodate a human pilot now removed, along with some of the associated constraints forced on aircraft designers, there is also an incentive to re-evaluate many previously discarded concepts that are impractical for full-scale manned aircraft, but which may well be beneficial when viewed in the context of UAVs and MAVs. One such idea that could now have merit when applied to an MAV-type platform is that of generating lift with a rotating cylinder.

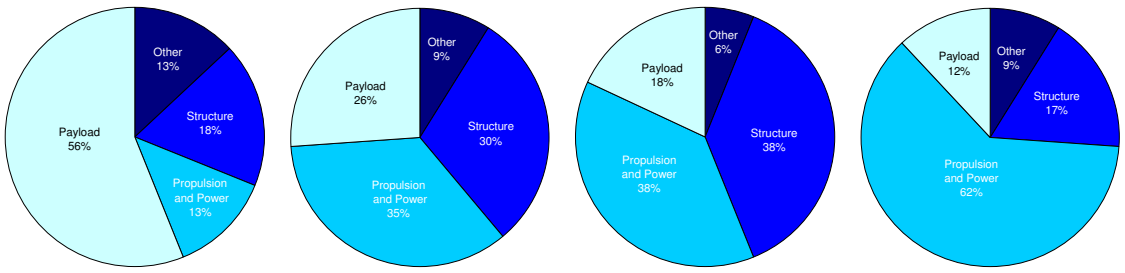

(a) Extender (3.10) (b) Dragon Eye (1.13) (c) MITE (0.46) (d) Black Widow (0.15)

Figure 1.1: Small-UAV weight budget comparison[1]. Numbers in brackets denote vehicle wingspan in metres.

At present, the inability to support useful payloads significantly restricts the usefulness of MAV craft. Successful exploitation of the large lift generating capabilities of the rotating cylinder ($C_L > 10$ is known to be possible) could greatly benefit all mission capability related areas. In particular, a significant increase in available payload weight could be achieved. This would enable the use of larger, more sophisticated sensors or the carriage of multiple sensors that could then be linked together to provide better autonomy, leading to advanced mission roles or novel applications.

Although continuing miniaturisation of technologies will always provide smaller, more capable payloads, the inherent extra lifting potential of a rotating cylinder platform would remain an advantage. This makes the idea worthy of investigation. The high value of the obtainable lift coefficients also raises the possibility of very low speed flight, creating a platform possessing some of the qualities of both fixed-wing and rotary-wing vehicles. High C_L values have also been associated with a reduction in the overall size of MAVs.[2]

1.1 The Rotating Cylinder for MAV Applications

Previous attempts at exploiting the large forces available from a spinning cylinder have failed to result in a successful venture and the general view has been that the concept

is not much more than a novelty. Indeed, the rotating circular cylinder has not been seriously considered as a means of primary lift generation for an aircraft since the early decades of the last century when the introduction of the Kutta-Joukowski theorem led to much speculation and investigation into the 'Magnus effect' and it's possible pertinence to aircraft flight.[3] More recent efforts at practical application of the concept have mostly concentrated on its use as a high-lift device (trailing or leading edge flap) for STOL type aircraft,[4–6] but have not reached fruition. To date, the only moderately successful application of the Magnus effect in an aeronautically related field has been the Flettner rotorship.

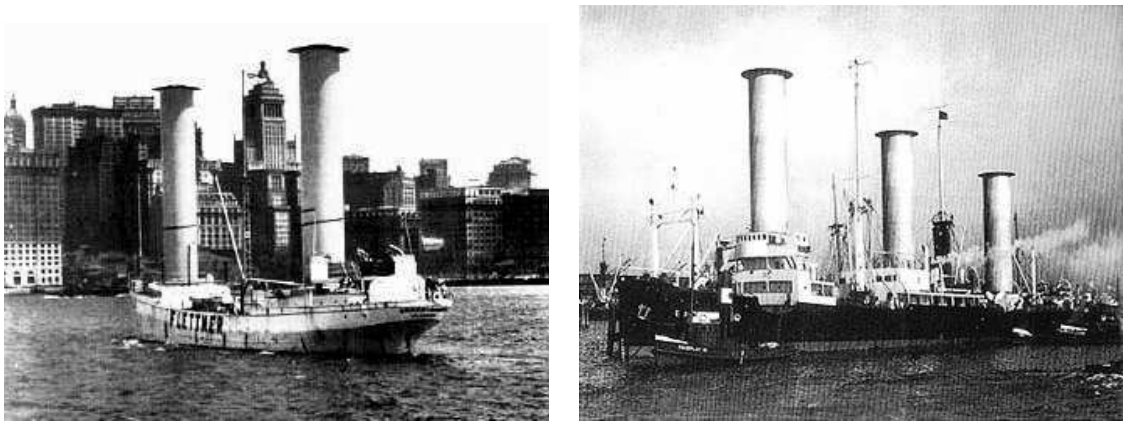

(a) The Buckau (b) The Barbara

Figure 1.2: The Flettner rotorships.

In 1925, Anton Flettner published a number of papers describing his application of the principles of rotating cylinders to the propulsion of ships.[7] He had originally been considering the use of aerodynamic metal sails, but realised the potential of rotating cylinders when he learned of recent experiments at the Aerodynamische Versuchsanstalt Göttingen (AVA), in Germany.[8–10] Confident that his idea would work, in 1926 he converted the sailship 'Buckau' (later renamed 'Baden Baden') by fitting it with two 18.5 m high, 2.8 m diameter cylindrical rotors orientated with the longitudinal axis vertical and capped with small endplates (see Figure 1.2a).

In a crosswind, rotation of the cylinders about the longitudinal axis produced a propulsive force acting perpendicular to the wind direction. This force was many times greater than that generated by a conventional sail of equivalent size, yet the drag of the new rigging was substantially lower. The rotors were also quicker and easier to adapt to a change in wind-speed than a sail, were able to utilise higher wind-speeds without fear of damage, and also greatly enhanced turning and manoeuvrability. The rotorship design was well received and, on the orders of the German navy, a second ship, 'Barbara', became the first vessel to be specifically designed and built as a rotorship (see Figure 1.2b).

Though in regular commercial service during the late 1920s, the rotorships did not gain widespread popularity and their dependence on wind conditions proved a crucial failing. The demand for a steady service and an abundance of cheap fuel meant that the concept of the Flettner rotor was abandoned in favour of propeller-driven craft. Despite a small revival during the fuel crisis of the 1970s, the potential of the rotorship was never fully realised.[11]

That Flettner was able to obtain a level of success that has so far eluded other attempted applications is a consequence of the operational conditions associated with a sailing ship setting. As Betz[8] noted, these were especially favourable to the rotating cylinder concept. For most cases in which lifting forces are required, the flow velocity is so high that, to obtain a sufficient lift as to be advantageous, the rotational speed of the cylinder becomes prohibitively large. The high power requirements and associated technical difficulties would then nullify any benefits that could be gained.

By contrast, the wind velocities at which the Flettner rotorships achieved maximum efficiency were not very high at all, being on the order of 5 to 10 m/s. Consequently, the required peripheral velocity was only moderately high (≈ 20 to 30 m/s) and, due to the large size of the cylinders, the necessary rotational rate remained quite low even at the highest wind speeds. The large drag associated with a bluff body such as a cylinder was also not so problematic: the conventional sail that it replaced performed even worse in this regard.

The unfavourable operating conditions associated with full-scale flight are just one reason why rotating cylinders are ill-suited to the task of providing lift for conventional-sized aircraft. Several other prominent objections may be raised. The lack of moving parts that a conventional wing provides is both mechanically and structurally more convenient. Furthermore, since the generation of lift from a rotating cylinder is not a passive process, a partial power failure on an aircraft with rotating cylinders in place of wings would create a strong inequality of lift that would present serious control difficulties. A complete power failure would be immediately disastrous.

The most basic objection to a rotor aircraft is the inefficiency of a rotating cylinder as a lifting medium. Existing data[12] suggests a maximum lift-to-drag ratio of between five and six, which is substantially less than that of a typical aerofoil. In noting the many attempts between 1850 and 1930 at applying the Magnus effect to generating lift, Klemin[13] concluded that this is the fundamental handicap that must be overcome if a rotor airplane design is to succeed. Prandtl[9] went further, stating that he saw no practical advantage in connection to using the Magnus effect for the purpose of generating lift for an airplane, as

a propeller, in windmills, or for similar applications. However, the use of rotating cylinders to generate lift for MAV-scale craft immediately eliminates many of these objections.

As with Flettner's rotorships, an MAV platform offers similarly favourable operating conditions for rotating cylinder application. With no crew or passengers to endanger and a low overall cost, vehicle loss due to power failure would be reduced to the level of any other system malfunction. The small size and flight speeds would dictate that the absolute values of drag and power remain relatively small and, although larger than for a fixed-wing MAV, the indications are that the power and propulsive requirements are likely to be within the limits of what is achievable with existing technologies of a suitable size. In any case, the anticipated improvements in mission capability resulting from a greater payload capacity would be expected to outweigh the associated costs of larger drag forces and increased power.

Most importantly, the poor performance of aerofoils when operating at the low Reynolds numbers of MAV flight means that the lift-to-drag ratios of a rotating cylinder and conventional wing are of similar magnitude in these conditions. Furthermore, the literature suggests that low drag and a high lift-to-drag ratio may be relatively unimportant for MAV-scale flight. Instead, multi-disciplinary optimisation (MDO) studies[2] indicate that the best improvements in design can be achieved by increasing the maximum lift.

In this regard, rotating cylinders would be well-suited to MAV application as, based on the incredibly high lift coefficients reported by CFD investigations ($C_L > 20$ for $Re \leq 200$), rotating cylinder aerodynamics is actually somewhat improved at low Reynolds number. The lift from a rotating cylinder is also largely unaffected by the problems associated with laminar separation bubbles that plague fixed-wing aircraft at low Re_c. With rotating cylinders, these effects are relegated to a generally unattractive region of the lift curve that would not, in any case, be suitable for MAV operation. Instead, at the point at which the maximum lift-to-drag ratio occurs, such effects have already been eliminated by the transition-inducing effects of rotation.

Despite such favourable aspects, an MAV application is not without its difficulties. Although the low flight speed also leads to correspondingly low peripheral velocities, the small size implies greater rotational rates will need to be implemented. Incorporating a rapidly spinning cylinder into an MAV design adds a further level of complexity to an already difficult problem and may bring technological difficulties that would increase overall structural weight and reduce the potential benefits to payload capability. To fully make use of this potential, and justify the increased complexity, requires a vehicle whose design enables most of the extra lift made available (for a given span) by the use of the

rotating cylinder concept to be reserved for payload weight. However, successful realisation of such a design is made more difficult by a significant lack of experimental data on all aspects of rotating cylinder flow.

1.2 Project Overview

The purpose of the present work is not primarily to build or design a demonstrator vehicle for a UAV platform, at or near the MAV size limit, that is centered around the use of rotating circular cylinders as the primary means of generating lift, but rather to determine the feasibility of such a vehicle and to improve the scientific and technical knowledge required for its development. Towards this end the following steps were carried out:

- Analysis of the existing literature with a view to identification, examination, and discussion of the shortcomings, inconsistencies, or gaps in the data that might impact on the project by preventing the feasibility assessment or by hindering the design and development of the platform.
- Commencement of a preliminary design study and performance analysis using the data collected from the literature to assess overall feasibility, estimate performance quantities for a range of possible vehicle masses and cylinder sizes, and provide a consideration of the stability and control of such a class of flight vehicle.
- Planning and execution of an experimental testing programme on an isolated rotating circular cylinder with emphasis on verifying the aerodynamic behaviour and filling any gaps in the literature. Specifically, this pertained to the collection of data regarding three-dimensional characteristics, power requirements, and lateral force and moment data.
- Examination of the aerodynamic characteristics of the vehicle as a whole through wind tunnel testing of a near-full-scale model of the proposed design.
- Reassessment and refinement of the design based on the outcome of the isolated cylinder and vehicle model tests with a view to the establishing of a preferred configuration and the future development of a prototype for free-flight tests.

By providing details of, and results from, the above outlined investigations, the present work thus aims to be of use to any future research efforts into rotating-cylinder-based aircraft.

1.3 Dissertation Overview

The outline for the rest of this document is as follows: Chapter 2 reviews the current state-of-the-art of MAVs. Beginning with a brief summary of general UAV activity, the chapter highlights the designs, technologies, and lessons learnt from the first decade of MAV research and discusses expected future developments. Due to the considerable growth of research activity in this field, the review in Chapter 2 is representative rather than exhaustive.

Chapter 3 provides a comprehensive overview of rotating cylinder flow and its typical features. Details on all aspects of the flow, from force behaviour through to wake phenomena and power requirements are included. The focus is on the comparison and analysis of the existing research so as to provide an understanding of how best to employ the cylinders and identify areas requiring further research.

Chapter 4 is the preliminary design study examining the feasibility of an MAV design based on rotating cylinders as the primary means of lift generation. The assessment considers possible designs in light of the aerodynamic behaviour and available technologies, presents performance estimates based on existing data and discusses the implications of the design on the stability and control of such a craft.

Chapters 5, 6, and 7 are concerned with the experimental tests on the isolated cylinder and vehicle model. They describe the experimental equipment, arrangements, and procedures used to carry out the experiments and analyse the results. The outcome of the tests, and the implications of the findings, are also thoroughly discussed. A particular focus of the discussion in Chapters 6 and 7 is the impact of the data on vehicle design.

Finally, Chapters 8 and 9 summarise the conclusions of the present study and give recommendations for future work.

2 Micro Air Vehicles: A Review

Despite the relatively short history of research into micro-aircraft, recent exponential growth in this field has led to the development of a large number of vehicles designed to operate in many different roles. This chapter provides background information on the history, role, design, and possible future development of MAV-scale aircraft. Although the focus is on MAVs, other classes of small-UAVs are, by necessity, discussed too. In addition, a brief summary of general UAV activity is also included so as to provide a context for the current proliferation of unmanned aircraft, of whatever size. The chapter begins with a clarification of the numerous terms and definitions that have emerged to describe all such aircraft.

2.1 A Note on Terminology

> *"UAV: A powered aerial vehicle that does not carry a human operator, uses aerodynamic forces to provide vehicle lift, can fly autonomously or be piloted remotely, can be expendable or recoverable, and can carry a lethal or non-lethal payload. Ballistic or semi-ballistic vehicles, cruise missiles, and artillery projectiles are not considered unmanned aerial vehicles."*

At present there exists no single internationally recognised definition of a UAV. The above quote is taken from the US Department of Defence's (DoD) dictionary of military terms[14] and was chosen as representative of the vehicle class discussed throughout this document. Further, the DoD has been at the forefront of this technology and many of their terms and standards have become the defacto terms and standards for the entire field. The UK definition of a UAV, as provided by the CAA's airworthiness requirements for unmanned flight,[15] is far simpler than its American counterpart (an aircraft which is designed to operate with no human pilot on board), but effectively the same. Alongside such all-encompassing definitions are many different unofficial classification systems for unmanned craft, of which the most commonly accepted are by mission group (Tactical, Strategic, Combat etc.) or design environment (HALE, MALE etc.), though some nations favour classification by mass or speed.

Micro air vehicles occupy the extreme end of the UAV spectrum and are the only type to be classified solely by size. Though generally defined as having a maximum characteristic dimension (span or length etc.) of 6" or less, there are actually many different interpretations of the term and in recent years some agencies have expanded the definition

to include vehicles with a maximum dimension of less than 0.5 m.[16]

Between the limits of UAV and MAV are a wide range of different sized vehicles that go by various names such as gun-launched UAV, man-portable UAV, back-packable UAV, parasite UAV, maritime UAV, micro UAV, mini aerial vehicle, and so forth. Until recently, all such craft were classified by the DoD under the slightly nebulous term of 'small-UAV' (S-UAV), but this has now seemingly fallen out of use. In their most recent documents,[17] the term 'mini-UAV' has been adopted instead. Although generally being applied to vehicles with a wing span of less than 10 ft, no formal definition for this term appears to exist, reflecting the fact that no official classification criteria for UAV either by size or weight has been adopted by the DoD or any other organisation.

The situation has recently been further complicated by a switch in DoD terminology[17] away from UAV in favour of Unmanned Aircraft System (UAS), within which the flying component of the system is referred to as an Unmanned Aircraft (UA). This change in terminology was designed to reflect the fact that the aircraft is only one component of a system that is made up of multiple parts, including ground stations, personnel, and other elements, and is in line with the Federal Aviation Authority (FAA) decision to treat UAVs as aircraft for regulatory purposes.

Where unmanned aircraft are discussed in this document it is generally in reference to the actual vehicle itself, rather than the system as a whole; thus, the term UAV, as opposed to UAS, will be retained. Where a specific craft is discussed, UAVs of any type will be referred to by the manufacturers designation, if any, or by the operational designation if it is in service. If necessary, a short comment on size, weight, or mission class will also be made. For general descriptive purposes, the term mini-UAV will be applied to describe any UAV with characteristic dimension greater than 6" but less than or equal to 10 ft. The term MAV will be reserved for those crafts with a characteristic dimension of less than or equal to 6". Where both vehicle types are referred to simultaneously they will be described as small-UAVs.

2.2 Unmanned Aerial Vehicles

Whilst it is only recently that the field of UAVs has publicly come to the fore, there has in fact been a long tradition of military usage of unmanned systems throughout much of aviation history, though many of these craft were not UAVs as specifically defined above. Hot air balloons filled with explosives were used at least as far back as 1849, whilst 'drones' or 'Remotely Piloted Vehicles' (RPV) have been used for simple recon-

naissance, for anti-aircraft gunnery training, or as crude cruise missiles since the early decades of the twentieth-century. The use of unmanned craft of a more sophisticated nature began during the Vietnam War when technology had progressed to a sufficient level as to enable UAVs (such as the Teledyne Ryan AQM-34 Firebee photo-reconnaissance drone) to be more effective. Since then, UAVs of one type or another have played a role in the majority of recent conflicts, including the Balkans, both Persian Gulf campaigns, and Afghanistan, where their role is still ongoing. Much of this involvement has been in a limited or secondary role, but the success of UAV deployment in Kosovo, Afghanistan, and Iraq has led to a significant increase in worldwide UAV spending that, along with increasing payload capabilities, growing intolerance to loss of life, and increased press and public awareness, is likely to further add to the proliferation of this technology.

Though most UAV research and production now occurs in the US, the majority of smaller tactical UAV systems are fielded and tested in Israel and Europe, both early adopters of unmanned technology.[18] Israel was the first country to employ what would now be regarded as a UAV. Begun in 1974 as a response to the regional political situation of the late 1960s and early 1970s, Israel's UAV programme has made it the most experienced user and a worldwide leader reportedly having some forty-five live UAV programmes (as of 2009).[19] Unmanned vehicles were also quickly taken-up in Europe, where Belgium has operated the EPERVIER (Sparrowhawk) system since 1977. At least sixteen EU member states now have an active UAV programme and several have been pursuing an Unmanned Combat Aerial Vehicle (UCAV) system through multinational programmes such as 'nEUROn' and 'Barracuda'.[16,20] Although the UK is not a participant in either programme it remains at the forefront, alongside France and Germany, of European UAV activity.

Unmanned aerial vehicles are currently a high priority as the UK has cancelled plans for its next-generation manned combat aircraft. Furthermore, the technology-transfer problems encountered with the Joint Strike Fighter, has led to the UK pursuing an independent UAV capability.[21] Current UK UAV efforts are managed by the Ministry of Defence's (MoD) Unmanned Air Systems team, which was formed from the merger of the UK Government's Strategic Unmanned Air Vehicles (Experiment) programme (SUAVE) and the Tactical Unmanned Air Vehicles (TUAV) Project team, and is responsible for directing UK acquisition policy on unmanned aircraft and guiding future research. Systems presently under development include the Desert Hawk III mini-UAV; a UCAV technology demonstrator programme, codenamed 'Taranis'; and the Watchkeeper TUAV, intended as a replacement for the ageing Phoenix and expected to enter service in 2010.

In contrast to its current position, US involvement with the field of unmanned aircraft

was initially erratic. Despite flirting with UAV technology during World War II (under the aborted Operation Aphrodite) and having several programmes during the 1960s, by the end of the Vietnam War all the various American UAV projects were cancelled due to defence budget cuts. US interest was later rekindled by Israel's use of UAVs during the 1982 invasion of Lebanon. Israeli experiences with the Scout and Mastiff mini-UAVs convinced leaders in the US Navy of the need to acquire the Scout and, furthermore, to pursue the development of their own reconnaissance drones. This decision would lead to the 1986 procurement of the Pioneer full-scale UAV. Following particularly successful deployments of Pioneers during the first Gulf War, American military officials further recognized the worth of unmanned systems and the 1990s saw the introduction of the Hunter, Predator, Shadow, and Global Hawk systems (see Figure 2.1). The success of these systems has led directly to the growth in demand for UAV technology currently being experienced.

(a) RQ-2B Pioneer

(b) RQ-5A Hunter

(c) RQ-4 Global Hawk

(d) MQ-1 Predator

Figure 2.1: Operational UAV systems.

To date, unmanned aircraft have primarily been tasked with the provision of reconnaissance, but the increasing sophistication of modern UAVs is leading to more varied scope in the types of missions being performed. These now include roles as expendable communications jammers, mobile communications relays, and several emerging roles in signal intelligence, target monitoring, and battle damage assessment. From a broad perspective,

UAVs are generally preferred for those tasks for which manned missions are ill-suited or present unacceptable risks.

When applied to such missions, commonly known as 'the dull, the dirty, and the dangerous',[17,22] UAVs offer several advantages over manned aircraft. UAVs are able to free up personnel from man-intensive extended sentry and reconnaissance missions, whilst offering better sustained alertness (the dull); they can perform aerial surveyance and physical sampling of radiologically, chemically, or biologically contaminated areas without risk to human life (the dirty); or can undertake high-risk Suppression of Enemy Air Defences (SEAD) missions with less need for supporting aircraft, a lower political and human cost of mission failure, and a higher probability of success (the dangerous). The advantages offered by unmanned systems within these areas has led some to suggest that UAVs may at some point almost fully supplant manned aircraft in a large number of roles.

Though there have been other similar claims made throughout the last century of manned flight that subsequently turned out to be false (the 1957 UK Defence White Paper setting forth the future of the RAF is a particularly good example), the growing spread of unmanned technology and the seriousness with which the defence sector is taking UAVs cannot be ignored. In their 2005 roadmap[17] for the long-term strategy of US UAV development and acquisition, the DoD noted that UAVs have matured to the point where it is no longer necessary to look for niche missions. Instead of asking "Can we find a mission for this UAV?", the question now is "Why are we still doing this mission with a human?".

The growing trend towards the use of unmanned systems will undoubtedly transform the way many military and military support operations are conducted. However, the proliferation of this technology should not be seen as a indication of manned aircraft inadequacy but rather as another facet of the continuing drive to replace man-power with technology.[23] This is of particular importance in the current era where many armed forces are in the process of restructuring or reducing their military power yet also seeking to maintain the ability to purposefully intervene wherever their interests are threatened.

The possible future development and deployment of UAVs in military roles was outlined in the 2002 DoD roadmap,[22] which covered the expected evolution in design and usage of UAVs during the twenty-five year period from 2002 to 2027. This anticipated the introduction of F-16 sized UAVs in a number of combat and combat support roles occurring as early as 2012. Such missions would be made possible by improvements in power, communications, and sensor capabilities, which would allow these craft to operate with a significant degree of autonomy and be able to engage in real-time multi-vehicle coordination and cooperation. An expectation that Vertical Take-Off and Landing (VTOL) Rotary

UAVs with very high endurance capabilities would begin to emerge by 2012 was also expressed. By the end of the development period, morphing airframe UAV systems that are able to change their shape to serve the current mission and environmental conditions were envisaged. The use of shape memory alloys and stretching skins would allow such crafts to perform aerodynamic manoeuvres impossible for manned aircraft.

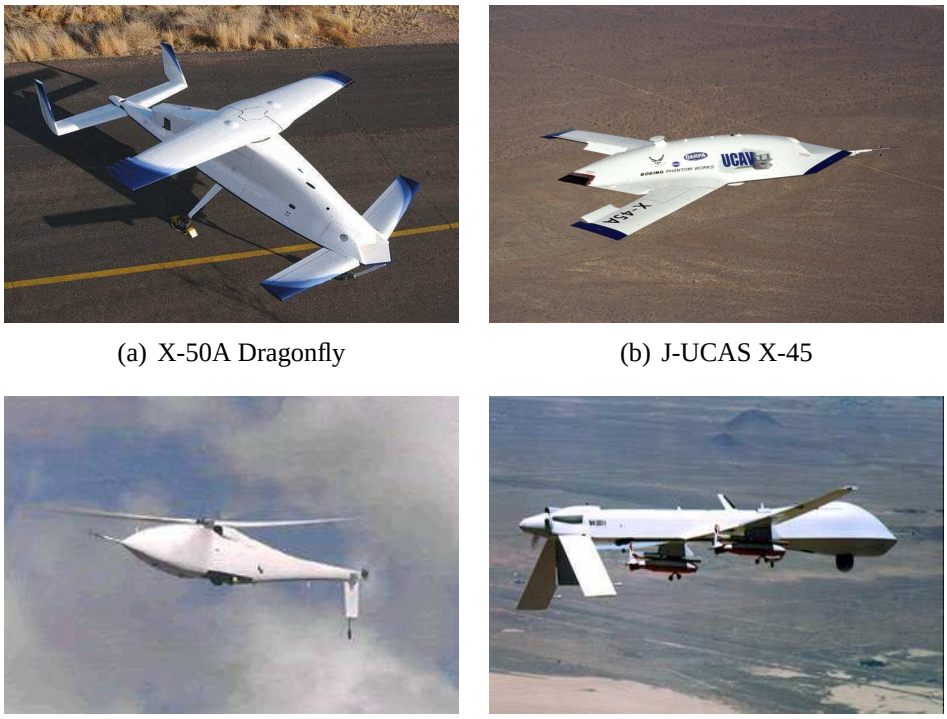

(a) X-50A Dragonfly (b) J-UCAS X-45

(c) A-160 Hummingbird (d) Predator/FINDER integration

Figure 2.2: Developmental UAV programmes.

Though highly speculative, many of the possibilities highlighted in the roadmap, including the introduction of rotary-wing designs, combat UAVs, and interactions between different UAV systems can already be seen in recent developmental programmes such as the J-UCAS combat UAV, the 5 ft FINDER mini-UAV (designed for deployment from a Predator aircraft), the A-160 Hummingbird VTOL rotary-wing UAV, and Boeing's Dragonfly Canard Rotor/Wing programme (see Figure 2.2). However, the actual development of UAV design and capabilities will be very much dependent on sudden changes in funding, political will, and military thinking. The 2005 DoD roadmap[17] outlined many of the same long-term goals listed above but was less specific about the timeline. Since then, the J-UCAS programme has been largely cancelled and the US Army has eliminated two of the planned developmental UAVs from its Future Combat System (FCS), which has itself undergone considerable restructuring.

Despite the natural tendency to concentrate on military applications, many scientific and

civilian uses for UAVs have been mooted and many more can be easily imagined. Following an initial period of inertia, such uses are now beginning to emerge in the fields of police surveillance, drug enforcement, border control, and 'search and rescue' applications following disasters.[24–27] Though demand is growing there are several regulatory, safety, and technological obstacles that must still be overcome. However, it is possible that, in time, the commercial applications of UAVs may come to predominate over military ones by a significant degree, just as is the case with the manned aviation market.[16]

2.3 The DARPA MAV Initiative

The idea of miniature flight vehicles first came to prominence in 1993 with the RAND Corporation's 'Future Technology-Driven Revolutions in Military Operations' workshop.[28] Born from RAND's interest in microsystems, the concept of 'microdrones' was discussed as part of the larger topic of mobile micro-robots. Despite some initial scepticism the idea gained momentum and, in 1995, investigations into the feasibility of micro-fliers were conducted at MIT's Lincoln Laboratory[29,30] and at the US Naval Research Laboratory (NRL). Together with the RAND workshop, this activity prompted the involvement of the Defence Advanced Research Projects Agency (DARPA) which, in 1996, instigated a multi-year developmental programme to focus attention on this area. It is through this initiative that the commonly recognised definition of an MAV platform was established.

To justify DARPA involvement, a suitably difficult objective was deemed necessary and so a maximum characteristic dimension of 6" was imposed. This particular choice meant that the proposed MAVs would be an order of magnitude smaller than the smallest UAV platform in operation at the time, the 4 ft wing span SENDER aircraft operated by the NRL. Additionally, a notional weight of 50 g, which included a day/night imaging payload, was suggested and a typical mission outlined: After launch the vehicle would be expected to fly a distance of 1 km to the designated target area where it would loiter for 30 minutes in turbulent conditions, with wind-speeds of up to 25 mph, before returning to base. The envisaged scenario would require the vehicle to be quiet and inconspicuous yet relatively robust, possessing of the ability to manoeuvre amongst obstacles such as trees or buildings whilst making repeated ascents and descents from altitudes of 350 ft.

Requirements for the command module and control system were also established. The system would be used in a squad-level combat environment so it needed to be light enough to be man-portable, simple enough to be operable by an unskilled user, and yet provide a high degree of autonomy. Whilst not of primary concern, a desire to keep the overall cost as low as possible was also expressed. Though more than a decade old, the DARPA

specifications remain a useful benchmark, particularly since no other agency, American or otherwise, has provided an alternative. Whilst the DARPA parameters have since become an accepted industry standard, the DoD has stated that "the requirements described are neither doctrinally or technically based and are not considered immutable".[22]

(a) MicroSTAR

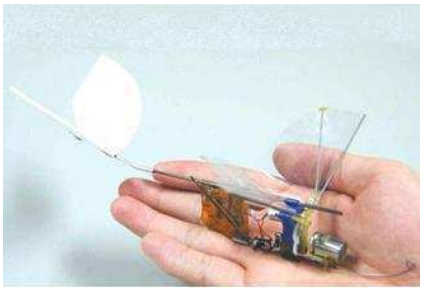

(b) Microbat

(c) SLADF

(d) Kolibri

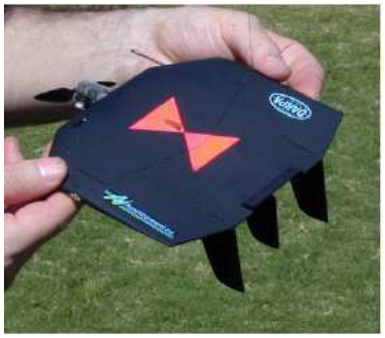

(e) Black Widow

Figure 2.3: DARPA initiative MAV designs.

The DARPA initiative aimed to develop both fundamental flight-enabling technologies and mission-capable system demonstrators. Research into advanced propulsion and power systems included a Micro-Electromechanical Systems (MEMS) based micro gas turbine, developed by MIT;[31] an IGR Inc. demonstration of a very lightweight solid-oxide fuel cell; and a very small gas turbine engine by M-DOT. A flapping-wing propulsion solution was also explored, with three separate programmes, run by the California Institute of Technology (Caltech), UCLA, and AeroVironment;[32] the University of Toronto Institute for Aerospace Studies and SRI International; and Vanderbilt University,[33] being funded.

Each programme employed a different approach to achieving a flapping wing action. The Caltech design used a standard direct current (DC) motor and gear box, the SRI device used electrostrictive polymer actuators, and the Vanderbilt device used piezoelectric actuators. Of the three, Caltech's palm-sized 'Microbat' ornithopter design (see Figure 2.3b) was the more widely reported. In 2003, a 9" version of Microbat, weighing only 14 g, reportedly flew under radio-control for a record 25 minutes at flight speeds of ≈ 7 m/s.[34]

Four different vehicle designs were also developed under the DARPA programme (see Figure 2.3). Two, the Lutronix Kolibri shrouded propeller design and Microcraft's Small Lift-Augmented Ducted Fan (SLADF), were rotorcraft with a VTOL capability. The SLADF could also fly horizontally by pitching over and developing lift from the aerofoil-shaped circular duct and an optional wing. The Lockheed Sanders MicroSTAR (later acquired by BAE Systems) and AeroVironment Black Widow were both fixed-wing designs. The Black Widow is particularly notable for being probably the most impressive vehicle to emerge from DARPA's funding of MAV research.

A (broadly) circular 'flying-wing' design of 6" span, the Black Widow was developed over a four year period, passing through twenty iterations from conception to the final vehicle.[35] Made primarily from Expandable Polystyrene (EPS) foam, with balsa wood control surfaces, the vehicle weighed approximately 60 g and was powered by lithium batteries. In flight tests it successfully reached speeds of up to 35 mph (15 m/s), a maximum straight line range of 17 km (though communications range was limited to 1.8 km), a maximum altitude of 769 ft, and an endurance time of 30 minutes. The Black Widow programme was an important step in MAV development, achieving several key results and demonstrating the importance of careful design and optimisation to maximise the efficiency of both the critical, individual subsystems (such as propulsion and power) and the entire vehicle itself. On a technological front, a basic avionics suite for an MAV-sized craft was shown to be entirely feasible and a custom-built colour video camera plus down-link transmitter of total mass 3 g was developed. Despite this success, little of this technology has come into use today.

Whilst the US Army and Marines had been receptive to the basic MAV concept, the initial phase of the DARPA programme concluded in 2000 with the general consensus that, for the present, a 6" vehicle was unable to provide the performance capabilities sought after by the military. The focus has now shifted to vehicles in the 8" to 16" size range, which are better suited to existing payload and propulsion technologies. Relaxing the size constraint brings several other benefits too. Increased size improves the aerodynamics of the lifting surfaces and allows MAVs to use more powerful telemetry transmitters with simpler, smaller low-gain antennas. Without this, many first generation vehicles required a large (6 ft) antenna at the ground station so as to receive the low power signals emitted by the MAV. This resulted in the total system size, as defined by vehicle plus Ground Control Unit (GCU), for a 15 cm craft being similar to that for a larger 100 cm vehicle, and negated some of the advantages of developing a MAV-scale craft.[2]

In 2001, DARPA's MAV programme progressed to the Advanced Concepts Technology Demonstration phase (ACTD), whose primary goal was to further develop and integrate

MAV technologies into militarily useful and affordable backpackable systems (suitable for dismounted soldier, Marine, and Special Forces missions), and then get them into the hands of the military quickly. Whilst the initial DARPA programme was more concerned with the fundamental technologies and components for small-scale flight, the ACTD phase expanded the scope to include advanced communications and information systems, advanced sensors, electronic packaging technologies, and lightweight, efficient, high-density power sources. Multi-purpose structures, that combine a structural role with other critical system functions such as power, damage repair, or ballistic protection, were also explored through the associated Synthetic Multi-Functional Materials programme.

(a) MAV FCS Class I UAV

(b) GoldenEye 80 FCS Class II UAV

Figure 2.4: The MAV and OAV programmes.

A particular focus of the ACTD has been the development of lift-augmented ducted fan mini-UAVs capable of autonomous flight, precision landing, and independent re-launch in restricted environments without using runways or helipads. The ACTD efforts aimed to produce a small (less than 10 kg weight), backpackable vehicle for inclusion in the US Army's FCS as the Class I UAV, providing an unmanned reconnaissance capability at the platoon level. The 13" diameter Honeywell vehicle, known simply as the Micro Air Vehicle (MAV), is the preferred platform to fill this role (see Figure 2.4a). The Class I UAV programme has now entered a military utility evaluation phase, which included a 2007 deployment to Iraq to help keep American troops safe by identifying improvised explosive devices from the sky, and is expected to be fielded to Infantry Brigade Combat Teams in 2011.

Small VTOL UAVs were also pursued by the related DARPA/US Army Organic Air Vehicle (OAV) programme, which aimed to develop a possible candidate to meet the, now cancelled, FCS Class II UAV requirements for a vehicle to carry out reconnaissance and surveillance in support of over-the-hill operations at the company level (see Figure 2.4b). With a weight of approximately 35 kg, OAV was intended primarily as a vehicle-mounted

system that would be carried and launched from either a High Mobility Multipurpose Wheeled Vehicle (HMMWV) or one of the FCS autonomous ground vehicles. Initial designs for the OAV were based on Allied Aerospace's iSTAR family of ducted fan designs, which were themselves derived from the Microcraft SLADF system produced under the original DARPA MAV initiative.

2.4 The Role of MAVs

Beyond the initial DARPA discussion, potential military applications for MAVs were the subject of several end-user conferences that resulted in the creation of three notional mission scenarios. The primary mission proposed was that of over-the-hill (OTH) Reconnaissance, Surveillance, and Target Acquisition (RSTA). The second was a jungle scenario requiring a loiter capability and high agility, and the final mission type was an 'urban canyon' scenario that called for both VTOL and hover capabilities. Each suggested mission type necessitated a different compromise between speed, range, manoeuvrability, and logistical complexity. Within each scenario the MAV would be used to provide support to small-unit ground forces at the platoon level or below, fulfilling any one of a number of situational awareness roles including artillery spotting, sensor dispersal, signal jamming, communication relay, denied area reconnaissance, battle damage assessment, or moving-target indication.[36]

More recently there has been a considerable lack of end-user involvement in dictating the mission and capability requirements of MAVs. This has been a particular problem in Europe, where workshops designed to address the unmet technological requirements for MAV usage have found it difficult to attract end-user interest.[37] Useful information on this issue is again provided by the DoD. Their opinion, as an end-user, on both mini-UAVs and MAVs was revealed in a short appendix to the 2002 UAV roadmap.[22] Although this outlined a belief that small-UAVs have the potential to solve a wide variety of difficult problems for which larger platforms may be unsuited, it also stated that, whilst "The fundamental relevance of small UAVs...*is* indeed a function of their size",[22] this should not be taken to mean that "their small size imparts some unique function or mission relevance to them that is missing in larger vehicles".[22] Nor should their low cost, and resulting expendability, be perceived as a unique capability.

Rather, the DoD sees the relevance of small-UAVs in the operational impact of simple logistics, whereby the small size of these vehicles offers a "flexibility in operational employment that larger, more logistically complex and intense UAVs do not".[22] This mobility means mini-UAVs and MAVs can be used to provide an immediate response to a

changing scenario, allowing for real-time OTH reconnaissance, information about the immediate battlefield, or behind-next-building intelligence for urban conflicts to be gathered and relayed to battlefield commanders with little or no time-delay. Larger vehicles cannot offer such responsiveness because of their more extensive logistical support requirements.

Furthermore, instead of deployment as independent systems, the use of smaller UAVs in conjunction with larger, more capable vehicles is the DoD's envisaged role for both mini-UAVs and MAVs. Parallel deployment of UAVs in this manner reinforces the strengths of both whilst mitigating some of the smaller systems weaknesses, the most pressing of which is the lack of all-weather operations. The small size and low mass of these vehicles, in particular the MAVs, results in a greater susceptibility to less-than-ideal weather. Consequently, climatic conditions such as high wind, rain, and snow can impact on endurance and interfere with imaging and communications systems. Other critical shortfalls arise from the short range and low endurance, which will dictate how and where small-UAVs will be deployed.

Although their size may not be perceived as the primary relevance of small-UAVs, it can nevertheless be quite advantageous to their otherwise restricted payload capability and limited performance. With a reduced likelihood of detection, small platforms are able to approach far closer to an area of interest than a full-sized vehicle and so provide an opportunity to place payloads close to targets, and then benefit from this proximity. Simple, yet illustrative, examples provided by Coffey & Montgomery[1] show how proximity can greatly enhance the capability of mini-payloads in areas as diverse as radar jamming, aerial photography, and signal collection, so that small-UAVs can perform similar tasks, with similar results, as larger aircraft, but with less sophisticated technology.

An alternative view of the role which small-UAVs may play in military operations was proposed by Weed.[38] In his monograph on UAV procurement, he outlined a strategy in which UAV operations at the army brigade level are centered around large numbers of small-UAVs of 6 ft span or less. With an ability to deploy and operate in a greater variety of environments, Weed argued that small-UAVs provide advantages to employability and functionality (in terms of coverage, mission flexibility, and mission customisation) at less overall cost than the present approach, in which small numbers of larger, more capable craft are deployed. Thus, while the more complex unit's capabilities are far superior, the synergistic effect of fielding numerous less effective small-UAVs may be ultimately more efficacious.

In addition, as UAVs have suffered a historically high attrition rate, Weed[38] noted that by adopting an approach of having a large quantity of smaller, simpler assets, the loss of

a single vehicle has less impact on operations than if there are only a small number of highly sophisticated aircraft. The simplicity and compactness of small-UAVs would also act to reduce susceptibility to the two main means of loss (mechanical failure and enemy action) as small-UAVs are less likely to be intercepted and tend to have fewer system components that might possibly fail.

Whether or not such a broad change in strategy actually does come to pass, it seems probable that mini-UAVs will, in some form, take over from their larger counterparts in many of the roles for which unmanned craft are well suited, particularly the more prosaic research and surveillance tasks where conventionally sized UAVs are either too expensive, too inflexible, or too large.[39] However, the more extensive role envisaged by Weed is not inconceivable. In the past, technological limitations and the then-prevalent view that aircraft, whether manned or unmanned, should be relatively large meant that mini-UAVs were generally used as specialised tools for reconnaissance or to accomplish other routine functions. The continuing migration of capability from larger to smaller platforms (sensor capabilities first demonstrated on the 48.7 ft wing span RQ-1A Predator in 1994 are now available on the 14 ft wing span RQ-7 Shadow[17]), coupled with the impact of the DARPA MAV initiative, has enabled a paradigm shift in military thinking on the relevance of small-UAVs.

Though mini-UAVs are becoming more central to military strategy, it may be some time before MAV-sized craft are equally successful. For UAVs with wing spans less than 2 ft, currently available technology appears to offer very few missions.[1] Without considerable improvements in performance or progress in multi-vehicle coordination, MAVs will likely be precluded from the majority of military operations, even those for which they should be well suited. Instead, MAVs may play a considerable role in civilian operations, where the weaknesses of MAV-sized craft are not so significant.

Emerging non-military applications for the MAV class are similar to those suggested for larger UAVs and include hazardous substance detection and identification (whether radiological, biological, or chemical), disaster management, traffic monitoring, aerial photography for real estate purposes, police surveillance, local security for national buildings, forestry/wildlife surveys, meteorological sampling, and power line inspections.[39–41] As a result of their more easily transportable nature, MAVs are particularly suited to use in remote locations that are currently too costly or complex to monitor with large craft, or urban areas where larger aircraft may find it difficult to operate due to the lack of space.

Michelson[42] has attributed the present lack of success in the use of MAVs not only to the technical difficulty of the problem but also to some poor employment assumptions.

Where the DoD has said that the small size of MAVs does not impart some special ability, Michelson went further by saying that he believed their size, as defined by the DARPA initiative, to actually be a hinderance to the type of outdoor asset that was originally envisaged. He noted that, as not all technologies are scalable, the imposed size constraints will restrict MAVs to small radio antennas that operate best at short wavelengths and high frequencies (≈ 2 GHz). This type of radio wave does not easily pass through obstacles and so limits usage to line-of-sight operation.

Consequently, even the simplest OTH reconnaissance mission scenario would likely require the MAV to attain an altitude that would be sufficient to mask the presence of a larger air vehicle of perhaps ten times the size. Such an aircraft would be able to provide better performance, have a more capable payload, and be less vulnerable to environmental conditions than the typical MAV. Therefore, Michelson concluded that the difficulty in flying at the 15 cm scale is unwarranted because existing mini-UAV assets, such as the FQM-151 Pointer or NRL Dragon Eye, are already capable of addressing those tasks and missions generally associated with MAVs.

In spite of these issues, Michelson[42] also stated that a strong case for MAV-sized craft does exist, but that current efforts and expectations for an outdoor asset have been misdirected. Rather, the mission space for which such small size is an advantage is "indoors and in confined spaces, where the environment is controlled or at least protected".[42] In these conditions, MAVs offer the potential to rapidly and covertly penetrate buildings, tunnels/caves, bunkers, and other enclosures by non-obvious means and then navigate their interiors more effectively than other assets, such as ground robots. In Michelson's view, this would present a new paradigm in reconnaissance whereby close-in interaction, rather than a stand-off capability, is encouraged. Key to such activities will be small size, slow flight, and the ability to navigate without GPS, which typically will not work indoors.[42]

2.5 Design Philosophy

MAV design differs from other manned and unmanned aircraft in several important ways. Firstly, given their small size and typical flight velocities, MAVs are considered 'low Reynolds number' craft. This is a slightly ambiguous term that carries different meanings to different designers, but where MAVs are concerned the term is generally taken to describe operation at $Re_\ell \leq 2 \times 10^5$. This is some two orders of magnitude smaller than typical military or civilian aircraft and one order of magnitude smaller than most larger UAVs. Operation at such low Reynolds number presents numerous challenges in several key areas, including the performance of lifting and control surfaces, flight dynamics and

control, thrust generation, and powerplants.

Secondly, the small dimensions of MAVs affects all technological aspects of their design, limiting the choice of structural materials and dictating the use of the smallest, lightest (and cheapest) sensors, power systems, and payloads. Such restriction does not exist at larger scales and can often further compound the problems introduced by low Reynolds number flight. Finally, a further difference exists in the overarching design philosophy.

At MAV scales, the typical method of constructing a vehicle and then incorporating the required modules and subsystems into the resulting available space is problematic due to the imposed size constraints.[36] Instead, an integrated design solution, where each part of the vehicle plays multiple roles, has been presented as the best option for this class of vehicle. In this view, the wings could double as an antenna for communication and data transmission whilst the power source might be integrated into the vehicle as part of the structure of the fuselage itself.[42] This type of design would require a degree of integration that has not been demonstrated anywhere else. At present, MAV designs lack the suggested level of integration, though there are a number of emerging examples, such as the AeroVironment Wasp and the Georgia Institute of Technology's Entomopter, that indicate how future MAVs may be developed.

Designing an MAV as an 'integrated system of systems' also requires that particular attention be given to some design aspects that would otherwise be secondary logistical concerns for conventional UAVs. The packaging, assembly, and reconditioning of an MAV are critical for efficient use by field troops, who will often need to deploy the system in a hurry, and the design thus needs to cater for this. Furthermore, for unmanned aircraft, system size is often more important than vehicle size because of transportation and cost factors. This is particularly so for MAVs, and achieving the smallest system size requires that the development of the vehicle and its ground support equipment be considered simultaneously in the design process.

An alternate approach to the problem of 'airframe stuffing' is that adopted for the Air Force Research Laboratory's (AFRL) developmental Sensorcraft full-scale UAV concept. Whilst previous UAVs have followed the conventional route of vehicle design, the Sensorcraft concept reversed the traditional process by selecting the optimum mix of sensors prior to the start of the design process, which is then moulded to fit around the chosen systems, with sensor apertures embedded in the fuselage as necessary. This does, however, limit the vehicle to those roles that can be performed with the original choice of sensors.

Recent combat experience with the 2.4 ft wing span Dragon Eye mini-UAV during the second Iraqi conflict suggests that limiting sensor choice in this way is not well-suited

for military MAV roles. Used by the US Marine Corps throughout Operation Iraqi Freedom, the majority of Dragon Eye flights were unplanned, with activities being dictated by changing opportunities and specific tactical requirements.[43] This situation saw Dragon Eye operate in a number of different roles. Given that such usage is likely to be commonplace in military MAV applications, a design that allows a rapid interchange of sensor modules would be better able to provide the necessary flexibility to allow the MAV to carry out different missions as the need arises. However, for civilian or scientific applications, where a dedicated role for the MAV is more likely, a Sensorcraft-type approach may have merit.

2.6 Current and Future Developments

Whilst the DARPA initiative went some way towards demonstrating that MAV-sized vehicles were capable of executing militarily relevant missions, it also revealed the difficulties of flight at such small scales and highlighted those areas requiring further research without which MAVs will struggle to garner the level of acceptance that larger unmanned craft now enjoy. Regardless of configuration, the future development of MAVs is hindered by limited understanding of the aerodynamics of flight at low Reynolds numbers. Technical barriers in small-scale power generation and storage, autonomous control and navigation, communication, and propulsion must also be overcome. In addition, advances in structural materials technology may be necessary, particularly where miniaturisation and the achievement of integration is concerned.

Such technical barriers are linked to the main operational challenges to be met, which are centered around the need for improvements in agility, range, payload capacity, and data transfer rates, whilst simultaneously decreasing size and structural weight. More fundamental questions also remain regarding the operational role of MAVs, particularly in the area of mission capability. These may prove the largest obstacle to the proliferation of this class of UAV. Current MAV activities and possible future approaches towards addressing these challenges are discussed below.

2.6.1 Operational Role and Design

Despite the post-DARPA shift in focus to mini-UAVs, the desire for bird-sized or smaller aircraft has not diminished. In 2001, Mueller & DeLaurier[44] suggested that the long term goal for MAV design is for a vehicle with total mass of 30 g, a maximum dimension of between 6 cm and 8 cm and an endurance of 20 to 30 minutes at cruise speeds between 30

and 65 kph. The more recent review by Hu & Zhou[45] concluded that future MAVs would be closer to 1 cm in size. However, the timescale for the development of such vehicles now appears to have been pushed back by some margin.

The DoD's view on the relevance of small-UAVs would seem to suggest that simply making the platform as small as possible should not be the goal of future MAV development. On the other hand, there may be some applications where a very small size may provide the best solution. Thus, two classes of MAVs may eventually emerge: one that is of the order of 2 to 15 cm in size, and a second class of 1 cm or smaller vehicles. The larger vehicles would be similar to the existing notion of an MAV, but smaller and more capable, and would carry out many of those roles expressed in this and other documents. The second class would operate in extreme numbers, so that even if most of the units fail some would likely survive long enough to carry out the task, and be effectively disposable, but would only be suited to a limited number of roles.

This type of disposable 'flying sensor' has been investigated at Stanford University with the Mesicopter[46] (a centimeter-sized quad-rotor electric helicopter) and at UC Berkeley with 'Smart Dust'[47] (see Figure 2.5). Typical applications suggested for these designs are the investigation of meteorological and atmospheric conditions in dangerous environments, such as within hurricanes and tornados or on the surface of Mars. Cooperative action of MAVs to enhance capability is also desirable for more typical, larger MAVs and is a current topic of research.[48,49] However, the near-term need is said to be for MAVs that can perform the baseline mission with a single vehicle,[50] which will be more readily accomplished with an 8 cm to 15 cm sized platform.

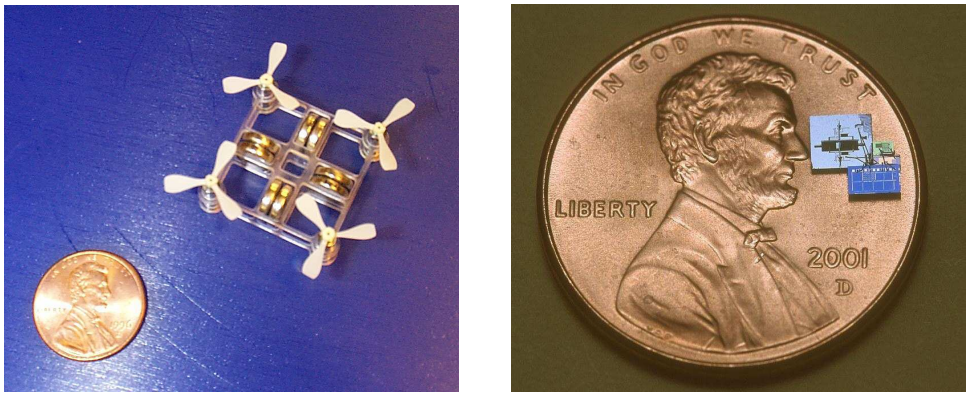

(a) Mesicopter[46] (b) Smart Dust[47]

Figure 2.5: Recent developments in ultra small 'flying sensors'.

To reach the level of future design sophistication envisaged by many in the MAV community will require a considerable increase in research funding and a concerted effort into

developing MAV-scale technology. Though MAVs may ultimately benefit from the interest currently shown in mini-UAVs, the change in focus following the end of the DARPA initiative has resulted in a prevalent lack of MAV funding from military sources. That the market for 6" and smaller MAVs is not readily identifiable, and may not be possible to cultivate, is perhaps the greatest challenge to be overcome.[37] The lack of end-user interest and feedback also makes it difficult to conclusively state the purpose and missions of MAVs, further hampering design development. This has led some to suggest the commercial toy and electronics market as an alternative avenue for further funding,[51] but such a move may harm the credibility of MAVs.

However, the focus by DARPA on MAVs, and the relative simplicity and low cost of these smaller vehicles, has resulted in a large number of academic, civil, and military research institutes now having some kind of MAV or mini-UAV programme.[16] The results of wind tunnel tests and CFD simulations performed for such internal programmes should help address the lack of reliable aerodynamic and performance data at low Reynolds number and may be useful for methods aimed at advancing, optimising, and automating MAV design.[52,53] The numerous annual inter-university MAV design competitions[2,54–58] that have been running since the earliest days of the concept also provide a useful proving ground for the development and validation of innovative ideas. All such activity, and the fact that large numbers of MAVs can be developed in a relatively short time, may lead to a rapid evolution in design and capabilities.

2.6.2 Fixed-Wing MAVs

Just as the field of fixed-wing aircraft is the most mature for full-scale flight so the majority of existing MAV designs are also of this nature. Relatively simple in concept and easily implemented, the concentration on fixed-wing MAVs has resulted in a larger number of varied designs (as seen in Figure 2.6) and a higher level of development, in terms of performance, as compared to other types. Current designs have demonstrated good forward flight capabilities, with maximum speeds of the order of 20 m/s and flight durations of about 30 minutes, as well as impressive levels of autonomy.

For fixed-wing MAVs a large wing area is desirable to keep wing loading low and so reduce power requirements and increase manoeuvrability. Constraining the maximum dimension to 6" prevents designers from increasing the span, leaving an increase of the chord as the only viable option. It follows that in order to maximise the lifting area for a given dimension, the span and chord of the wings should be the same. As a result, many fixed-wing MAVs are of the low-aspect-ratio (LAR), flying-wing type. As well as

providing a large wing area, this design also gives a large volume for housing payloads and systems and provides a stiff yet simple structure that is typically easy to manufacture. Equally importantly, LAR wings (specifically those with $AR < 2$) tend to perform better than slender wings at low Re.[44]

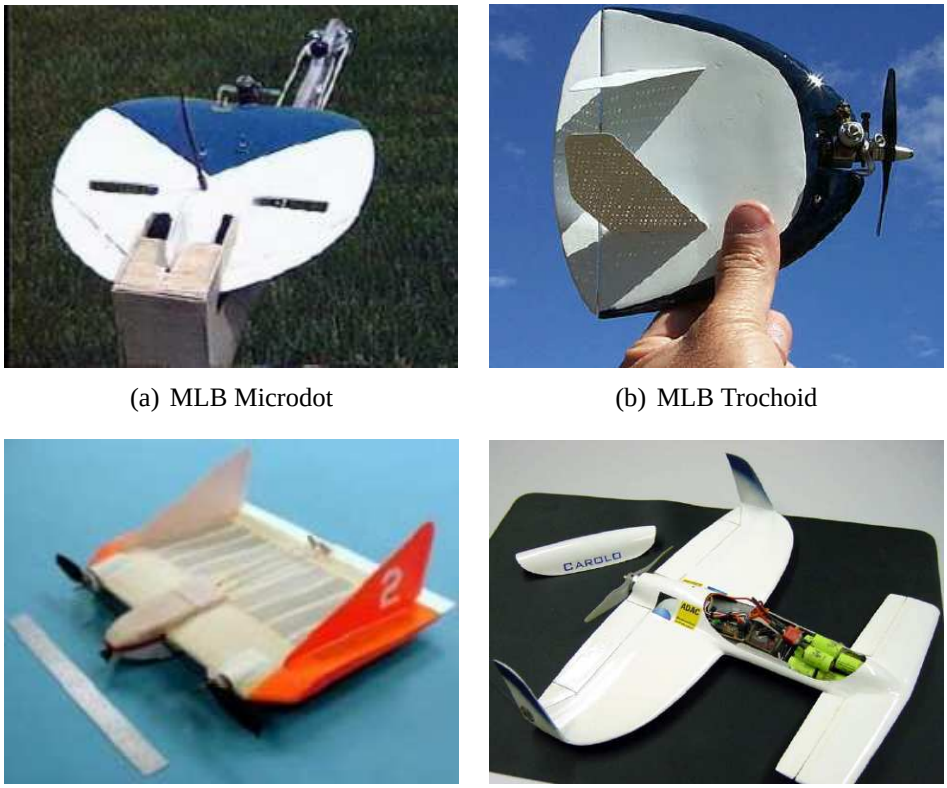

(a) MLB Microdot (b) MLB Trochoid

(c) NRL MITE 2 (d) ILR Carolo

Figure 2.6: Fixed-wing MAVs.

The majority of challenges facing fixed-wing MAVs stem from the poor aerodynamic performance of their lifting surfaces at low Reynolds numbers. Under the typical conditions of MAV flight viscous forces play a much more significant role and it becomes difficult to generate lift while maintaining low drag. Aerofoils designed for much higher Reynolds regimes tend to perform poorly in these conditions. Applied to low Reynolds number tasks they suffer from lower lift coefficients, higher drag coefficients, and stall at lower angles of attack. As a result, the aerodynamic efficiency of fixed-wings, as defined by the lift-to-drag ratio, deteriorates rapidly for Reynolds numbers less than $Re_c = 1 \times 10^5$. Such effects occur because, at these low Reynolds numbers, the characteristics of the boundary layer differ to those experienced by larger craft.

The greater tendency towards laminar boundary layers for $Re_c < 1 \times 10^6$ leads to laminar separation bubbles that have a great deal of influence on the aerofoil's behaviour, partic-

ularly where drag is concerned.[59] Reducing the depth of the separation bubble causes the associated pressure drag to decrease and so most methods of increasing performance concentrate on minimising the effects of these separation bubbles by 'thinning' them out.[59] This typically involves reducing the convex nature of the aerofoil's upper surface in the region where transition to turbulent flow occurs. As this can be most simply and effectively achieved by decreasing the thickness-chord ratio of the aerofoil, it has led to a preponderance of thin aerofoil ($t/c \leq 6\%$) use for MAVs and similar applications, but there is still uncertainty on the best approach.

Although there is a need to develop efficient aerofoils suitable for low-aspect-ratio wings at low Reynolds numbers,[44] optimisation of fixed-wing configurations also needs to be explored further to determine what the best aerodynamic characteristics for aerofoils at MAV-scale flight actually are. MDO investigation suggests that, where fixed-wing craft are concerned, low drag and high lift-to-drag ratios are relatively unimportant for meeting mission constraints whilst large power-to-weight ratios and a high lift generating capacity are far more important. The study by Morris & Holden[2] has also indicated that the primary factor restricting further size reduction in fixed-wing MAVs was the value of $C_{L\text{max}}$. Analysis revealed that an increase in the maximum lift coefficient from $C_{L\text{max}} = 1.2$ to $C_{L\text{max}} = 2$ would allow a 23% reduction in maximum linear dimension. Improvements in propeller efficiency, specific fuel consumption, and specific power each enabled reductions of the order of 10%, whilst elimination of parasite drag was shown to only offer a 7% reduction at most.

Improvements in lifting capability for fixed-wing craft may arrive through increased understanding of LAR wing aerodynamics at low Reynolds numbers. Though such wings are typically seen as being aerodynamically less efficient, the flow around LAR wings is characterised by complex three-dimensional phenomena including wing-tip vortical flows, transition, separation and reattachment, and the mutual interactions thereof. Such phenomena have been shown to significantly influence flight performance for low-aspect-ratio, fixed-wing MAVs by augmenting the lifting capability and increasing the stall angle of the wing.[2] The growth in interest in MAV platforms has lead to an increase in both experimental[60,61] and numerical[62–64] studies of low Reynolds number and low AR aerodynamics; however, the behaviour of LAR wings at low Re_c remains poorly understood.

Improving the performance of the lifting and control surfaces at low Reynolds numbers would also enable enhancements in the stability and control of fixed-wing MAVs. This is important as many of the capabilities required for some of the suggested mission scenarios are not possible with current fixed-wing designs as they lack the agility and versatility necessary for manoeuvres such as rapid flight beneath a forest canopy or within an urban

environment. Poor stability and control of fixed-wing craft has also been found to affect mission performance, particularly the quality of video imagery captured.[2]

The replacement of hinged control surfaces with active wing control using electrically actuated piezoelectric structures that differentially alter lift,[37] or adaptive wings having a flexible morphing structure have been suggested as possible ways to improve agility. Research at the University of Florida has focused on a bat-like membrane-wing concept MAV, which is thought to be able to provide several advantages over rigid fixed-wings.[65,66] The flexible polymer membrane allows the wing to adapt to changes in the airflow and permits operation at much higher angles of attack without stalling. This reportedly provides a much smoother flight in gusty conditions, greatly improving the precision with which the MAV can be flown. However, wind tunnel testing revealed that the increase in stall angle came at a cost of a lower maximum lift-to-drag ratio ($C_L/C_D \approx 3$).

For conventional control methods, questions remain about the size and location of control surfaces. Some wing planform shapes are known to suffer poor aileron effectiveness as the control surfaces are located close to a region of strong vortical flow. Experiments in circular wing design by the MLB company[2] suggest that control effectiveness can be restored by adding a nearby slot between the upper and lower wings surfaces, but this comes at the cost of reducing the available internal payload volume. A non-standard propeller location has also been shown to be beneficial, as the propeller wash helps keep the flow attached to the control surfaces even for quite high angles of attack, though this too may reduce wing volume.[67] The beneficial effect of propeller wash in both improving control and augmenting lift has also been noted by other researchers.[2]

2.6.3 Rotary-Wing MAVs

Research and development in small rotary-wing UAVs with a VTOL capability has been a significant outgrowth of the original DARPA MAV initiative. Rotary-wing designs can offer significant advantages over fixed-wing MAVs, particularly where the vehicle is required to hover or manoeuver in a restricted environment. However, this agility comes at the cost of increased power demands: a vehicle in hover consumes approximately twice as much power as a similarly loaded fixed-wing vehicle engaged in forward flight. Rotorcraft also suffer from poor performance in horizontal flight, though this may be mitigated by the use of external sources (such as manned/unmanned vehicles or munitions) to deliver rotary-wing MAVs close to the designated target.

The majority of existing rotary-wing MAVs have been of a ‘flying ducted fan’ nature.

These have proven a popular choice as they currently seem the most suitable configuration for flight and imaging in complex environments such as under forest canopies or in buildings (as indicated by the attention given to ducted fan designs through the MAV ACTD and OAV programmes). In addition, a ducted fan/shrouded propeller solution provides a number of useful advantages over a free propeller.

Ducted fans produce approximately 30% more thrust than conventional open propellers, which translates into larger payloads, longer range, and higher cruise speeds. The use of a duct also reduces the rotor noise signature (improving stealthiness), decreases sensitivity to changes in axial velocity, and makes it safer for the operator to handle the craft at launch. Furthermore, since micro-rotorcraft missions will require these vehicles to fly at low-altitudes, in close proximity to people, buildings, and other obstacles, the duct also acts as an effective means of physically protecting the rotors and other critical hardware from casual impact damage.[68]

(a) University of Maryland MICOR[57]

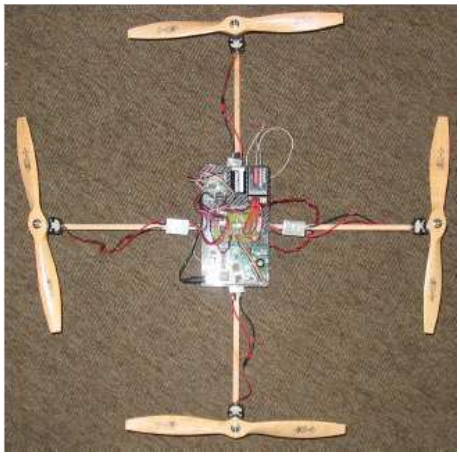

(b) Pennsylvania State University Quadrotor[69]

Figure 2.7: Non-ducted-fan rotorcraft MAV designs.

Non-ducted-fan design types also exist but are less prominent. The conventional main rotor/tail rotor configuration has not generally been pursued as compactness is adversely affected by the tail boom and the large size of the rotor required.[57] Configurations with two or more rotors, such as the University of Maryland's Micro Coaxial Rotorcraft,[57] the European consortium led project MARVEL,[70] the EADS Quattrocopter MAV,[71] and the Pennsylvania State University Quadrotor design[69] (see Figure 2.7) have received more attention. The last three are all examples of quadrotor designs, with four lifting rotors, that offer several advantages to agility and control.

A feasibility study at UCLA[72] considered the merits of both active (helicopter) and passive

(autogyro) designs for rotary-wing MAVs and concluded that the autogyro was the more promising of the two as it was able to carry a greater payload than the helicopter and at a lower speed, thus providing greater manoeuvrability. With no need for an anti-torque device, the overall weight of the passive design was also lower and the gyroscopic effect of the autogyro's rotor was found to be beneficial to stability. Despite this, rotary-wing MAVs have invariably been active designs.

Regardless of rotor configuration, the technical challenges for small rotary-wing UAV systems are numerous and the status of research into the low Reynolds number aerodynamics of rotary-wings is as limited, if not more so, than that for fixed-wings. The popularity of ducted fan MAV designs has lead to an increased focus on general rotary-wing aerodynamics for MAV applications,[68, 73] though further research is still needed to enable the exploitation of unsteady aerodynamics for MAV-sized rotorcraft (possibly through active morphing of blades by changing twist, camber, and planform[37]) and to increase their performance in forward flight.

Developments in noise prediction and suppression as well as a simplification of flight controls are also required for rotary-wing MAVs. Incorporating a reliable semi-autonomous control system in these small vehicles, so that the operator does not have to constantly monitor their performance or location, will be especially challenging as they are only able to carry the smallest microprocessor systems and power supplies along with very lightweight and inexpensive sensor systems.[69]

2.6.4 Flapping-Wing MAVs

Whilst fixed-wing MAVs suffer from a reduction in aerodynamic efficiency at the low Reynolds numbers at which they operate, the converse is true for flexible flapping wings. This method of propulsion is clearly the solution favoured by small natural fliers, such as birds and insects, which fly at similar speeds and are of a similar size to the conventional notion of a MAV. Flapping-wing flight at this scale has several promising advantages, notably the ability to fly at low speeds (3 to 5 m/s), excellent hovering capabilities, a low acoustic signature, and very good mobility in all directions. Extremes of agility, such as upside-down flight and VTOL, are also possible, making flapping wings particularly well suited to urban or indoor mission scenarios.

Despite seeming to offer the most promise of the three principle configurations, flapping wing MAV designs are by far in the minority and are no longer being actively pursued by the DoD.[22] This is largely because the lack of understanding regarding basic aerody-

namics and flight dynamics at low Re is even more endemic for flapping-wing flight than either fixed- or rotary-wings. The increased mechanical complexity associated with this configuration is also a factor.

Existing flapping-wing designs may be separated into two main types: those which attempt to mimic nature (biomimetic designs) and those which are inspired by nature, but do not try to copy it (biomorphic or bio-inspired designs). Further delineation of designs into ornithopters, in which the wing shape and flapping motion are based on or copied from the wing kinematics of birds, and entomopters, which are modelled on the kinematics of insect flight, may also be made. Differences in bird and insect flight mean that the choice of wing morphology and flapping kinematics affects the capabilities of the vehicle being designed. Avian-based designs are generally better suited to small angles of attack and long endurance flight whilst the much stronger vortical system created by insect-like wings allows for greater feats of aerial agility, such as hovering and vertical take-off.

The majority of previous efforts at flapping-wing flight have been biomimetic in approach. Such mimicry of nature has been criticised by several researchers as being overly simplistic.[42,74] Indeed, adherence to the solutions produced by nature would in some cases actually result in an inferior design. As Michelson[42] noted, the optimal means for getting from point A to point B along a prepared road surface in the minimum amount of time and with the least energy expenditure is the wheel, a structure which does not occur anywhere in nature as a method of locomotion. In contrast, biological inspiration, wherein a biological model is used as a starting point, but the design is not constrained by the limitations of the model, is thought to be the superior design philosophy, and may produce an even better solution than the original biological source.

Furthermore, a completely biomimetic solution is difficult to design with current technology and even more difficult to implement. As a result, existing biomimetic designs are heavily simplified, being unable to wholly replicate neither the actual morphology of bird and insect wings nor the flapping mechanisms they use to modulate the flight envelope in terms of speed, direction, and orientation.[42] Wing shape morphing and active flow control, as used by birds to optimise the flow around the wing to certain conditions, would be particularly difficult to obtain with current technology. A successful engineering implementation would likely require significant progress in the area of MEMS technology and the use of advanced intelligent materials that are not presently available.[75]

Given such difficulties, and the additional degree of complexity of avian wingbeat kinematics, flexible insect-like wings may be simpler to realise, easier to move without active control systems, and possibly less power consuming than articulated bird-like wings. The

insect-like manoeuvrability and hover capabilities that entomopters can provide may also be more desirable for MAV applications. In either case, irrespective of design philosophy, or choice of inspiration, more research will be needed to determine which aspects of bird and insect flight are truly necessary for successful, controlled, small-scale flapping-wing flight and which phenomena (stroke geometry etc.) are caused or required by biological constraints such as physiological (muscle) or neurological (eyesight) limitations.

Examples of biomimetic flapping-wing MAV designs include the aforementioned Caltech/UCLA/AeroVironment Microbat (see §2.3), which adopted a morphology and flapping mechanism similar to a bird or bat, and Berkeley's Micromechanical Flying Insect (MFI) project to develop a 25 mm (wingtip-to-wingtip, see Figure2.8a) autonomous device that uses biomimetic principles to try and capture some of the high flight performance achieved by true insects.[76,77]

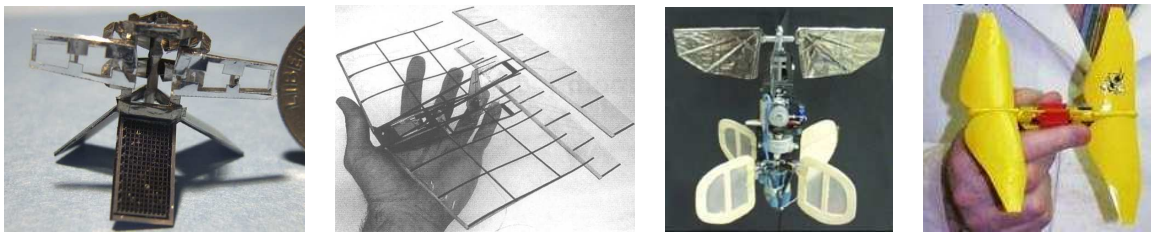

(a) MFI (b) NPS MAV (c) Mentor (d) Entomopter

Figure 2.8: Flapping-wing MAV and mini-UAV designs.

Biomorphic designs include the Naval Postgraduate School's (NPS) highly unconventional vehicle that combines a low AR fixed-wing mainplane with two trailing flapping wings of higher AR, positioned one above the other (see Figure 2.8b), and which was inspired by the way birds exploit flight in ground-effect to improve performance, and the Mentor mini-UAV, developed by the University of Toronto and SRI International as part of the DARPA initiative's study into flapping-wing propulsion. Although it used a hummingbird for inspiration, Mentor's design is distinctly un-avianlike: it has four wings and uses tail-like fins for stability and control (see Figure 2.8c). During a 2003 test flight, Mentor reportedly became the first ornithopter to successfully hover under its own power.[34]

Perhaps the most advanced current flapping-wing MAV is that designed by the Georgia Institute of Technology's Aerospace Laboratory as part of their Entomopter programme (see Figure 2.8d) for the development of a machine that both flies and crawls like an insect.[42,78,79] The vehicle is powered by a purpose-built reciprocating chemical muscle (RCM) that drives the twin-wing flapping mechanism, inspired by the wing kinematics of the hawkmoth, and enables Entomopter to fly. Ambulatory and swimming locomotion

behaviours are also powered through the RCM, which operates in a similar fashion to the piston and cylinder of a steam engine[78] and has a specific energy that is said to be much greater than that of current batteries.[22]

The Entomopter also displays impressive levels of design integration. As well as driving the propulsion mechanism, the RCM technology has the advantage of being able to provide power to the onboard systems and any MEMS devices too. Excess exhaust gas from the RCM is also used for the operation of gas bearings, as an ultrasonic obstacle avoidance ranging system, and for full flight control of the vehicle through independent circulation-controlled lift modification.

2.6.5 Power and Propulsion

The storage of propulsive and systems energy represents one of the key obstacles to improving MAV performance. Lightweight, efficient power supplies with high energy densities are needed to maximise endurance and improve the sensor capabilities of MAV systems or they will remain power-limited for the foreseeable future. Advances in energy sources are also required for the provision of a hover capability for VTOL rotary-wing MAVs and flapping-wing MAVs without sacrificing endurance.

The choice of power source is also closely tied to the propulsion system employed. However, selection of a propulsion system for an MAV can be problematic since the commonly used technologies of conventional aircraft do not scale well when miniaturised; as UAVs decrease in size below 10 kg the choice of efficient propulsion systems decreases dramatically. Regardless of such difficulties, a suitable solution must be found as engine reliability is a very important factor in securing user acceptance, particularly for military applications. Furthermore, the performance of the propulsion system is critical to the overall success of the vehicle as a whole and so needs to be optimised.

The simplest, cheapest, most available propulsion solution for small-UAVs remains the propeller. Typical propellers for current designs consist of small plastic propellers from model aircraft, which are often crudely modified to fit size constraints. Such a haphazard approach is detrimental to performance, which already tends to be quite low at the Reynolds numbers in question, typically between 50% and 75%. Experiments suggest that efficiency can be greatly improved (to $\approx$89%) by the use of a serrated turbulator strip positioned at the 20% chord point,[80] or by custom-designing of the propeller.[35] An increase in reliable small-diameter, low Reynolds number propeller performance data will be vital to improving the efficiency of small-UAV propulsion systems.[81]

Early MAV designs used small internal combustion engines (ICE), as typically used on model aircraft, to drive their propellers. Since fossil fuels have such a high energy density (see Figure 2.9a), these engines are still useful for most small-UAV missions, but their noise signature, weight, poor efficiency, and unreliability are less than ideal. The logistics of carrying liquid fuel around are an added undesirable feature. That being said, efficient ICEs under one horsepower have not been fully researched and there is potential for much progress in this area.[37] Recent years have also seen the emergence of very small gas turbine generators and jet engines (such as the MIT micro gas turbine,[31] the QinetiQ Microjet,[82] and the DARPA-funded M-Dot Midge) that are suitable for some mini-UAVs and which may, with further development, also become available to MAVs.

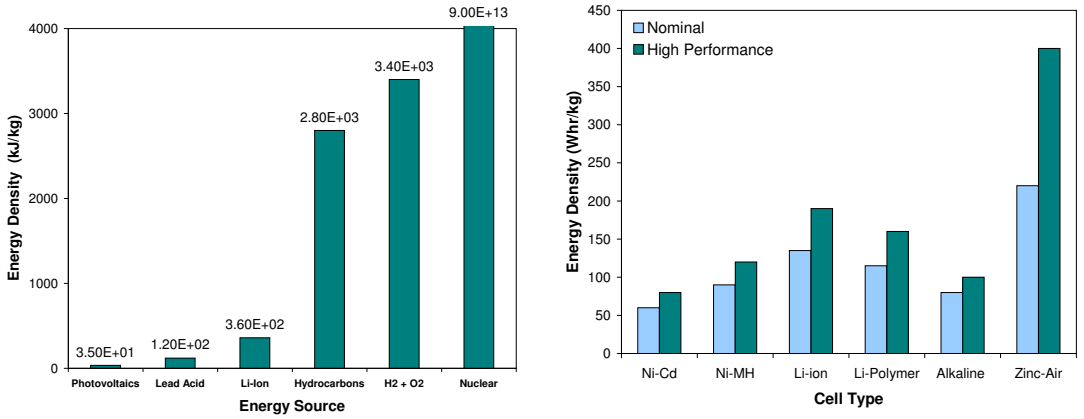

(a) Comparison of different power sources (b) Comparison of common battery types

Figure 2.9: The energy density of common power sources.

The majority of current MAVs drive propellers using electric motors that are powered by batteries. Reliable, cheap, safe, and accepted by consumers, they are the most suitable choice for most small-UAV platforms and will remain so for the time being. Electrically powered motors also benefit from a low acoustic signature, ease of start, and relative performance insensitivity to altitude and temperature. However, their low energy densities, combined with the lack of available space and a constraint on weight, reduce most craft to flight times of a few tens of minutes at best.

Short-term improvements in the power supply problem are likely to come from continuing progress in traditional battery technology. Developments in lithium batteries, which offer the best performance of all commercial battery types (see Figure 2.9b), have resulted in significant logistical improvements for MAVs. The introduction of new high-density zinc-air cells, specially developed for the UAV/MAV market and with a flexible planar nature that allows them to be configured into almost any shape, should have a similarly beneficial impact.[83,84] The advent of small, high performance, brushless DC motors has

also enhanced the performance of electric propulsion systems and optimisation through analytical study may provide additional advances.[85]

Integration of the power system with another subsystem would also be beneficial to the limited performance of existing technologies, as illustrated by the AeroVironment Wasp mini-UAV (see Figure 2.10a). A product of DARPA's Synthetic Multi-functional Materials programme, the Wasp is a 32 cm (13"), 170 g flying-wing design whose wing structure is made from a synthetic battery material, so that as well as carrying the aerodynamic loads, the wing also doubles as a plastic lithium-ion battery that can provide an average 9 W of power at 143 Whr/kg. In the summer of 2002, the Wasp set what is believed to be an MAV endurance world record by flying for 1 hour and 47 minutes.[86] Without such integration, endurance would have been significantly reduced, or vehicle weight greatly increased.

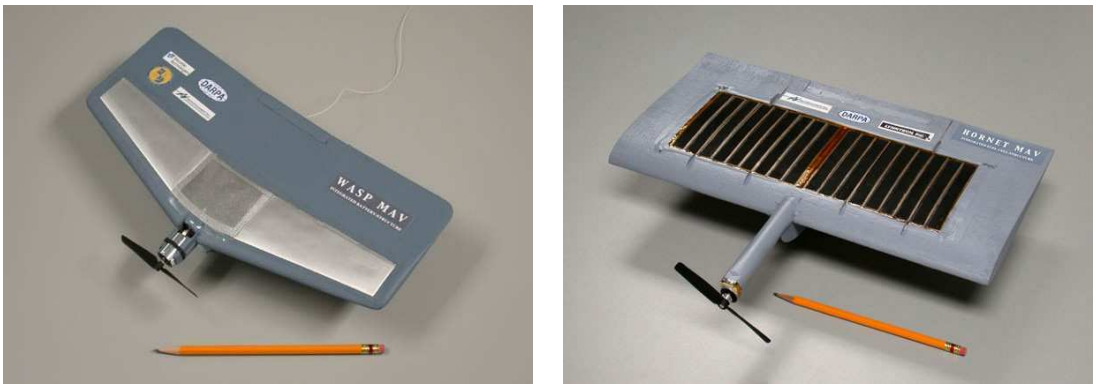

(a) WASP (b) Hornet

Figure 2.10: Second generation AeroVironment mini-UAVs.

A long-term solution to the power requirements of small-UAVs may come from the introduction of compact fuel cells that promise a much higher power density than currently available electro-chemical cells. In addition, fuel cells free the end-user from the lengthy recharging times necessary with batteries, suffer no leakage of charge, and exhibit no 'memory effect' reduction of storage capacity with age. However, in some cases, they produce a far larger heat signature than conventional power sources. The use of fuel cells in mini-UAVs was explored as part of DARPA's Synthetic Multi-Functional Materials programme.

In March 2003, the AeroVironment Hornet mini-UAV (see Figure 2.10b) completed the first successful flight of a UAV powered entirely by fuel cells. The 15" flying-wing design was flown three times for a total endurance of fifteen minutes during which the onboard hydrogen-oxygen fuel cell, which was integrated into the wing so that it also functioned as

an aid to structural rigidity, provided power for the motor, pumps, servos, radio channel link, and other avionics systems.[87] A specific energy of up to 400 Whr/kg is thought to be possible using this system and the fuel cell is estimated to provide an endurance three-times greater than that with batteries of comparable weight.

2.6.6 Structures

Current MAVs are based on simple platforms, built mainly from 'hobby shop materials' (such as balsa wood, polystyrene foams, glues, and sticky tape) using model airplane technology. Most designs are mini- rather than micro-sized and have a distinct lack of integration. The materials and structures aspects of future designs will largely depend on the specific MAV design and performance requirements set by end-users (mission constraints such as observability will have an impact on the structural materials used); however, developments in miniaturisation, with respect to material size and weight and the structural design principles applied, as well as improvements in design integration through the introduction of multi-functional structures and materials, are thought to be the main issues that need to be adressed.[88] Providing the necessary structural capabilities will likely require purpose-designed materials, though this may adversely affect affordability.

Recent experiences suggest that the requirement for materials that provide sufficient structural ruggedness and damage tolerance should also not be underestimated. During deployment in Iraq, the 2.4 ft wing span Dragon Eye mini-UAV was found to be "too flimsy", easily breaking apart on repeated landings. Partly as a result of this, partly as a result of a lack of endurance, from 2006, all ongoing and future procurements for the Dragon Eye were redirected to the larger (4.3 ft wing span), sturdier RQ-11 Raven mini-UAV.[89] Such issues are likely to be even more prevalent at MAV sizes and careful thought must be given to structural requirements in terms of storage, transport, assembly, launch, resistance to in-air collision, and landing. Environmental robustness (weather, climate) and, due to their small size, the influence of dirt on functionality should be considered too.[44]

2.6.7 Control and Navigation

Due to their low weight and size constraints, control of early MAVs generally relied on the same sort of electronics as used in remote control (RC) model aircraft. Despite its ready availability, such equipment was never intended for the level of performance required from MAVs, and its usage restricts capability by limiting flight agility and the degree of autonomy. The level of autonomy also depends on the number of sensors carried and the

way they are fused together, which is limited by the low lifting capability of MAVs. As a result, early MAVs were remotely-piloted craft rather than truly autonomous vehicles. Furthermore, the use of unsophisticated control technology, combined with low natural stability, high sensitivity to turbulence, and a susceptibility to rapid angular acceleration, meant that the first generation of MAVs could only be flown by skilled pilots. For military applications there is a strong desire for a vehicle that is highly autonomous and requires no special expertise or support to operate.

The continued miniaturisation of hardware (gyroscopes, accelerometers, pressure transducers, etc.) has improved things and many of the larger mini-UAVs are now able to employ small, commercially available autopilot systems that typically weigh from 85 g to 250 g, but are highly capable. Such systems offer advanced abilities, including automated take-off and landing, GPS waypoint navigation, telemetry, altitude/airspeed sensors, and ground control software for in-flight re-tasking, as well as more prosaic tasks like servo control, all integrated into a single unit. This type of device is still too large for most MAVs and much heavier than the basic electronics currently used. Additionally, whilst it adds functionality that greatly improves the capabilities of this type of vehicle, it also adds considerable cost (the Micropilot MP2028g costs $5,000).

As well as a deficit of high quality sensors, actuators, and computational units of suitably small size and weight, the problem of miniaturisation of flight control systems is complicated by the increase in frequency of flight dynamics as aircraft size decreases, resulting in MAVs requiring higher bandwidth actuators than their larger counterparts. Application of MEMS components, ultrasonic devices, and piezoelectric actuators are foreseen for future MAVs. Such components are expected to improve reliability, save weight, and reduce overall power consumption. MEMS devices can also provide the bandwidth and accuracy needed in flight control sensing and computing, so that mini-UAV and MAV flight agility can improve.

Further stability and control advances will also be necessary before MAVs will be able to fully cope with the demands of the various operational environments they will face. Flight in differing weather conditions will require MAVs to contend with strong gusts that may often be equal to, or greater than, the forward airspeed of the vehicle itself. Sub-canopy, indoor, and urban scenarios pose the greatest problem for control systems as they will require precision manoeuvres around obstacles, such as buildings or trees, whilst operating in an enclosed space. A very powerful flight control system will be needed to provide autonomous operation in these conditions.

This aspect of MAV design is drawing a great deal of attention from the research com-

munity.[90–95] In particular, vision-based control systems, such as the statistical horizon detection algorithm developed at the University of Florida,[96–99] have proven popular. This system uses the vehicle's on-board camera to locate the horizon in real-time and provide feedback for stability and control in both pitch and roll motion. Tests have shown the control of a vehicle using this algorithm to be significantly enhanced, as compared to manual control. Similar systems have been investigated by other researchers.[100,101]

Along with the onboard control system, thought must also be given to the ground control unit. As the point of interface with the human operator, GCU ergonomics, particularly the arrangement of the information display, are of great significance. Above all, the GCU should be simple enough to allow for intuitive use of the requisite controls and the relevant information (e.g. the current course of action) should be visible at a glance. Such human factors are not often considered in the context of technical issues, but are thought to be a key aspect of obtaining end-user acceptance and require further research.[37]

2.6.8 Payload Capability

Payload carrying capacity is key to assessing the mission capabilities of small-UAVs. For the typical mini-UAV, particularly those of wing span greater than 4 ft, there are a number of advanced payloads, of suitable size, weight, and cost, now available. These include high performance television cameras, infrared sensors for day/night surveillance, acoustic sensors, chemical-biological sensors, and electronic surveillance equipment.[1] For current MAVs and smaller mini-UAVs (less than 2 ft wing span), the available payload weight, which can be as little as 7 g, severely limits the availability of useful sensors. The majority of existing MAVs carry a video camera as their primary sensor and micro-sized camera technology is sufficiently well developed that it is possible to obtain a basic imaging system that weighs less than 2 g.[35] However, data and power intensive payloads, such as Synthetic Aperture Radar (SAR), are beyond the capabilities of those platforms at the lower end of the size spectrum and are expected to remain so for the foreseeable future.[1]

Improving the low lifting capability of MAVs would not only increase the available number of sensor types, but would also allow for more sophisticated technology to be used. At present, even when a suitably sized sensor is available, it may, by necessity, be relatively unsophisticated, affecting the quality of data recorded. An increased payload capacity would also improve data quality by enabling the carriage of multiple sensors that could work in unison to provide a better sensing ability. In addition, sensor capability and data quality are strongly linked to the post-processing of the data collected. For example, to maximize its value, raw video images may need to be adjusted for camera alignment,

combined into larger image maps, and possibly have features identified and extracted. Currently, little commercial software exists to process the vast amount of data that will be generated by fleets of mini-UAVs or MAVs.[2,50]

The airborne communications equipment performing video down-link and command up-link are also limited by the small size and low payload weights. At the larger end of the mini-UAV scale, the payload carrying capacity is sufficient to allow directional antennas, and enough power may be available to reach long distances and even communication satellites. For MAVs and the smaller mini-UAVs, omnidirectional transmission with necessarily small, high-frequency antennas and low transmit powers is required because size and weight constraints prevent the use of more capable devices. This has limited the radio communications of MAVs and smaller mini-UAVs to between 2 and 5 km, effectively restricting vehicle range too.

This communication limitation is also a serious restriction on the missions that small-UAVs can undertake and poses one of the greatest scaling challenges: how to send data over great distances without requiring excessive power and weight.[50] Possible solutions to the communications problem include the use of cellular communication architecture,[1] high-gain antennas, reduced data rates, or burst transmission communication schemes.[50] Under some circumstances, small-UAVs may be able to communicate to a larger ‘mother ship’, which would act as a communication relay, eliminating the need for a long-range telemetry link.

3 The Flow Past a Rotating Circular Cylinder

The flow past a stationary circular cylinder in crossflow has attracted considerable interest because of its simple geometry and representative behaviour of general bluff-body flow. Results for the flow past a rotating circular cylinder in crossflow are comparatively scarcer and its behavior is not so well understood, although that is not to say that the subject has not been a focus of research. Indeed, the rotating cylinder has attracted continuing interest for more than 150 years because of the considerable practical benefits to be obtained in the field of lift enhancement, drag reduction, and bluff-body flow control.

Although the problem has been examined both theoretically and experimentally, the complexity of the flow has meant that analytical treatments are more limited and most of the research is either experimental or numerical. Previous studies have shown the flow past a rotating cylinder to be highly dependent on a number of parameters, including Reynolds number (based on cylinder diameter), cylinder peripheral-to-freestream-flow velocity ratio, aspect ratio, end effects, surface roughness, freestream turbulence, and wind tunnel blockage. Of these, the velocity ratio and Reynolds number are of primary importance. However, the influence of the secondary parameters can be substantial: variations in these quantities from one experiment to the next are responsible for the often considerable scatter and disagreement that is visible in the literature.

This chapter catalogues the available information on rotating circular cylinders so as to provide a repository of knowledge that would be useful for the development of a small-UAV based on this geometry. This includes a historical overview of research into the Magnus effect, including attempts at application of the phenomenon; information on the nature and behaviour of the aerodynamic forces and discussion of their origin from boundary layer behaviour and the surface pressure distribution; data for the torque and power requirements to spin the cylinder; consideration of the characteristic wake flow and associated vortex shedding phenomena; the impact of yaw angle; and the effects of flow interaction due to proximity between multiple cylinders. In addition, the application and suitability of standard wind tunnel wall interference correction methods to rotating cylinder flow, as it pertains to the experimental phase of the present research, is examined.

3.1 Definitions and Notation

This section introduces the notation used to define the physical dimensions and parameters that will be employed throughout the rest of the report to describe the flow past an isolated

three-dimensional rotating cylinder. For the purposes of comparison, the choice of notation system was intended to reflect, as much as possible, that which is most commonly adopted throughout the literature. Any differences are designed to make interpretation of the results of the present tests more intuitive.

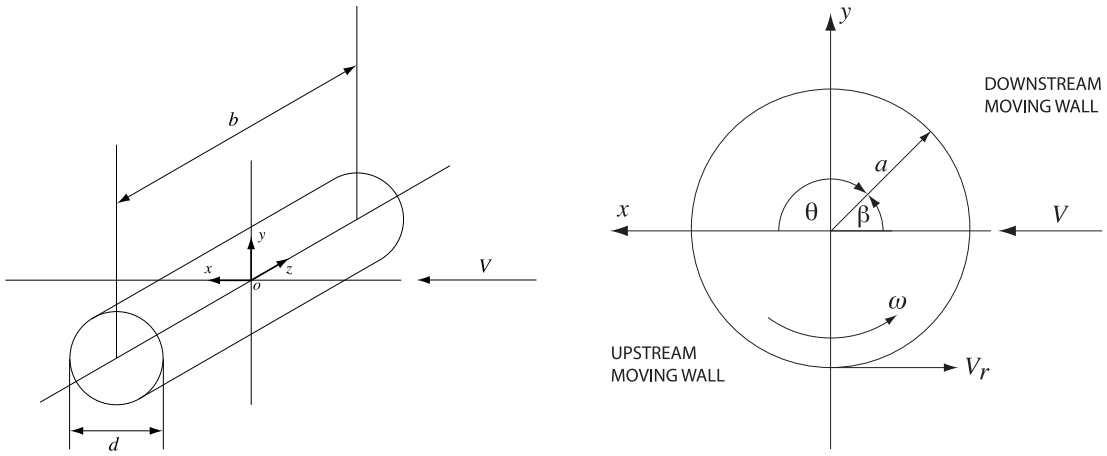

(a) Cartesian coordinate system

(b) Polar coordinate system

Figure 3.1: The rotating circular cylinder: axes, dimensions, and notation.

For simplicity, a frame of reference (f_c) that is fixed to the cylinder in translation, but does not rotate with it, is assumed. This particular frame was chosen as it is also analogous to a wind tunnel test of a rotating cylinder. Within this frame, cartesian coordinate system $oxyz$, with origin at the cylinder's center of gravity, is adopted for describing the flow past the cylinder (see Figure 3.1a). Note that the choice of orientation of $oxyz$ reflects the current experimental arrangements. It is also useful to define a polar coordinate system with radial coordinate r and angular coordinate θ, both measured in the xy plane. The origin of this polar coordinate system is coincident with that of $oxyz$ and θ is measured positive clockwise from the positive x axis. Angle β represents the supplement of θ (see Figure 3.1b).

Within frame f_c, the three-dimensional cylinder, having length b, diameter d, and aspect ratio

$$AR = \frac{b}{d} \tag{3.1}$$

is assumed to translate through a viscous incompressible fluid with constant velocity V in the direction of the negative x axis, such that the flow at infinity has a uniform velocity of magnitude V in the opposite direction. It follows that x is the streamwise direction, y is

the lateral direction, and z is the spanwise direction. As it translates, the cylinder rotates about the z axis in an anticlockwise manner, with constant angular velocity of magnitude ω. The associated peripheral velocity at the surface of the cylinder, V_r, is calculated from the angular velocity and the radius, a, such that

$$V_r = \omega a \tag{3.2}$$

The rotational rate (in rpm) corresponding to a given V_r may be determined from

$$N = \frac{60\omega}{2\pi} \tag{3.3}$$

For a circular cylinder as shown in Figure 3.1, where the rotation is in an anticlockwise sense and the fluid moves from right to left, the upper surface of the cylinder will be the downstream moving wall. Along this surface the velocities V and V_r are in the same direction and reinforce each other. For the same cylinder in the same flow, the lower surface will be the upstream moving wall. Here the velocities V and V_r are in opposition and interfere with each other. Note that the two walls are delineated by the boundary layer origin point. Unlike for a stationary wall, this is not always located at the front stagnation point (see §3.4).

The primary parameters influencing the flow around the cylinder are known to be the Reynolds number, Re, and velocity ratio, Ω. The Reynolds number is based on the freestream velocity, the coefficient of kinematic viscosity of the fluid, ν, and a characteristic length; for a circular cylinder, the diameter is typically used. Hence, Reynolds number may be calculated using

$$Re = \frac{Vd}{\nu} \tag{3.4}$$

The velocity ratio is determined by non-dimensionalising the cylinder peripheral velocity by the freestream velocity. Thus,

$$\Omega = \frac{V_r}{V} \tag{3.5}$$

Note that the velocity ratio is analogous to the angle of attack for aerofoils in the sense that the aerodynamic behaviour of the cylinder varies directly with it.

Increasing the velocity ratio creates a variation in the relative velocities around the surface of the cylinder, giving rise to pressure asymmetries that are the chief cause of the aerodynamic forces and moments acting on the cylinder. When discussed, these pressures are expressed in terms of the conventional pressure coefficient

$$C_p = \frac{p - p_\infty}{\frac{1}{2}\rho V^2} \tag{3.6}$$

where p is the local static pressure, p_∞ is the freestream static pressure, and ρ the fluid density.

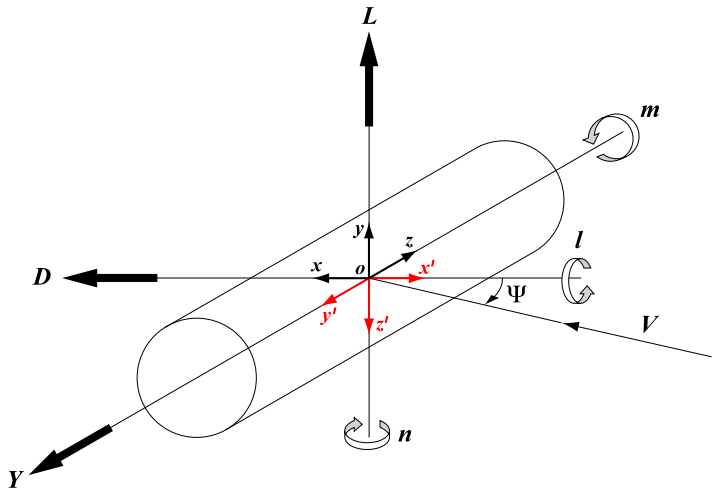

Figure 3.2: Forces and moments on a rotating cylinder (Arrows denote positive directions).

The system of forces and moments that can act on the cylinder is shown in Figure 3.2. Note that in this case coordinate axes $ox'y'z'$ are preferred over $oxyz$ and Ψ is the yaw angle. The generated forces and moments are reduced to coefficient form in the usual manner i.e. with respect to the dynamic pressure, a characteristic area, and if necessary, a reference length. The area is taken to be the projected area, as defined by the cylinder's span and diameter. Hence, the lift, drag, and sideforce coefficients are expressed as

$$C_L = \frac{L}{\frac{1}{2}\rho V^2 bd} \tag{3.7}$$

$$C_D = \frac{D}{\frac{1}{2}\rho V^2 bd} \tag{3.8}$$

$$C_Y = \frac{Y}{\frac{1}{2}\rho V^2 bd} \tag{3.9}$$

Lateral moments are nondimensionalised using the cylinder span as the reference length. Hence, the rolling moment and yawing moment coefficients are given by

$$C_l = \frac{l}{\frac{1}{2}\rho V^2 b^2 d} \tag{3.10}$$

$$C_n = \frac{n}{\frac{1}{2}\rho V^2 b^2 d} \tag{3.11}$$

where l and n are the rolling moment and yawing moment respectively.

The torque, Q, required to rotate the cylinder is expressed by the torque coefficient, C_Q, where

$$C_Q = \frac{Q}{\frac{1}{2}\rho V^2 b d^2} \tag{3.12}$$

The associated power requirements are given in terms of the power coefficient C_P, where

$$C_P = \frac{P}{\frac{1}{2}\rho V^3 b d} \tag{3.13}$$

and P is the power. The relationship between torque and power may be shown to be given by

$$C_P = 2\Omega C_Q \tag{3.14}$$

The wake of a rotating cylinder is known to exhibit periodic vortex shedding phenomena in the same manner as for a stationary cylinder. Such activity may be described in terms of the Strouhal number, St. This is a non-dimensional parameter relating to the natural frequency, f_s, at which vorticity is shed, and is defined as

$$St = \frac{f_s d}{V} \tag{3.15}$$

Note that, with regards to comparison between present results and the existing literature, if the notation and definitions used in the literature differed from that detailed in this

section, the relevant results were adjusted to match the current system before the data was compared.

3.2 Historical Overview

Throughout most of its history, the flow past a rotating circular cylinder has been examined as a means to understanding the 'Magnus effect', a phenomenon whereby a body translating and rotating in a fluid experiences a force at right angle to the direction of motion. Although the effect itself is generally identified with the 1853 experiments of Gustav Magnus,[102] it had already been known for some time that bullets and other projectiles tended to depart from their ballistic trajectory when spinning about the longitudinal axis. Indeed, more than a century earlier, artillerist Benjamin Robins[103] had studied and reported on this behaviour, noting that the rotation about the longitudinal axis caused an asymmetry of the flow that led to a curvature in the trajectory of the musket balls he had experimented with. His work first appeared in print in 1742.

Whilst Robins' tests were the first experimental investigations of the Magnus effect, the first discussion of the phenomenon was earlier still, having been driven by observations from ball games that pre-dated those of the artillerists. Gleick[104] has suggested that, in 1672, Sir Isaac Newton made mention of the effect, with regards to the behaviour of a sliced ball, after observing tennis players at his Cambridge college. Supposedly, Newton even ventured an explanation in terms of different pressures acting on opposing sides of the ball. Both Walker[105] and Bateman[106] have made similar comments regarding Newton and the Magnus effect, but such claims remain unsubstantiated.

Given the historical timeline, it would seem to be more proper to use the term 'Robins effect' or possibly 'Robins-Magnus effect', so as to acknowledge Robins' detailed contributions to the understanding of the phenomenon. However, for the purposes of this document, which is specifically concerned with the forces arising from the rotation of a cylinder, the term 'Magnus effect' is retained in recognition of Magnus' examination of this particular geometry.

Though crude and purely qualitative, Magnus' experiments with a brass cylinder[102] established that the previously noted deviation arising from rotation was caused by a transverse force whose direction was towards the side where the peripheral velocity and the freestream velocity were in the same direction. Magnus also realised that this force arose due to the interaction between the peripheral velocity and the freestream that, by the Bernoulli effect, led to an asymmetrical pressure distribution about the object in question:

on the side where the two velocities reinforced each other the pressure was lower than where they interfered. However, Magnus' overall explanation of the phenomenon was not wholly satisfactory, being limited by the state of the theory of flow that existed at the time.

The first mathematical explanation as to the nature of the force was provided in 1877 by Lord Rayleigh[107] when his examination of what he called 'irregular flight' as it applied to the trajectory of a tennis ball introduced the classic model of potential flow around a cylinder with circulation. The model is obtained by the superposition of different elementary solutions to Laplace's equation, which governs potential flow. The linear addition of the solution for a uniform stream to that of a doublet produces a flow with a closed circular stagnation streamline, which acts to separate the flow due to the doublet from that due to the uniform stream. This dividing streamline can be replaced by a solid body of identical shape without changing the nature of the flow, so that the resulting pattern represents the potential flow past a two-dimensional non-rotating circular cylinder. Lifting flow past a spinning cylinder is obtained by the additional superposition of a line vortex, located at the origin of the circle, with strength K that is directly proportional to the rotation speed of the cylinder.

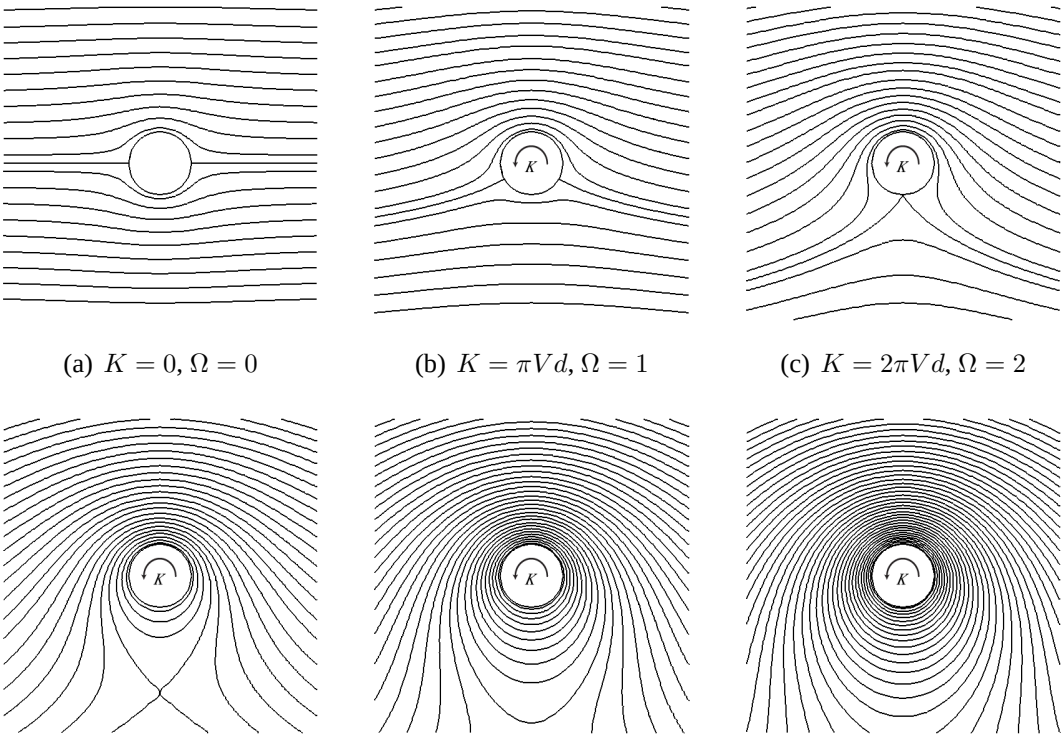

(a) $K = 0, \Omega = 0$ (b) $K = \pi V d, \Omega = 1$ (c) $K = 2\pi V d, \Omega = 2$

(d) $K = 4\pi V d, \Omega = 4$ (e) $K = 6\pi V d, \Omega = 6$ (f) $K = 8\pi V d, \Omega = 8$

Figure 3.3: Potential flow streamlines (flow is assumed to be from right to left).

The effects of increasing rotation in potential flow are shown in the streamline patterns of Figure 3.3. They indicate that, as the circulation increases, the fluid velocity near the downstream moving wall increases, whilst that near the upstream moving wall decreases. Hence, the effect of increased rotation is to decrease the pressure on the downstream moving wall and increase it on the upstream moving wall, exactly as noted by Magnus in his experiments. A further consequence of rotation is seen in the behaviour of the stagnation points. For $K = 0$ (i.e. a stationary cylinder) the familiar situation of two stagnation points at $\theta = 0^\circ$ and $\theta = 180^\circ$ occurs. With increasing vortex strength, the stagnation points begin to move towards each other along the upstream moving wall. When $K = 2\pi V d$, they coincide at $\theta = 270^\circ$ (see Figure 3.3c) and will move off the surface completely when the vortex strength is increased further. This situation creates a closed streamline about the cylinder, within which it continues to rotate, carrying around with it a region of fluid that is separated from the rest of the flow.

Experimental investigation of rotating cylinder flow began in earnest at the beginning of the twentieth century, when discussion of the Magnus effect was very much in fashion. As part of his historic work on boundary layers, Prandtl[9] carried out flow visualisation tests using cylinders as early as 1907, but made no force measurements and concentrated primarily on the cases of a stationary cylinder and two oppositely rotating cylinders positioned one above the other. In connection with these experiments, an isolated rotating cylinder was tried once, without however, much importance being attached to the matter. Prandtl would later perform more extensive flow visualisation tests with isolated rotating cylinders using much better apparatus.[108]

The first quantitative measurements of the Magnus force were probably those carried out by the Frenchman M. A. Lafay[109,110] in 1910. His tests covered quite a broad range of Reynolds numbers ($5.7 \times 10^4 \leq Re \leq 1.98 \times 10^5$), enabling Lafay to also be the first to discover the inversion of the Magnus effect that occurs at low Ω and high Re (see §3.3.3). At about the same time as Prandtl and Lafay, the Russian, Dimitri Riabouchinsky, also began paying attention to the Magnus effect. He studied auto-rotating bodies and rotating cylinders at the Koutchino Institute of Aerodynamics, near Moscow. No results from Riabouchinsky's tests with cylinders are known to exist, though some of his work is mentioned briefly by Ahlborn[111] and Tokaty.[112]

A second flurry of experimental investigations into the nature of the Magnus effect occurred in the early 1920s. The 1923 investigation that was carried out at the Aerodynamische Versuchsanstalt Göttingen (AVA) by Ackeret, with the involvement of both Betz and Prandtl[8–10] (hereafter referred to as the Göttingen tests), is notable for its contribution to the success of the Flettner rotorships (as detailed in §1.1). In discussing the tests,

Betz[8] remarked that the nature of the Magnus effect was so thoroughly investigated by the AVA that Flettner was immediately able to utilise the results in his designs. In truth, the Göttingen tests were actually quite limited as they focused only on force measurements, and then, only at a single Reynolds number of $Re = 5.1 \times 10^4$. Furthermore, the drag data does not match well with the results of later tests, such as those of Reid[113] or Swanson.[12] The Göttingen tests did, however, mark the first investigation of the effects of endplates on rotating cylinder flow.

Reid's 1924 tests[113] were the first Magnus effect experiments in the United States and employed a much larger aspect ratio cylinder ($AR = 13.3$) than any preceding study, producing noticeably different results, particularly for the drag. Swanson[12] noted that the most interesting of Reid's results were never published, but no explanation for either the reasons why they went unpublished nor any details on the nature of the unpublished results was given. Meanwhile, in the UK, Thom began a series of experiments[114–119] that remains one of the most extensive investigations of the Magnus effect to date.

During his decade long investigation, Thom experimented with a number of different aspects of rotating cylinder flow, including end conditions, surface roughness, aspect ratio, and blockage effects. He also performed some of the earliest surface pressure and boundary layer measurements too. However, Thom's investigations were not performed in a completely systematic fashion and so not all the tests were equally extensive. Experiments with different Reynolds numbers, aspect ratios, or endplates were not always tested throughout the same velocity ratio range, thus leaving gaps in the data. Such failings make Thom's results less useful than they might otherwise have been.

This focus on the Magnus effect spurred a number of contemporaneous efforts towards practical application of the phenomenon. As well as his famous rotorships, Flettner also turned his attention to applications in windmill design.[112, 120, 121] Following extensive testing, he developed a prototype windmill having a four-rotor propeller positioned atop a 30 m tower that housed an electric generator. Each rotor was almost 5 m long and slightly tapered, with axial rotation being driven by a small motor built into the inside of the cylinder shell. Though rotor propellers were said to offer several advantages over conventional windmills they never achieved widespread commercial use. A four-rotor propeller design was also proposed by Föttinger as a means of ship propulsion.[122]

A similar application was pursued by Julius Madaras, who patented an idea for a means of power generation that involved the use of several cylindrical rotors.[123] Positioned vertically, each rotor sat on a special type of railroad car that was pushed around a circular track when the wind was strong enough to generate a sufficiently large transverse force.

Power was extracted from the system by electrical generators attached to the wheels of the rail car. The Madaras Power Plant Project, as it was called, went into planning in the USA during the 1920s and a pilot scheme, using a single full-scale rotor, was begun in 1933. Before a substantial estimate of its efficacy could be made, the project was cancelled when the rotor was blown down by high winds.[120] A later re-examination of the concept by Whitford *et al.*[124] suggested that a racetrack shaped course would provide a greater level of energy production.

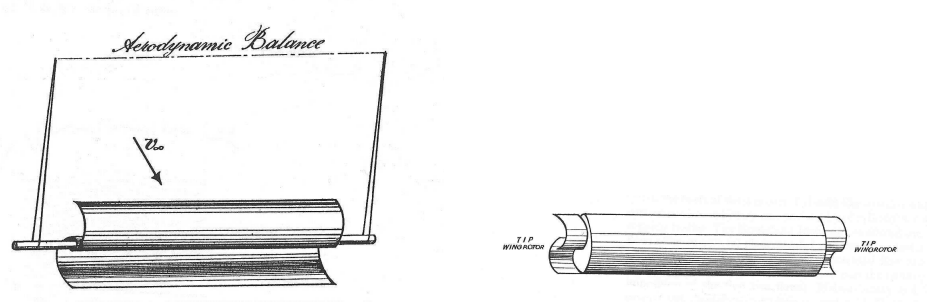

(a) Wing-rotors (b) Combined rotors

Figure 3.4: Soviet rotating wing programmes from 1938–1941.[112]

Wolff's tests[125,126] are notable as they represent an early attempt at application of rotating cylinders to aircraft, in this case by fitting the cylinder to the leading edge of a conventional wing. Wolff hoped that this would increase the maximum lift coefficient of the wing, but he was largely unsuccessful. The use of a rotating cylinder as this type of high-lift device was also investigated by the German AVA in Göttingen.

In the period prior to and during World War II, the experiments of Busemann,[127] von Holst,[128] and Küchemann[129,130] examined the use of a spinning cylinder and spinning wing as a trailing edge addition to a fixed main-plane. Following the end of the war there was a certain amount of British interest[131,132] in these little-known activities but, although the rotating flap was seen as an attractive high-lift scheme, nothing substantial ever developed. Similar work on rotating cylinders, wing-rotors, and combined rotors (see Figure 3.4) was carried out by the Soviets at the Zhukovsky Academy of Aeronautics in Moscow[112] between 1938 and 1941.

Such tests were the forerunners of later efforts to employ rotating cylinders as boundary layer control devices. This concept, known as Moving Surface Boundary Layer Control (MSBLC), had been demonstrated by Prandtl as early as 1910. Rather than making direct use of the large forces generated by rotation, MSBLC exploits the motion of the cylinder's surface to prevent separation of the boundary layer from the lifting body to which the cylinder is attached. This effect is achieved in one of two ways: by preventing the initial

growth of the boundary layer through restriction of the relative motion between the surface of the wing and the freestream, or by re-invigorating an existing boundary layer through the addition of supplementary momentum.

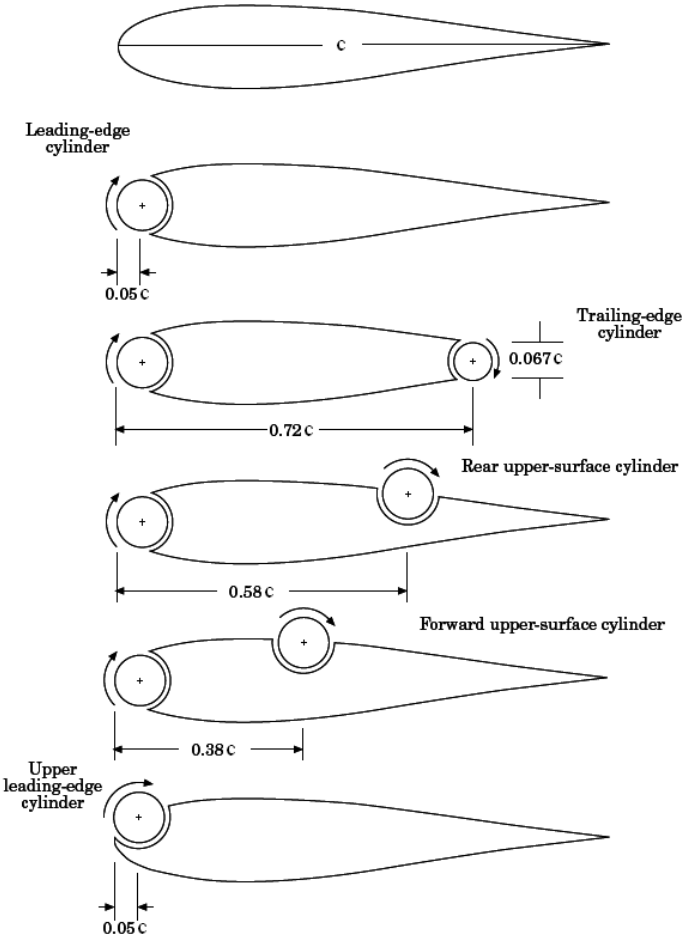

Figure 3.5: Overview of typical rotating cylinder configurations for MSBLC application.[133]

Studies of this kind were particularly popular in the 1960s and 70s, during which rotating cylinders were applied to a variety of different tasks, including the control of torpedoes,[134] in ship manoeuvrability,[135] as a high-lift device for aircraft,[136] and as a means of controlling boundary layer separation in a subsonic diffuser.[137] Different configurations and locations of the cylinder were also considered (see Figure 3.5). Though they have so far failed to result in a successful venture, MSBLC applications have continued to attract research attention to the present day.[6, 133, 138–141]

Perhaps the most notable example of this type of application comes from a NASA programme of experiments investigating several different slow-flight systems. The programme included a rotating cylinder flap design[4, 142–144] that NASA hoped would drastically increase slow-speed performance, providing improved turning effectiveness and

greater flap lift. Evaluation of the concept was carried out using a modified North American Rockwell YOV-10A prototype aircraft, the wing of which was refitted to incorporate a two-segment Fowler flap with a hydraulically driven rotating cylinder positioned at the flap's leading edge (see Figure 3.6). The cylinder was spun at speeds of up to 14,000 rpm, energising the boundary layer and preventing separation of the airflow from the flaps. At the same time, it also deflected the propeller thrust, providing a powered-lift component that was over and above that derived from the wing.

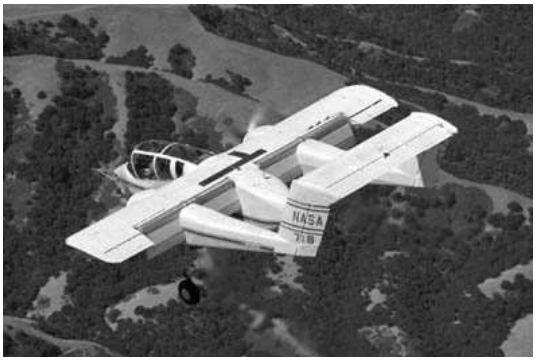

(a) Modified Rockwell YOV-10A prototype aircraft[145]

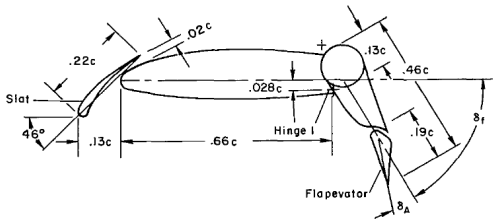

(b) Flap and slat geometry[4]

Figure 3.6: The NASA rotating cylinder flap programme.

The modified aircraft was first tested in the 40 ft x 80 ft wind tunnel at NASA Ames,[4,142] before beginning a series of flight tests[143] to evaluate the low-speed handling qualities and performance characteristics. These tests showed the rotating cylinder flap to be "an effective and efficient" high-lift device that, despite greater drag than a conventional flap, was able to provide the high lift coefficients, low speeds, and steep descent angles necessary for the desired STOL performance whilst also being relatively mechanically simple (providing trouble free operation for over 80 hours of tests) and having power requirements that were lower than those for a blowing boundary layer control flap at the same lift.

However, the tests also revealed adverse stability and control characteristics at flap deflections above 75° that prohibited the aircraft from being flown to its full potential. In summarising the flight test results, Weiberg *et al.*[142] noted that the deterioration in performance as approach speed was reduced was not due to some inherent failing of the rotating cylinder flap but was a result of operating at low speeds and high lift coefficients. These conditions led to unstable pitch characteristics, a low longitudinal control margin, low directional stability, and lateral instability.

Post-war investigation of rotating cylinder flow was more sporadic than in the early decades of the twentieth century, but included several important studies. The work of

Kelly & Van Aken[146] and Jaminet & Van Atta[147] has provided the only known experimental data for very high ($Re = 9 \times 10^5$) and very low ($Re = 50$) Reynolds regimes respectively, while Swanson's[12] tests remain the most comprehensive examination of the forces on rotating cylinders, with extensive measurements of the lift and drag obtained for Reynolds numbers between $3.5 \times 10^4 \leq Re \leq 5.01 \times 10^5$ and across a velocity ratio range of $\Omega \leq 17$. Alongside the force readings, Swanson also performed the first boundary layer measurements since Thom[117] and introduced the idea of the boundary layer origin point (see §3.4). Furthermore, his results confirmed the earlier arguments of Davies[148] and Krahn[149] on the nature of the inversion of the Magnus effect. If Swanson's paper can be criticised, it is in the lack of detail concerning the experimental arrangements.

The 1980s produced a small resurgence in experiments aimed at fundamental understanding of rotating cylinder flow, generating more studies than the previous three decades combined. New measurements of the boundary layer[150–153] and the surface pressure distribution[154,155] were performed, complementing and extending the earlier works of Thom[116] and Miller.[156,157] Also of note are the studies of Diaz *et al.*[158,159] and Massons *et al.*,[160] which remain the only in-depth quantitative investigations of the nature of the rotating cylinder wake and its associated vortex shedding.

In contrast, the last fifteen years have seen a distinct fall in the number of experimental studies of rotating cylinders. This is, perhaps, not so much indicative of a reduction of interest in the subject as it is a consequence of the transition towards other means of investigation. The difficulties associated with the physical testing of a rapidly rotating body, coupled with the advent of sufficiently powerful computers, have meant that CFD methods are now an attractive, cost effective alternative to traditional experiments. Accordingly, most of the more recent work on rotating cylinders has been of the CFD simulation type, with the interest stemming primarily from the convenience of using the simple geometry of rotating cylinder flow as a prototypical problem in unsteady separation.

The earliest numerical work on rotating cylinder flow was probably that by Thoman & Szewczyk[161] in 1966. Although a small quantity of studies followed in the 1970s,[162,163] more substantial numbers did not begin to appear until the 1980s,[164–167] coinciding with a rise in computing power. Even so, these early studies were quite basic in their scope, being limited to small velocity ratios ($\Omega \leq 0.5$) and very low Reynolds numbers ($Re \leq 40$), where the flow field remains steady. This restriction on Reynolds number was due to a poor convergence rate and other numerical stability problems. The computational cost of three-dimensional simulations and the limitations of the available numerical tools also meant that the early studies dealt only with two-dimensional flow-fields. Developments in computing power have now allowed for larger Ω and higher Re to be investigated, though

three-dimensional simulations remain very much in the minority.

In addition, the advancement in Reynolds number capability has proceeded much slower than the increase in the value of Ω that may be successfully investigated. The majority of studies have been limited to Reynolds numbers below $Re = 1 \times 10^3$, with most of those being at $Re \leq 200$, this being approximately the highest value at which the flow can be expected to remain two-dimensional and laminar.[168] For higher Re the cost of computation can, depending on the choice of numerical scheme adopted, very quickly become impractically high.

Difficulties in obtaining converged results have constrained those few studies[169–175] that have been performed at higher Reynolds numbers ($Re > 1 \times 10^3$) to examination of an early transient period only, or have limited the range of velocity ratios able to be investigated. More critically, these high Re studies have nearly all been two-dimensional in nature, even though the flow is, by this point, intrinsically three-dimensional. Any conclusions drawn from such work are thus questionable. Progress in the available numerical methods and the continuous increase in computer power are beginning to improve this situation: recent three-dimensional simulations[176] at much higher Reynolds numbers ($Re = 5 \times 10^4$) are now starting to provide useful quantitative results for comparison with experimental data.

However, in general, numerical studies of rotating cylinders tend to be primarily focused on discussion of the nature of the unsteady flow, as opposed to explicit quantitative comparison with the experimental literature. Of particular interest has been the study of the formation and development of vortices in the wake at low velocity ratios. For studies that extend to higher velocity ratios ($\Omega > 2$), the two aspects of rotating cylinder flow that have drawn the most attention are the ability of a rotating cylinder to suppress vortex shedding and the question of the maximum lift that can be generated. A few studies, such as that by Chew *et al.*,[175] are more extensive, producing quantitative data on many aspects of rotating cylinder flow from force coefficient values through to pressure distributions and wake shedding frequencies. Such studies illustrate the strength of the numerical simulation approach, which offers the ability to collect multi-faceted results in a way that would be very difficult for an experimental study.

3.3 The Lift and Drag of a Rotating Cylinder

The determination of the lift and drag of a rotating circular cylinder is the most common objective of investigations into this arrangement. As a result, there is a sizeable amount

of information in the literature regarding the variation of C_L and C_D with velocity ratio. Although most of this data is experimental, results from analytical and numerical studies are also available. However, despite the quantity of results, there remains a lack of conclusiveness on force behaviour. In particular, the nature of the lift and drag curves at high velocity ratio, the issue of the maximum possible lift, and the effects of the secondary parameters have not been definitively addressed.

3.3.1 Analytical Results

The most basic analytical results for the forces on a rotating cylinder are obtained from the potential flow model. That this model is only applicable to a two-dimensional cylinder in an inviscid, incompressible, and irrotational fluid limits the usefulness of its predictions; in particular, the assumption of inviscid flow leads to a prediction of zero drag, known as d'Alembert's paradox. The model also predicts the lift of a rotating cylinder to be a linear function of the velocity ratio and to increase indefinitely with rising Ω (see Figure 3.7). Using the Kutta-Joukowski theorem the lift coefficient for a rotating cylinder can be shown to be given by

$$C_L = 2\pi\Omega. \tag{3.16}$$

The first attempt at an analytical representation of wake phenomena was made in 1928 by Bickley,[177] using a modified version of potential flow. In this approach, an additional vortex was included downstream of the cylinder to represent the shed vorticity in the wake. Consequently, an image vortex positioned within the cylinder was required to maintain the cylinder surface as a streamline. Bickley found that, when the added 'wake' vortex was made to move downstream, the model predicted a non-zero drag force that increased with the square of the circulation. Bickley's model reportedly produces better agreement with experiments for the lift force too, which is now seen to be a parabolic function of the circulation.[12]

Beyond potential theory, the preferred strategy of the analytical approach to rotating cylinder flow has been through the use of boundary layer theory. Studies such as those of Glauert,[178,179] Moore,[180] and Wood[181] have investigated the effects of rotation at both high and low Re and large and small Ω. Despite their increased sophistication, these studies are generally only valid for those situations where boundary layer separation is completely suppressed and their results are still very limited in the level of agreement with experimental data.

3.3.2 Experimental Results 1: Overview

Although there is some disagreement on the performance at higher velocity ratios, the quantitative force measurements all show that the rotating cylinder is capable of generating much more lift (approximately ten times more) than a conventional aerofoil of the same projected area, although this extra lift comes at the cost of a large drag force that is many times greater than that produced by a well-designed aerofoil or wing.

The origin of this circulation around a rotating cylinder has often been said to be a result of the friction from the no-slip condition between the two separation points transferring the rotational motion of the cylinder surface to the fluid, so that it is set into opposing motion.[180,182] However, studies[183–185] indicate that this effect only occurs in the very thin boundary layer region next to the cylinder. In his tests with rotating tangent ogive-nosed cylinders, Brown[184,185] noted that the air outside the boundary layer does not follow the rotation of the cylinder, indicating that no viscous shear was transmitted to this portion of the flow pattern. Furthermore, the very existence of an inverse Magnus effect (see §3.3.3) proves that such a process cannot be the origin of the circulation.

Instead, as several authors have concluded,[9,12,183] the circulation around a rotating cylinder is a consequence of asymmetric boundary layer separation on the upstream and downstream moving walls as caused by moving wall effects. Boundary layer separation is moved back on the side of the cylinder that is moving with the fluid, and is moved forward on the side opposing the freestream. The wake then shifts to the side moving against the fluid, causing the flow to be deflected on that side, and the resulting change in free stream flow creates a lift force on the spinning cylinder. The large magnitude of the lift is due to the far greater downwards deflection of the air by a rotating cylinder, as compared to a wing.

Typical results for the experimentally determined variation of the lift, drag, and lift-to-drag ratio with Ω are given in Figure 3.7. The data shown are those of Swanson,[12] whose tests are probably the most extensive experimental examination of the forces on a rotating cylinder. In addition, Swanson felt that his arrangements produced the closest approach to two-dimensional flow of any of the other studies. Whilst Swanson's data illustrates the high values of lift available, as compared to a typical aerofoil, it also reveals that the lift for viscous flow is considerably less than that predicted for two-dimensional potential flow. A substantial change in the lift-curve slope may also be noted at $\Omega \approx 3$, though no upper limit to C_L is observed. The value of the lift at high Ω is a point of contention in the literature and there remains a great deal of ambiguity with regards to the maximum lift coefficient that can be achieved with a rotating cylinder.

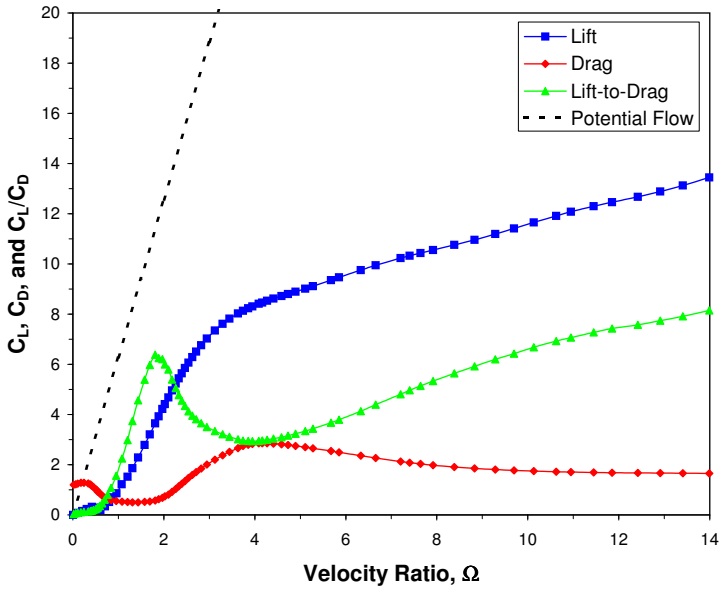

Figure 3.7: Swanson's[12] results for the lift and drag of a rotating cylinder.

Whilst the lift for potential flow increases indefinitely with velocity ratio, Prandtl[9,108] argued the existence of a maximum theoretical lift coefficient for real flows. Prandtl believed that the situation that exists for potential flow at $\Omega = 2$, when the front and rear stagnation points have rotated such that they are coincident on the upstream moving wall at $\theta = 270°$ and a closed streamline forms around the cylinder, would for real flows prevent the shedding of vorticity and the further generation of circulation. Prandtl noted that observations from his flow visualisation tests at $Re = 4 \times 10^3$ (see §3.7) suggested that, in a real flow, the topology at $\Omega = 4$ was equivalent, or at least very similar, to that for an inviscid flow at $\Omega = 2$. Thus, he suggested this point, $\Omega = 4$, as the location of the maximum C_L, where the value of the lift would be the same as that for potential flow at $\Omega = 2$, namely $C_{L_{max}} = 4\pi$.

The early force measurements by Lafay[109,110] and others produced significantly smaller lift coefficients ($C_{L_{max}} \approx 1.8$ for $AR = 3.5$) than were theoretically thought possible and did not violate Prandtl's limit, but these tests had been performed on short aspect ratio cylinders without endplates. Later experiments with large aspect ratio cylinders (see §3.3.4) and endplates (see §3.3.5), as well as two-dimensional numerical simulations at low Re (see §3.3.7), indicate that Prandtl's limit does not hold. Furthermore, Prandtl's conclusion was based on his well known flow visualisation observations and photos,[108] but several authors[12,186] have suggested that his apparatus was flawed and the patterns seen were not truly representative of the flow past a rotating cylinder (see §3.7).

The overall reduction of C_D for $\Omega \leq 1$ seen in Figure 3.7 is a consequence of the coming

together of the separation points, due to the effects of rotation on boundary layer separation, leading to a narrowing of the wake. As the velocity ratio increases beyond $\Omega = 1$ the drag increases also, reaching a value much greater than that on a stationary cylinder. This increase in drag occurs even though the wake profile is still decreasing in area (see §3.7). The drag is seen to peak at $\Omega \approx 3$, close the observed 'knee' in the lift curve. Beyond this point, Swanson found that further increases in the velocity ratio now resulted in a fall in drag.

Swanson attributed the continued increase in C_D beyond $\Omega = 1$ to flow reattachment over the rear of the cylinder accompanied by rotation of the wake and the separation points, in the same sense as the rotation of the cylinder, until they are located near the lower extremity of the cylinder ($\beta = 270°$) when $\Omega = 3$. The subsequent reduction in C_D for $\Omega > 4$ was said to be a result of further rotation of the wake towards the front of the cylinder ($\beta = 0°$) and the resultant changes to the flow pattern and pressure distribution. Other studies often show quite different drag behaviour to Swanson's results and there remains considerable disagreement and uncertainty regarding the variation of drag with velocity ratio at high Ω.

In any case, the combination of high lift and high drag means that the maximum lift-to-drag ratio remains modest (< 8). In related work with autorotating wings,[183] such low lift-to-drag ratios have been attributed to the energy lost by shed vortices. Swanson's results indicate that the location of this maximum C_L/C_D may actually occur at very high velocity ratios ($\Omega > 14$), though an earlier peak value is also noted at $\Omega \approx 2$. In the rest of the literature the position of maximum lift-to-drag is generally reported to occur somewhere in the range $1.5 \leq \Omega \leq 2.5$. The unsystematic nature of the available data makes it difficult to determine whether the wide range of values is a result of the influence of aspect ratio or Reynolds number, or whether it is simply due to a lack of data around the location of the peak preventing an accurate definition of its position.

3.3.3 Experimental Results 2: Effect of Reynolds number

The dependence on boundary layer separation characteristics, which are strongly influenced by Reynolds number, means that the Magnus effect itself also depends on Re. The effects of rotation of the cylinder on separation of a purely laminar or purely turbulent boundary layer are seen to be rather straightforward. However, when moving wall effects influence flow separation via boundary layer transition, not only is the total effect more complicated, but it also has a much larger influence on the flow phenomena, particularly at low velocity ratios.

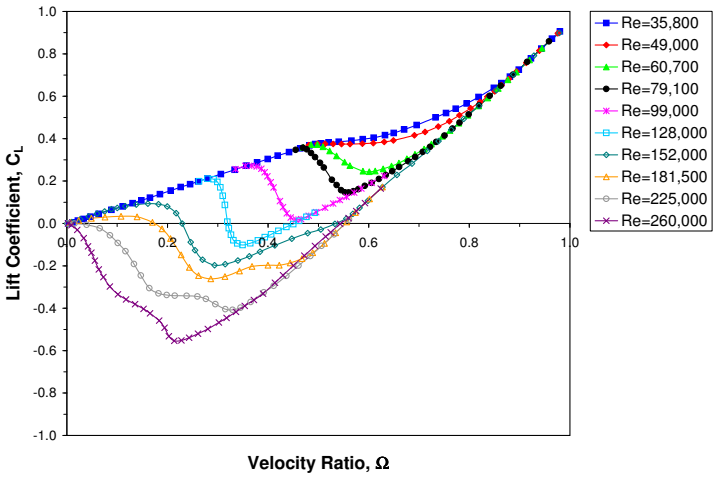

(a) Lift coefficient: subcritical Re

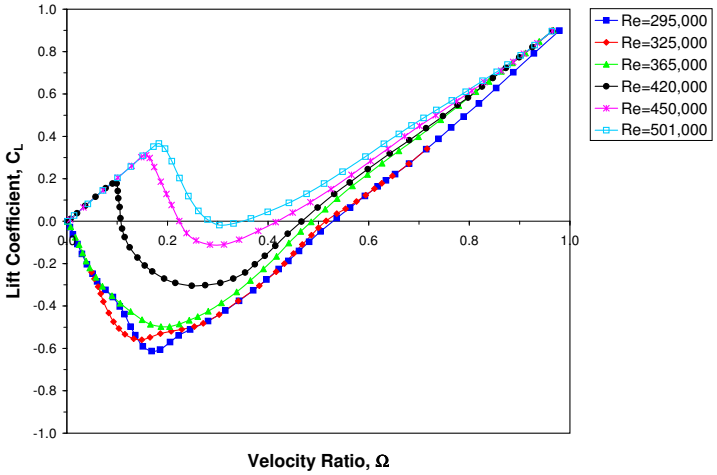

(b) Lift coefficient: critical and supercritical Re

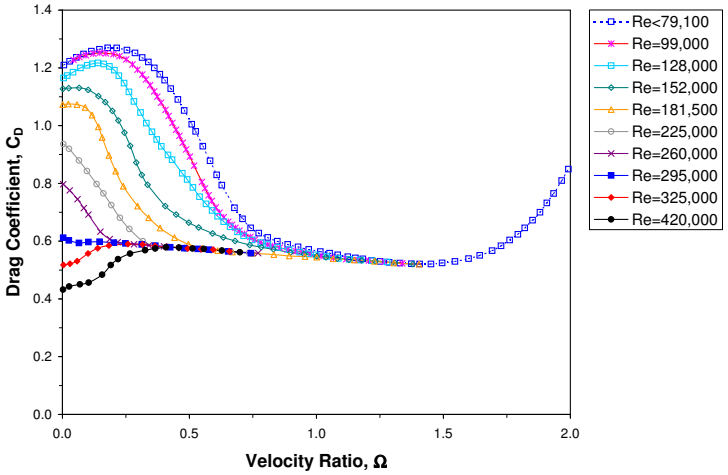

(c) Drag coefficient

Figure 3.8: Swanson's[12] results for the effect of high Reynolds number on the lift and drag of a rotating cylinder.

In 1910, Lafay[109,110] tested a rotating cylinder of aspect ratio $AR = 3.5$, without endplates, in an open-jet wind tunnel for $5.7 \times 10^4 \leq Re \leq 1.98 \times 10^5$ and $\Omega \leq 1.3$. He discovered that for Reynolds numbers greater than $Re = 8.8 \times 10^4$, and at least as high as $Re = 1.98 \times 10^5$, the Magnus effect was inverted at low velocity ratios, such that the transverse force was in the opposite direction to that predicted by Magnus. Lafay confirmed the inversion by measuring the pressure around the cylinder, noting that at low velocity ratios and high Reynolds numbers, the pressure on the upstream moving surface was indeed less than on the downstream moving surface. When he increased the velocity ratio towards $\Omega = 1$, the pressure once again reached a minimum on the downstream moving wall side and the conventional Magnus force was restored.

Later tests with rotating cylinders by Reid[113] and Thom[115] also noted this effect, as did experiments with spheres and golf balls by Maccoll[187] and Davies.[148] That inversion was not seen in all the early experiments is due to the fact that the Reynolds number for many of these tests was too low to instigate such changes. In addition, the sensitivity of the equipment may also not have been sufficient to measure the small magnitudes of lift involved. Davies' 1949 work is of particular interest as it also included the first explanation for the inversion, involving differential transition and the effective, or relative, Reynolds number based on the rotation of the body.

In 1956, Krahn[149] published a more detailed explanation for Lafay's observations of an inverse Magnus effect, describing the inversion "as a transition effect of the boundary layer from laminar to turbulent flow".[149] He suggested that rotation of the cylinder destroys the symmetrical nature of the flow and so turbulence appears on the two sides of the cylinder at different Re, the transition being dependant on the speed of the flow relative to the surface of the cylinder. However, Krahn carried out no tests to confirm his ideas and, due to uncertainties in the exact value of the critical Reynolds number controlling the inversion, his numerical data were only approximate.

Krahn's concept was later partially proved by the tests of Kelly & Van Aken[146] and then confirmed through Swanson's[12] detailed experiments. More recent investigations of the inversion include those of Tanaka & Nagano[188] and Griffiths & Ma,[189] but their results do not agree well with Swanson's. This is most likely due to differences in experimental conditions; in particular, the cylinder aspect ratio.

Swanson's force measurements (see Figure 3.8) reveal that the inversion phenomenon, and force coefficient dependency on Reynolds number in general, exists only for $\Omega < 1$. Within this range, negative lift coefficients are seen to be present only for $Re > 1 \times 10^5$ and reach a maximum value ($C_L \approx -0.6$) at critical freestream conditions ($Re = 3.25 \times$

10^5), where the effect is strongest: at these Reynolds numbers negative lift occurs as soon as the velocity ratio is non-zero. Swanson also reasoned that at or near the peak negative lift coefficient, the boundary layer on the upstream moving surface reaches a fully developed turbulent state.[12]

Increasing the Reynolds number away from the critical value causes the magnitude of the negative lift to slowly decrease until it disappears altogether for $Re > 5.01 \times 10^5$. However, the nonlinearity in the lift curve due to lift loss persists until much higher Re: the Kelly & Van Aken results[146] indicate that linearity of the lift curve at low Ω is only restored somewhere between $Re = 6.05 \times 10^5$ and $Re = 9.07 \times 10^5$. Swanson's data also confirms Krahn's prediction that the value of Ω that defines the onset of the lift loss will increase in magnitude the more that the freestream Reynolds number differs from the critical Re.

The results of Figure 3.8 also show that the magnitude of the lift-curve slope at low velocity ratio is greatest at critical freestream Re. In these conditions, $|dC_L/d\Omega|$ is approximately seven times greater than at low Ω (prior to the onset of the lift loss) in laminar flow. For supercritical Re the magnitude of the slope at low Ω is smaller, but still approximately twice as large as for laminar conditions. Tests at high postcritical Re by Kelly & Van Aken[146] confirm that the lift-curve slope is considerably greater for a turbulent boundary layer as compared to a laminar one: for $\Omega \approx 0.3$ and $Re = 1.01 \times 10^5$, the lift has reached $C_L \approx 0.23$, whereas for the same velocity ratio at $Re = 9.07 \times 10^5$, $C_L \approx 1$.

Kelly & Van Aken have suggested that such a difference occurs because a laminar boundary layer is much less efficient in vorticity transport than a turbulent one. Ericsson[190] noted that because the lift-curve slope is greater for turbulent conditions, where C_L is primarily generated by the upstream moving wall effect, than it is in laminar conditions, where the downstream moving wall effect is dominant, this suggests that the upstream moving wall effect is the greater of the two. Such results, and the phenomenon of Magnus effect inversion in general, may (with reference to the ideas of Davies,[148] Krahn,[149] Swanson,[12] and Ericsson[190]) be explained by examination of the competing influence of moving wall effects on transition and separation of the boundary layer in different Reynolds number and velocity ratio regimes.

For the stationary case ($\Omega = 0$), separation of the upper and lower boundary layers occurs symmetrically about the cylinder axis in both laminar and turbulent conditions, thus $C_L = 0$. However, even with only a little rotation, moving wall effects begin to induce an asymmetry of the separation positions. In purely subcritical flow ($Re \ll 3 \times 10^5$) and at low velocity ratio, say $\Omega = 0.3$, the jet-like effect of the downstream moving

wall results in the filling out of the boundary layer velocity profile and the delay of flow separation, so that the separation point on this surface moves rearwards from its subcritical position when $\Omega = 0$ towards the super-critical position. On the upstream moving wall, the separation point at $\Omega = 0$ is already subcritical and is largely unaffected by the separation-promoting properties of moving wall effects on this surface. Thus, the greater length of attached flow on the downstream moving wall produces positive lift. As long as the Reynolds number remains low, say $Re < 2 \times 10^4$, there is no transition of the boundary layers prior to separation and further increases in Ω result in the magnitude of C_L continuing to grow. This is the regular Magnus effect as discussed in §3.3.2.

As the freestream Reynolds number increases towards the critical value, the effect of increasing Ω on the relative velocities also substantially changes the relative Reynolds number, and so influences boundary layer transition. On the downstream moving wall the relative velocity of the fluid with respect to the wall is decreased and the relative Reynolds number is $Re_{rel} = Re_\infty(1-\Omega)$, where Re_∞ is the freestream Reynolds number. Thus, flow conditions on this wall are effectively the same as those for a lower Reynolds number than the freestream velocity would imply. Similarly, on the upstream moving wall the relative fluid velocity is increased and the effective Reynolds number is $Re_{rel} = Re_\infty(1 + \Omega)$, which is a greater value than the freestream Re implies and changes the boundary layer accordingly.

If Re_∞ and Ω are sufficiently large, the increase in the relative Reynolds number on the upstream moving wall will promote early transition to a turbulent boundary layer prior to the flow separating. However, since Re_{rel} is decreased on the downstream moving wall, boundary layer transition on this surface is delayed. This difference causes the flow on the upstream moving surface to remain attached for a longer period than on the downstream moving wall. The resulting region of low pressure counteracts the normal Magnus effect and causes an almost discontinuous loss of lift force.

Further increases in both Re and Ω lead to a progressively greater length of attached flow on the upstream moving wall, causing a continuing drop in C_L that eventually leads to either negative lift coefficients (if the freestream Reynolds number is high enough) or a substantial dip in the lift curve. A reduction in drag is also observed in this region, with both such effects being most pronounced at critical Re conditions.

Eventually, when the velocity ratio is sufficiently high, regular moving wall effects on the delaying or promoting of separation forces the flow to separate from the upstream moving wall prior to transition by moving the separation point forward of the transition point. This restores the greater length of attached flow on the downstream moving wall

that is responsible for the regular Magnus effect and causes a gradual recovery in the lift.

Where the inversion resulted in negative values of C_L the lift coefficient now slowly reduces in magnitude, until at some velocity ratio, Ω_K, the upper and lower separation points are at the same distance from the forward stagnation point and the Magnus force is again zero. With further increases in velocity ratio, the positive Magnus effect permanently takes over and C_L continues to rise. Krahn[149] estimated the value of Ω_K to be approximately $\Omega_K = 0.5$, but the actual position is dependent on the freestream Reynolds number (see Figure 3.8). For Reynolds numbers up to 3×10^5, $\Omega_K \approx 0.55$; by $Re = 5.01 \times 10^5$ it has dropped to $\Omega_K \approx 0.35$.[12]

For low supercritical Reynolds numbers the inversion is still prominent, but is now caused by the downstream moving wall effect delaying transition, causing it to move downstream of the separation point and thus tending to change the separation position from a supercritical type back to a subcritical type. As before, this produces a discontinuous loss of lift by changing the relative lengths of attached flow in favour of the upstream moving wall. However, in postcritical flow ($Re \gg 3 \times 10^5$), moving wall effects on transition due to increasing Ω give way to their effects on separation and the separation-promoting nature of the upstream moving wall now moves the separation point on this surface from the supercritical position back towards the subcritical position. As for purely laminar flow, this creates a longer length of attached flow on the downstream moving wall, restoring the regular Magnus effect and leaving C_L to increase in magnitude.

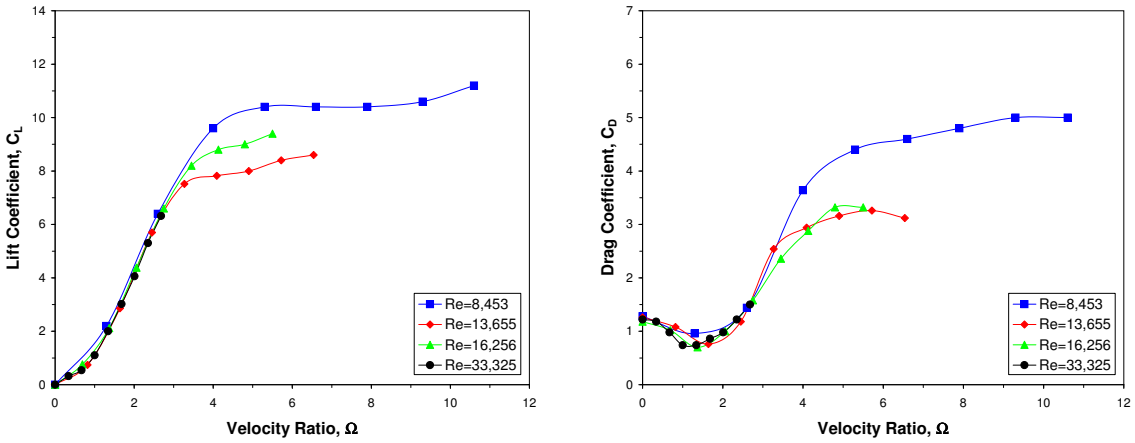

(a) Lift coefficient

(b) Drag coefficient

Figure 3.9: Thom's[115] results for the effect of low Reynolds number on the lift and drag of a rotating cylinder of aspect ratio $AR = 8.1$.

In addition to the change in force behaviour at the higher Reynolds numbers, the literature also seems to suggest that a second region of Reynolds number dependency may exist

when $\Omega > 2.5$ and $Re < 3 \times 10^4$. Under these conditions, Thom[115] reported a tendency for both lift and drag coefficients to increase as Reynolds number was reduced. The effect was quite dramatic, producing a 23% increase in C_L and C_D as Reynolds number was decreased from $Re = 1.63 \times 10^4$ to $Re = 8.45 \times 10^3$. However, Thom freely admitted that, due to the limitations of the force balance, he placed no great confidence in the accuracy of the results at the Reynolds numbers and velocity ratios in question. Furthermore, examination of his data (see Figure 3.9) indicates that the trend is somewhat inconsistent, supporting the notion that it may have been a result of experimental error. No other force data for similar Re and AR are known to exist, preventing a fuller assessment of the validity of the results.

3.3.4 Experimental Results 3: Effect of Aspect Ratio

The effects on the aerodynamic characteristics of a rotating cylinder, without endplates, due to varying the aspect ratio are illustrated in Figure 3.10. The variation in lift seen at low velocity ratios ($\Omega < 1$) is a consequence of the various Reynolds numbers at which the different results were obtained (as detailed in §3.3.3). There is insufficient data to assess the influence of aspect ratio, if any, in this region. It is interesting to note that, except for the smallest value of AR, the influence of aspect ratio on C_L does not appear to become apparent until $\Omega \geq 1.5$. For larger velocity ratios, increasing aspect ratio results in larger lift coefficients and delays the point at which there is a reduction of the lift curve slope. Swanson[12] suggested leakage flow and consequent pressure equalisation around the ends of shorter cylinders as possible reasons for the reduction in lift at low AR.

The results for high velocity ratios also dispute Prandtl's notion of a maximum lift coefficient equal to $C_{L_{max}} = 4\pi$ at $\Omega = 4$. In particular, the results of Tokumaru & Dimotakis[191] indicate that C_L can be made larger than the Prandtl limit (by more than 20%) at high Ω through increasing the aspect ratio; however, although the lift continued to rise for high Ω, the rate at which it did so became gradually smaller when $\Omega > 4$. Tokumaru & Dimotakis suggested that diffusion, unsteady flow processes, and three-dimensional effects were the reason for the violation of Prandtl's limit as they allowed the flow outside the closed streamline to receive vorticity from the flow inside the closed streamline. In this way the theoretical maximum lift coefficient can be exceeded. Such an explanation has been disputed in other studies[192] and a more reasonable conclusion would seem to be that Prandtl's original conjecture on $C_{L_{max}}$ was simply incorrect.

A trend with respect to aspect ratio is not as strongly defined for the drag coefficient data, though there is a suggestion that a larger aspect ratio causes a reduction in C_D at

high velocity ratios (Figure 3.10b). There is also far more scatter in the results at low Ω, indicating that drag is more sensitive to differences in the experimental conditions than lift. However, a beneficial effect of low aspect ratio at $\Omega = 0$ is seen, and is in keeping with the known effects of inflow due to low AR for stationary cylinders.[193] Interestingly, for $\Omega > 4$, the form of the three-dimensional drag curves is considerably different to Swansons[12] nominally two-dimensional result. In addition, there exists a considerable difference between Reid's[113] drag curve and all other published results that is difficult to account for.

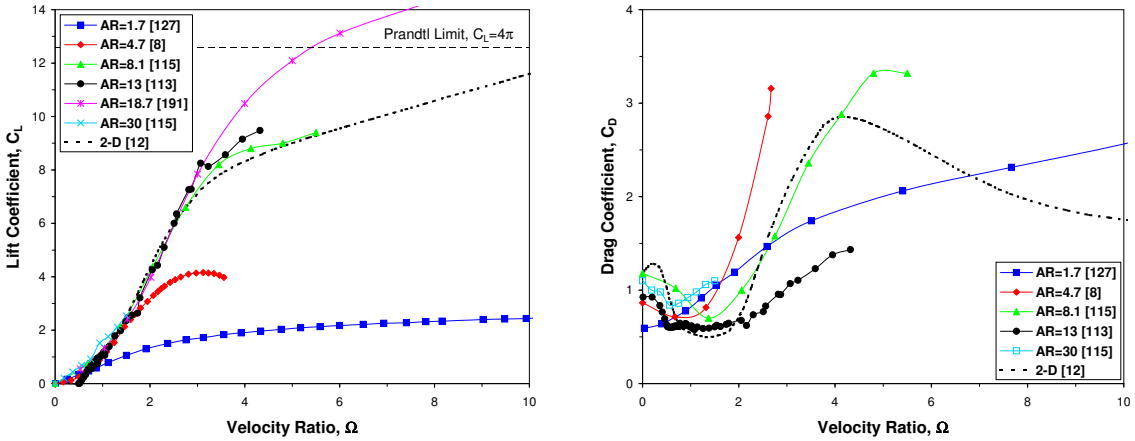

(a) Lift coefficient

(b) Drag coefficient

Figure 3.10: Effect of aspect ratio on the lift and drag of a rotating cylinder.

3.3.5 Experimental Results 4: Effect of Endplates and End-shape

The application of endplates to improve the performance of a rotating cylinder dates back to the early decades of the twentieth-century. First used as part of the Göttingen tests,[8–10] endplates were employed to try and increase the maximum lift on the cylinder, which in earlier tests without endplates had not been very close to Prandtl's theoretical maximum of $C_{L_{max}} = 4\pi$. Prandtl ascribed the reduction of maximum lift to the combined effects of flow separation on the tunnel walls and an inflow of fluid from the cylinder tip region towards the low pressure region at the mid-span. This was said to cause the pressure on the cylinder to increase and the flow to separate earlier through a thickening of the boundary layer on the downstream moving wall.

To combat this, Prandtl investigated the use of circular endplates to prevent the noted inflow and limit interference from the wall boundary layer. Tests with fixed plates were unable to prevent the inflow of air around the tips, but results with the endplates attached to the cylinder, so that they rotated with it, were far more favourable, causing a 150%

increase in the maximum lift from $C_{L_{max}} \approx 4$ at $\Omega = 4$ to $C_{L_{max}} \approx 10$ at the same velocity ratio. Two different sizes of endplates were tried during the experiments ($d_e/d = 1.7$ and $d_e/d = 2$, where d_e is the endplate diameter), and it was reported that increasing the endplate size had a beneficial effect on performance.

In keeping with the Göttingen tests, the predominant endplate type considered throughout the rest of the available literature has been circular endplates that spin with the cylinder. Jaminet & Van Atta[147] used square stationary plates in their tests, but took no force measurements. Examination of the results from the existing studies of endplates confirms that the addition of rotating endplates does indeed cause the value of C_L produced at high velocity ratios ($\Omega > 4$) to be approximately doubled (see Figure 3.11a).

The results are also in accordance with the notion that the Prandtl limit may be violated, and suggest that a larger plate size produces more lift, in much the same way as a larger aspect ratio does. However, the fact that most of the tests with large plates were performed with high aspect ratio cylinders makes it difficult to separate the influence of one from the other. As a final note, the lift generated through the use of sufficiently large endplates is seen to be approximately half that predicted by potential flow, which is in keeping with observations that the flow patterns for viscous flow past a rotating cylinder are similar to those at half the velocity ratio in inviscid flow.

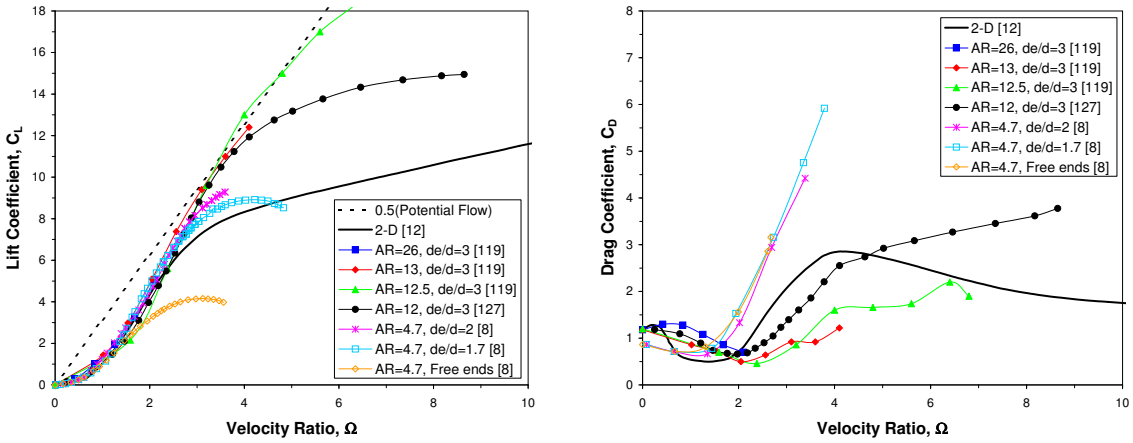

(a) Lift coefficient

(b) Drag coefficient

Figure 3.11: Effect of endplates on the lift and drag of a rotating cylinder.

The effect of endplates on drag behavior is less well defined. Prandtl[9] indicated that spinning endplates acted to separate each tip vortex into two separate parts, reducing their kinetic energy and decreasing the induced drag. A comparison of the Göttingen results with and without endplates (see Figure 3.11b) confirms a minor reduction in the

drag when plates of size $d_e/d = 2$ were employed, but suggests that the smaller size of $d_e/d = 1.7$ was ineffective in reducing C_D. Thom[119] connected drag behaviour with the endplate size relative to the thickness of the fluid layer dragged round with the cylinder at high Ω, noting that the rise in C_D occurs when the size of this hollow cylinder of air matches the plate diameter d_e. Examination of the drag data indicates that the use of larger plates ($d_e/d \geq 3$) can result in a considerable reduction of the drag at high velocity ratios. However, as with the lift, the influence of aspect ratio on the observed results cannot be ruled out.

In his final report on the subject of rotating cylinders, Thom[119] expanded the concept of endplates by examining the effect of using multiple circular discs, which he called fins, positioned at regular intervals along the span. He hoped that the use of these fins would produce a flow that was more similar to the potential flow state at $\Omega = 2$, for which the front and rear stagnation points merge and detach from the cylinder surface. In this condition, no wake forms as the air around the cylinder is contained within the enclosed streamline region, so that the drag would thus be very small.

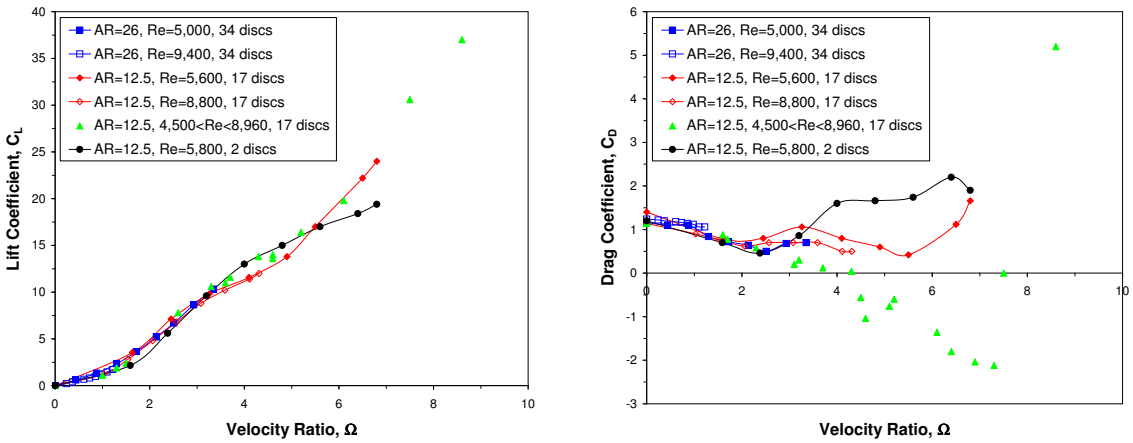

(a) Lift coefficient

(b) Drag coefficient

Figure 3.12: Thom's[119] results for the effect of multiple endplates of size $d_e/d = 3$ on the lift and drag of a rotating cylinder.

The experiments considered three different configurations. In the first, plates of size $d_e/d = 3$ were positioned at intervals of $\Delta z/b \approx 0.03$ along the span of a large aspect ratio cylinder ($AR = 26$). In the second, the same size plates were positioned at intervals of $\Delta z/b \approx 0.06$ along the span of a smaller cylinder ($AR = 12.5$). A small number of tests with plates of size $d_e/d = 1.5$ positioned along the larger cylinder, using the smaller interval, were also performed. In all cases, test conditions of $4.5 \times 10^3 \leq Re \leq 1.25 \times 10^4$ and $\Omega \leq 9$ were maintained. The results were then compared to data obtained with only

two endplates of size $d_e/d = 3$.

Thom reported that the use of discs along the entire span enabled very high lift coefficient at high velocity ratios ($C_L = 36$ at $\Omega = 8.6$, see Figure 3.12a). This effect on the lift was attributed to secondary flow around the numerous fins. A drag penalty, as compared to the plain case, was noted for $\Omega < 2$, but the fins had a drastic effect on C_D at higher rotational rates. For all non-zero Ω, drag values continuously decreased until they became negative for $\Omega > 4$, reaching a minimum value of $C_D = -2.12$ before beginning to increase again at $\Omega > 7.3$ (see Figure 3.12b). Thom suggested that the onset of negative drag (i.e. the apparent production of thrust) may have been a by-product of wall interference from using a closed working section for the tests, and that it did not necessarily translate to negative drag in free-air conditions. No attempt at correction of the results was mentioned.

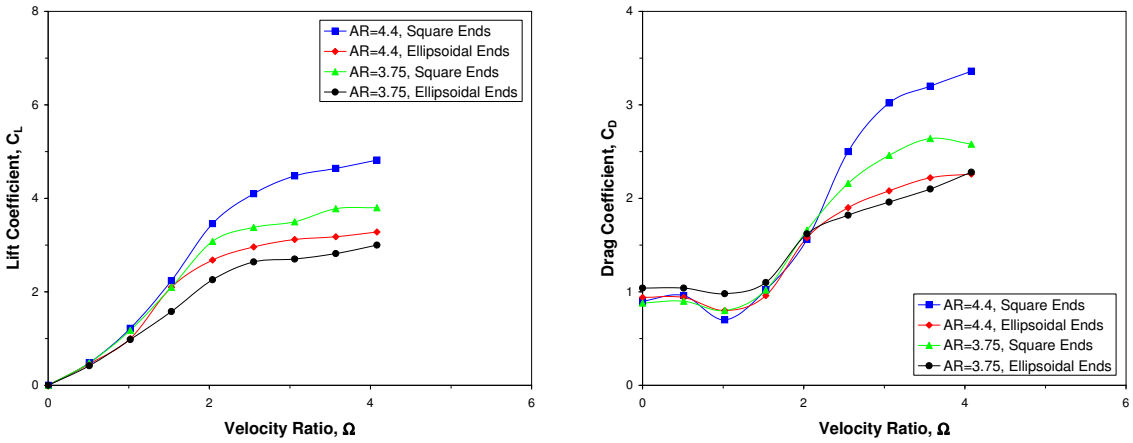

(a) Lift coefficient

(b) Drag coefficient

Figure 3.13: Thom's[115] results for the effect of endshape on lift and drag at $Re = 2.19 \times 10^4$.

It should also be noted that Thom had previously expressed doubt over the accuracy of his results at the sort of low Reynolds number used in the experiments, and that the negative drag was only seen in one set of tests performed with a new balance; in the other experiments, a reduction of drag due to the fins was observed, but C_D remained positive at all times. Furthermore, Thom's work with multiple endplates was carried out with large aspect ratio cylinders, which would have affected the results, making it difficult to attribute the improved lift and drag wholly to the use of fins.

As part of his extensive investigation into the effects of end conditions, Thom[115] also briefly examined the influence of endshape on lift and drag. In 1924, he tested regular-shaped 'square ended' cylinders against 'rounded ended' cylinders with ellipsoidal tips at flow conditions of $Re = 2.19 \times 10^4$ and $\Omega \leq 4$. Two different aspect ratios ($AR = 3.75$

and 4.4) were considered. The results (see Figure 3.13) showed that the cylinder with ellipsoidal ends generally produced less drag and less lift than a regular cylinder of the same diameter at the same Reynolds number. This reduction in magnitude was more pronounced for the lift than the drag, and appeared sooner too: a change in C_L was apparent for all $\Omega > 1$, but the drag only differed significantly for $\Omega > 2$.

3.3.6 Experimental Results 5: Effect of Surface Roughness

Surface roughness is a long established and effective means of influencing the flow around a stationary circular cylinder across a broad range of Reynolds numbers that span the transition between sub-critical to post-critical regimes and beyond. For subcritical flows, the effect of surface roughness on drag is to cause the large reduction in C_D that usually occurs at or near the critical Reynolds number to be displaced to lower Re by promoting premature transition to turbulent flow.

By contrast, the effect of surface roughness on rotating cylinder flow has largely been ignored in the literature. Until very recently, the first, and only, examination of the effects was by Thom[115,119] in 1925. These tests were quite crude, with roughness being effected by gluing sand (of unspecified size) to the surface of a cylinder of $AR = 8.1$ that was tested in the range $\Omega \leq 5.56$ and $1.63 \times 10^4 \leq Re \leq 3.33 \times 10^4$. Thom noted only a small effect from the roughness, with a slight increase in C_L at high velocity ratios, but a corresponding increase in C_D at the same Ω (see Figure 3.14). Zdravkovich[120] noted that at the Reynolds numbers of the tests the laminar boundary layer is extremely stable and suggested this as a reason for the lack of effect.

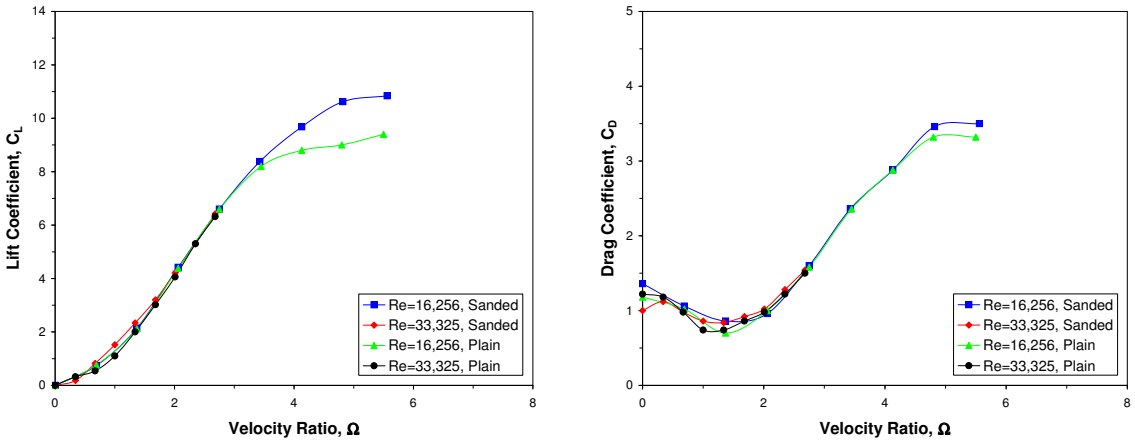

(a) Lift coefficient

(b) Drag coefficient

Figure 3.14: Thom's[115] force results with a sanded cylinder of aspect ratio $AR = 8.1$.

Recent experiments investigating the effect of arc-type grooves for the case of a rotating cylinder suggest roughness is more effective at low velocity ratios. In 2005, Takayama & Aoki[194] performed a series of experiments using a grooved cylinder, of $AR = 2.15$ and fitted with endplates of $d_e/d = 1.375$, that was tested in the range $4 \times 10^4 \leq Re \leq 1.8 \times 10^5$ and $\Omega \leq 1$. A total of thirty-two spanwise U-shaped grooves were added around the circumference of the cylinder and three different groove depths were investigated (see Figure 3.15). Pressure tappings on both the un-grooved portions and inside the grooves were used to measure the surface pressures, and the lift and drag coefficients were then calculated from integration of the pressure distributions. Measurements were also made with a smooth cylinder, for which Takayama & Aoki found both lift and drag to be Reynolds dependent in the same way that Swanson[12] showed (see Figures 3.16a and 3.17a), so as to act as a basis for comparison.

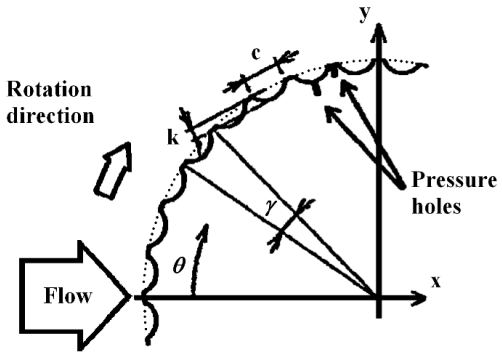

Type	A	B	C
k (mm)	0.30	0.58	0.94
d (mm)	80		
c (mm)	6.76		
γ (deg)	11.25		
k/d	3.75×10^{-3}	7.25×10^{-3}	11.75×10^{-3}

Figure 3.15: Cross-section and specification of Takayama & Aoki's[194] cylinder with grooves.

With the addition of grooves, the lift and drag characteristics when $\Omega > 0$ depended on the initial conditions for the grooved cylinder at $\Omega = 0$: specifically, the Reynolds dependent reduction in lift and drag with increasing velocity ratio was now limited to those values of Re for which sub-critical or critical conditions existed when the cylinder was stationary. For the type A groove (smallest depth), the presence of critical Reynolds number conditions was limited to the range $6 \times 10^4 \leq Re \leq 9 \times 10^4$. The type B grooves pushed the location of the critical Reynolds region down to $Re < 6 \times 10^4$. The use of type C grooves (where the groove depth was greatest) revealed only supercritical behaviour throughout, presumably because the critical Re region had been wholly shifted to $Re < 4 \times 10^4$. Outside of these regions of subcritical and critical flow the lift and drag behaved as they would for supercritical flow. In this regime, lift increases monotonically with Ω and drag (for $\Omega \leq 1$) is constant (see Figures 3.16b to d and Figures 3.17b to d).

Although increasing the groove depth resulted in the progressive elimination of the Re dependent reduction in lift and drag, it was not completely beneficial. Whilst the lift curve slope was initially increased by the addition of grooves (by a factor of ≈ 2.5), with greater

groove depth it was slowly reduced in magnitude: with the type C grooves, the lift curve slope was of the same value as for a smooth cylinder, but without any non-linearity in the shape of the curve. Similarly, although the drag is at first reduced, and the relationship between drag and velocity ratio decoupled, by the use of grooves, increasing the groove depth causes the value of C_D to progressively rise. Such behaviour is a consequence of the effects of the grooves on separation.

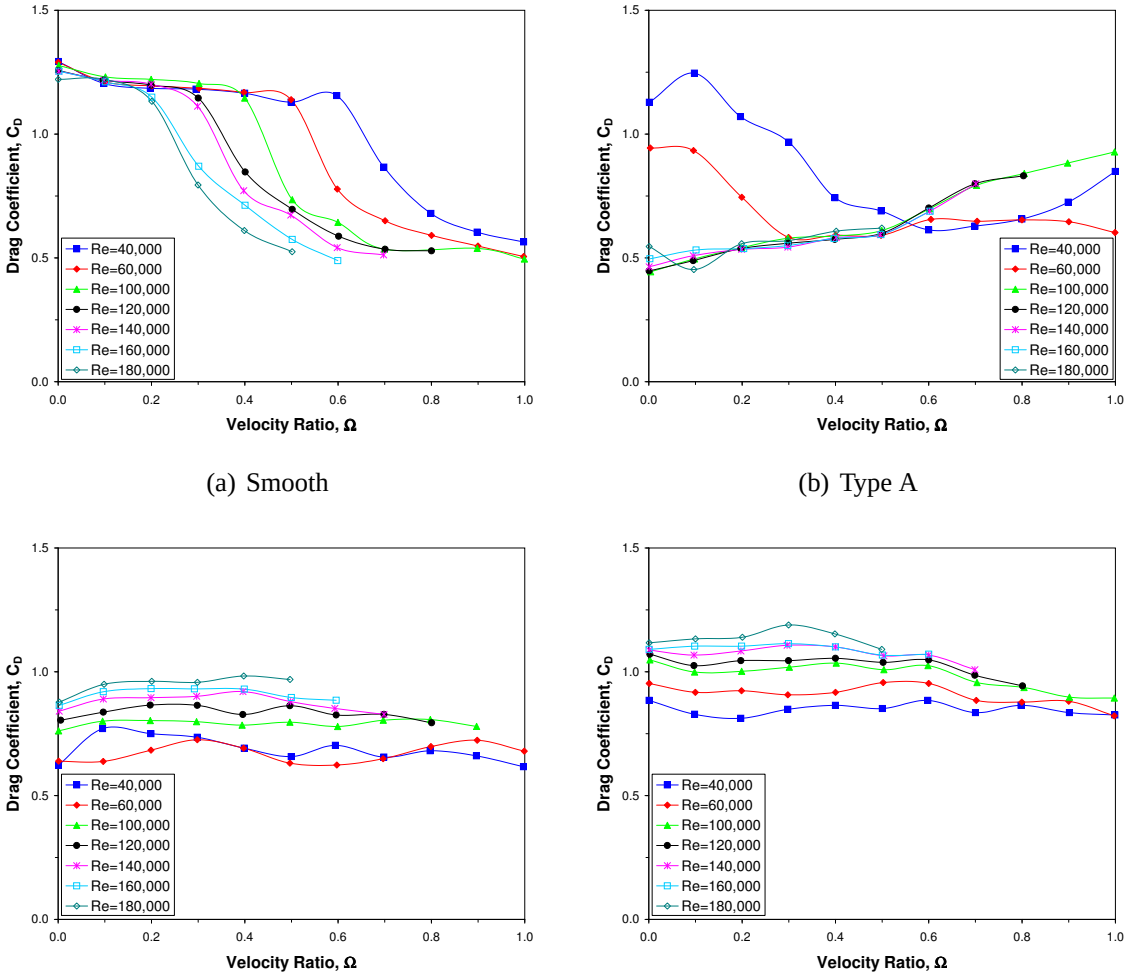

(a) Smooth

(b) Type A

(c) Type B

(d) Type C

Figure 3.16: Drag of a grooved cylinder.[194]

With sufficient groove depth the flow is already turbulent from the start ($\Omega = 0$) and there is no sudden downstream shifting of the separation point on the upstream moving wall that is associated with the inversion of the Magnus effect. Instead, for $Re = 1 \times 10^5$ and $\Omega \approx 0.4$ (where Magnus effect inversion would otherwise occur), the wake was found to have rotated further in the direction of rotation than would be the case for a smooth cylinder, hence the initial increase in C_L that is visible in the lift coefficient data for a grooved

cylinder. However, Takayama & Aoki also reported that as groove depth was increased the separation point on the downstream moving wall moved upstream, thus making the separation points on the two sides of the cylinder more symmetrical and causing an increase in the wake width. These changes are responsible for the increase in drag and reduction in lift, as compared to type A and type B grooves, that are seen in the type C results.

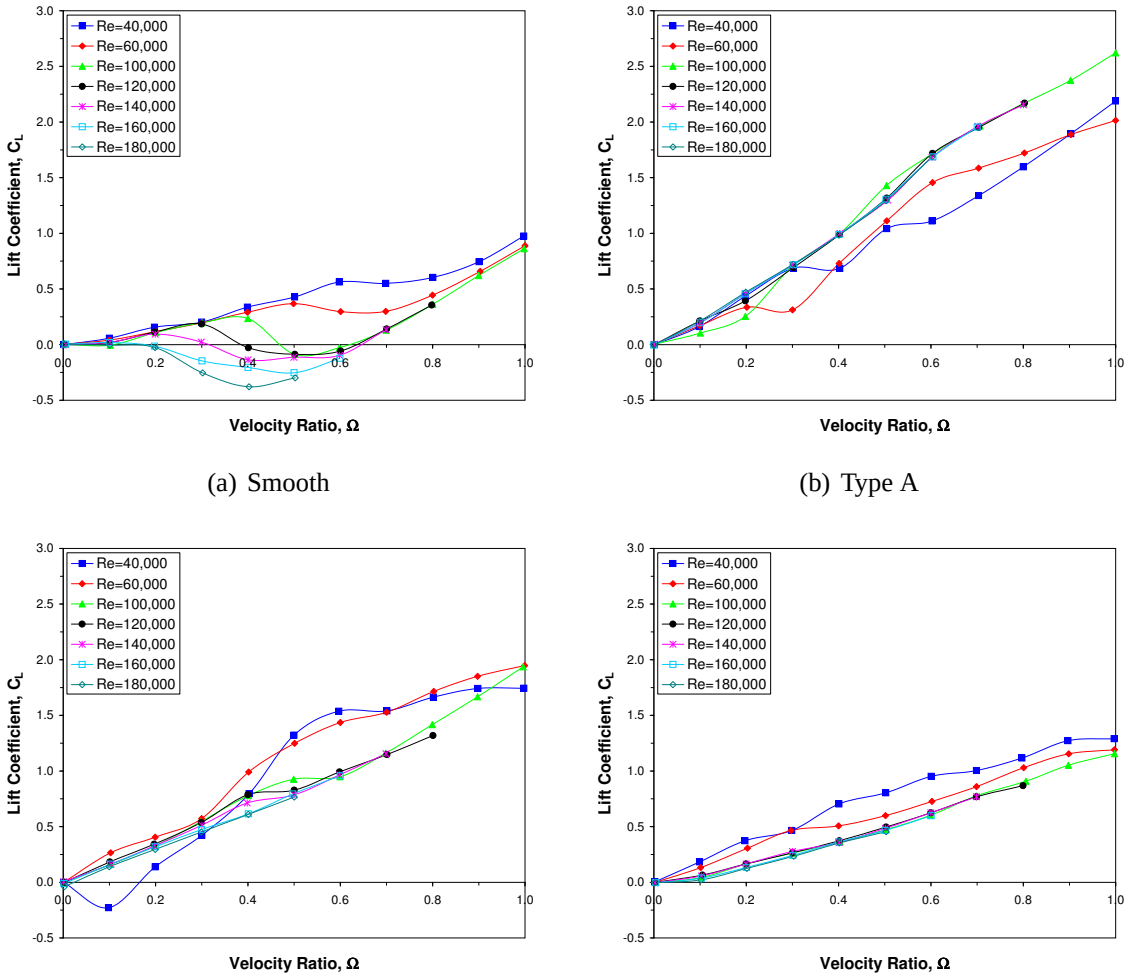

(a) Smooth

(b) Type A

(c) Type B

(d) Type C

Figure 3.17: Lift of a grooved cylinder.[194]

The Takayama & Aoki results show that the effects of spanwise grooves on a rotating cylinder are equivalent to the effects of the grooves when $\Omega = 0$, which are themselves in keeping with the known effects of distributed surface roughness on stationary cylinders.[195,196] This would suggest that the effects of surface roughness on a rotating cylinder should be identical to those of grooves, i.e. both stationary and rotating cylinders should respond to surface roughness in the same way. The lack of any effect of roughness re-

ported in the Thom data may be a consequence of the low Reynolds numbers and the lack of detailed measurements at low velocity ratios. In addition, the simplistic fashion in which those tests were performed and the choice of roughness employed, which may not have been suitable for the Reynolds numbers at which the tests were run, could also have had an effect. In any case, more experiments are needed to confirm the apparent benefits of surface roughness, particularly with regards to the force behaviour when $\Omega > 1$.

3.3.7 Numerical Results

Lift and drag results from a number of computational studies, spanning the entire range of Reynolds numbers for which data are available, are shown in Figure 3.18. The more extensive results are for a narrow range of Reynolds numbers between $100 \leq Re \leq 1 \times 10^3$. Results at higher and lower Re are either very limited in number, and their legitimacy questionable, or limited to only a small range of velocity ratios ($\Omega \leq 1$).

Force results for very low Reynolds numbers ($Re < 50$) generally come from the early computational studies performed in the 1970s and 1980s. Data from these sources tends to show considerable discrepancies, and even contradictions, regarding the magnitude of the aerodynamic force coefficients and their behaviour with changing velocity ratio. Some of these early numerical works have since been criticised by later researchers for their use of course grids, small domains, and inadequate outer boundary conditions.[197] The scatter in their force coefficient results is likely explained through such issues. A lack of experimental force measurements in this Reynolds number range has prevented any validation of the numerical results, adding to the uncertainty.

The majority of studies at Reynolds numbers higher than $Re = 1 \times 10^3$ are usually directed towards the understanding of vortex shedding phenomena, rather than the determination of C_L and C_D. When lift and drag results are presented, they tend to focus only on the fluctuating nature of the forces, not on the mean values. The Elmiligui *et al.*[176] results are a notable exception, and also include data from three-dimensional simulations, but the velocity ratio range is too small to provide a meaningful comparison with either experimental results or other CFD data. The only other three-dimensional numerical study[198] of rotating cylinder flow provided data for just a single velocity ratio of $\Omega = 5$.

Analysis of Figure 3.18 indicates that the lift results appear to be largely independent of Reynolds number. A number of studies[197, 199, 200] have reported that the slope of the lift curve increases slightly with decreasing Re, but any such effect is much less prominent than the substantial Reynolds number related changes in the drag. This difference in re-

sponse to changing Re arises from the contrasting importance of the pressure and viscous contributions to lift and drag.

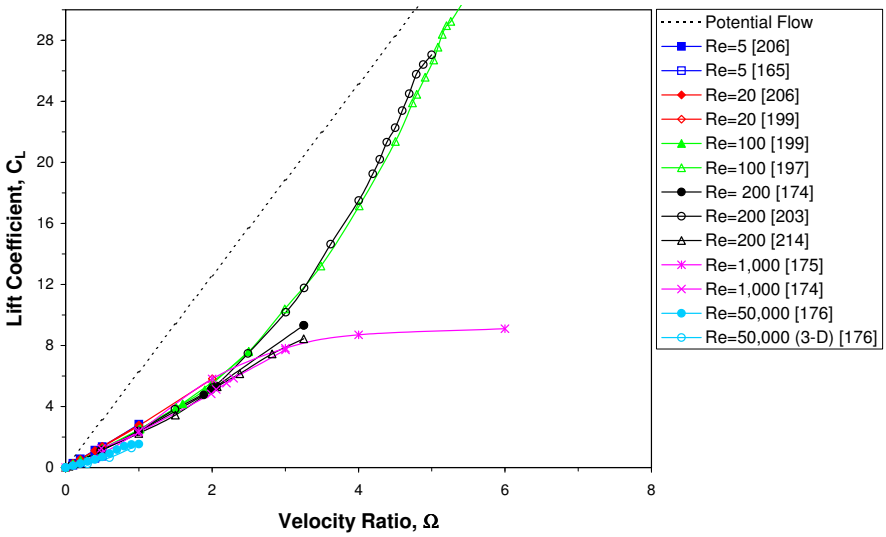

(a) Lift Coefficient

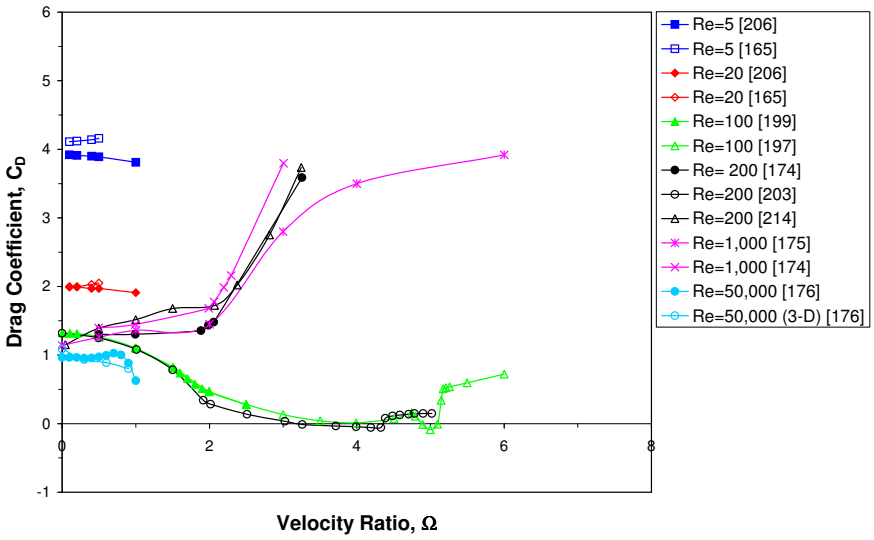

(b) Drag Coefficient

Figure 3.18: Numerically derived force data for a rotating cylinder. Unless otherwise noted, results are for a two-dimensional cylinder.

Both experimental and numerical works indicate that the majority ($> 90\%$) of the lift comes from the pressure distribution, and that the magnitude of the pressure contribution to lift increases with increasing Re.[155, 199] Since a rise in Reynolds number mostly affects the frictional forces, which have only a negligible contribution to the total lift, the value of C_L is practically unaffected by the Reynolds number. In contrast, the friction drag is known to be of the same order as the pressure drag, and both components are found to

decrease with increased Reynolds number.[200] Thus, C_D depends more strongly on Re. This is particularly so at very low Reynolds numbers, resulting in the large change in the magnitude of the drag coefficient seen between the results at $Re = 5$ and those at $Re = 20$.

Substantial differences between the various data sets are also apparent in the variation of lift and drag with velocity ratio. In keeping with the experimental data, the numerical results for $\Omega \leq 2$ are largely in agreement and the lift is similar to potential flow, in that C_L is seen to be a linear function of the velocity ratio, though it is much smaller in magnitude than the values predicted by theory. For higher velocity ratios, the numerical lift results are broadly divided into three: (1) those that indicate that the lift continues to increase with velocity ratio, violating the Prandtl limit and drawing ever more closer to the potential flow values (for $\Omega = 12$, Stojković *et al.*[197] reported a lift value of $C_L = 74$ whereas potential flow at the same value of Ω predicts a lift coefficient of $C_L = 75$); (2) those that suggest a more modest lift increase, which may or may not reach an upper limit; and (3) those that simply do not extend to high enough velocity ratio to be definitively counted amongst the other two types.

The existence of an upper limit for lift in some of the two-dimensional numerical results is, although in keeping with experimental findings, somewhat surprising as the levelling off of C_L seen in experimentally derived data seems to be associated with the three-dimensional effects of a finite aspect ratio. In support of their findings, Chew *et al.*[175] have suggested that asymptotic values of lift and drag at high velocity ratio occur because for $\Omega > 2$ the two-dimensional flow structure approaches some form of self-similarity that manifests as a similarity in the pressure and shear stress distributions (see §3.4.3 and §3.5). The formation of a dividing streamline and its interference with vortex shedding were also noted as reasons for the existence of a maximum lift. Sengupta *et al.*[192] have criticised the hybrid vortex method used by Chew *et al.*[175] (who did themselves note that it can give rise to large numerical diffusion) and suggested that the use of this technique may be responsible for the difference between other results and those of Chew *et al.*

A similarly fundamental difference occurs between the various drag data sets too. The results from those simulations which reported the lift to continuously increase show that the drag coefficient continuously decreases with velocity ratio, to the point where small amounts of net thrust are produced at high Ω. Such negative drag is said to arise because the pressure component of C_D decreases quickly at high velocity ratio, becoming negative, whilst the skin friction component increases more slowly with velocity ratio.[197,199] For these studies, the combination of near-zero drag and very high lift produces lift-to-drag ratios in excess of $C_L/C_D = 1000$. By contrast, the drag results from the data sets

that predicted a more modest lift indicate that C_D continuously increases with velocity ratio, initially doing so quite slowly before a more rapid rise for $\Omega > 2$.

Neither of the two types of results described above completely captures the response seen in the experimental drag data. Examination of Figure 3.18b shows that the first type of result correctly predicts the gradual reduction in C_D that occurs for $\Omega \leq 1.5$, but fails to predict the sharp rise at higher velocity ratio. The second type correctly predicts this increase, but fails to predict the reduction of C_D at low Ω.

The considerable disagreement in the numerically predicted values of the lift and drag is made more puzzling by the fact that the flow patterns observed in most computational simulations are qualitatively the same. At least some of the deviation between the force results of different studies may be regarded as a consequence of the dissimilar numerical strategies employed, but there is no obvious link between any particular method and a particular trend in lift and drag; the studies from which the conflicting data for $Re = 100, 200$ were drawn (as shown in Figure 3.18) were all performed using different numerical methods, yet some agree and some do not. Nor can a trend with regards to Reynolds number be established.

3.4 Boundary Layer Measurements

Initial discussion of the boundary layer on a rotating cylinder was begun by Prandtl[108] as a means to explaining the Magnus effect, but his comments were purely qualitative. Later investigation of boundary layer phenomena has largely concentrated on the determination of the location of the separation points, measurement of the boundary layer velocity profiles, and measurement of the shear-stress distribution. Most of this work has been experimental in nature, though some numerical and analytical results are available. The latter have also focused on understanding the nature of the time-dependent development of the boundary layer and ascertaining the minimum value of the velocity ratio necessary to completely inhibit boundary layer separation.[182, 201]

That the rotating circular cylinder has both an upstream moving and downstream moving wall has meant that the problem has also drawn interest as a more general study of unsteady separation. Furthermore, since many of the same separation and vortex initiation dynamics are evident on both the rotating cylinder and more complex bodies, such as pitching wings and autorotating bodies, the simple geometry of the rotating cylinder offers an insight into the boundary layer separation behaviour observed in these more complicated cases.[155]

3.4.1 Velocity Profiles and Boundary Layer Thickness

Thom[117] performed what may be the first experimental measurements of the boundary layer on a rotating cylinder. He tested a cylinder of $AR = 5.41$, that spanned the tunnel horizontally, for $Re = 1.85 \times 10^4$ and $\Omega = 2$. However, Thom's results were derived from measurements of the total and static pressure in the boundary layer, in both still and moving air, that were taken on separate runs (i.e. not concurrently) and so may be of limited use. Furthermore, Thom noted also that the positioning of the tubes may have adversely affected the results too. Thom's findings showed that the boundary layer was distorted by rotation so that it was thicker on the side where the direction of rotation opposed the freestream, and thinner where the direction of rotation coincided with the freestream. Thus, the effective body shape was distorted by rotation. In addition, Thom noted that the boundary layer as a whole was thicker at lower rotational speeds and that there was no net circulation in the wake.

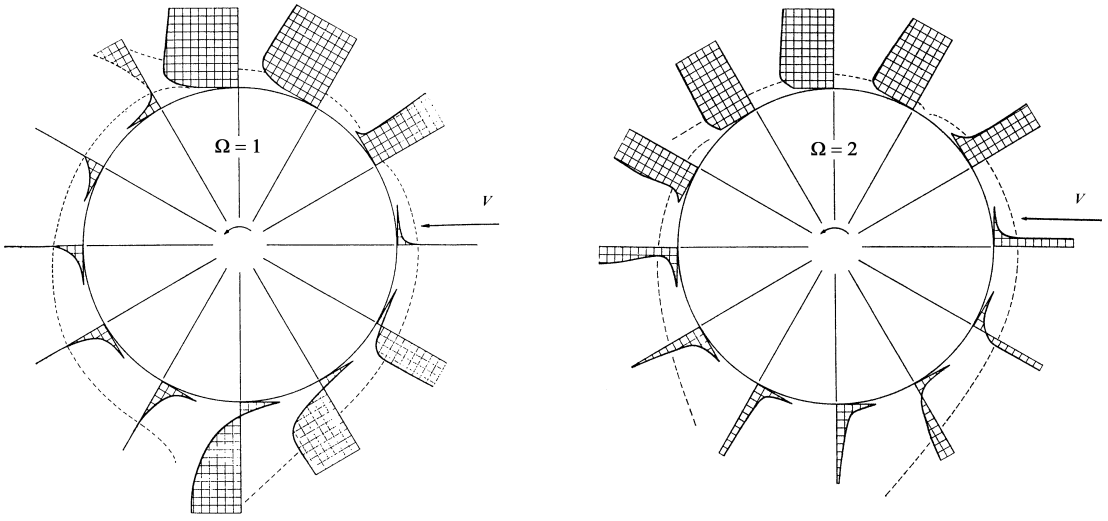

(a) $\Omega = 1$ (b) $\Omega = 2$

Figure 3.19: Swanson's[12] velocity profiles around a rotating cylinder at $Re = 4 \times 10^4$.

The next experimental investigation of the boundary layer was by Swanson.[12] Alongside his extensive force tests, Swanson carried out measurements of the boundary layer velocity profile at $Re = 4 \times 10^4$ and $1 \leq \Omega \leq 2$. His findings (see Figure 3.19) led him to suggest that the origin of the boundary layer on a rotating cylinder (which he defined as the point from which the shear in the boundary layer has opposite direction on opposite sides of the body) did not coincide with the front stagnation point, as it does when the cylinder is stationary. Rather, Swanson argued that the origin lay where the surface velocity was equal to the freestream i.e. at the point of zero relative velocity (see Figure

3.20). Thus, due to the effects of rotation on the relative velocities, increasing Ω causes the boundary layer origin to become displaced in the direction of rotation, contrasting the movement of the stagnation point.

Swanson's analysis of the boundary layer also revealed several more items of note. Swanson used evidence from the force characteristics to reason that for $\Omega \geq 1$ both the upstream moving and downstream moving surface boundary layers are in a fully developed turbulent state. He suggested that the fact that the drag of a rotating cylinder at $\Omega \approx 1$ is at a minimum value that corresponds to that measured on a stationary cylinder with fully developed turbulent boundary layers, as well as the fact that no further dependence on Reynolds number was seen in the behaviour of either the lift or the drag coefficients for $\Omega > 1$, supported this assumption.

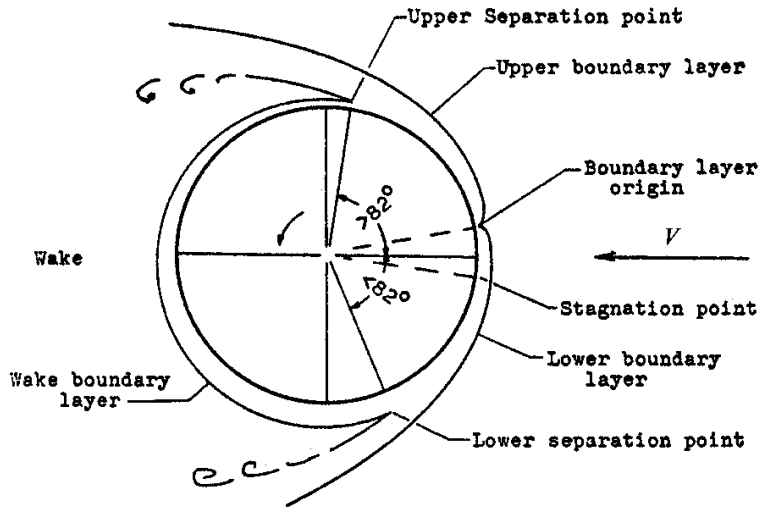

Figure 3.20: Swanson's[12] concept of the origin of the boundary layer on a rotating cylinder.

Additionally, Swanson observed that the 'knee' of the lift curve at $\Omega = 3$ coincided with the boundary layer origin reaching the meridian of the cylinder ($\beta = 90°$). Swanson noted that, at this point, his definition of a boundary layer origin was no longer applicable, as for all velocity ratios greater than $\Omega = 3$ the cylinder surface is everywhere travelling at a velocity beyond that which can be attained by the fluid near the wall. In much the same way that Prandtl predicted an upper limit to the lift would occur when a closed streamline formed around the cylinder, Swanson felt that when the boundary layer origin reached the top of the cylinder this situation might impose a similar restriction on C_L. However, his lift results showed that C_L continued to increase beyond this threshold, albeit at a slower rate.

Swanson attributed this increase in lift past the 'knee' to rotation of the flow pattern due to the pressure field induced by changes in the vorticity shed from the downstream moving surface boundary layer, and he suggested that some limit should exist as the wake formed from the separating boundary layers rotates around to a position near the front of the cylinder ($\beta = 0°$). No such limit was reached within the extent of the data taken by Swanson ($\Omega \leq 17$).

Peller[151–153] confirmed Swanson's argument on the origin of the boundary layer by measuring the thickness distribution, δ, along both the upstream and downstream moving surfaces at $Re = 4.8 \times 10^4$ and $\Omega \leq 2$. Comparison of Peller's boundary layer profiles to Swanson's generally showed good agreement (see Figures 3.19 and 3.21). Peller attributed discrepancies between the two results to differences in Reynolds number and inaccuracies resulting from Swanson's method, which did not include any hotwire measurements.

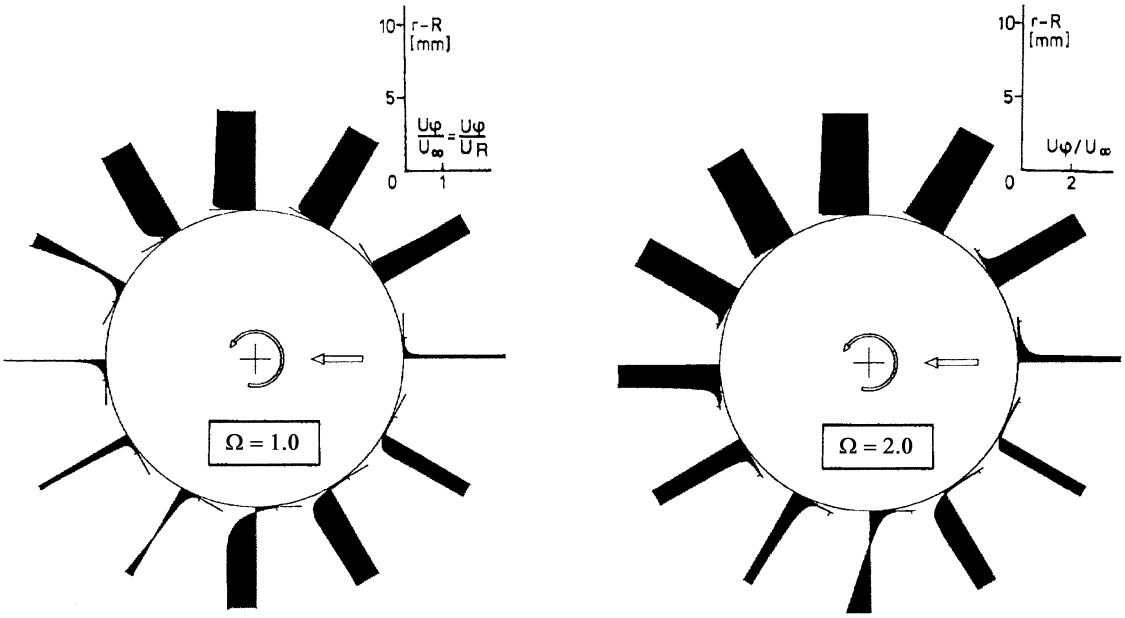

(a) $\Omega = 1$ (b) $\Omega = 2$

Figure 3.21: Peller's[152] velocity profiles around a rotating cylinder at $Re = 4.8 \times 10^4$.

Using his results, Peller recorded the separation angles as measured from both the forward stagnation point and the approximate location of the boundary layer origin (see Figure 3.22). He noted that only when the cylinder was stationary did the two angles coincide and concluded, like Swanson, that only for this condition of $\Omega = 0$ are the stagnation point and the boundary layer origin the same. Peller also repeated his boundary layer measurements with a cylinder surface temperature of $100°$ C and reported that wall temperature had a strong beneficial effect on the velocity profiles near the separation points.[152]

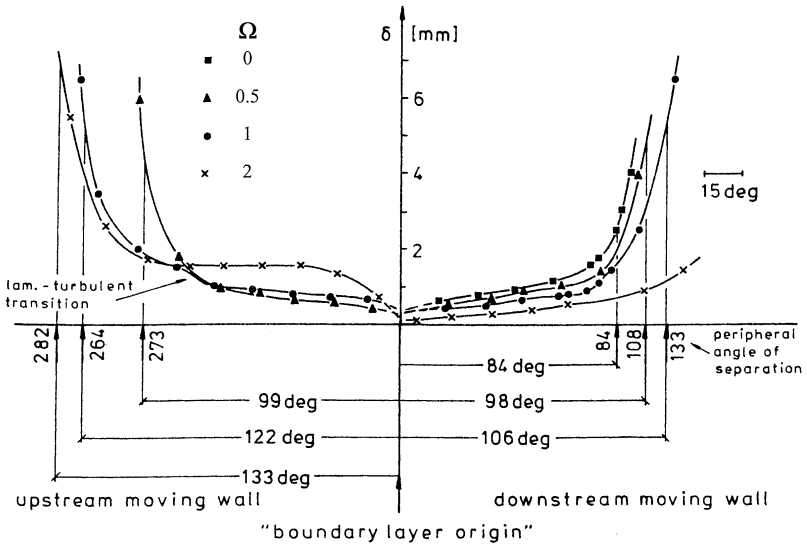

Figure 3.22: Peller's[152] results for the distribution of boundary layer thickness at $Re = 4.8 \times 10^4$.

3.4.2 Location of the Separation Points

It is known that the separation points on a rotating circular cylinder are affected by rotation and behave differently from the non-rotating case. For instance, the effects of rotation mean that, where they occur, separation points for a rotating cylinder are not located at the wall, but at a certain height above it. In addition, separation is delayed on the downstream moving wall because the cylinder surface imparts kinetic energy to the local boundary layer. On the upstream moving wall the rotation opposes the freestream and reduces the kinetic energy of the boundary layer, which promotes early separation. As such, the boundary layer separation points, and the wake as a whole, are displaced in the direction of rotation of the cylinder. However, for large enough velocity ratios (typically $\Omega > 2$) the effects of rotation are such that separation is completely suppressed on both walls.[108, 182]

Both experimental[152, 155, 202] and numerical[169, 175] studies generally show the separation point for the downstream moving wall to move in an almost linear fashion with increasing velocity ratio (see Figure 3.23). Results for the upstream moving wall reveal far less change with Ω. Such findings are consistent with the delay of separation on the downstream moving wall and explain the narrowing of the wake with increasing Ω. The literature also indicates that for higher Reynolds numbers ($Re > 6 \times 10^4$) the boundary layer separation point on the upstream moving wall is strongly dependent on both Re and Ω.[155] For example, at $Re = 1 \times 10^5$, Takayama & Aoki[194] have reported a sudden downstream shift in the position of the separation point on the upstream moving wall when

$\Omega \approx 0.4$. This motion makes the separation points more symmetric and the observation is consistent with the phenomenon of Magnus effect inversion and its associated loss of lift.

Results from the surface pressure measurements of McLaughlin *et al.*[155] for $3.6 \times 10^4 \leq Re \leq 1.78 \times 10^5$ indicate that the location of the separation point on the downstream moving wall is largely insensitive to Reynolds number. This appears to be in conflict with the data shown in Figure 3.23. However, the visible differences in the downstream moving wall separation point locations may also stem from the difference in aspect ratio of the test cylinders, or may be associated with the fact that several studies[12,150,169] have noted that there are often considerable time-dependent variations in the position of the separation points. Thus, the data obtained from any particular study may differ from other results depending on which point in the oscillation cycle, described as sinusoidal by Cheng *et al.*,[169] measurements were taken.

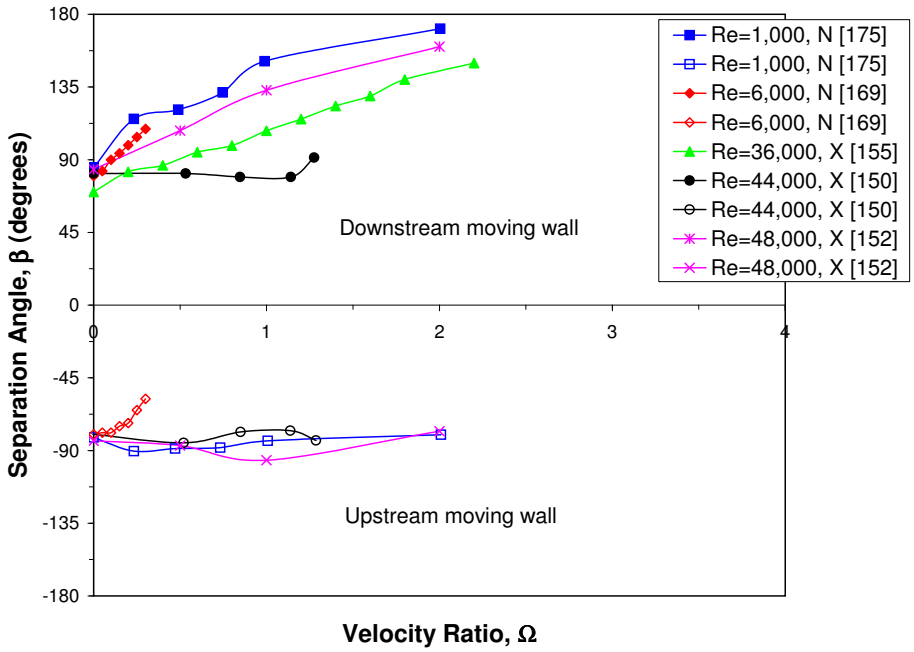

Figure 3.23: The variation of the separation point angular location with velocity ratio. 'N' denotes data from numerical studies whereas 'X' denotes experimental results.

More generally, discrepancies between the various results for the separation point locations may be associated with the difficulty of defining a separation point for a moving wall. This is because application of the classical vanishing wall stress criterion that is usually used to identify separation is limited to steady flow over fixed walls and is not necessarily a meaningful indication of separation in the case of a moving wall. Thus, studies investigating the separation points on a rotating cylinder have generally preferred the so-called MRS criterion, in which the separation point is defined as the point where

both the skin friction and the fluid velocity become zero within the attached boundary layer as it appears to an observer moving with the separation, as this is said to be a more appropriate criterion for separation on moving walls.

However, whilst the MRS model for the downstream moving wall is supported by both experimental[152,202] and theoretical[182] studies, the evidence for its applicability to the upstream moving wall is less conclusive. Although, the flow visualisation study of Ludwig[202] and analytical study by Ece *et al.*[182] appear to support the MRS criterion for both walls, Peller[152] reported that, based on his experimental findings, the MRS method could not be used at all for the upstream moving wall. Instead, reliable determination of the separation points on this wall could only be established through simultaneous observation of the velocity profiles, the root-mean-square values of velocity fluctuations, and the boundary layer thickness. A similar approach was adopted by Aldoss & Abou-Arab[150] in their experiments.

3.4.3 Shear Stress Distribution

Investigation of the shear stress distribution around a rotating cylinder appears to be limited to the work of Aldoss & Abou-Arab,[150] Cheng *et al.*,[169] and Chew *et al.*[175] Aldoss & Abou-Arab[150] estimated shear stress based on their experiments with a cylinder of $AR = 10.5$ at $\Omega \leq 1.25$ and $Re = 4.42 \times 10^4$. The magnitude of the mean shear stress was seen to be a function of both the angular position around the cylinder's circumference and the velocity ratio (see Figure 3.24). Shear stress increased with Ω on the upstream moving wall (where the relative velocity is larger) and decreased with Ω on the downstream moving wall. This decrease only occurred for $\Omega < 1$, after which the shear stress then began to increase on the downstream moving wall too. However, shear stress on the downstream moving wall remained smaller than on the upstream moving wall throughout. The change to increasing shear stress on the downstream moving wall was said to possibly be due to transition to turbulent flow on the cylinder's surface. Such behaviour is consistent with the changes in the relative velocities between the fluid and the cylinder.

Similar trends were reported in the numerical studies of Cheng *et al.*[169] and Chew *et al.*[175] However, the study by Chew *et al.* also found that a limiting value of the mean shear stress occurred at high Ω, which Chew *et al.* took to mean that the growth of the recirculating region with velocity ratio imposes a fixed velocity gradient at the wall that does not change even though the cylinder itself may be rotating faster. In addition, the mean shear stress distribution on the surface of the cylinder showed self-similarity for $\Omega > 3$.

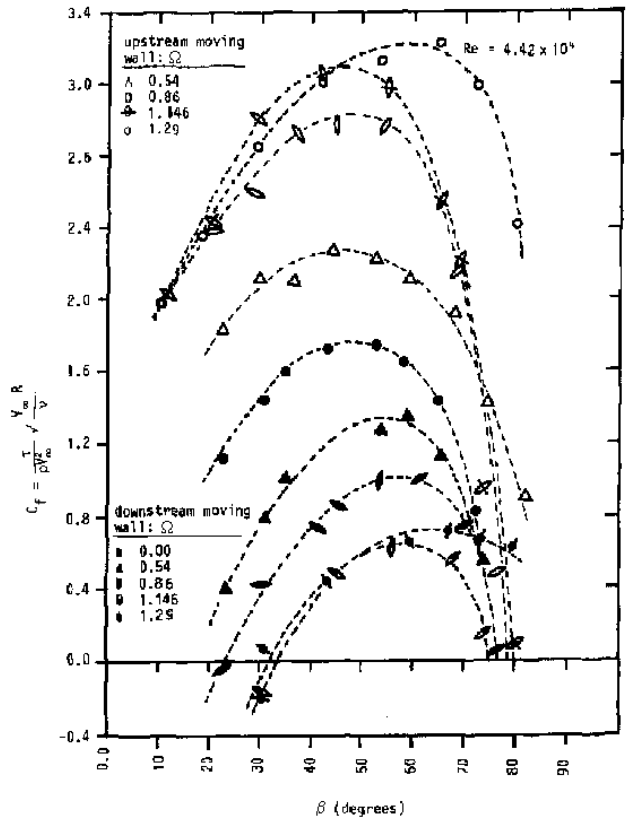

Figure 3.24: Experimental[150] shear stress distribution for a rotating cylinder at $Re = 4.42 \times 10^4$.

3.5 Surface Pressure Distribution

Experimental investigations of the variation of the lift and drag with velocity ratio are mainly limited to direct measurements of the forces, and, hence, often give little physical insight into the details of the flow behaviour around the cylinder. Determination of the aerodynamic forces through measurement of the pressure distribution around the surface of a rotating cylinder can be much more helpful in this regard, yet such investigations are quite scarce. This is because of the difficulty associated with physical measurement of the pressure at a point on a rotating body. Analytical and numerical assessments of the pressure distribution are more readily accomplished, but suffer from the same restrictions and failings as other data determined by these means of investigation.

3.5.1 Analytical Results

Analytical studies based on boundary layer theory, such as those of Glauert[178,179] and Moore,[180] do not generally provide information on the surface pressure distribution, thus

leaving potential flow as the main theoretical reference point. A selection of predicted pressure distributions for inviscid flow at a range of velocity ratios are shown in Figure 3.25. In accordance with the streamline patterns of Figure 3.3, the most notable trends observable are the very large magnitudes of the minimum pressure and the disappearance of the stagnation points for $\Omega > 2$.

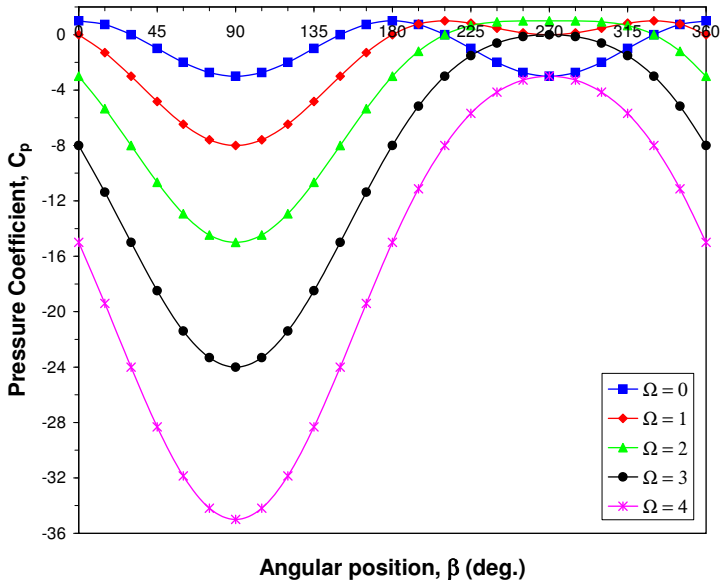

Figure 3.25: Potential flow surface pressure distribution for a rotating cylinder.

3.5.2 Experimental Results

The earliest quantitative measurements of the pressures around a rotating cylinder were by Lafay[109] in 1910. Lafay's method for measuring the pressure was somewhat crude, involving a stationary probe placed adjacent to the spinning surface of the cylinder (see Figure 3.26a). Though effective, this approach came with several technical problems and operational limits. In addition, Lafay did not produce a detailed graphical representation of the pressure distribution, but used the actual pressure readings to confirm his observations of the inversion of the Magnus effect.

The first extensive investigation of the pressure distribution was performed by Thom[116] as part of his comprehensive series of experiments into many aspects affecting the flow around a rotating cylinder. Using a cylinder of $AR = 7.7$ (spanning the test section and with no endplates), Thom took measurements around the mid-span of the cylinder for $7.8 \times 10^3 \leq Re \leq 3.1 \times 10^4$ and $\Omega \leq 4$. The apparatus for these pressure tests was largely internal to the cylinder (see Figure 3.26b), allowing for a less intrusive measurement of

the flow than Lafay's experiments. However, it should be noted that, in his report, Thom acknowledged the high level of difficulty in measuring the pressure on the surface of a rotating cylinder and he stated that he did not regard his results as having a great degree of accuracy, particularly at the lower test speeds (i.e. higher Ω).

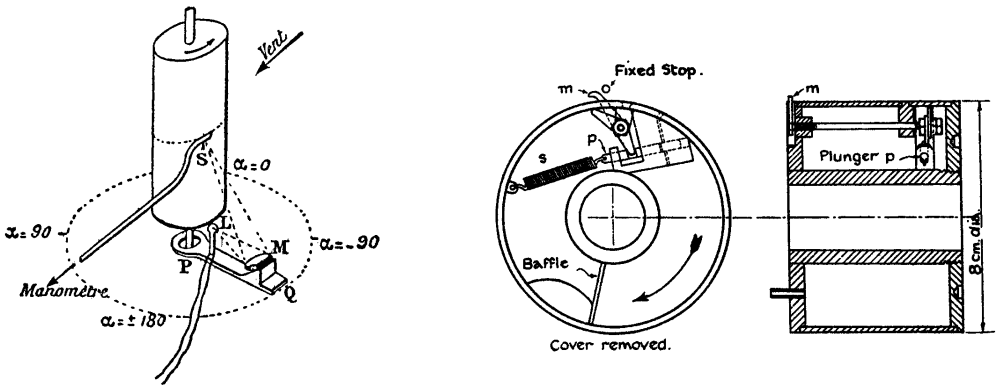

(a) Lafay's apparatus[112] (b) Thom's apparatus[116]

Figure 3.26: Experimental arrangements for measuring the pressure around a rotating cylinder.

The results of Thom's experiments (see Figure 3.27) confirmed the motion of the stagnation point in the direction opposite to the rotation of the cylinder, as predicted by potential flow and observed by Prandtl via his earlier flow visualisation tests.[9,108] They also indicated that the surface pressure in the region corresponding to the width of the wake was quite constant for $\Omega < 3$, though it became somewhat less so at higher velocity ratios. In addition, whilst it was known that an asymmetrical pressure distribution was formed by rotation of the cylinder, Thom's experiments allowed the magnitude of the asymmetry to be properly quantified.

On the downstream moving wall, rotation caused a drastic decrease in the value of the minimum pressure coefficient, which dropped from $C_{p_{min}} = -1.1$ at $\Omega = 0$ to $C_{p_{min}} = -10.5$ at $\Omega = 4$. In contrast, rotation caused the pressure on the upstream moving wall to increase and no minimum pressure was observed on this wall for any velocity ratio greater than zero. This suggests that the flow on the upstream moving wall separated without going through an adverse pressure gradient, and was probably caused by the separation promoting nature of the moving wall effects when V and V_r are in opposition.[154] Thom's results also showed that, as Ω increased, the position of $C_{p_{min}}$ on the downstream moving wall moved in the direction of rotation (i.e. towards the rear of the cylinder), which constitutes an increase in drag, and is qualitatively different to the predicted distributions of potential flow, where the suction peak is always located at $\beta = 90°$.

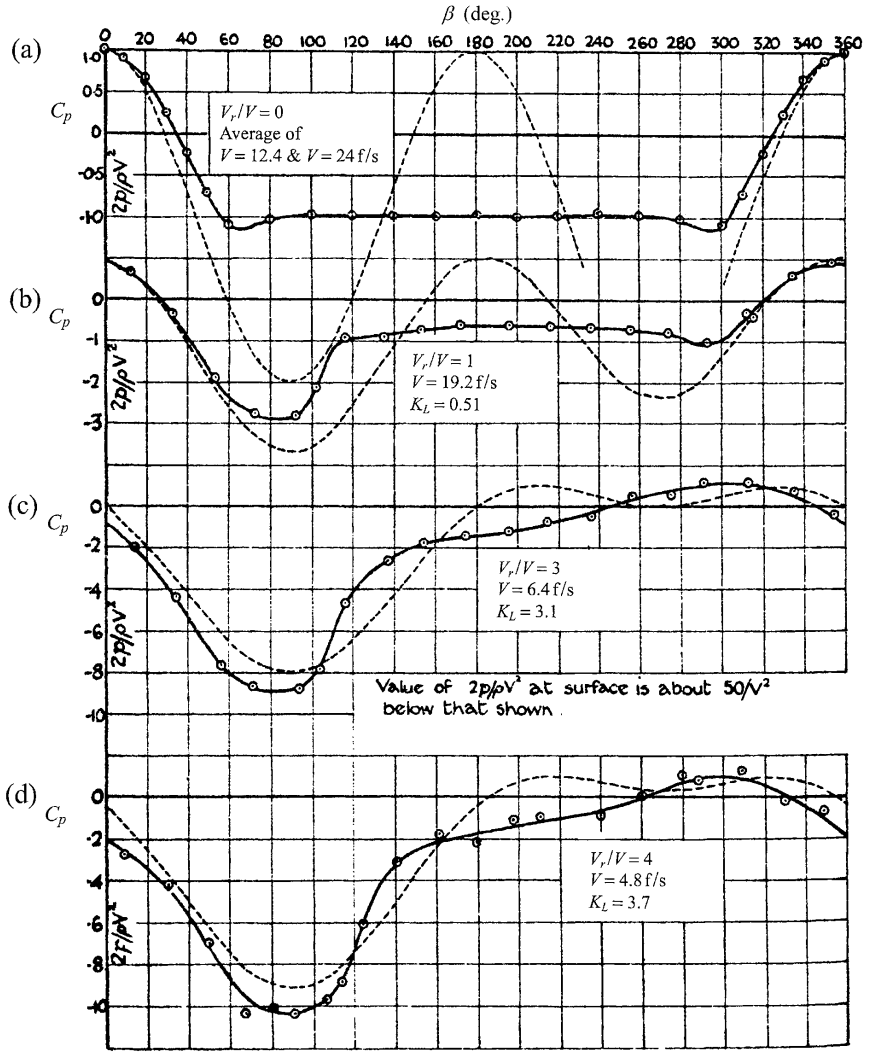

Figure 3.27: Mean pressure distribution around the center section of a rotating circular cylinder of aspect ratio $AR = 7.71$, as measured by Thom[116] for (a) $\Omega = 0$, $1.98 \times 10^4 \leq Re \leq 3.9 \times 10^4$; (b) $\Omega = 1$, $Re = 3.1 \times 10^4$; (c) $\Omega = 3$, $Re = 1 \times 10^4$; and (d) $\Omega = 4$, $Re = 7.8 \times 10^3$. The dashed line represents the potential flow distribution associated with the integrated C_L from the measured pressure curve (these being $\Omega = 0$, $\Omega \approx 0.15$, $\Omega \approx 1$, and $\Omega \approx 1.15$ respectively).

Overall, the differences between the actual pressure distribution for a real flow and that predicted by potential flow at the same velocity ratio were found to be considerable, being most apparent in those regions where viscous effects were dominant (i.e. in the wake) and in the much reduced magnitude of the suction peak. Furthermore, unlike the theoretical pressure distributions, Thom's results showed that positive pressure coefficients continued to occur somewhere on the surface of the cylinder up to the limit of his tests at $\Omega = 4$. In potential flow, the pressure is everywhere negative for $\Omega > 3$. Thom's results did, however, show that, at higher velocity ratios, the measured pressure distribution compared quite favourably with the potential flow distribution associated with the value of the lift

coefficient determined by integration of his pressure readings (see Figures 3.27c and d).

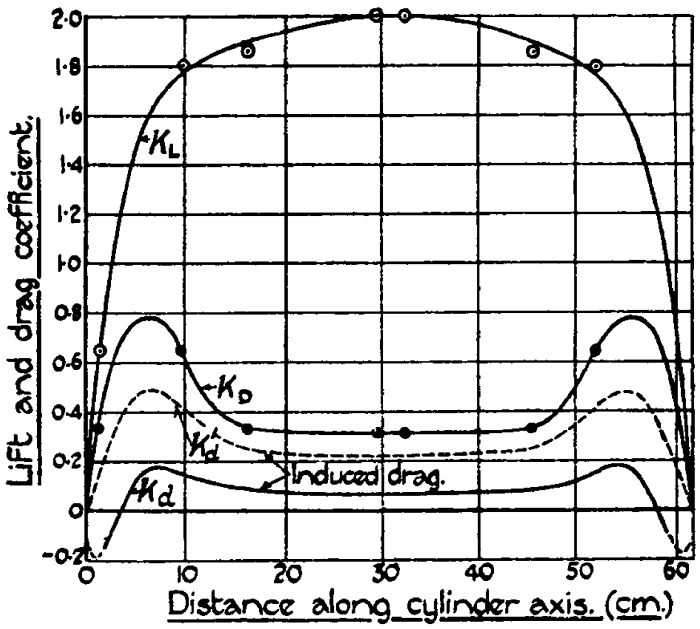

Figure 3.28: Thom's[116] spanwise distribution of lift and drag for $Re = 1.56 \times 10^4$, $AR = 7.71$, and $\Omega = 2$. Note that $K_L = 0.5C_L$ and $K_D = 0.5C_D$.

By taking pressure measurements at different spanwise locations, Thom[116] was also able to illustrate the spanwise distribution of lift and drag (see Figure 3.28), though unlike the tests on the center section, these measurements were limited to $\Omega = 2$. The results indicated a non-uniform, approximately elliptic, lift distribution, suggesting the presence of trailing vortices and induced drag. Interestingly, the profile drag was found to be higher towards the ends than at the center. Thom attributed this to either a mix of experimental error and the influence of the tunnel wall boundary layer or a faulty method of calculating induced drag. Whilst lift and drag were found to fall to zero at the tips, this was said to not be due to a decrease in flow velocity in this region, which was only seen to reduce by some 10%. As far as is known, the results by Thom remain the only experimental data on the spanwise distribution of lift and drag on a rotating cylinder.

Thom's pressure measurements were not repeated until Miller[156,157] carried out his own tests in 1976 and 1979. Miller experimented with both a circular cylinder[156] and a Magnus rotor[157] (an asymmetrically shaped body that is essentially a circular cylinder, but fitted with four driving vanes that make it capable of autorotation when in a moving airstream). Miller's apparatus was either completely internal to the cylinder or positioned outside of the wind tunnel, thus allowing for a far cleaner measurement of pressure than even Thom's attempts. However, the cylinder was of very small aspect ratio ($AR = 1.64$ with

endplates of size $d_e/d = 1.93$) and only the data for three velocity ratios ($\Omega = 0.17$, 0.77, and 2.05) were actually given. These pressure distributions were presented in polar form, making it more difficult to compare Miller's results with those of other tests (see Figure 3.29).

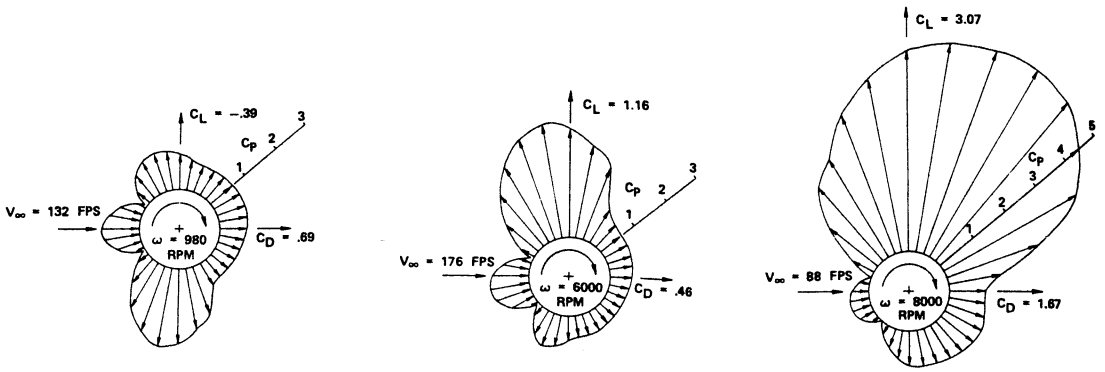

(a) $\Omega = 0.17$, $Re = 3.44 \times 10^5$ (b) $\Omega = 0.77$, $Re = 4.49 \times 10^5$ (c) $\Omega = 2.05$, $Re = 2.24 \times 10^5$

Figure 3.29: Polar representation of mean pressure distribution about a rotating cylinder.[156] Note that arrows pointing away from the cylinder indicate negative pressure coefficients.

Further measurements of the pressure distribution around a rotating circular cylinder were provided by Chew[154] in 1987, McLaughlin *et al.*[155] in 1991, and Takayama & Aoki[194] in 2005. The results of these later measurements were qualitatively quite similar to Thom's data and confirmed many of the observations seen in those tests, including the movement of the stagnation point, the change in the peak suction location, and the constant base pressure for $\Omega < 3$. However, comparison between different data sets (see Figure 3.30) shows only limited quantitative agreement in the actual pressure coefficients, particularly with regards to the value of the minimum pressure, for which no trend based on either Re or AR may be established. However, on the whole, the results indicate that the location of the suction peak moves in the direction of rotation as aspect ratio is decreased, which is consistent with the higher drag of low AR cylinders.

Despite the differences seen in Figure 3.30, a comparison of the lift curves obtained from integration of the pressure distributions shows good agreement between results from different experiments, especially for $\Omega < 2$ (see Figure 3.31a). Those differences that can be observed in the pressure-derived C_L curves are consistent with the variations in the aspect ratios of the cylinders used in the experiments, suggesting that this parameter is the chief cause of the noted dissimilarity between the various pressure distributions. Comparing the integrated lift coefficients against those from direct measurements also reveals good agreement, with the pressure-derived results correctly showing signs of inversion of the Magnus effect when the Reynolds number is high enough.

By contrast, the drag data (see Figure 3.31b) show little agreement between the various results, though the discrepancies are much like the dissimilarity between the results from different direct force measurement experiments (as shown in Figure 3.10). Note that the negative value of C_D seen in Thom's[116] results at high velocity ratio was said to probably be due to experimental error, as the measurement was taken at a very low speed, where the pressure was very small.

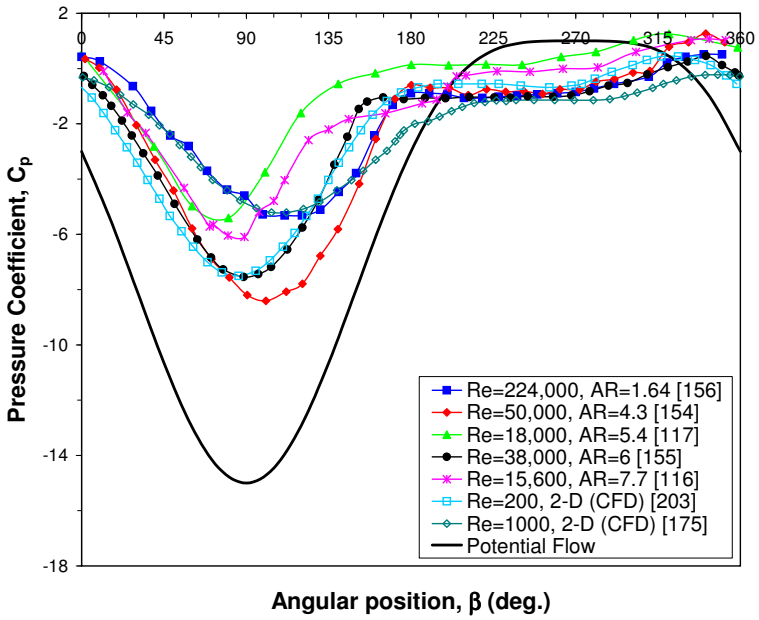

Figure 3.30: Comparison of analytical, experimental, and numerical pressure distribution data at $\Omega = 2$.

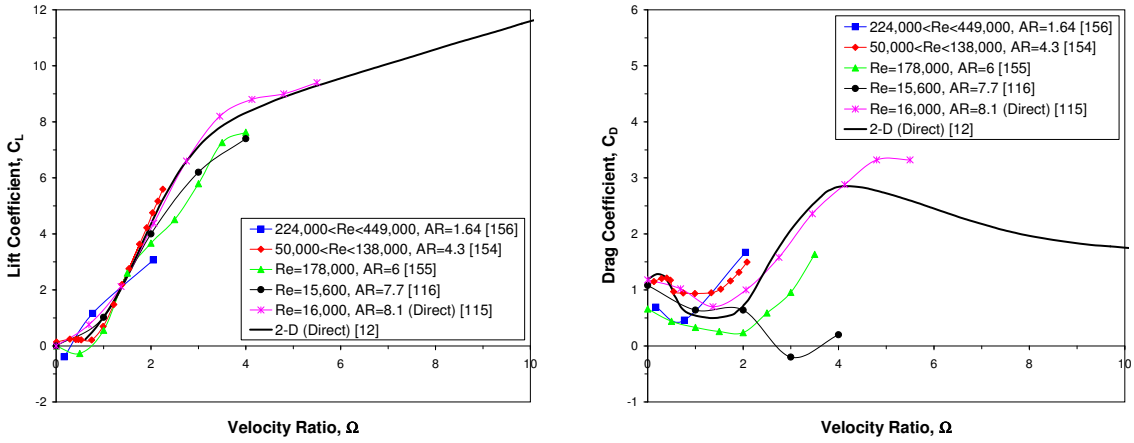

(a) Lift Coefficient

(b) Drag Coefficient

Figure 3.31: Comparison of lift and drag data derived from pressure distribution integration with that from direct balance measurements.

3.5.3 Numerical Results

Qualitative and quantitative differences in the surface pressure distributions obtained by numerical simulation are, unsurprisingly, similar to those visible in the CFD force coefficient data. Those studies that indicate the lift to increase indefinitely with velocity ratio generally show that, whilst at low Ω the pressure distribution is qualitatively different to inviscid flow, increasing the velocity ratio causes the pressure distribution to more closely approach that of potential theory. This type of result is exemplified by the work of Mittal & Kumar[203] and Mittal,[198] as shown in Figure 3.32. Similar results have been obtained by Padrino & Joseph[200] and others. The key difference between these results and the experimental data is in the magnitude of the minimum pressure and the greater negative shift of the distribution with increasing velocity ratio. Thus, while Thom's results for three-dimensional flow at $Re = 7.8 \times 10^3$ indicated that the measured pressure distribution at $\Omega = 4$ was quite similar to that for potential flow at $\Omega = 1.15$, Mittal & Kumar found that, for two-dimensional flow at low Reynolds number, the pressure distribution for $\Omega = 4$ closely matched that from potential flow at $\Omega = 3$.

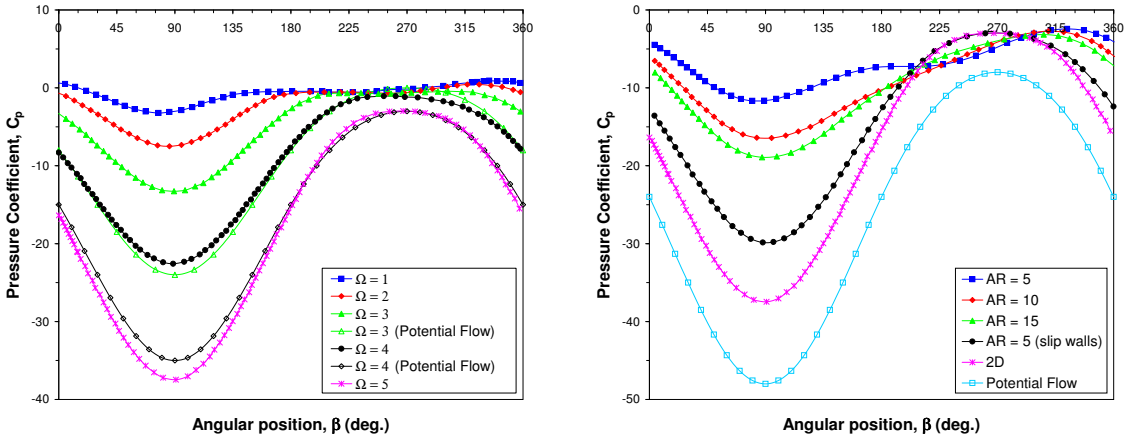

(a) Two-dimensional results at various Ω[203]

(b) Three-dimensional results at $\Omega = 5$[198]

Figure 3.32: Numerically predicted surface pressure distributions at $Re = 200$.

In a later study, Mittal[198] also examined the influence of aspect ratio, noting that, in comparison to the two-dimensional case, finite cylinder simulations showed that three-dimensional effects tended to decrease the suction generated on the cylinder, such that $C_{p_{min}}$ was seen to progressively reduce as aspect ratio decreased (see Figure 3.32b). In addition, the location of the peak suction C_p was observed to move towards the front of the cylinder as AR was reduced. Although this is contrary to experimental observations regarding the effects of AR on the position of the suction peak, it conforms to the trend of progressively decreasing C_D with Ω seen in most CFD-based force data.

In contrast to such results, but in keeping with their prediction of an asymptotic limit to the lift and drag, the Chew *et al.*[175] data showed more modest values of the minimum pressure at high velocity ratio and the shape of the distribution was somewhat different too. For $\Omega > 2$, the pressure distributions also began to exhibit a self-similarity (see Figure 3.33) that Chew *et al.* associated with the development of self-similarity for the entire two-dimensional flow structure, and which was said to be responsible for the asymptotic values of C_L and C_D at high Ω. In addition, the Chew *et al.* pressure distributions showed the same motion of the suction peak with increasing velocity ratio (rearwards, in the direction of rotation) as is seen in the experimental findings. Such a shift in the location of $C_{p_{min}}$ is much less visible in other CFD results, if not wholly absent.

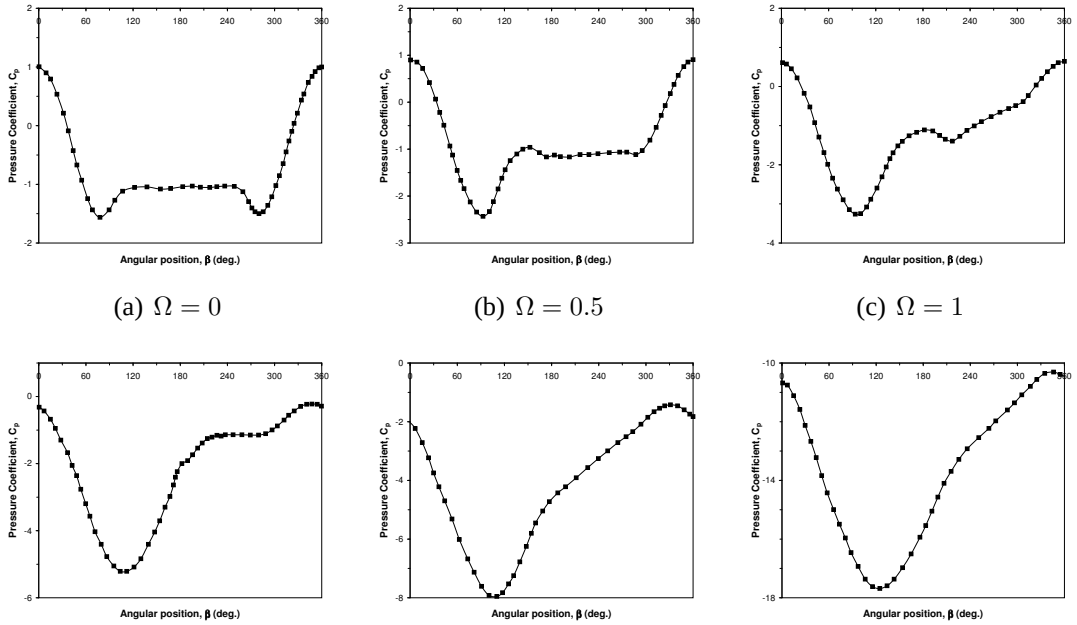

(a) $\Omega = 0$ (b) $\Omega = 0.5$ (c) $\Omega = 1$

(d) $\Omega = 2$ (e) $\Omega = 3$ (f) $\Omega = 6$

Figure 3.33: The Chew *et al.*[175] numerically predicted surface pressure distribution for two-dimensional flow at $Re = 1 \times 10^3$.

3.6 Torque and Power Requirements

Many of the past experimental tests on rotating cylinders have been tied to practical applications, such as ship propulsion,[7,135] wind-based power generation,[158,159] high-lift devices,[4,142] heat exchangers,[151–153] and structural dynamics.[204] Despite this, there is a significant lack of data for such basic quantities as the torque and power required to spin the cylinder. What little information is available is mostly analytical or numerical in origin, whilst the existing experimental measurements are somewhat limited and the data uncertain.

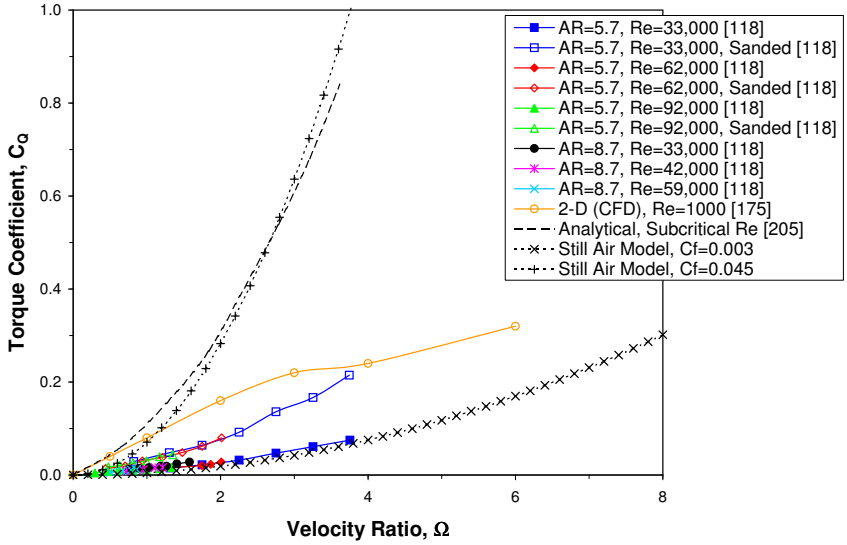

(a) Torque Coefficient

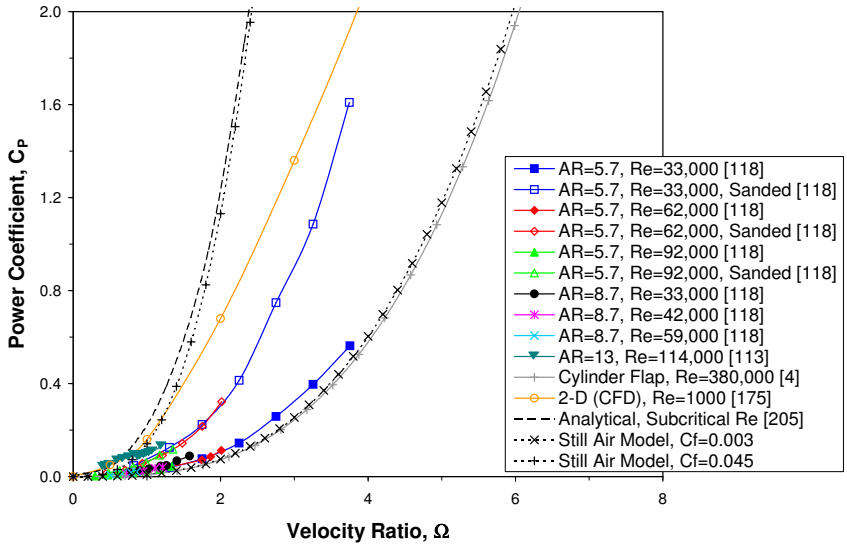

(b) Power Coefficient

Figure 3.34: Torque and power requirements for a rotating cylinder.

A comparison of various results for C_P and C_Q from a number of different sources is shown in Figure 3.34. Note that, where necessary, some of the data have been modified so that they match with the definitions of the torque and power coefficients outlined in Equations 3.12 and 3.13. Such data show the torque coefficient to be quite small, generally being less than 10% of the value of the lift or drag at the same velocity ratio, and indicate a slightly parabolic increase in C_Q with Ω. Power requirements are seen to be of a more substantial magnitude and show a more rapid, obviously parabolic, rise in C_P with velocity ratio. However, Figure 3.34 also clearly demonstrates the considerable disagree-

ment that exists between different studies. Further observations on the trends in torque and power requirements made by the various studies are discussed in more detail below.

3.6.1 Analytical Results

Analytical estimates of the torque and power requirements to maintain cylinder rotation are generally of little practical interest because of the limitations of the techniques employed. Theoretical studies, such as those of Glauert[178] and Moore,[180] tend to involve the examination of only a small range of velocity ratios, or produce results that, due to the assumptions made in the analysis, are applicable only to very high or very low Re. For example, Glauert[178] gave a quantitative estimate of the torque on a rotating cylinder at high Reynolds numbers, but the results of his study were restricted to $\Omega \leq 0.1$. Data from these sources also tends to show little similarity with other studies.

Of more use is the study by Aldoss & Mansour.[205] As well as extending across a broader velocity ratio range ($\Omega \leq 3.8$), the method used, which was based around Thwaite's method for laminar incompressible boundary layers, also produced force results that showed at least some agreement with previous experiments (something that many analytical studies do not do), thus lending confidence to the assessment of the torque coefficient. Even so, although the Aldoss & Mansour results showed C_Q to increase linearly with Ω, the actual values do not match well with the experimental measurements of Thom.[115,118] In their discussion, Aldoss & Mansour speculated that their assumption of a linear pressure distribution within the wake may have affected the analysis.

A comparison of the existing results for C_Q and C_P with values predicted by a very simple analytical model based around a rotating cylinder that is assumed to be spinning in still air is also shown in Figure 3.34. In this analysis, the torque is given by

$$Q = \frac{1}{2} F d \tag{3.17}$$

where F is the frictional force over the wetted surface of the cylinder. This is assumed to be a function only of the peripheral velocity, V_r, such that

$$F = \frac{1}{2} \rho V_r^2 \pi d b C_f \tag{3.18}$$

where C_f is the skin friction coefficient. Hence, from Equation 3.17, the torque required

to spin the cylinder is seen to be

$$Q = \frac{1}{4}\rho V_r^2 \pi d^2 b C_f \tag{3.19}$$

If Equation 3.19 is now non-dimensionalised according to Equation 3.12, then the torque coefficient for finite Ω (i.e. when $V \neq 0$) may be estimated as

$$C_Q = \frac{1}{2}\pi C_f \Omega^2 \tag{3.20}$$

and, from Equation 3.14, the power coefficient will be

$$C_Q = \pi C_f \Omega^3 \tag{3.21}$$

The predicted torque and power coefficients obtained through this model show that the data from the literature lies approximately in the range $0.003 \leq C_f \leq 0.045$. This range is found to be consistent with values of the equivalent friction factor derived from experimental measurements[10,115] of C_Q using cylinders rotating in still air. Analytical and numerical results are seen to lie towards the upper end of this C_f range, but further investigation is required to establish any meaningful trends in terms of Re or other parameter.

3.6.2 Experimental Results

Early experimental results for the torque coefficient of a rotating cylinder were largely obtained for the case of $V = 0$. During the Göttingen tests of 1923, Ackeret[10] measured the torque on a cylinder of $AR = 4.7$, without endplates, spinning in still air. The results also included a single data point apparently taken by Lafay[109,110] under similar conditions in 1910. Ackeret's findings indicate that, for a laminar boundary layer, the torque coefficient (as based on V_r^2 and a) is reduced with increasing V_r. A turbulent boundary layer resulted in a considerably smaller decrease in the torque and Ackeret speculated that for high enough Re there would be no reduction at all.

The only other experimental measurements of the torque coefficient known to exist are those of Thom. As part of his 1925 tests, Thom[115] made a small number of measurements of the air torque on a rotating cylinder, noting C_Q to be proportional to some power of the rotational rate between one and two. In 1932, he carried out more detailed tests[118]

with two different cylinders of $AR = 5.7$ and 8.7 for $3.3 \times 10^4 \leq Re \leq 9.3 \times 10^4$ and $\Omega \leq 4$. One cylinder was made of smooth brass the other of wood. Thom also tested the brass cylinder again after its surface had been sanded to simulate surface roughness. For all three cases, the torque was measured in both still and moving air.

As with his earlier tests, Thom found the torque to be proportional to the product of wind speed and rotational rate. Results for both the smooth brass and wood cylinders were nearly identical, and the torque was seen to increase with velocity ratio in a slightly parabolic manner. In addition, the torque coefficient data showed no influence from either Reynolds number or aspect ratio, though the range of each parameter assessed was admittedly quite small. However, surface roughness had a much more drastic effect, increasing the measured torque by two to three times that of the plain case (see Figure 3.34).

The tests also showed that the resultant force on the cylinder acted at approximately $0.008d$ from the cylinder's longitudinal axis for most of the velocity ratio range tested (increasing and decreasing slightly for very high and very low Ω respectively). When the cylinder was roughened the eccentricity was also increased by a similar amount as the torque. Thus, Thom suggested that it was this eccentricity of the 'center of pressure' of the resultant force (including both pressure and viscous components) that produced the torque.

Direct experimental measurements of the power required to spin a rotating cylinder are limited to those of Reid[113] in 1924 and Weiberg & Gamse[4] in 1968 (Note that the results attributed to Thom in Figure 3.34b were derived by the present author using Equation 3.14 and Thom's values for C_Q). Reid's measurements of the power required to sustain a particular rate of rpm were taken for both wind-on and wind-off cases, with the wind-on measurements being performed at a speed of $V = 15$ m/s, or $Re = 1.14 \times 10^5$. The results indicated that power requirements for a particular rpm were smaller when $V > 0$. Reid suggested that this was due to a decrease in air friction that was caused by a reduction in the relative velocity of the air to the cylinder surface around most of the circumference. Note that Reid made no mention of any correction of his results for motor efficiency.

Weiberg & Gamse recorded power requirements during their wind tunnel tests with a rotating cylinder flap. These tests were far more extensive than Reid's and the Reynolds number ($2.75 \times 10^5 \leq Re \leq 3.8 \times 10^5$) and velocity ratio range ($\Omega \leq 6.7$) were also somewhat higher than most experiments. The power to spin the cylinder was determined from measurements of the electrical power input to the drive motors and corrected for a motor efficiency of 92%, obtained from a dynamometer calibration of the motors. The results showed the power requirements to be a function of N^3 and nearly independent of

airspeed (within the limits of their tests, see Figure 3.35). This invariance of P with V suggests that the power coefficient may vary with Reynolds number, which is contrary to the trends seen in the C_P curves based on Thom's torque measurements.

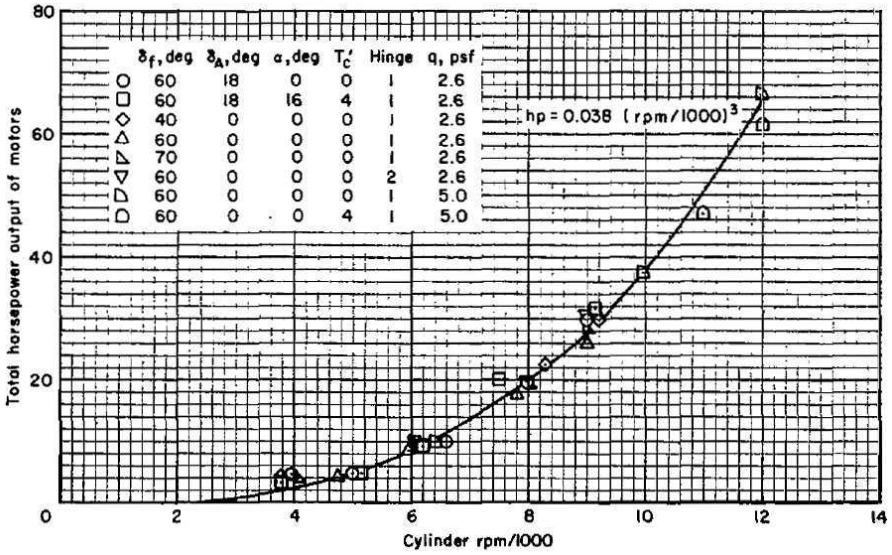

Figure 3.35: Invariance of rotating cylinder flap power requirements with velocity, as measured by Weiberg & Gamse.[4]

It should be noted that the Weiberg & Gamse curve shown in Figure 3.34b was plotted from their suggested equation for the power, given as

$$P = 0.038 \left(\frac{N}{1000} \right)^3 \tag{3.22}$$

where P is in horsepower, together with the values of the cylinder dimensions, as given in their reports. However, it is unclear exactly how big the cylinder was or which definition of horsepower was adopted (the present author assumed 1 hp = 746 W), thus adding some uncertainty to the Weiberg & Gamse results.

3.6.3 Numerical Results

Like other CFD results for rotating cylinder flow, numerically derived assessments of the torque and power requirements are restricted to low Reynolds numbers ($Re \leq 1 \times 10^3$). In addition, some studies, such as that of Ece *et al.*,[182] consider only the temporal variation of the torque rather than the time-averaged mean values and their relationship with the velocity ratio.

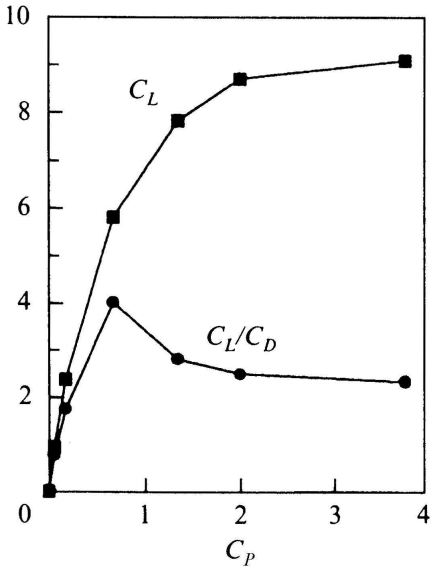

Figure 3.36: Chew *et al.*'s[175] numerical power coefficient results for $Re = 1 \times 10^3$.

The most extensive numerical analysis of C_Q and C_P was performed by Chew *et al.*[175] for two-dimensional flow at $Re = 1 \times 10^3$ and $\Omega \leq 6$. The results showed that for $\Omega \geq 4$ the torque coefficient tended towards an asymptotic limit, which was consistent with the argument of these authors regarding self-similarity at high velocity ratio (see Figure 3.34a). By contrast, the power coefficient continued to increase with Ω (see Figure 3.34b). Whilst this asymptotic behaviour in C_Q is not consistent with the experimental data, it should be noted that the Chew *et al.* results for high velocity ratios ($\Omega = 4$, 5, and 6) are confirmed by the numerical work of Padrino & Joseph,[200] who also calculated C_Q at $Re = 1 \times 10^3$.

Chew *et al.* also examined power efficiency by plotting a graph of lift-to-drag ratio against power coefficient (see Figure 3.36). This revealed that the maximum value was reached very early on at $C_P = 0.6$, after which further increases in power input did not give rise to increased aerodynamic efficiency, but actually decreased it. Similarly, the maximum lift coefficient was reached at $C_P \approx 2$ and was not much improved at higher C_P. Chew *et al.* concluded that the usefulness of the Magnus effect as a means of lift generation is thus limited.

Based on the findings of their own simulations, Mittal & Kumar[203] reached a similar conclusion. They presented two-dimensional numerical results for the total power coefficient required to both spin and translate the cylinder at $Re = 200$. Power requirements were seen to be fairly constant in the range $\Omega \leq 2$, but rose rapidly with further increases in velocity ratio (see Figure 3.37), thus making lift generation via the Magnus effect very power-intensive and reducing the benefits of the large lift forces generated at high Ω.

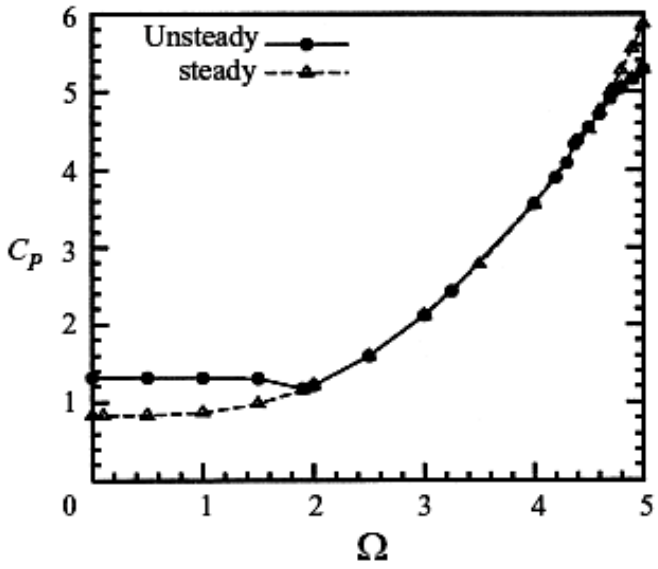

Figure 3.37: Mittal & Kumar's[203] results for the total power requirements to both translate and rotate a cylinder at $Re = 200$.

3.7 The Wake of a Rotating Cylinder

For small velocity ratios, the wake of a rotating cylinder is known to be similar to that of a stationary cylinder, so that flow separation produces a broad wake with a dominant periodicity caused by alternate vortex formation and shedding, particularly at low Re. Increasing the velocity ratio induces several changes in the cylinder's wake, the most important of which are found to be: the development of asymmetry in the size and strength of the vortices shed from the upstream and downstream moving walls; a progressive, asymmetric change in the position of the separation points that leads to the narrowing and biasing of the wake (towards the side where V and V_r are in opposition); the creation of closed streamlines about the cylinder; and the eventual suppression of the periodic nature of the wake.

Examination of the wake of a rotating cylinder has primarily been performed numerically. However, these computational studies have largely been constrained to investigation of the symmetrical range ($5 \leq Re \leq 40$), regular range ($41 \leq Re \leq 200$), and the lower end of the irregular range (up to $Re = 1 \times 10^4$). Only a few studies have considered higher Re. Experimental studies, comprising both flow visualisation tests and hotwire measurements, are surprisingly few in number and have also tended to concentrate on the examination of relatively low Reynolds numbers ($Re \leq 9 \times 10^3$). What little experimental information[188] there is for high Re indicates that vortex shedding, of one form or another, persists for Reynolds numbers at least as high as the critical Re.

3.7.1 Flow Topology, Vortex Shedding, and the Effects of Rotation

Early analysis of the wake of a rotating cylinder came from Prandtl's[108] flow visualisation study at $Re = 4 \times 10^3$. The streamline patterns from his water tank tests (see Figure 3.38) show a certain similarity with those of potential flow (Figure 3.3), particularly with regards to the biased nature of the wake at high Ω. The results led Prandtl to propose the presence of two distinct regimes, delineated by a critical velocity ratio, Ω_c. For $\Omega < \Omega_c$, vortices were formed and shed alternately from the two sides of the cylinder. For $\Omega \geq \Omega_c$, Prandtl observed the formation of a single anticlockwise vortex on the upstream moving wall of the cylinder. This vortex was found to grow in size as the flow developed, eventually being cast downstream when the steady state for that particular velocity ratio was achieved. No other vortices were subsequently shed, leaving Prandtl to conclude that alternate shedding had stopped. Prandtl placed the value of the critical velocity ratio at $\Omega_c = 2$ and associated the cessation of vortex shedding with the gradual narrowing, lengthening and biasing of the near-wake that occurs with increasing Ω. Prandtl also noted the creation of closed streamlines about the cylinder when $\Omega = 4$, commenting that the flow pattern for this velocity ratio was similar to that in potential flow at $\Omega = 2$.

Prandtl's visualisation tests have been criticised by a number of authors for the fact that the images were taken at uniform pressure on the free surface of a tank of water and are thus not fully representative of the flow past a rotating cylinder. Swanson[12] wrote that comparisons between Prandtl's flow patterns and those obtained by F. N. M. Brown[184,185] using a smoke tunnel showed striking differences, particularly in the motion of the front stagnation point. Consequently, Swanson concluded that the actual wake flow behind a rotating cylinder will be very different to the flow patterns obtained by Prandtl. However, Prandtl's findings on the general nature of the wake are supported by the extensive and important flow visualisation study of Coutanceau & Ménard.[186]

These authors used flow visualisation via solid tracers in a water tank at low Reynolds numbers ($Re = 200$, 500, and 1×10^3) to exhaustively detail the process of vortex formation and shedding in the near-wake behind an impulsively started rotating and translating cylinder. The findings showed that rotation destroyed the symmetry of the vorticity generated by the cylinder, resulting in the formation and shedding of vortices of different sizes and strengths. This was said to occur because of the differences in the relative velocities between the fluid and the upstream and downstream moving walls. The opposition of velocities on the upstream moving wall created a region of high relative velocity, which resulted in greater shear and larger vorticity. For the downstream moving wall, the situation was reversed; thus, the formation of vortices on this wall was more readily affected by velocity ratio.

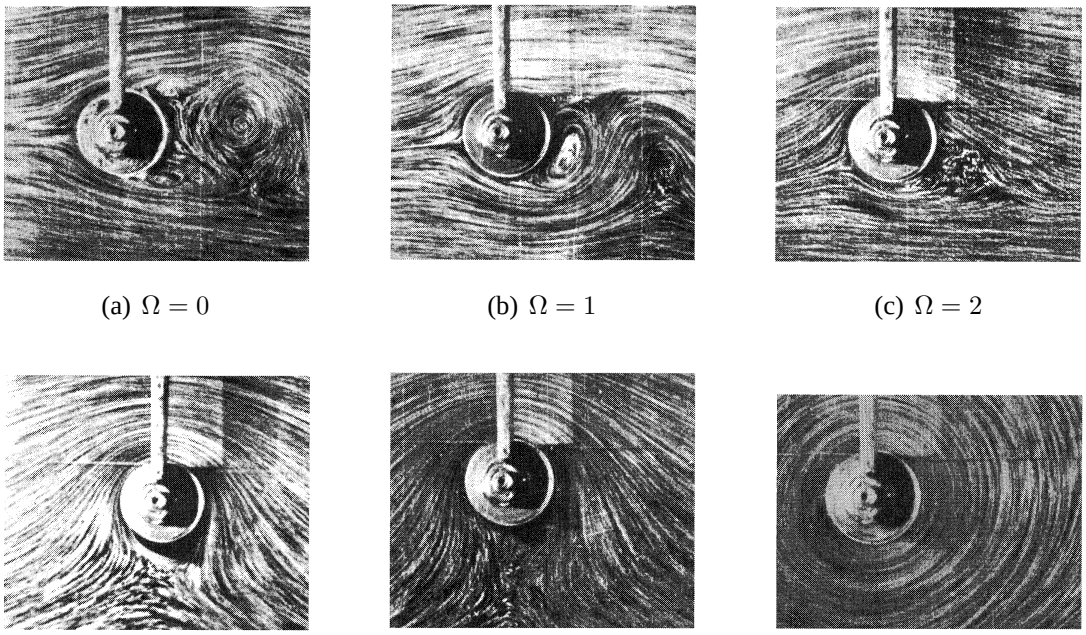

(a) $\Omega = 0$ (b) $\Omega = 1$ (c) $\Omega = 2$

(d) $\Omega = 4$ (e) $\Omega = 6$ (f) $\Omega = \infty$

Figure 3.38: Prandtl's[108] water surface flow visualisations at $Re = 4 \times 10^3$.

For all $\Omega > 0$, Coutanceau & Ménard found that vortices formed on the upstream moving wall earlier than on the downstream moving wall. The first vortex to form was created just after the onset of the motion and was shed into the stream in a time that was largely unaffected by either Ω or Re. The formation of the second vortex, on the downstream moving wall, was found to be affected by rotation as soon as $\Omega > 1$, such that its appearance in the flow was progressively delayed and its size and strength continuously decreased until, for sufficiently high Ω, the second vortex completely disappeared. As in Prandtl's tests, the critical velocity ratio at which this occurred was found to be $\Omega_c \approx 2$. For velocity ratios in excess of this value, no other vortex was created, after the first one, during the time period of the tests, leading Coutanceau & Ménard to conclude that the vortex street had been destroyed. The disappearance of the downstream moving wall vortex was said to be connected with the fact that, for $\Omega > 2$, rotation of the cylinder no longer reduced the fluid relative velocity on the downstream moving wall, but now accelerated it.

Coutanceau & Ménard[186] also reported that the global structure of the wake was not found to be significantly different at $Re = 1 \times 10^3$, as compared to the lower test Reynolds numbers, but that the relative influence of rotation was smaller and its effects delayed. In addition, new phenomena regarding the formation of secondary vortices, which occasionally formed near the cylinder wall and merged to create larger vortices that were then shed downstream, also occurred at the higher Re. Similar findings regarding secondary

vortices and the microscale structure of the flow were reported by the numerical study of Badr *et al.*[166] at the same Reynolds number.

A number of CFD studies[166, 167, 169, 175, 192, 203, 206, 207] have used the Coutanceau & Ménard experimental results as a benchmark to compare against their own streamline patterns, with strong agreement being reported by all. That being said, Sengupta *et al.*[192] have noted that the experimental flow patterns reveal the presence of extra vortices near the shoulder (at $\theta = 90°$) that fail to appear in the numerical simulations. They suggested that these differences are attributable to the experimental arrangements used by Coutanceau & Ménard; in particular, the point where the cylinder passes through the water tank was said to create vortices that moved in a spanwise direction with time, altering the streamline pattern and rendering the flow three-dimensional. The results by Polidori *et al.*[208] for $Re = 1 \times 10^3$ using the same apparatus as Coutanceau & Ménard, but with a nonrotating cylinder, seem to confirm this to be so.

Computational studies have also provided further topological analysis of the near-wake and the mechanics of vortex detachment and shedding. Such investigation has shown that the formation and evolution of the main and secondary vortices is affected by both increasing velocity ratio and Reynolds number.[166] For very low Reynolds numbers ($Re \leq 46$) the wake is, like that of the stationary cylinder, characterised by a lack of oscillatory features, with no vortex shedding, regardless of velocity ratio. For $60 \leq Re \leq 1 \times 10^3$ the flow pattern described by the numerical studies is largely the same as that noted by Prandtl in his flow visualisation tests at $Re = 4 \times 10^3$, but the flow topology at $Re > 1 \times 10^4$ is said to be significantly different from lower Re.[173] In particular, there is a change in which vortex is shed first. However, all such investigations have been performed in the context of two-dimensional flow. Conclusions drawn from these studies at high Re, where the wake will only remain two-dimensional in the starting flow for a limited time, are thus somewhat dubious.

Numerical studies[199, 203, 209] at low Reynolds number ($Re \leq 200$) also indicate that the formation of closed streamlines around the cylinder, dividing the flow into inner and outer regions, first occurs at $\Omega = 0.5$, a much lower velocity ratio than suggested by both potential theory ($\Omega = 2$) and experimental observations ($\Omega = 4$). For such small Ω, the closed streamlines are said to exist only in a region that is very close to the body and are difficult to see. Mittal[203] suggested that the difference with potential flow arose because the speed on the cylinder surface is constant for the real flow case, unlike the potential flow case. Experimental and computational results are, however, all in agreement that the size of the closed streamline grows with increasing velocity ratio, but decreases with increasing Re.

High Reynolds number ($Re \geq 1 \times 10^3$) may also change the point at which the closed streamlines form. The numerical study of Chew *et al.*[175] at $Re = 1 \times 10^3$ first observed closed streamlines around the cylinder at the same point as in potential flow, i.e. $\Omega = 2$. They remarked that, in real flows, this would lead to the formation of three-dimensional Taylor vortices in the inner region, where centrifugal effects are important. Such toroidal vortices have been observed via flow visualisation by Taneda[210] and Matsui,[211] who associated them with the suppression of vortex shedding.

The most detailed quantitative experimental investigations into the nature of the wake of a rotating cylinder were carried out by Diaz *et al.*[158,159] In two separate studies, they took hotwire measurements of the distribution of streamwise and lateral velocity components in the wake behind a cylinder of size $AR = 30$. Multiple probe locations between $3 \leq x/d \leq 150$ and $-8 \leq y/d \leq 8$ (with particular emphasis on $-0.6 \leq y/d \leq 0.6$) were examined at a single Reynolds number of $Re = 9 \times 10^3$ and velocity ratios of $\Omega \leq 2.5$.

Based on their results, Diaz *et al.*[158,159] made several observations on the nature of the flow, noting that as velocity ratio increased: the Reynolds stresses in the plane of symmetry of the wake were significantly reduced from their value at $\Omega = 0$; the mean velocity profiles become progressively more asymmetric; the fluctuating velocity field became increasingly damped, particularly for $\Omega > 1$; wake width was continually decreased, particularly for $\Omega > 1$; and the wake was displaced in the direction of rotation (i.e., towards the side where V_r and V are in opposition).

In addition, Diaz *et al.* reported that, at low velocity ratios, the near-wake was dominated by well defined, highly energetic Kármán vortices, and the characteristic length and velocity scales were not much changed from those for the stationary cylinder. Consequently, for $\Omega < 1$, vortex shedding activity was said to be practically unaffected by rotation. Beyond this threshold there was a sharp initial decrease in vortex street activity, attributed to an increase in the random modulation of the process. As Ω increased further, the vortices were seen to become progressively more diffuse until the process became completely random and shedding ceased at $\Omega = 2$. For higher velocity ratios, no coherent structures associated with Kármán vortex activity existed in the near-wake and Diaz *et al.* considered it to be fully turbulent from its inception.

On the basis of these findings, Diaz *et al.* suggested the existence of two distinct regimes in the wake of a rotating cylinder, similar to Prandtl's idea, but with the critical juncture now at $\Omega = 1$. Diaz *et al.* stated that, at this point, a fundamental change in the process of Kármán vortex formation occurred due to the dissimilarity induced by rotation to the lateral velocity profiles in the regions immediately above and below the cylinder. The

decay of Kármán vortex activity for $\Omega > 1$ was said to be linked with the onset of completely asymmetrical upper and lower velocity distributions, and the eventual suppression of shedding at $\Omega = 2$ was connected with the associated increase in the thickness of the thin layer of entrained fluid rotating with the cylinder.

Surface pressure measurements by McLaughlin *et al.*[155] for much higher Re ($3.6 \times 10^4 \leq Re \leq 1.78 \times 10^5$) support the notion of a significant change in the wake structure occurring when $\Omega > 1$. However, these authors attributed the cessation of vortex shedding to increasing turbulence of the boundary layer on both sides of the cylinder and the fact that turbulent separated shear layers are less likely to form large cohesive vortices.

In further commenting on their findings, Diaz *et al.*[159] attributed the decrease in wake width to the reduction and redistribution of wake kinetic energy over all relevant frequencies, whilst the displacement of the wake was said to be caused by the high momentum transfer conditions occurring in the region below the upstream moving wall of the cylinder: for $\Omega \leq 1$, boundary layer separation and vortex shedding were more prevalent from the upstream moving surface, causing a net downward transfer of momentum within the wake that balances the generated lift.

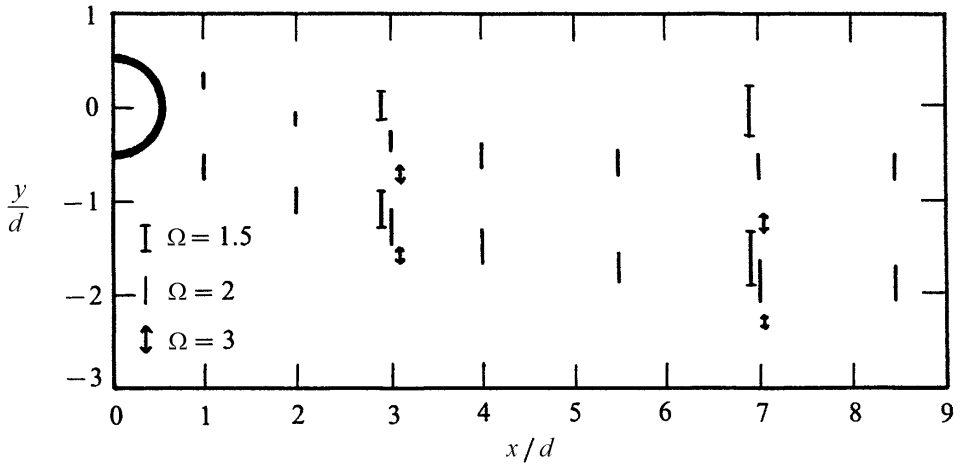

Figure 3.39: Position of the turbulent/non-turbulent interface in the wake of a rotating cylinder.[212] Mean values of the interface are centered on the vertical bars that represent rms values. The cylinder is rotating in a clockwise sense.

The extent of the biasing of the near-wake is expressed quantitatively in the results of the related tests by Massons *et al.*[212] They used image processing techniques to digitally analyse cinematographic recordings of dye-injection flow visualisation tests and locate the position of the turbulent/non-turbulent interface in the wake of stationary and rotating cylinders. The tests employed a cylinder of $AR = 11.67$ and examined downstream

distances of $1 \leq x/d \leq 8.5$ at $Re = 2 \times 10^3$ and $\Omega \leq 4$.

The results clearly illustrate the deflection of the wake, and the reduction of its width, with increasing velocity ratio (see Figure 3.39). The unsteady nature of the wake is indicated by the size of the root-mean-square (rms) values of the position of the interface. This fluctuation is associated with periodic shedding of vortices. That the rms values at $\Omega = 3$ are considerably smaller than those for lower velocity ratios is consistent with the suppression of vortex shedding at high Ω. Also apparent is that, for a given x/d station, the rms value of the interface is greater on the upstream moving wall side than it is on the downstream moving wall side. This is in keeping with the separation promotion properties of the upstream moving wall and the resulting asymmetry in the size and strength of the shed vortices.

3.7.2 The Critical Velocity Ratio

Both numerical and experimental studies are generally in agreement that, for all Reynolds numbers for which vortex shedding from a rotating cylinder occurs ($Re > 46$), there is always a critical velocity ratio beyond which shedding is subsequently suppressed. Only a small number of numerical studies have contested this fact.[213,214] The analytical studies of Moore,[180] Glauert[178,215] and Wood[181] also indicate that, for high enough Ω, it is possible to obtain steady flows with no vortex shedding at both high and low Re. However, these studies were based not on the full Navier–Stokes equations, but on steady boundary layer theory, and their applicability to the investigation of the unsteady separated flow associated with vortex shedding is questionable.

The numerical and experimental data on the variation of the critical velocity ratio with Reynolds number can be combined to illustrate the transition between steady and time-periodic wake flows (see Figure 3.40). The results of the CFD simulations are seen to be in good agreement with the only available experimental data at similar Reynolds number, and both sets of data show the critical velocity ratio to be a logarithmic function of Re. The curve also suggests that, whilst increasing Reynolds number tends to destabilise the flow past a circular cylinder, rotation acts to stabilise it.[199]

By contrast, Jaminet & Van Atta[147] reported that, for $Re < 48$, rotation could always be used to artificially induce vortex shedding at lower Reynolds numbers than would otherwise be expected. However, the cause of this induced shedding seems to stem from problems with the experimental set-up (specifically, the whipping motion arising from rotational eccentricity of the cylinder, see §3.7.6), rather than being an inherent consequence

of rotation.

In general, the numerical and experimental data at low Reynolds number suggests that as Re increases the critical velocity ratio for suppression approaches a limiting value of $\Omega_c = 2$. This is in agreement with critical velocity ratio values reported by studies at higher Re, such as Prandtl's[108] flow visualisation findings for $Re = 4 \times 10^3$ and the Diaz *et al.*[158] hotwire results for $Re = 9 \times 10^3$. However, some studies have indicated a larger critical velocity ratio: Flow visualisation by Calamote[216] for $1 \times 10^3 \leq Re \leq 8 \times 10^3$ and $\Omega \leq 8$ showed shedding to finally disappear when $\Omega \approx 2.5$. At this point the two boundary layers met and vorticity was swept downstream in a sort of 'plume'. The numerical simulation by Chou[217] at $Re = 1 \times 10^3$ found the vortex street was only completely suppressed when $\Omega \geq 3$. Similarly, Chew *et al.*,[175] also at $Re = 1 \times 10^3$, did not give a definitive critical value of the velocity ratio for which vortex shedding was suppressed, but they agreed that the vortex street structure began to deteriorate as soon as $\Omega > 2$ and finally disappeared for $\Omega > 3$.

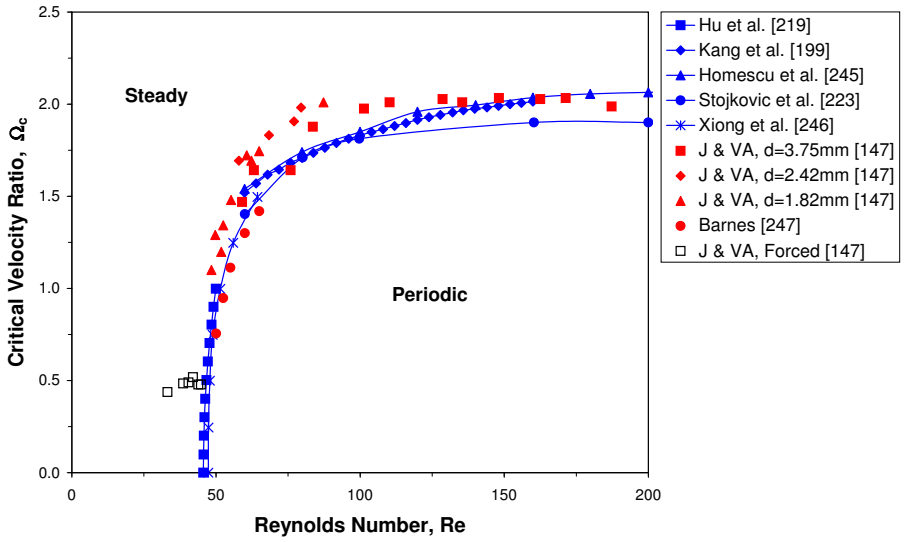

Figure 3.40: Reynolds dependent transition between steady and periodic flows for a rotating cylinder.

Based on the results of their two-dimensional numerical study for $\Omega \leq 3.25$ and $Re = 200$, Chen *et al.*[213] have proposed that vortex shedding is not suppressed at high velocity ratios. For $\Omega < 2$, Chen *et al.*[213] reported very good agreement with the experiments of Coutanceau & Ménard[186] and the associated numerical work of Badr & Dennis.[167] For higher Ω, examination of equivorticity contours showed that, contrary to the findings of most other studies, the shedding of more than one vortex continued beyond the expected suppression threshold of $\Omega = 2$. However, in these conditions, vortex shedding was found to be highly asymmetric, with the downstream moving wall vortex being considerably

weaker than the upstream moving wall one.

Other differences were also observed: vortex strength and size were seen to decrease with each shed vortex; there was a much longer period of time between successive vortices; and rather than appearing alternately on opposite sides of a vortex street, the vortices now seemed to form a sort of 'single file'. Chen *et al.* also noted that, for $\Omega = 3.25$, the third vortex shed had the same rotational sense as the second, and they speculated that, for such high Ω, vortices might be shed from the upstream moving wall only, rather than alternating between the two.

Chen *et al.* believed that experimental researchers have failed to detect the shedding of vortices at high Ω because their flow visualisation experiments were frame dependent: since streamlines appear different depending on how they are viewed, the camera would have to move with the core of the vortex for it to be successfully observed, which is clearly difficult to arrange. Furthermore, Chen *et al.* claimed that other numerical and experimental studies also did not extend to large enough dimensionless time to witness vortex shedding when $\Omega > 2$. Mittal & Kumar[203] have refuted this idea of continuing vortex shedding, stating that Chen *et al.* were misled on the issue because they themselves did not compute the flow for a long enough time. However, the numerical analysis by Ou & Burns[214] at $Re = 200$ has also found vortex shedding to continue beyond $\Omega = 2$. No experimental results in support of these claims appear to exist.

In contrast to such studies, Tanaka & Nagano[188] encountered suppression of vortex shedding at much lower velocity ratios than would be expected for the given Reynolds numbers. They placed a hotwire probe behind a low aspect ratio cylinder ($AR = 2.4$) at a distance of $x/d = 2.89$ and took measurements for $\Omega < 1.1$ and $4.8{\times}10^4 \leq Re \leq 3.71{\times}10^5$. The results suggested a critical velocity ratio of between $0.66 \leq \Omega_c \leq 0.77$, the exact value varying with Re. In his comprehensive book on flow around circular cylinders, Zdravkovich[120] speculated that the high Reynolds numbers and distant location of the probe might have affected the results. In addition, that the blockage ratio was much larger ($d/B = 0.18$) than in other arrangements may also have been a factor.

3.7.3 Strouhal Number Evolution

The variation of the Strouhal number with velocity ratio for $\Omega < \Omega_c$ is a further point of contention within the literature. Figure 3.41 shows a comparison of Strouhal number data from a variety of different experimental and numerical studies and reveals a fundamental difference between the results. Whereas the experimental data universally indicates an

overall rise in St with velocity ratio, the numerical data are split in two: the results of some studies support the experimentally observed trend, whilst the rest indicate a slight overall decrease in St with Ω. This qualitative difference exists even at those Reynolds numbers where data from the two means of study overlap.

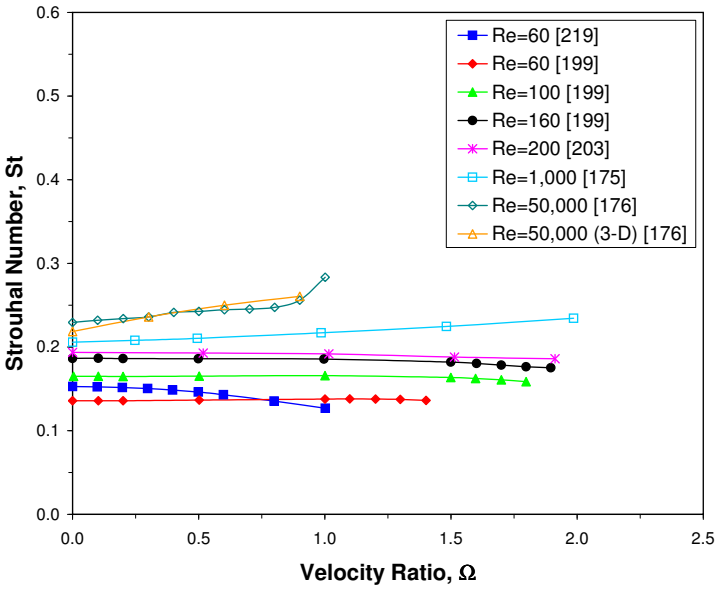

(a) Numerical Results

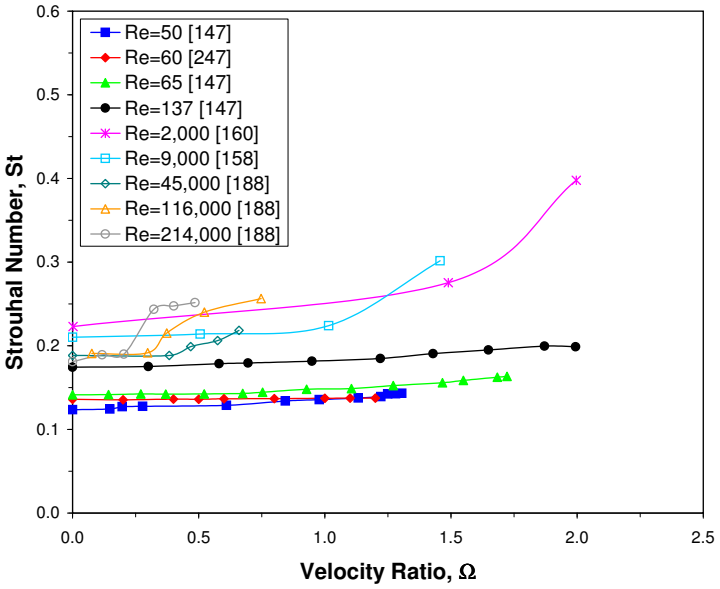

(b) Experimental Results

Figure 3.41: Comparison between numerical and experimental results of the Strouhal number variation with velocity ratio.

Whilst this disagreement may be in part attributable to the failings of some of the numeri-

cal methods employed (as discussed by Van Atta[218] and Kang *et al.*[199] with regards to the Hu *et al.*[219] data), it should be noted that all the computationally derived results shown in Figure 3.41 were obtained using different numerical schemes. Consequently, it is not possible to link a particular trend (i.e. increasing or decreasing St) with a particular method, which suggests that numerical artefact is not the primary cause of the discrepancy.

That all the numerical studies which indicate an increase of St with Ω were performed at Reynolds numbers in excess of $Re = 1 \times 10^3$, whilst those that show St to decrease are all for $Re < 200$, suggests that Reynolds number effects may be the cause of the apparent disagreement between the experimental and numerical data. It is known from the study of stationary cylinders that a change in flow pattern occurs between $200 \leq Re \leq 1 \times 10^3$, and a similar change in the flow past a rotating cylinder may thus be responsible for the switch in the trend of Strouhal number variation with velocity ratio. However, such an explanation is apparently refuted by the experimental findings of Jaminet & Van Atta,[147] which indicate that the trend of increasing St also exists for $Re \leq 200$. Furthermore, a number of studies,[167,174,186,200] both experimental and numerical, have reported that the flow at $Re = 200$ is very similar to that at $Re = 1 \times 10^3$ and above (up to $Re = 1 \times 10^4$).

Mittal & Kumar[203] have suggested that the difference in findings is, perhaps, related to the interaction between the vortex shedding mechanism and centrifugal instabilities that might exist for three-dimensional flows such as those in experimental tests. Since all the experimental results indicate an increase in St with Ω, this would seem a plausible explanation. Furthermore, such instabilities have been reported in the experiments of Diaz *et al.*,[158,159] the flow visualisation tests of Matsui,[211,220,221] and the three-dimensional numerical simulations by Mittal.[198] However, it does not explain the existence of two-dimensional numerical studies that support the trend of increasing Strouhal number.

Mittal & Kumar[203] further defended their findings by explaining that the trend of reduction of St with Ω was consistent with the observation that an increase in velocity ratio causes the wake to narrow. They argued that the reduction in the lateral width of the wake implies that the shear layers are closer to each other, resulting in a shorter characteristic length. Thus, from simple physical arguments, this would suggest a larger time scale for shedding, a lower frequency, and hence, a lower Strouhal number.

In support of the experimentally observed trend, Van Atta[218] used a similar argument to Mittal & Kumar, but reached a different conclusion. He noted that, as Ω increases, the separation points are asymmetrically displaced and come closer together, so that the distance between vortices shed from the upstream and downstream moving walls is reduced. If this characteristic shedding length scale decreases, then it follows that the shedding

frequency, which is inversely related to the length scale, would increase. Therefore, Van Atta concluded that, for fixed Re, one would expect the Strouhal number to increase with increasing Ω. A similar explanation to Van Atta's was also proposed in the numerical studies of Chew *et al*.[175] and Cheng *et al*.[169]

Support for the experimental results may also be inferred from the study of vortex shedding from stationary cylinders. It is known that the Strouhal number for an infinitely long stationary cylinder increases when Re passes beyond the critical regime,[120,222] and that this is caused by a change in wake width. For sub-critical flow, the cylinder experiences laminar boundary layer separation and the wake width is approximately the same as the cylinder diameter. For critical and supercritical flow, the accompanying transition to turbulent separation causes the separation points to move further downstream, which reduces the wake width, forces the free shear layers to interact earlier, and increases the value of St. Since the effects of cylinder rotation on the separation points and wake width seem equivalent to the described transition-induced motion, this would appear to validate the experimental findings.

Despite the difference in overall trend, several similarities between the graphs of Figure 3.41 may be seen. Both experimental and computational results generally agree that, for $\Omega < 1$, the Strouhal number is largely unaffected by rotation, remaining quite similar to the expected value for a stationary cylinder. The results also show that, for a given Ω, the Strouhal number increases with Reynolds number, matching the known Strouhal number behaviour of a stationary cylinder. Furthermore, the experimental and numerical data at comparable Re are quantitatively very similar. Examination of the data also suggests that, for $\Omega > 1$, the rate of change of St with Ω may be governed by the Reynolds number.

Reynolds number effects may also be responsible for the qualitative differences between the Strouhal number results of Tanaka & Nagano[188] and the other experimental data. The high test Reynolds numbers ($4.8 \times 10^4 \leq Re \leq 3.71 \times 10^5$) of this study may mean that the unusual shape of the Strouhal number curve is due to a change in vortex shedding activity near the critical Re, similar to that which occurs for a non-rotating cylinder in this range. That being said, the rapid rise in St with Ω that defines the Tanaka & Nagano results is not just restricted to near-critical Re. Alternatively, this sharp increase in Strouhal number may be linked with the sudden downstream shift in the upstream moving wall separation point that accompanies Magnus effect inversion, and which only becomes prominent when $Re > 2 \times 10^4$, this being outside the Re range of the other experimental studies. Three-dimensional effects from the very low aspect ratio of the cylinder ($AR = 2.4$) or experimental error, perhaps associated with the large blockage ratio of the tests ($d/B = 0.18$), are other possible origins for the unusual results.

3.7.4 Secondary Vortex Shedding

Recent numerical simulations by Mittal & Kumar[203] and Stojković *et al.*[197,223] suggest that, following initial suppression at Ω_c, vortex shedding from a rotating cylinder resumes within a small envelope of periodicity at high velocity ratio. For $\Omega \leq 1.9$, Mittal & Kumar's[203] results at $Re = 200$ were in agreement with other numerical and experimental findings. When $\Omega > 1.9$, vortex shedding was seen to stop and for $1.91 \leq \Omega \leq 4.34$ the flow was found to remain stable. However, at $\Omega \approx 4.35$, shedding unexpectedly resumed and the flow remained periodic until $\Omega > 4.74$. Similarly, the two-dimensional numerical study for $60 \leq Re \leq 200$ and $\Omega \leq 6$ by Stojković *et al.*[223] revealed that a secondary shedding phase appeared in the range $4.35 \leq \Omega \leq 5.45$, the exact point of onset being dependent on Reynolds number: with increasing Re the second shedding mode appeared at progressively smaller values of Ω.

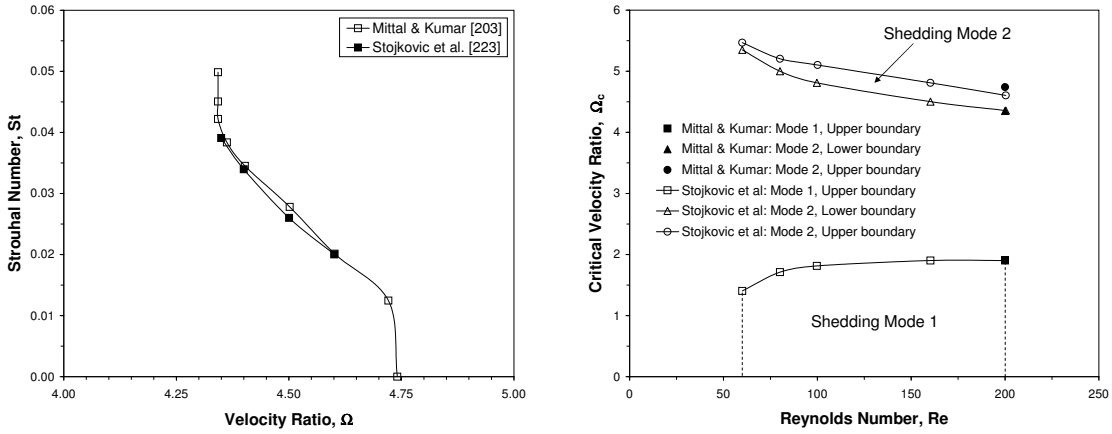

(a) Strouhal number evolution at $Re = 200$ (b) Location of the second shedding mode

Figure 3.42: Comparison between the Mittal & Kumar[203] and Stojković *et al.*[223] results on the nature of the second shedding mode.

Both studies noted that the characteristics of the shedding occurring in this second stage of instability were markedly different from that which takes place for $\Omega < \Omega_c$. Whereas in the first shedding stage both anticlockwise and clockwise vortices are shed alternately, only anticlockwise rotating vortices were shed during the secondary stage, and the Strouhal number was seen to be both quite small by comparison ($St \leq 0.05$) and more strongly dependent on velocity ratio. Furthermore, the amplitude of unsteadiness in the aerodynamic coefficients was much increased. A comparison of the Stojković *et al.* and Mittal & Kumar results on the apparent location and nature of this new shedding mode is shown in Figure 3.42. Such strong agreement between two separate works employing different numerical methods adds validity to the findings. In addition, both studies took appropriate

steps to ensure that the new shedding mode was not generated by numerical artefact.

Mittal & Kumar provided a detailed explanation for the existence of this two-stage shedding behaviour, suggesting that it was a consequence of the changes caused by rotation to the flow field. They noted that, ordinarily, vortex shedding can only occur if vorticity of large enough strength is released into a region of slowly moving, preferably recirculating, fluid. Thus, for $\Omega \geq \Omega_c$, vortex shedding is hampered by the formation of closed streamlines around the cylinder and the small size of the wake, such that any vorticity that does diffuse outside of the closed streamline is quickly advected away by high-speed flow.

However, at those velocity ratios associated with the second shedding phase this situation is changed. Whilst the clockwise vorticity is again advected away by high-speed flow, the anticlockwise vorticity is now fed into a region of slow moving flow, close to the stagnation point (which has moved due to the influence of rotation). As a result, vorticity is able to build up until it is eventually shed into the wake. The process happens slowly, so that the length of the shedding cycle increases, leading to a low shedding frequency and a small Strouhal number. When the velocity ratio increases further, the vorticity decays too quickly to diffuse out of the closed streamline region and so never reaches the outer flow, resulting in a return to stable flow.

The explanation given by Stojković *et al.* was less specific. They attributed the secondary shedding phase to an oscillation between two different flow types, one dominated by the effects of rotation, and that is more consistent with potential flow (this type was said to occur at higher Ω than the second shedding phase), and one where viscous effects more strongly influence the flow (this type was said to occur at lower Ω than the second shedding phase). The appearance of the second shedding phase at smaller Ω with greater Re was attributed to a reduction in the influence of viscous forces when Re is increased. Stojković *et al.* also predicted that the second region of unsteadiness should occur at other Reynolds numbers above $Re = 200$, but would occupy a different velocity ratio range.

The existence of such a secondary phase of vortex shedding at Reynolds numbers that are more realistically associated with practical application would be of significant interest. However, there do not appear to be any results that show this to be so. If such a secondary phase of shedding does exist at higher Re, its features are not visible in the results of Diaz *et al.*[158,159] for $Re = 9 \times 10^3$ and $\Omega \leq 2.5$, nor in the data from Massons *et al.*[212] for $Re = 2 \times 10^3$ and $\Omega \leq 3$. Given that the onset of the second phase appears to occur at progressively higher Ω with decreasing Re, it may simply be a matter of testing at the appropriate velocity ratio for a given Re. These existing experimental results would thus define the lower boundaries from which further tests should begin.

3.7.5 Effect of Shedding on Force Coefficients

One consequence of vortex shedding is to create periodic unsteadiness in the values of the aerodynamic coefficients. For a stationary cylinder, this effect causes the lift to fluctuate (about a zero-mean value) at the same rate as the shedding frequency, whilst the drag fluctuates twice as fast. In contrast, most numerical studies[174, 199, 204] have reported that, for a rotating cylinder, both the lift and drag fluctuate synchronously at the vortex shedding frequency. Furthermore, the amplitude of these fluctuations is said to be quite large, often being comparable in size to the mean value of the force. Experimental observations of the fluctuating nature of the forces are more sparse, with most studies only reporting the magnitude of the mean forces. Although no quantitative data seems to be available, some qualitative comments do exist,[12] these being in agreement with the numerically-based observations.

In most cases, the amplitude of unsteadiness in lift is found to be greater than that in drag, though both are reported to be constant in time (except for an early transient period following start-up). Most studies also note that the fluctuations are decreased by increasing velocity ratio due to the suppression of shedding; for $\Omega > \Omega_c$, fluctuations are practically nonexistent. Interestingly, both Mittal & Kumar[203] ($Re = 200$) and Stojković *et al.*[197] ($Re \leq 100$) have concluded that the unsteadiness in the aerodynamic coefficients was a maximum for $\Omega = 1.5$. This is somewhat surprising as, depending on Re, vortex shedding has typically been either significantly degraded or fully suppressed by this stage.

3.7.6 Vortex Shedding Lock-on

The fluctuating lift due to the presence of a vortex street can also cause a cylinder to oscillate in the transverse direction, especially if the body's natural frequency is close to the shedding frequency. Similarly, for a body undergoing forced vibration, if the forcing frequency lies in the vicinity of the shedding frequency it can cause a 'lock-on' effect wherein the combined system of cylinder-plus-wake act together and vortex shedding occurs at the vibration frequency, rather than the natural shedding frequency associated with the given flow conditions. This lock-on effect causes vortex shedding to be almost perfectly correlated across the span, which in turn can cause the amplitude of the oscillation to increase. Such behaviour is well documented for the case of a stationary cylinder[224–226] and has also been demonstrated for rotating cylinders.

During their experiments at low Reynolds numbers ($Re \leq 200$), Jaminet & Van Atta[147] found that a consequence of using very large aspect ratio cylinders ($34 \leq AR \leq 70$)

was that eccentricity in the motion of the cylinder occurred if the model was not perfectly straight, or if the clearance required for lubrication of the bearings allowed for eccentric rotation. Despite efforts to eliminate such factors altogether, Jaminet & Van Atta reported that lateral vibration and whipping of the cylinder was found to have interfered with the process of vortex shedding.

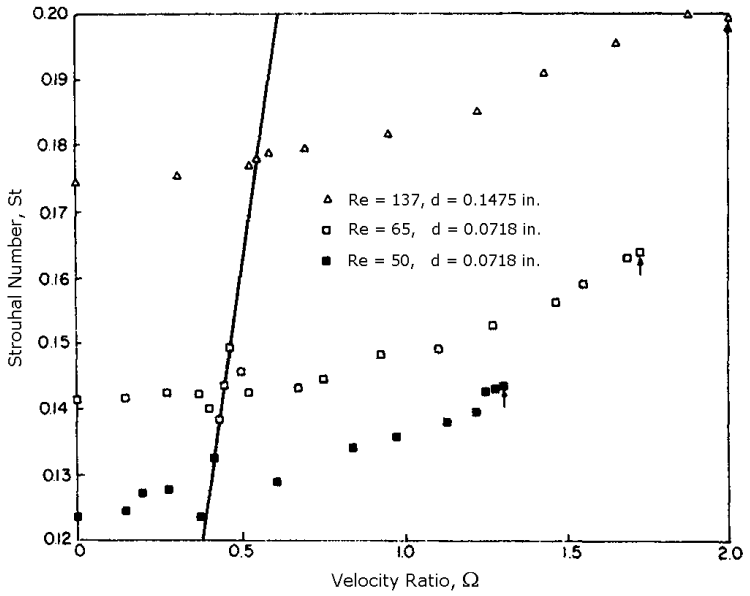

Figure 3.43: Effect of eccentricity on the Strouhal number.[147] The solid line indicates regions where the shedding frequency was synchronised with the vibration frequency. The arrows denote the points at which shedding was suppressed.

Both types of perturbation had the same effect of synchronising the shedding frequency to the rotation rate, with the magnitude and frequency of the perturbation influencing the extent to which the shedding rate was affected. Within the synchronisation range, vortex shedding was found to be highly stable and regular, exactly as in the non-rotating case. When the velocity ratio was increased further the shedding frequency no longer followed the rotation rate, returning instead to its expected value (see Figure 3.43). In addition, for those Reynolds numbers where shedding was not expected to occur ($Re < 50$), Jaminet & Van Atta reported that oscillation of the cylinder could be used to artificially induce vortex shedding.

3.8 The Effects of Yaw on a Rotating Cylinder

The effects of yaw on a rotating cylinder appear to be practically unstudied. The only investigation known to exist is the experimental study of Howerton,[227] though this was

very limited in its nature. The tests spanned a Reynolds number range of $2.4\times10^4 \leq Re \leq 5 \times 10^4$, but the velocity ratio was limited to $\Omega \leq 0.7$ and only a single yaw angle was considered. Furthermore, only the lift and drag were recorded, with no measurements of sideforce, yawing moment, or rolling moment taken. Thus, information on lateral forces and moments would seem to be completely absent from all of the available literature.

Howerton's[227] tests examined the aerodynamic forces on two adjacent, independently rotating circular cylinders in crossflow. Each individual cylinder had an aspect ratio of $AR = 8.25$, and a small clearance of 1/16" (≈ 1.6 mm) was maintained between the two. The tests were primarily concerned with the evaluation of the effects of differential rotation of the two cylinders on lift and drag at zero yaw, but a second configuration, where the cylinders were positioned offset from the perpendicular by $30°$, was also investigated (see Figure 3.44). For these yawed tests, the rotation rate of both cylinders was kept the same. Preliminary experiments with oildots showed little tendency for spanwise flow, indicating that the adopted arrangements closely approximated two-dimensional flow.

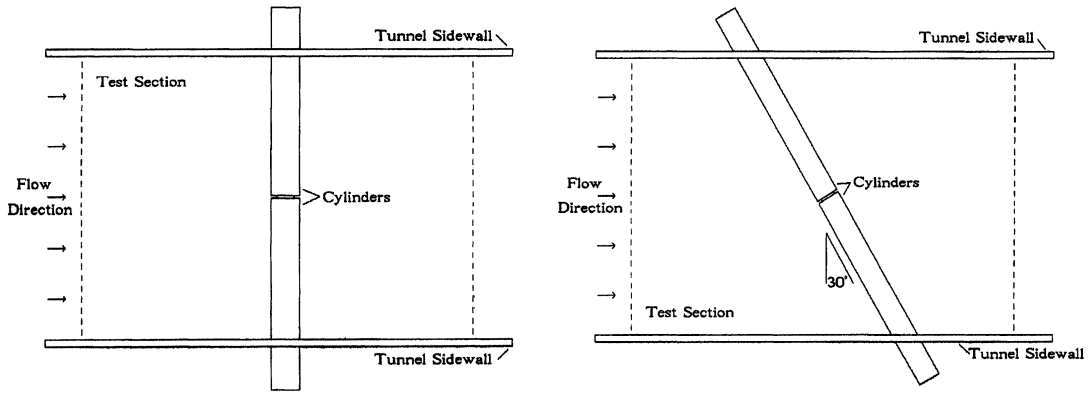

(a) Primary Configuration (b) Secondary Configuration

Figure 3.44: Configuration of cylinders in wind tunnel for Howerton's[227] tests.

The objective of Howerton's yawed tests was to determine whether the crossflow component or the normal component of velocity was the only factor in developing the lift and drag. For this purpose, the tunnel speed for the yawed tests was chosen so that the normal velocity component matched the freestream velocity used in the non-yawed tests. This normal component was used in the non-dimensionalisation of the forces measured when the cylinder was offset, the results of which were then compared with the force coefficients obtained when the cylinder was in direct crossflow. Based on his results (see Figure 3.45), Howerton reported that, for the approximately two-dimensional configuration adopted and the range of Reynolds numbers and velocity ratios tested, the assumption of treating the normal component of velocity as the only significant contributor to the lift

and drag was valid. However, it should be noted that Howerton estimated the error in his force data to be as much as 7.5%. In addition, his results for zero yaw do not match well with those of Thom[115,118,119] or Swanson[12] at similar Re.

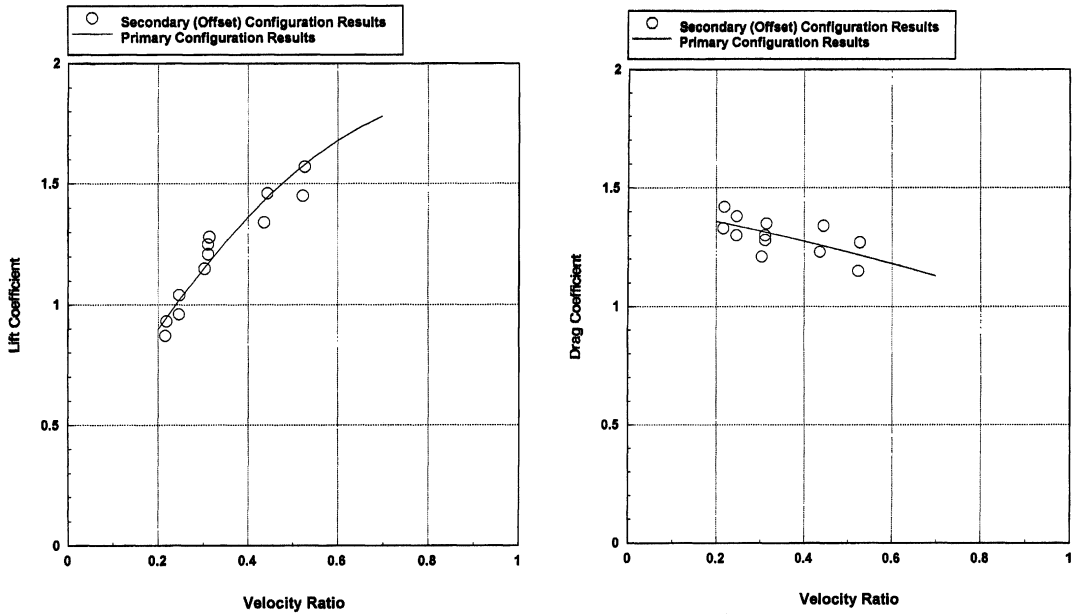

(a) Lift Coefficient (b) Drag Coefficient

Figure 3.45: Howerton's[227] results for the forces on a yawed rotating cylinder at $\Psi = -30°$.

Examination of the literature for stationary yawed cylinders hints at other possible effects that may have some bearing on the flow past a yawed rotating cylinder. Work by Zdravkovich *et al.*[193] on short ($AR \leq 8$) non-rotating circular cylinders indicates that a bistable and hysteretic spanwise asymmetry in the pressure distribution about the xy plane may influence the yawing and rolling moments of low aspect ratio cylinders even at zero yaw. Angles greater than $\Psi = 2°$ were found to enhance the asymmetry, though the resulting yawing and rolling moment coefficients remained small throughout (≤ 0.3). In addition, the literature for stationary cylinders suggests that yaw angle also affects the frequency (St is reduced) and form of vortex shedding.[120] Given the similarity between shedding from rotating and stationary cylinders, especially at low Ω, such changes in shedding phenomena may be expected to occur with a rotating cylinder too, though this remains unconfirmed.

3.9 Multiple Cylinders

Studies with multiple stationary cylinders indicate that interference effects at close proximity can drastically change the flow around the cylinders, producing unexpected forces,

changes to the pressure distributions, and alterations to vortex shedding phenomena, either by intensification or suppression.[120,228] The study of interference flows between two rotating cylinders in close proximity has largely been ignored, and does not feature strongly in the available literature. When it has been examined, it has mostly been approached in purely theoretical terms, such as in the work of Watson[229] and Ueda *et al.*[230] This type of analytical study is usually carried out for Stokes flow conditions, where the Reynolds number is extremely low ($Re < 1$), and so tend to be of little practical interest. A small number of flow visualisation studies, such as Prandtl's tests,[9,108] also exist, but are purely qualitative. Useful information on the interference effects between two rotating cylinders is thus limited to the experimental work of Howerton.[227]

3.9.1 Overview of Interference Between Stationary Cylinders

The different arrangements of two parallel stationary cylinders with axes positioned at right angles to the flow direction are typically classified into one of three groups (see Figure 3.46). In the first, the cylinders are in tandem, one behind the other at any longitudinal spacing, S. In the second, the cylinders face the flow one on top of the other at any transverse spacing, T (known as 'side-by-side'). All other combinations of longitudinal and transverse spacing represent a staggered arrangement. A comprehensive review of interference effects for tandem, side-by-side, and staggered stationary cylinders is given by Zdravkovich.[120]

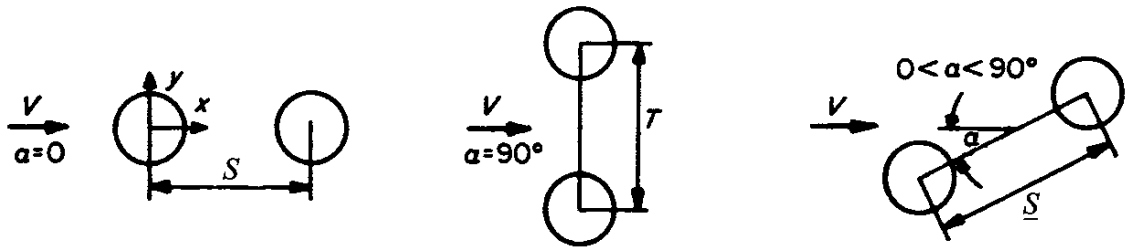

(a) Tandem (b) Side-by-side (c) Staggered

Figure 3.46: Classification of multiple cylinder configurations.[222] Note that S, T, and $\underline{S}$ are measured center-to-center.

A simplified version of Zdravkovich's suggested interference flow regimes for all three arrangements is shown in Figure 3.47. Note that this diagram is only applicable to Reynolds numbers between $1 \times 10^3 \leq Re \leq 1 \times 10^5$ (which are of particular interest for the present work). For higher and lower Re there is known to be considerable modification of the interference effects.[120] Primarily, interactions between the cylinders are governed by the

spacing ratios (S/d, T/d) and the Reynolds number, but are also known to be influenced by such parameters as freestream turbulence, surface roughness, and aspect ratio.

The effects of changing cylinder spacing are largely felt through an alteration (that can be both beneficial or detrimental) of the drag forces and shedding phenomena, and may be loosely divided into those due to proximity interference (arising as a result of the physical nearness of one cylinder to the other) and those due to wake interference (a consequence of one cylinder being immersed in the wake of the other, but not necessarily in very close proximity). The level of interference experienced can also be either partial (where only one cylinder is affected) or combined (where both cylinders mutually interfere).

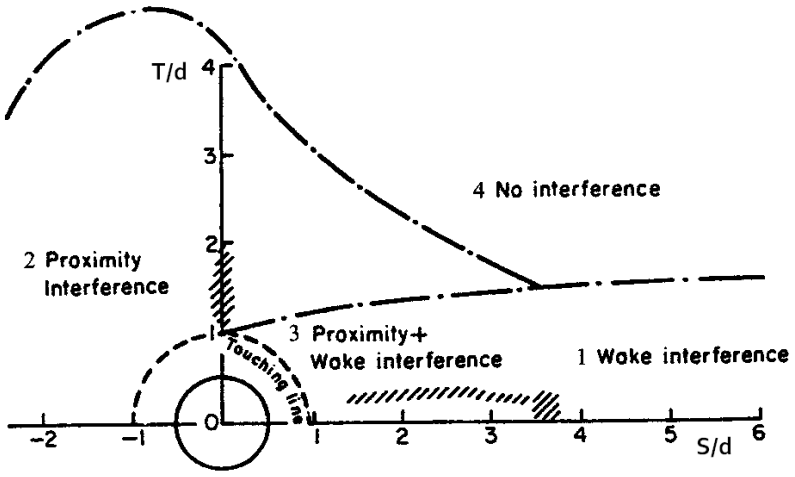

Figure 3.47: Simplified diagram of Zdravkovich's[120] interference flow regions between two stationary cylinders for $1 \times 10^3 \leq Re \leq 1 \times 10^5$. Hatched regions indicate bistable flow.

3.9.2 Interference Between Rotating Cylinders

Rotation adds an extra degree of complexity to the interference effects between two or more cylinders in close proximity. Cylinder-to-cylinder interactions will be dependent on the directions of rotation (whether co-rotating or counter-rotating) and the velocity ratios of the two cylinder (whether equal or unequal). In any case, the extent of both the proximity interference and wake interference regions may be expected to change with increasing velocity ratio, so that there would be one such interference diagram as Figure 3.47 per value of Ω. In particular, wake interference regions will be altered by the biasing of the wake that occurs at higher Ω. As a result, the interference flow regimes for a rotating cylinder would not be expected to be symmetrical about the S/d axis (except, perhaps, at the lowest velocity ratios).

As noted, the literature on interference effects between rotating cylinders is very limited.

None of the existing studies have investigated tandem or staggered arrangements, whilst side-by-side configurations have been considered only in the aforementioned theoretical analyses and flow visualisation tests. Prandtl's tests concentrated on the case of two counter-rotating, touching cylinders ($T/d = 1$), but provide no useful information on the flow pattern other than the observation that vortex shedding is eventually suppressed as Ω is increased. The analytical investigations are more varied, examining both equal and unequal co-rotating and counter-rotating cylinders at various T/d, but the assumptions made and low Reynolds numbers considered mean that the results are of no practical value.

Howerton's experimental tests considered a slightly different configuration than most multiple cylinder investigations, but are important as they provide information on the effects of interference due to differential rotation of the cylinders, which is of interest to the present work. The arrangements for Howerton's tests have been fully described in §3.8, but are summarised here for convenience. The cylinders were neither tandem, side-by-side, nor staggered. Instead, they shared the same axis of rotation, but were separated by a small spanwise distance of 1/16". Each cylinder had aspect ratio $AR = 8.25$ (see Figure 3.44), the test Reynolds number range was $2.4 \times 10^4 \leq Re \leq 5 \times 10^4$, and the velocity ratio was limited to $\Omega \leq 0.7$.

Differential rotation was implemented by changing the rotational rate of one of the cylinders to a value that was slightly higher or lower than the rate at which the other cylinder spun. The case of both cylinders spinning together at the same rate was taken as a baseline, against which the results for differential rotation were compared (see Figure 3.48). A total range of conditions between $\pm$60% from the baseline were examined in steps of 20%. At each step, the change in lift and drag was recorded so as to assess the impact of interactions between the cylinders on the forces generated by the system as a whole.

In general, interaction effects between the cylinders were found to be nearly non-existent for low values of differential Ω (less than $\pm$20% difference), but became more important as the disparity in velocity ratios was increased. In any case, even for a high disparity in Ω ($\pm$60%), interference effects caused only a minimal change in the drag of the two-cylinder-system ($\approx 1\%$), with a slightly greater change in the lift coefficient ($\approx 4\%$). However, Howerton also noted that the error margin of his results ($\approx 7.5\%$) was of a similar magnitude to the changes apparently induced by differential rotation; thus, only general trends can be inferred from the data. Furthermore, Howerton's results with no differential rotation rate (effectively a single cylinder scenario) indicated much smaller lift coefficients than those measured by Thom[115,119] and the drag data showed differences to that of Swanson,[12] with C_D generally being higher. Hence, it is unclear how reliable Howerton's observations actually are.

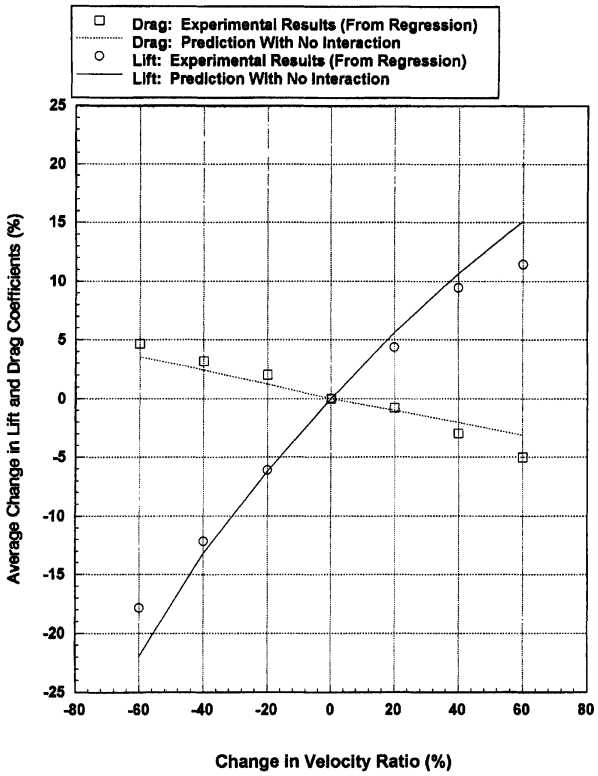

Figure 3.48: Howerton's[227] results for the effects of differential rotation on lift and drag of two coaxial cylinders at $2.4 \times 10^4 \leq Re \leq 5 \times 10^4$. Cylinder separation was 1/16".

3.10 Wind Tunnel Wall Corrections

The substantial experimental component of the present research necessitates that consideration be given to the evaluation of the accuracy and validity of the results. Primarily, this entails an assessment of the effects of tunnel wall constraint on the measured data so as to prevent an incorrect determination of the aerodynamic coefficients, something which is often overlooked in existing rotating cylinder studies. As a result, information on this matter is very limited. Guidance may be sought from examination of methods applicable to general bluff-body flows, as wall as analysis of blockage effects, and their correction, for a non-rotating cylinder. Correction techniques of interest may then be considered in light of what little information on this subject is available in the literature for rotating cylinders.

3.10.1 Overview of Conventional Wall Interference

Generally, the primary effect of wall constraint is regarded to manifest through an apparent change in the freestream velocity, and is assumed to have both normal and streamwise

components. For a model positioned in the center of a wind tunnel, these may be considered independent to each other. The vertical component represents a change in the flow direction and is known as lift interference, since it is usually associated with the circulation around the model; specifically, the constraint imposed on the velocity field of the bound and trailing vortices. The streamwise component represents an increase in the longitudinal flow speed and is known as blockage interference. Blockage is commonly assumed to consist of two independent parts: a solid blockage component due to the volume occupied by the body, and a wake blockage component due to the reduction of flow speed in the wake. Wake blockage also induces a longitudinal static pressure gradient across the model that affects the measured drag.

The exact magnitude and nature of the wall interference on a model is governed by the aerodynamic characteristics of the model, its size relative to the working section (often expressed in terms of the so-called 'model blockage' parameter, defined as either the ratio of total model frontal area to tunnel cross-sectional area, A/C, or the ratio of model reference area to tunnel cross sectional area, S/C), the freestream Mach number, and the tunnel type: interference will differ depending on the cross-sectional shape of the working section and whether it is open or closed. Special conditions such as slotted or perforated walls will also have an effect. Therefore, the methodology required to correct the flow field will differ from case to case. In the following discussion only those methods applicable to closed rectangular or octagonal subsonic wind tunnels, as employed in the present research, are considered.

The simplifying assumptions on which conventional wall interference models are built result in corresponding limits to the applicability of the theories. Typically, the model should be less than $0.8B$ in span (where B is the tunnel width), wings should be uniformly loaded, and the lift not too large. Critically, the standard theories assume that the body in question gives rise to an essentially streamline flow, where wake effects are small and drag is low. For flow past a stalled wing or bluff body, such as a cylinder, these techniques tend to underestimate the effects of blockage.

More modern methods to assess wall interference eschew a purely analytical approach in favour of multiple measurements of the wall static pressure inside the working section. These boundary measurement methods provide advantages in regards to model and wall representation, particularly for bluff bodies, but can be somewhat impractical, needing as many as 100 to 200 wall pressure readings to give good results.[231] Even more advanced methods involve adaptive tunnels with variable geometry and on-line processing of corrections,[232] but such methods are not readily available or easily implemented in the typical wind tunnel. Consequently, the relative simplicity of the analytical approach is generally

more convenient.

3.10.2 Correction Models for General Bluff-Body Flows

The effects of wall constraint on the flow around a bluff body (defined as a body having leading-edge separation without re-attachment or having large regions of separated flow further aft on the body[232]) are even now not fully understood. As a result, there is no entirely satisfactory method for applying boundary corrections to these geometries. Nevertheless, several techniques that cater for such cases as a stalled wing or a flat plate normal to the flow have been developed, the most commonly employed of which are briefly discussed below. More details may be found in the relevant AGARD reports[232, 233] and ESDU data sheets.[234]

The founding approach to the analytical estimation of wake blockage for bluff models in closed test sections was by Maskell.[235] He argued that it was unrealistic to suppose that the effect of wall constraint on bluff-body flow can be separated into solid and wake blockage components, since this approach may only be adopted when the influence of the wake on the pressure field over the body can be regarded as a second order effect, as it can for most streamline flows. In contrast, the pressure field over a bluff body depends strongly on the wake structure and generally bears little relation to the attached flow field of the body, from which conventional solid blockage is derived. Thus, Maskell concluded that bluff-body flow would seem to require a mathematical model that is quite different from that adopted for streamline flow.

In his analysis, Maskell used an approximate relation describing the momentum balance in the flow outside the wake, supported by wind tunnel measurements on three-dimensional flat plates normal to the freestream, to formulate a theory for the wake blockage produced by separated flows. The analysis was predicated on a number of assumptions: (1) That the pressure distribution was invariant under wall constraint; (2) That separated flows from three-dimensional bodies tended to become axially symmetric far downstream; (3) That the base pressure was constant over the separated region and was equal to the static pressure on the wake boundary; and (4) That the constraining effect of the test section walls distorted the wake by reducing its expansion and that this reduction was in proportion to the contraction of the external stream around the wake.

The first of these assumptions is fundamental to Maskell's method. It implies that blockage only scales the pressure field by a constant speed increase, without changing its shape. Consequently, for Maskell's theory to be applied to a particular geometry, the location

of any separation or reattachment points for that body must be independent of wall constraint. The remaining assumptions have been shown[236,237] to not be critical to the validity of Maskell's method.

Although derived from analysis of non-lifting flat plates, Maskell's method may, with a slight modification, also be applied to lifting flows. Ordinarily, the correction in Maskell's equation is due to the separated-flow component of drag that in the case of a non-lifting body accounts for almost all of the drag. When the wake-blockage correction is applied to bodies that have drag contributions from sources other than flow separation, the different components must be estimated so that Maskell's correction can be applied only to the drag resulting from flow separation. The remaining drag components should be corrected in the conventional fashion. For a wing or aircraft, this drag breakdown is readily done. In other cases, the breakdown may be less certain and the correction is often applied to the total drag coefficient instead.

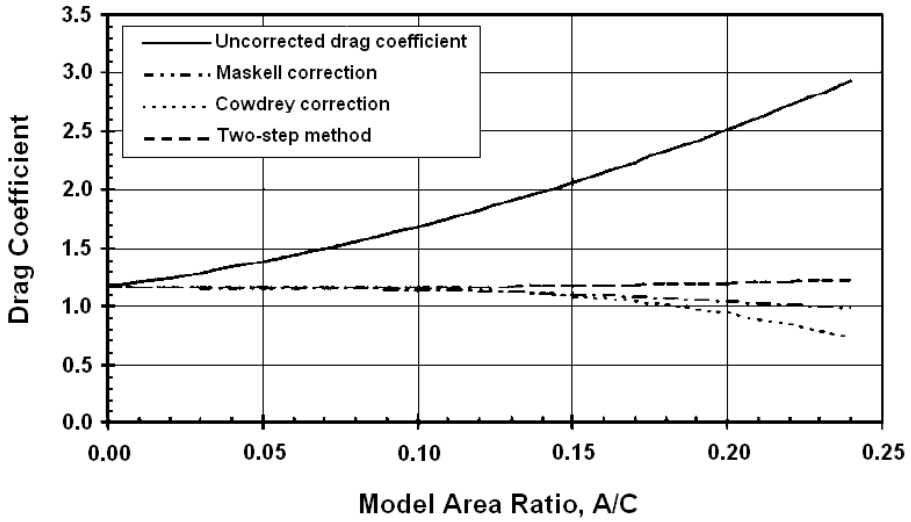

Figure 3.49: Comparison of separated-flow corrections for three-dimensional normal flat plates.[232]

When applied to many two-dimensional and three-dimensional bluff bodies, Maskell's method has been found to overpredict the correction for large blockage ratios. Hackett[238] argued that this was a consequence of assumption (4) of Maskell's approach, which effectively combines the incremental drag correction arising from wake distortion due to boundary constraint with the dynamic pressure correction. To remedy this, Hackett modified Maskell's analysis by separating the correction into its two constituent components: a blockage-induced incremental velocity and a drag increment. He argued that the resulting 'two-step' version of the analysis should provide a superior adjustment to both the drag and other forces and moments.

A comparison of Maskell's method to Hackett's two-step version[238] and Cowdrey's later analysis[237] shows that the tendency of Maskell's method towards overcorrection at high blockage is indeed removed by use of the two-step derivation (see Figure 3.49). By contrast, the Cowdrey method is seen to overcorrect the data more so than even the Maskell method, particularly when $S/C > 0.2$. However, for $S/C \leq 0.12$ all three approaches produce identical results.

3.10.3 Blockage Effects and Correction for a Nonrotating Cylinder

There are a number of studies that have specifically focused on the effects of wall constraint on the flow past a stationary circular cylinder in a wind tunnel, though much of this previous work has been performed in the context of nominally two-dimensional flow. Furthermore, since a stationary cylinder is a non-lifting body, there is no attention given in the literature to the establishment of specific lift interference methods for this geometry. Rather, the literature considers only the determination of blockage interference and its subsequent effect on the flow. Examination of such work reveals a lack of overall consensus on the effects of blockage and the best way to correct for them. Nevertheless, the literature for nonrotating cylinders provides a measure of guidance regarding the selection of a suitable method to correct experiments on a rotating cylinder.

The results of most tests investigating wall interference on a stationary cylinder indicate that the Strouhal number, drag coefficient, and surface pressure distribution around the cylinder are dependent on the blockage ratio. The Strouhal number and drag coefficient usually increase as blockage increases, though competing effects can sometimes act to keep C_D fairly constant.[239] Increasing blockage is also known to cause the magnitudes of the minimum pressure coefficient ($C_{p_{min}}$) and base pressure coefficient ($C_{p_{base}}$) to increase too.[240] However, the effect of blockage on the form of the pressure distribution and the position of the separation points is a matter of dispute. Resolution of the influence of blockage on such characteristics is of critical importance as the applicability of many of the correction models for bluff-body flow is dependent on the outcome.

Fackrell[241] remarked that it seemed likely that the separation position on curved bodies could change due to an effective increase in Reynolds number caused by wall constraint. However, he noted also that the results of his tests with a circular cylinder at $Re = 1 \times 10^5$ suggested that the assumption of fixed separation points was adequate. Similarly, tests with cylinders by Modi & El-Sherbiny,[242] also at a Reynolds number of $Re = 1 \times 10^5$, showed that there was little change in the separation positions for blockage ratios at least as large as $d/B = 0.36$.

By contrast, the study by West & Apelt[239] reported that the actual shape of the pressure distribution around a circular cylinder was changed when blockage was greater than $A/C = 0.06$. The change was said to be the result of an upstream shift in the separation position that occurred for all aspect ratios tested ($AR = 4$, 6, 8, and 10) and for Reynolds numbers at least as high as $Re = 6 \times 10^4$. The shift was associated by West & Apelt with changes in the tunnel floor pressures that were caused by increasing blockage.

Given their results, West & Apelt concluded that whilst blockage effects were negligible at low blockage ratios ($A/C \leq 0.06$), for those cases where the shape of the pressure distribution was changed, the commonly used correction techniques based on the method of images concept (which do not account for such changes) were inappropriate for correcting pressure data in the region where the change occurs ($70^\circ \leq \beta \leq 120^\circ$). Nor could they be expected to adequately correct the drag coefficient. This view is in direct contrast to that expressed in other studies, where it has been reported that some conventional correction procedures are effective for stationary cylinders at low blockage ratios. In particular, Modi & El-Sherbiny[242] reported that Maskell's correction method may be employed at low blockage ratios, but is not valid beyond $d/B = 0.2$.

In view of the lack of a well established method for correcting bluff-body flows, Farell *et al.*[240] carried out their own experimental investigation to assess the validity and accuracy of the available blockage correction methods when applied to low-speed flow past a non-rotating cylinder spanning a wind tunnel. They defined blockage by d/B and examined the range $0.068 \leq d/B \leq 0.205$. To eliminate the possibility that a change in flow conditions would move the separation points they used surface roughness to ensure that the flow was fully turbulent. Interestingly, in their discussion of bluff body blockage, these authors maintained the division of the effect into solid and wake components that Maskell had rejected.

Farell *et al.* corrected their measurements using both the Maskell[235] and Allen & Vincenti[243] methods and then compared the results. For blockage ratios less than $d/B = 0.15$, the two methods both yielded corrected values for the pressure and drag coefficients that were nearly independent of constraint. However, there was a consistent difference in the magnitude of the corrected results predicted by the two models. Extrapolation of the experimental data to zero blockage led Farell *et al.* to favour the Allen & Vincenti method. This is surprising as Fackrell[241] found Allen & Vincenti's velocity correction technique to undercorrect at low blockage ratios and overcorrect at high blockage.

The results of the tests by Farell *et al.* also revealed a number of other interesting findings. Firstly, the pressure difference $C_{p_{base}} - C_{p_{min}}$ was found to be largely unchanged for

blockage ratios up to $d/B = 0.205$. Since this value represents the pressure rise sustained by the boundary layer prior to separation, its near independence from blockage led Farell *et al.* to suggest that a turbulent boundary layer is relatively insensitive to local changes in the flow velocity caused by blockage effects. Secondly, some of their early tests with the cylinder model varied the blockage ratio by moving the walls of the wind tunnel rather than changing the model size. In these cases, the three-dimensionality of the flow at the free ends of the cylinder was found to overshadow the effects of blockage. Finally, Farell *et al.*[240] also suggested that the effects of blockage may differ depending on whether the flow is subcritical or supercritical, this being particularly so at the larger blockage values ($d/B > 0.15$).

3.10.4 Blockage Effects and Correction for a Rotating Cylinder

It is assumed that wall constraint will have a similar effect on the flow past a rotating cylinder as it does when the cylinder is stationary. Hence, there is a requirement for correction methods suitable for this arrangement. The bluff body blockage correction models described in §3.10.2 and §3.10.3 have typically been developed with flat plates or stationary cylinders in mind and no specific correction procedure for a rotating cylinder is known to exist. When considering the applicability of these existing blockage correction methods to rotating cylinder flow, there are a number of questions and issues that are specific to this geometry which have to be addressed.

At low velocity ratios a large separated wake is prevalent and the rotating cylinder could be considered as a typical bluff body. For $\Omega < 2$, depending on the Reynolds number, there may also be well-defined vortex street that makes the wake unsteady. This raises the question of whether rotating cylinder flow needs to be corrected with unsteady wind tunnel wall correction models comparable to those intended for other unsteady flows, such as oscillating aerofoils. In this regard, it should be noted that whilst the wake of a stationary cylinder is also unsteady, the correction of this flow for wall interference has not been treated any differently in the literature than steady flows. Similarly, in his tests with autorotating wings, Smith[183] used Maskell's method to correct his wind tunnel data for blockage. Although the method was derived for steady flow, Smith assumed it to be valid for his tests because the wing rotated rapidly enough for the shed vortices to be closely spaced and they were observed to quickly merge into a wake of relatively uniform size. This assumption would seem applicable to rotating cylinder flow too.

With increasing velocity ratio the size of the wake is rapidly reduced and vortex shedding, and its accompanying unsteadiness, is eventually suppressed. For high velocity ratios

(say $\Omega > 4$), the pressure distribution begins to approach that predicted by potential flow, albeit at a lower effective Ω, suggesting that, for these conditions, the wake exerts less of an influence on the pressure field than at low Ω, and thus raises the question of whether it would now be reasonable to apply the conventional correction techniques based on streamlined flow. At such high velocity ratios there will also be a closed streamline around the cylinder that is not symmetrical about the x axis. This changes the effective shape of the cylinder and will mean that it is no longer positioned on the tunnel centerline. Whilst any consequence of this can be expected to be small, it may still require consideration.

In addition to the changing nature of the wake, a rotating cylinder correction model may also have to address the very strong deflection of the wake that occurs at high Ω and the accompanying large lift forces. In conventional lift interference, the induced velocity is assumed to have no component along the tunnel axis; therefore, there is no lift effect on the tunnel speed or dynamic pressure. Instead, the transverse component of the induced velocity (upwash) varies along the tunnel axis, creating an effective curvature of the flow that is generally regarded as being equivalent to a change in aerofoil camber and incidence.

Since the aerodynamic characteristics of a rotating cylinder are only a direct function of Ω, not α, lift interference may be expected to have less of an effect on rotating cylinder flow, requiring only a simple correction of the force measurements due to rotation of the wind axes. Furthermore, Smith's[183] experience of correcting autorotating wings for lift interference suggests that it may be possible to ignore the effects altogether. Smith used the standard streamline curvature and downwash corrections, as detailed in Pope & Harper,[231] but found the lift correction to be very small in comparison to the blockage term. However, as Smith did not compare his data against any pre-existing results, it is not possible to assess how successful the application of these techniques to a body rotating about an axis transverse to the freestream actually was.

The research on blockage for stationary cylinders also indicates that the suitability of a given correction method may depend on Reynolds number. For the case of a rotating cylinder there is then the added question of whether the choice of model should depend on the freestream Reynolds number or be governed by boundary layer transition effects caused by rotation. Depending on the tunnel speed, a condition in which the freestream Reynolds number is subcritical, but the boundary layer is turbulent may easily occur at some velocity ratios. Thus, the choice of correction model may be required to vary with both Ω and Re.

Alongside such specific questions, the general applicability of bluff body correction tech-

niques to the case of a spinning cylinder is also dependent on the effects of constraint on the location of the separation positions, which remains uncertain. Measurements by Swanson[12] and others indicate that the boundary layer is fully turbulent from inception for all $\Omega \geq 1$. Hence, the observation by Farell *et al.*[240] that a turbulent boundary layer is relatively insensitive to blockage effects implies that any effects of constraint on the position of the separation points should be restricted to low velocity ratios, whereas at high Ω the assumption of fixed separation points on which methods such as Maskell's[235] and Fackrell's[241] are based should be satisfied. As there are no known results from tests specifically aimed at investigating the change in the separation positions with blockage ratio for a rotating cylinder, such speculation cannot be confirmed. However, Peller's[151–153] measurements of the boundary layer may provide relevant information.

Despite the high blockage ratio of his tests ($d/B = 0.3$), Peller's[151] results regarding the position of the separation points compared well with previous findings at similar Re by Swanson.[12] Thus, Peller suggested that for velocity ratios at least as high as $\Omega = 2$, the effect of tunnel constraint on the boundary layer development was minimal. In addition, Peller concluded that his measurements showed that the immediate influence of rotation was negligibly tied-in with the effects of blockage and short aspect ratio.

The results of surface pressure measurements such as those of Chew[154] and McLaughlin *et al.*[155] are more ambiguous about the impact of Reynolds number, and hence wall constraint, on the separation points. These studies show that, whilst the location of the separation point on the downstream moving wall is largely insensitive to Reynolds number, boundary layer separation on the upstream moving wall is strongly dependent on both Re and Ω. That being said, McLaughlin *et al.* also reported that, for low velocity ratios, the pressure distributions on the upstream moving wall were found to be coincident regardless of Reynolds number, and they suggested that alterations to the pressure distribution caused by changes to Re were minor relative to the scaling effect of changing the velocity ratio.

The difficulty in choosing an appropriate method for correcting wall interference is further exacerbated by the lack of discussion of correction methods in the existing literature on rotating cylinder flow, thus leaving most of the above-mentioned questions unanswered. Only Thom[115] and Peller[151–153] have explicitly commented on correction methods to be applied to forces measured on a rotating cylinder, and then only in the context of two-dimensional flow. Griffiths & Ma[189] indicated that they had corrected their results for the effects of blockage, but gave no details of the methods used, nor any information on the blockage ratio of the tests. Modi *et al.*[141] echoed the aforementioned failings of conventional blockage correction techniques, and stated that, in the absence of a reliable

procedure to account for the effects of wall constraint, they had opted to purposely leave their data uncorrected. In all other publications, blockage corrections have either been applied yet not mentioned, or presumably, ignored completely.

Thom's[115] discussion of the effects of tunnel walls on the measured lift and drag was concerned only with the constriction of streamlines. Thom connected the prevention of streamlines around the cylinder from bulging with an increase in velocity of magnitude

$$\frac{\Delta V}{V} = \left(\frac{d}{H}\right)^2 \tag{3.23}$$

and then calculated an appropriate correction from the potential flow equations for the stream function of a two-dimensional rotating cylinder. On examination, this approach appears similar to a discussion of solid blockage for a stationary cylinder; No mention of wake blockage effects was made. Thom reported that his method worked quite well when applied to his own results, successfully bringing lift coefficients measured at $d/H = 0.26$ into line with results at $d/H = 0.13$. The method did not work so well with the drag coefficients though.

Peller's[151–153] discussion was also performed in the context of two-dimensional flow. His cylinder spanned the height of the working section, having a rather large blockage factor of $d/B = 0.3$. This was somewhat intentional as Peller's work was concerned with the use of rotating cylinders in cluster heat exchanger applications, where blockage can be considerable and flow conditions non-ideal. Peller considered only solid blockage in his discussions, and did not appear to differentiate between stationary and rotating cylinders when selecting blockage correction methods. He presented a list of several different velocity correction formulae developed for heat exchanger applications,[151] though all such equations predict far larger values for the velocity correction than conventional solid blockage correction methods. For his own work, Peller used Lock's method as outlined in Pankhurst & Holder.[244]

Even if blockage is not explicitly discussed, there is usually enough information given in individual journal articles or technical reports to enable an assessment of the blockage ratio at which the existing body of force results were obtained. In this way, those data obtained under 'blockage free' conditions can be identified and then used to assess changes due to blockage in other data sets. However, there are some studies where the available details are insufficient and either the cylinder diameter or tunnel section size is omitted. Furthermore, the often large variations in aspect ratio, end conditions, and Reynolds numbers that exist between different experimental studies would make it difficult to be sure

that any differences are actually due to wall constraint rather than some other factor. The lack of reliable numerical data at comparable Reynolds number to the experimental literature is another hurdle to assessing the effects of blockage on the available force data. Even with such difficulties, it is worth comparing the blockage ratios of various experimental studies and seeing what, if anything, may be inferred about their results.

Such a comparison (see Table 3.1) indicates that the studies by Thom,[115,119] Jaminet & Van Atta,[147] Diaz *et al.*,[158,159] Massons *et al.*,[160] and Tokumaru & Dimotakis[191] are at low enough blockage that the effects of constraint can be considered negligible (by Apelt & West's[239] 6% criterion). However, of these, only the studies by Thom and Tokumaru & Dimotakis provided force coefficient data, the others being solely concerned with the nature of the wake. Furthermore, the study by Tokumaru & Dimotakis did not measure drag and took no direct measurements of the lift, but rather calculated the value of C_L semi-empirically via measurements of the local velocity field. Note also that a number of important experimental studies[8–10,12,146] provide insufficient information to conclusively assess the blockage ratio, leaving the accuracy of their data ambiguous.

Table 3.1: Blockage ratios of experimental studies.

Author	d/B	S/C
Reid (1924)	0.075	0.095
Thom (1925)	0.02–0.13	0.008–0.13
Thom (1926)	0.13	0.13
Thom (1931)	0.19	0.19
Thom (1932)	0.12–0.19	0.12–0.19
Thom (1934)	0.04–0.08	0.04–0.08
Jaminet & Van Atta (1969)	0.002–0.005	0.0004–0.0008
Tanaka & Nagano (1973)	0.18	0.18
Miller (1976, 1979)	0.13	0.039
Diaz *et al.* (1983, 1985)	0.033	0.033
Coutanceau & Ménard (1985)	0.071–0.107	0.087–0.13
Peller (1986)	0.30	0.30
Massons *et al.* (1989)	0.054	0.054
Aldoss & Abou-Arab (1990)	0.095	0.095
McLaughlin *et al.* (1991)	0.17	0.17
Tokumaru & Dimotakis (1993)	0.051	0.048
Takayama & Aoki (2005)	0.44	0.42

Plotting the data of Thom at low blockage against that for much higher d/B reveals no real trend associated with blockage ratio. In particular, the drag results are seen to be much more strongly dependent on aspect ratio (see Figure 3.50a). This is not unexpected

given the comments by Farell *et al.*,[240] with regards to stationary cylinders, on the ability of three-dimensional effects to dominate those due to blockage. Comparison of the lift results (see Figure 3.50b) indicates that two separate types of curves may be observed: those for blockage ratios of $d/B \leq 0.13$ and those for higher blockage. The difference is mostly appreciable at low velocity ratios, manifesting in the same manner as the kinks in the lift curve arising from inversion of the Magnus effect.

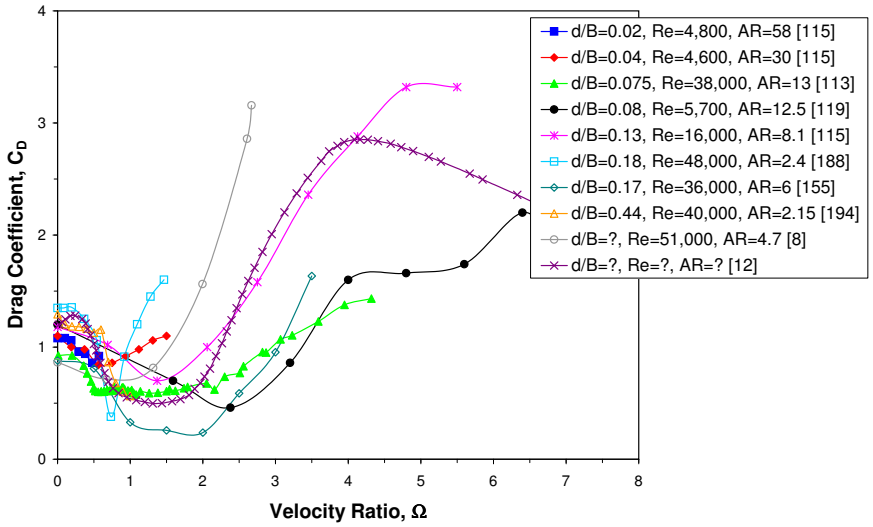

(a) Drag coefficient

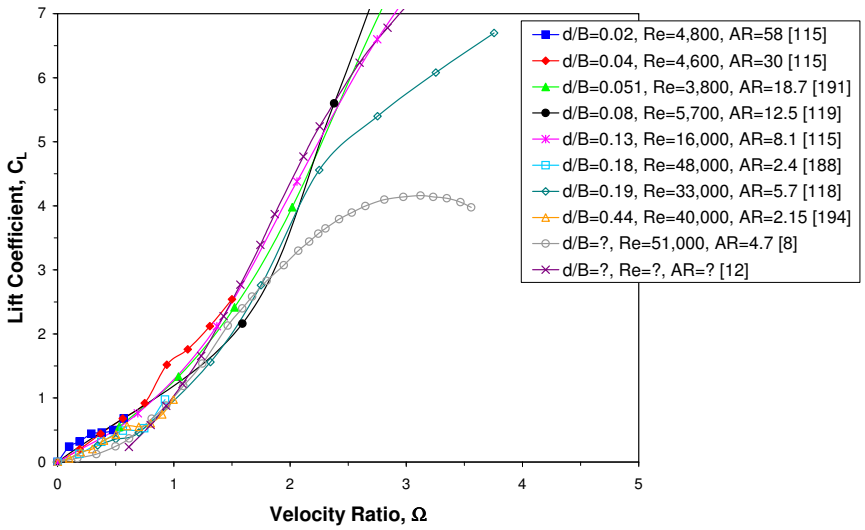

(b) Lift coefficient

Figure 3.50: Comparison of force coefficients at different blockage ratios.

Unfortunately, all the data for high blockage also tends to be associated with Reynolds numbers where inversion of the Magnus effect would naturally occur anyway. Thus, it

is not clear whether the loss of lift at high d/B is due to a blockage-induced change in effective Reynolds number, or simply part of the natural flow pattern. However, the results do seem to suggest that, for $d/B \leq 0.13$ and $\Omega \leq 1.5$, the results are practically identical and apparently insensitive to blockage. This may be because the effects of rotation on the location of the separation points dominate those due to local changes in Reynolds number due to wall constraint. Any differences in force results at the higher velocity ratios are more likely to be a result of the three-dimensional effects that come to dominate the flow at high Ω, and how they differ from one experimental arrangement to the next, as opposed to blockage.

4 Preliminary Design Study and Feasibility Analysis

A number of difficulties were encountered when examining the feasibility of applying rotating cylinders to MAVs and attempting to develop possible designs. The most obvious problem stems from the almost complete lack of any preceding work of a similar nature that could be used both as a starting point and a guide for the design process. A search of the literature revealed that whilst rotor designs have been suggested for conventional aircraft in the past (a design is pictured and discussed briefly in a 1932 article by Klemin,[248] see below) such instances are very few in number and any discussion is typically of limited content and highly critical of the concept. For example, in the Klemin article the rationale behind the different aspects of the unusual design went largely unmentioned and the focus of the discussion was primarily on the unsuitability of rotor designs.

A further, related difficulty is that guidance for the development of a design incorporating rotating cylinders cannot simply be sought by consulting the large repository of data regarding conventional aircraft design as much of this information would be of questionable or limited applicability. This lack of guidance is exacerbated when pursuing an MAV-sized vehicle, for which a dedicated design methodology has not yet been formalised and, though there is much to be gained from examining other attempts at MAV development, the available information is neither as established nor as well organised as for conventional aircraft.

However, the fundamental problem faced when attempting to develop a rotating-cylinder-based MAV is one that is common to all MAV designs: the lack of an officially defined design specification or typical mission scenario for this class of UAVs. Having a designated role about which to tailor the design is always important because it is generally poor practice to first develop a UAV platform (of whatever kind) and then try and find a mission for it,[17] but it assumes added prominence in the design of a successful MAV because of the strict size and weight constraints. Mission requirements would also be instrumental in defining the specific design of the MAV by dictating such aspects as the required speed, endurance, signature, survivability, and sensor placement. Consequently, in the absence of suitable guidelines, a decision was made to consider only a simplified, generic design with which to assess the concept of rotating cylinder MAVs as a whole and provide baseline data for future development.

This chapter examines possible designs for an MAV based around rotating cylinders and uses existing data on the aerodynamics of rotating cylinders to provide an estimation of the general performance of such a craft. In addition, the practical feasibility of successfully providing the required rotation, propulsion, power, control, and communications systems

within the size and weight constraints of the MAV class using currently available technologies and structural materials, whilst simultaneously being able to exploit the lifting potential of the rotating cylinder to provide a superior payload capability, was assessed.

4.1 Design Specifications

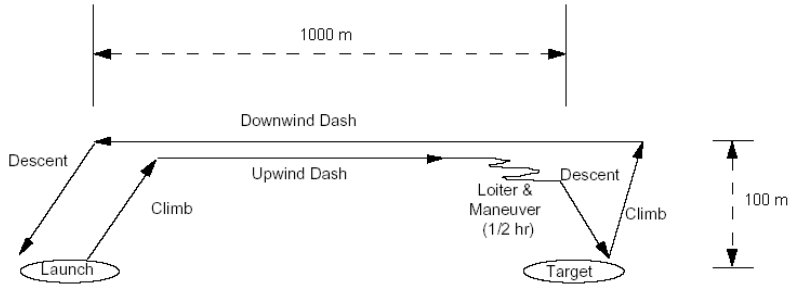

Figure 4.1: Generic MAV mission scenario for design competitions.[56]

Lacking an explicit, end-user-defined, design specification and mission profile for an MAV, the vehicle size constraints and performance requirements detailed by the original DARPA initiative were merged with some of the criteria established for the many MAV design competitions[2,56] to produce a basic framework within which to perform the design analysis. The adopted specifications are summarised in Figure 4.1 and Table 4.1. Note that although a vehicle conforming to the DARPA MAV definition was ideally sought, the size and weight constraints were expanded to allow investigation of the perhaps more realistically achievable mini-UAV sizes and weights too. Also, the desired payload capacity was chosen so as to provide an advantage in comparison to existing vehicles of a similar size (see Figure 4.2). Finally, a capability for low speed flight was also specified.

Parameter	**Specification**
Max. dimension	≤ 0.4 m
Weight	≤ 500 g
Cruise altitude	100 m
Cruise velocity	10–15 m/s
V_{min}	≤ 5 m/s
Range	> 1000 m
Endurance time	> 30 min
Payload	$\geq 20\%$

Table 4.1: Desired MAV specifications.

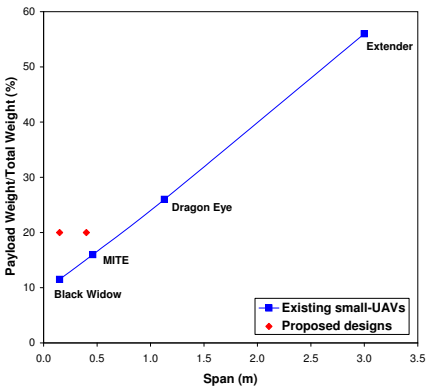

Figure 4.2: Payload capacity comparison.

4.2 Configuration

As well as considering designs involving rotating cylinders, initial investigations also examined whether a rotating wing might actually be more advantageous to MAV applications than a cylinder. Of particular interest were wings with an S-shaped profile, as used on Savonius-type vertical-axis wind turbines. Such wings display autorotation phenomena at low velocity ratios (typically at $\Omega \approx 0.5$) and so would not need a motor and power supply to drive the wing and generate lift, a considerable advantage in developing an MAV-scale craft. In addition, the literature indicates that spinning wings in general do not suffer from Reynolds-dependent nonlinearity of the lift curve at low velocity ratios.[183] This is because the mechanism through which lift is generated by an autorotating wing is very different to that for a rotating cylinder. As a result, rotating wings tend to produce substantially more lift than a cylinder in the region $\Omega \leq 1$.

However, the lift produced by rotating wings in the autorotating range is far smaller than that achievable by a cylinder undergoing forced rotation at high Ω and the lift-to-drag ratio is not much greater than unity ($C_L/C_D \approx 1.5$).[112, 129, 183, 248, 249] Furthermore, despite the benefits to power requirements and weight, the lack of an active drive mechanism can actually be disadvantageous to vehicle performance and control as a whole because the velocity ratio at which the wing rotates, and hence the magnitude of lift generated, is fixed by the design of the rotor and cannot be easily changed in response to new flight conditions or mission requirements.

A Savonius rotor or other rotating wing may, as with the rotating cylinder, be driven to rotate at a higher velocity ratio than that for autorotation. Under these conditions the flow pattern begins to resemble that over a rotating cylinder and the wing now generates much more lift than in the autorotation range, although studies[129, 183, 249] seem to indicate that both the lift and lift-to-drag ratio remain less than that for a rotating cylinder at the same velocity ratio, particularly in the region $1 \leq \Omega \leq 3$. However, a lack of comparable data at the same AR and Reynolds number makes a comprehensive analysis of rotating cylinder performance relative to that for a rotating wing difficult.

In any case, forced rotation of a spinning wing would also clearly negate any advantages to power requirements enjoyed by an autorotating design. In addition, previous research[183, 250, 251] has also shown that vortex shedding is not suppressed with increasing velocity ratio for a rotating wing; thus, even at high Ω, there would always be a large unsteady component to the forces and moments acting on the wing. When coupled with the reduced aerodynamic efficiency, these properties suggest that the rotating cylinder appears to be better suited to MAV application than the rotating wing.

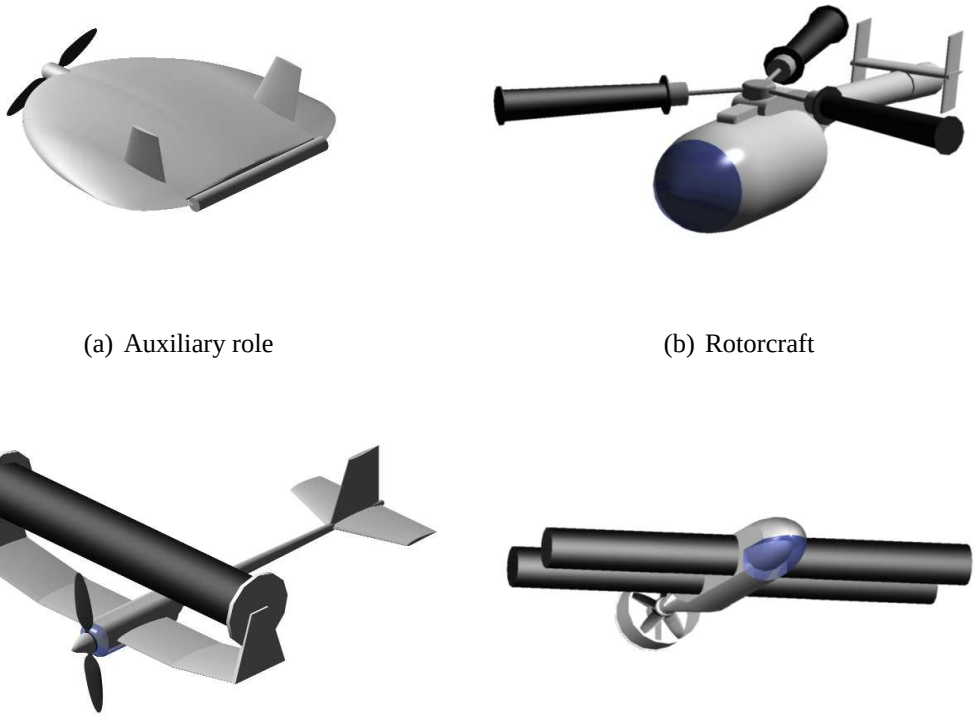

(a) Auxiliary role (b) Rotorcraft

(c) Single cylinder (d) Multiple cylinders

Figure 4.3: Conceptual designs for a rotating cylinder MAV.

Having constrained the configuration to include the use of rotating cylinders in some capacity, a number of different design possibilities (see Figure 4.3 and Table 4.2) were then considered and compared on the basis of the following criteria: size and weight, simplicity, controllability, and aerodynamic performance, which was further subdivided into total drag, maximum lift (this also being indicative of payload capacity), and power requirements for both spinning the rotors and translational flight. The primary design choice was deemed to be between using the rotating cylinder as the main provider of lift or using it in an auxiliary capacity, e.g. as an MSBLC-type high-lift device.

This latter role has, to date, been the preferred approach for attempted rotating cylinder application in aircraft and does offer certain advantages. The resulting design would in essence be a modified fixed-wing vehicle and the literature indicates that both the lift curve slope of the aerofoil, $dC_L/d\alpha$, and the pitch stiffness, $dC_m/d\alpha$, would remain unchanged by the addition of a rotating cylinder, whilst the maximum lift and stall angle can be expected to be greatly increased (by a factor of two or three) over typical values for an unmodified wing.[6] In addition, the power required to drive the cylinder is reported to be quite low[4,139] and tests by Tennant *et al.*[252] have shown that the lift coefficient generated

by a forebody-cylinder combination is both generally greater than that produced by an isolated cylinder of the same area and does not exhibit a nonlinear response due to Magnus effect inversion at low Ω and high Re.

The benefits provided by an MSBLC-type design must be balanced against the difficulties associated with embedding a rotating cylinder, and its drive mechanism, into the wing of an MAV, particularly given the preference for thin aerofoil use at MAV scales so as to mitigate the problems associated with low Re_c flight. Manufacturing complications would also arise due to the need to follow any wing taper and the requirement for a very small clearance between the cylinder and the body so as to prevent adverse effects on performance from communication between the high pressure and low pressure regions.[6]

Furthermore, the necessarily small size of the cylinder would also result in a requirement for very high rotational rates that may be mechanically prohibitive. For example, assuming a flying wing design of maximum chord $c = 15$ cm and a suitably low thickness-chord ratio appropriate for low Re_c flight, say $t/c \approx 0.06$, this implies a maximum possible cylinder diameter of $d = 9$ mm. Consequently, to reach $\Omega = 3$ (where studies[4,141,253] indicate that the maximum improvement in $C_{L_{max}}$ and α_s occurs) would, at a flight speed of $V = 10$ m/s, require a cylinder rotation rate in excess of $N = 64,000$ rpm. Even for a larger vehicle size, say of 30 cm chord, or a lower velocity ratio of $\Omega = 2$ (where the lift-to-drag ratio is said to reach a maximum), the required rotational rate would still be greater than $N = 40,000$ rpm.

Table 4.2: Evaluation matrix for selection of general MAV configuration.

Property	**Weighting**	**Auxiliary**	**Rotary**	**Single**	**Double**	**Multiple**
Size/Weight	0.19	4	2	4	3	1
Complexity	0.15	2	1	3	4	2
Controllability	0.10	2	5	1	3	4
Total Drag	0.17	5	3	4	3	2
Total Lift	0.22	2	4	3	4	5
Power	0.17	5	1	4	3	1
Total	1.00	3.40	2.59	3.33	3.37	2.50

If, instead, the rotating cylinder concept is to be used as the main provision of lift, then several further choices present themselves. The first concerns the number of cylinders to be employed; the second regards the specific arrangement of the cylinder as a lifting surface. The use of a single cylinder would require only one motor, simplifying the mechanical aspects of the design and reducing both vehicle weight and power requirements, but it raises questions about the arrangement of the vehicle as a whole and the achieve-

ment of roll, pitch, and yaw control. Such a design may require a hybrid approach, with small conventional wings or other control surfaces employed alongside the main cylinder. The available payload space and capacity may also be adversely affected with such an unusual arrangement.

Alternatively, if a design involving multiple rotating cylinders were adopted, the cylinders could then simply be employed as direct replacements for either fixed or rotary wings. For example, in an idea similar to Flettner's work with windmills,[112] several cylinders could be linked together around a central hub to form an unconventional rotor for a helicopter MAV. This is an attractive solution that would benefit from both the hover capability of a rotary-wing vehicle and the high lift coefficients of the rotating cylinder, but it is not without its difficulties.

To ensure a uniform level of lift across the entire rotor span, each cylinder would need to be tapered so that the diameter increases as it extends towards the rotor tip, which may result in added manufacturing complications; mechanical complexity would be considerably increased due to rotation of components about two different axes; the need for multiple motors and anti-torque devices would strongly impact on size and weight constraints; finally, the effects of advancing/retreating rotor performance asymmetry would also have to be considered. Although there is no equivalent stalling behaviour where rotating cylinders are concerned, inverse Magnus effect phenomena may be initiated under certain conditions, leading to a loss of lift that is much like stall in effect, if not origin.

Using the cylinders as direct replacements for fixed wings may simplify the arrangement of the vehicle by allowing the rotors to be positioned around some sort of central fuselage, which would also provide space for housing the payload, sensors, and other onboard systems. In such a configuration, an even number of rotors would generally be preferable so as to retain symmetry of shape, and a design involving two rotating cylinders would create a vehicle that more closely resembled a standard aircraft layout. Despite this, there may be considerable advantages to be gained from using a greater number of rotors. A design with four or more cylinders would offer both a very large lifting force and the possibility of superior roll, pitch, and yaw control through differential rotation of each cylinder. However, such designs would be expected to incur an increase in vehicle size, weight, total drag, and overall power requirements.

The use of multiple rotors in close proximity to each other would also require the mapping of the interference effects between the cylinders within the S/d–T/d plane (similar to Figure 3.47) for all Ω of interest. The literature for non-rotating cylinders indicates that such effects are likely to be highly complex and that a downstream or transverse separation

of as much as $6d$ may be required to avoid detrimental interactions, such as vortex-induced vibrations. Large spacings of this type could not be easily implemented at MAV scales without either an increase in overall vehicle size or a reduction in cylinder diameter, with a consequent rise in the required rotational rates. A less than optimum spacing could be employed, but may compromise aerodynamic performance. That being said, close proximity between two stationary cylinders can, in some cases, result in a much reduced C_D for both cylinders. A similar effect may thus occur for rotating cylinders too.

Interestingly, the specific option of four rotating cylinders arranged about a central fuselage appears to be the only design with previous representation in the literature, having been attempted at a conventional scale by J. C. Guest and L. C. Popper in New York City during the early 1930s. Information on the design of this 'spindle rotor' airplane comes primarily from the description provided in an article by Klemin,[13] although this was actually a response to an earlier article in the contemporary magazine *Popular Aviation*. Efforts to locate the original article have proved unsuccessful.

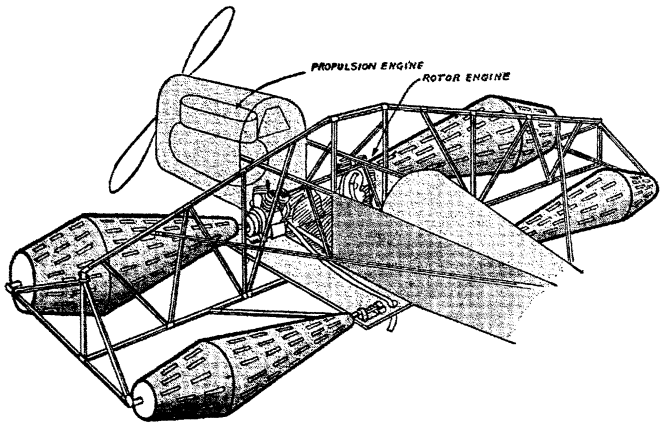

Figure 4.4: Diagrammatic view of 1930s 'spindle rotor' aircraft.[13]

Klemin's article reveals that whilst propulsion was of the conventional propeller type, instead of the usual wings the aircraft had four cylinders mounted in two banks of two, with the front row being somewhat larger than the back (see Figure 4.4). A truss was used to support the ends of each cylinder and the large forward rotors were reported to be driven by two small engines. The design of the rotors themselves was also highly irregular, with each cylinder being asymmetrically tapered so that the inboard and outboard tip diameters were of very different sizes and the position of the maximum cylinder diameter was off-center relative to the mid-span.

However, because of the nature of Klemin's article, many aspects of the design remain unexplained. For instance, although the front cylinders are said to be driven, the method of

rotation of the rear cylinders is not noted and it is unclear if all four cylinders can be made to operate independently. Similarly, the particular shape of the rotors, their apparently slotted surface, and the consequences for the aerodynamic performance of the cylinders is not discussed, although information provided by Iversen,[251] who may have had access to the original *Popular Aviation* article, indicates that a lift coefficient as high as $C_L = 15$ and a drag coefficient of $C_D = 5$ were reported. No further details on the success or otherwise of the attempt to develop the design are known to exist.

A comparison of the possible vehicle configurations using figures of merit (see Table 4.2) revealed that the auxiliary cylinder, single main cylinder, and double main cylinder designs all achieved similarly high scores. However, on consideration, the auxiliary and single cylinder designs were ultimately rejected in favour of pursuing investigation of the double main cylinder design. This solution, with two rotating cylinders used as direct replacements for conventional wings, is closely analogous to traditional aircraft designs and was seen as the most logical starting point from which to begin the study of rotating cylinder MAVs, particularly given the paucity of data on the design of such a vehicle. Examination of this arrangement would thus provide useful data for the assessment of the fundamental shortcomings or benefits of the concept that could then be used in attempting to develop more complex configurations that may differ wholly from conventional designs.

The choice of general configuration was also influenced by the shortcomings of the other two top-scoring designs. Specifically, the auxiliary cylinder option was primarily rejected as it was felt that the very small size of the rotor in such a design would not fully exploit the lifting potential of the rotating cylinder, whereas the single main cylinder option came with considerable uncertainty over the precise arrangement of the vehicle, which made selection of a suitable, non-arbitrary, starting design difficult. In addition, the lack of a well-defined mission profile and design specification was also instrumental in the choice of configuration by creating a preference for a more straightforward design.

4.3 Performance Estimates

A preliminary assessment of the likely performance of an MAV based around rotating cylinders was carried out by creating a mathematical model of the adopted mission profile and using the experimental data from the earlier tests of Weiberg & Gamse,[4] Swanson,[12] Reid,[113] Betz,[8] Tokumaru & Dimotakis,[191] and Thom,[115–119] together with a simple model of the atmosphere, to model the variation of the lift, drag, torque, and power coefficients for a twin rotor design. This analysis provided an indication of whether the performance

requirements would be too high to make such a craft viable. Note that neither the initial launch phase, the retrieval phase, nor the methods employed for these stages of the mission, were considered in the analysis.

The response of lift and drag to velocity ratio, aspect ratio, and Reynolds number was modelled through a combination of curve fitting via the least-squares method together with bicubic interpolation using a fourth order Lagrange interpolating polynomial. A lack of suitable data meant that only the performance for Reynolds numbers between $1 \times 10^4 \leq Re \leq 5 \times 10^5$, aspect ratios between $1.7 \leq AR \leq 15$, and velocity ratios of $\Omega \leq 4$ could be reliably modelled. Note also that, based on the trends apparent in the available data (see Figures 3.8 and 3.10), the influence of aspect ratio on the lift coefficient was only modelled for $\Omega > 1$, whereas for the drag, which was more susceptible to end effects, aspect ratio variation was modelled for all Ω. Modelling of Reynolds number effects on both C_L and C_D was restricted to the region $\Omega \leq 1$.

A lack of data prevented any modelling of the effects of Re or AR on the torque and power coefficients, which were thus assumed to vary only with Ω. The small number of available studies regarding the variation of C_Q and C_P also meant that there was considerably more uncertainty in the estimated power requirements for spinning the cylinders than in those quantities based on the assumed lift and drag behaviour, whose dependence on multiple data sources provided greater confidence in the results. Thus, overall, the analysis may be considered to provide a useful indication of performance rather than being definitive.

Power requirements for spinning the cylinders (P_R) were calculated using the average of the Thom[118] and Weiberg & Gamse[4] experimental measurements of C_Q and C_P, which predicted the lowest values of P_R, and the much higher computational estimates of Aldoss & Mansour.[205] These values were combined with the drag data, which were used to assess the power for horizontal translational flight (P_T), and an estimate for the onboard control and communications systems power requirement (P_S), which was placed, conservatively, at about 4 W by examining typical values for other small UAV designs, so as to determine the total power requirement for flight, P. Hence, if

$$P = P_T + P_R + P_S \tag{4.1}$$

and

$$P_T = D_{tot} V \tag{4.2}$$

where D_{tot} is the total drag of the vehicle as a whole, whilst

$$P_R = Q\omega \tag{4.3}$$

then from Equations 3.2, 3.5, 3.8, and 3.12, the total power for a vehicle with two cylinders of length b and diameter d is given by

$$P = \rho V^3 bd(C_D + 2\Omega C_Q) + P_S \tag{4.4}$$

or

$$P = \rho V^3 bd(C_D + C_P) + P_S \tag{4.5}$$

Note that, as a first attempt at estimating the power required for forward motion of the aircraft, the value of D_{tot} was assumed to be the same as the combined drag of both cylinders, with no adjustment made for the contributions of the fuselage, tail, fin, or other components of the design. This removed the need to make specific assumptions about the vehicle layout and is not an unreasonable approach as the high drag of the cylinders means they are likely to account for the vast majority of the total drag of any final design. Also, if constant velocities and shallow angles of climb and descent ($\gamma \leq 10°$) are assumed, then the power requirements given by Equations 4.4 or 4.5 can be used to indicate vehicle performance across the entire mission scenario.

Table 4.3: Performance model constraints.

Parameter	**Constraint**
RPM, N	$\leq 20{,}000$
Power, P	≤ 50 W
Velocity ratio, Ω	$1.2 \leq \Omega \leq 3$
Aspect ratio, AR	$1.7 \leq AR \leq 15$
Rotor span, b	≤ 0.2 m
Mass, m	≤ 500 g

The performance model was used to identify those combinations of rotor geometry, vehicle total mass, and operating velocity ratio that best matched the desired design and performance criteria. Viable configurations were identified by varying the input values of

b, d, Ω, and V to the performance model and using appropriate constraints (see Table 4.3), based on the design specification and maintaining practical feasibility, to identify those combinations of parameters providing suitably sized rotors that produced enough lift at the cruise velocity ratio to support the vehicle's weight and which needed neither too high a rotational rate nor very large power requirements.

Note that the constraints applied to the analysis were each set with a specific reasoning in mind. The limitations placed on the total power and maximum rotational rate were based on the typical operational limits of commercially available electric motors of an appropriate size and weight. Therefore, these two constraints are not strict physical limits that must be adhered to and were only implemented so as to confine the analysis to the identification of more realistic solutions. Operation outside the imposed limits is not impossible, but may currently be practically very difficult. Future technological development should allow these restrictions to be relaxed.

The constraint on the operating velocity ratio range reflects the desire to cruise at or near the position of maximum lift-to-drag ratio (expected to be at $\Omega \approx 2$). This would also be close to the velocity ratios for minimum drag and minimum power (which are typically located between $1 \leq \Omega \leq 1.5$, depending on rotor geometry). Furthermore, operation at such high velocity ratios would mean that vortex shedding from the cylinders would be considerably reduced, or even wholly suppressed. This avoids the large amplitude oscillation in the aerodynamic forces associated with shedding, which could otherwise greatly increase structural loads and might impact on stability and control too.

The velocity ratio constraint also took into account the inadvisability of flight at $\Omega \leq 1$, where Reynolds number effects are prominent. Below this limit, the vehicle could, under the appropriate conditions, experience a dramatic loss of lift that might even result in negative C_L values. In setting the constraint on desirable operating range, a lower limit of $\Omega = 1.2$ rather than $\Omega = 1$ was implemented so as to include a suitable buffer zone against the onset of Re effects. This was intended to help identify those solutions whose operating velocity ratio was not so close to the critical value of $\Omega = 1$ that a sudden change in the environmental conditions (through turbulence or gusts) or a perturbation in rotational rate N would unexpectedly initiate Magnus effect inversion phenomena.

Finally, the vehicle mass restriction and rotor size constraint (which was applied to the span of a single cylinder and chosen so as to provide a maximum dimension of 0.4 m) were both in accordance with the design specification and the type of platform sought. The associated aspect ratio range constraints were chosen somewhat arbitrarily and were primarily based on the available data for modelling the cylinders' aerodynamic behaviour.

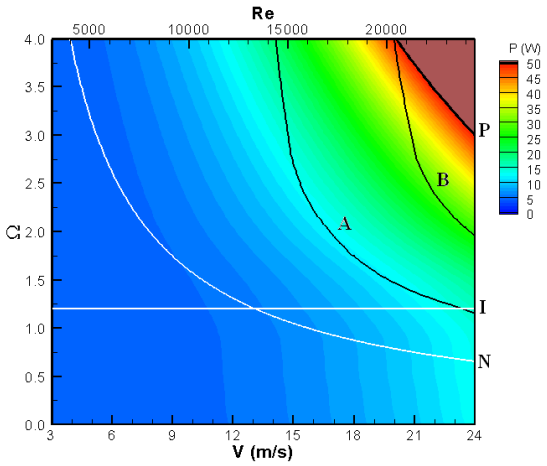

(a) $d = 0.015$, $b = 0.045$, $AR = 3$

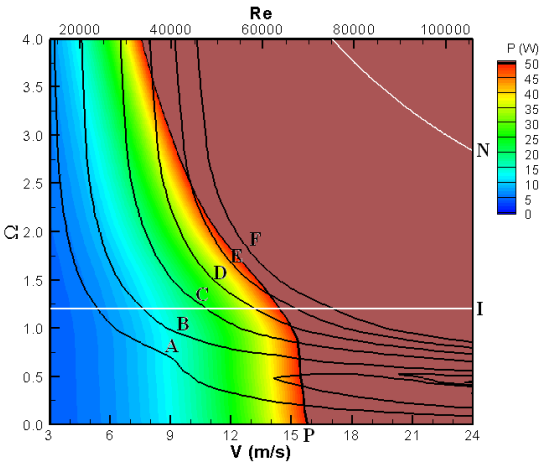

(b) $d = 0.065$, $b = 0.195$, $AR = 3$

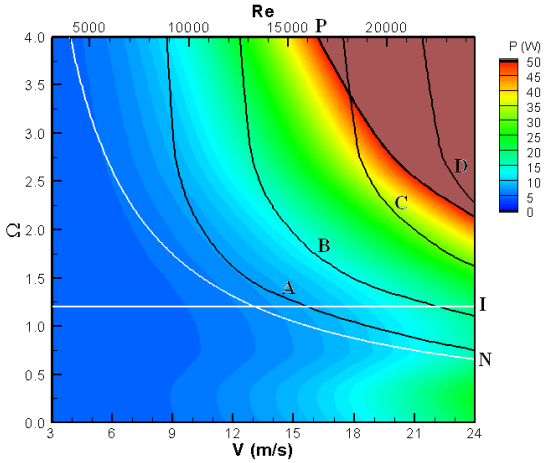

(c) $d = 0.015$, $b = 0.075$, $AR = 5$

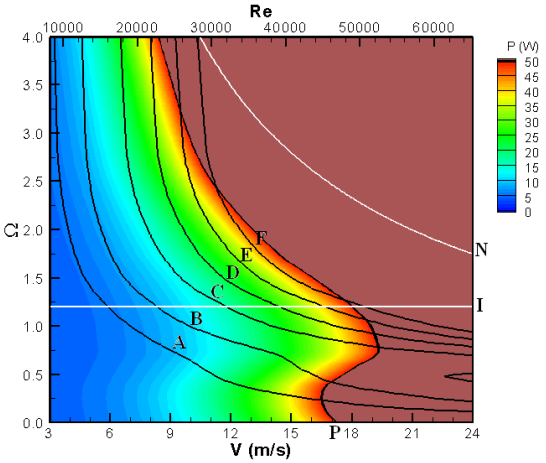

(d) $d = 0.04$, $b = 0.2$, $AR = 5$

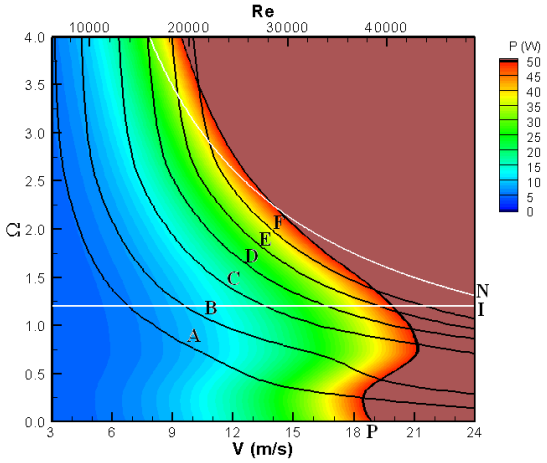

(e) $d = 0.03$, $b = 0.2$, $AR = 6.67$

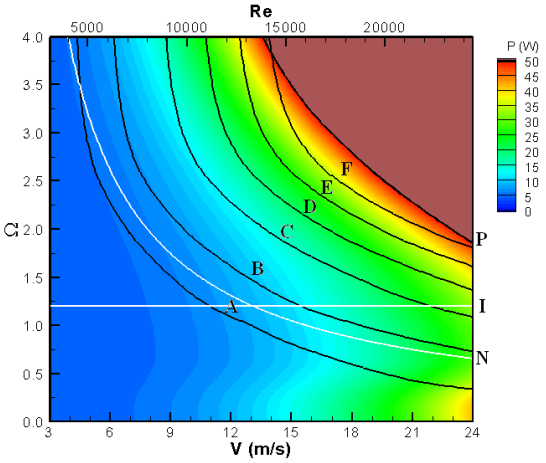

(f) $d = 0.015$, $b = 0.15$, $AR = 10$

Figure 4.5: Operational space of different rotor geometries. Curves A to F denote the limits of steady horizontal flight for a given vehicle mass (A = 50 g, B = 100 g, C = 200 g, D = 300 g, E = 400 g, and F = 500 g). Curve I denotes the minimum recommended operating velocity ratio ($\Omega = 1.2$). Curve N denotes the recommended upper limit on the rotational rate (N = 20,000 rpm). Note also that contours for $P > 50$ W have been omitted. This boundary is delineated by curve P.

The analysis found there to be multiple combinations of cylinder span, cylinder diameter, V, and Ω that were estimated to provide the required performance at a given vehicle mass, although the number of possible solutions was seen to reduce as m was increased. The most favourable solutions were selected from the identified configurations by giving preference to those combinations of parameters that required smaller values of N and P and which did not operate too close to any of the imposed constraint boundaries. Rotor geometries having aspect ratios of $AR \geq 5$ were also preferred as the available data for smaller AR is less reliable and the results of the analysis when $AR < 5$ more suspect.

Selection of preferred solutions also considered the size of the operational space associated with a given rotor geometry. This was determined by using the performance model to generate surface plots of the varying power requirements for fixed b and d across the entire range of flight speeds and velocity ratios of interest and then superimposing a series of boundaries representing the applied constraints on Ω, N, and P. Curves defining the locus of points (in terms of V and Ω) for which the available lift is equal to a fixed weight between 50 g and 500 g, and which thus identify the limit of steady horizontal flight at a given total mass, were also included (selected results are shown in Figure 4.5). In this way the operational space for a given vehicle weight and rotor size is revealed to be the area between the appropriate weight boundary for level flight and the boundaries for minimum Ω, maximum N, and maximum P.

For example, no vehicle of mass 300 g that employed two rotors of size $b = 0.2$ m and $d = 0.03$ m would be able to sustain level flight at speeds or velocity ratios to the left of boundary D, as this rotor configuration would not produce enough lift to support the aircraft's weight (see Figure 4.5e). Similarly, operation to the right of curves N or P would be difficult with current technology but could be possible if a suitable drive system and power supply to spin the cylinders were identified or developed. Operation below curve I is also possible but could leave the vehicle open to a sudden change in C_L. Since the size of the operational space is associated with the available power, which is closely tied to the performance capabilities of the aircraft in climb and manoeuvering, solutions with a larger operational space were thus preferred.

The analysis also revealed general trends about the performance of different rotor configurations, which were then used to select the most favourable solutions at three representative weights across the entire range considered (see Table 4.4). Note that the analysis indicated that a vehicle conforming to the general definition of an MAV (6" maximum dimension and 50 g total weight) was theoretically possible. However, the performance requirements for this option were found to be at the utmost limits of practical feasibility and the design was ultimately rejected in favour of more appropriate solutions.

As would be expected, small diameter rotor designs were primarily limited by the required rpm, with very high rotational rates needed to produce even moderate velocity ratios. In addition, small d cylinders also produced less lift, which increased both the minimum speed required for level flight at a given mass and the velocity ratio needed at a given flight speed (this can be seen in the way that curves A to F are pushed up and to the right as d reduces, see Figure 4.5).

Large diameter cylinders were, except at the utmost extremes of V and Ω, not subject to constraints due to rpm, but rather tended to be limited by the high power associated with the large drag forces generated by a large rotor (this can be seen in the way that curve P is pushed down and to the left as d increases, see Figure 4.5). The analysis also indicated that, regardless of rotor configuration, it was the power requirements for translational motion that were the dominant factor in determining the total power necessary for flight. The power needed to spin the cylinders did not become a limiting factor in performance until the largest values of V and Ω investigated.

Table 4.4: Approximate cruise performance for three possible rotating-cylinder-based small-UAV configurations. Cylinder dimensions are for a single rotor.

Parameter	**m=50 g**	**m=250 g**	**m=500 g**
Cylinder diameter	0.03 m	0.04 m	0.035 m
Cylinder span	0.15 m	0.2 m	0.2 m
Aspect ratio	5	5	5.71
Cruise velocity	5.3 m/s	9.1 m/s	12.7 m/s
V_{min} at $\Omega = 4$	4.4 m/s	7.3 m/s	10.2 m/s
Cruise Ω	2.0	1.9	2.1
Cruise C_L	3.1	3.3	3.6
Cruise C_D	1.5	1.4	1.5
Cruise C_L/C_D	2.1	2.2	2.3
Cruise thrust	0.24 N	1.12 N	2.11 N
P_T	1.2 W	10.2 W	26.8 W
P_R	0.5 W	3.5 W	11.3 W
Total power	5.7 W	17.7 W	42.1 W
Cruise RPM	6,750	8,260	14,550

Although increasing aspect ratio had a beneficial effect on the lift force, total drag, and power requirements, very high AR designs were generally found to be most suitable for low mass values ($m < 200$ g). This was a result of the constraint on span b, which forced high AR rotors to have a small diameter and meant that the necessary rotational rates could only be kept at a reasonable value with low mass designs that were able to sustain flight at low velocities. Low AR designs were also limited to low mass values, though

this was due to a general lack of lift. Similarly, insufficient lift at high Ω meant that a very-low-speed capability ($V < 3$ m/s) was also, regardless of AR, only possible with low mass designs ($m < 100$ g). Overall, the best performance was achieved with medium sized aspect ratios ($4 \leq AR \leq 7$), which provided a suitable capability across a wider range of values of V, Ω, and m.

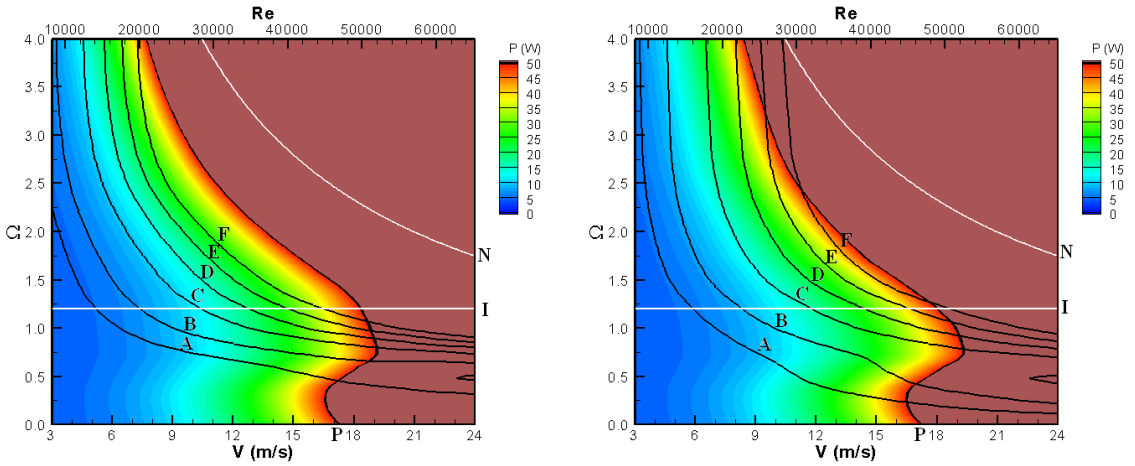

(a) Endplates of size $d_e/d = 2$

(b) No endplates

Figure 4.6: Effect of endplates on the estimated performance of a vehicle with two $AR = 5$ rotors (of individual diameter $d = 0.04$ m and span $b = 0.2$ m). See Figure 4.5 for explanatory notes.

Whilst the analysis indicated that a viable vehicle seems quite possible, the overall power requirements were found to be high when compared to reported values for typical fixed-wing MAV and mini-UAV designs, thus making the concept less attractive. This unfavourable comparison is confirmed by estimations of the power requirements in straight and level flight for the corresponding fixed-wing aircraft equivalent of each of the three design configurations presented in Table 4.4. For these cases, P_T is given by

$$P_T = \frac{1}{2}\rho V^3 S_w C_{D_0} + \frac{2W^2}{\pi AR \rho V S_w e} \tag{4.6}$$

where S_w is the wing planform area, C_{D_0} is the profile drag coefficient (based on S_w), W is the aircraft weight, and e is the Oswald efficiency factor (assumed to be 0.83).

In calculating P_T, values of W corresponding to the three values of m in Table 4.4, as well as their associated values of the flight speed V, were assumed. For all three cases a circular wing planform ($AR = 4/\pi$) with diameter equal to the total span of the rotors on the equivalent rotating-cylinder-based design was also assumed. A reasonable estimate of C_{D_0} was made for each of the three vehicle sizes, and associated chord Reynolds numbers,

considered by using empirical data[80] for aerofoils at low Re_c.

Comparison of Tables 4.4 and 4.5 suggests that a rotating-cylinder-based MAV design would typically need about four times as much power (ignoring P_S) as the equivalent fixed wing craft. The primary cause of this increase is the high drag of the cylinders, and not the power required to rotate them (compare P_T and P_R). However, rather than a fixed wing aircraft, a more reasonable comparison may be against a rotary-wing type design, where the power is used for direct lift. Typical power requirements for such designs are not readily available but may be estimated using a simple momentum actuator disc model[254] in which the power for horizontal translational flight is given by

$$P_T = 2\rho S_a \left[\frac{C_{D_0} V^3}{4} + \frac{C_{D_0}^2 V^4}{16U} + \frac{1}{U} \left(\frac{W}{2\rho S_a} \right)^2 \right] \tag{4.7}$$

where S_a is the actuator disc planform area, C_{D_0} is the profile drag coefficient of the fuselage (as based on disc area and assumed to be $C_{D_0} = 0.02$), and U is the resultant speed through the disc, which may be determined from the following equation:

$$U^4 - V^2 U^2 - \frac{1}{2} C_{D_0} V^3 U = \frac{1}{16} C_{D_0}^2 V^4 + \left(\frac{W}{2\rho S_a} \right)^2 \tag{4.8}$$

Power requirements for hovering flight were estimated from

$$P_H = \sqrt{\frac{W^3}{2\rho S_a}} \tag{4.9}$$

Values of V and W were again assumed to be the same as those from Table 4.4 and the actuator disc diameter was taken to be equal to the total span of the rotors on the equivalent rotating cylinder design.

Although the power requirements for the rotating cylinder configurations were also found to be higher than their rotary-wing equivalents (see Table 4.5), it must be noted that the estimated power requirements for P_T and P_H are those for an ideal actuator disc. In practice, a real rotor would require considerably greater power input, suggesting a somewhat more favourable comparison, particularly in regards to hovering flight, than was the case with fixed-wing craft. Nevertheless, a reduction in total power requirements seems necessary if a practical rotating-cylinder-based small-UAV is to be developed.

Table 4.5: Estimated power requirements of equivalent fixed-wing and rotary-wing small-UAV designs.

Fixed Wing	**m=50 g**	**m=250 g**	**m=500 g**
Wing span	0.3 m	0.4 m	0.4 m
Cruise velocity	5.3 m/s	9.1 m/s	12.7 m/s
C_{D_0}	0.02	0.015	0.013
P_T	0.44 W	3.44 W	9.43 W
Rotary Wing	**m=50 g**	**m=250 g**	**m=500 g**
Disc diameter	0.3 m	0.4 m	0.4 m
Cruise velocity	5.3 m/s	9.1 m/s	12.7 m/s
P_T	0.39 W	3.29 W	9.26 W
P_H	0.83 W	6.92 W	19.6 W

Whilst the performance analysis suggests that significant reductions in power could be achieved with high aspect ratio rotors this was usually accompanied by undesirable side effects. High AR rotors with large d meant a larger surface area, a greater drag force, and higher thrust requirements. Similarly, large AR rotors with small d resulted in a need for high rotational rates. A possible reduction in the power necessary for flight with no detrimental consequences could be achieved by using a low aspect ratio cylinder, with a reasonable diameter and smaller area, but augmenting the aerodynamic performance through an appropriate change in the end conditions.

In this regard, the use of endplates may be highly beneficial as they provide an effective means of increasing lift without having to increase either cylinder aspect ratio or surface area. Existing experimental results[8,113] indicate that aerodynamic performance similar to that for a cylinder of $AR = 13.3$ can be achieved with an $AR = 4.7$ cylinder through the use of endplates of size $d_e/d = 2$. This arrangement (see Figure 4.6) would allow a 250 g vehicle employing two cylinders of diameter $d = 0.04$ m and span $b = 0.2$ m to cruise at only $V = 7.9$ m/s (at $\Omega = 1.9$), thus reducing power requirements by 34%, drag by 38%, and the required rpm by 14% (as compared to the values from Table 4.4).

However, the exact effect of endplates on drag behaviour is uncertain and the consequences for lateral forces and moments unknown, having never before been investigated. Other measures for changing the flow past a circular cylinder, such as surface roughness, are currently poorly understood when the cylinder is rotating and any benefits to lift and drag at the velocity ratios of interest are unclear. Hemispherical endshapes are known to reduce the drag at velocity ratios of $\Omega \geq 2$, but they also reduce the value of the lift coefficient and are thus not as advantageous as endplates.

4.4 Stability and Control

The development of an MAV using rotating cylinders instead of conventional wings clearly requires a modified approach to establishing stability and control than is usually employed. This section considers the possible behaviour of such an aircraft and details the assembling of modified equations of motion for an aircraft having two rotating cylinders.

4.4.1 Independence from Angle of Attack

The greatest difference between a rotating cylinder design and a conventional aircraft arises from the fact that the lift and drag of the vehicle are no longer predominantly tied to the geometric angle of attack, α. Changes in angle will not cause a significant variation in the amount of lift and drag being generated as the pressure distribution around a rotating cylinder is largely unaffected by α. Increasing or decreasing the angle of attack will simply rotate the pressure distribution (and hence the force vectors) backwards or forwards, although for small α even this effect may be neglected.

Instead, the forces and moments acting on this type of aircraft will now be dependent largely on changes to the velocity ratio Ω, which in turn is dependent only on the velocity of the aircraft V (assuming constant rotation of the cylinders). However, the effect of angle of attack on the aerodynamic performance of such a vehicle cannot be completely ignored due to contributions to both lift and drag from other components, such as the fuselage and any control surfaces, which will still depend on α. There may also be some conditions for which the influence of angle of attack on the cylinders is substantial.

This situation complicates the analysis of the stability of the design as the forces and moments acting on the vehicle will be partly dependent on α and partly on Ω. However, since the angle of attack is itself dependent on the velocity V through the relationship

$$\alpha = \tan^{-1}\left(\frac{w}{V}\right) \tag{4.10}$$

then from Equation 3.5 this implies that, for small angles,

$$\Omega = \frac{V_r}{w}\tan\alpha \approx \frac{V_r\alpha}{w} \tag{4.11}$$

where α is in radians. Equation 4.11 connects the response of the cylinders with that of

the other aerodynamic surfaces (which vary with α) and could thus be used to investigate the stability of the aircraft analytically. For instance, the contribution to pitch stiffness from the cylinders could be analysed using the following approach:

$$\frac{\partial C_m}{\partial \alpha} = \frac{\partial C_m}{\partial \Omega} . \frac{\partial \Omega}{\partial \alpha} \tag{4.12}$$

where $\partial\Omega/\partial\alpha$ is determined from Equation 4.11.

4.4.2 Gyroscopic Effects

A second difference in behaviour lies in the gyroscopic moments that will be generated as a result of the rotation of the cylinders. Such gyroscopic effects arise when an action that displaces the angular momentum vector of a spinning body from its original orientation (this typically being in alignment with the spin axis) occurs. It may be shown that, due to the spin of the body, the displacement is resisted and the expected motion associated with the action does not occur, but is instead translated into motion about a third axis that is orthogonal to both the spin axis and the axis about which the action was initiated.

For instance, if a moment is applied about the local x axis of a body spinning about the local y axis, then the gyroscopic response prevents the body from rotating about the x axis and causes it to rotate (or precess) about the local z axis instead. Similarly, a moment about the z axis will result in precession about the x axis. Furthermore, the inverse effect is also found to be true: precession of the spin axis about the x or z axes results in induced moments about the z or x axes respectively. However, motion about the spin axis will not result in any induced moments or precessional rates about any other axis. Thus, there are no gyroscopic effects in the plane at right-angle to the spin axis.

For a rotating cylinder MAV with typical body-fixed axes, the spin axis will be the y axis, thus implying that such a vehicle will experience gyroscopically-induced rolling and yawing moments but will have no gyroscopic effects induced in the xz plane. This suggests that there will not be any cross-coupling of longitudinal and lateral motion due to rotation of the cylinders. Under the simplified conditions applicable to a rotating cylinder MAV (fixed nutation angle of 90°), it may also be shown that any gyroscopically-induced moments and precessional rates are governed by the following form of equation:

$$M_1 = I_2 \omega_2 \omega_3 \tag{4.13}$$

where M_1 is the applied/induced moment about axis 1, ω_3 is the applied/induced precessional rate about axis 3, and I_2 and ω_2 are, respectively, the moment of inertia and rotational rate about the spin axis (axis 2).

The examination of gyroscopic motion also lends itself to predicting the possible handling characteristics of the proposed design. Since any applied force which deflects a gyroscope out of its plane of rotation will actually be felt in the same direction as effectively applied but 90° ahead of (in the direction of rotation) the point of application, thus an MAV with rotating cylinders will, for positive lift conditions, have a tendency to behave as follows:

- An applied right rolling moment results in a right yaw precession response.
- An applied left rolling moment results in a left yaw precession response.
- An applied right yawing moment results in a right roll precession response.
- An applied left yawing moment results in a left roll precession response

The converse will tend to be true for applied precessional motions (i.e. right roll precession induces a left yawing moment and so on). In practice, the actual response will depend on the point of application of the force and so the aircraft may well execute a coupled roll-yaw response similar to the aileron adverse yaw behaviour of conventional aircraft. Combined motion can also occur as a result of the displacement of the spin axis not being completely resisted due to energy losses in initiating the induced response. Such gyroscopically-determined coupled motion will be in addition to any aerodynamic roll-yaw cross-coupling effects.

It should be noted that gyroscopic effects are also experienced by conventional aircraft designs, where they are caused by propellers, fan rotors, or other spinning components. However, at high speeds, these effects are generally very small in comparison to the aerodynamically generated forces and moments affecting the aircraft and so are usually ignored. For an MAV class vehicle, gyroscopic effects from the rotating cylinders, as well as any propellers, may be much more significant due to the low flight speeds, small dimensions, and the consequent small magnitude of the aerodynamic forces and moments.

Thus, the actual effects of gyroscopic motion on the stability and control of a rotating cylinder MAV will depend on how closely the cylinders approximate the motion of a gyroscope and the relative magnitude of the aerodynamic forces and moments to the gyroscopic moments; particularly, whether there are any conditions where these components are of similar size. It can be expected that the cylinders will behave as weak gyroscopes

and that any induced effects should themselves be of a low magnitude as they would be kept small by the necessarily low mass and correspondingly low moments of inertia of the cylinders. Avoiding high rates of yaw and roll would also mitigate gyroscopic effects, though this may be difficult on an MAV class vehicle.

4.4.3 Longitudinal Static Stability

Given that the contribution to vehicle pitching moment due to a rotating cylinder is unlikely to vary significantly with angle of attack this suggests that, like a typical wing-body combination, a rotor-fuselage combination may not be naturally stable in pitch. However, since it is usually possible for $dC_m/d\alpha$ to be made negative for virtually any combination of lifting surfaces and bodies by placing the center of gravity far enough forward, the question of pitch stability for a rotating cylinder aircraft would seem to depend largely on the specific layout of the vehicle and the arrangement of the aerodynamic surfaces.

The presence of the rotating cylinders also means that there will be a reaction torque on the body of the aircraft that must be countered if the vehicle is to have attitude control. When the cylinders are rotating so as to generate positive lift, the torque on the body may be seen to be such that it will tend to pitch the nose of the vehicle downwards. Thus, the case of an MAV with rotating cylinders is analogous to a conventional aircraft with a wing having positive camber, i.e. the initial pitching moment, C_{m_0}, will be negative. For fixed-wing craft this would not be a satisfactory flight configuration as, given that $dC_m/d\alpha < 0$ is generally required for stability, a negative value of C_{m_0} would not allow the aircraft to be trimmed at positive lift conditions.

For a rotating-cylinder-based aircraft the sign of C_{m_0} is not restrictive in this manner as the lift is not intrinsically tied to angle of attack. However, a means of trimming the rotor torque remains necessary. With conventional designs the requirement for a positive C_{m_0} is usually satisfied through the use of an aft-positioned horizontal tail set at a suitable negative incidence, or a canard configuration at a positive incidence. Such an approach would also seem to be the simplest way to trim the torque due to the rotors, provide attitude control, and contribute to the necessary pitch stiffness too.

Difficulties with the use of a horizontal tail in this way may arise from the very low chord Reynolds numbers at which the tail would operate (likely to be of the order of $Re_c = 2 \times 10^4$ or less). The reduced aerodynamic performance of wings at low Re_c and the small tail area may mean that it cannot provide a sufficient pitching moment for equilibrium. However, the much larger lift force from the cylinders could be used, through

positioning of the vehicle center of gravity so that it is sufficiently aft of the rotor center of pressure, to trim out much of the induced torque on the body, thus lessening the level of performance that would be required from the tail.

4.4.4 Equations of Motion

The use of rotating cylinders as the primary means of generating lift on an aircraft requires that the equations of motion be modified to include the presence of spinning rotors. Simplified equations of motion for such an aircraft are thus presented below. Note that the equations are subject to the following initial simplifying assumptions:

1. The Earth is assumed to be flat and fixed in inertial space.
2. The effects of altitude, longitude, and latitude on the acceleration due to gravity may be neglected and a uniform gravitational field of strength g is assumed.
3. The mass of the aircraft remains constant with respect to time.
4. Wind velocity is assumed to be zero.
5. The aircraft is assumed to be a rigid body such that the coordinates of any point on the aircraft, relative to a body fixed axes system $oxyz$, do not change.
6. The shape and mass distribution of the aircraft are assumed to be symmetric about the xz plane.
7. All attached rotors are assumed to possess axial symmetry.
8. The angular velocity of the cylinders remains constant with respect to time.

Assumptions 1 to 3 were deemed reasonable given the general type of aircraft under discussion (a low speed, short range, and low altitude electric vehicle). No other assumptions about the specific layout of the aircraft (such as the type, location, or number of control surfaces or the presence of propellers) were made. Assumptions 4 and 5 are recognised as being somewhat unrealistic but were assumed for simplicity. Assumption 6 is very nearly true for most aircraft and can be reliably assumed. Assumption 7 is required to prevent the location of the center of mass changing with rotation of the cylinders. Assumption 8 is acceptable since the aircraft will spend the majority of its time in level flight with the cylinders at a constant velocity ratio. When the rotor angular velocities are increased or decreased, the change is thus assumed to occur instantaneously.

With reference to Figure 4.7, the equations of motion for the aircraft were formulated in frame f_e, which is an inertial frame of reference that is, in accordance with assumption 1, fixed to the Earth and in which Newton's laws are valid. $Ox_e y_e z_e$ is a cartesian coordinate system fixed to this frame. Once formulated the equations were, for mathematical convenience, translated to a body carried frame f_b within which coordinate system $oxyz$ forms a set of body-fixed axes, with origin at the aircraft's center of gravity, that move and rotate with the aircraft. The notation used throughout the formulation and presentation of the equations is also illustrated in Figure 4.7.

In addition, the following mathematical conventions were adopted: Vector quantities in the equations are denoted by boldface fonts and have a subscript indicating the coordinate system in which the components of the vector are given. A right superscript on a position, velocity, or acceleration vector denotes the frame of reference that the vector is measured relative to. A left superscript on a derivative denotes the frame in which the derivative is taken. Matrices are denoted by square brackets, with a subscript on the matrix denoting the coordinate system in which the elements of the matrix are assembled.

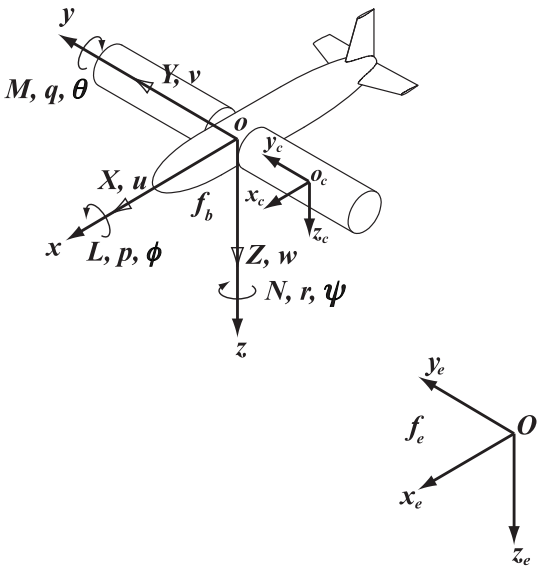

Figure 4.7: Reference axes and notation for presentation of equations of motion. Note that u, v, and w are the components of the linear velocity of the center of gravity relative to the atmosphere along the x, y, and z axes respectively. p, q, and r are the components of angular velocity of the body about the x, y, and z axes respectively. X, Y, and Z are the components of the resultant aerodynamic and thrust forces acting on the aircraft in the x, y, and z directions respectively. L, M, and N are the components of the resultant aerodynamic moments about the x, y, and z axes respectively. ϕ, θ, and ψ are the Euler angles defining the orientation of $oxyz$ relative to $Ox_e y_e z_e$ (such that $-\pi \leq \phi \leq \pi$, $-\frac{\pi}{2} \leq \theta \leq \frac{\pi}{2}$, and $-\pi \leq \psi \leq \pi$). Arrows denote positive directions.

The presence of two rotating cylinders on the aircraft primarily affects its angular momentum, $\mathbf{H}$. For a vehicle of mass m with two rotors having angular velocities of Γ_1 and Γ_2

(assumed to be able to vary independently), the angular velocity of the complete aircraft, as expressed in body axes $oxyz$, will be given by

$$\boldsymbol{\omega}_b^e = \begin{bmatrix} p \\ q \\ r \end{bmatrix} + \begin{bmatrix} 0 \\ \Gamma_1 \\ 0 \end{bmatrix} + \begin{bmatrix} 0 \\ \Gamma_2 \\ 0 \end{bmatrix} \tag{4.14}$$

The total angular momentum may then be shown to be given by

$$\mathbf{H}_b = [I]_b \begin{bmatrix} p \\ q \\ r \end{bmatrix} + [J]_b \begin{bmatrix} 0 \\ \Gamma_1 \\ 0 \end{bmatrix} + [J]_b \begin{bmatrix} 0 \\ \Gamma_2 \\ 0 \end{bmatrix} \tag{4.15}$$

where $[I]_b$ is the matrix of moments and products of inertia for the complete system (body plus both cylinders) in $oxyz$, such that

$$[I]_b = \begin{bmatrix} I_{xx} & -I_{xy} & -I_{xz} \\ -I_{yx} & I_{yy} & -I_{yz} \\ -I_{zx} & -I_{zy} & I_{zz} \end{bmatrix}_b \tag{4.16}$$

and $[J]_b$ is the matrix of moments and products of inertia for a single cylinder in $oxyz$, such that

$$[J]_b = \begin{bmatrix} J_{xx} & -J_{xy} & -J_{xz} \\ -J_{yx} & J_{yy} & -J_{yz} \\ -J_{zx} & -J_{zy} & J_{zz} \end{bmatrix}_b \tag{4.17}$$

Since the sum of external moments (about the center of gravity) acting on the aircraft is given by the time derivative of the angular momentum, it may be shown that, in frame f_b, this will be given by

$$\sum \mathbf{G}_b = [I]_b \, {}^b\dot{\boldsymbol{\omega}}_b^e + (\boldsymbol{\Omega}_b^e \times ([I]_b \, \boldsymbol{\omega}_b^e)) \tag{4.18}$$

where $\mathbf{G}_b$ is the vector of external moments acting on the aircraft, as expressed in $oxyz$, and $\boldsymbol{\Omega}_b^e$ represents the angular velocity of $oxyz$ with respect to $Ox_e y_e z_e$, as defined in

$oxyz$. This may be seen to be given by

$$\mathbf{\Omega}_b^e = \begin{bmatrix} p \\ q \\ r \end{bmatrix} \tag{4.19}$$

Thus, carrying out the necessary vector and scalar multiplications from Equation 4.18, and collecting like terms, produces three scalar equations that completely describe the rotational motion of the aircraft:

$$L = I_{xx}\dot{p} - I_{xz}(\dot{r} + pq) - (I_{yy} - I_{zz})qr - J_{yy}r(\Gamma_1 + \Gamma_2) \tag{4.20}$$

$$M = I_{yy}\dot{q} - I_{zx}(r^2 - p^2) - (I_{zz} - I_{xx})pr \tag{4.21}$$

$$N = I_{zz}\dot{r} - I_{zx}(\dot{p} - qr) - (I_{xx} - I_{yy})pq + J_{yy}p(\Gamma_1 + \Gamma_2) \tag{4.22}$$

These may be rearranged to state vector form (by solving Equations 4.20 and 4.22 simultaneously) to give

$$\begin{aligned} \dot{p} &= \frac{I_{zz}L + I_{xz}N + (I_{zz}(I_{yy} - I_{zz}) - I_{xz}^2)qr + I_{xz}(I_{xx} - I_{yy} + I_{zz})pq}{I_{xx}I_{zz} - I_{xz}^2} \\ &+ \frac{J_{yy}(\Gamma_1 + \Gamma_2)(I_{zz}r - I_{xz}p)}{I_{xx}I_{zz} - I_{xz}^2} \end{aligned} \tag{4.23}$$

$$\dot{q} = \frac{M + I_{xz}(r^2 - p^2) + (I_{zz} - I_{xx})pr}{I_{yy}} \tag{4.24}$$

$$\begin{aligned} \dot{r} &= \frac{I_{xx}N + I_{xz}L + I_{xz}(I_{yy} - I_{zz} - I_{xx})qr + (I_{xx}(I_{xx} - I_{yy}) + I_{xz}^2)pq}{I_{xx}I_{zz} - I_{xz}^2} \\ &+ \frac{J_{yy}(\Gamma_1 + \Gamma_2)(I_{xz}r - I_{xx}p)}{I_{xx}I_{zz} - I_{xz}^2} \end{aligned} \tag{4.25}$$

The absence or presence of rotating bodies fixed to the aircraft has no bearing on the equations of translational motion, the kinematic equations for the orientation of a rigid body, nor the navigational equations for the position of the center of gravity (providing the coordinates of the flight path), which remain as follows:

$$\dot{u}^e = \frac{X}{m} - g\sin\theta - qw^e + rv^e \tag{4.26}$$

$$\dot{v}^e = \frac{Y}{m} + g\cos\theta\sin\phi - ru^e + pw^e \tag{4.27}$$

$$\dot{w}^e = \frac{Z}{m} + g\cos\theta\cos\phi - pv^e + qu^e \tag{4.28}$$

$$\dot{\phi} = p + q\sin\phi\tan\theta + r\cos\phi\tan\theta \tag{4.29}$$

$$\dot{\theta} = q\cos\phi - r\sin\phi \tag{4.30}$$

$$\dot{\psi} = q\sin\phi\sec\theta + r\cos\phi\sec\theta \tag{4.31}$$

$$\begin{aligned}\dot{x} = {} & u^e\cos\theta\cos\psi + v^e(\sin\phi\sin\theta\cos\psi - \cos\phi\sin\psi) \\ & + w^e(\cos\phi\sin\theta\cos\psi + \sin\phi\sin\psi)\end{aligned} \tag{4.32}$$

$$\begin{aligned}\dot{y} = {} & u^e\cos\theta\sin\psi + v^e(\sin\phi\sin\theta\sin\psi + \cos\phi\cos\psi) \\ & + w^e(\cos\phi\sin\theta\sin\psi - \sin\phi\cos\psi)\end{aligned} \tag{4.33}$$

$$\dot{z} = -u^e\sin\theta + v^e\sin\phi\cos\theta + w^e\cos\phi\cos\theta \tag{4.34}$$

Equations 4.23 to 4.34 thus represent the nonlinear equations of motion for an aircraft with two rotating cylinders as the primary means of generating lift (as expressed in a body-fixed axes system and subject to the aforementioned assumptions). Note that the additional terms due to the cylinders in Equations 4.20 to 4.22 are in agreement with the discussion in §4.4.2 regarding the form of the equation governing gyroscopic moments (Equation 4.13) and their absence in the xz plane (so that Equation 4.21 is unchanged from that in conventional analysis).

Although modern computers allow the evaluation of the performance of an aircraft and its control systems through nonlinear simulation, the study of linear algebraic equations derived from application of small-disturbance theory to the equations of motion, and in which the nonlinear aerodynamic coefficients are replaced by stability derivatives, may also provide a great deal of insight. In particular, the relative importance of the various stability derivatives under different flight conditions may be determined, highlighting their effect on the stability of the aircraft's motion and providing information about the vehicle's manoeuvrability, its natural stability, and the effectiveness of the control surfaces. For this reason, it is often beneficial to continue to examine the small perturbation equations regardless of other available analytical tools.

In linearising the equations, the motion of the aircraft can be considered to be the result of small disturbances away from some initial steady-state reference flight condition. Thus, each variable, including the rotational rates of the cylinders, may be written as the sum of a steady state value (denoted by subscript $_0$) plus a change caused by the disturbance (denoted by prefix Δ). For instance,

$$u^e = u^e_0 + \Delta u^e \tag{4.35}$$

and

$$\Gamma_1 = \Gamma_{1_0} + \Delta\Gamma_1 \tag{4.36}$$

The initial condition of flight is conveniently chosen as one in which the aircraft spends most of its time and in which the velocities and accelerations are known. In general, there are two choices: equilibrium (unaccelerated) flight along a straight path with constant linear velocities (relative to inertial space) and zero angular velocity, or steady flight during which the linear and angular velocities (relative to the body fixed coordinate system, $oxyz$) remain constant. Simplification of the analysis may be achieved by setting the

initial flight condition to be that of equilibrium flight.

Linearisation then proceeds from the adoption of the usual methods and assumptions of small perturbation theory:

9. All steady-state term values (u_0^e, v_0^e,. . . etc.) are assumed constant such that the time derivative of such terms is zero.

10. Disturbances away from the initial steady flight condition are assumed to be small such that the products and squares of all disturbance terms are negligible in comparison to the disturbances themselves.

11. The disturbance angles are assumed to be small such that the sines of these angles may be taken to be equal to the angles themselves, the cosines of these angles may be taken to be equal to 1, and any squares or products of these angles may be neglected.

12. Since the disturbances are assumed small, changes in the air density encountered by the aircraft during a disturbance can be ignored.

13. The initial steady-state flight condition of the aircraft is assumed to be that of equilibrium flight. This represents steady, unaccelerated, symmetric flight at a climb angle of θ_0 (not assumed small) with no angular velocity. Thus, $v_0^e = p_0 = q_0 = r_0 = \phi_0 = \psi_0 = 0$. For this flight condition the reference rate of rotation for both cylinders must be the same. Thus $\Gamma_{1_0} = \Gamma_{2_0} = \Gamma_0$.

If assumptions 9 to 13 are applied to Equations 4.23 through 4.34, and the reference state values are eliminated from the right hand side of these equations, then the linearised equations of motion are as follows:

$$\Delta\dot{u}^e = \frac{\Delta X}{m} - g\Delta\theta\cos\theta_0 - w_0^e\Delta q \tag{4.37}$$

$$\Delta\dot{v}^e = \frac{\Delta Y}{m} + g\Delta\phi\cos\theta_0 - u_0^e\Delta r + w_0^e\Delta p \tag{4.38}$$

$$\Delta\dot{w}^e = \frac{\Delta Z}{m} - g\Delta\theta\sin\theta_0 + u_0^e\Delta q \tag{4.39}$$

$$\Delta\dot{p} = \frac{I_{zz}\Delta L + I_{xz}\Delta N}{I_{xx}I_{zz} - I_{xz}^2} + \frac{2J_{yy}\Gamma_0(I_{zz}\Delta r - I_{xz}\Delta p)}{I_{xx}I_{zz} - I_{xz}^2} \tag{4.40}$$

$$\Delta\dot{q} = \frac{\Delta M}{I_{yy}} \tag{4.41}$$

$$\Delta\dot{r} = \frac{I_{xz}\Delta L + I_{xx}\Delta N}{I_{xx}I_{zz} - I_{xz}^2} + \frac{2J_{yy}\Gamma_0(I_{xz}\Delta r - I_{xx}\Delta p)}{I_{xx}I_{zz} - I_{xz}^2} \tag{4.42}$$

$$\Delta\dot{\phi} = \Delta p + \Delta r \tan\theta_0 \tag{4.43}$$

$$\Delta\dot{\theta} = \Delta q \tag{4.44}$$

$$\Delta\dot{\psi} = \Delta r \sec\theta_0 \tag{4.45}$$

$$\Delta\dot{x} = \Delta u^e \cos\theta_0 - u_0^e\Delta\theta\sin\theta_0 + \Delta w^e \sin\theta_0 + w_0^e\Delta\theta\cos\theta_0 \tag{4.46}$$

$$\Delta\dot{y} = u_0^e\Delta\psi\cos\theta_0 + \Delta v^e + w_0^e\Delta\psi\sin\theta_0 - w_0^e\Delta\phi \tag{4.47}$$

$$\Delta\dot{z} = -\Delta u^e \sin\theta_0 - u_0^e\Delta\theta\cos\theta_0 + \Delta w^e\cos\theta_0 - w_0^e\Delta\theta\sin\theta_0 \tag{4.48}$$

It can be seen that if all the rotor angular velocity terms are set to zero, Equations 4.40 and 4.42 return to their usual form for when gyroscopic effects are ignored. It is also interesting to note that, as a result of the assumption of symmetry of shape about the xz plane, terms due to perturbations in the cylinder spin rates do not appear in the linearised equations.

In conventional analysis, the aerodynamic forces and moments arising during a disturbance ($\Delta X, \Delta M, \ldots$ etc.) are next taken to be functions of the perturbations in u^e, v^e, w^e, p, q, and r and are typically modelled by Taylor series expansions about the equilibrium state. Thus, for the force in the x direction,

$$
\begin{aligned}
\Delta X \;=\; & \left(\frac{\partial X}{\partial u}\right)_0 \frac{\Delta u}{1!} + \cdots + \left(\frac{\partial^\infty X}{\partial u^\infty}\right)_0 \frac{\Delta u^\infty}{\infty!} + \cdots + \left(\frac{\partial X}{\partial r}\right)_0 \frac{\Delta r}{1!} + \ldots \\
& + \left(\frac{\partial^\infty X}{\partial r^\infty}\right)_0 \frac{\Delta r^\infty}{\infty!} + \left(\frac{\partial X}{\partial \dot{u}}\right)_0 \frac{\Delta \dot{u}}{1!} + \cdots + \left(\frac{\partial^\infty X}{\partial \dot{u}^\infty}\right)_0 \frac{\Delta \dot{u}^\infty}{\infty!} + \ldots \\
& + \left(\frac{\partial X}{\partial \dot{r}}\right)_0 \frac{\Delta \dot{r}}{1!} + \cdots + \left(\frac{\partial^\infty X}{\partial \dot{r}^\infty}\right)_0 \frac{\Delta \dot{r}^\infty}{\infty!} + \cdots + \Delta X_C
\end{aligned}
\tag{4.49}
$$

where the stability derivatives, such as $(\partial X/\partial u)_0$, are evaluated at the reference condition and ΔX_C is a time-dependent force that results from activation of the controls.

In general, second order and higher terms may be neglected from the Taylor series expansions. Similarly, the effects of derivatives with respect to the time rate of change of a velocity are generally small enough that they can be neglected. However, since the flow field at the tail is affected by the downwash from the wing and so depends on the time history of the wing motion, the effect of the time rate of change of incidence is accounted for by the retention of Z and M derivatives due to $\Delta \dot{w}^e$.

The assumption of symmetry of external shape also dictates that half of the stability derivatives may be taken to be zero. Small disturbances to motion within the plane of symmetry, that is a change in u^e, w^e or q, will not result in the creation of a force or moment out of the xz plane; thus, ΔY, ΔL, and ΔN due to such motion is equal to zero. Disturbances outside the plane of symmetry (Δv^e, Δp, and Δr) can produce forces and moments within the plane of symmetry, but in general, these are only second order effects. Hence, the stability derivatives for symmetric forces and moments with respect to asymmetric disturbances, and vice versa, may all be set to zero and the forces arising during a disturbance are commonly modelled as follows:

$$\Delta X = X_u \Delta u^e + X_w \Delta w^e + X_q \Delta q + \Delta X_C \tag{4.50}$$

$$\Delta Y = Y_v \Delta v^e + Y_p \Delta p + Y_r \Delta r + \Delta Y_C \tag{4.51}$$

$$\Delta Z = Z_u \Delta u^e + Z_w \Delta w^e + Z_{\dot{w}} \Delta \dot{w}^e + Z_q \Delta q + \Delta Z_C \tag{4.52}$$

$$\Delta L = L_v \Delta v^e + L_p \Delta p + L_r \Delta r + \Delta L_C \tag{4.53}$$

$$\Delta M = M_u \Delta u^e + M_w \Delta w^e + M_{\dot{w}} \Delta \dot{w}^e + M_q \Delta q + \Delta M_C \tag{4.54}$$

$$\Delta N = N_v \Delta v^e + N_p \Delta p + N_r \Delta r + \Delta N_C \tag{4.55}$$

where, for brevity, the following notation is assumed

$$\left(\frac{\partial X}{\partial u}\right)_0 = X_u, \quad \left(\frac{\partial X}{\partial w}\right)_0 = X_w, \quad \left(\frac{\partial X}{\partial q}\right)_0 = X_q, \ldots \text{etc.} \tag{4.56}$$

This simplification also allows the linearised equations of motion for a conventional aircraft to be grouped into purely longitudinal and purely lateral modes of motion. For an aircraft with rotating cylinders instead of wings, the existence of independent symmetric and asymmetric modes is not invalidated by the presence of the cylinders since the spin axis of the rotors is aligned with the body-fixed y axis, and so gyroscopic moments from rotation of the cylinder spin axis only arise from, and only result in, asymmetric disturbances. However, it is unclear if the longitudinal and lateral forces and moments can be considered to depend only on longitudinal and lateral perturbation velocities respectively.

Since the aerodynamic characteristics of the cylinders are dependent on Ω, which is itself a function of V and so dependent on Δu^e and Δw^e, then changes to both the longitudinal and lateral forces and moments would be expected to occur due to perturbations in the symmetrical velocities. If true, this invalidates the assumptions made in conventional analysis that permit the separation of the equations of motion into two independent groups. However, given the complete lack of data on the lateral forces and moments for a rotating cylinder, a definitive conclusion cannot be drawn, but the uncertainty would seem to prevent further meaningful simplification or analysis of the linearised equations.

Consequently, a full investigation of the dynamic stability of an aircraft with rotating cylinders, through the solution of either the linear or nonlinear equations of motion, first requires the complete determination of the aerodynamic force and moment coefficients (including their variation with changing Ω, Ψ, α, V, Re, and AR) for both the cylinders and the aircraft as a whole. Thus, such an analysis is also dependent on the establishment of a preferred vehicle configuration, a detailed knowledge of this layout, including the nature of the control system, and information on the effect of downwash from the rotors on any other aerodynamic surfaces. An analytical approach to the determination of the stability derivatives would also require an understanding of the spanwise distribution of lift and drag under different conditions. However, only Thom's[116] measurements (based on the surface pressure distributions at a single Re, AR, and Ω) are presently available.

4.5 Practical Feasibility

With the performance estimates indicating that a viable rotating cylinder design was theoretically possible, a survey of commercially available technologies and materials was

performed in order to assess the practical feasibility of the concept. Specifically, the survey aimed to determine whether an operational vehicle that conformed to one of the three configurations identified as most favourable by the performance estimates (see Table 4.4) could be constructed using suitable components that would provide the required capability (in terms of payload weight, range, and endurance) within the weight limits associated with the size of the rotors, the flight speed, and the preferred operational velocity ratio range. Note that the survey considered only COTS technology and materials for reasons of simplicity and cost.

In assessing the required components for a successful design, estimating vehicle weight, and determining feasibility, a number of assumptions were made regarding the general layout of the vehicle. As well as a twin rotor system, each configuration was assumed to include a basic aerodynamically-shaped fuselage (of suitable dimensions to house all the necessary components but within the platform size limits), a conventional empennage comprising of a fin and tail, and a tractor propeller. The structural weight of the vehicle was then estimated in accordance with this arrangement. In addition, the rotor system was assumed to be capable of driving each cylinder independently.

The assumed nature of the design and the choice of components and materials for its construction were also influenced by recommendations provided in the literature by previous efforts at MAV and mini-UAV development. Information on the best approach to establishing the propulsion, power, and control systems, together with details on the size, weight, performance, and suitability of typical components and materials was used to identify the most appropriate equipment for the desired performance, thus enabling a reasonable assessment of the practical feasibility of the concept to be made. This information was particularly useful as it is not always available from the original equipment manufacturer.

Such recommendations resulted in the pursuit of a vehicle that used electric propulsion and employed a direct-drive system for both the propeller and cylinders, this method having been shown to be more efficient than a geared drive system at the small scales of MAV flight.[35] In addition, previous experience indicated that the use of brushless electric motors should (due to higher power output, greater efficiency, and generally smaller size and weight) be favoured over conventional brushed types and that lithium-polymer batteries should (due to their light weight and very small form-factor) be considered the preferred power source. Similarly, the choice of structural materials was made based on the experiences of previous designers regarding the machinability and resistance to damage of different material types.

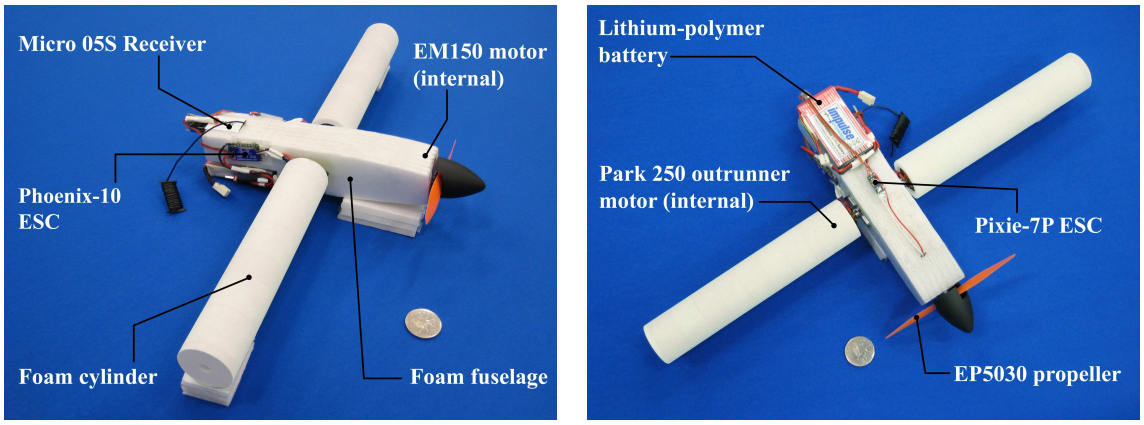

(a) Top view (b) Bottom view

Figure 4.8: Unoptimised prototype rotor system and partial fuselage for basic rotating cylinder mini-UAV design. Total system weight, without payload, is 215 g.

On completion, the investigation into the feasibility of the concept indicated that the construction of a vehicle capable of providing the full level of performance outlined in the design specification was, for all three vehicle weights considered, unachievable with currently available COTS components and materials. For the smallest vehicle size considered, such a design would need to weigh more than twice the 50 g maximum weight associated with the rotor size and operating conditions. The 250 g and 500 g configurations came closer to matching the required performance within the applied constraints on platform size and weight and a viable vehicle could be constructed in both cases if the desired payload capability of 20% was wholly ignored. Alternatively, more basic designs having a much reduced performance, but providing the necessary payload capability, could also be constructed within the applied constraints. A prototype of such a basic vehicle was constructed for the 250 g configuration (see Figure 4.8 and Table 4.6).

The failure to construct a fully functional vehicle was, except for the 50 g vehicle, not associated with the need for a rotor system, which was itself found to be entirely achievable using only commonly available, relatively inexpensive materials, and could generally be constructed for less than 25% of the total vehicle weight. Instead, the primary reasons for the inability to match the design specifications were the high power and the lack of a suitable battery type that met all the requirements in terms of cell size, weight, and performance.

Estimates of the power for spinning the cylinders and maintaining forward motion were used with the mission profile to calculate flight times and energy requirements so as to determine the necessary battery capacity for each vehicle configuration. This indicated that, once the efficiency of the motors, propellers, and other components involved were

taken into account, batteries with a capacity of 650 mAh, 2250 mAh, and 5500 mAh (with discharge rates of at least 1A, 4A, and 9 A respectively) would realistically be required to fulfill the envisaged mission profile with the 50 g, 250 g, and 500 g vehicles. Such batteries are commercially available but are currently bigger and heavier than would be acceptable in the present context.

The high drag of the cylinders also contributed to the inability to develop a fully functional aircraft by imposing a higher performance demand on the propulsion system than would otherwise be indicated by the overall size and weight of the vehicle. This made selection of a suitable solution somewhat difficult and no ideal candidate system could be determined. Brushless motors of the required capability were always smaller in size than the equivalent conventional motor, but only offered a weight advantage at the levels of performance necessary for the 500 g vehicle; for smaller sizes, brushless motors tended to be heavier than their conventional counterparts. Brushed motors able to provide the correct performance were generally of a reasonable weight, but their lower efficiency resulted in an increase in the necessary battery capacity. Consideration was given to the use of a ducted fan propulsion system as its greater efficiency should lead to a reduction in weight, but a suitably small unit that matched the performance requirements could not be identified.

Table 4.6: Breakdown of weights for prototype of basic 250 g rotating cylinder mini-UAV design having two cylinders of size $d = 0.04$ m and $b = 0.2$ m.

Rotor System	**No.**	**Total Weight (g)**
Depron foam cylinders	2	20
E-flite Park 250 outrunner brushless motor	2	30
Castle Creations Phoenix-10 brushless ESC	2	12
Propulsion System		
GWS EM150 brushed motor	1	40
GWS EP5030 nylon propeller	1	2
Castle Creations Pixie-7P brushed motor ESC	1	3
Control System		
Hitec micro 05S radio receiver	1	8.6
Falcon 1.6 servo	2	3.2
Carbon fibre push-rods and linkages	2	4
Power Supply		
7.4 V 900 mAh 20C lithium polymer battery	1	57
Structure		
Depron foam fuselage and empennage	1	10
Screws, fastening, mounting brackets etc.	-	10
Payload	-	50
	Total	249.8

It should also be noted that the assembled prototype used a drive system in which the cylinders' outboard ends were unsupported. Whilst preliminary tests suggested that this approach was adequate, it is generally undesirable to apply a bending moment to a motor shaft in this way. Thus, in practice, a support system similar to that depicted in Figure 4.4, or some other alternative design, may be necessary. This would likely result in an increase in structural weight, making successful vehicle development all the more difficult.

Although a fully-functional vehicle built from COTS components was not currently possible, the shortfall in performance does not seem insurmountable and a vehicle approaching or exceeding the desired specifications is likely to be realisable using just COTS materials through future technological developments. The required level of performance could conceivably be met at present if more advanced, more expensive, less readily available, but generally lighter materials and components were used in conjunction with custom-development of individual subsystems (which has been shown to drastically reduce vehicle weight[35]) and the implementation of a more sophisticated design. In particular, a greater level of integration between subsystems and the use of multi-role materials should lead to substantial weight reductions and performance enhancements. However, achieving increased integration requires investigation of the most favourable vehicle configuration and the best arrangement of any aerodynamic surfaces and propellers relative to the rotors.

Renewed investigation into, and subsequent greater understanding of, the flow past a rotating cylinder could also lead to further improvements in vehicle size, weight, and performance by providing much needed clarification on the variation of C_L, C_D, and C_P with velocity ratio. The lack of such data meant that the choice of motors and other components needed for the rotor and propulsion systems was generally made conservatively as the estimated requirements for the operating conditions were somewhat uncertain. A greater understanding of rotating cylinder flow may also provide new means of improving the rotors' aerodynamic performance through increased lift, reduced drag, and lower power requirements at a given velocity ratio. Any such improvement would be of significant practical benefit to the development of a fully operational vehicle as the requirements placed on the power and propulsion systems were found to be the most difficult to fulfill.

Overall, the feasibility analysis and preliminary design phase indicated that the concept of the rotating cylinder small-UAV warranted further investigation. As a result, a wind tunnel testing programme that was intended to address some of those areas of uncertainty highlighted by the design analysis was initiated. Thus, the programme was focused around experiments aimed at clarifying and extending the understanding of the flow past a rotating circular cylinder and included an examination of the preferred configuration for an MAV or mini-UAV of the proposed design.

5 Tests on an Isolated Rotating Cylinder

The history of experimental investigation into rotating cylinder flows is an example of somewhat unsystematic and fragmentary research. The data that exists in the moderate Reynolds number range that is of interest for the present study ($2 \times 10^4 \leq Re \leq 1 \times 10^5$) is incomplete and occasionally contradictory. In particular, reviewing the literature highlights the uncertainty in the results regarding the drag performance of finite aspect ratio rotating cylinders, where the arrangements strongly influence the outcome of testing, and the question of the maximum lift that can be generated. Understanding and predicting the behaviour of these two forces is of paramount importance to the successful development of an MAV based around rotating cylinders as the primary means of lift generation.

A further problem is that much of the existing experimental investigations have not been performed with a practical application in mind, but rather as a general study of the fundamental physics of the flow. Where the experimental tests have been tied to practical applications they have typically not been related to aircraft flight. Consequently, the available data does not address many aspects that would be important in this context. This is reflected in the surprising lack of experimental data for such basic quantities as the torque and power required to spin the cylinder. Similarly scarce is information on the effects of yaw. Both of these are important in the design of a flight vehicle, particularly an MAV. More generally, there also appears to be a deficit of detailed information concerning the nature of the wake.

Much of the more recent data on rotating cylinder flow come from increasing numbers of numerical simulation studies. Despite this focus, CFD results are of little practical interest and cannot be used to address the uncertainty in experimental data due to the lack of overlap between results from the two methods of investigation. Most of the numerical studies are limited to very low Reynolds number regimes ($Re \leq 200$), where no experimental force results appear to be available: experimental data only exists for Reynolds numbers of $Re \geq 2 \times 10^3$. The importance of Reynolds number matching is highlighted by Chang & Chern's[173] results, which suggest that the topology of the flow at higher Re is different from that at low Re.

Furthermore, the computational cost of three-dimensional simulations, and the limitations of the available numerical tools, has meant that nearly all the available CFD studies deal with two-dimensional geometries only. For realistic and accurate simulation at higher Reynolds numbers the three-dimensionality of the flow must be accounted for. As a result, despite an existing body of experimental and numerical data, there remains a need for further testing.

With such a view in mind, a series of experiments were carried out on an isolated rotating circular cylinder in crossflow with the intent to confirm its aerodynamic properties. These tests differed from many previous experiments on rotating cylinders in that they were not aimed at simulating two-dimensional flow, but were concerned with examining the results of three-dimensional flow about a three-dimensional cylinder, for which data are scarce.

A particular focus of the tests was on the effects of endplates. The existing literature demonstrates their ability to simply, yet effectively, improve the aerodynamic performance of a rotating cylinder, particularly when of low aspect ratio, but it is incomplete. Previous works have generally focused on their ability to produce a more two-dimensional flow, for which larger plates are preferred. Consequently, nearly all previous experiments with endplates have concentrated on sizes greater than $d_e/d = 1.7$; the effects of smaller plates and the relative merits of different plate sizes and configurations have not been specifically investigated. Such an assessment is of interest as, in the context of the present application, a low AR cylinder is preferable but large endplates may be undesirable.

Furthermore, despite analysis of their ability to enhance two-dimensionality and discussion of their effects on lift and drag, many of the other possible effects of endplates on the aerodynamic characteristics of a rotating cylinder (e.g. effects on power requirements, lateral force and moment coefficients, vortex shedding etc.) have not been quantified. As such, the current tests involved examination of the influence of endplate size, number (one plate or two), and arrangement relative to the cylinder (spinning versus stationary). The effects of each configuration on the forces and moments, power requirements, and wake phenomena were determined. The consequences of yawing the cylinder were also assessed.

This section details the equipment and arrangements used to carry out the isolated cylinder tests, explains the methods and procedures employed to analyse the results, and includes a comprehensive discussion of the findings. This involved a comparison of the present results with pre-existing data to determine the veracity and accuracy of both, highlighting any new, important results.

5.1 Experimental Arrangements

Testing of the isolated cylinder model was carried out in City University's Handley Page laboratory using two closed-circuit variable speed subsonic wind tunnels of differing design (designated T2 and T3). By making full use of both facilities it was possible to expand the scope of the experiments and produce more useful data. Development of the

test model required not only the design and manufacture of the cylinder itself, but of all surrounding systems too. Specifically, this involved the creation of a family of endplates of varying size, the construction of suitable support structures to mount the cylinder in the tunnels, and the implementation of methods for controlling and determining the cylinder rotation rate. A description of all such aspects of the isolated cylinder model, along with information on the wind tunnels, is given below.

5.1.1 The Wind Tunnels

The T2 tunnel has a rectangular working section (with 45° corner fillets) of dimensions 1.12 m x 0.815 m x 1.68 m and is vented to atmosphere at the rear. T2 can generally be operated at speeds of between 16 and 45 m/s, wind speed being assessed by using a Furness FCO332 differential pressure transmitter to measure the difference between tunnel working section and contraction pressures. The velocity distribution of the approach flow is known to be quite uniform, with a maximum variation of about 1.75% from the mean, but generally varying by less than 0.5% across the majority ($> 80\%$) of the working section. Nominal turbulence intensity levels are below 0.7%. T2 is fitted with a six-component overhead balance positioned directly above the working section and has motor drives to control both incidence and yaw.

During the planning phase of the experiments the start-up speed of T2 was determined to be a limiting factor with regards to the range of velocity ratios for which measurements could be taken: at a speed of $V = 16$ m/s the maximum achievable velocity ratio was estimated to be only $\Omega = 1.7$. For meaningful testing to be carried out, it was felt that this should be extended to at least $\Omega = 2$ and preferably beyond. To increase the available velocity ratio range required either a reduction of the minimum tunnel speed, or operation of the motor at very high rotational rates. The latter option was limited by the choice of motor, and also by the support structure used to connect the cylinder to the T2 balance.

Preliminary experimentation with the drive system revealed that the motor could only be reliably operated to a maximum of $N = 7000$ rpm before unacceptable vibration of the structure was noted. This was not fast enough to enable testing at $V = 16$ m/s across the entire desired range of velocity ratios. Thus, with no alternative motor readily available and no guarantee that a different motor would not still cause excessive vibrations, the first option of reducing the start-up speed of T2 was undertaken.

To facilitate this, a wide-slatted louvre door (see Figure 5.1a) was installed downstream of the working section (at position C, Figure 5.1b) for some of the T2 tests. By using

the louvre door in one of three configurations a significant reduction in the start-up speed of T2 could be achieved. Leaving the slats fully open made little change to the start-up speed, thus keeping Ω_{max} at approximately 1.7. When the slats were set to $45°$, the minimum speed was reduced to 12 m/s. In this condition, $\Omega_{max} \approx 2.1$. Finally, with the slats fully closed, speeds as low as 6 m/s were possible and Ω_{max} was approximately 4. To ensure that there were no adverse consequences to data accuracy from using this approach, a short series of experiments to assess the effects of the louvre on the flow, and any subsequent influence on the aerodynamic coefficients, were performed. These indicated that, in general, the system produced acceptable data (see §5.5.1 for full details).

Although of similar size and overall design to the T2 tunnel, T3 differs by having an octagonal working section (vented at the rear, with maximum dimensions of 1.15 m x 0.89 m x 1.5 m) and only a three-component balance (lift, drag, and pitching moment). Furthermore, though T3 has a motorised pitch arm, it lacks a yaw mechanism. The velocity distribution in T3 is known to be less reasonably uniform than T2, with a maximum variation of about 3% from the mean and a typical variation of about 1.5%, but nominal turbulence levels are slightly smaller, at about 0.5%.

Speed control for T3 is effected through a modern inverter, which gives a wider usable test range (of between 3 and 45 m/s) than T2. This superior degree of control allowed investigation of large velocity ratios without the need for correspondingly high rotational rates. As with T2, the wind speed in T3 was assessed by measuring the difference between tunnel working section and contraction pressures. Primarily, this was achieved through a Furness FCO16 digital water manometer; however, at low wind speeds the digital manometer did not offer a sufficient resolution to precisely determine tunnel speed. As such, a Casella micro-manometer with vernier scale was used for all tests at $V \leq 7$ m/s.

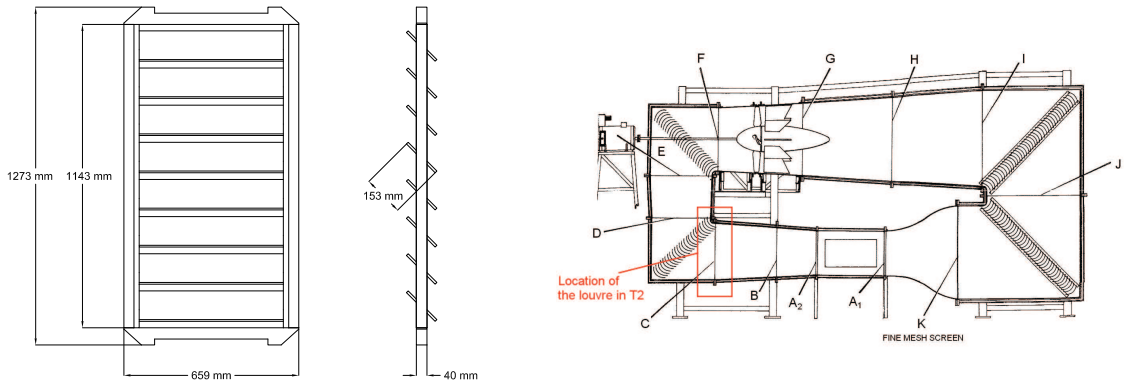

(a) The louvre door

(b) The T2 wind tunnel

Figure 5.1: The use of louvre doors in the T2 wind tunnel.

5.1.2 The Cylinder

Sizing of the cylinder model was greatly influenced by initial designs for the proposed MAV, but was ultimately constrained by both balance force limits and the characteristics (power and rpm) of the available motor. Model dimensions were also required to be such that the test Reynolds numbers would be similar to the expected Reynolds number range of the MAV ($2 \times 10^4 \leq Re \leq 1 \times 10^5$) whilst, for the purpose of comparison, also being in the same range as previous published experimental results. Model size with regards to tunnel blockage was also a consideration.

With these constraints in mind, and having decided on an initial aspect ratio of $AR = 5$, a parametric study was carried out to compare balance force and moment limits against motor power/rpm characteristics and so determine the best size for the model. This suggested that the use of a cylinder with a span between 400 mm and 500 mm would provide the best compromise between conflicting requirements. On the basis of this finding, a suitable model was designed and manufactured.

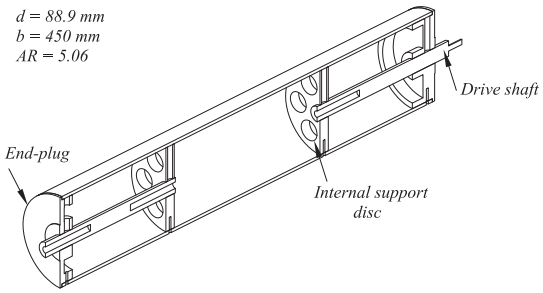

(a) Cylinder internal structure

(b) Endplate family

Figure 5.2: The cylinder model and endplates.

The final model primarily consisted of a hollow piece of aluminium tubing of external diameter $d = 88.9$ mm, length $b = 450$ mm and shell thickness 3.2 mm. This was spun on a steel shaft of 15 mm diameter, which in an effort to reduce weight did not run the length of the span, but was split in two, so that each section was approximately one third of the cylinder's total length. The shaft sections exited the cylinder through aluminium endplugs located at either end of the central tube and used to hold the shaft in place. The internal free end of each shaft section was supported by a thin aluminium disc that was fixed to the inner wall of the cylinder (see Figure 5.2a). This type of design allowed for the investigation of different aspect ratios without necessitating the construction of a

completely new model: to alter AR, only the central tube need be replaced.

5.1.3 Endplates

Circular endplates (see Figure 5.2b) were used in some tests to investigate their ability to minimise end effects, increase lift, and decrease drag. Initially, the endplates were fixed to the cylinder's endplugs so that they spun with the cylinder. This arrangement was chosen as being more representative of the likely final design: it would be difficult to fit an MAV with the more effective, as suggested by the literature,[111,120,147] stationary endplates. Even so, a small number of later tests did investigate the effects of stationary plates. In these experiments, the endplates were fixed to the model's support structure rather than to the cylinder, and a 0.5 mm gap existed between the plates and the cylinder's end walls. A smaller gap of 0.25 mm was also examined.

Endplate dimensions were chosen so as to complement the work of Betz,[8] Thom,[115,119] and Busemann.[127] Initial tests were carried out with an endplate-to-cylinder diameter ratio of $d_e/d = 2$. The effect of reducing endplate size was then investigated by gradually decreasing the size ratio to $d_e/d = 1.5$, 1.25, and finally 1.1. Later tests examined larger endplates of size $d_e/d = 2.5$ and 3. All endplates were 2 mm thick and had a 11° chamfer over the outer 8 mm of the diameter, reflecting previous work by Apelt & West.[239] These six different endplate sizes were combined to give a total of nineteen separate end configurations, encompassing the use of two free ends, two plates of the same size, one plate and one free end, and combinations of two different sized plates. Note that when the cylinder had one free end, the endplate was always positioned at $z/b = 0.5$, whilst when mismatched plates were used, the larger plate was always positioned at $z/b = -0.5$.

5.1.4 Support Structure

With testing taking place in two non-identical wind tunnels it became necessary to develop separate mounting structures for T2 and T3. In general, the design of these support systems was a compromise between the desire for a rigid structure that would help prevent vibration and the requirement for a less intrusive design so as to minimise aerodynamic interference.

The T2 support system comprised two struts that extended vertically upwards from behind the endplates, connecting the model directly to the balance plate (see Figure 5.3). The struts were constructed from hollow rectangular beams of cold-drawn mild bright steel,

with shell thickness 1.6 mm and cross-section 35 mm x 17 mm. Semi-circular sections of wooden dowling were attached to the front and back of each vertical strut to effect a more aerodynamic shape. Wider supports at the lower ends of each strut were used to house a pair of single-row radial ball bearings that supported the cylinder shaft.

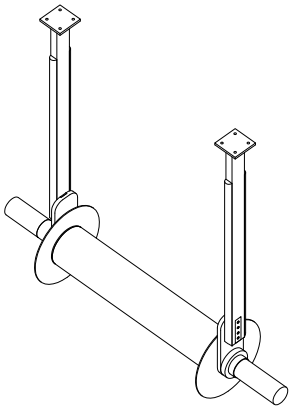

(a) The T2 struts

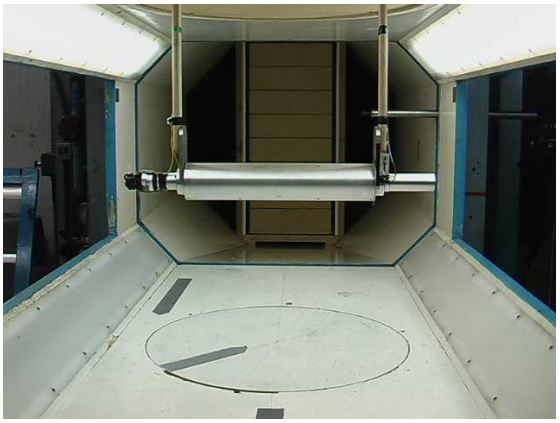

(b) The cylinder in T2

Figure 5.3: Cylinder support structure for T2.

The T3 support structure was constructed from the same mild steel bars as the T2 supports, and had the same overall design, except for the addition of a stepped arrangement and crossplate (see Figure 5.4). This was necessary to accommodate the constraints imposed by the octagonal geometry of T3's working section. To minimise interference, the crossplate was kept as far away from the cylinder as possible, being approximately 15 mm from the upper wall of the tunnel. Since the balance plate for the T3 tunnel is located much further away from the horizontal centerline of the working section than is the case with T2, the T3 struts were also slightly longer than those used in T2 testing.

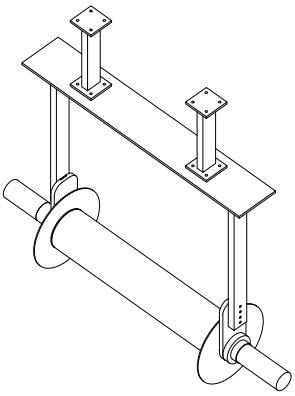

(a) The T3 struts

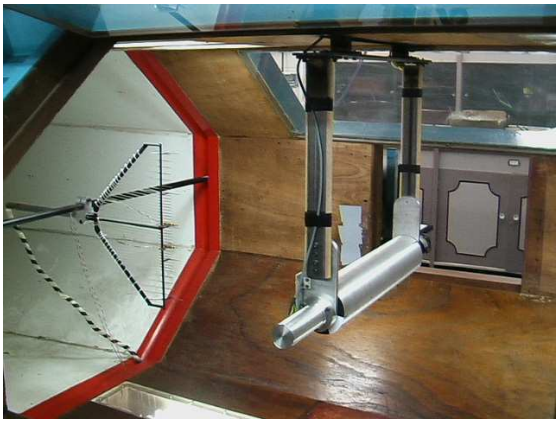

(b) The cylinder in T3

Figure 5.4: Cylinder support structure for T3.

In both T2 and T3, the cylinder was mounted horizontally, in the middle of the tunnel working section, such that its mid-span was coincident with the tunnel centreline. Area blockage for the model plus support struts was found to be $A/C \approx 0.08$ in T2 and $A/C \approx 0.09$ in T3. The cylinder diameter-to-tunnel height ratio was slightly bigger, being $d/B \approx 0.11$ for T2 and $d/B \approx 0.10$ for T3. On the whole, model blockage was larger than ideally desired ($d/B \leq 0.06$), but was a consequence of having to balance the many different constraints on cylinder sizing. The ratio of cylinder span to tunnel width was $b/B \approx 0.4$ for both T2 and T3.

5.1.5 Cylinder Rotation and Speed Control

A Graupner Ultra 3300-7 variable speed DC electric motor was used to drive the cylinder. This particular model was chosen for its good efficiency, high maximum speed, and high shaft power output. A direct-drive method was employed so as to avoid the complication of gearboxes. The motor was mounted on to the side of one of the struts supporting the cylinder, with connection between the motor and cylinder shafts accomplished via an integral-clamp-style jaw-coupling. To maintain symmetry of shape, a 'dummy motor' was attached to the strut on the non-motor end of the cylinder. This dummy structure was made to be approximately the same size and weight as the motor and its mounting assembly.

Power was supplied to the motor by two heavy-duty, type 063, lead-acid batteries (12 V, 370 A cranking power, 45 Ah each). The use of a battery rather than a DC power-pack allowed for the implementation of high rotation rates where current draw was in excess of 10 A (the limit of the available power-packs). Variation of the cylinder rpm was achieved by placing a 6.35 Ω rheostat in series with the motor (see Figure 5.5). Changing the resistance of the rheostat had the effect of altering the motor's armature current and torque, thus allowing the motor's speed to be increased or decreased as required.

Note that, although this is a simple and practical method of speed control, it does suffer from several drawbacks: power and heat are wasted in the rheostat, leading to a low overall efficiency; an uneven power curve means there is typically very little low end torque; and speed regulation may often be poor, even for a fixed setting of the rheostat. Indeed, when testing at very high rotational speeds it became difficult to set the motor speed to a fixed value and it was found to experience a fair amount of drift. Considerable effort was made to keep this drift as small as possible and, regardless of rotational rate, care was taken to ensure that the cylinder rpm had stabilised sufficiently before any data readings were taken (see §5.3.5).

The speed control circuit was also used to measure the power supplied to the motor (see Figure 5.5). A digital voltmeter measured the voltage across the motor whilst current was measured using a 60 mV, 60 A brass-ended shunt resistor that was in series with the motor. A second digital voltmeter, placed in parallel with the shunt, displayed the current in units of 1 mV to 1 A. This method of current measurement was employed to allow for testing at very high velocity ratios, where the motor may draw more than 10 A of current (the limit of most digital ammeters).

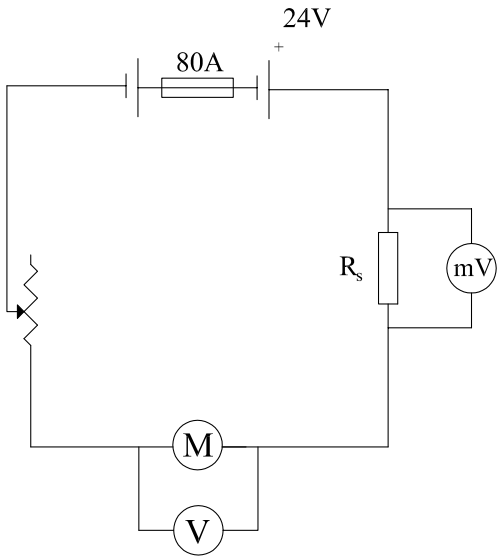

Figure 5.5: Circuit diagram for motor speed control and power measurement.

Measurement of the cylinder rotational rate was through a reflective opto-coupler placed parallel to the endplate on the non-motor side of the support structure at a distance of about 5 mm (see Figure 5.6a). Alternating black and white segments on this endplate provided a changing input to the opto-coupler when the cylinder was rotating, and a custom built interface allowed its output to be displayed on a Racal-Dana 1990 120 MHz universal counter. This provided a continuous, real-time reading of the cylinder rpm that helped to better manage any drift. The accuracy of this optical system was tested against both a contacting mechanical tachometer and a stroboscope, with the difference between the readings from all three means being less than one percent.

In some instances, the above method of speed determination was not possible and the procedure had to be modified. For example, in those tests carried out with stationary endplates the opto-coupler could not be used as the endplates did not spin, so the rotation rate of the cylinder was instead determined by evaluation of the motor speed constant, K_v. This parameter expresses the motor speed per volt, allowing the motor rotational rate

to be assessed purely from a measurement of the applied voltage.

To calculate K_v, readings of the voltage across the motor at several different rpm were obtained using the opto-coupler for the case of the cylinder without endplates. These were then used to plot a graph of motor speed N against voltage V that, as expected, indicated a highly linear and strongly repeatable relationship between the two (see Figure 5.6b). Applying a least-squares linear regression to the data produced an equation that was found to predict the value of the cylinder's rpm for any measured motor voltage to an accuracy of more than 99%, as compared to the actual measured value, at all but the lowest rotational speeds. For $N \leq 600$ rpm, the accuracy of predictions fell to 95%. This difference is believed to be due to the low-speed characteristics of the motor.

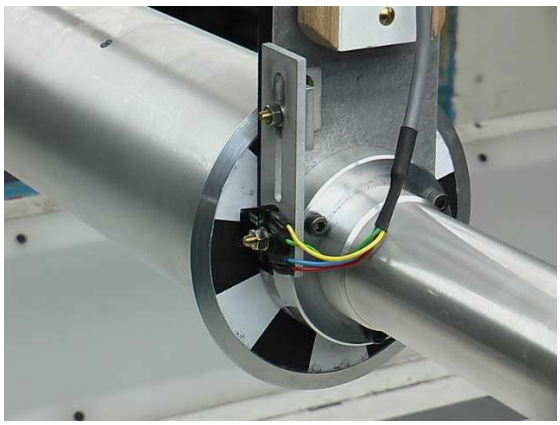

(a) Opto-coupler and input segments

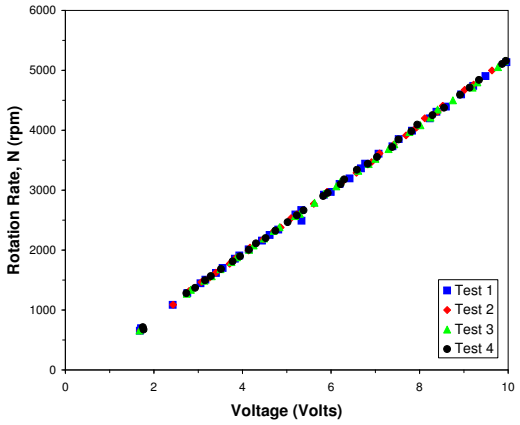

(b) Determination of the motor speed constant, K_v

Figure 5.6: Measurement of the cylinder rotational rate.

5.1.6 Wake Measurements

Taken alongside the force, moment, and power readings were a series of different pressure measurements designed to investigate the wake region of the flow. These measurements were primarily meant as an aid to checking the validity of force data by confirming that cylinder wake-flow phenomena conformed to known behaviour. The tests involved the measurement of both the time-averaged and time-varying pressure within the wake by use of pressure transducers and a wake rake.

The rake, as shown in Figure 5.7, comprised forty pitot tubes and five static tubes, the latter being located in a plane parallel to the former, but offset by 25 mm. The rake was initially positioned vertically within the plane of the cylinder's mid-span ($z/b = 0$), at a downstream distance of $x/d = 3$, and with its centreline approximately one diameter below the cylinder's lateral axis (as represented by $y/d = 0$). This choice ensured that

the majority of the pitot tubes were located on the upstream moving wall side of the cylinder, and was made with the expectation, as suggested by the literature,[12,108,158,159] that the wake would be deflected in the direction of rotation as higher velocity ratios were implemented.

Later tests moved the rake to three more downstream locations: $x/d = 4$, 5, and 7. As the downstream separation distance increased it became necessary to alter the position of the rake's centerline in order to fully capture the widening wake profile. In each case, pressures were recorded at $z/b = 0$. For $x/d = 3$ and 5, pressures were also measured at twenty-three other spanwise stations in the range $-0.51 \leq z/b \leq 0.45$; it was not physically possible to take measurements at $z/b > 0.45$ due to limitations in the traverse mechanism used to move the rake. Note that the wake rake could be positioned to an accuracy of ± 1 mm, equivalent to $\pm 0.011d$.

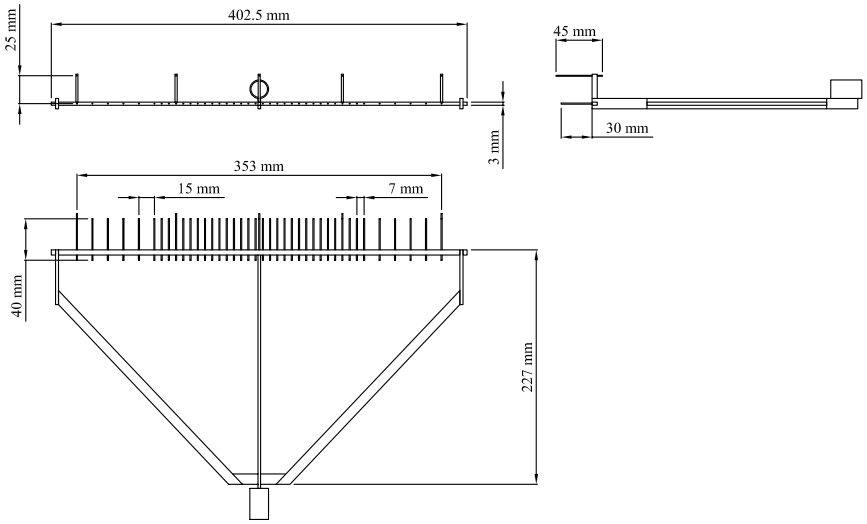

Figure 5.7: Wake rake dimensions.

Rake pressures were measured using a Pressure Systems, Inc. ESP-miniature pressure scanner (rated at ± 2.5 psig) and a Chell CANdaq self-contained data acquisition system, which together are able to provide an accuracy of $\pm 0.06\%$ full-scale deflection. Each tube on the rake was connected to one of the scanner's sixty-four ports, the output from which was acquired by the CANdaq system and relayed, via Ethernet, to a PC running a custom software package that controlled how the data was acquired.

For every combination of x/d, z/b, and Ω that was to be investigated, data was sampled at a rate of 100 Hz over a period of 10 s, so that during each run 1000 readings were taken for each of the pitot and static tubes on the rake. However, despite the high level of

sensitivity available, pressure values at the lowest test speeds ($V < 7$ m/s) were too small to be reliably measured with this system. Results based on measurements taken at these speeds provided only an indication of overall trends and were viewed with scepticism, unless corroborated by more reliable data.

(a) The wake rake in T2 (b) The dynamic pressure transducers

Figure 5.8: The wake rake and dynamic pressure transducers.

Further information on the wake was gathered using three Kulite CTQH-187 series (type B) dynamic pressure transducers rated at 5 psi. Contained within brass housings (see Figure 5.8b), the transducers were attached to the wake rake and positioned so as to concentrate measurements on the cylinder's upstream moving wall side (See Figure 5.9). The first transducer was located as close as possible to the cylinder's lateral centreline at $y_1/d = -0.06$, the second was midway between the centerline and the lower perimeter at $y_2/d = -0.25$, and the last slightly below the level of the cylinder's lower surface at $y_3/d = -0.6$. Note that whenever it was necessary to move the rake laterally, the dynamic pressure transducers were also relocated so as to maintain these relative positions.

The transducers were used to record voltage signals that were representative of the fluctuating pressure field in the wake. These signals were digitally sampled at a rate of 300 Hz, over a period of 60 s, by using a PC running the CED Spike2 software package. Connection between the transducers and the computer was through a Fylde 379TA transducer–amplifier and then through a CED 1401 analogue-to-digital converter (ADC). The sampling rate was chosen on the principle that, in order to avoid aliasing during fast Fourier analysis, the sampling frequency should be at least twice as fast as the highest frequency expected in the spectra. Thus, with some tests performed at $V = 16$ m/s (where for $\Omega = 0$, $St \approx 0.21$ and $f_s \approx 40$ Hz), and with the expected increase of f_s with Ω and the existence of harmonic frequencies in mind, this informed the selection of 300 Hz as the sampling rate.

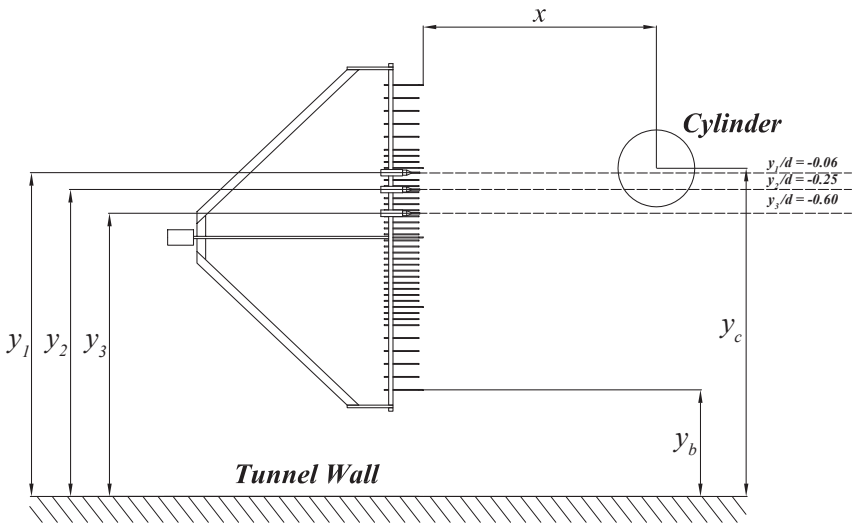

Figure 5.9: Wake rake and pressure transducer positioning.

5.1.7 Flow Visualisation Methods

A brief programme of flow visualisation tests was performed during experimental testing as a means of assessing interference effects arising from the use of a louvre door in T2 and to examine some of the wake behaviour more closely. Two different visualisation techniques were employed: smoke visualisation was used to investigate wake structure, whilst oildots examined surface flow. Visualisation tests were performed in both T2 and T3, though the unfavourable octagonal geometry of T3 prevented all but the simplest investigations in that tunnel. Overall, the number and scope of these tests were somewhat limited by the available equipment.

Oildot tests were performed for the stationary cylinder case only. In each test, several rows of oildots, made using 3-in-1 oil, were placed along the entire span of the upper surface of the cylinder between $35° \leq \beta \leq 145°$. A digital photograph of the oildot positions before and after the tunnel was activated was then taken. Photos were always taken from the exact same position and orientation relative to the cylinder. In this way, the motion of the oildots was more easily assessed.

An Aerotech ATE Ltd. smoke generator and wand probe were used for the smoke visualisation tests. The generator was used to pump fluid from an internal reservoir, along the length of the probe, to the tip, where an electrical heating element vaporised the fluid, creating a smoke plume with which to visualise the wake flow. Two different fluids were

experimented with during the tests. The first, Shell Ondina EL, was a medicinal quality white oil. The second was a simple 9-to-1 mix of water and glycerol. For the majority of tests, the probe was located at the mid-span, several diameters upstream of the model, and with its tip positioned level with the cylinder's longitudinal axis. However, other streamwise and spanwise locations were also investigated. In all cases, a black card screen was attached to the door on the far side of the wind tunnel so as to provide a contrasting background against which to better view the pale smoke against, and a Panasonic NV-MX500 digital video camera was used to record the results.

5.2 Testing Procedure

Experimental investigation of the isolated cylinder consisted of three stages. Testing began with a brief period of preliminary experiments, conducted solely in T2, which were used to validate the experimental arrangements in that tunnel. This was followed by an extensive series of T3 tests that formed the bulk of the investigation. Finally, a second series of T2 experiments, to investigate performance under yaw, were performed. Full details of the tests carried out within each stage and the methods used are provided below.

5.2.1 Preliminary T2 Testing

The initial set of tests were carried out to assess the feasibility of using a louvre door to reduce the start-up speed of T2, and to investigate any adverse effects on force data arising from this method. For expediency, only the isolated cylinder with endplates of $d_e/d = 2$ was examined during this phase, and the assessment of the effects of the louvre on the aerodynamic coefficients considered only lift and drag. Wake pressure measurements using the rake and transducers were also taken alongside the force readings to examine changes to the flow pattern due to the louvre. These measurements were taken both with and without the cylinder present. Pressure measurements in an empty tunnel were taken at $3 \leq x/d \leq 5$ and for multiple spanwise locations corresponding to the entire length of the model. With the cylinder present, time-averaged pressure measurements were taken with the rake located at $z/b = 0$ and for $3 \leq x/d \leq 7$. Dynamic pressure readings, using all three transducers, were taken for the $x/d = 3$ case only.

All the preliminary tests were carried out at the aforementioned test speeds of $V = 7$, 12, and 16 m/s. These three velocities were sufficient in providing test Reynolds numbers and velocity ratios that suitably covered the range of interest ($4.1 \times 10^4 \leq Re \leq 9.1 \times 10^4$ and $\Omega \leq 4$ respectively). Data readings were taken at fairly large intervals of $\Delta N \approx 600$

rpm, with the corresponding interval in Ω being dependent on the freestream velocity and atmospheric conditions ($\Delta\Omega \approx 0.3$ at $V = 7$ m/s and $\Delta\Omega \approx 0.2$ at $V = 16$ m/s).

Note also that, initially, force measurements were taken for both the case where the rotational rate was continuously increased and that when it was continuously decreased. No significant difference in the lift and drag coefficients was observed and all subsequent tests were carried out for the case of Ω increasing only. Similarly, investigation showed that the direction of rotation of the cylinder and whether rotation or the freestream was initiated first had no effect on the magnitude of the measured forces and moments.

To provide consistency, a fixed operating procedure for the tests was established. For each run, cylinder rotation was initiated at the lowest possible rate, after which the tunnel was switched on and its velocity increased until the required speed was reached. At this point, the rotation rate of the cylinder was increased to the first value at which data was to be logged. After collecting the data, the rotation rate was increased to the next value of interest and so on until all rotation rates of interest, for that test run, had been examined.

Actual sampling of all the data at each point of interest comprised a 60 s time period during which lift and drag readings were measured, at a sample rate of 10 Hz, via the T2 data acquisition and balance control system. The mean value for the one minute testing period was then calculated for use in determining force coefficients. Readings from the wake rake and pressure transducers were taken simultaneously with the force data, and were sampled in the manner described in §5.1.6. Measurements of the cylinder rotational rate were taken manually from the counter's display, with multiple readings made throughout the testing period and later averaged to give the mean value.

At the end of the first period of T2 testing, a brief series of flow visualisation tests were conducted as an aid to understanding some of the more unexpected results obtained. Oil-dot tests on the stationary cylinder were performed for all configurations of louvre door present and not present. Smoke flow visualisation of the wake was carried out with the smoke generator positioned as described in §5.1.7, though only the mid-span position was investigated in these preliminary tests. All smoke visualisation tests were carried out for $\Omega \leq 2$, both with and without the louvre door present.

5.2.2 T3 Testing

This phase of testing was concerned solely with the behaviour of the isolated cylinder at zero yaw. All six endplate sizes were used during T3 testing and nineteen different

endplate configurations, including a comparison of stationary endplates with spinning endplates, were examined. Due to the limitations of the T3 balance, measurement of the aerodynamic coefficients was restricted to lift and drag only. Wake pressure measurements, with the rake positioned at $-0.55 \leq z/b \leq 0.45$ and $3 \leq x/d \leq 5$, were taken alongside the force data, though time-varying pressure measurements were limited to $z/b = 0$. Power requirements to spin the cylinder were assessed for each configuration, and new flow visualisation tests with the smoke generator positioned at several locations along the span were also carried out.

With its superior speed control facility, T3 enabled examination of the full range of Reynolds numbers of interest, including those not covered by the T2 experiments. As such, a total of five test speeds ($V = 3$, 5, 7, 12 and 16 m/s) were used during this phase. These particular values were chosen with specific aims in mind. The three highest speeds matched those used during T2 testing and provided comparative data for assessing any detrimental effects of using the louvre door. Furthermore, at these speeds, data point interval was sufficiently small (see Table 5.1) as to provide detailed information on the inversion of the Magnus effect, which as a Reynolds number dependent phenomena was also useful in assessing any effects from the turbulence levels in the tunnels. The lowest speed was chosen as it provided data at a Reynolds number of $Re \approx 2 \times 10^4$, matching that suggested by initial performance calculations as the cruise Reynolds number of the proposed MAV. The final choice of 5 m/s provided a suitable bridge between the other data sets.

Table 5.1: Investigatable velocity ratio range for various wind tunnel speeds.

Tunnel speed (m/s)	**Reynolds number**	**Velocity ratio range**	**Minimum interval**
3	1.8×10^4	$1.00 \leq \Omega \leq 7.80$	0.30
5	3.0×10^4	$0.60 \leq \Omega \leq 4.60$	0.18
7	4.2×10^4	$0.40 \leq \Omega \leq 4.20$	0.15
12	7.1×10^4	$0.25 \leq \Omega \leq 2.00$	0.08
16	9.5×10^4	$0.20 \leq \Omega \leq 1.45$	0.05

Taken together, these speeds enabled investigation of a velocity ratio range of $\Omega \leq 7.8$. Furthermore, the use of five test speeds meant that the principal range of interest ($\Omega \leq 4$) was covered by multiple data sets obtained at different speeds. Such an overlap of data improved confidence in the results by making it easier to spot any errors arising from testing at the lower speed settings, where reduced accuracy of force and moment coefficient determination was more of a problem.

Experimental procedures with regards to cylinder and tunnel operation during T3 testing were identical to those for T2. Data readings for all the T3 tests were generally taken at intervals of $\Delta N \approx 200$ (equivalent to $\Delta\Omega \approx 0.05$ at $V = 16$ m/s and $\Delta\Omega \approx 0.30$ at $V = 3$ m/s), though some motor speeds were avoided as they coincided with structural resonance frequencies of the cylinder and support struts. Each endplate configuration proved to have its own specific vibrational response; consequently, different motor speeds were avoided for different tests. As with T2, each test comprised a 60 s time period in which force and moment data were recorded at a sampling rate of 10 Hz using T3's purpose-built data acquisition system. Multiple readings of the cylinder rotational rate, motor current, motor voltage, and tunnel speed were taken manually during testing and later averaged. Wake pressure measurements were taken separately from the force data through an extensive series of tests specific to this purpose.

5.2.3 Main T2 Testing

The second phase of T2 testing was primarily aimed at examining the behaviour of the cylinder under yaw, where endplates could generate large forces and moments. Yaw angles of between $-30^\circ \leq \Psi \leq 5^\circ$ were examined, in steps of five degrees, for fifteen of the nineteen possible endplate configurations; stationary endplates were not examined in this phase. All tests were performed at the same three tunnel speeds as the initial T2 tests, but this time, lateral forces and moments were also of interest and no wake pressure readings were taken. Data point interval was varied with each test speed so as to best investigate the specific velocity ratios of interest. As in T3, structural vibration was also an influence.

The method of testing was generally the same as in the other phases, with the addition of a systematic approach to setting the yaw angle. Beginning with the cylinder at zero yaw, cylinder rotation was initiated and the tunnel then started and set to the required speed. The cylinder was then repositioned to the desired yaw angle in such a way that Ψ was always decreasing. This ensured that any hysteresis effects in the balance output were consistent, and so allowed for their removal. With the yaw angle set, the rotational rate was increased through all the desired values, with data taken at each point of interest. A second method in which the cylinder was set, as before, to each rotational rate and then swept through the entire range of yaw angles (ending up at zero yaw again) was also examined. No significant difference was noted in the behaviour of the cylinder and the remaining tests were all carried out using the first method described above.

The procedure for sampling of data during these tests was identical to that from the preliminary T2 tests, though now all six forces and moments were recorded, and multiple

manual measurements of the motor current and voltage were also taken alongside the rotational rate. As with all other tests, these were later averaged.

5.3 Analysis of Data

On acquisition, the raw data collected from the wind tunnel tests was then converted into useful results. Typically, this meant reducing the force, moment, power, and pressure measurements to coefficient form. In general, this was done using the equations outlined in §3.1; however, modifications were sometimes necessary so as to accommodate the methods through which the data were recorded. The varying nature of the tests in each tunnel meant that this often required a different process for each data set. Details of how the results from the different tests were analysed are given below.

5.3.1 Analysis of Force and Moment Measurements

The mean values of the force and moment data at a given Ω were reduced to coefficient form with respect to the dynamic pressure and the cylinder's projected area, as described in §3.1. Within this method, an allowance was made for any wind-off and wind-on strut contributions. The former was only applicable to the T2 data, where a wind-off reading that varied with yaw angle was noted. The latter was applicable to both T2 and T3 results, where strut contributions were found to be a function of Reynolds number and (for T2 only) yaw angle. Thus, for lift,

$$C_L = \frac{L - L_0(\Psi)}{\frac{1}{2}\rho V^2 db} - C_{L_{strut}}(Re, \Psi) \tag{5.1}$$

where $L_0(\Psi)$ was the yaw-dependent wind-off strut contribution to lift and $C_{L_{strut}}(Re, \Psi)$ was the yaw and Reynolds number dependent wind-on strut contribution to C_L. Similar equations were used for the determination of all other force and moment coefficients, whether derived from T2 or T3 data sets.

The influence of the supporting structure was generally found to have the greatest impact on the measurement of the drag force. However, at non-zero yaw angles, the strut contribution in T2 also became significant for sideforce and rolling moment. Furthermore, in T3, the enforced presence of a crossplate on the struts meant they affected the lift and pitching moment data too. Thus, variation or miscalculation of the strut contribution was

of great concern when determining the aerodynamic coefficients, and considerable attention was paid to the accurate determination of strut effects, so as to provide the best quality results possible.

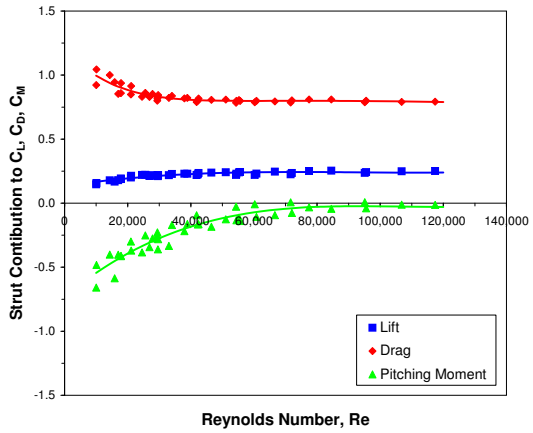

(a) Wind-on variation with Reynolds number at $\Psi = 0°$ in T3

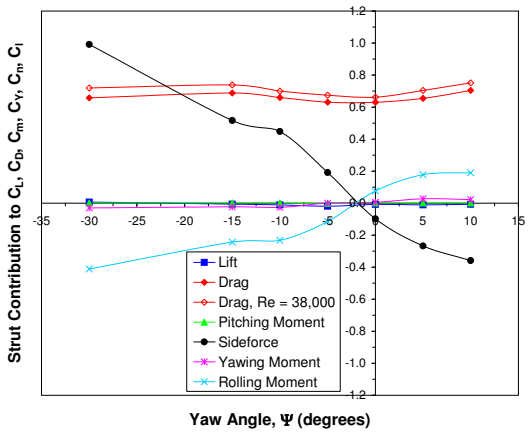

(b) Wind-on variation with yaw angle at $Re = 6.8 \times 10^4$ in T2

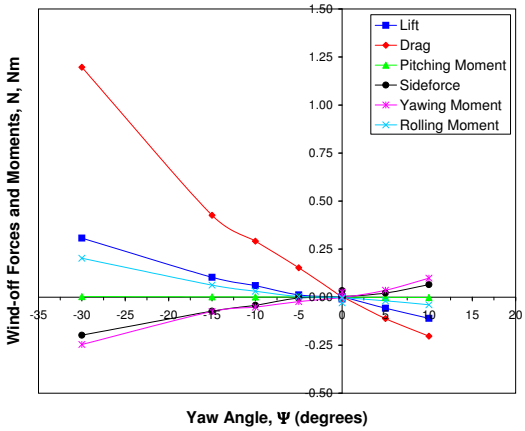

(c) Wind-off variation with yaw angle for no endplates case in T2

Figure 5.10: Wind-on and wind-off strut contribution to forces and moments in T2 and T3.

In both T2 and T3, wind-on strut contributions were measured by testing the support structure by itself at all possible combinations of tunnel speed and yaw angle at which force and moment data were recorded (see Figures 5.10a and b). Wind-off strut-only readings were obtained across the entire range of yaw angles tested and for all endplate configurations (see Figure 5.10c). The results of these tests indicated that wind-on strut contributions were, except for the drag in T2, independent of Reynolds number for $V \geq 7$ m/s, but varied greatly with yaw. To account for strut effects, a polynomial curve was fitted to all the strut data and the resulting equations used to eliminate the correct value of the relevant strut contribution from the measured aerodynamic coefficients.

It should be noted that this approach is a rather simplistic one that does not allow for interference effects between the rotating cylinder and the support rig. The actual situation regarding the components of the measured forces and moments is more complex. In all, three components exist: that due to the cylinder itself, that due to the struts themselves, and that due to interference effects between the two. Hence, for drag,

$$C_{D_m} = C_{D_{cyl}} + C_{D_{strut}} + C_{D_{int}} \tag{5.2}$$

where C_{D_m} is the measured drag and

$$C_{D_{int}} = C_{D_{int_{C/S}}} + C_{D_{int_{S/C}}} \tag{5.3}$$

In this approach, $C_{D_{int_{C/S}}}$ represents the effect of the rotating cylinder on the struts and $C_{D_{int_{S/C}}}$ the effect of the struts on the rotating cylinder. These terms may be further divided into non-rotating and rotating components, the latter of which are not necessarily constant with increasing Ω. As such, a complete assessment of the strut contributions would need to determine such interference effects across the entire range of velocity ratios tested. However, the nature of the experimental arrangements made it difficult to apply typical methods for the removal of interference contributions, particularly those associated with rotation. Even so, comparison of the present data with pre-existing results suggests that the failure to take these effects into account is not of great significance.

5.3.2 Analysis of Power Measurements

Readings of the motor voltage and current taken during testing were used to calculate the power supplied to the motor. This calculation produced a value for the total power required to rotate the cylinder, within which was also included that lost due to motor inefficiency. To determine the shaft power, i.e. that required to rotate the cylinder only, motor efficiency was estimated using a simple mathematical model of a DC motor together with the relevant performance constants (the no-load current, maximum torque, maximum speed, and motor speed constant) for the Ultra 3300-7, as obtained from the motor manufacturer's data sheets.

The shaft power coefficient was then calculated by subtracting the wind-off readings of the voltmeter and ammeter from all wind-on readings and multiplying the product of these two terms by an efficiency factor that was a function of rotational rate, N. i.e.

$$C_P = \frac{\text{IV}}{\frac{1}{2}\rho V^3 db}\ \eta(N) \tag{5.4}$$

where I and V are the measured motor current and voltage respectively. The final results were used to examine cylinder power requirements with respect to end configuration, velocity ratio, cylinder rpm, and Reynolds number.

5.3.3 Analysis of Time-Averaged Wake Pressure Measurements

Wake total pressure measurements obtained with the rake were time-averaged and converted to coefficient form in the usual manner. Thus,

$$C_{p_{tot}} = \frac{H - p_\infty}{\frac{1}{2}\rho V^2} \tag{5.5}$$

where H is the local total pressure at a given pitot tube on the wake rake. The resulting pressure coefficients were used to create surface plots for the investigation of global changes in the lateral and spanwise wake structure. This entailed monitoring the change in the wake pressures with velocity ratio at a given spanwise location, as well as the spanwise variation at a constant velocity ratio.

5.3.4 Analysis of Dynamic Wake Pressure Measurements

After capture, the dynamic wake pressure measurements were processed using the Spike2 data acquisition and analysis programme. The sampled transducer voltages were digitally filtered within Spike2 to ensure that only the relevant pressure components were analysed. First, the DC offset was removed, then a digital band stop filter (for $48 \leq f \leq 52$ Hz) was applied to eliminate the 50 Hz mains frequency AC signal. Spectral analysis was then carried out by using Spike2's built-in fast Fourier transform (FFT) algorithm to transform the recorded pressure waveforms from the time domain to the frequency domain, and so obtain the frequency power spectrum. The FFT was applied using a standard Hann window function and a data block size of 512, which yielded a time resolution of 1.706 s and frequency resolution of 0.58 Hz.

For each transducer location and velocity ratio tested, the corresponding power spectrum was visually inspected to identify the frequency of the dominant spectral peak. With some

exceptions, this peak was usually located at the shedding frequency, f_s. Once identified, this frequency was then used to calculate the Strouhal number, as defined in Equation 3.15. To understand the changes in the wake, the variation with velocity ratio of both the Strouhal number and the amplitude of the dominant frequency peak was then assessed.

5.3.5 Uncertainty Estimates

An estimate of the total uncertainty in the power, force, and moment measurements was made through the usual error propagation methods. The standard error in the mean of the repeat measurements taken at each data point was assessed from the standard deviation of each data set. From this, the average uncertainty in all force and moment coefficients was derived (see Table 5.2). That the typical uncertainties for lift, drag, and pitching moment were greater in T2 was primarily due to the lack of damping in the T2 balance. Similarly, the greater uncertainty in the lateral force and moment coefficients, as compared to the longitudinal coefficients, was partly due to the vibration of the support structure and partly due to the general smallness of the value of these coefficients. Note that the uncertainty in the forces and moments was found to increase slightly with velocity ratio, but no effect due to endplate configuration was observed.

It should also be noted that both the accuracy and precision with which the T3 tunnel speed can be determined, and the force resolution capabilities of the balance, are known to be reduced when $V < 7$ m/s. As such, the results obtained for $V = 5$ m/s and $V = 3$ m/s (i.e. $\Omega > 4$) are not as certain as other measurements (a further $\pm 1.5\%$ uncertainty). This increasing uncertainty can also be seen in the greater spread of the data points for the higher velocity ratios. Some of this increased variation may also have been due to the Reynolds dependent nature of the strut contribution to the measured forces and moments. At the lowest Reynolds numbers, the T3 strut-only data was itself more spread out, and the contribution to lift and drag may have been incorrectly accounted for. Results from this high-Ω region are included in the following discussion to illustrate the behaviour of the cylinder at higher values of Ω, particularly with respect to the effects of endplates, but they have not been used in refining the performance models for the cylinder MAV. For this task the data were limited to $\Omega \leq 4$.

The uncertainties in the velocity ratio and power coefficient were found to be largely independent of the wind tunnel in which the tests were performed. The total uncertainty in Ω was estimated to be $\pm 1.5\%$ at low velocity ratios ($\Omega < 1$), rising to $\pm 3.5\%$ at the highest Ω. The primary source of this uncertainty was due to difficulty in fully stabilising the motor speed during the data logging period. Through careful monitoring, the magnitude

of motor speed drift was contained to approximately ± 10 rpm at low rotational rates, increasing to ± 30 rpm at the highest rotational rates. Uncertainties in C_P were assessed by estimating the uncertainty in the current and voltage readings, with the average value of the total uncertainty for the power coefficient in both T2 and T3 being $\pm 1.7\%$.

Table 5.2: Estimates of average uncertainty in T2 and T3 force and moment data. Note that uncertainties are rounded up to nearest 0.5%.

Quantity	**% Uncertainty in T2**	**% Uncertainty in T3**
Lift coefficient	± 2.0	± 1.5
Drag coefficient	± 1.5	± 1.5
Pitching moment coefficient	± 3.0	± 2.5
Sideforce coefficient	± 3.5	–
Yawing moment coefficient	± 6.0	–
Rolling moment coefficient	± 6.5	–

5.4 Wind Tunnel Boundary Corrections

In the general case, the choice of method for the correction of wall constraint depends on the nature of the experiments, the required precision and accuracy of the data, and the available resources. For a stationary cylinder, even with no consensus in the literature on the best approach, a suitable model can be fairly easily chosen from those available by consideration of these issues together with the experimental details, such as blockage ratio, Reynolds number, extent of three-dimensionality of the flow, and so on. On the basis of the discussion in §3.10, selection of a correction method for a rotating cylinder appears rather more involved, and there is very little guidance on the issue to be found in existing works. Consequently, rather than choosing a single correction method to apply to the results, a comparison between two different approaches (the first, a conventional correction method for streamline flows, the second, Hackett's correction for bluff bodies) was performed. Based on the discussion in §3.10.4, no assessment of lift interference was attempted.

5.4.1 Conventional Blockage Correction Equations

In conventional blockage theory, the total correction factor for the increment in the axial velocity of the tunnel, ϵ, is given by the sum of the solid and wake blockage components. The typical approach to determining the required correction for solid blockage in

three-dimensional flow involves representing the body by a doublet, with a doubly infinite distribution of image systems to model the tunnel boundaries. The resulting correction, based on Lock's analysis,[255] is given as

$$\epsilon_s = \tau\Lambda\left(\frac{A}{C}\right)^{\frac{3}{2}} \tag{5.6}$$

where τ is a factor that depends on the shape of the cross-section of the tunnel, Λ is a body-shape factor, A is the maximum cross-sectional area of the body, and C the frontal cross-sectional area of the tunnel. Note that, in all cases, the values of τ and Λ were obtained graphically from material presented in Pope *et al.*[256] and the frontal area of the support struts was included in the value of A.

For three-dimensional wake blockage, the relevant correction factor is typically determined by representing the wake by a source that is matched by a downstream sink, and then using a doubly infinite system of image source-sink pairs to represent the tunnel boundaries.[231] Given its dependence on the wake, the incremental velocity at the model is generally expressed in terms of the drag coefficient, so that the effect becomes more pronounced at higher C_D, where the wake is larger. The correction factor may thus be determined using

$$\epsilon_w = \frac{1}{4}\frac{S}{C}C_{D_m} \tag{5.7}$$

where C_{D_m} is the measured drag, C is the frontal cross-sectional area of the tunnel, and S the reference area upon which the drag coefficient is based.

Equations 5.6 and 5.7 were used to determine the values of the individual blockage components, which were then summed together to obtain the total correction factor to be applied to the velocity, i.e.

$$\epsilon = \epsilon_s + \epsilon_w \tag{5.8}$$

The corrected velocity at the model was then calculated from

$$V_\infty = V_m(1 + \epsilon) \tag{5.9}$$

where V_∞ is the free air velocity and V_m the measured velocity. The correction to the dynamic pressure may then be shown[232] to be given by

$$q_\infty = q_m(1+\epsilon)^2(1-M_m^2\epsilon) \tag{5.10}$$

where q_∞ is the true dynamic pressure (free from constraint), q_m is the measured dynamic pressure, and M_m the measured Mach number. For low speeds, the effects of compressibility may be ignored, and for small ϵ, second and higher order terms may be neglected. Thus, the correction simplifies to

$$q_\infty = q_m(1+2\epsilon) \tag{5.11}$$

Force and moment coefficients resulting from tunnel balance measurements were corrected so as to correspond to this equivalent dynamic pressure. For example, by combining Equations 3.7 and 5.11, the corrected lift is seen to be given by

$$C_{L_\infty} = \frac{C_{L_m}}{(1+2\epsilon)} \tag{5.12}$$

where C_{L_m} is the measured lift coefficient and C_{L_∞} the corresponding free air lift coefficient. A similar result occurs for all other force and moment coefficients. Power coefficients, which are dependent on V^3, required correction by $1+3\epsilon$. In addition to such changes, the velocity ratio must also be adjusted to account for the increase in freestream velocity. Thus, from Equations 3.5 and 5.9

$$\Omega_\infty = \frac{\Omega_m}{(1+\epsilon)} \tag{5.13}$$

5.4.2 Hackett's Equation for Wake Blockage

Hackett's method[238,257] for the correction of wake blockage for bluff bodies is essentially an extension of Maskell's[235] approach, but is preferred as it is said to provide a superior adjustment to both the drag and other forces and moments. On application of his assumptions (see §3.10.2), Maskell's analysis produces a correction in the dynamic pressure; however, Hackett argued that, because of its momentum-based derivation, Maskell's

correction for wake constraint should actually be in the form of a drag increment instead. Furthermore, Hackett suggested that the inclusion of both dynamic pressure and incremental drag blockage components into a single adjustment meant that, if left as a dynamic pressure correction, Maskell's method would properly correct the drag, but the other forces and moments would be overcorrected because the dynamic pressure correction has too large a value. Thus, Hackett modified Maskell's analysis by separating the correction into its two constituent components: a blockage-induced incremental velocity and a drag increment.

In this 'two-step' version of the analysis, the correction to the dynamic pressure becomes

$$\frac{q_\infty}{q_m} = 1 + \varepsilon(C_{D_{\infty_1}} - \Delta C_D)\left(\frac{A}{C}\right) \tag{5.14}$$

where ε is a blockage factor that is dependent on the base pressure coefficient, $C_{D_{\infty_1}}$ is the drag coefficient corrected by Maskell's original one-step method, and ΔC_D is a term which contains the incremental drag correction due to the wake distortion arising from boundary constraint. Its value is given by

$$\Delta C_D = \frac{C_{D_m}}{1 + \varepsilon C_{D_m}(A/C)} + \left(\frac{C_{D_m}}{2\varepsilon C_{D_m}(A/C)}\right)\left(1 - \sqrt{1 + 4\varepsilon C_{D_m}(A/C)}\right) \tag{5.15}$$

where C_{D_m} is the measured drag coefficient. The value of $C_{D_{\infty_1}}$ was obtained from Maskell's original equation in drag increment form:

$$\frac{C_{D_m}}{C_{D_{\infty_1}}} = 1 + \varepsilon C_{D_m}\left(\frac{A}{C}\right) \tag{5.16}$$

Note that, for lifting flows, the analysis is typically modified so that the correction is applied only to the drag resulting from flow separation. In this case, the term C_{D_m} from Equations 5.15 and 5.16 is replaced by C_{D_s} such that

$$C_{D_s} = C_{D_{tot}} - C_{D_i} - C_{D_f} \tag{5.17}$$

where C_{D_f} is the component of drag due to skin friction, C_{D_i} the induced drag component, and $C_{D_{tot}}$ the measured total drag coefficient.

For the purposes of the analysis, C_{D_f} was assumed to be of negligible value, whilst the value of C_{D_i} was estimated by plotting a graph of the measured C_D against C_L^2 (see Figure 5.21). The gradient of the linear portion of the graph was then determined and the induced drag assessed. An estimation of the value of ε for the cylinder aspect ratio in question was obtained from the following expression, as detailed by Ewald *et al.*[232]

$$\varepsilon = 0.96 + 1.94e^{-0.06AR} \tag{5.18}$$

Since Hackett's equation provides a direct estimation for the change in dynamic pressure, the value of the correction factor calculated from Equation 5.14 was applied directly to the lift coefficient data as follows

$$C_{L_\infty} = \frac{C_{L_m}}{1 + \varepsilon(C_{D_{\infty_1}} - \Delta C_D)(A/C)} \tag{5.19}$$

Slightly different processes were necessary for both the drag and velocity ratio, so that

$$C_{D_\infty} = \frac{C_{D_m} + \Delta C_D}{1 + \varepsilon(C_{D_{\infty_1}} - \Delta C_D)(A/C)} \tag{5.20}$$

and

$$\Omega_\infty = \frac{\Omega}{1 + 0.5\varepsilon(C_{D_{\infty_1}} - \Delta C_D)(A/C)} \tag{5.21}$$

5.5 Results and Discussion

The results of tunnel testing with the isolated cylinder model are presented and discussed in this subsection. Where possible, the data were examined and evaluated in comparison with other published results, with particular points of interest including the magnitude of the maximum lift coefficient, the exact nature of the drag curve at high velocity ratio, and the value of Ω for which the lift-to-drag ratio is a maximum. Results regarding the effects of endplates, yaw, and velocity ratio on the pitching moment have not been included in this discussion as C_m could not be measured using the chosen experimental arrangements. Note that the same definitions and notation outlined in §3 are retained throughout this section.

5.5.1 Validation of T2 Data, Error Estimates, and Blockage Corrections

The use of the louvre door during T2 testing prompted an analysis of the effects on all data obtained with this arrangement. Primarily, this involved a comparison of T2 force results at both high and low Re against those in T3, obtained without the need for the louvre. In addition, wake pressure measurements (both with and without the cylinder) and oildot flow visualisation test results were examined for changes to the flow pattern arising from the influence of the louvre.

For the 'no cylinder' tunnel pressure measurements, an initial test performed without either the cylinder or louvre present and with the tunnel running at 35 m/s was used as a reference condition against which the effects of the door were assessed. At this reference speed the flow was highly uniform (as discussed in §5.1.1). When the louvre door was added, with slats fully open so that $V = 16$ m/s, there was a very slight decrease in the uniformity of the flow. This was not necessarily due to the louvre: even without the louvre present, simply reducing the tunnel speed to 16 m/s produced a similar effect. However, progressive closure of the louvre slats caused the flow uniformity to become steadily worse, with far more unsteadiness and fluctuations in the pressures across the working section. Thus, it may be concluded that the addition of the louvre had a noticeable effect on the flow in T2.

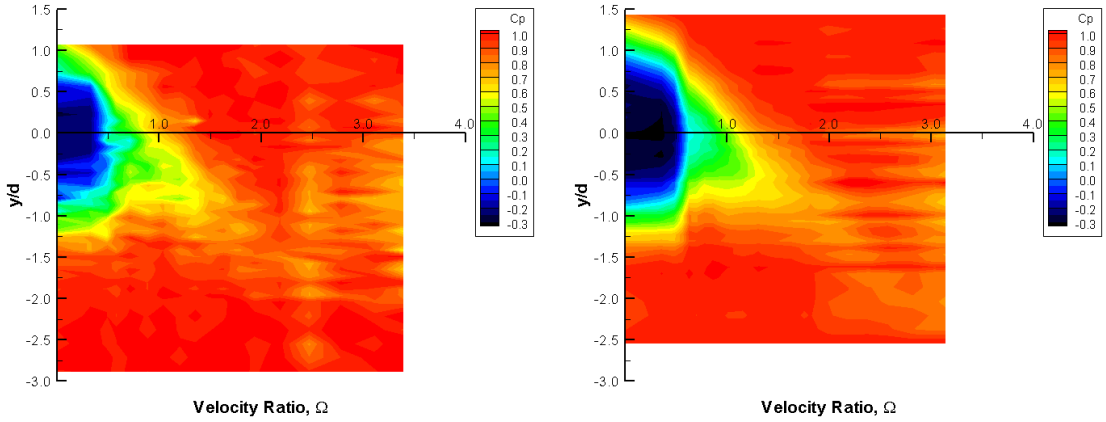

(a) T2: $Re \approx 7.1 \times 10^4$ and $x/d \approx 3$ (b) T3: $Re \approx 7.4 \times 10^4$ and $x/d \approx 3$

Figure 5.11: Comparison of wake total pressure variation with velocity ratio for T2 and T3. Data comes from tests with endplates of size $d_e/d = 2$.

Even so, actual tests with the cylinder present were more favourable. A comparison of the T2 and T3 data for the variation with velocity ratio of the time-averaged total pressure coefficient in the wake behind the cylinder with endplates of size $d_e/d = 2$ is shown in

Figure 5.11. Despite the change in flow regularity (visible in the much less smoother variation of the T2 pressure readings) the results from the T2 and T3 tests at similar Re show good agreement. There is a slight difference regarding the magnitude of pressure coefficients in the wake at low velocity ratios, but this may also be due to slight differences in both the Reynolds number and the downstream location of the rake in each run. Oildot tests with the cylinder stationary also confirmed that the louvre caused little change to the position of the separation points, which were found to be located between $80° \leq \beta \leq 85°$ regardless of the louvre configuration. This is in good agreement with Achenbach's[258] result ($\beta = 81°$) for a low-aspect-ratio stationary cylinder ($AR = 3.33$) at similar Reynolds number ($Re = 6 \times 10^4$).

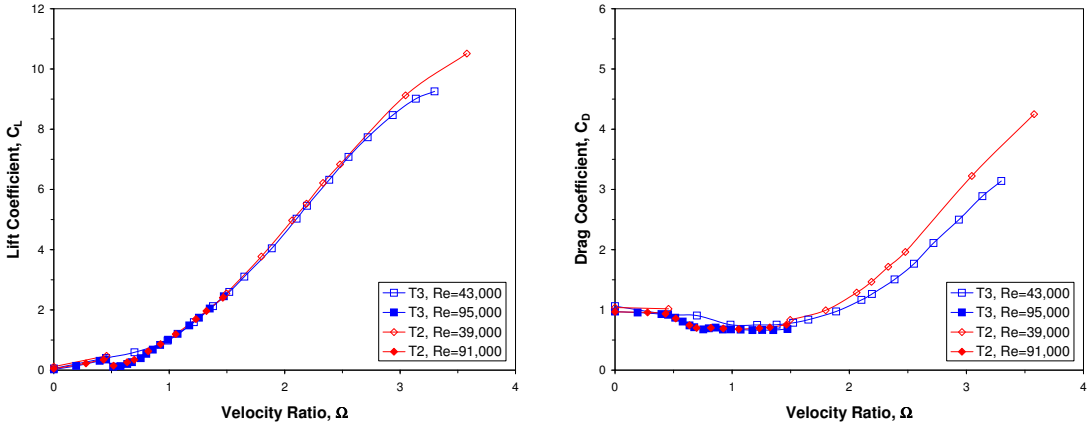

(a) Lift Coefficient (b) Drag Coefficient

Figure 5.12: Comparison of lift and drag data for T2 and T3 tunnel tests. Data comes from tests with endplates of size $d_e/d = 2$.

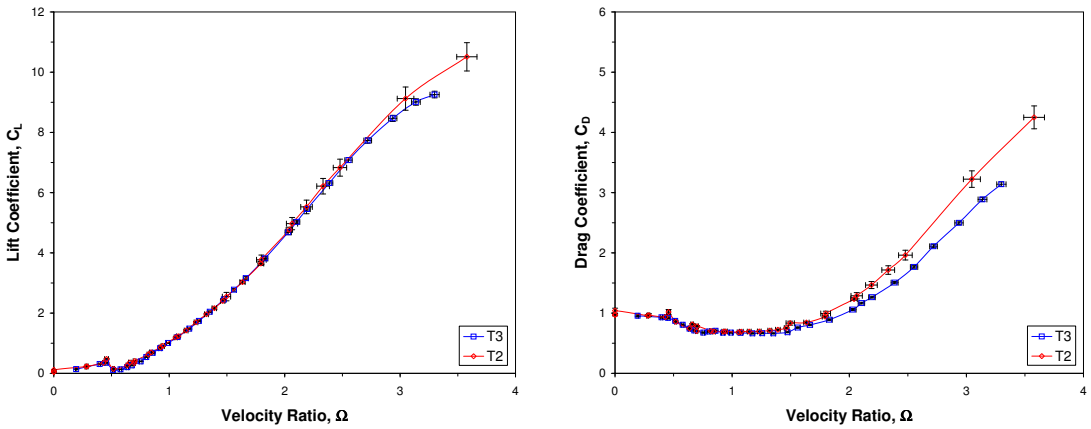

(a) Lift Coefficient (b) Drag Coefficient

Figure 5.13: Uncertainty estimates for T2 and T3 lift and drag coefficients. Data comes from tests with endplates of size $d_e/d = 2$.

Furthermore, the use of the louvre also appeared to have only a minimal effect on the force measurements obtained in T2. Figure 5.12 compares the lift and drag data from the T2 tests with those obtained in T3. These results show that there is practically no difference in the lift data, though much more disagreement is visible in the drag data, reflecting the sensitivity of this parameter to experimental arrangements. Similarly large variations in drag were occasionally noted in the data from different repeat tests in the same tunnel (whether T2 or T3), with the same cylinder configuration and the same Reynolds number, and so are not necessarily due to the louvre.

It is also interesting to note that there is very good agreement between all data sets at similar Re for $\Omega \leq 1$. In this regime, the flow is more sensitive to changes in Reynolds number and one would expect increased turbulence from the louvre to perhaps have the greatest impact at these low velocity ratios. For high velocity ratios, the boundary layers are known to be fully turbulent from inception and any changes in the flow from the louvre would not be expected to strongly influence the forces. This would imply that the discrepancy in the drag results originates from some other source.

The addition of error bars based on the estimated uncertainty in the force data to the curves of Figure 5.12 indicates that much of the difference between the T2 and T3 drag results falls within the limits of experimental error (see Figure 5.13), and so may be explained by such problems as the loss of accuracy in force and speed determination at low V and the difficulties in correctly determining strut contributions. The change in wall constraint between the two tunnels may also have played a role, but since the model frontal area ratio (A/C) in T2 is actually less than in T3, correction by conventional means would actually increase the difference between the two sets of results. Indeed, little improvement in the similarity may be seen in the conventionally corrected results of Figure 5.14.

Application of Hackett's bluff body blockage correction technique also produced mixed results (see Figure 5.14). Correction of the data by this method reduced lift to far below the values of the uncorrected results, and reduced the similarity of the present findings with published data. This was particularly so when an attempt was made to apply the correction only to the separated drag component, indicating that perhaps a faulty method was used. In contrast to the lift results, application of Hackett's method to the drag was generally more successful at producing agreement between the T2 and T3 data at high velocity ratio, even when the separated drag component was assessed. However, this was not always the case, especially for the smaller endplate sizes ($d_e/d < 1.5$) or with two free ends. For these conditions, the determination of the induced drag component, C_{D_i}, was less certain due to the difficulty in determining the slope of the graph of C_D versus C_L^2, which for small d_e/d was non-linear at both high and low Ω (see Figure 5.21a).

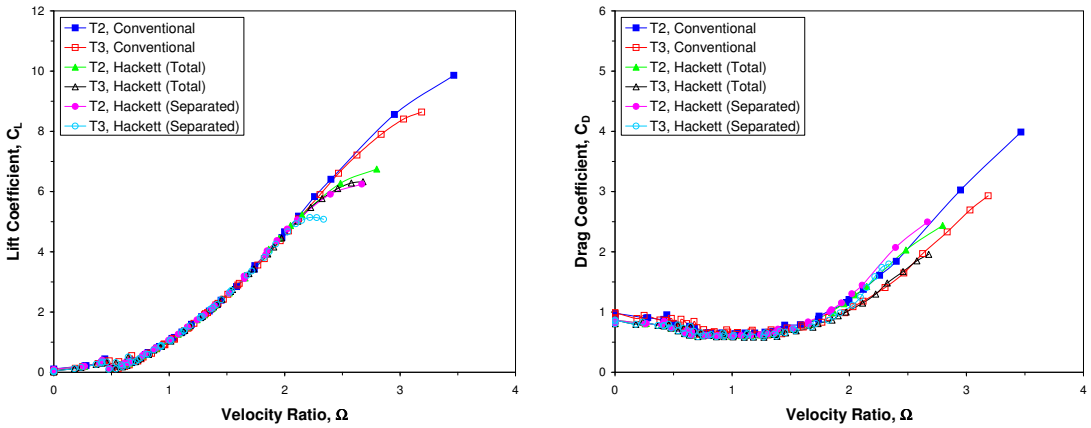

(a) Lift Coefficient

(b) Drag Coefficient

Figure 5.14: Comparison of blockage correction methods. Data comes from tests with endplates of size $d_e/d = 2$. The term 'Total' indicates that the correction was based on the total measured drag. The term 'Separated' indicates that the correction was based on the estimated separated-flow component of drag only.

The existence of good agreement in the uncorrected lift and drag for velocity ratios at least as high as $\Omega = 2$, one of the main regions of interest, and the uncertainty over the suitability of blockage correction methods and their application meant that a decision was made to present the rest of the isolated cylinder data in this section without any corrections applied, so as to not alter the data through exposure to incorrect methods. The difference in drag at higher velocity ratios meant that the T2 drag data was treated somewhat sceptically, but remained useful for the purposes of comparison.

5.5.2 Comparison with Published Data

The aerodynamic characteristics of the cylinder without endplates (effectively $d_e/d = 1$) were used as a reference level to which the performance of the other end configurations was compared. These results, in comparison to existing data, are shown in Figure 5.15. For the lift coefficient, the current findings are found to be in excellent agreement with the trend based on aspect ratio that is established by the preceding studies; in particular, the similarity with the study by Betz[8] at $AR = 4.7$ confirms the validity of the results. However, the present results also indicate a pronounced limiting of C_L when $\Omega > 3$ that is not generally visible in other data sets. Presumably, this is due to the differences in AR.

This limiting of C_L is in agreement with Swanson's[12] comments on his own results, in which he indicated that if there was to be a limit to the lift from a rotating cylinder it might be expected to occur when the boundary layer origin point has migrated, due to

rotation, from the front stagnation point to the lateral meridian at $\beta = 90°$. Swanson's boundary layer measurements indicated that this occurs at $\Omega = 3$. Although Swanson saw no such limiting of C_L in his own lift results, his suggestion agrees well with the present data for the cylinder without endplates. However, this behaviour is changed by endplate size and does not hold true with larger d_e/d (see §5.5.4). Also, this limiting of the lift appears to be associated with the evolution of the trailing vortex system (see §5.5.8) and is not necessarily related to the motion of the boundary layer origin point.

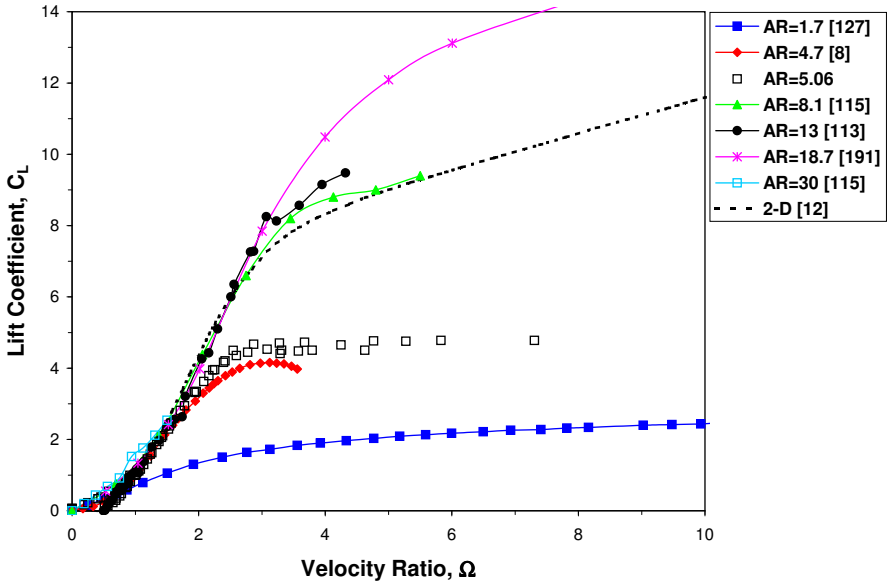

(a) Lift coefficient

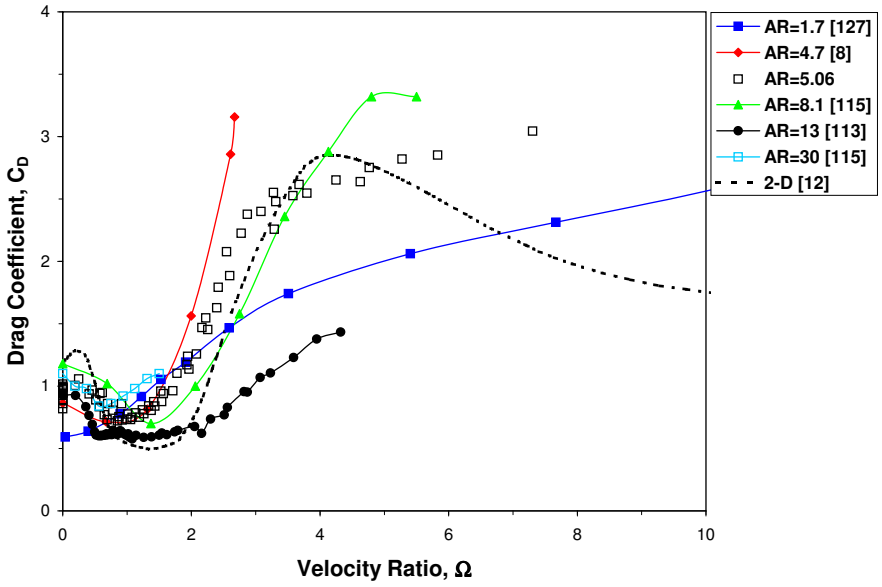

(b) Drag coefficient

Figure 5.15: Comparison of results for cylinder with no endplates to existing data.

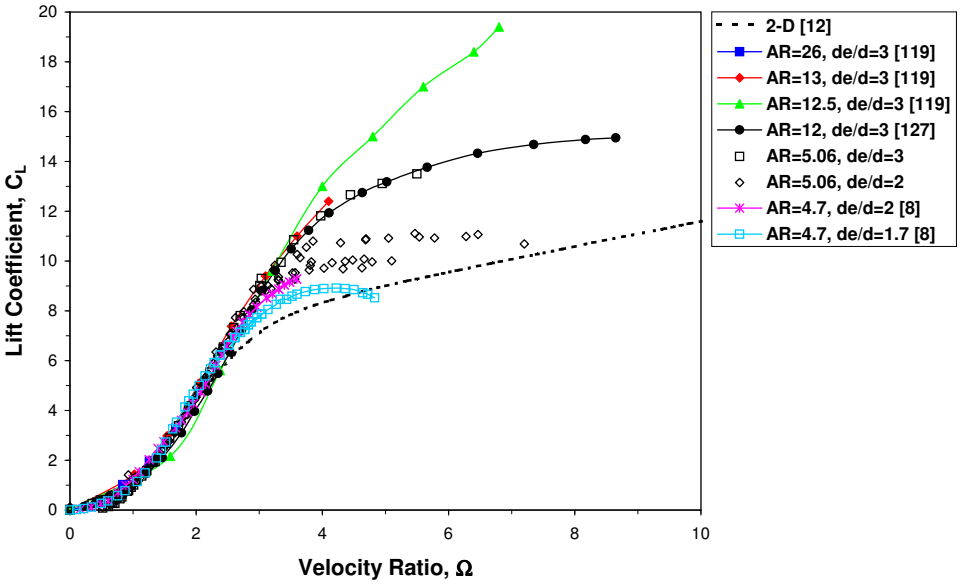

(a) Lift coefficient

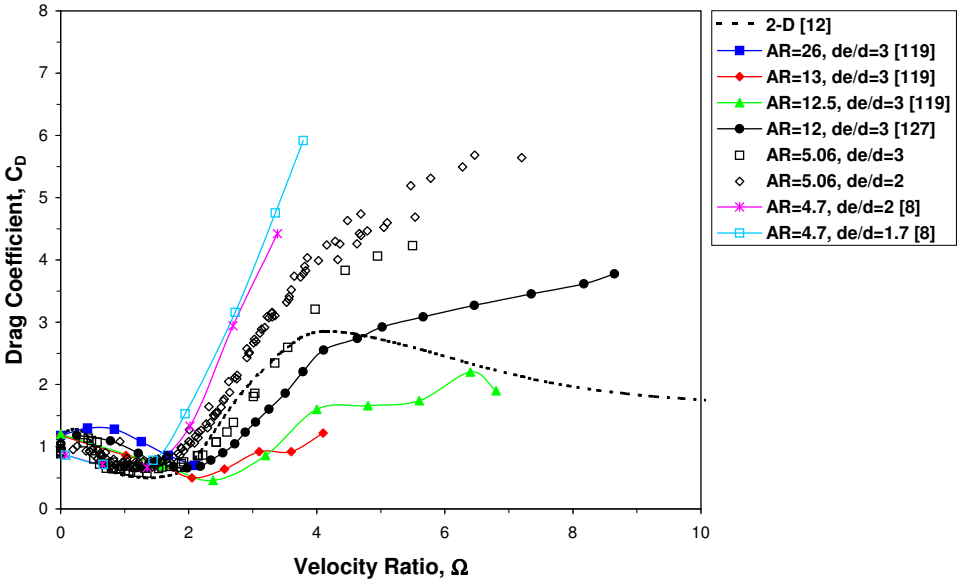

(b) Drag coefficient

Figure 5.16: Comparison of results for cylinder with endplates to existing data.

By contrast to the lift results, drag coefficient trends do not display such good agreement with previous data and there is far more scatter in the results. As with the lift coefficient, a limiting of drag at high Ω is seen in the current data but is missing from previous experimental results. This may be due to the fact that the cylinder tested in the present experiments had two almost completely free ends, whilst the cylinders from the previous tests were all positioned so that they spanned the walls of the wind tunnel (typically

with a slight clearance). In such an arrangement, which does not appear to promote two-dimensional flow, the tunnel walls may have acted like stationary endplates, so changing the end conditions and affecting the results (see §5.5.6). Interaction with the wall boundary layer would also change the end flow.

A comparison of current results obtained with the use of spinning endplates against those from other studies that used endplates of the same size ratio is somewhat complicated by the lack of systematic data to account for the influence of aspect ratio; that being said, there is generally a very good agreement with previous test results (see Figure 5.16). The current findings also indicate that endplate size ratio may be more important than aspect ratio in determining the lift performance: the lift curve for the present $AR = 5.06$ tests with $d_e/d = 3$ is the same as that obtained by Busemann[127] using the same size plates but with a cylinder of $AR = 12$, and is also comparable to that for a cylinder of $AR = 18.7$ (see Figure 5.15). By contrast, aspect ratio appears more important than endplate size to the drag behaviour and there is, again, generally more variation between current values of C_D and the previous results.

5.5.3 Effects of Reynolds Number

The Reynolds dependent nature of the lift and drag at low velocity ratio provided a further opportunity to validate the results by comparing the current T2 and T3 data to those from Swanson's[12] detailed study of Magnus effect inversion. For the lift coefficient, such a comparison (see Figure 5.17a) shows that there is only fair agreement between the present results and those of Swanson. Although all the data sets compare very well outside of the inversion region, in the current results the loss of lift created by the inversion phenomenon at a given Reynolds number was less pronounced, so that the current tests effectively appear to be associated with a lower Re than indicated by the freestream.

Discrepancies between current results and Swanson's findings were, given the differences in the experimental arrangements, not unsurprising. The low aspect ratio, use of endplates, the effects of the louvre door, and wall constraint were all expected to substantially affect the data. However, the nature of the results suggests that the difference with Swanson's findings was not due to wall constraint as this should increase the effective Reynolds number and enhance the drop in C_L. Similarly, since the T2 and T3 data are in very good agreement, the difference is unlikely to be a result of the use of the louvre. Nor was the difference changed or improved by using endplates, of any size (see §5.5.4). Instead, this difference may be a consequence of end disturbances and three-dimensionality arising from the low aspect ratio interfering with the sudden downstream shift of the separation

line on the upstream moving wall (from which Magnus effect inversion derives), so that the location of the separation line is correlated along a shorter extent of the span and the total lift loss is reduced (see §5.5.8). Strut interference may also have played a role.

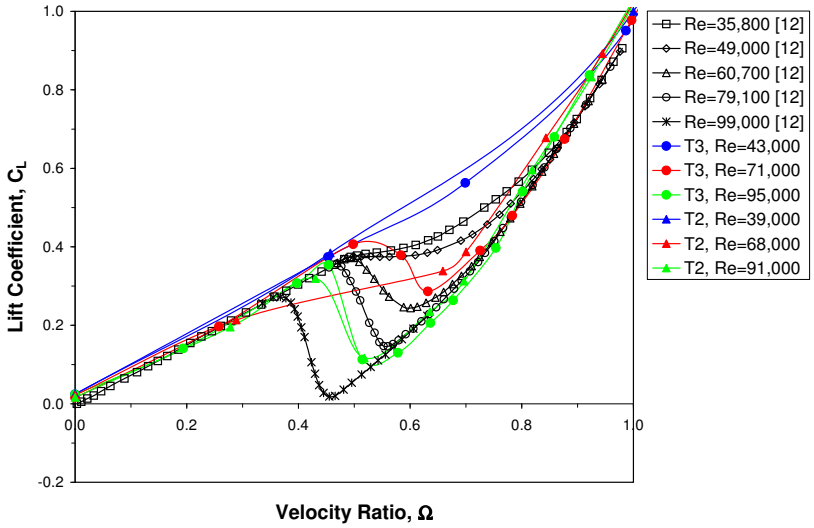

(a) Lift coefficient

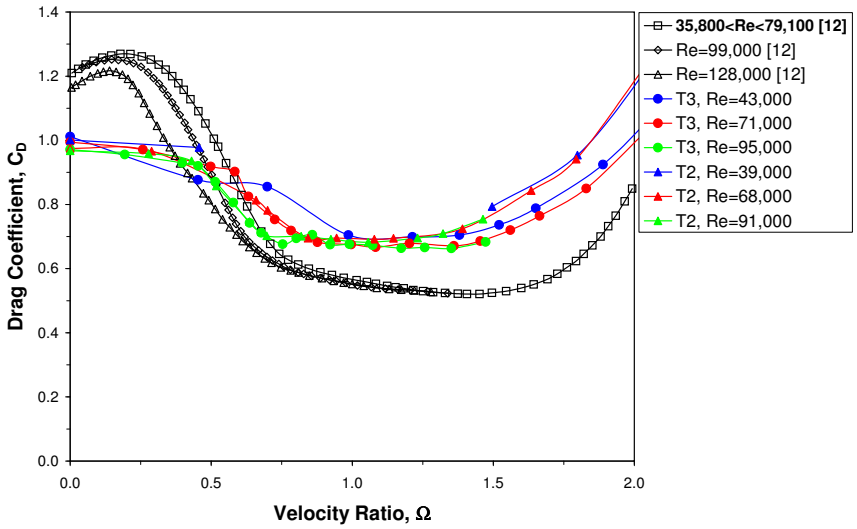

(b) Drag coefficient

Figure 5.17: Effects of Reynolds number at low velocity ratio for the cylinder with two endplates of size $d_e/d = 2$.

The current drag results are also seen to be substantially different to those of Swanson, most noticeably at near-zero velocity ratios (see Figure 5.17b). The same trend of decreasing C_D with increasing Re is noticeable, but the shape of the curve for $\Omega < 0.5$ is radically different and the reduction in drag is much less pronounced. This also appears to be a consequence of the low cylinder aspect ratio, as current values of C_D at $\Omega = 0$

match well with published data obtained under similar conditions. Zdravkovich *et al.*[193] found that the drag coefficient for a $AR = 5$ stationary cylinder with two free ends at Reynolds numbers between $1.33 \times 10^4 \leq Re \leq 8.8 \times 10^4$ varies from $0.75 \leq C_D \leq 0.82$. They also reported that there appears to be considerable scatter in the results that might be a genuine feature of the flow at low AR and high Re.

This reduction in the measured drag at $\Omega = 0$ relative to the value for a stationary cylinder in two-dimensional flow ($C_D = 1.2$) is caused by an inflow of fluid around the free ends of the cylinder and into the near wake, where it causes the pressure over the rear surface of the cylinder to rise. This then reduces the pressure difference between the front stagnation point and the base of the cylinder, so causing a decrease in drag. That the data shown in Figure 5.17b was obtained with large endplates, which reduce the amount of inflow, explains why the measured drag was slightly greater than that of Zdravkovich *et al*. Results with smaller plates were closer to the published values, being around $C_D \approx 0.9$. The lack of correction for interference drag between the cylinder and the support struts may also have been a contributing factor.

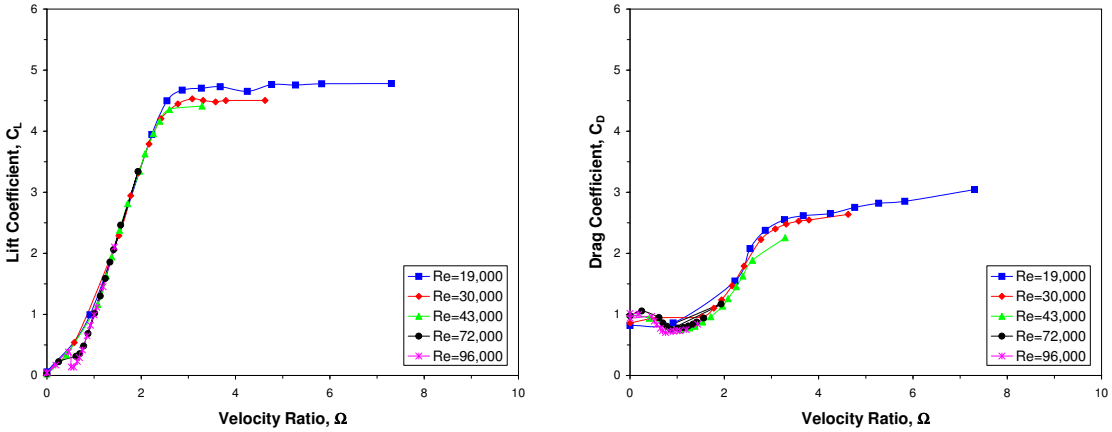

(a) Lift coefficient

(b) Drag coefficient

Figure 5.18: The effects of low Reynolds number on lift and drag for the cylinder without endplates.

In addition to the well-established variation with Reynolds number at high Re, the results also seemed to suggest that a second region of Reynolds number dependency may exist when $\Omega > 2.5$ and $Re < 4 \times 10^4$. Under these conditions all the curves showed the same trend, but a slight increase in the lift at high Ω was noted as Re decreased. A similar effect was seen in the drag data (see Figure 5.18). This finding is in keeping with results reported by Thom,[115] whose data extended down to much lower Reynolds numbers, going as low as $Re = 4.6 \times 10^3$, where he found the increase in the force coefficients to be more pronounced. However, just as Thom placed no great confidence in the accuracy of his

results (see §3.3.3), a similar lack of certainty must be expressed in the present findings. The accuracy of the measurements taken at the low test velocities that corresponded to the Reynolds numbers in question is known to be reduced in comparison to the other data, and the magnitude of the effect is small enough that the apparent variation may simply be the result of experimental scatter.

5.5.4 Symmetric End Conditions: Effect of Endplate Size

The effects of endplate size on lift and drag when using two equi-sized plates are shown in Figures 5.19 and 5.20. The lift results indicate that, regardless of endplate size, a limiting value of C_L will eventually always be reached. However, increasing the ratio d_e/d had the same effect as that established in Figure 5.15 for an increase in aspect ratio: it caused the maximum attainable lift to be increased, and delayed the occurrence of this maximum to higher velocity ratios. This effect was quite substantial and the findings indicate that increasing the endplate size will eventually result in the lift at high velocity ratios being in excess of the Prandtl limit, regardless of the actual aspect ratio of the cylinder.

Note also that, as with aspect ratio, the effects of endplate size were not visible until $\Omega > 1.5$. Plate size seemingly had no effect on the lift at low Ω, where the influence of Reynolds number was found to be in keeping with the values and trends of Figure 5.17 for all plate sizes tested. This suggests that the differences between Swanson's[12] data on the inversion of the Magnus effects and the present results at high Re and low Ω is indeed due to the influence of end disturbances, whether from the free-ends or the use of endplates.

Quantitatively, the relationship between plate size and the increase in the maximum lift coefficient was rather straightforward: for a given endplate size, the percentage increase in the maximum lift (based on $\Omega > 4$) relative to that for the no-endplates case was approximately the same as the percentage increase in the plate size ratio relative to $d_e/d = 1$. Thus, for $d_e/d = 1.1$ (10% plate size increase), the increase in $C_{L_{max}}$ was 8%; for $d_e/d = 1.25$, it was 18%; for $d_e/d = 1.5$, it was 56% and so on (see Figure 5.20a). Alternatively, one could say that, for a given plate size, the ratio of the maximum lift coefficient relative to that for the no endplates case was approximately equal to d_e/d.

The drag data showed a similar, but more complex, relationship with endplate size (see Figures 5.19b and 5.20b). At low, non-zero, velocity ratios, the differences in C_D between the various endplate sizes were mostly associated with Reynolds number effects, as discussed in §3.3.3, rather than d_e/d. For $\Omega \geq 1.5$, the data obtained with the smaller plate sizes ($d_e/d \leq 1.5$) showed a rapid rise in drag with velocity ratio. This increase

is believed to be associated with the large induced drag component that results from the increase in lift coefficient at high Ω. For large plates, the onset of this increase in C_D was pushed back, such that for $d_e/d = 3$ it did not occur until $\Omega > 2$. This delay seemingly stems from the ability of larger endplates to reduce lift-dependent drag (see Figure 5.21).

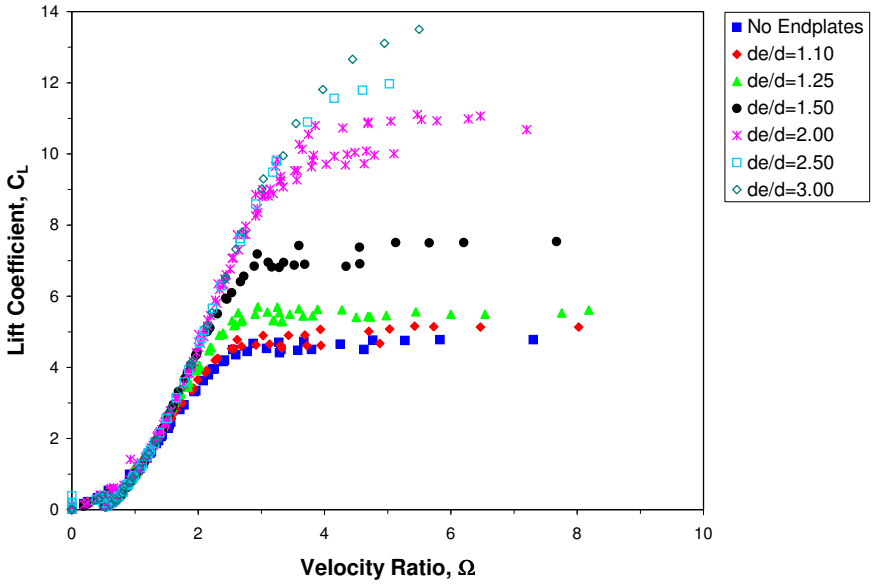

(a) Lift coefficient

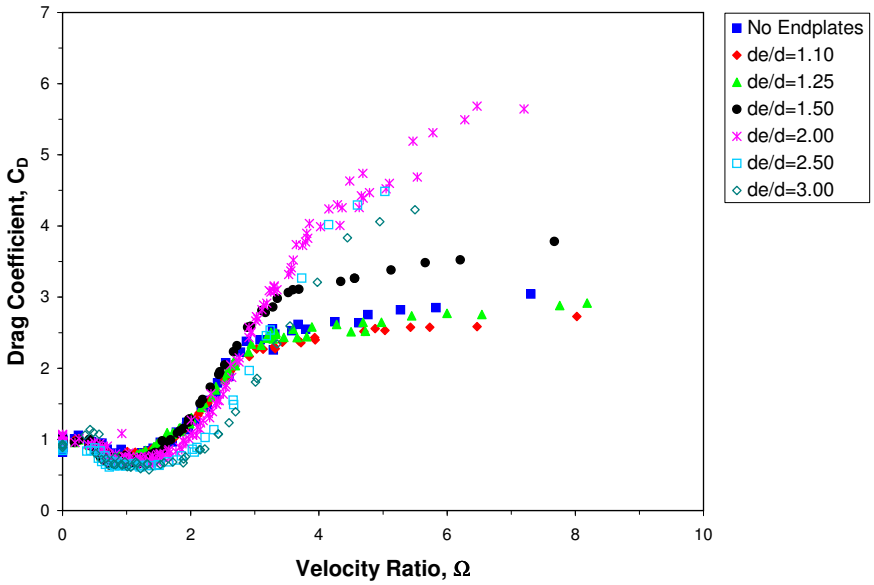

(b) Drag coefficient

Figure 5.19: Effects of endplate size on lift and drag.

As a result of the delay, for all $d_e/d \geq 2$ a region of reduced drag, as compared to $d_e/d = 1$, was found to exist at moderately high velocity ratios (see Figure 5.20b). The

extent and magnitude of this reduction increased with plate size, so that for $d_e/d = 3$, C_D was reduced for all velocity ratios between $0.55 \leq \Omega \leq 3.5$, with a peak reduction of 36% at $\Omega = 2.5$. It is believed that the unusually long region of low drag visible in Reid's[113] results (see Figure 5.15) may be explained by a similar effect, though in Reid's case it likely resulted from the large aspect ratio of his cylinder ($AR = 13.3$).

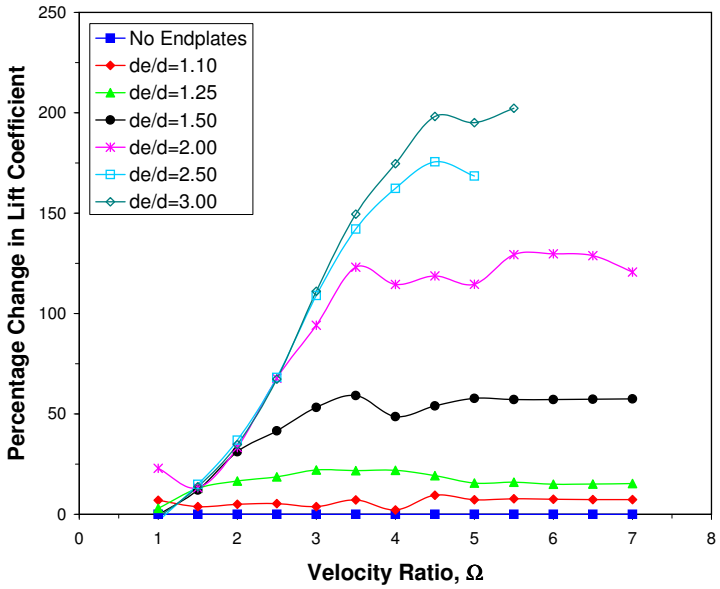

(a) Percentage increase in lift coefficient relative to $d_e/d = 1$

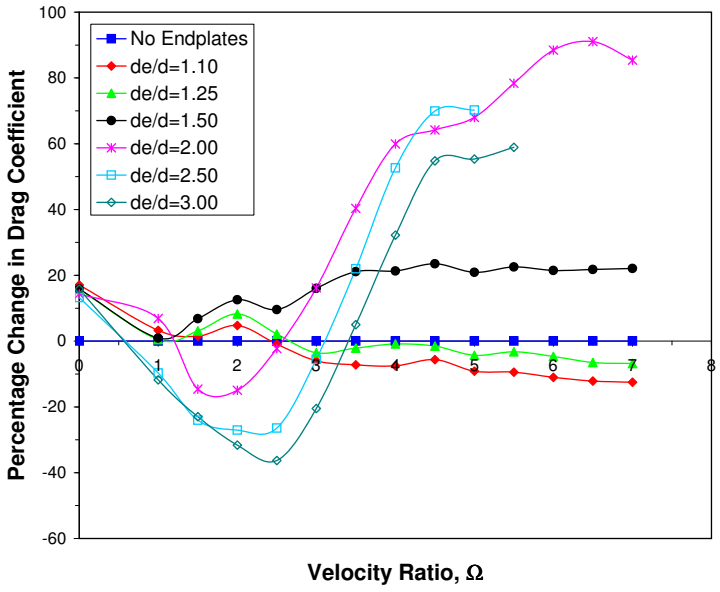

(b) Percentage increase in drag coefficient relative to $d_e/d = 1$

Figure 5.20: Relative effects of endplate size on lift and drag.

The advantageous nature of large endplates only persisted until $\Omega \approx 3$, where the drag

behavior for the smaller plate sizes drastically changed. At this point, the increase in drag was suddenly arrested, and although a limit of the type seen for the lift was apparently never reached, the growth in C_D was far smaller for all subsequent velocity ratios. The point at which this change occurred and the severity of the change was directly related to plate size: the larger the plates, the later the change, and the less pronounced it was. The results also suggested that, when $\Omega > 3$, the drag for the smallest plate sizes ($d_e/d = 1.1$ and 1.25) was not only less than that with larger plates, but was also less than with no endplates. However, the effect was quite small (5 to 10% reduction) and may simply be due to experimental scatter.

As a consequence of this more complicated drag behavior, the choice of endplate size for the best drag performance was found to be dependent on velocity ratio. At low velocity ratios ($\Omega < 1$), smaller plates generally gave slightly smaller drag coefficients. For applications at moderate velocity ratios ($1 < \Omega < 3$), larger plates are preferred, so as to delay the increase in induced drag. For high velocity ratio applications ($\Omega > 3$), smaller plates are again more desirable as the drag quickly approaches a limit.

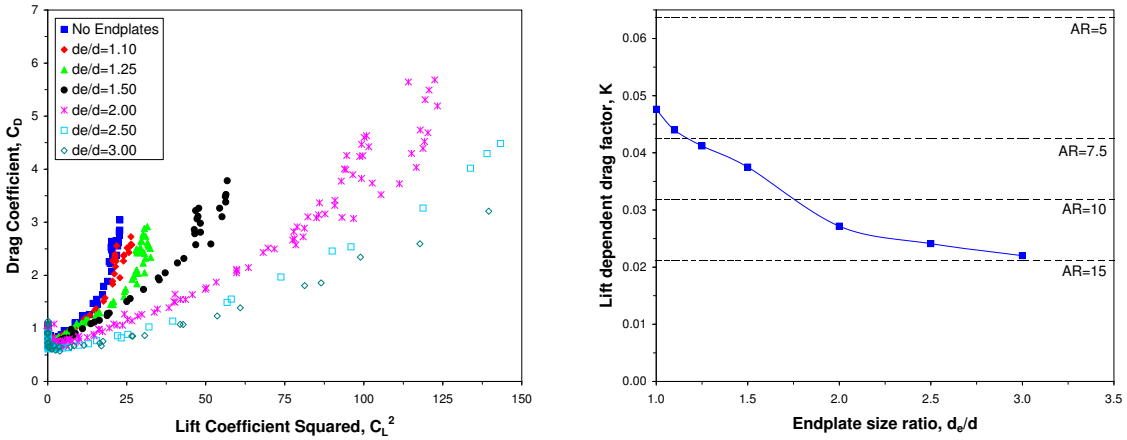

(a) Drag variation with lift-squared

(b) Estimation of variation of K with d_e/d

Figure 5.21: The effects of endplates on lift-dependent drag. Note that dashed lines indicate the theoretical value of K when $e = 1$ for various AR.

Examination of Figure 5.21 suggests that with increasing d_e/d the total drag for a rotating cylinder (when $\Omega > 1$) more closely approximates the form

$$C_D = C_{D_0} + KC_L^2 \tag{5.22}$$

where C_{D_0} is the profile drag (independent of lift) and K is the lift-dependent drag factor. This may be written as

$$K = k_1 + \frac{k_2}{\pi AR} \tag{5.23}$$

where k_1 is the lift-dependent profile drag factor and k_2 the induced drag factor. Alternatively,

$$K = \frac{1}{\pi ARe} \tag{5.24}$$

where e is the Oswald efficiency factor, such that, from Equations 5.23 and 5.24,

$$e = \frac{1}{\pi ARk_1 + k_2} \tag{5.25}$$

Comparison of the estimated values of K with theoretical, ideal, values when $e = 1$ suggests that the use of endplates reduces lift-dependent drag by increasing the effective aspect ratio of the cylinder (see Figure 5.21b). With larger endplates ($d_e/d \geq 1.5$) the factor by which AR increases is seen to be roughly the same as the size ratio d_e/d. That K was estimated to be less than the ideal value for $AR = 5$ even for the cylinder without endplates is likely primarily due to the difficulty of accurately determining the slope of the graph of C_D against C_L^2 when $d_e/d \leq 1.5$. For these cases the linear portion of the curve is, at best, limited to $1 \leq \Omega \leq 3$. However, since it may be expected that $k_2 \geq 1$, the results for small d_e/d also suggest the possibility that k_1 may be slightly negative, so that the lift-dependent component of profile drag reduces with increasing C_L. This would seem consistent with the behaviour of the wake of a rotating cylinder as Ω increases.

The nature of the lift and drag curves resulted in the peak lift-to-drag ratio occurring at fairly low Ω. Figure 5.22 shows that the peak was generally close to $\Omega = 2$, but that its exact position was weakly dependent on plate size: from an initial position of $\Omega \approx 1.9$ when $d_e/d = 1$, the location of the maximum lift-to-drag was then pushed to slightly higher Ω as plate size increased, reaching $\Omega \approx 2.2$ for $d_e/d = 3$. The complicated relationship between plate size and drag meant that only when $d_e/d > 2$ was the magnitude of C_L/C_D substantially increased beyond that with no endplates. Even so, the maximum attainable value of the lift-to-drag ratio remained modest ($C_L/C_D < 7$ even when $d_e/d = 3$).

For high velocity ratios ($\Omega > 4$), the lift-to-drag ratio approached a limiting value of $C_L/C_D \approx 2$ for $d_e/d \leq 2$ (reducing slightly with decreasing d_e/d) and $C_L/C_D \approx 3$ when $d_e/d > 2$. In this regards, the rotating cylinder is found to be like other high-lift devices in that the generation of very high values of C_L comes at the consequence of a much reduced

lift-to-drag ratio. It is also interesting to note that for $\Omega \leq 1$ and low Reynolds numbers ($Re \leq 4 \times 10^4$), where the loss of lift due to inversion of the Magnus effect is small, the lift-to-drag ratio was approximately the same as the velocity ratio. Furthermore, for all end configurations tested, the lift-to-drag ratio tended towards a value of $C_L/C_D \approx 1$ at $\Omega \approx 1$.

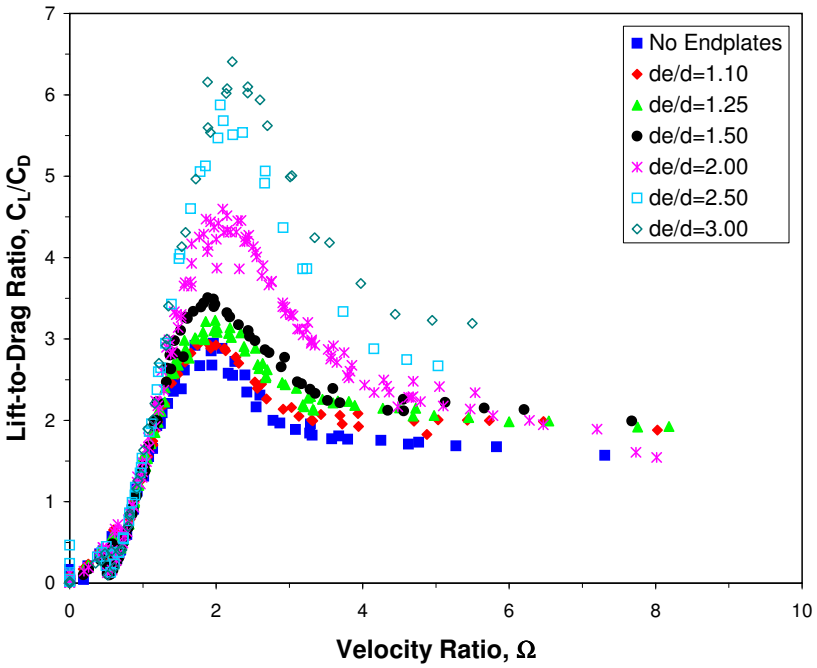

Figure 5.22: Effect of endplate size on lift-to-drag ratio.

The effects of symmetric end conditions on the lateral forces and moments acting on an isolated rotating cylinder at zero yaw are shown in Figure 5.23. Although small variations with changing velocity ratio may be noted in the sideforce, yawing moment, and rolling moment coefficients, the actual values of C_y, C_n, and C_l were so close to zero magnitude that the lateral forces and moments generated by a rotating cylinder with symmetric end conditions may, within the limits of the tests, be considered to be practically independent of Ω.

Similarly, the effects of Reynolds number for these arrangements was also negligible and there was no appreciable influence of high Re on the behaviour at low Ω. The findings do indicate that C_y and C_n are at least somewhat susceptible to the influence of endplate size, with the results for $d_e/d \geq 1.5$ showing a slight linear increase with velocity ratio, but even then only for $\Omega > 2.5$. However, all such variations with Re, Ω, and d_e/d were greatly magnified with asymmetric end conditions (see §5.5.5) or when the cylinder was yawed (see §5.5.10).

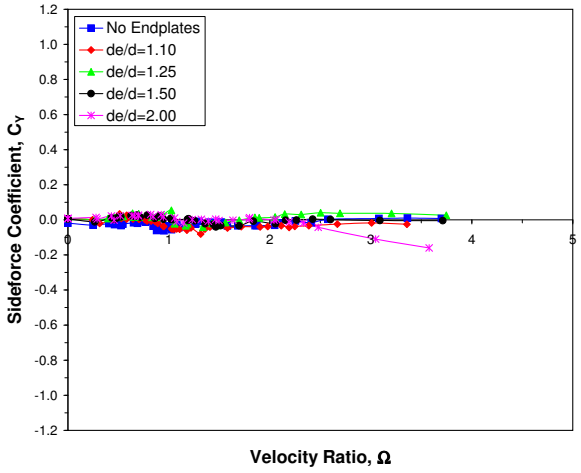

(a) Sideforce coefficient

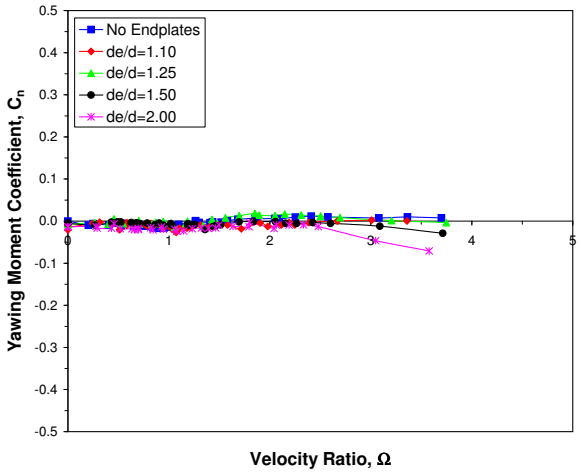

(b) Yawing moment coefficient

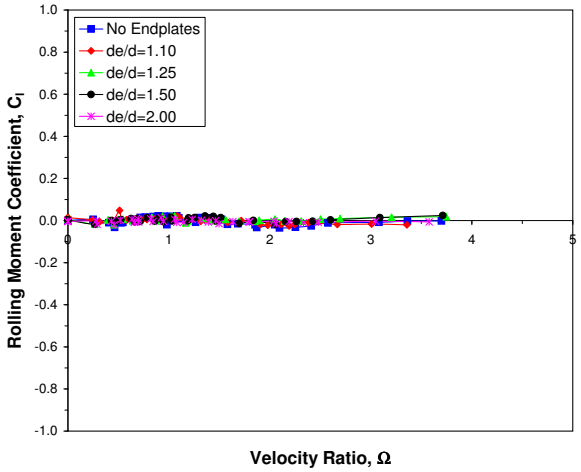

(c) Rolling moment coefficient

Figure 5.23: Effect of endplate size on lateral forces and moments on a rotating cylinder at $\Psi = 0^\circ$.

5.5.5 Asymmetric End Conditions: Effect of Endplate Arrangement

Tests with a single endplate showed that the effects on lift of having one free end were invariably detrimental, and the improvement in C_L at high Ω was approximately half of that with two plates of equal size (see Figure 5.24a). The effect of one free end on the drag when using small endplates was minimal. For larger plates ($d_e/d \geq 2$), a free end changed the shape of the drag curve so that it matched that of smaller plates, with a limiting of C_D at $\Omega > 3$. However, the region of reduced drag at moderate Ω was now much diminished (see Figure 5.24b). Tests with two plates of unequal size provided an intermediate response and revealed that the influence of the larger plate dominated that of the smaller one where lift was concerned, whilst the opposite was true for drag (see Figures 5.24c and d). The magnitude of this effect scaled with the relative difference in plate sizes.

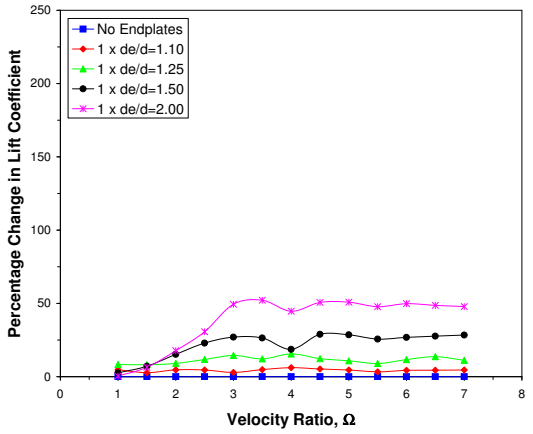

(a) Percentage change in lift with a single endplate

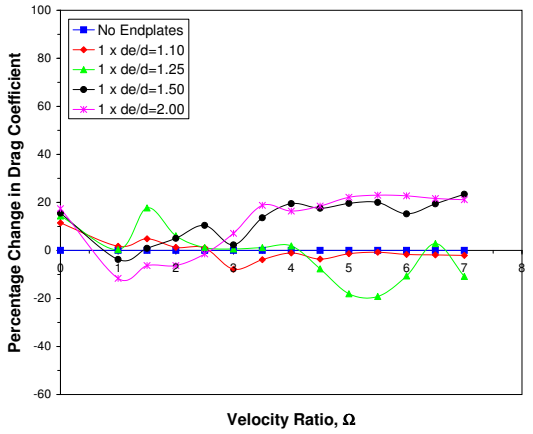

(b) Percentage change in drag with a single endplate

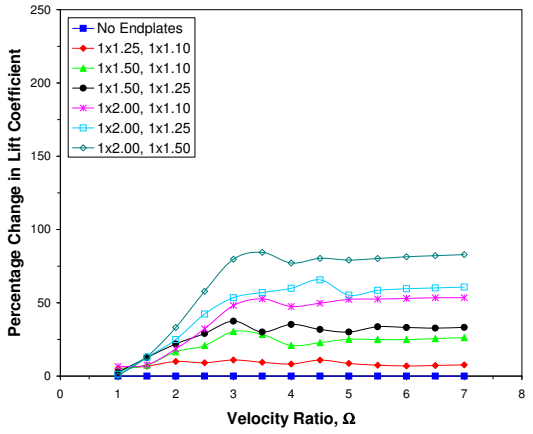

(c) Percentage change in lift with unequal endplates

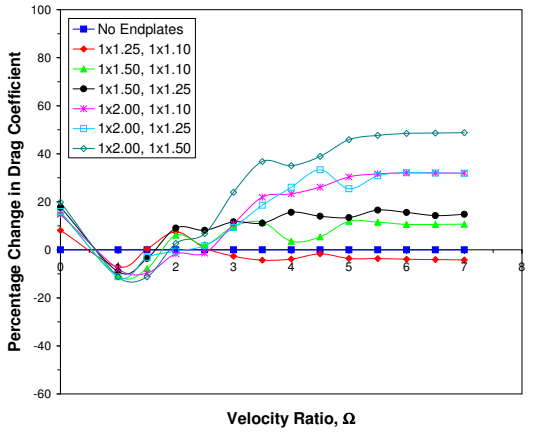

(d) Percentage change in drag with unequal endplates

Figure 5.24: Effects of various asymmetric end arrangements on lift and drag.

Such changes to C_L and C_D meant that the maximum lift-to-drag ratio with one free end was invariably less than with two plates of the same size and, in most cases, practically the same as that with no endplates. When the cylinder was tested with a single endplate of size $d_e/d = 2$, the value of $(C_L/C_D)_{max}$ was somewhat better than other cases, but was still less than that with two plates of size $d_e/d = 1.5$. For all combinations of mismatched plates, the lift-to-drag ratio was found to be marginally better than most configurations with one free end, but even then the maximum value of C_L/C_D achievable was never much more than that obtained with one endplate of size $d_e/d = 2$.

Asymmetric end conditions involving one free end or mismatched endplates were found to be much more important to the behaviour of the lateral forces and moments, and their use resulted in values of C_Y, C_n, and C_l that were nearly always of far greater magnitude than those generated by any symmetric end configuration, though always much smaller than C_L and C_D. This change in the response was proportional to the magnitude of the asymmetry in end conditions: the greater the difference between the port and starboard ends, the more pronounced the change from the performance obtained with symmetric end conditions. For cases with one free end, this meant that the magnitude of the lateral forces and moments was directly dependent on the endplate size ratio, d_e/d. With mismatched endplates, the magnitudes were proportional to the relative difference between the two endplates being used rather than the actual values of d_e/d. In all cases, the sign of the lateral forces and moments was dependent on the position of the endplate (or largest endplate for mismatched pairs) relative to the center of gravity. Changing this arrangement (say, by moving the endplate from port to starboard, or vice versa) altered the sign.

Except for some minor differences, the trends in C_Y, C_n, and C_l were generally the same whether the cylinder was fitted with mismatched endplates or had one free end (see Figures 5.25 and 5.26). In both cases, the response of the lateral forces and moments to changing Ω and asymmetric end conditions appeared consistent with the nature of the flow structure created by these configurations, as discussed in §5.5.8 and illustrated in Figure 5.33. It is believed that this asymmetric flow has an effect on the local (sectional) lift and drag that drives the growth of C_Y, C_n, and C_l. This dependence on C_L and C_D is supported by the trends at high Ω, which seemed to suggest that the sideforce, yawing moment, and rolling moment may all approach an upper limit when $\Omega \geq 4$. Whilst this has not been explicitly confirmed through experiments, it is consistent with the fact that the lift and drag are both seen to plateau in this velocity ratio range. The results also showed that, for asymmetric end conditions, the variation of the lateral forces and moments with velocity ratio was only comparable to that with symmetric ends (as shown in Figure 5.23) when the smallest endplates ($d_e/d < 1.25$), or combinations of endplates, were used and became more complex when large endplates ($d_e/d \geq 2$) were employed.

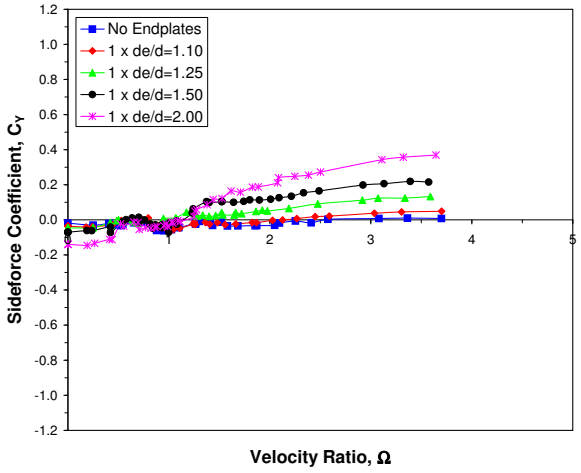

(a) Sideforce coefficient

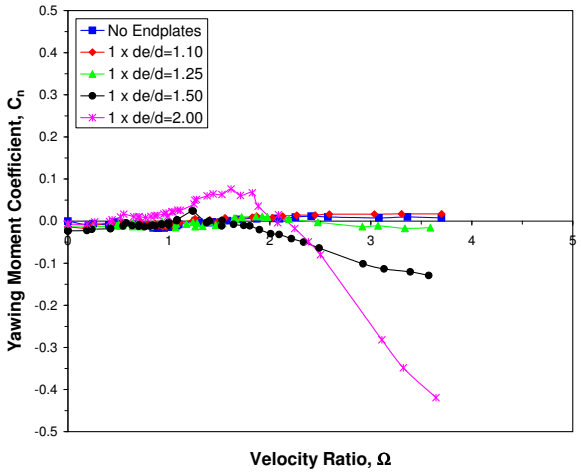

(b) Yawing moment coefficient

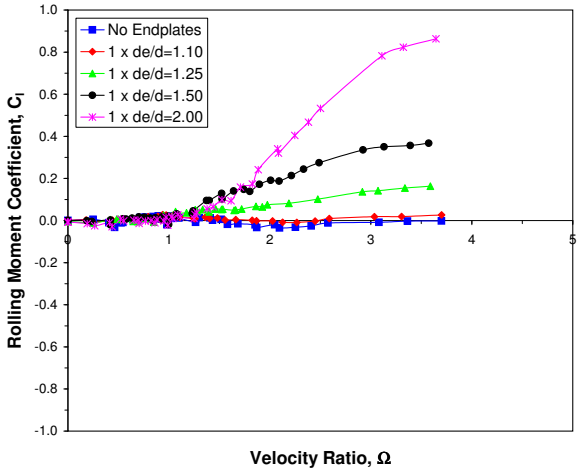

(c) Rolling moment coefficient

Figure 5.25: Effect of one free end on the lateral forces and moments on a rotating cylinder at $\Psi = 0°$. Note that the endplate was always located at $z/b = 0.5$.

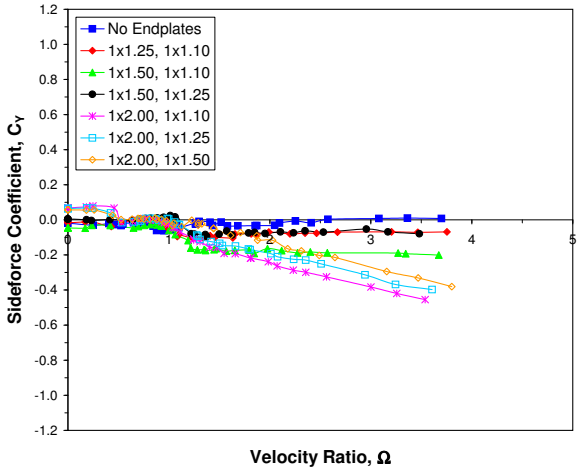

(a) Sideforce coefficient

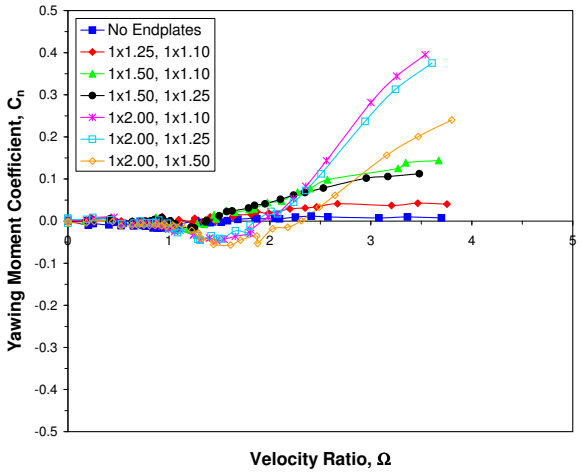

(b) Yawing moment coefficient

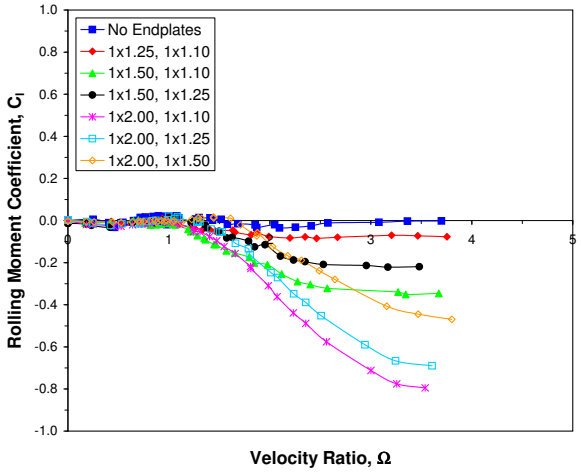

(c) Rolling moment coefficient

Figure 5.26: Effect of mismatched endplates on the lateral forces and moments on a rotating cylinder at $\Psi = 0°$. Note that the larger endplate was always located at $z/b = -0.5$.

Examination of the lateral force and moment results also reveals that the yawing moment and rolling moment performance was quite closely related, with the form of the curves of C_n versus Ω and C_l versus Ω always being very similar regardless of end configuration. For $\Omega \leq 1.3$, both C_n and C_l remained near zero in magnitude and largely independent of Ω. Beyond this point, lateral moments showed a continuous, generally linear, increase with velocity ratio, the magnitude of which was closely linked to endplate size. It is also interesting to note that the yawing moment and rolling moment coefficients generated with asymmetric end conditions were always of opposite sign, and the rolling moment was, for most velocity ratios, seen to be approximately twice as large as the yawing moment associated with the same end configuration.

The sideforce coefficient was found to always be of the same sign as C_n, but it exhibited a variation with velocity ratio for all Ω tested, not just $\Omega > 1$. A particularly pronounced change, which may be related to the Reynolds-number-dependent changes to the lift and drag at low velocity ratios, occurred for $\Omega \leq 0.6$, and became even greater when $d_e/d \geq 2$. In addition, for $d_e/d > 1.25$ there was also a significant non-zero sideforce at $\Omega = 0$. Although the sideforce response to changing velocity ratio for $\Omega \leq 1.3$ was found to be non-linear and complex, it should be noted that the magnitude of C_Y still remained quite low. At higher velocity ratios, this response changed to a generally linear increase in C_Y with Ω and the magnitude of C_Y was largely the same as for the associated yawing moment.

5.5.6 Results with Stationary Endplates

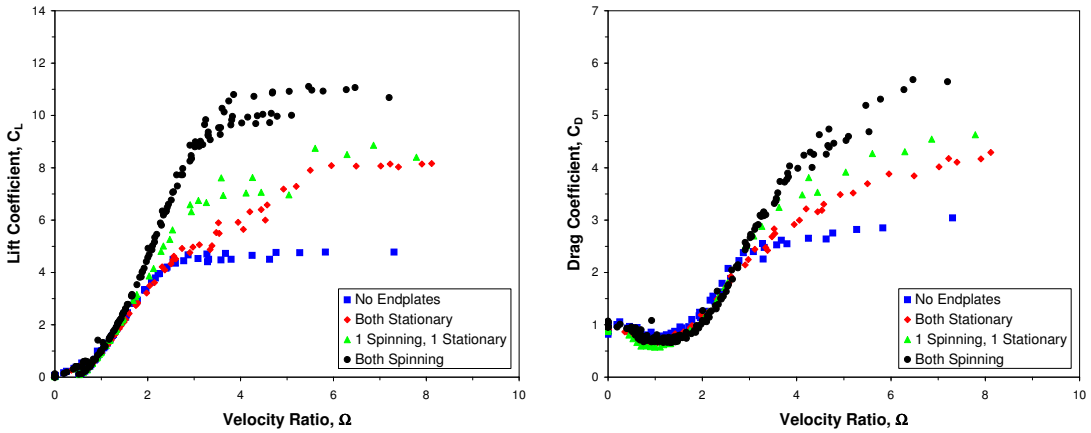

(a) Lift coefficient

(b) Drag coefficient

Figure 5.27: Effects of stationary endplates, of size $d_e/d = 2$, on lift and drag.

Figure 5.27 displays the effects on the lift and drag of having two stationary endplates. As with endplate size, whether the plates were spinning or stationary was found to be unimportant until $\Omega \geq 1.5$, and stationary plates made no difference to Magnus effect inversion at high Re. At higher velocity ratios, the overall performance increase arising from the use of stationary plates was substantially less than that achieved with two spinning endplates. The lift curve with both plates stationary was seen to be very similar to that for the no endplates case, except that the lift plateau was now displaced to $\Omega = 6$. However, the drag behavior lacked the limiting of C_D associated with having two free ends. Consequently, the lift-to-drag ratio was not much changed from that for the no endplates case (see Figure 5.28). These results suggest a fundamental change in the flow as compared to that with spinning endplates. Mixing one spinning plate and one stationary plate produced an intermediate situation that was slightly closer to the behavior with both endplates spinning, though not much more so.

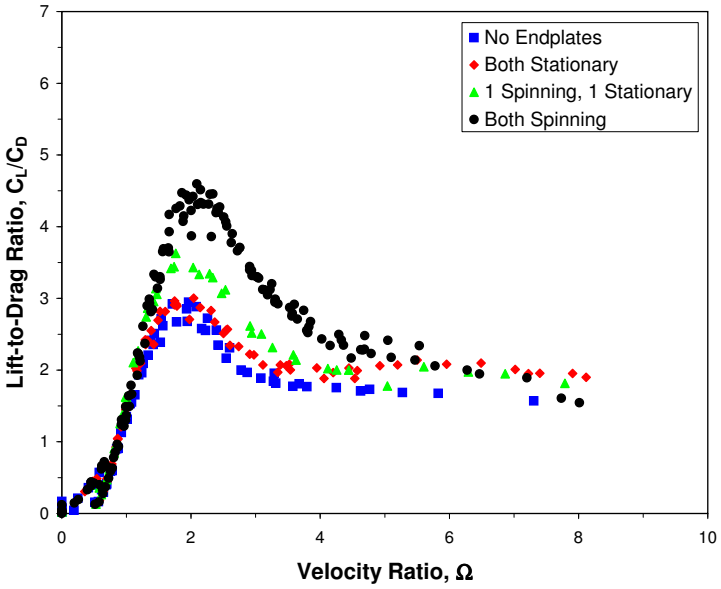

Figure 5.28: Effect of stationary endplates, of size $d_e/d = 2$, on lift-to-drag ratio.

5.5.7 Power Requirements

Power requirements for spinning the cylinder at various Reynolds numbers and for differing end configurations are shown in Figure 5.29. Based on his measurements, Reid[113] indicated that power requirements were greater when the cylinder rotated in still air because of the increased air friction arising from the larger relative velocity between the cylinder and the freestream. The current results revealed no such difference. In fact, the results show little dependency on either Reynolds number or end-conditions: only for

$d_e/d \geq 2.5$ were power requirements significantly affected by endplate size or arrangement. Whilst this may be expected, the large difference between the power requirements for $d_e/d = 2$ and $d_e/d = 3$ is quite surprising, but was verified by repeated measurements. The apparent lack of influence from Reynolds number, or possibly just from velocity, is in keeping with the results of tests by Weiberg & Gamse,[4] based around a rotating cylinder flap, which also found the power to be independent of V.

The strongest factor affecting the power requirements was found to be the condition of the bearings. With worn bearings the value of C_P was more susceptible to changes in Re and d_e/d, though still not excessively so. Results obtained at the beginning of the testing period were repeated at the end of the experimental phase, when the cylinder had undergone many months worth of testing, but showed only a small increase in power requirements (less than 10%). In their tests with rotating cylinder as high-lift devices, both Weiberg & Gamse[4] and Modi *et al.*[6] have also remarked on the close dependence of power requirements on bearing friction.

Figures 5.29c and d indicate that the lift generated from a rotating cylinder is both rather costly in terms of power required and rapidly reaches a saturation point beyond which no extra benefit in C_L is obtained, regardless of the amount of power input. This is a consequence of the form of the lift curve and may be different at large aspect ratios ($AR > 10$) or with very large endplates ($d_e/d > 3$). Aerodynamic efficiency, as determined by C_L/C_D, also quickly reaches a maximum and is itself not improved by further power input but rather is actually decreased. These results are qualitatively similar in nature to the numerical findings of Chew *et al.*[175]

The actual values of the power coefficients were found to closely match the analytical results of Aldoss & Mansour,[205] but did not agree well with the values of C_P calculated from the results of Thom's[118] experimental torque coefficient measurements (see Figure 5.29e). This may be due to errors in estimating the efficiency of the motor. Note also that the power coefficients of Figure 5.29e are primarily those from measurement of P at $Re = 1.7 \times 10^4$. Values of C_P for all higher Re were found to be substantially reduced (up to 50% smaller for $\Omega \leq 4$), though still not in line with those of Thom. Such differences may be due to errors in the determination of the tunnel speed at very low V.

In the present context, the total power coefficient to both rotate and translate the cylinder is also of importance. Plotting this quantity, as given by the sum of C_P and C_D at a given Ω, against velocity ratio for the case of $Re = 1.7 \times 10^4$ indicates that, for $\Omega \leq 4$, the drag-based contribution to total power requirements is dominant as C_D is generally of equal or greater magnitude than C_P in this range (see Figure 5.29f). Consequently, for some low

velocity ratios, this resulted in a doubling of the total power requirements, as compared to those for only spinning the cylinder. Note that the shape of the curve of Figure 5.29f is seen to agree well with that obtained numerically by Mittal & Kumar[203] (see Figure 3.37).

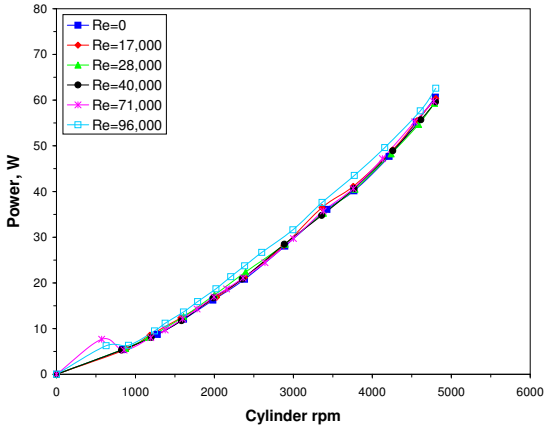

(a) Effect of Reynolds number for $d_e/d = 2$

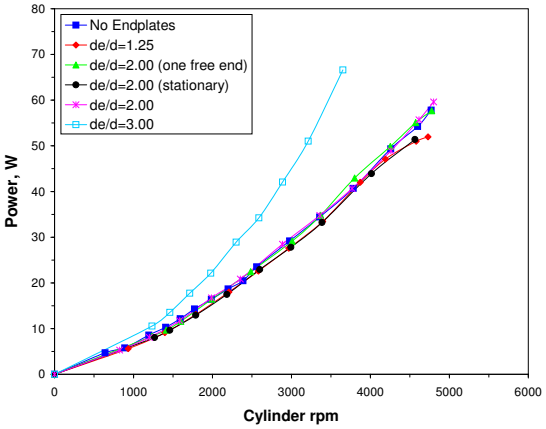

(b) Effect of end configuration for $Re = 4 \times 10^4$

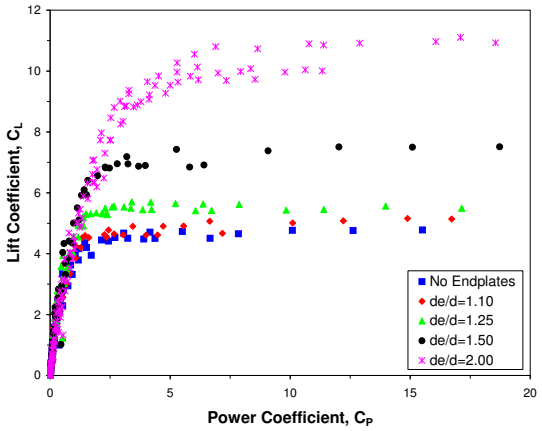

(c) Effect of power input on lift

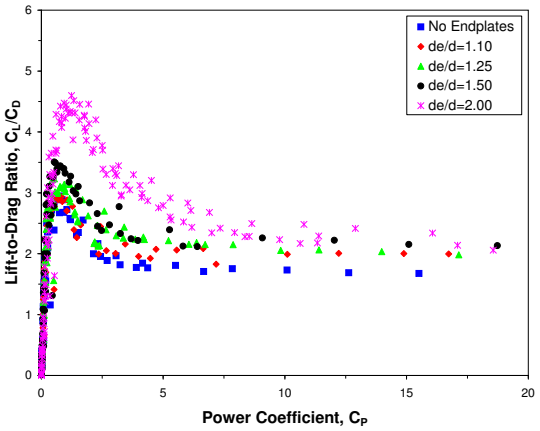

(d) Effect of power input on lift-to-drag ratio

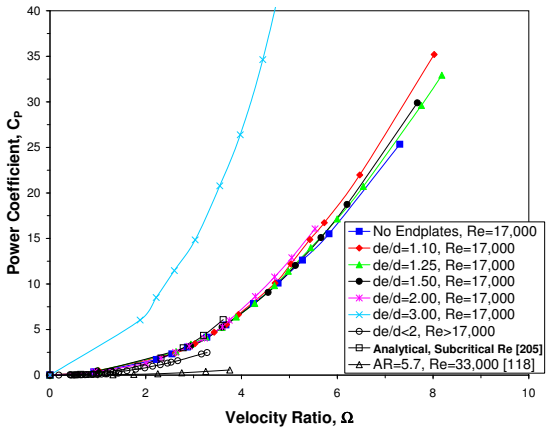

(e) Comparison with other data for $Re = 1.7 \times 10^4$

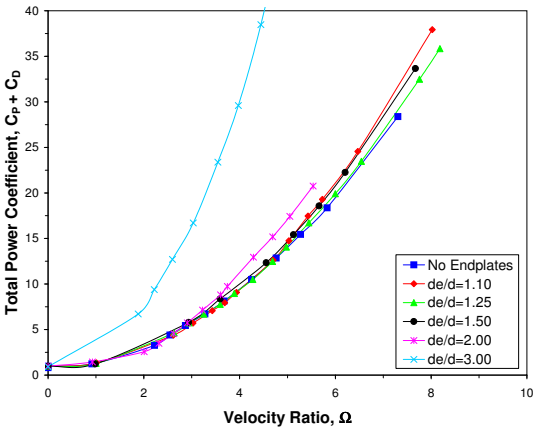

(f) Total power coefficient at $Re = 1.7 \times 10^4$

Figure 5.29: Power requirements for a rotating cylinder.

5.5.8 Wake Pressure Measurements

Figure 5.30 shows a series of pressure plots of the spanwise and lateral variation of the time-averaged total pressure in the wake of the cylinder without endplates for $\Omega < 3.5$ and $Re = 7 \times 10^4$. These plots were used to understand the changes in force behavior caused by different end conditions. The highly three-dimensional nature of the flow is clearly illustrated in Figure 5.30a, where $\Omega = 0$, by the lack of spanwise uniformity of the wake. The influence of the ends can be seen to extend some $1.5d$ along the span, leaving only a small region near the center where the flow may be considered nominally two-dimensional. The smaller wake width near the tips (most clearly seen when $\Omega = 0$) was probably the result of enforced transition to turbulent boundary layer separation in this region as a result of disturbances produced by the ends.

The rapid reduction of wake width due to the influence of rotation on the separation points is visible in Figures 5.30b and c. The particularly dramatic change at $\Omega = 0.63$ was a result of phenomena related to the inversion of the Magnus effect, as discussed in §5.5.3. In addition, the vertical deflection of the wake is readily apparent once $\Omega > 1$. At this point, it was no longer possible to accurately measure the wake pressure with the pitot tubes, which perform badly with inclined flows. When coupled with the reduction of wake width due to rotation, this caused the separated wake to seem to disappear.

A velocity ratio of $\Omega = 1$ was also the point at which vortices at the cylinder tips became more pronounced (see Figure 5.30e). Such vortices have also been observed on stationary cylinders[193] and are known to originate from the separated shear layers from the sharp edges of the cylinder (or the endplates). A trailing vortex system is then formed when these two counter rotating vortices are swept downstream. This system, though similar to that on a wing, was found to be much more dynamic. With increasing velocity ratio the tip vortices moved both inboard and downwards, towards the mid-span position, and the vortex core was seen to strengthen. This continued until $\Omega = 2.6$, whereupon the shape of the vortices became increasingly deformed and their strength was reduced. The spanwise motion of the vortices was also slowed, and seemingly stopped at $\Omega \approx 2.8$.

Interestingly, from comparison with Figures 5.19a and b, the initial prominence of the vortices at $\Omega = 1$ is seen to coincide with the beginning of the end of the identical force behavior that otherwise generally existed (Reynolds number effects notwithstanding) at low Ω for all end conditions. Furthermore, the point at which vortex strength began to diminish appeared to match the point at which, for $d_e/d = 1$, the lift began to plateau. Similarly, the point at which the drag increase was arrested apparently corresponds with the termination of the vortices' spanwise motion.

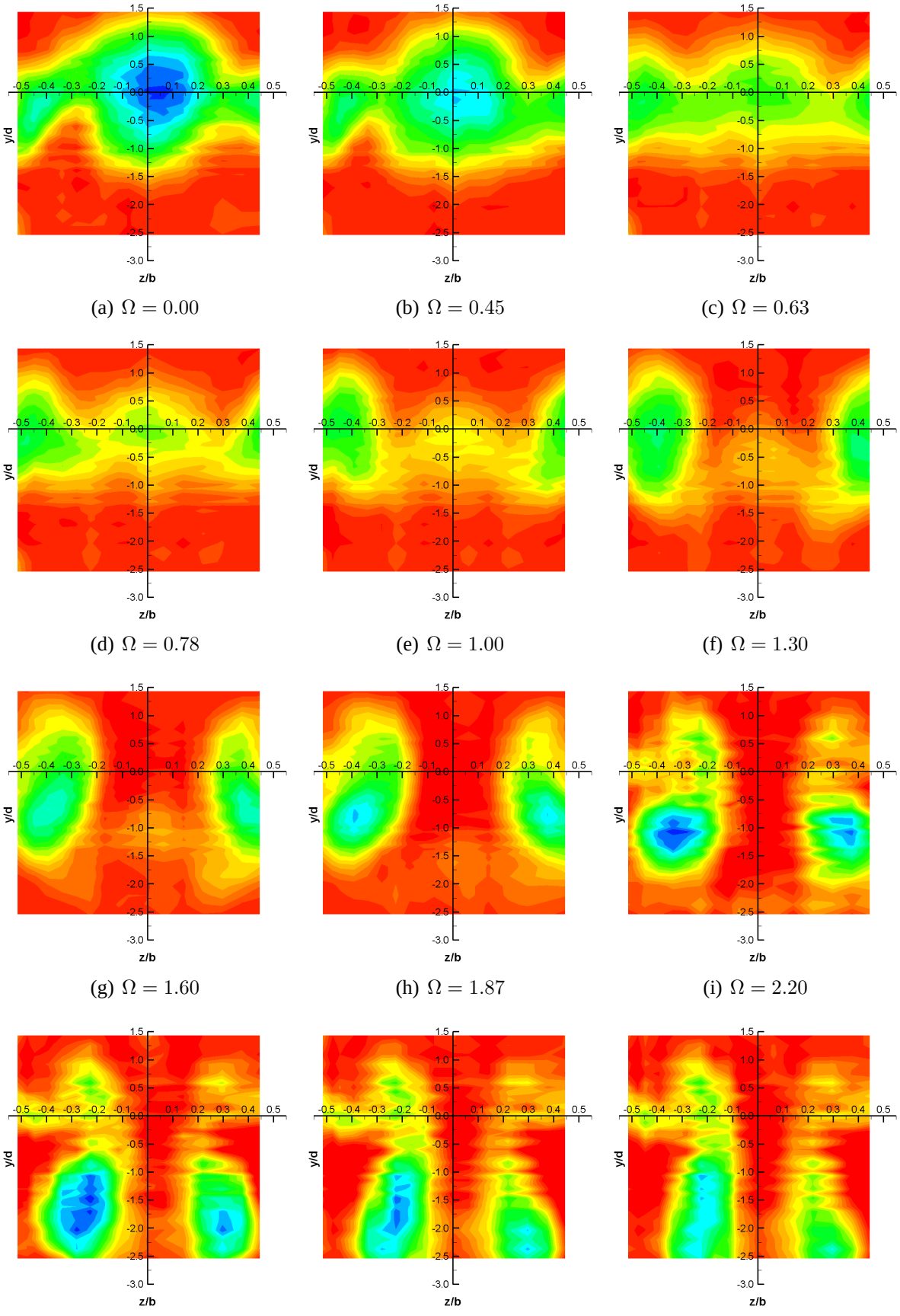

(a) $\Omega = 0.00$ (b) $\Omega = 0.45$ (c) $\Omega = 0.63$

(d) $\Omega = 0.78$ (e) $\Omega = 1.00$ (f) $\Omega = 1.30$

(g) $\Omega = 1.60$ (h) $\Omega = 1.87$ (i) $\Omega = 2.20$

(j) $\Omega = 2.60$ (k) $\Omega = 3.05$ (l) $\Omega = 3.20$

Figure 5.30: Spanwise variation of total pressure in the wake at $x/d = 5$, $d_e/d = 1$, and $Re = 7 \times 10^4$. See Figure 5.32 for legend.

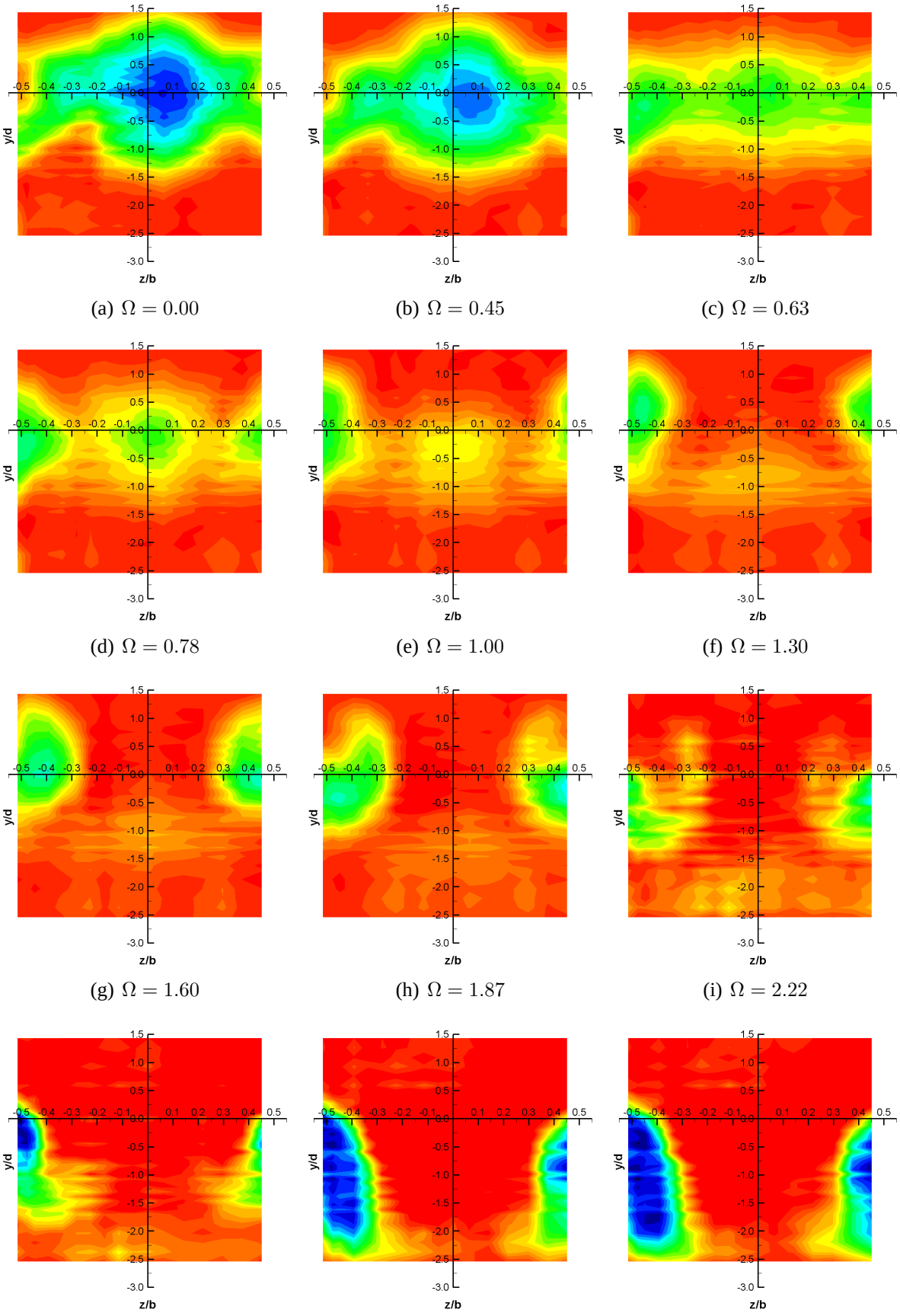

(a) $\Omega = 0.00$ (b) $\Omega = 0.45$ (c) $\Omega = 0.63$

(d) $\Omega = 0.78$ (e) $\Omega = 1.00$ (f) $\Omega = 1.30$

(g) $\Omega = 1.60$ (h) $\Omega = 1.87$ (i) $\Omega = 2.22$

(j) $\Omega = 2.62$ (k) $\Omega = 3.10$ (l) $\Omega = 3.20$

Figure 5.31: Spanwise variation of total pressure in the wake at $x/d = 5$, $d_e/d = 2$, and $Re = 7 \times 10^4$. See Figure 5.32 for legend.

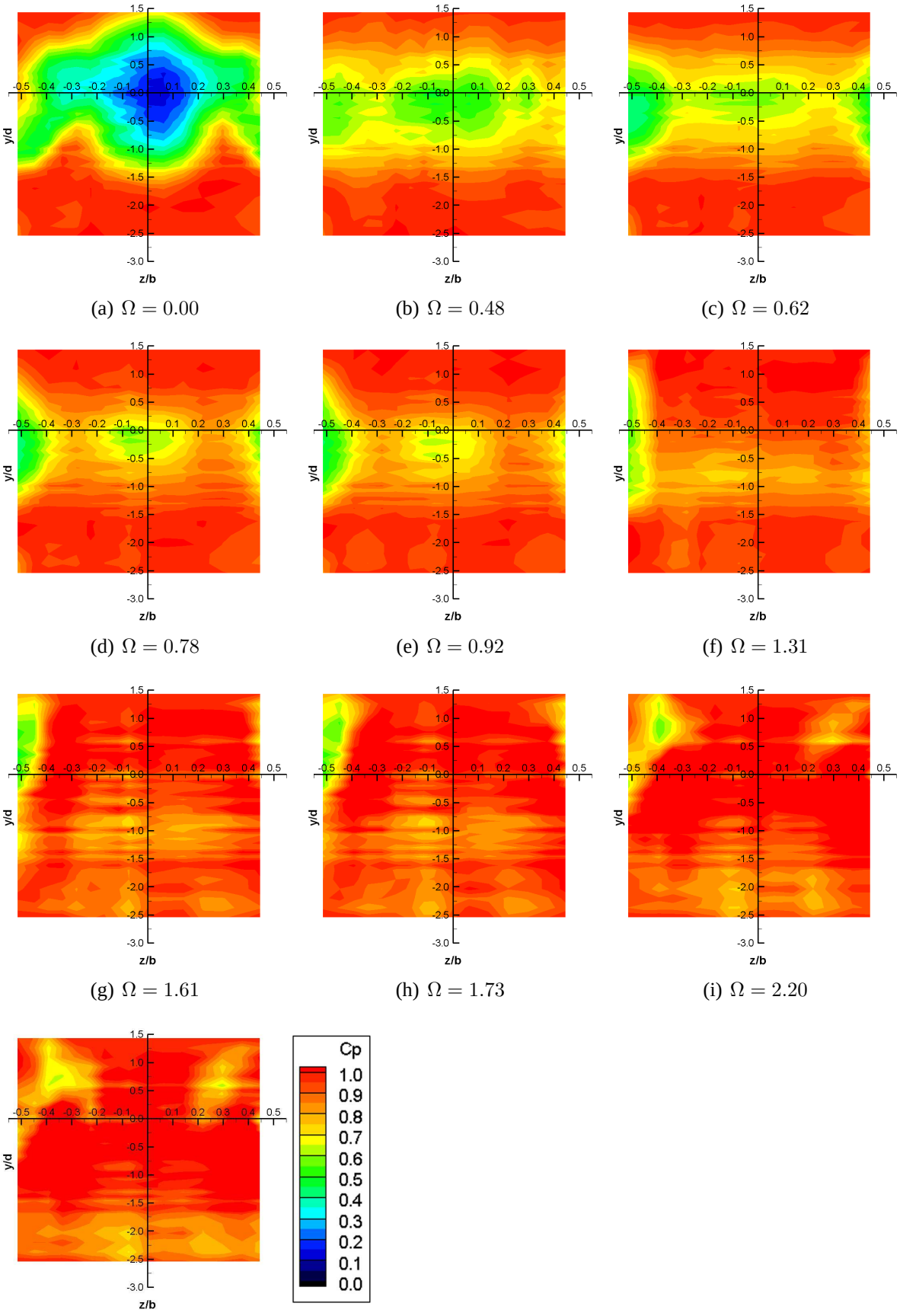

(a) $\Omega = 0.00$ (b) $\Omega = 0.48$ (c) $\Omega = 0.62$

(d) $\Omega = 0.78$ (e) $\Omega = 0.92$ (f) $\Omega = 1.31$

(g) $\Omega = 1.61$ (h) $\Omega = 1.73$ (i) $\Omega = 2.20$

(j) $\Omega = 2.37$

Figure 5.32: Spanwise variation of total pressure in the wake at $x/d = 5$, $d_e/d = 3$, and $Re = 7 \times 10^4$.

At this point, a brief discussion is necessary regarding the pronounced port-starboard asymmetry, of both shape and magnitude, visible in the wake structure. Investigation has suggested that this occurrence is related to problems with the experimental arrangements; in particular, it is the result of physical asymmetries between the motor and non-motor sides of the support struts that the dummy motor cannot fully replicate, together with flow asymmetries arising from a slight (1°) misalignment between the T3 balance and the tunnel centerline. In addition, other physical asymmetries, such as non-uniform surface roughness due to minor scratches and small surface imperfections that accumulated over the testing period, and inherent three-dimensionality stemming from the low aspect ratio, may have also played a role.

Of these sources of error, the asymmetry in the support structure appears to have been the most important, as comparison of Figures 5.30a, 5.31a, and 5.32a suggests that the asymmetry in the wake structure is improved with larger d_e/d (where the cylinder is more shielded from outside influences). In any case, whatever its cause, a comparison with data obtained in T2 suggests that any impact from this asymmetry on the aerodynamic coefficients was relatively minor.

Tests with small endplates ($d_e/d = 1.1$ and 1.25) revealed the form and evolution of the wake to be very similar to the no endplates case. This is in agreement with the similarity between the force data for these end conditions. With two endplates of $d_e/d = 1.1$ or 1.25, the formation of the tip vortices occurred at roughly the same velocity ratio as for $d_e/d = 1$ and their spanwise motion and eventual weakening again coincided with the limiting of the lift and drag. However, with increased plate size, the strength of the vortex core before it begun to weaken was noticeably stronger. Plate size also influenced the overall vortex shape, which became less regular as d_e/d was increased.

Figure 5.31 shows the variation of wake pressures with velocity ratio when $d_e/d = 2$. For $\Omega = 0$, there was only a limited improvement in the ability to promote two-dimensionality, though a more pronounced low pressure region near the mid-span may be noted. This is a consequence of the endplate size: without endplates, inflow around the cylinder ends and into the wake occurs much more readily and so wake pressures are higher. A difference, relative to Figure 5.30a, in the wake structure near the endplates (at $z/b \approx -0.45$, see Figure 5.31a) for the stationary cylinder may also be observed. This change was likely due to freestream flow interaction with the boundary layer on the endplate and became more pronounced with increasing d_e/d.

More substantial differences in the wake of the cylinder with large endplates began to appear when the velocity ratio was increased beyond $\Omega = 1$. The size of the vortical

structures was initially much smaller than with no endplates and their downward motion somewhat slower. Furthermore, the vortices did not form circular structures, but rather highly elongated ellipses that, within the limits of the tests, did not actually migrate towards the centerline. Note also that for $\Omega = 2.62$, when the strength of the vortices in Figure 5.30 was beginning to weaken, the vortices occurring when $d_e/d = 2$ were not yet even fully formed, and continued to develop in strength up to the last measured velocity ratio of $\Omega = 3.3$. Comparison with the lift and drag curves of Figure 5.19 confirms that, at this velocity ratio, both forces are still increasing in magnitude, or perhaps are only just beginning to plateau.

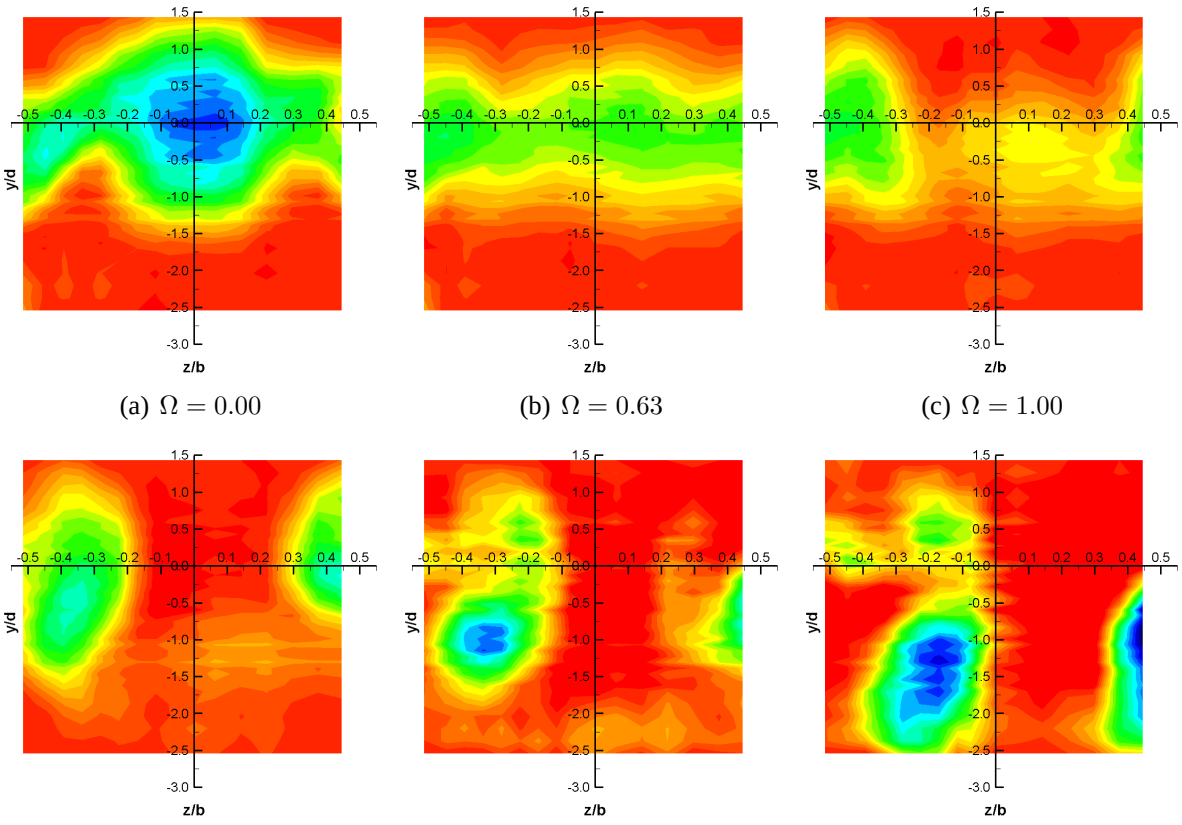

(a) $\Omega = 0.00$ (b) $\Omega = 0.63$ (c) $\Omega = 1.00$

(d) $\Omega = 1.60$ (e) $\Omega = 2.22$ (f) $\Omega = 3.05$

Figure 5.33: Spanwise variation of total pressure in the wake at $x/d = 5$, $d_e/d = 2$ (with one free end), and $Re = 7 \times 10^4$. See Figure 5.32 for legend.

The changes in wake structure associated with large endplates are further illustrated in Figure 5.32. Here it can be seen that, for $d_e/d = 3$, the formation of the tip vortices is even more heavily delayed: they have not yet begun to form even when $\Omega = 2.37$. Unfortunately, it was not possible to extend the tests to higher velocity ratios due to very strong structural vibrations resulting from the large size of the plates. Note that the unusually quick reduction in wake width seen in Figure 5.32b is unexplained. It was present in several repeat measurements and appears to be a consequence of the large plate size.

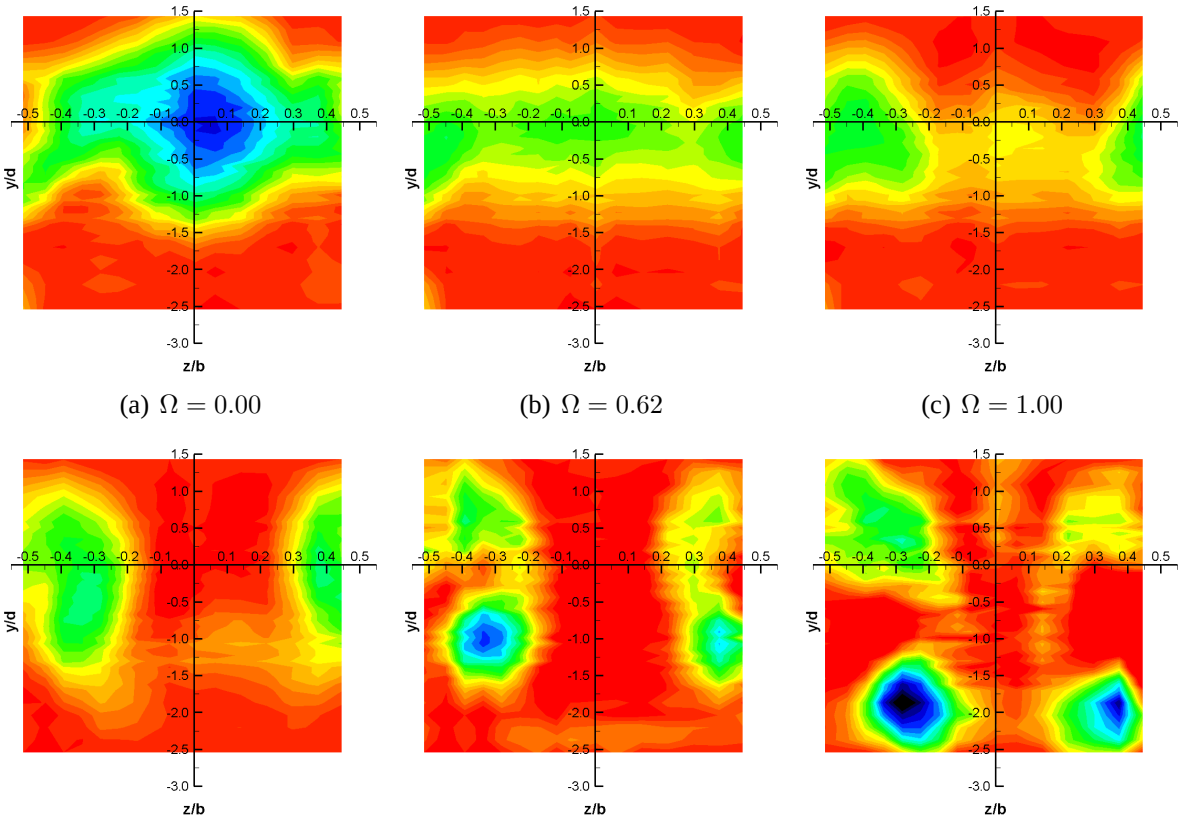

(a) $\Omega = 0.00$ (b) $\Omega = 0.62$ (c) $\Omega = 1.00$

(d) $\Omega = 1.58$ (e) $\Omega = 2.20$ (f) $\Omega = 3.08$

Figure 5.34: Spanwise variation of total pressure in the wake at $x/d = 5$, $d_e/d = 2$ (stationary plates with a 0.5 mm gap between cylinder and endplate), and $Re = 7 \times 10^4$. See Figure 5.32 for legend.

Figure 5.33 highlights the nature of the wake when the cylinder had one free end and one endplate, of size $d_e/d = 2$. It is readily apparent that when $\Omega > 1$ two different wake structures, one associated with no endplates, one with plates of $d_e/d = 2$, exist together in a sort of hybrid flow. However, whilst the presence of the endplate resulted in a stronger and more regularly shaped vortex than was the case with two free ends (contrast Figures 5.30k and 5.33f), comparison with the force coefficient data suggests that it was the free end, through the spanwise motion of its associated vortex, that dictated the point at which the lift and drag plateau. A similar result occurred with mismatched endplates. Such an asymmetric wake structure, and the associated differences in the lift and drag generated by the port and starboard portions of the cylinder, is also responsible for the increased magnitude of the lateral forces and moments generated with asymmetric end conditions.

Figure 5.34 shows the wake structure when the endplates were stationary. For low Ω, this was largely the same as for spinning plates, which is in agreement with the force data of Figure 5.27. However, the changes that once again emerged when $\Omega > 1$ suggest a fundamental difference between spinning and stationary endplates. The tail-like structure

that connects the vortex to the tip was far more pronounced (especially so at high velocity ratios) and the shape of the vortices was both more uniform and much stronger than with no endplates. Interestingly, the strength of the vortex core appears as strong, if not stronger, than for the equivalent velocity ratio with spinning plates, but the size, shape, and position of the vortices were considerably different.

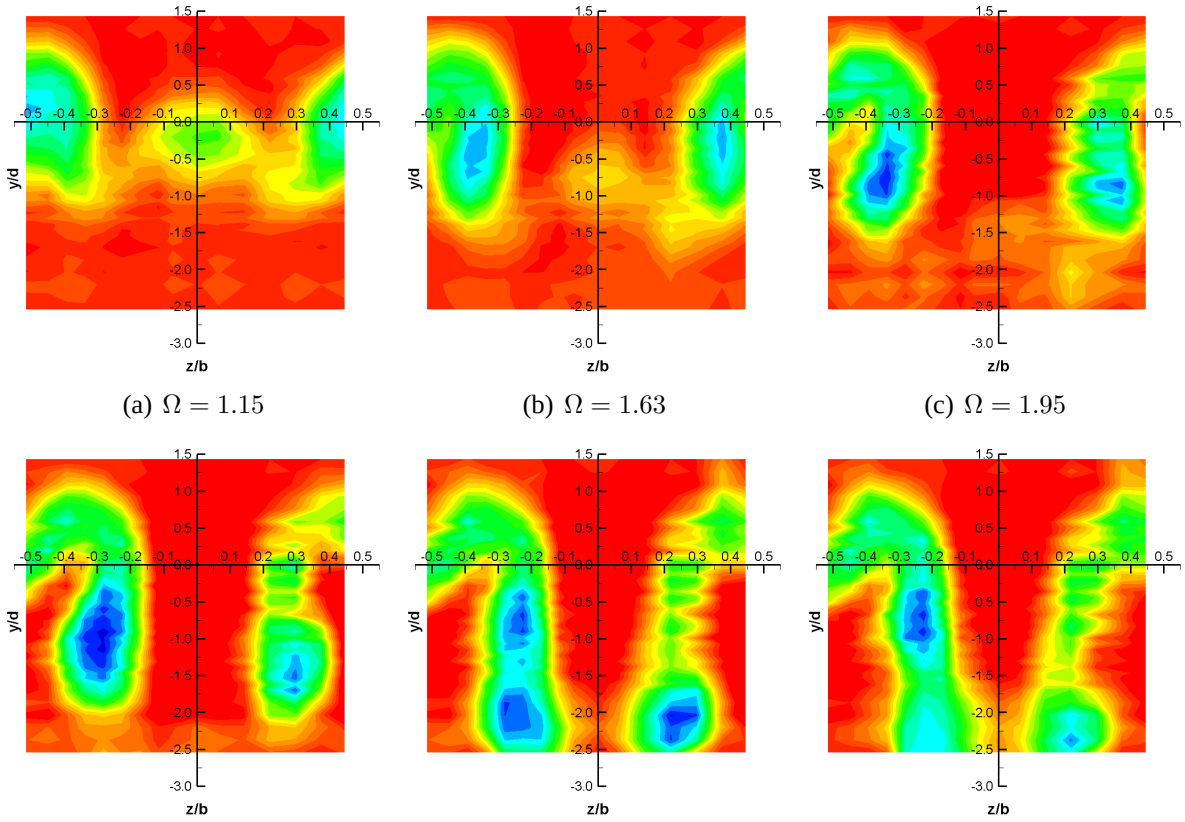

(a) $\Omega = 1.15$ (b) $\Omega = 1.63$ (c) $\Omega = 1.95$

(d) $\Omega = 2.36$ (e) $\Omega = 2.79$ (f) $\Omega = 3.10$

Figure 5.35: Spanwise variation of total pressure in the wake at $x/d = 3$, $d_e/d = 1$, and $Re = 7 \times 10^4$. See Figure 5.32 for legend.

It is again notable that the spanwise motion of the vortices coincided with a change in the drag at $\Omega = 3$, but not the lift, which appears to be mostly driven by vortex strength rather than position and so does not begin to plateau until $\Omega = 6$. The size of the gap between the cylinder end-wall and the endplates was found to be important to wake structure. For smaller gaps (0.25 mm), the wake at $\Omega \leq 2.2$ began to bear slightly more resemblance to that for spinning plates of the same size, but force data were not noticeably different when a smaller gap was implemented.

The results of tests with the rake at different downstream locations showed there to be a considerable change in the wake structure with increasing x/d (see Figures 5.35 and 5.36). The tests showed that the trailing vortex system did not seem to fully form until

at least $x/d = 3$ and that both the strength and shape of the vortices were changed with downstream distance, such that vortices were less circular in structure at $x/d = 3$, but had a stronger core than at $x/d = 5$. Furthermore, based on their spanwise position, the vortices must both rotate and translate closer together as they move downstream. Other, quite drastic, changes were observed when $\Omega > 2.5$: the 'tail' connecting the vortex core to the cylinder tip was more readily apparent when $x/d = 3$, and for some end conditions ($d_e/d \leq 1.25$) the vortices exhibited a 'dual core' structure when $\Omega > 2.55$. Note that these findings on the existence and evolution of the trailing vortex system, at both $x/d = 3$ and $x/d = 5$, were corroborated by smoke flow visualisation tests in T2 and T3.

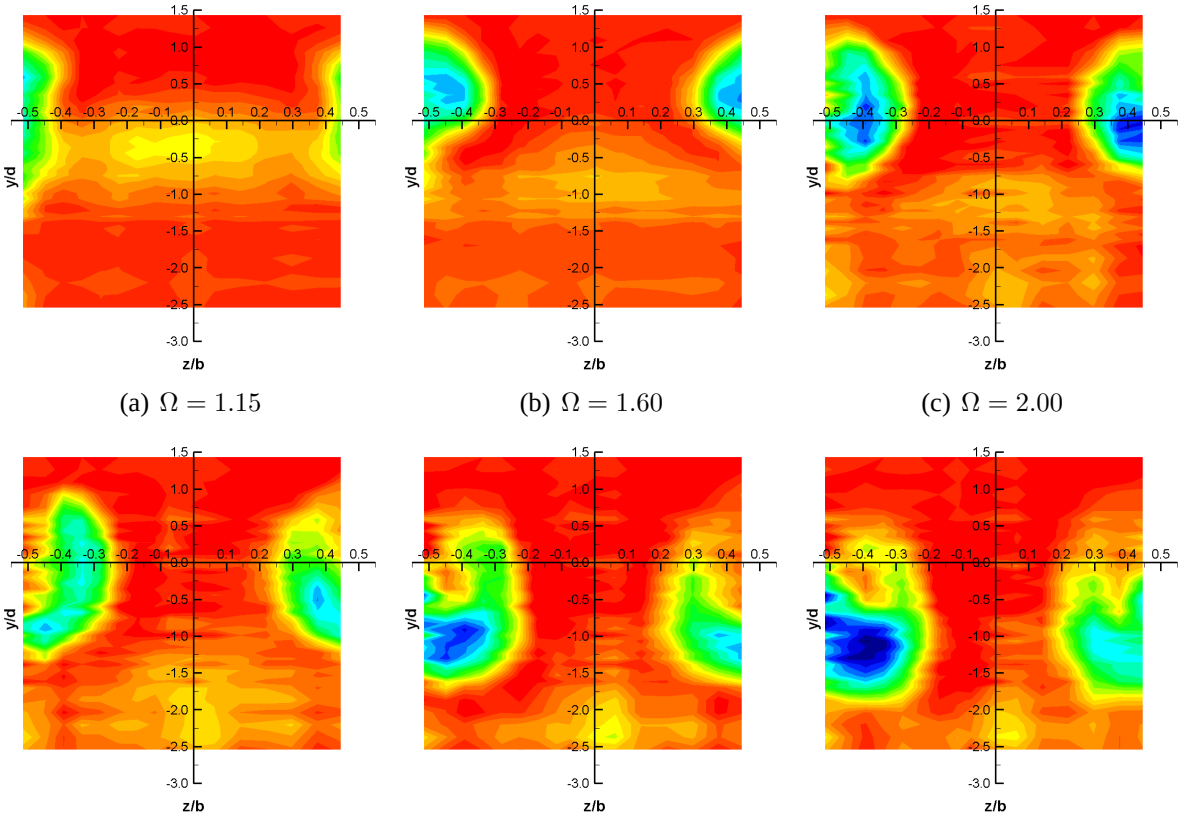

(a) $\Omega = 1.15$ (b) $\Omega = 1.60$ (c) $\Omega = 2.00$

(d) $\Omega = 2.42$ (e) $\Omega = 2.82$ (f) $\Omega = 3.20$

Figure 5.36: Spanwise variation of total pressure in the wake at $x/d = 3$, $d_e/d = 2$, and $Re = 7 \times 10^4$. See Figure 5.32 for legend.

Based on the wake pressure measurements and force readings, it seems apparent that the use of endplates controls the forces and moments acting on a rotating cylinder by manipulating the lift and drag. This is done in two ways. Firstly, endplates prevent inflow around the tips and stop the pressure equalization that would otherwise occur. Secondly, they control the formation of the trailing vortex system. The first effect is visible at low velocity ratios, where larger plates tend to give a slightly larger C_D, particularly for $\Omega = 0$. At high velocity ratios, the second effect is more dominant. Small plate sizes allow the

early growth of the tip vortices, which then move inwards towards the mid-span, drawing in higher pressure air. This both reduces drag and limits lift. Larger plates produce more powerful vortices, but delay their occurrence until much higher Ω, and seemingly prevent their inwards migration. This allows both lift and drag to increase for longer.

With symmetric end conditions the vortices that form at either end of the cylinder are the same for all velocity ratios and the associated lift and drag distribution along the cylinder span is always symmetric about $z/b = 0$. In these conditions the lateral forces and moments appear largely negligible. By using different sized endplates at either end, or by having one free end, this creates a hybrid situation where tip vortices of different size and strength, and which move inboard at different rates, are formed. This is largely detrimental to the lift and drag performance and also changes the spanwise distribution of C_L and C_D so that it is no longer symmetric about $z/b = 0$. In these conditions much larger values of C_Y, C_n, and C_l are generated. The sign of the lateral forces and moments may also be controlled through this asymmetry by changing the end at which the endplate (or largest endplate if using mismatched pairs) is located, see Figures 5.25 and 5.26.

5.5.9 Vortex Shedding Phenomena

Spectral analysis of the time-varying wake pressures showed that vortex shedding phenomena was affected by both endplate size and Reynolds number. In some instances, these effects impacted on the quality of the data recorded and impeded analysis. The best results were obtained from the power spectra of tests at $Re = 4.1 \times 10^4$, with endplates of size $d_e/d = 2$ attached, and with the rake at $x/d = 3$. These are shown in Figures 5.37 and 5.38. For higher or lower Re, a dominant peak at f_s was more often absent from the power spectra, making it harder to interpret the results. For $Re > 4.1 \times 10^4$, this may have been a consequence of the growing irregularity of vortex shedding as Reynolds number is increased. For lower Re, it was probably due to the very low magnitude of pressures involved. A similar difficulty in identifying a dominant spectral peak occurred when testing without endplates or with small endplates ($d_e/d \leq 1.5$); in these cases shedding always appeared more irregular. Also, with increasing downstream distance, shedding activity seemed to decay quite quickly and the individual power spectra at $x/d = 5$ were both more chaotic and had much smaller frequency peaks than when $x/d = 3$.

Despite the changes in the spectra for higher Re, there was little actual difference in the value of St for all Reynolds numbers between $4.1 \times 10^4 \leq Re \leq 9.8 \times 10^4$. The Strouhal number for a given Ω was, however, found to change slightly with both x/d and d_e/d, respectively increasing and decreasing in magnitude by a small amount ($\approx 10\%$). Even

so, the same overall trend of increasing St with Ω was observed throughout, and in all cases the critical velocity ratio for suppression remained the same. Note also that the results for all three transducer locations were found to show the same overall trends.

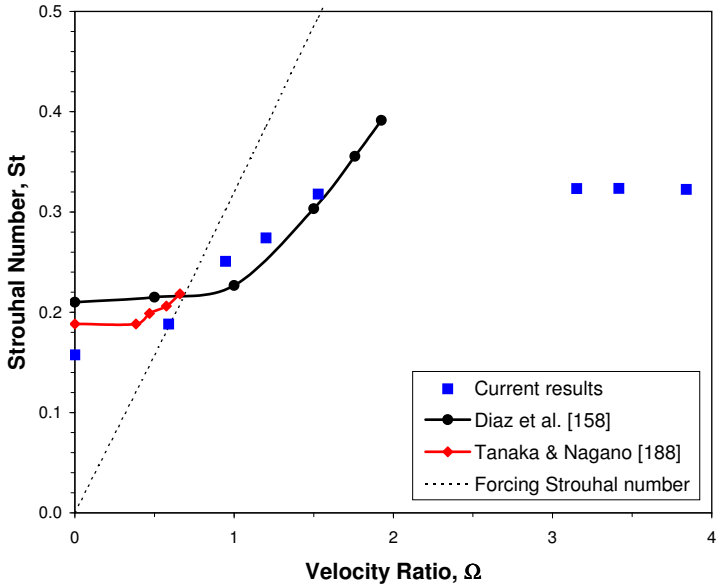

Figure 5.37: Strouhal number variation with velocity ratio for $x/d = 3$, $y/d = -0.6$, $d_e/d = 2$, and $Re = 4.1 \times 10^4$.

Individual variations between the spectra for each y/d did exist, but were wholly consistent with the differing proximity of each transducer to the positions on the cylinder surface from which vortices were shed. Thus, the amplitude of the spectral peaks for $y/d = -0.6$ (which was close to the point of shedding from the upstream moving wall) was generally greater than that for $y/d = -0.06$ (which was initially located between the two sides of the vortex street, where vortices are more diffuse). The biasing and narrowing of the wake with increased Ω also affected the spectra for each transducer in different ways, particularly where harmonic peaks were concerned, but the Strouhal number across all y/d locations remained effectively the same up to the point at which shedding was suppressed. Consequently, the results of Figures 5.37 and 5.38, along with the associated discussion that follows, may be considered representative of the data for all conditions tested.

Comparison with existing data shows that, overall, the present Strouhal number results agree qualitatively with the trend of increasing St with Ω and the eventual suppression of vortex shedding at $\Omega_c = 2$, as established by the experimental studies of Diaz *et al.*,[158,159] Tanaka & Nagano[188] and others (see Figure 5.37). However, a good quantitative match with the existing literature was only noted at mid-level velocity ratios ($1 \leq \Omega \leq 1.5$); the results at both higher and lower Ω, especially $\Omega = 0$ and $\Omega > 3$, are markedly different. Such departures from previous findings appear to be due to the low AR of the cylinder.

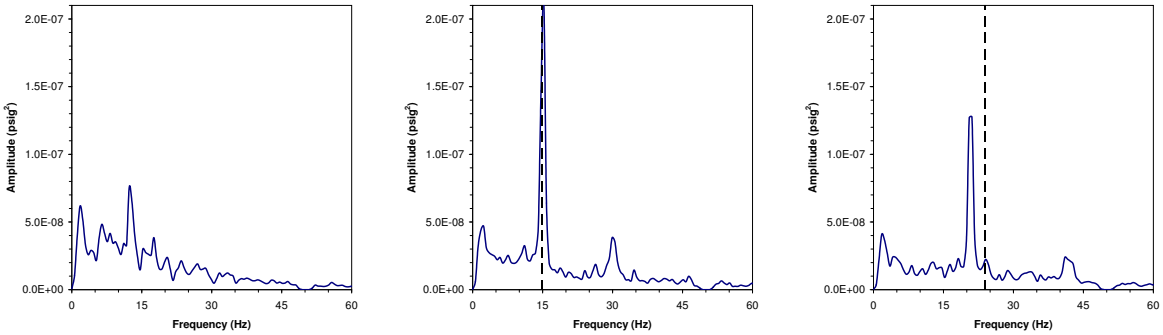

(a) $\Omega = 0.00$ (b) $\Omega = 0.58$ (c) $\Omega = 0.95$

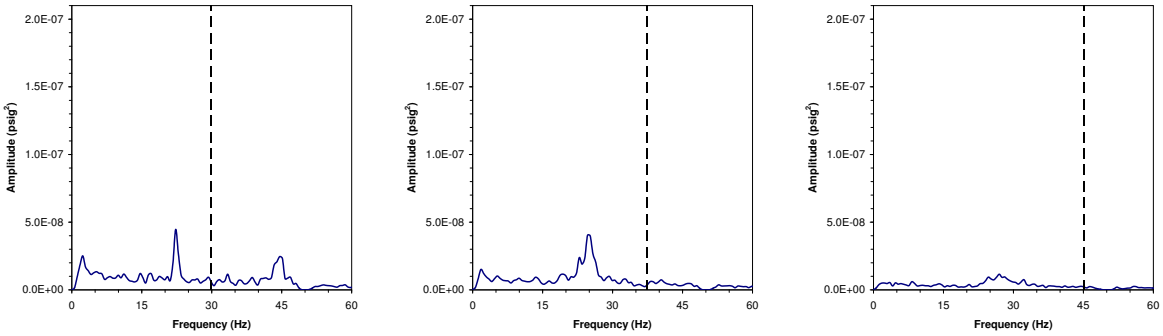

(d) $\Omega = 1.21$ (e) $\Omega = 1.54$ (f) $\Omega = 1.88$

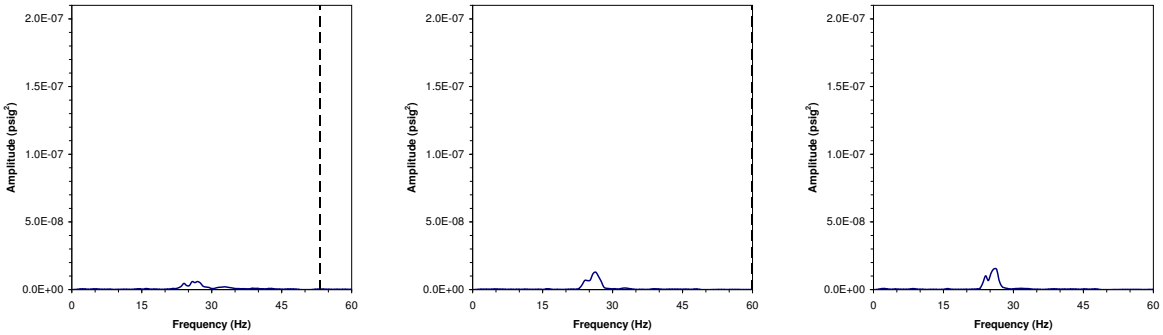

(g) $\Omega = 2.16$ (h) $\Omega = 2.45$ (i) $\Omega = 2.77$

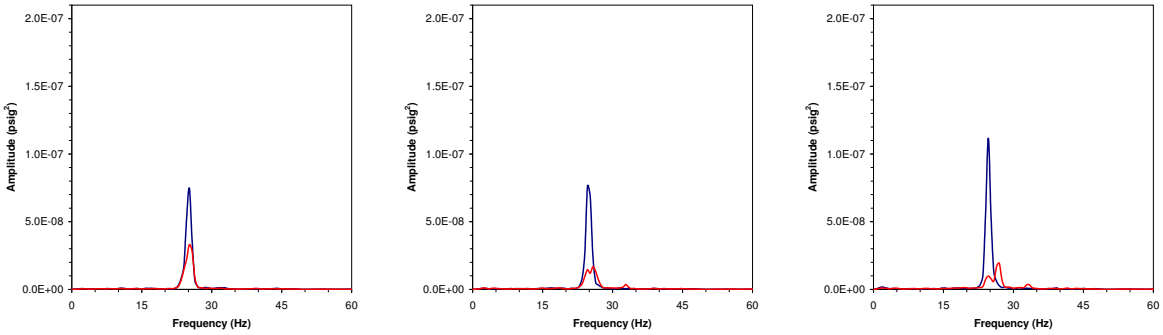

(j) $\Omega = 3.14$ (k) $\Omega = 3.40$ (l) $\Omega = 3.85$

Figure 5.38: Power spectra for $y/d = -0.6$, $x/d = 3$, $Re = 4.1 \times 10^4$, and endplates of size $d_e/d = 2$. Blue curves indicate results obtained with Ω continuously increasing. Red curves indicate results obtained with Ω continuously decreasing. Where appropriate, dashed lines are used to indicate the forcing frequency.

The Strouhal number associated with the most prominent peaks in the spectra for $\Omega = 0$, $Re = 4.1 \times 10^4$, $d_e/d = 2$, and $x/d = 3$ was found to be $St = 0.165$. The value of St obtained for the same Re and d_e/d but with the rake at $x/d = 5$ was a slightly larger $St = 0.173$, whilst that for $d_e/d = 1$, $x/d = 3$ and the same Re was a much lower $St = 0.13$. Such low values of St at $\Omega = 0$ are consistent with the effects of finite aspect ratio and a comparison with published data obtained under similar arrangements reveals good agreement. Zdravkovich *et al.*[193] reported that the Strouhal number for a stationary cylinder of $AR = 5$ at $Re = 1.1 \times 10^5$ varied between $0.15 \leq St \leq 0.19$; the irregularity caused by low AR and high Re making it impossible to assign a single value. Norberg's[259] experiments with a cylinder of $AR = 5$, having circular endplates of size $d_e/d = 10$, found the Strouhal number to be $St \approx 0.185$ at $Re = 4 \times 10^4$. This suggests that the current values are quite reasonable.

The results with the cylinder stationary also highlighted the effects of high Re on the vortex street. Figure 5.38a shows that for $\Omega = 0$ a single dominant peak was somewhat difficult to identify and that low-amplitude spectral activity was distributed across a broad range of frequencies ($f \leq 40$ Hz). These features appear to be an inherent part of the wake of a stationary or rotating cylinder under the test conditions and probably occur as a result of the irregularity of vortex shedding at the range of Reynolds numbers tested at. Such an assumption is supported by the fact that the level of spectral activity at frequencies outside the shedding peak was seen to increase with proximity to the lower extremity of the cylinder, where the upstream moving wall vortex is shed from, and to decrease rapidly as the suppression velocity ratio was approached, disappearing completely at Ω_c.

Other potential origins for the spectral activity at frequencies outside of the shedding peak were also considered. It is possible that this activity may be associated with the choice of window function applied in the FFT process; however, analysis of the original data using different functions (Hamming, Kaiser) revealed no significant changes. Pressure measurements from a test with the cylinder not in the tunnel were used to determine whether the activity was in some way associated with the freestream flow, but the form of the power spectrum in these conditions was considerably different. An example of the power spectrum found to be associated with the freestream is that shown in Figure 5.38g.

Comparison with previous studies also shows that the current results lack the typically observed region of constant Strouhal number for $\Omega \leq 1$; instead the findings indicate a rapid increase in St for all non-zero Ω. Such a difference with the Diaz *et al.* results could be dismissed as a consequence of the larger aspect ratio ($AR = 30$) and lower Reynolds number ($Re = 9 \times 10^3$) of their experiments. By contrast, the lack of similarity between the present low-Ω results and the data of Tanaka & Nagano was more surprising

as their Reynolds number ($Re = 4.5 \times 10^4$), downstream probe location ($x/d = 2.83$), and cylinder aspect ratio ($AR = 2.4$) all quite closely match those of the current tests. Whilst the much higher blockage ratio of the Tanaka & Nagano tests ($d/H = 0.18$) may account for the disparity, the more likely cause of the difference between current findings and all the existing results is 'lock-on' phenomena, as described in §3.7.6.

In the present experiments, strong structural vibration of the cylinder occurred at rotation rates between $600 \leq N \leq 1600$ rpm. For the $Re = 4.1 \times 10^4$ tests, this range corresponded to $0.44 \leq \Omega \leq 1$. The forcing Strouhal number based on the rotational frequency of the cylinder within this range (and beyond) is plotted on the graph in Figure 5.37. The closeness of this line to the Strouhal number results at $\Omega = 0.58$ and 0.95, and the level of vibration observed, indicates that the shedding frequency may have become synchronised with the rotation rate, so causing the Strouhal number to increase with N rather than remaining at its natural level. At higher rpm, the rotational frequency and shedding frequency were no longer close enough to induce lock-on; thus, the Strouhal number returned to its true value and the results show more similarity with the data of Diaz *et al*.[158,159]

That rotation and vibration of the cylinder may have lead to lock-on phenomena occurring at low velocity ratios is also supported by the fact that, with the cylinder rotating, a spectral peak associated with the vortex shedding frequency became much more prominent than when the cylinder was stationary. This change was particularly notable in the spectra for $\Omega = 0.58$ (compare Figures 5.38a and b) and appears to indicate that rotation of the cylinder initially acted to stabilise the irregularity of vortex shedding caused by high Re and low AR. It is known that lock-on can cause vortex shedding to be almost perfectly correlated across the cylinder span producing a more stable shedding process.[147,224]

For $\Omega > 1$, the shedding frequency peak underwent a large reduction in amplitude (compare Figures 5.38c and d). This was a result of both the progressive degradation of vortex shedding activity and the biasing of the wake, which deflected the path of the vortices away from the transducer locations. The biasing and narrowing of the wake also allowed vortex activity from both the upper and lower shed vortices to be transmitted to the transducers, resulting in the appearance of a second spectral peak (centered on the second harmonic frequency, $f = 2f_s$) that was always smaller and wider than that associated with the main shedding frequency, as seen in Figures 5.38b to d. With increasing velocity ratio the frequency spectra also began to manifest changes indicative of the suppression of vortex shedding. For $1.54 \leq \Omega \leq 2$, the progressive reduction in the amplitude of the shedding peak was now also accompanied by a fundamental change in shape towards a broadband peak (see Figures 5.38e to g). Accordingly, the Strouhal number for this region

is undefined.

That the critical velocity ratio was $\Omega_c \approx 2$ and that shedding was suppressed for all higher velocity ratios is apparent in the fact that the spectra obtained for all three transducer locations at $x/d = 3$ and $2 \leq \Omega \leq 2.45$ were effectively identical in form to that obtained in a reference test in which the cylinder was absent from the tunnel while pressure measurements using the rake and transducers were made. The general form of the frequency spectrum under these conditions is illustrated in Figure 5.38g. Note that for these velocity ratios, the deflection of the wake meant that the transducer at $y/d = -0.6$ was still largely in the wake whilst those at $y/d = -0.25$ and $y/d = -0.06$ were not. Thus, the similarity across all three transducers suggests that, with the suppression of shedding, the wake flow was now effectively indistinguishable from the freestream.

The most interesting results were obtained at the higher velocity ratios ($\Omega > 2$) where the unexpected re-emergence of a dominant spectral peak in the results suggests there was a return to some sort of periodicity in the wake. Figures 5.38h and i show that between $2.45 \leq \Omega \leq 2.77$ a small amplitude 'bump', centered on $f = 25$ Hz, appeared in the frequency spectra for $d_e/d = 2$ and $x/d = 3$. When $\Omega > 2.77$, this became a sharp, distinct peak (still located at $f = 25$ Hz) whose frequency remained invariant with further increases in velocity ratio, but whose amplitude grew considerably. Unlike the results at low velocity ratios ($\Omega < 1.5$), no activity was seen at any other frequency and the spectra for all three y/d locations were always identical. This behaviour was seen to persist up to the limit of testing at $\Omega = 3.85$, but was found to exhibit a degree of hysteresis. The nature of the frequency peak was dependent on whether measurements had been obtained with the velocity ratio continuously increased upwards from $\Omega = 0$ (Figure 5.38, blue curves) or continuously decreased downwards from $\Omega \approx 4$ (Figure 5.38, red curves).

A similar result was obtained with the rake further downstream at $x/d = 5$, but the spectral peak was much smaller in amplitude and was located at approximately half the frequency of that observed at $x/d = 3$, suggesting it may have been a subharmonic. The general reduction in clarity of the spectral peaks experienced in all the results at $x/d = 5$ may also have affected the results at this position. The results with smaller endplate sizes or with two free ends also showed activity similar to that described, but indicated that the velocity ratio at which this change in the power spectrum occurred was dependent on d_e/d, as discussed below.

This re-emergence of a dominant frequency peak at high velocity ratios shows some resemblance to the secondary shedding phase noted in the low-Re computational work of Stojkovic *et al.*[197,223] and Mittal & Kumar[203] (discussed in §3.7.4). The onset of the ac-

tivity at $\Omega = 3.14$ and its persistence to higher Ω is in keeping with the notion that the secondary phase appears earlier and lasts longer as Re increases. However, such similarities are only superficial and a close examination reveals considerable differences between the present findings and the nature of the secondary shedding seen in CFD studies.

For instance, the value of St associated with this high-Ω frequency peak was the same as the last definitively identifiable Strouhal number for the first shedding phase ($St = 0.32$ at $\Omega \approx 1.6$). This is a much higher value than that reported in the CFD studies, where the Strouhal number for the second phase ($St \approx 0.05$) was always found to be considerably smaller than in the first phase. Furthermore, the CFD data of Stojkovic *et al.*[223] showed that, in the second phase, St reduces with Ω. In contrast, the present data show that, for $\Omega > 3.14$, St remained constant with increasing Ω. Most tellingly, the form of the spectra for $\Omega > 3.14$ was identical across all three transducer locations, even for those values of y/d for which the transducer would not, at these velocity ratios, be expected to be within the wake. This suggests that the spectral peak seen at $\Omega > 3.14$ was not associated with vortex shedding from the wake.

Instead, the re-emergence of a strong peak in the power spectra for $d_e/d = 2$, $x/d = 3$, and $\Omega > 2.77$ seems to coincide with the evolution of the large trailing vortex system described in §5.5.8. As previously noted, these vortices initially began to dominate the wake at $\Omega \approx 1.5$ and were seen to both increase in strength and move towards the mid-span as the velocity ratio was increased further. The exact shape, strength, and position of the vortices at high velocity ratio was also found to be strongly dependent on both end conditions and downstream location from the cylinder. For $d_e/d = 2$, $x/d = 3$, and $\Omega > 2$ the vortices are seen to be located quite close to the mid-span, where the transducers were positioned (see Figure 5.36).

Hence, a periodicity of the pressures near the cylinder mid-span that is associated with the rotation of these vortices may be responsible for the interesting results at high Ω. That this behaviour was much weaker at $x/d = 5$ is then a consequence of the development of the vortical structures as they move downstream. At $x/d = 5$, the trailing vortices were found to be much stronger, but they had now rotated away from the mid-span by a substantial amount (compare Figures 5.31k and 5.36f). In this condition the vortices may not have been able to influence the centerline as strongly as when the rake was at $x/d = 3$.

That the spectral peak at high Ω is related to the activity of the tip vortices is supported by the results with smaller endplate sizes and those without endplates. In each of these other cases, the high-Ω spectral peak was far less prominent than for $d_e/d = 2$, but the point at which the spectra began to change always coincided with the specific motion of

the tip vortices towards the mid-span for that particular end condition. Thus, for the no endplates case, where the vortices more quickly approach the mid-span (as indicated by Figure 5.35), there was a change in the spectra when $\Omega > 2.2$; for tests with endplates of $d_e/d = 1.5$, a change occurred at $\Omega \approx 3$, and so on. Furthermore, association with the tip vortices would also explain why such high-Ω activity has not previously been reported. The existing studies of vortex shedding from a rotating cylinder have generally been performed at low Ω and with large aspect ratio cylinders, where the tip vortices are less likely to influence the mid-span (where measurements are typically taken).

5.5.10 Results with a Yawed Rotating Cylinder

The results of tests with a yawed rotating cylinder revealed that aerodynamic performance was strongly affected by non-zero yaw, particularly for $|\Psi| \geq 15°$. The influence of yaw angle was found to be complex and was typically closely tied to the cylinder's end conditions. In general, the results showed little agreement with Howerton's[227] limited experiments; however, yawing and rolling moment data for $\Omega = 0$ and $\Psi = 0°$ was similar to results by Zdravkovich *et al.*[193] for low aspect ratio ($AR \leq 8$) stationary cylinders.

For lift and drag, the effects of yaw were largely the same for both symmetric and asymmetric end conditions, although asymmetric ends meant that the onset of yaw effects occurred at smaller Ψ. For the lateral forces and moments, there was generally a greater difference between the response to yaw with asymmetric end conditions and that with symmetric ends. This difference was primarily related to the influence of velocity ratio, which was always of greater importance with asymmetric end conditions. In most cases, the use of large endplates ($d_e/d > 1.5$) tended to complicate the effects of yaw and the smallest response to changing Ψ was always achieved with two free ends (see Figures 5.39 and 5.40). The results also showed that high yaw angles sometimes affected the forces and moments at low Ω, presumably by augmenting the influence of Re in this region.

It should be noted that the results revealed there to often be some quite substantial asymmetry between the force and moment coefficient results (particularly the drag and side-force coefficients) obtained at $\Psi = 5°$ and those at $\Psi = -5°$. This discrepancy remains unexplained but is most likely to have arisen due to small errors in the assessment of the strut and wind-off contributions at non-zero yaw. Although every effort was made to accurately account for these contributions, even a slight variation could have had a significant effect due to the relative smallness of the lateral forces and moments. Alternatively, the asymmetry may have resulted from some inherent feature of the flow pattern, as seen in the T3 wake pressure data, or from a small yaw offset between the balance and wind

axes in the T2 tunnel.

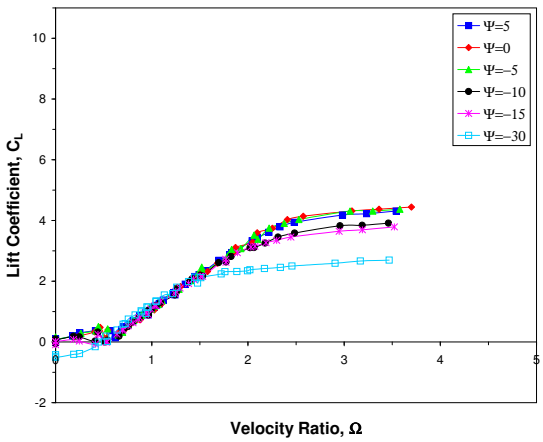

(a) Lift

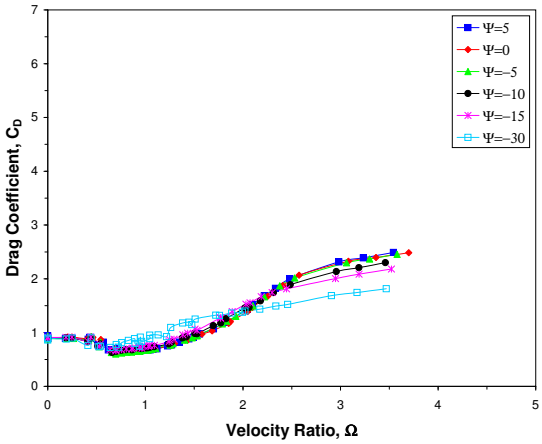

(b) Drag

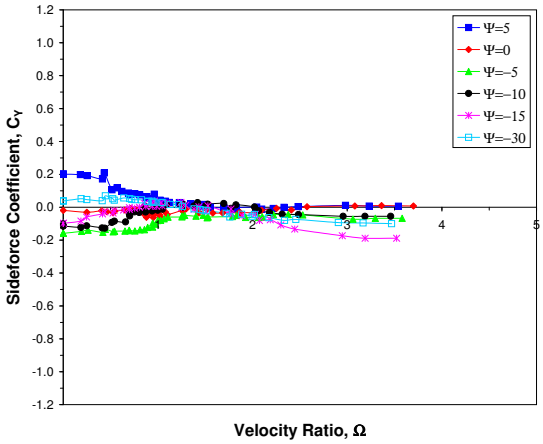

(c) Sideforce

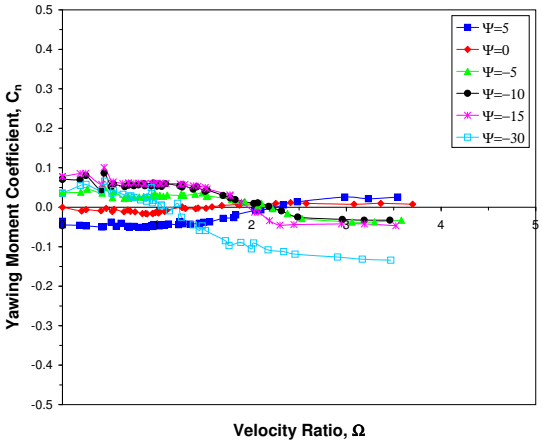

(d) Yawing moment

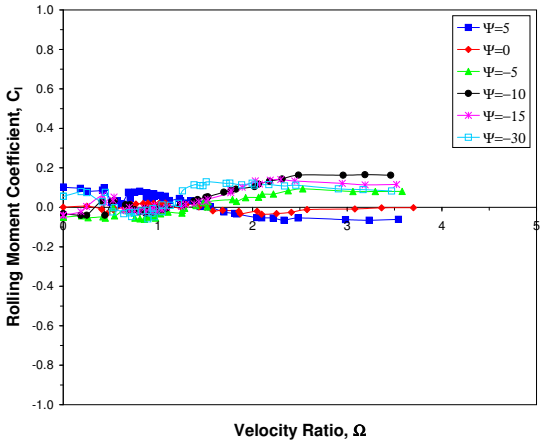

(e) Rolling moment

Figure 5.39: Variation of the aerodynamic forces and moments with velocity ratio for a rotating cylinder having no endplates ($d_e/d = 1$) at non-zero yaw.

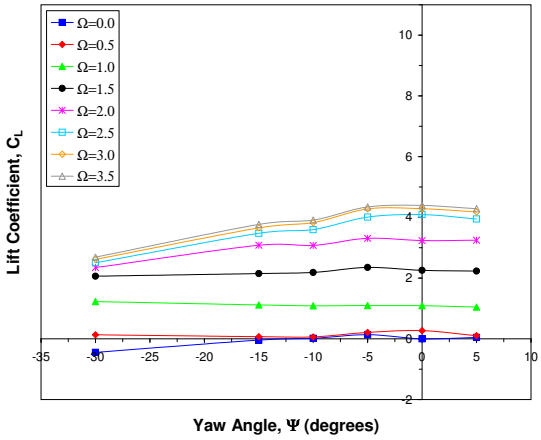

(a) Lift

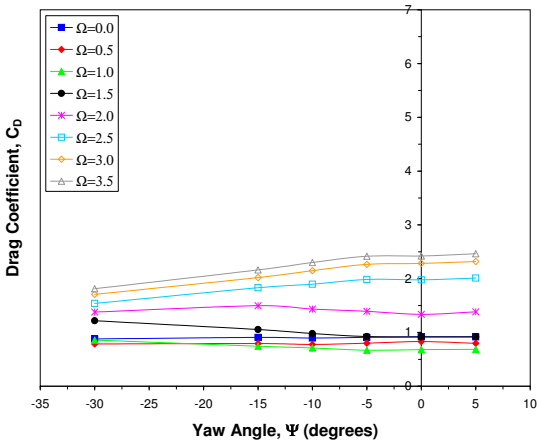

(b) Drag

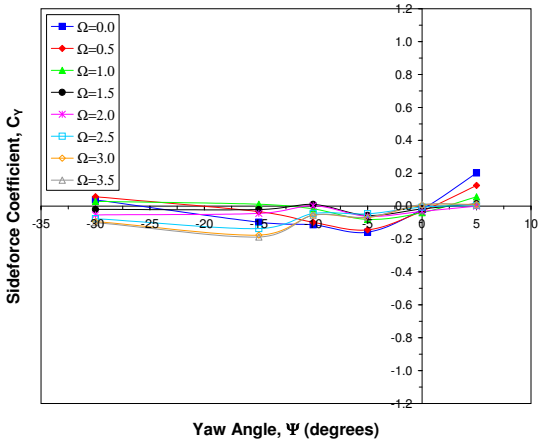

(c) Sideforce

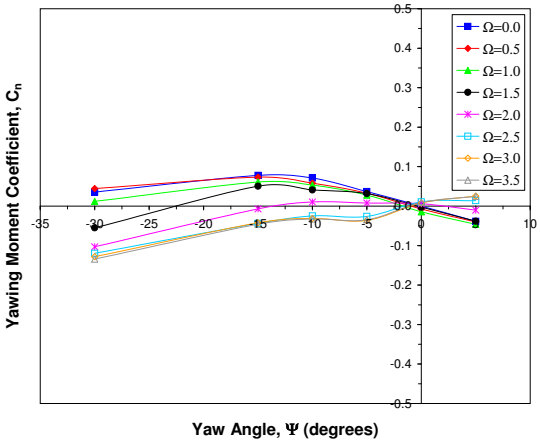

(d) Yawing moment

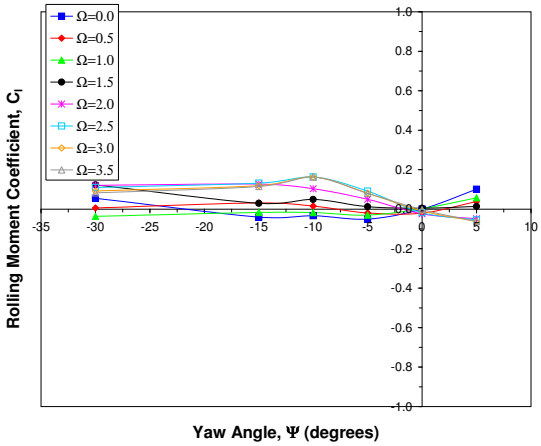

(e) Rolling moment

Figure 5.40: The effects of yaw on the aerodynamic forces and moments on a rotating cylinder with no endplates ($d_e/d = 1$).

In general, the effect of yaw on C_L was to cause a progressive loss of lift as Ψ was increased (see Figures 5.41 and 5.42). This affected the value of the maximum achievable lift coefficient at high velocity ratios but did not change the overall form of the lift curve nor alter the gradient of the linear portions, even for large yaw angles. Increasing yaw angle also caused the reduction in lift to manifest at ever lower velocity ratios, though never below $\Omega = 1.5$. This limit on the influence of yaw held true for all end conditions tested. Consequently, for velocity ratios between $0.5 \leq \Omega \leq 1.5$, the lift was practically unaffected by either yaw angle or endplate configuration, even for $\Psi = -30°$. At higher velocity ratios, the independence of lift from yaw angle was governed by the end conditions.

Symmetric and asymmetric end conditions employing two large endplates were able to delay the majority of the lift loss to higher yaw angles ($|\Psi| > 15°$), but thereafter experienced a rapid and profound reduction of $C_{L_{max}}$ (up to 60% relative to zero yaw). By contrast, configurations using small endplates experienced the lift loss associated with yaw at much lower angles (often as low as $|\Psi| \leq 5°$) but underwent a more gradual reduction in C_L, with a smaller loss of maximum lift (about 40% relative to zero yaw). Note that with one free end the benefits of larger plates began to subside earlier, whilst for $\Omega > 3$ the onset of lift loss always occurred at quite low yaw angles ($|\Psi| \leq 10°$) regardless of end conditions.

Overall, the tests revealed that no configuration of endplates could prevent lift loss at all non-zero yaw angles, and by $\Psi = -30°$ the lift curve for all end conditions was effectively the same. Although larger endplates did, for $\Omega > 1.5$ and high yaw, still produce more lift than with smaller endplates, this extra lift was much less pronounced than at zero yaw. Hence, it may be concluded that increasing the yaw angle reduced the influence of endplate size and arrangement on C_L and that for large yaw angles the lift was now only weakly tied to end configuration.

Despite the overall negative effect of Ψ on lift, increasing the yaw angle caused some end configurations to exhibit a small improvement in C_L at some velocity ratios. The data for all combinations of mismatched plates indicated a fairly prominent increase in lift, relative to zero yaw, when $\Omega > 2$ and $-10° \leq \Psi \leq -5°$. The magnitude of this increase was governed by the relative asymmetry between the two ends and reached a value of $\Delta C_L \approx 0.5$ with the largest asymmetry. Note that this increase was not observed for any configuration with one free end. A much smaller rise in C_L that occurred for all end conditions at $\Omega = 1$ and $\Psi = -30°$ was also indicated by the data; however, this latter effect was small enough that it may simply have been due to experimental error.

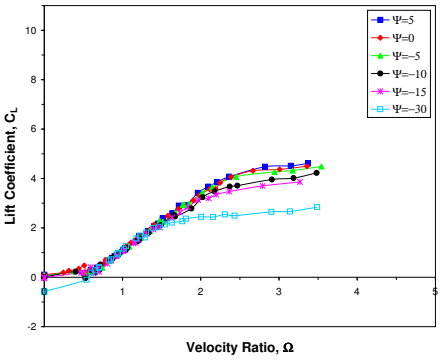

(a) 2 x $d_e/d = 1.1$

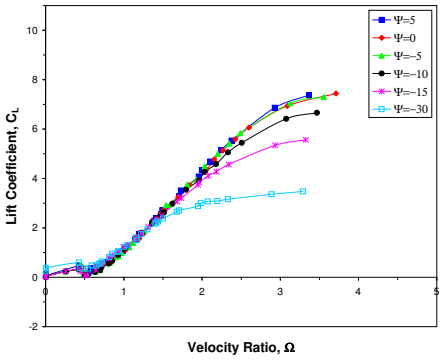

(b) 2 x $d_e/d = 1.5$

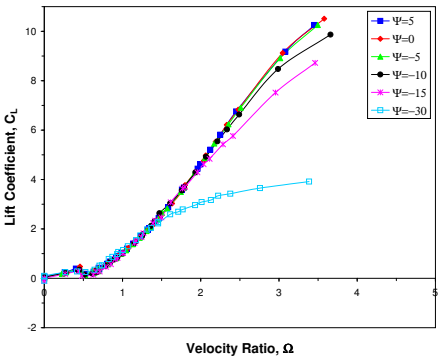

(c) 2 x $d_e/d = 2$

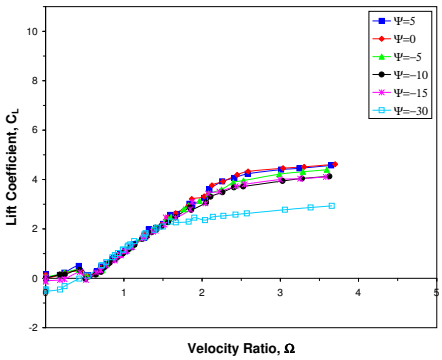

(d) 1 x $d_e/d = 1.1$

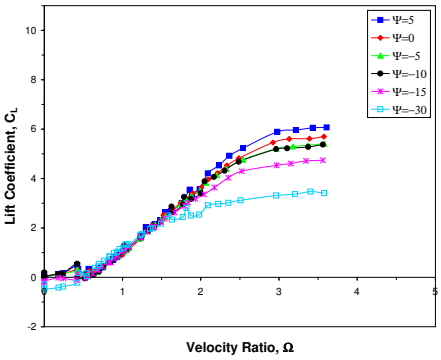

(e) 1 x $d_e/d = 1.5$

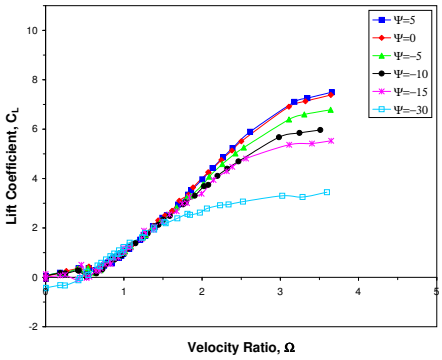

(f) 1 x $d_e/d = 2$

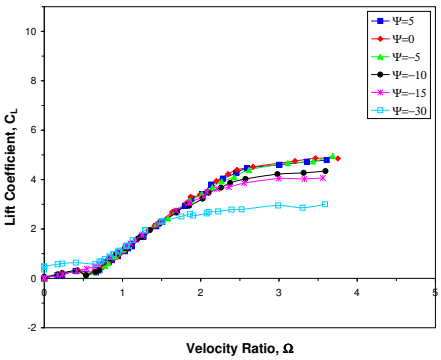

(g) $d_e/d = 1.25$, $d_e/d = 1.1$

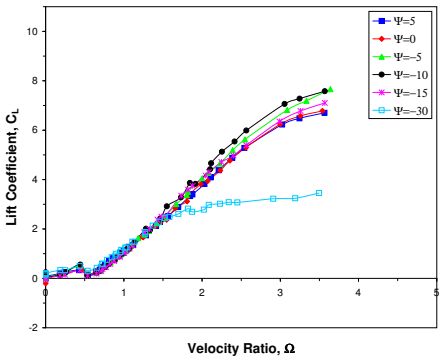

(h) $d_e/d = 2$, $d_e/d = 1.1$

Figure 5.41: The variation of lift with velocity ratio for a rotating cylinder at non-zero yaw.

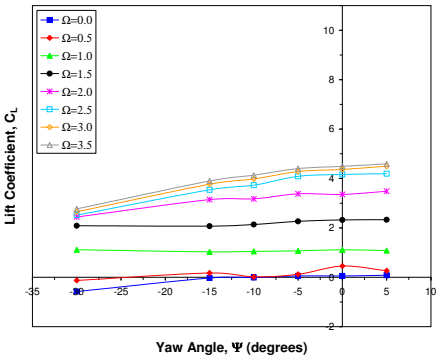

(a) 2 x $d_e/d = 1.1$

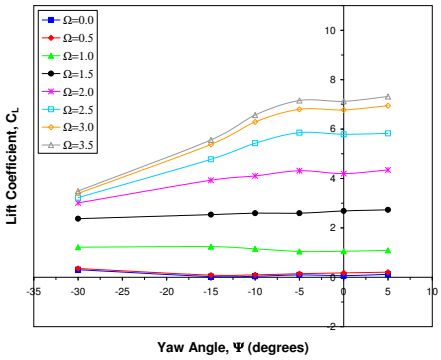

(b) 2 x $d_e/d = 1.5$

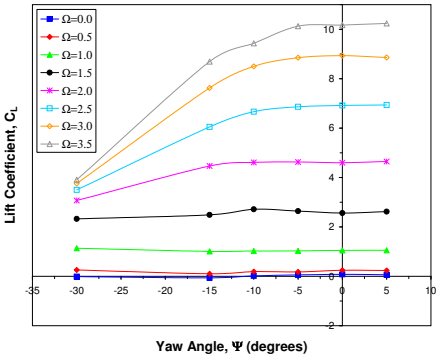

(c) 2 x $d_e/d = 2$

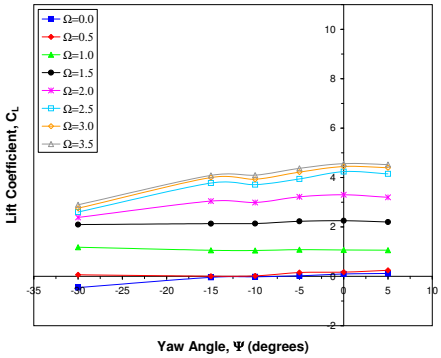

(d) 1 x $d_e/d = 1.1$

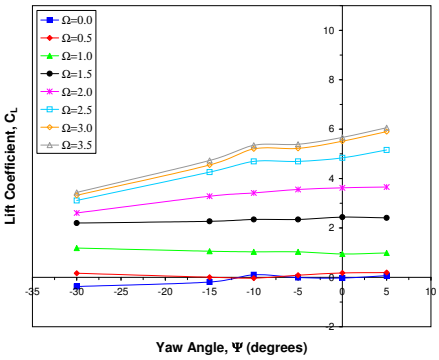

(e) 1 x $d_e/d = 1.5$

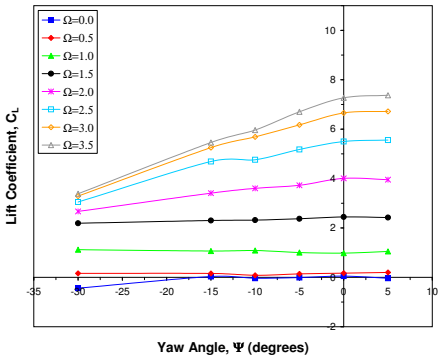

(f) 1 x $d_e/d = 2$

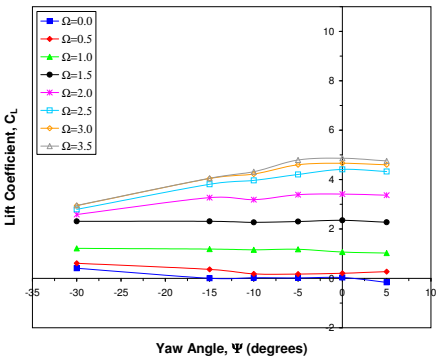

(g) $d_e/d = 1.25$, $d_e/d = 1.1$

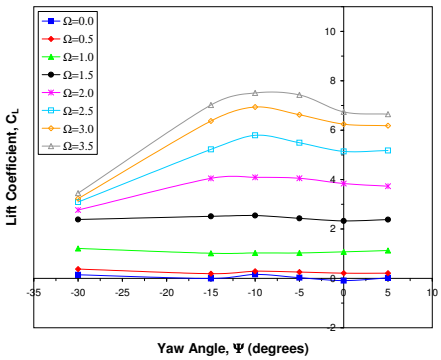

(h) $d_e/d = 2$, $d_e/d = 1.1$

Figure 5.42: The effects of yaw on the lift of a rotating cylinder.

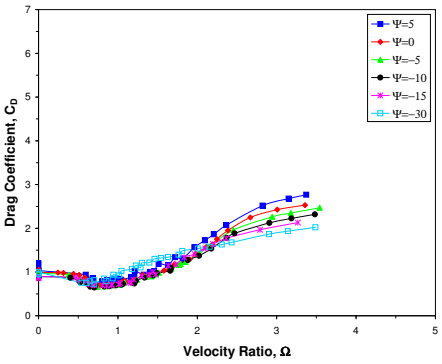

(a) 2 x $d_e/d = 1.1$

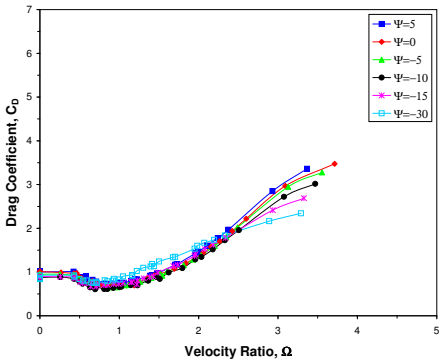

(b) 2 x $d_e/d = 1.5$

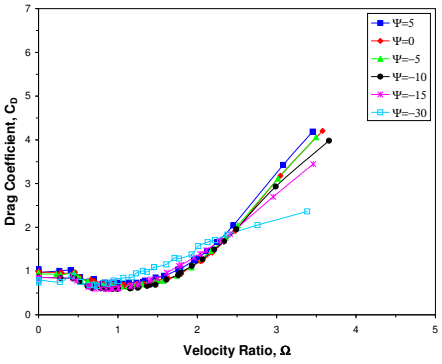

(c) 2 x $d_e/d = 2$

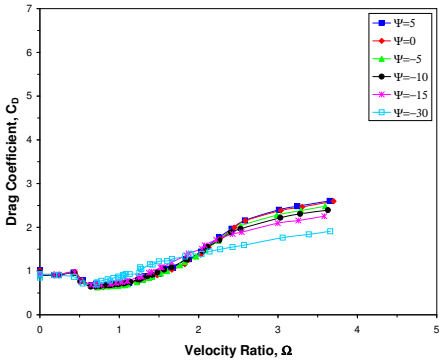

(d) 1 x $d_e/d = 1.1$

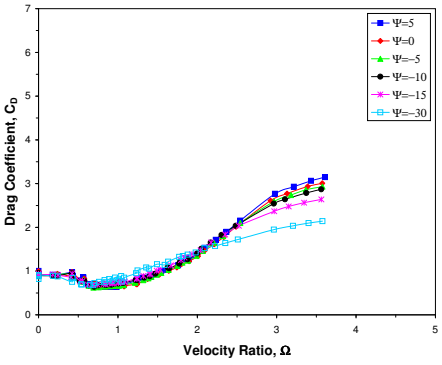

(e) 1 x $d_e/d = 1.5$

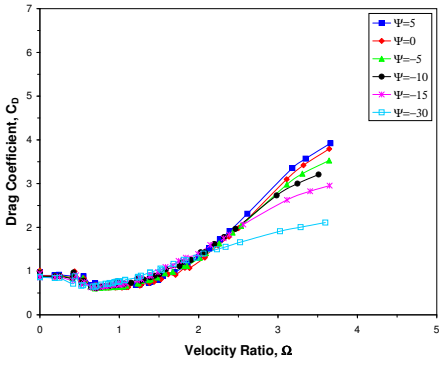

(f) 1 x $d_e/d = 2$

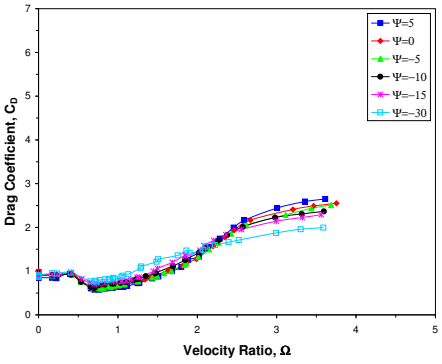

(g) $d_e/d = 1.25$, $d_e/d = 1.1$

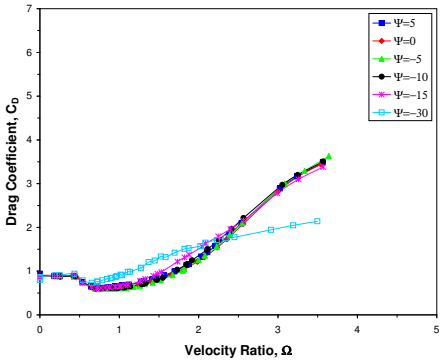

(h) $d_e/d = 2$, $d_e/d = 1.1$

Figure 5.43: The variation of drag with velocity ratio for a rotating cylinder at non-zero yaw.

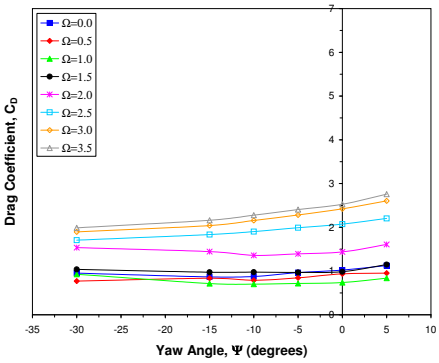

(a) 2 x $d_e/d = 1.1$

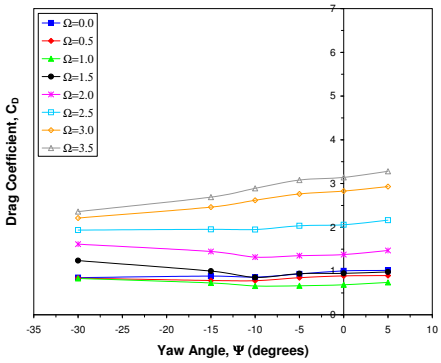

(b) 2 x $d_e/d = 1.5$

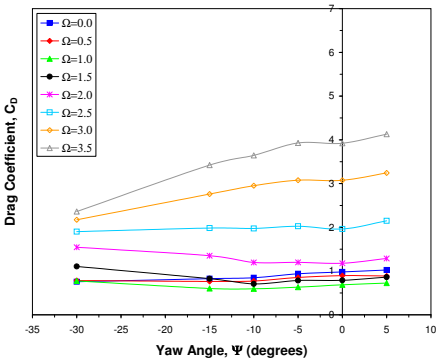

(c) 2 x $d_e/d = 2$

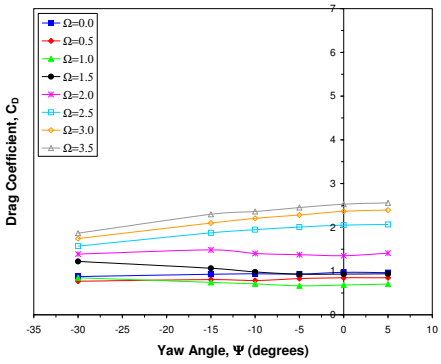

(d) 1 x $d_e/d = 1.1$

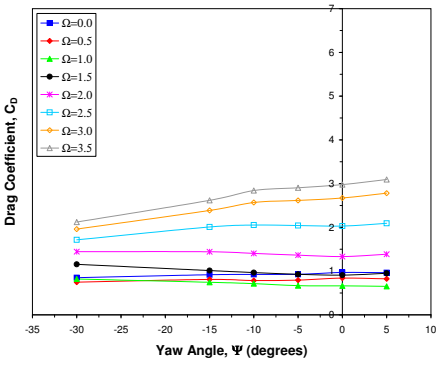

(e) 1 x $d_e/d = 1.5$

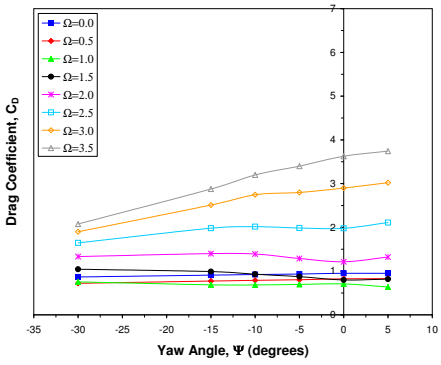

(f) 1 x $d_e/d = 2$

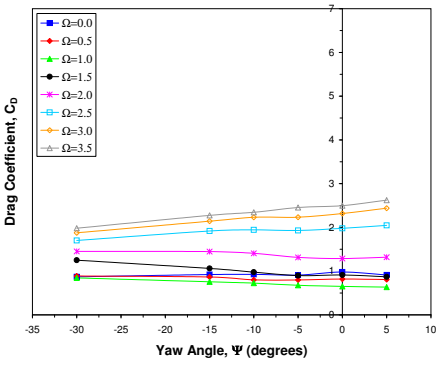

(g) $d_e/d = 1.25$, $d_e/d = 1.1$

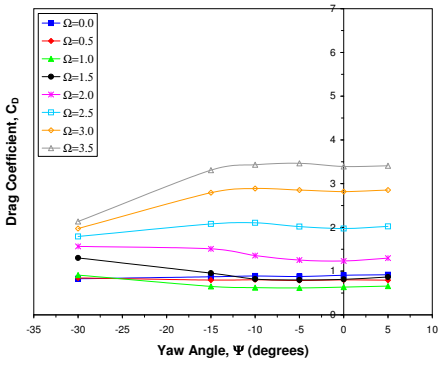

(h) $d_e/d = 2$, $d_e/d = 1.1$

Figure 5.44: The effects of yaw on the drag of a rotating cylinder.

For large yaw angles and high Reynolds numbers ($Re \geq 7 \times 10^4$) there was also a significant change in the lift behaviour at low velocity ratios. For those configurations that had either one free end, two very small endplates ($d_e/d = 1.1$), or two free ends, the lift in the region $\Omega \leq 0.6$ began to decrease in magnitude when $|\Psi| \geq 10°$. Eventually, for $\Psi = -30°$, the lift when the cylinder was stationary was found to be both negative and unexpectedly large ($C_L \approx -0.5$). With rotation of the cylinder the lift coefficient then became gradually less negative until it reached $C_L = 0$ at $\Omega \approx 0.6$. It is also interesting to note that, where the effect occurred, the initial magnitude of the negative lift, and the point at which C_L then became positive, were found to be the same regardless of plate size or arrangement.

A different, possibly related, effect was seen when testing with two mismatched plates of quite small size (both plates of size $d_e/d \leq 1.5$). In these cases, the lift at $\Omega = 0$ and $\Psi = -30°$ was also non-zero, but this time it was positive ($C_L \approx 0.5$). Cylinder rotation then caused C_L to increase slightly before it returned to its expected value at $\Omega \approx 0.6$. It should be noted that neither of the unusual effects seen at low Ω occurred when two equally sized plates of $d_e/d > 1.1$ were used. In those cases, the behaviour for $\Omega < 0.6$ was, regardless of yaw angle, the same Reynolds-dependent loss of lift observed at zero yaw (as seen in Figure 5.17).

Such unexpected changes in the lift curve may be associated with the effects of yaw on the influence of Reynolds number at low velocity ratios. Alternatively, this behaviour could be a result of an interaction between the cylinder flow and the wake of the upstream support strut, which for high yaw angles would impinge on the cylinder as it is swept downstream, possibly interfering with the location of the separation line. Given the geometry of the support structure, any such interference would be most pronounced on only one side of the cylinder, so that an asymmetry in the separation line on the upstream and downstream moving walls would now exist even for $\Omega = 0$, resulting in the noted changes to the lift curve. The use of large endplates would, as was observed, act to prevent such behaviour by shielding the cylinder from the strut wake.

The effects of yaw on the drag coefficient (see Figures 5.43 and 5.44) were largely the same as for the lift and the primary consequence of increasing Ψ was to cause a fall in C_D at high velocity ratio, the extent of which was greater with larger endplates. Other similarities with the lift were also noticeable. The typical level of reduction in the drag at high Ω and high yaw was comparable to the fall in the lift, and the ability of different endplate configurations to delay this reduction to higher yaw angles was the same as noted with C_L. Also, the drag for all end conditions tested was generally found to be independent of yaw for $|\Psi| \leq 10°$. However, unlike the lift, the value of C_D for higher

yaw angles depended on the velocity ratio. Whereas for $\Omega > 2.5$, increasing yaw resulted in the aforementioned fall in C_D, between $1 < \Omega < 2$ further increases in yaw beyond $|\Psi| = 10^\circ$ actually caused an increase in drag (in comparison to the zero yaw case). Interestingly, for most end conditions, the drag between $2 < \Omega < 2.5$ was largely independent of Ψ for all yaw angles tested.

As for C_L, high angles of yaw also reduced the influence of the end conditions on C_D and the drag for $\Psi = -30^\circ$ was largely independent of both endplate size and arrangement. However, whereas the form of the lift curve was unchanged by increasing yaw, the drag curve at $\Psi = -30^\circ$ was of a somewhat different shape to that at lower yaw. For $\Omega \leq 0.6$, the drag curve remained very similar to that for other yaw angles and never displayed any unusual effects due to high Ψ. Beyond this point, the drag for $\Psi = -30^\circ$ began to rise in a more linear fashion and at a much faster rate than for low yaw. This increase continued up to the limits of testing. Despite this change in the variation with velocity ratio, the net effect of high yaw on C_D remained the same: when $1 < \Omega < 2$, the drag at $\Psi = -30^\circ$ was greater than at smaller yaw angles; at higher velocity ratios, the drag was less than for smaller yaw angles, including $\Psi = 0^\circ$.

The results for the yawing moment and rolling moment at non-zero yaw showed that, as when $\Psi = 0^\circ$, the behaviour of C_n and C_l was closely related and the trends in both quantities due to changing Ω, different end conditions, and increasing yaw were quite similar (see Figures 5.45 to 5.48). Except for the largest yaw angles tested, these trends also matched well with some of the behaviour observed at zero yaw. Thus, for most Ψ:

- The yawing moment was generally of opposite sign to the rolling moment and C_n remained approximately half the magnitude of C_l.
- Symmetric end conditions produced yawing and rolling moments of much smaller magnitude than with asymmetric ends.
- The relative asymmetry between the port and starboard ends, along with the arrangement of the endplates about $z/b = 0$, was again more important than actual endplate size.
- Neither endplate size nor arrangement became significant to the effects of yaw on C_n and C_l until plates of size $d_e/d > 1.25$ were employed.

This last point meant that for small d_e/d and low velocity ratios ($\Omega < 1.5$) the response of C_n and C_l to yaw angle was nearly always the same for all end configurations. However, this response was divided into two distinct parts: one for low yaw angles ($-5^\circ \leq \Psi \leq 5^\circ$)

and one for all higher Ψ. In the first region, increasing the yaw angle caused a progressive offset in the value of C_n and C_l at $\Omega = 0$, so that for all non-zero yaw there was a non-zero yawing and rolling moment acting when the cylinder was stationary. The magnitude of these initial moments was primarily governed by yaw angle, changing linearly with Ψ, but also varied slightly with endplate size.

In the second region ($|\Psi| > 5°$, $d_e/d \leq 1.25$, and $\Omega < 1.5$), the linear increase in the yawing and rolling moments seen at low yaw showed a degree of levelling off, reducing the effects of yaw, until $\Psi = -30°$, where there was a slight fall in magnitude of both C_n and C_l. In both regions, increasing the velocity ratio had only a minimal effect on the value of C_n and C_l, though C_l was slightly more susceptible to the influence of Ω and both moments showed greater variation with velocity ratio when the cylinder had asymmetric ends. However, in general, the yawing and rolling moments could be said to remain approximately constant with changing velocity ratio until $\Omega \approx 1.5$.

Examination of the sign of the yawing and rolling moments acting at low Ω showed that C_n was of opposite sign to that of the yaw angle, whereas the initial rolling moment was always of the same sign to Ψ. Thus, for the limited conditions of $-5° \leq \Psi \leq 5°$ and $\Omega < 1.5$, but irrespective of end configuration, the gradient $dC_n/d\Psi$ was always negative and $dC_l/d\Psi$ always positive. From these terms, the important stability derivatives $dC_n/d\beta$ and $dC_l/d\beta$ were assessed on the basis that, for a wind tunnel test of a body under yaw, the relationship between the sideslip and yaw angles is given by $\beta = -\Psi$. Consequently, $dC_n/d\beta$ was positive at low Ω and low Ψ and $dC_l/d\beta$ was negative. This shows that for these conditions the isolated rotating cylinder possessed both directional and lateral stability (i.e. the cylinder was statically stable to both disturbances in yaw and roll). Note that the magnitudes of $dC_n/d\beta$ and $dC_l/d\beta$ in this region were found to be very similar, but were slightly dependent on the end conditions.

With further increases in velocity ratio beyond $\Omega = 1.5$ the effect on the yawing and rolling moment was no longer the same for all end conditions, even for $-5° \leq \Psi \leq 5°$, and was now dependent on endplate size and arrangement. With symmetric ends, the response to yaw was again divided into two regions, one for $|\Psi| \leq 5°$ and one for all higher yaw angles. The behaviour of C_n and C_l in these two regions was largely the same as for $\Omega < 1.5$. However, at low yaw, both $dC_n/d\Psi$ and $dC_l/d\Psi$ had now changed sign, and for all yaw angles, the velocity ratio now had much more of an effect than at low Ω. For $\Omega > 1.5$, increasing the velocity ratio caused a linear change in the magnitude of C_n and C_l, which was greater with larger d_e/d, until a plateau was reached for $\Omega \geq 3$. The magnitude of the yawing and rolling moments on this plateau was dependent on both Ψ and endplate size.

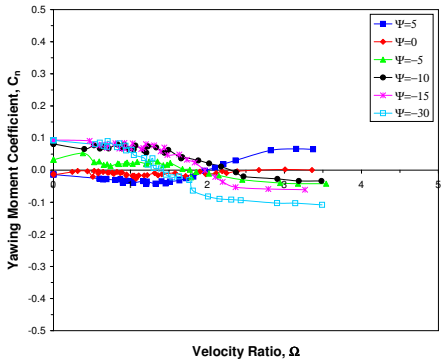

(a) 2 x $d_e/d = 1.1$

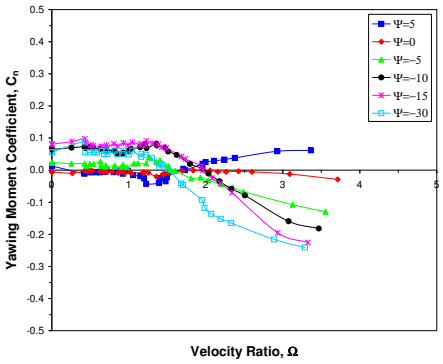

(b) 2 x $d_e/d = 1.5$

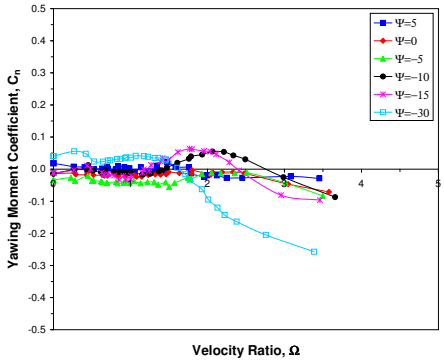

(c) 2 x $d_e/d = 2$

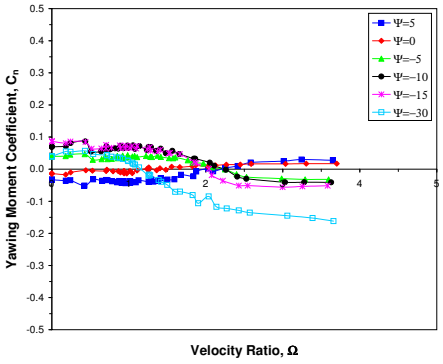

(d) 1 x $d_e/d = 1.1$

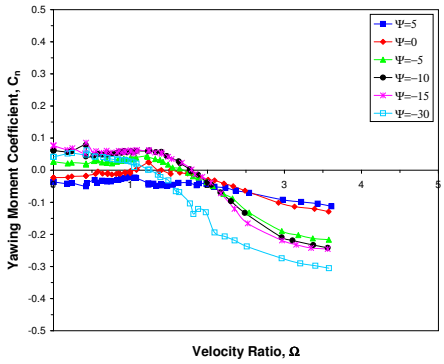

(e) 1 x $d_e/d = 1.5$

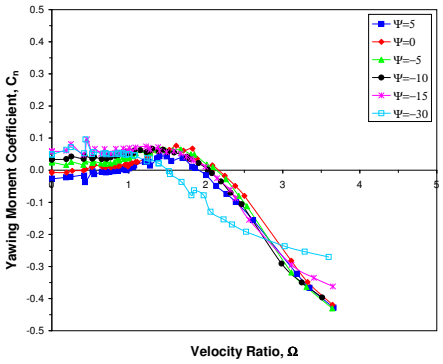

(f) 1 x $d_e/d = 2$

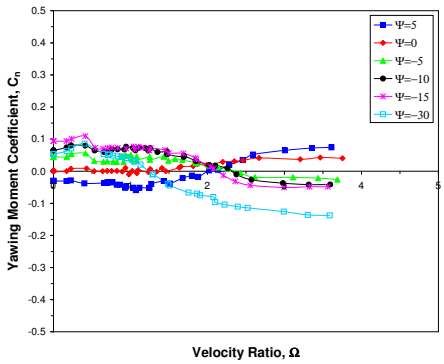

(g) $d_e/d = 1.25$, $d_e/d = 1.1$

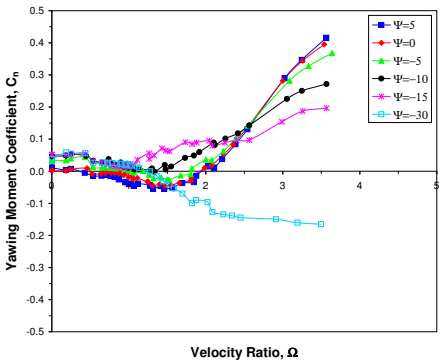

(h) $d_e/d = 2$, $d_e/d = 1.1$

Figure 5.45: The variation of yawing moment with velocity ratio for a rotating cylinder at non-zero yaw.

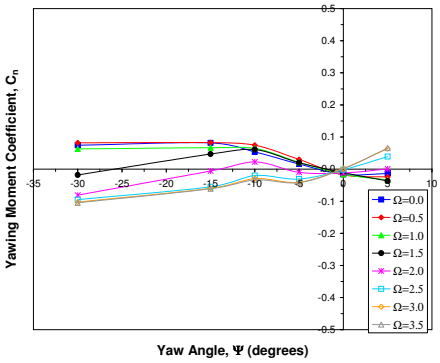

(a) 2 x $d_e/d = 1.1$

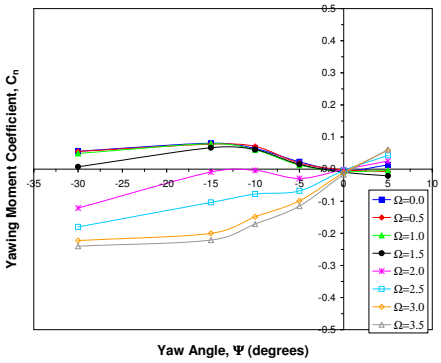

(b) 2 x $d_e/d = 1.5$

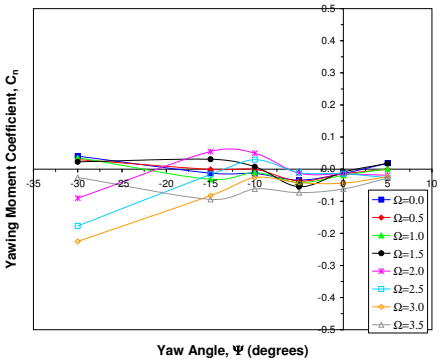

(c) 2 x $d_e/d = 2$

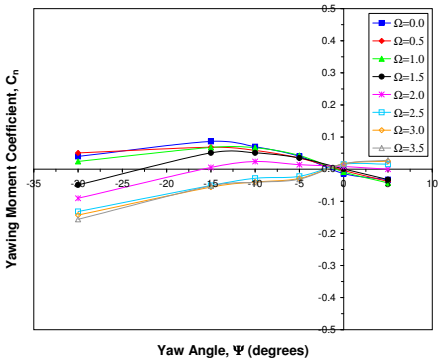

(d) 1 x $d_e/d = 1.1$

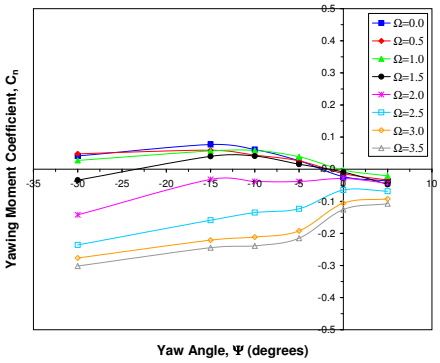

(e) 1 x $d_e/d = 1.5$

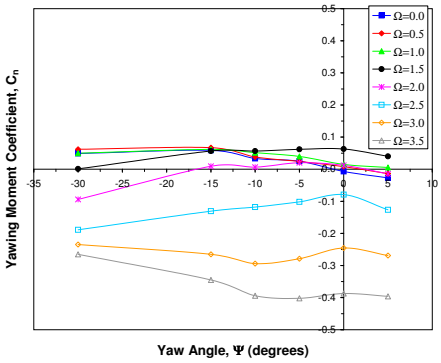

(f) 1 x $d_e/d = 2$

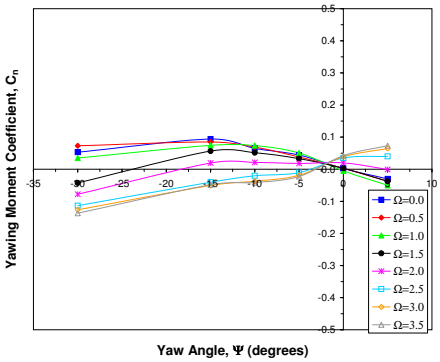

(g) $d_e/d = 1.25$, $d_e/d = 1.1$

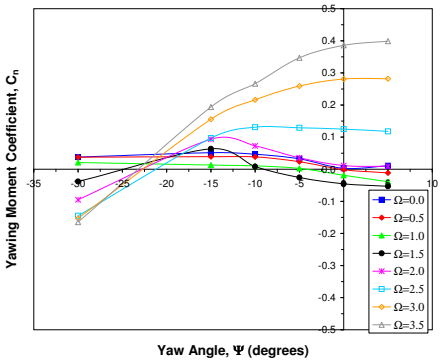

(h) $d_e/d = 2$, $d_e/d = 1.1$

Figure 5.46: The effects of yaw on the yawing moment on a rotating cylinder.

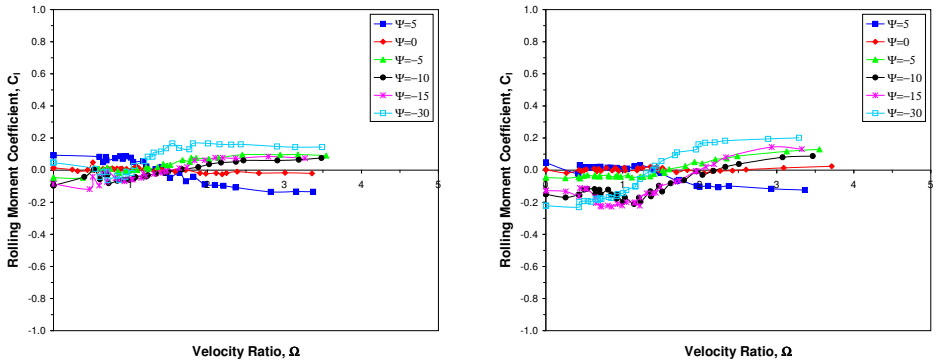

(a) 2 x $d_e/d = 1.1$ (b) 2 x $d_e/d = 1.5$

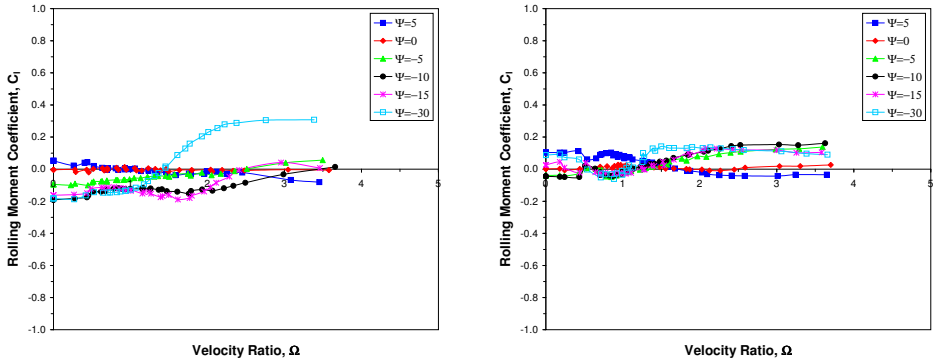

(c) 2 x $d_e/d = 2$ (d) 1 x $d_e/d = 1.1$

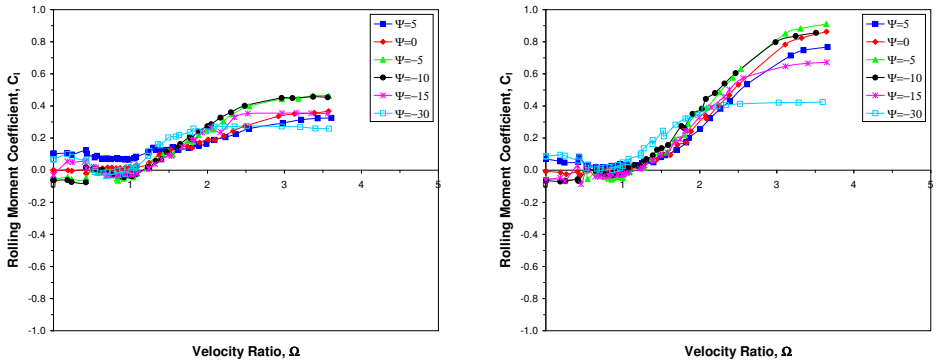

(e) 1 x $d_e/d = 1.5$ (f) 1 x $d_e/d = 2$

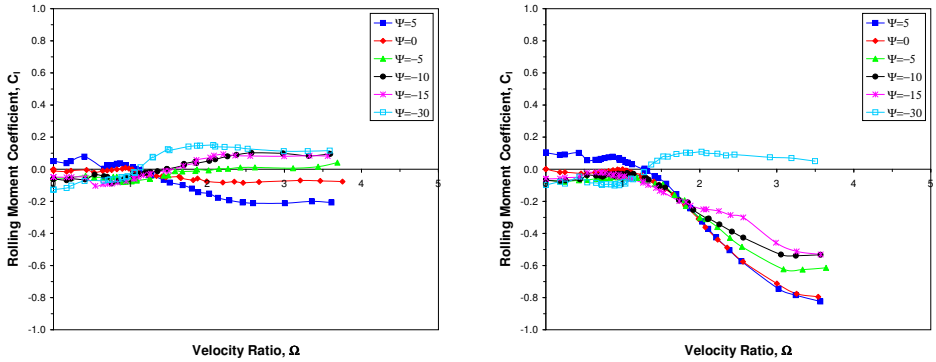

(g) $d_e/d = 1.25$, $d_e/d = 1.1$ (h) $d_e/d = 2$, $d_e/d = 1.1$

Figure 5.47: The variation of rolling moment with velocity ratio for a rotating cylinder at non-zero yaw.

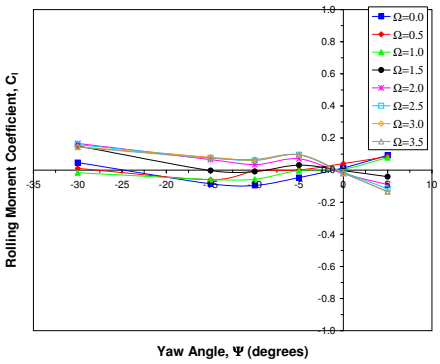

(a) 2 x $d_e/d = 1.1$

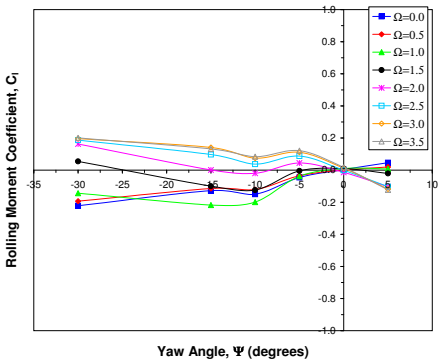

(b) 2 x $d_e/d = 1.5$

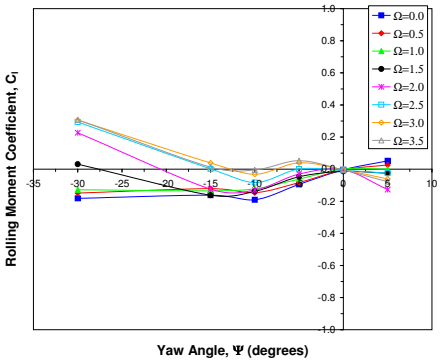

(c) 2 x $d_e/d = 2$

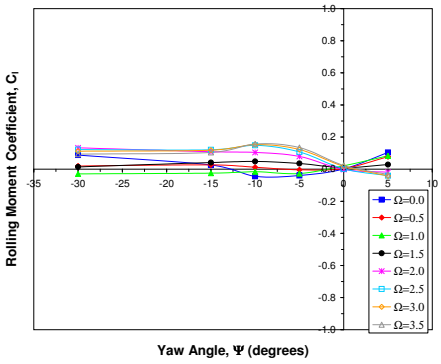

(d) 1 x $d_e/d = 1.1$

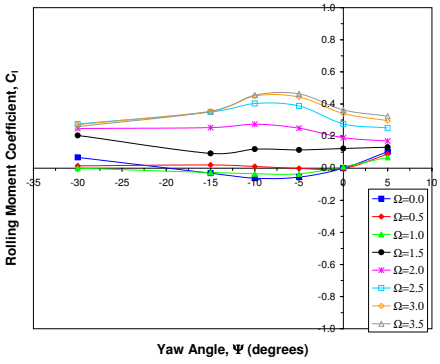

(e) 1 x $d_e/d = 1.5$

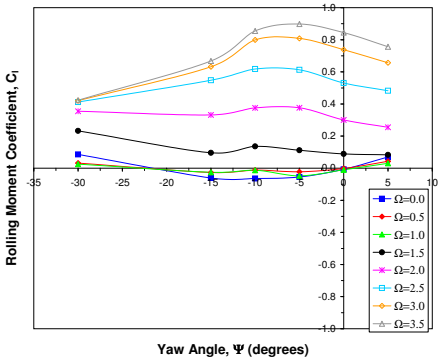

(f) 1 x $d_e/d = 2$

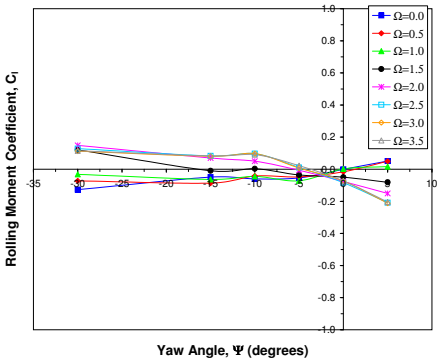

(g) $d_e/d = 1.25$, $d_e/d = 1.1$

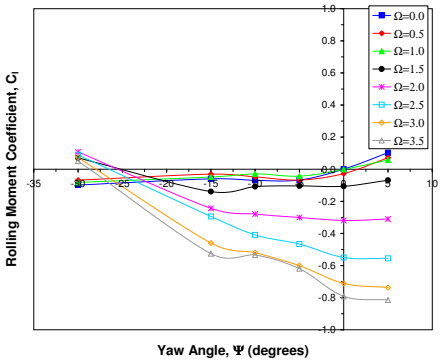

(h) $d_e/d = 2$, $d_e/d = 1.1$

Figure 5.48: The effects of yaw on the rolling moment on a rotating cylinder.

This change in the signs of the gradients $dC_n/d\Psi$ and $dC_l/d\Psi$ meant that for most Ψ there was a particular velocity ratio at which the magnitudes of $dC_n/d\beta$ and $dC_l/d\beta$ were zero, so marking the boundary between the cylinder being statically stable and unstable in yaw and roll. This transition point was generally the same for all $|\Psi| \leq 15^\circ$ and typically occurred somewhere between $1.5 \leq \Omega \leq 2.5$ for both the rolling moment and yawing moment. For symmetric end conditions this point also coincided with C_n and C_l being very close to zero magnitude. Thus, at this point, the yawing and rolling moments were independent of yaw angle and the rotating cylinder could be said to be trimmed, but it had only neutral directional and lateral stability. Such a trim point was not present in the results for higher yaw ($\Psi = -30^\circ$) and was also missing from the results with large endplates ($d_e/d = 2$), which for the yawing moment were significantly different to those with smaller plates and were possibly in error.

With one free end and an endplate of size $d_e/d < 1.5$ the response of the yawing and rolling moments to yaw for $\Omega > 1.5$ remained largely the same as with symmetric ends and a point of independence from yaw again occurred at $\Omega \approx 2$. However, the magnitudes of both C_n and C_l at this point were generally non-zero and became larger with increasing d_e/d. With a single endplate of size $d_e/d \geq 1.5$, the form of the yawing and rolling moment curves was also very different and there was now a linear increase in C_n and C_l for all $\Omega > 1.5$, much like that observed at zero yaw (see Figure 5.25). The nature of this increase was generally the same for all yaw angles tested, but became more rapid as d_e/d increased. The yawing and rolling moments with these end conditions were thus largely independent from the yaw angle for all $\Omega \geq 2$. The response with mismatched endplates was similar to one free end, but the effects of yaw at high velocity ratio and the influence of velocity ratio at low yaw were much more apparent than with the other types of end configuration.

In addition, the results for a yawed cylinder with mismatched endplates also revealed that the use of this type of asymmetric end condition caused the yaw angle at which both C_n and C_l were independent from velocity ratio to change. With symmetric endplates the results showed this condition to occur at $\Psi = 0^\circ$ (see Figure 5.23). With mismatched endplates, the point of independence from velocity ratio was seen to move to ever higher yaw angles as the asymmetry between the two ends increased. Thus, with two similar sized, but not equal, endplates the point of independence from Ω occurred close to $\Psi = 0^\circ$ (typically at $\Psi \approx -2.5^\circ$). With a large difference between the two plate sizes, this point now occurred at $\Psi \approx -20^\circ$. By contrast the data obtained with one free end showed a point of independence from velocity ratio to only occur at $\Psi = 0^\circ$ and only when using a small endplate ($d_e/d \leq 1.25$). For larger d_e/d, the yawing and rolling moments with one free end were never completely independent of velocity ratio.

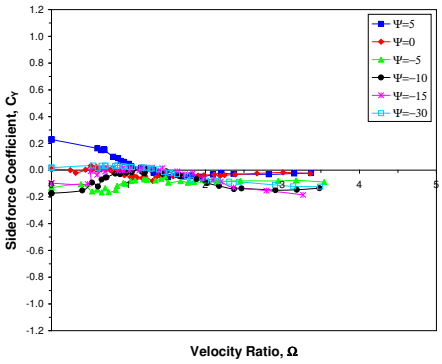

(a) 2 x $d_e/d = 1.1$

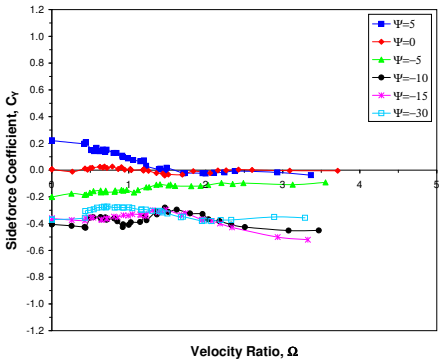

(b) 2 x $d_e/d = 1.5$

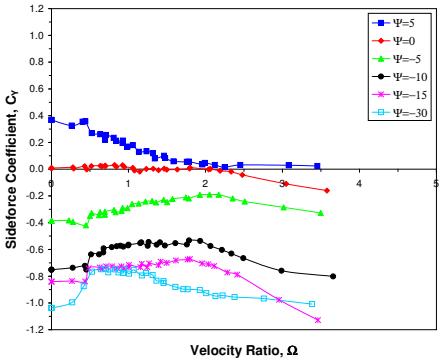

(c) 2 x $d_e/d = 2$

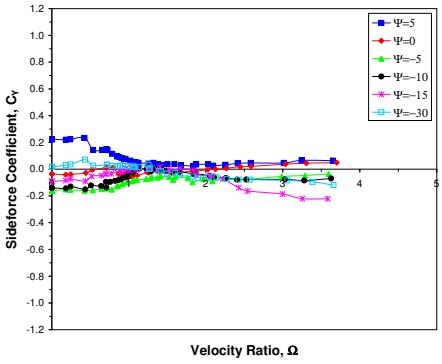

(d) 1 x $d_e/d = 1.1$

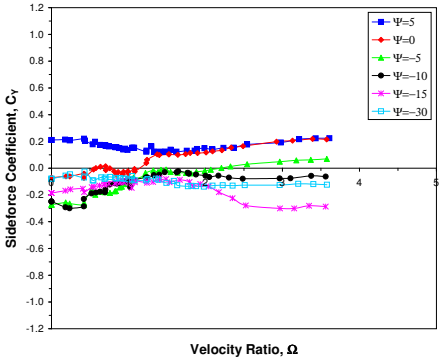

(e) 1 x $d_e/d = 1.5$

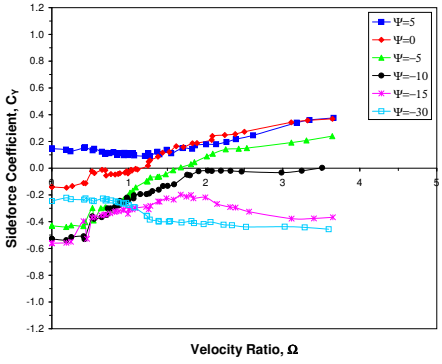

(f) 1 x $d_e/d = 2$

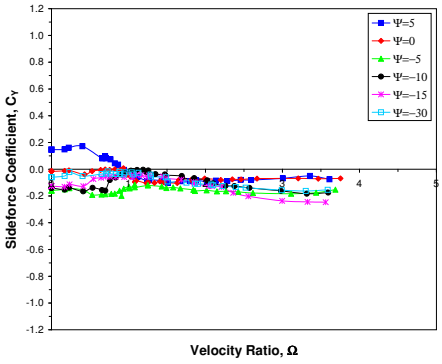

(g) $d_e/d = 1.25$, $d_e/d = 1.1$

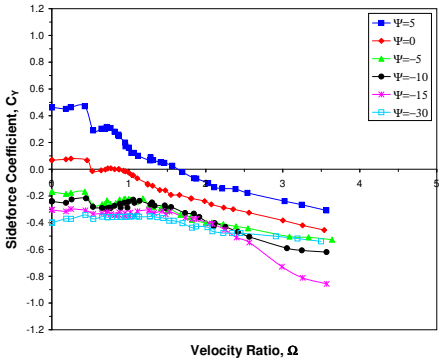

(h) $d_e/d = 2$, $d_e/d = 1.1$

Figure 5.49: The variation of sideforce with velocity ratio for a rotating cylinder at non-zero yaw.

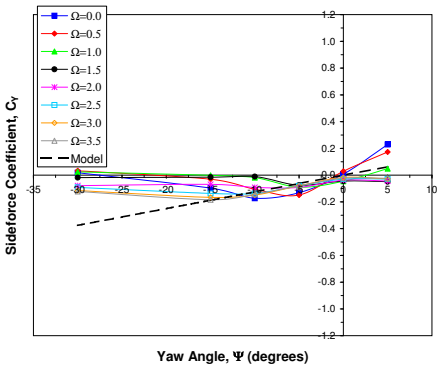

(a) 2 x $d_e/d = 1.1$

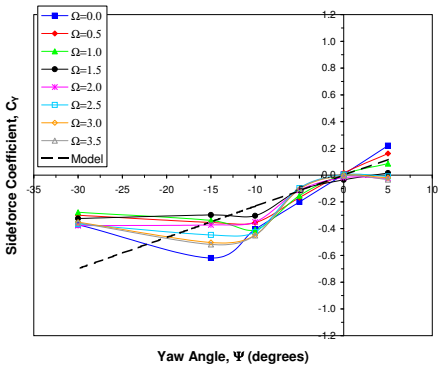

(b) 2 x $d_e/d = 1.5$

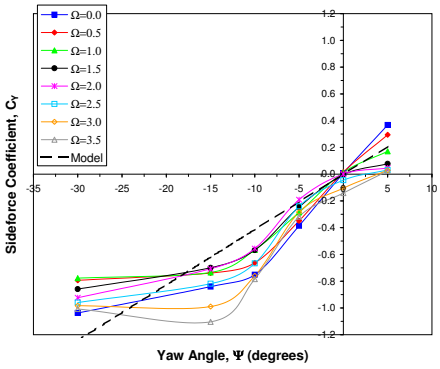

(c) 2 x $d_e/d = 2$

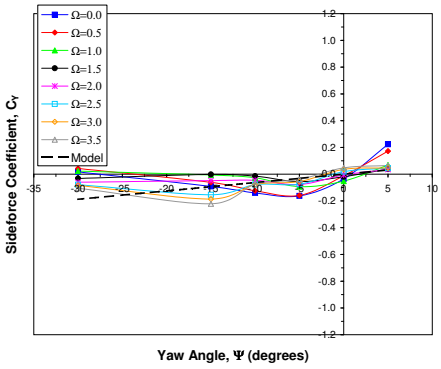

(d) 1 x $d_e/d = 1.1$

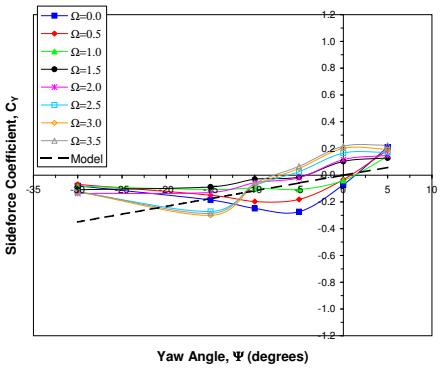

(e) 1 x $d_e/d = 1.5$

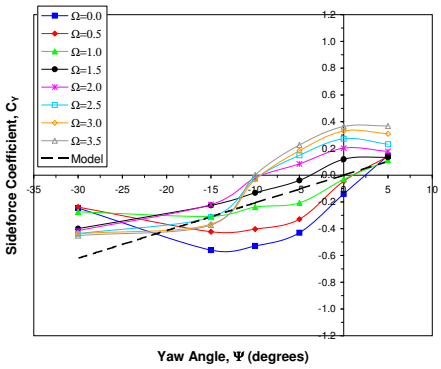

(f) 1 x $d_e/d = 2$

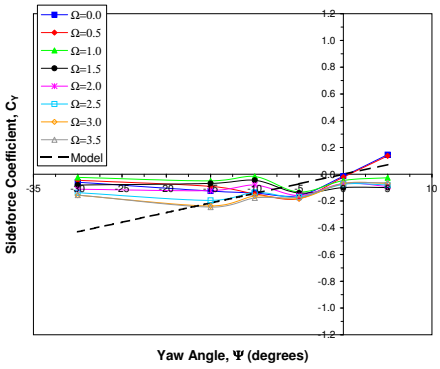

(g) $d_e/d = 1.25$, $d_e/d = 1.1$

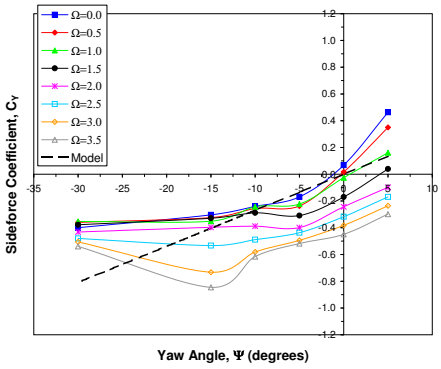

(h) $d_e/d = 2$, $d_e/d = 1.1$

Figure 5.50: The effects of yaw on the sideforce on a rotating cylinder.

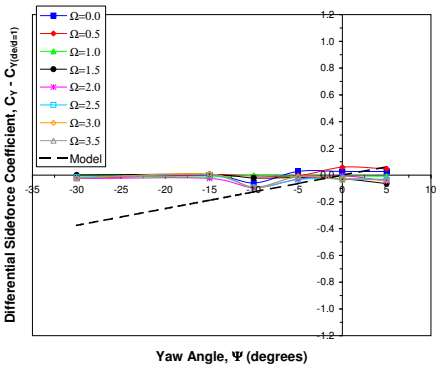

(a) 2 x $d_e/d = 1.1$

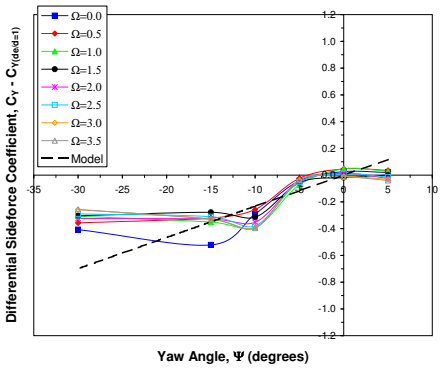

(b) 2 x $d_e/d = 1.5$

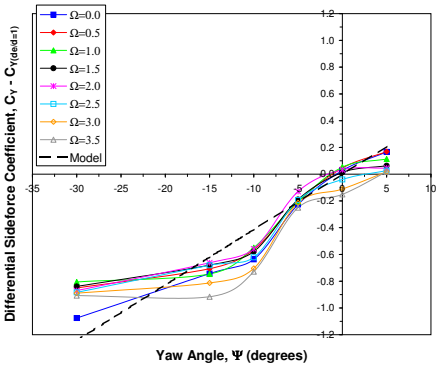

(c) 2 x $d_e/d = 2$

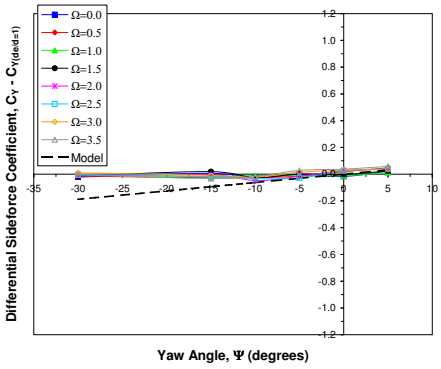

(d) 1 x $d_e/d = 1.1$

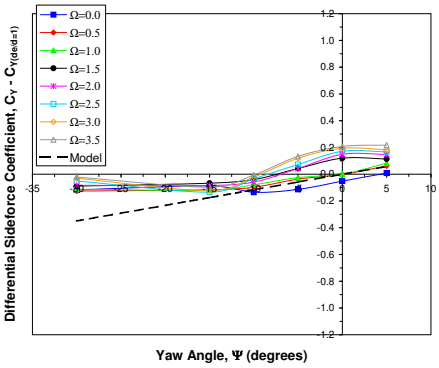

(e) 1 x $d_e/d = 1.5$

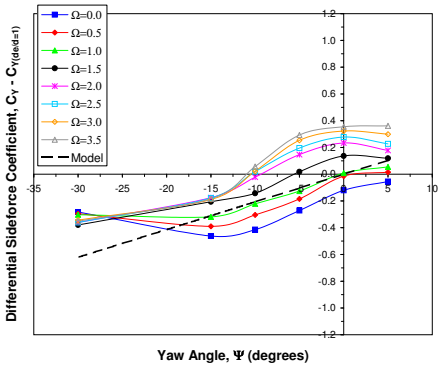

(f) 1 x $d_e/d = 2$

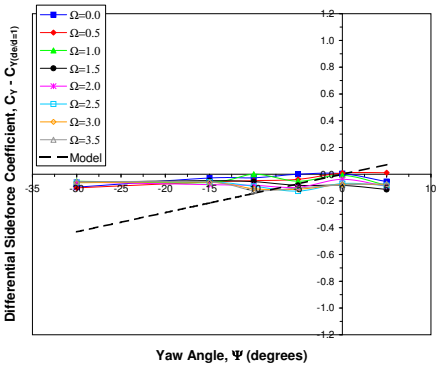

(g) $d_e/d = 1.25$, $d_e/d = 1.1$

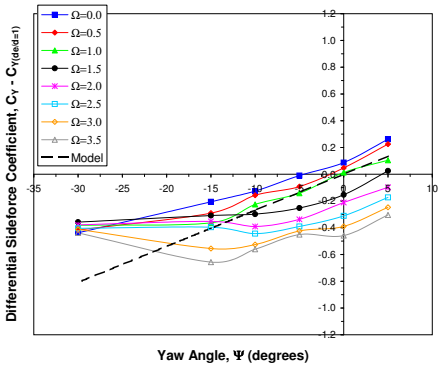

(h) $d_e/d = 2$, $d_e/d = 1.1$

Figure 5.51: Endplate influence on the sideforce on a rotating cylinder at non-zero yaw.

As with the lift and drag, the variation of C_n and C_l with velocity ratio at $\Psi = -30°$ was also somewhat different from that at lower yaw. However, unlike for C_L and C_D, the influence of d_e/d remained quite substantial at high yaw and the exact nature of the changes in the yawing and rolling moments was tied to the end conditions. It is also interesting to note that for $|\Psi| \geq 15°$ the trends in C_n and C_l were no longer quite so similar and the difference in magnitude between the two moments was much reduced. In addition, the shape of the curve of C_n versus Ω approximated that of the drag curve at the same Ψ, whilst the rolling moment curve generally showed a similarity with the lift curve shape at high yaw. This is in keeping with the notion that the yawing and rolling moment are driven by the drag and lift respectively. The results at high yaw also showed that, beyond $|\Psi| = 15°$, the effects of yaw tended to cause a change in both $dC_n/d\Psi$ and $dC_l/d\Psi$ at a given velocity ratio. This often resulted in a change in sign of either the generated moment, the gradient, or sometimes both.

The sideforce behaviour under yaw (see Figures 5.49 and 5.50) was found to be a cross between the response of the lift and drag to non-zero Ψ and that of the lateral moments. Specific similarities with C_L and C_D were apparent in the way that the form of the curve of C_Y against Ω for all non-zero yaw remained nearly the same with both symmetric and asymmetric end conditions and was not significantly altered by increasing d_e/d. In addition, like C_L and C_D, the magnitude of C_Y was more strongly governed by endplate size rather than arrangement (with the influence of d_e/d being stronger when $|\Psi| \geq 10°$) and there was only a minor change in the variation of C_Y with velocity ratio when $|\Psi| > 15°$. Interestingly, the initial sideforce at $\Omega = 0$ for $\Psi = -30°$ was typically less than that at lower yaw angles, indicating that high yaw actually decreased the sideforce.

In accordance with the results for the other forces and moments, the sideforce response to yaw when the cylinder was fitted with small endplates ($d_e/d \leq 1.25$) was unaffected by either plate size or arrangement and was largely the same as that observed with no endplates. However, overall, the variation of C_Y with yaw angle was more in keeping with that of the yawing and rolling moments. As with the lateral moments, the sideforce response to yaw for small d_e/d was split into low ($-5° \leq \Psi \leq 5°$) and high ($|\Psi| > 5°$) yaw regions that were similar in nature to those observed in the results for C_n and C_l.

Thus, in the first region, increasing the yaw angle caused a highly linear increase in the sideforce, whereas in the second region, the sideforce was much less strongly tied to yaw angle. At both high and low Ψ, the magnitude of $dC_Y/d\Psi$ for $\Omega < 1.5$ was generally independent of velocity ratio. In addition, as with the yawing and rolling moment behaviour, a point of sideforce independence from yaw angle occurred at $\Omega \approx 1.5$, which with symmetric end conditions also coincided with a near-zero magnitude of C_Y. For

higher velocity ratios there was then a change in the sign of $dC_Y/d\Psi$.

For $d_e/d > 1.25$ and symmetric end conditions there were still two regions of linear increase of sideforce with yaw angle, but the extent of the first region was made greater with larger d_e/d, doubling in size to between $-10° \leq \Psi \leq 5°$ when the cylinder was fitted with two endplates of size $d_e/d = 2$, and the magnitude of $dC_Y/d\Psi$ was increased too. In the second region, the gradient $dC_Y/d\Psi$ was again considerably shallower than at low yaw, and for $\Omega \geq 2.5$ it changed sign. With asymmetric end conditions and $d_e/d > 1.25$, the sideforce response to yaw was much more complex, being more dependent on the velocity ratio and generally no longer wholly linear. In addition, the magnitude of $dC_Y/d\Psi$ at a given Ω was smaller than with symmetric endplates, suggesting that asymmetric end conditions tended to reduce the influence of Ψ on the sideforce. For all configurations using large endplates, a point of independence from yaw angle typically occurred near $\Omega \approx 2$, but only for $|\Psi| \geq 15°$. As with the lateral moments, the magnitude of C_Y at this point was, for large d_e/d, always non-zero, even with symmetric end conditions.

Since the sideforce showed a greater sensitivity to increasing yaw angle, this meant that the gradient $dC_Y/d\Psi$ was typically larger than both $dC_n/d\Psi$ and $dC_l/d\Psi$, and the magnitude of C_Y at most velocity ratios, which had been significantly smaller than C_n and C_l when $\Psi = 0°$, was now much greater than both the lateral moments, being up to ten times larger at the highest yaw angles tested. Despite this change, the relationship between the sign of C_Y and that of the lateral moments remained the same as at zero yaw: the sideforce was typically of the same sign as the rolling moment but of opposite sign to the yawing moment. This also meant that $dC_Y/d\Psi$ was positive and the stability derivative $dC_Y/d\beta$ negative. Whilst $dC_Y/d\beta$ is usually also negative for a conventional wing too, the magnitude of this derivative for the rotating cylinder was much greater than for a typical wing, especially with large endplates.

The sideforce results for all non-zero yaw angles and all end conditions also showed that, for $\Omega \leq 0.5$, the sideforce exhibited the same sort of change in the curve of C_Y against Ω as seen in the other force and moment data at low velocity ratio. This low-Ω change was typically more pronounced than for the lateral moments, and became even greater with asymmetric end conditions, particularly at low yaw. More generally, for $\Omega \leq 1$, the initial effect of increasing Ω was to reduce the magnitude of C_Y so that it fell below its value at $\Omega = 0$. For most yaw angles, a further change in the variation of C_Y with velocity ratio was seen to begin at $\Omega \approx 1.5$ and may have been related to the changes in the lift and drag coefficients that occur at the same velocity ratio. The sideforce behaviour for higher velocity ratios ($\Omega \geq 2$) was largely the same for all yaw angles but was dependent on the endplate size and arrangements. For some conditions (small d_e/d or any symmetric end

arrangements), the sideforce at high velocity ratio was nearly constant with increasing Ω. With asymmetric ends and large d_e/d, the sideforce continued to change with Ω.

The influence of the endplates on the sideforce generated by the cylinder may be further examined by comparing the measured variation of C_Y with Ψ against values for the endplates in isolation, as estimated from a simple analytical model in which the endplates at non-zero yaw are treated as circular wings at an angle of attack. In this analysis, the contribution to the sideforce coefficient from a single endplate may be calculated as:

$$C_Y = \frac{\pi C_L}{4AR}\left(\frac{d_e}{d}\right)^2 \tag{5.26}$$

where C_L is the lift coefficient for the circular endplate-wing (as based on the endplate's planform area) and C_Y is the equivalent sideforce coefficient (as based on the cylinder's reference area).

The value of C_L at a given yaw angle was estimated using experimental data for non-rotating circular planform wings of similar thickness-chord ratio to the endplates.[60] These results suggested a value for the lift curve slope of $dC_L/d\Psi \approx 1.91$ per radian, so that $|C_L| \approx 0.5$ when $|\Psi| = 15°$. This value was then used to calculate the gradient $dC_Y/d\Psi$ for each endplate configuration so that the predicted variation of C_Y with Ψ could be plotted. The results of this process are shown in Figure 5.50, alongside the measured sideforce coefficients, and in Figure 5.51, where the predicted values of C_Y due to the endplates alone are compared to the difference between the measured C_Y for a given end configuration and that for $d_e/d = 1$ at the same yaw angle (as shown in Figure 5.40).

This comparison, in particular the results of Figure 5.51, generally reveals good agreement between measured values of the magnitude of C_Y and the gradient $dC_Y/d\Psi$ and those predicted for the equivalent endplates-alone case, but only when $|\Psi| \leq 10°$ and $\Omega \leq 1$. With increasing Ω, and at higher yaw angles, particularly $|\Psi| \geq 15°$, the measured results differ greatly from the endplates-alone model. For high yaw angles these differences may be associated, at least in part, with endplate stall, which was not modelled in the analysis. However, the change in the variation of sideforce with yaw angle that occurs when $|\Psi| \geq 15°$ also appears in the results with no endplates, and so may be intrinsic to a rotating cylinder. The effects of increasing Ω, most likely coupled with cylinder-endplate interactions and the influence of the cylinder itself, are seen to introduce significant nonlinearity to the variation of C_Y with Ψ, particularly for large d_e/d or a large asymmetry between port and starboard end conditions. For these cases, the magnitude of C_Y can also be substantially greater than that predicted for the endplates alone.

6 Tests on a Rotating Cylinder Mini-UAV

Following on from the experiments with the isolated cylinder, a second programme of wind tunnel tests was undertaken to investigate the aerodynamic performance of a near-full-scale model of a mini-UAV based around rotating cylinders. These tests addressed questions about the best configuration of such an aircraft by examining how the behaviour of the rotating cylinders changed when they were part of a complete vehicle configuration and exploring the interaction between the cylinders and the other components of the design. This section provides a detailed description of the test model, together with an overview of the experiments conducted, the methods of analysis of the data, and a discussion of the ensuing results.

6.1 Experimental Arrangements

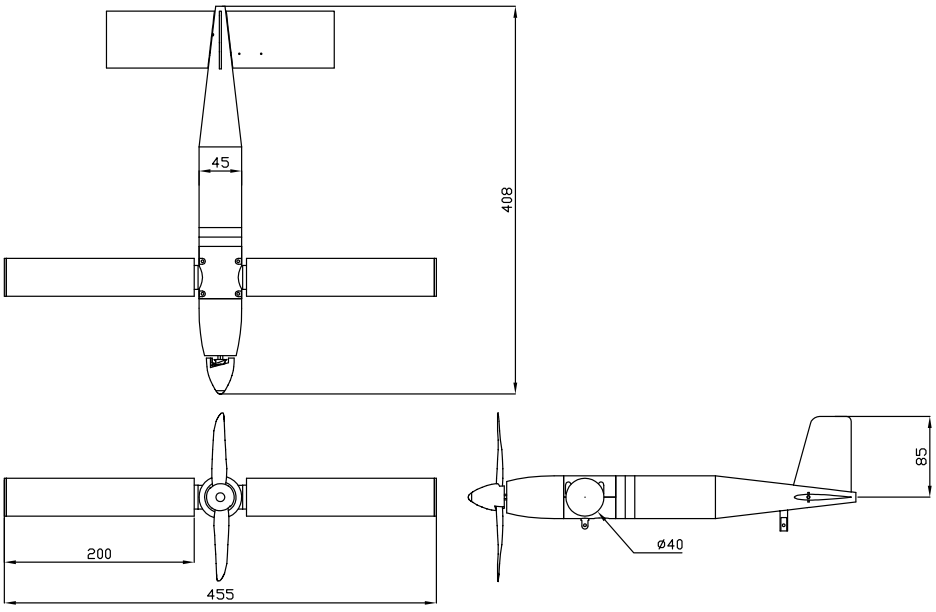

Figure 6.1: Overview of the rotating cylinder MAV test model. All dimensions in mm.

The design of the test model was heavily influenced by the discussion in §4 regarding the establishment of a preliminary layout for the proposed MAV and so was deliberately intended to be simplistic in nature. A view of the final design, with global dimensions highlighted, is shown in Figure 6.1 and model specifications are summarised in Tables 6.1 and 6.2. Note that, where given, c.g. locations and moments of inertia were determined using an accurate three-dimensional representation of the test model that was developed in the SolidWorks CAD software package. Such information is included in order to maintain

as complete a record of the model as possible.

The adoption of such a basic geometry for the test model was intended to provide baseline aerodynamic performance data that could serve as a reference for future research. This type of approach to MAV development has previously been employed by the Air Force Research Laboratory (AFRL) for their GENMAV generic MAV.[260] The test model was also designed to be a 'breakdown' model, allowing for different configurations of the aircraft to be built-up progressively through additions to the fuselage-alone case, and so enabling the relative effect of each component, and their interactions, to be evaluated.

Table 6.1: Model specifications.

Cylinder (Individual)		**EP7035 Propeller**	
Diameter	40 mm	Diameter	178 mm
Span	200 mm	Pitch	89 mm
Planform area	0.008 m^2	Blade width	13 mm
Aspect ratio	5.0	Material	Nylon
Fuselage		**Motors & Speed Control**	
Maximum diameter	45 mm	EM400	x 1
Length	368 mm	Vortex 35/48/939	x 2
Fineness ratio	8.1	Phoenix-45 ESC	x 2
Horizontal Tail		**Vertical Tail**	
Aerofoil section	SD8020	Construction	Flat plate
Mean aerodynamic chord	60 mm	Mean aerodynamic chord	52 mm
Thickness-chord ratio	0.1	Thickness	2 mm
Span	240 mm	Span	80 mm
Gross tail area	0.0144 m^2	Exposed fin area	0.0039 m^2
Aspect ratio	4.35	Aspect ratio	1.64
Root chord	60 mm	Root chord	61 mm
Taper ratio	1.00	Taper ratio	0.67
Leading edge sweep	0°	Leading edge sweep	15°

As well as the decision to adopt a basic geometry, the design and development of the model was also affected by the limitations of the available facilities and materials. Primarily, this meant that the size of the model was driven by the diameter of the motors employed to spin the cylinders, which were chosen so as to be capable of providing the necessary rotational rates for testing at the desired velocity ratios. This choice impacted on all other model dimensions and resulted in a final design that was slightly bigger than the originally envisaged maximum dimension of 0.4 m. In addition, the fact that the model had to be connected to the T2 balance enforced certain design and manufacturing decisions that would not normally be required in developing an operational MAV.

Table 6.2: Model component weights and balance. All weights are rounded to the nearest 0.5 g and include any associated screws or other fittings. Center of gravity positions are given relative to the origin of reference axes $o_i x_i y_i z_i$ (see Figure 6.11a). Moment of inertia values are determined in system $o_i x_i y_i z_i$ and are given in units of gm^2.

Component	**Wt. (g)**	**c.g. (mm)**	$\mathbf{I}_{xx}$	$\mathbf{I}_{yy}$	$\mathbf{I}_{zz}$	$\mathbf{I}_{xz}$
Nose fairing	6	103.4, 0, 0	0.001	0.061	0.061	0.000
EP7035 propeller	3	90.6, 0, 0	0.004	0.027	0.023	0.000
EM400 motor	81.5	51.6, 0, 0	0.009	0.231	0.231	0.000
Propeller adaptor	3.5	85.1, 0, 0	0.000	0.025	0.025	0.000
Cylinder	97	0, ± 121.2, 0	1.751	0.034	1.751	0.000
Endplug ($d_e/d = 1$)	4.5	0, ± 225.1, 0	0.234	0.001	0.234	0.000
Endplug ($d_e/d = 1.25$)	6.5	0, ± 225.5, 0	0.326	0.002	0.326	0.000
Vortex 35/48/939 motor	187	0, ± 124.4, 0	2.936	0.027	2.936	0.000
Motor mount	362.5	0, ± 63.6, 0	1.713	0.045	1.713	0.000
IR22X28X17 inner ring	29.5	0, ± 35.5, 0	0.040	0.005	0.040	0.000
HK2816 bearing	28.5	0, ± 35.5, 0	0.040	0.007	0.040	0.000
Fuselage	685	-76.8, 0, 0.08	0.210	9.973	9.966	-0.013
Fuselage plug	35.5	0, 0, 0	0.007	0.003	0.007	0.000
Horizontal tail	46	-244.5, 0, 0	0.238	2.758	2.997	0.000
Vertical tail	22.5	-254.3, 0, -42.2	0.052	1.513	1.461	0.243

However, because the model was not intended for free-flight, it was possible to take advantage of resources that would otherwise be unsuitable if strict weight limits and performance requirements had to be observed. This allowed for the use of larger and more powerful motors to drive the cylinders, extending the range of investigatable velocity ratios, and also enabled the use of a more sophisticated speed controller, which improved the quality of data obtained. Furthermore, the employment of engineering plastics and aluminium as construction materials provided a level of structural rigidity that would not be possible on an actual MAV, greatly reducing any aeroelastic effects. Though ultimately unrealistic, such choices simplified both the design and manufacture of the model and its aerodynamic behaviour, so aiding analysis. Full details of the design and development of each individual component of the model are given throughout the rest of this subsection.

6.1.1 The Cylinders

Cylinder sizing was primarily guided by the preliminary design study. Each cylinder was essentially a hollow tube made from Ertacetal H, an acetal homopolymer, with external diameter $d = 40$ mm, length 198 mm, and shell thickness 2.5 mm (see Figure 6.2). At the outboard end, the cylinders were fitted with an endplug, also constructed from Ertacetal

H, of which two different types were employed. The first had a maximum diameter that was the same as the diameter of the cylinder, thus providing an outboard end condition of $d_e/d = 1$. The second had a slightly larger maximum diameter (50 mm) and so acted like a small endplate of size $d_e/d = 1.25$. This choice of endplate size ratio was informed by the results of §5, which indicated that adverse lateral forces and moments occurred for $d_e/d > 1.25$. Both types of endplug extended the cylinder's length by 2 mm, giving each rotor an overall span of $b = 200$ mm and an individual aspect ratio of $AR = 5$.

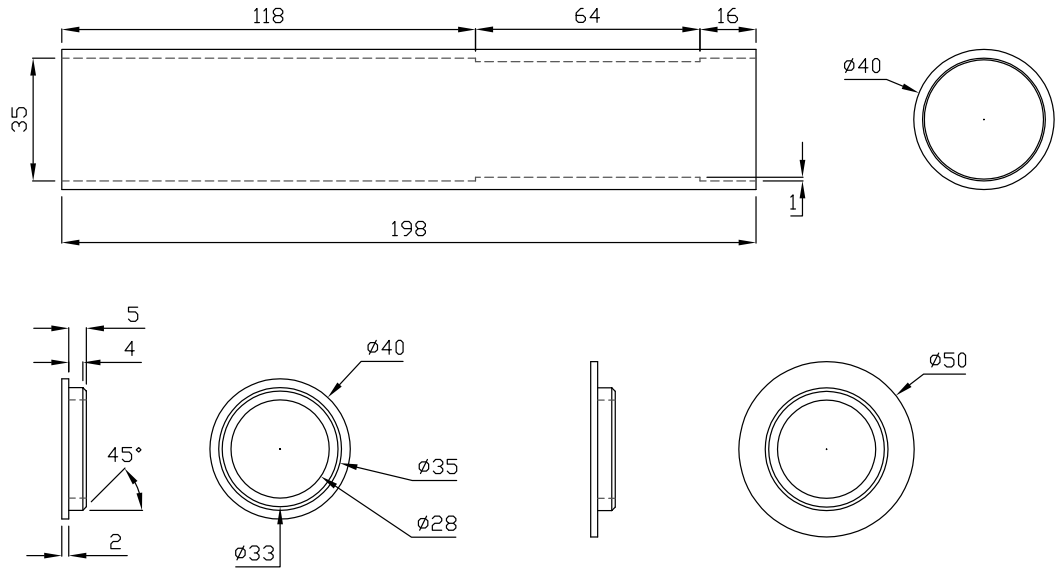

Figure 6.2: Cylinder and endplug dimensions. All dimensions in mm.

Note that the choice of material for the construction of the cylinders was made after examination of a number of different alternatives, including aluminium, several types of structural foams (specifically Depron foam, a brand name for a closed-cell form of extruded polystyrene; phenolic foam; and expanded polypropylene), and a number of engineering plastics (including perspex and Ertalon 66 SA, a form of extruded nylon). The decision to use Ertacetal H reflected the overall greater suitability of this material to the current task, it having provided a better combination of rigidity, machinability, dimensional stability, thermal resistance, and low weight than the other options considered. Cost and availability were also influential in the final choice.

6.1.2 Cylinder Rotation and Speed Control

Cylinder rotation was driven by two Welgard Vortex 35/48/939 external rotor three-phase brushless electric motors, one for each cylinder. Like other brushless motors, this type of motor, commonly called an 'outrunner', has its windings located on the stator rather

than the rotor (as is the case with a brushed DC motor). However, unlike a conventional 'inrunner' brushless motor, the outrunner has its stator positioned inside of the rotor, which now forms part of the outer case, so that the motor spins its outer shell around its windings. This arrangement means that outrunner motors produce more torque for a given motor size than their conventional equivalents, allowing them to be much smaller than a typical brushless or brushed motor of equal performance. This reduction in motor size was useful in keeping cylinder dimensions down to acceptable levels, whilst still providing a degree of performance that allowed the full range of desired experiments to be performed.

The specific choice of the Vortex 35/48/939 (which had diameter 35 mm, length 48 mm, and weighed 187 g) was made after a series of investigatory tests with a number of smaller motors, such as the 42 g EMAX CF2822, indicated that they would have lacked the performance necessary to enable testing at all the rotational rates of interest. Thus, the larger, heavier Vortex motors were preferred. Similarly, whilst the decision to drive each cylinder with its own individual motor complicated the overall design of the model, it expanded the scope of the possible tests.

Along with a decrease in size and an improvement in performance, the use of an outrunner motor also provided a more natural means of connection between the cylinders and motors (for power transmission) and simplified the problem of how to house the motors within the limits of the desired model geometry. Since the outer casing of each motor underwent rotation, the motors could be located entirely inside of their respective cylinder, close to the mid-span, and with the inner wall of the cylinder in simple press-fit contact with the motor's outer casing (see Figure 6.3). This meant that the cylinder was forced to rotate together with the motor.

Housing the motors within the cylinders in this fashion would have been far more difficult to implement with a brushed or brushless inrunner as the mounting holes on these motors are not located in a favourable position and the outer casing is not typically machined with any great precision. Power transmission would also have been more complex. However, the adopted arrangement did necessitate that, for the lift from the two cylinders to be in the same direction, the motors had to be made to spin with opposite senses.

To connect the cylinders to the rest of the model, each motor was, at its rear, attached to a brass mount that extended back through the cylinder to the vehicle fuselage, where the mount's inboard endcap was clamped tightly into place (see §6.1.3). A central hole in the mount allowed the wiring for the motor to exit the cylinder, whilst a HK2816 drawn-cup needle roller bearing, positioned between the motor mount and the inner wall

of the cylinder cavity, and a IR22X28X17 precision ground steel inner ring, that acted as a rollway for the bearing, were used to provide additional support for the inboard end of the cylinders. Note that as well as being a means of connecting the cylinders to the model, the brass mounts also acted as conductors of heat away from the motors and helped prevent overheating.

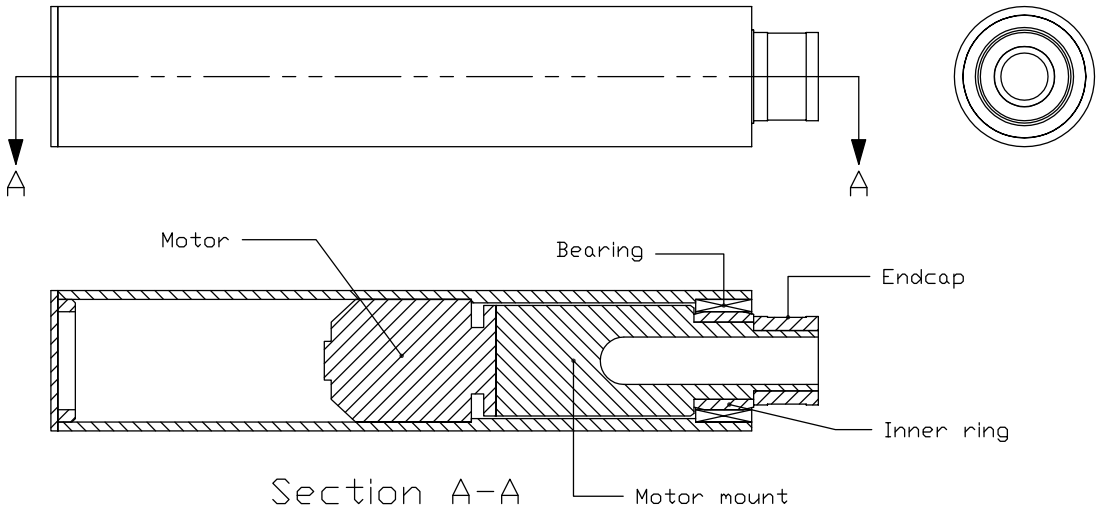

(a) Rotor internal structure

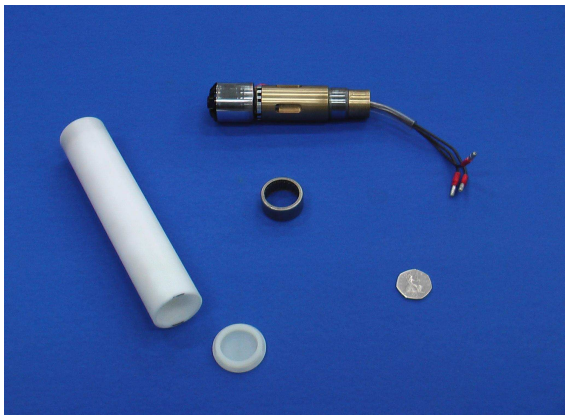

(b) The components of the rotor

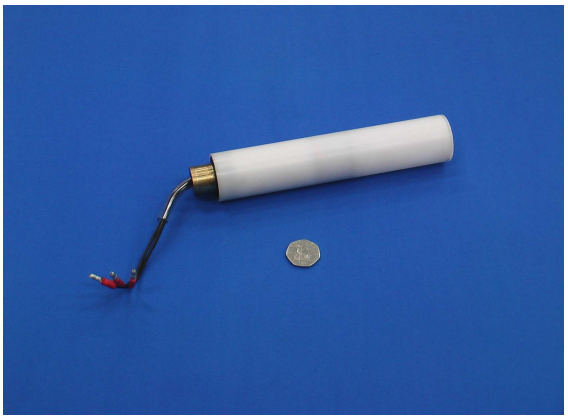

(c) The assembled rotor

Figure 6.3: The mechanism for rotation of the cylinders.

Despite the associated benefits, the use of a brushless motor did, however, complicate both the supply of power to the motors and the control of their speed. Unlike a brushed motor, power cannot be directly applied to a brushless motor as it does not have a brush-based mechanical commutation system to periodically reverse the current and drive the rotation of the motor. Instead, a brushless motor depends on an electronically controlled commutation system that uses a solid-state circuit to perform the same power distribution found in a brushed DC motor. This circuitry, known as an electronic speed controller or

ESC, intelligently powers each phase of a brushless motor in the correct sequence, and at the appropriate rotor positions, to keep the motor turning. The ESC also functions as an interface between the motor and the battery that provides variable power to the motor and allows proportional speed adjustments to be made.

For this application, the Vortex motors were controlled using two purpose-built brushless motor electronic speed controllers (one for each motor) that were based around the commercially available Castle Creations Inc. Phoenix-45 programmable sensorless ESC, but with some modifications. These speed controllers were not housed within any part of the model but were kept in specially-constructed enclosures outside of the wind tunnel. As with typical brushless ESCs, the modified Phoenix-45s were able to electronically start the motors, manage their acceleration, control their speed, and adjust their timing to maximise efficiency.

However, unlike a typical ESC, the modified Phoenix-45s were also able to provide a tachometric capability. This addition was necessary since the speed of a brushless motor is not dependent on the applied voltage across the motor in the same way that it is for a brushed motor, and so the motor rpm could not be ascertained purely from knowledge of the motor speed constant K_v, as was possible with the isolated cylinder tests. Furthermore, an optical tachometer similar to that used with the isolated cylinder was deemed unsuitable due to the design and arrangement of the model.

Instead, a tachometric capability was achieved by feeding the commutation signal generated by the Phoenix-45 into separate circuitry that employed a Microchip PIC16F88 microprocessor unit and custom-written software program to process the signal and determine the motor rpm. The output from each of these units was then connected to a Blackstar Meteor 100 frequency counter that was used to display each cylinder's rotation rate to the nearest 10 rpm, the reading on the counter being updated at a rate of 1 Hz. The accuracy of this measurement system was assessed by comparing the output rpm values to results obtained with a stroboscope. This showed that, at any given rotation rate, the difference in the results from both methods was at most ± 1 rpm.

Further modifications to the Phoenix-45 ESCs included the addition of aluminium heat sinks and an automatic temperature cut-off sensor that acted to prevent overheating. These were necessary for safe operation of the speed controllers outside of their normal environment, where they would ordinarily be cooled by a fast-moving airstream. Other measures to protect the sensitive ESCs against over-current and both over- and under-voltage were also implemented. In addition, since commercially available ESCs are generally intended for application to model aircraft, they are designed so as to be operated using a throttle

stick from a typical remote control. This was deemed too inaccurate for the present application and a separate interface, enabling the motor speed to be changed via a dial, was incorporated into the speed controllers.

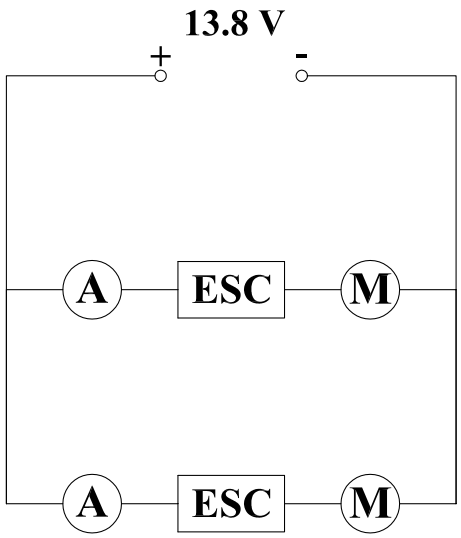

Figure 6.4: Circuit diagram for motor speed control and power measurement.

The power for both the motors and the speed controllers was supplied by a Samtex SEC 1223 AC-to-DC power converter, which used a mains input to provide a highly regulated output DC voltage of 13.8 V at 23 A. The speed control and power supply circuit also included two ammeters placed in series with the motors and ESCs (see Figure 6.4). These were used to measure the current drawn by each motor and so determine the power requirements for spinning the cylinders.

6.1.3 Fuselage

In keeping with the basic nature of the model, an axisymmetric fuselage based on simple geometric shapes was designed. In developing this fuselage, consideration was given to the typical design methodology applied to bluff bodies so as to help prevent or eliminate flow separation.[261,262] This examination of the literature indicated that the position of maximum thickness should be located as far forward as possible and that a gradual afterbody closure length of about three times the size of the maximum body diameter should be employed. However, fuselage sizing was also influenced by the size of the motors used to drive the cylinders and the propeller, as well as the need to accommodate the wiring for

these motors. In addition, the size of the horizontal and vertical tail moment arms was a factor too. Such requirements occasionally necessitated that compromises be made in the design and prevented the implementation of the optimum aerodynamic proportions.

The final fuselage design (see Figure 6.5) was constructed wholly from aluminium, the specific choice of which reflected the fact that as well as providing structural advantages it also enabled the entire body to act as a heat sink. This helped prevent the rotor and propeller motors, which were all totally enclosed within either the cylinders or the fuselage, from overheating. The fuselage was also manufactured so as to be quickly disassembled whilst still attached to the T2 balance, thus providing easy access to the internal components and allowing changes to the vehicle configuration to be made without having to uninstall the entire model. This design philosophy resulted in the fuselage being comprised of four principle sections.

At the front end was the nose section, which was based on an elliptic planform (minor radius 22.5 mm, major radius 74 mm) and used to house the motor for the propeller (see §6.1.5). A series of holes were drilled into the front of the nose so as to allow air to enter the propeller motor for cooling purposes, and a nose fairing was attached to this section for all the tests (see §6.1.5). The next part of the fuselage was a hollow cylinder (of diameter 45 mm, length 55 mm, and shell thickness 7.5 mm) to which the rotors were connected. This section was split horizontally into two equal portions that were used to clamp the endcaps of the motor mounts firmly into place. Note that this arrangement resulted in an average gap of about 10 mm between the cylinder inboard edge and the fuselage wall. Note also that a number of thin (10 mm) cylindrical extension rings could be added to either end of this part of the fuselage, enabling a degree of control over the location of the center of gravity.

The next section was the main portion of the fuselage, which was itself a hollow cylinder of diameter 45 mm and shell thickness 7.5 mm, but with a length of 85 mm. This section housed the wiring that connected the power supply and electronic speed controllers to the motors. Finally, at the aft end was the tailcone section, of length 148 mm and based on a simple truncated cone, to which the horizontal and vertical tails were attached. Note that no shoulder-radiusing of the juncture between the main fuselage and this afterbody section was implemented. Although this technique is usually a simple and effective means of preventing separation from axisymmetric bluff bodies, the study by Howard & Goodman[262] indicates that for Reynolds numbers (based on body diameter) of $Re_b < 4 \times 10^4$, the effects of shoulder radiusing on the drag are minimal. Other passive methods for the reduction of bluff body drag (such as circumferential rectangular or 'V'-shaped grooves) were reported to be similarly ineffective at such low Re_b.

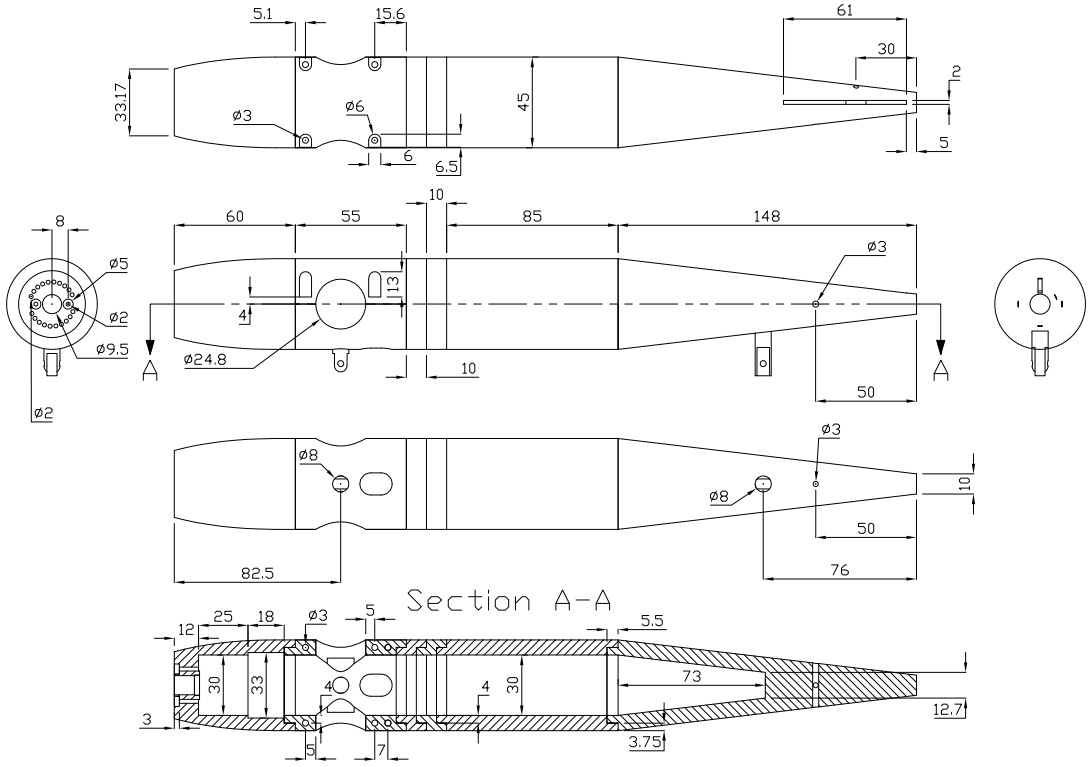

(a) Fuselage dimensions and internal structure

(b) The components of the fuselage

(c) The complete fuselage

Figure 6.5: The fuselage. All dimensions in mm.

6.1.4 Empennage

The model employed a conventional empennage arrangement comprising of a vertical fin and a horizontal tail, the designs of which were kept deliberately basic. This was particularly true for the vertical fin, which was constructed as a simple flat plate, made from aluminium, with thickness 2 mm, aspect ratio $AR = 1.38$, a mean aerodynamic chord of 52 mm, and no rudder (see Figure 6.6a and Table 6.1). The fin was attached to

the fuselage using a small flange that fitted into a slot on the fuselage tailcone and was held securely in place using a grub screw.

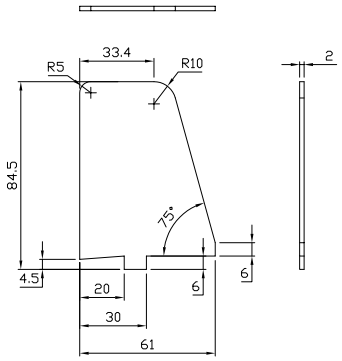

(a) Vertical tail dimensions

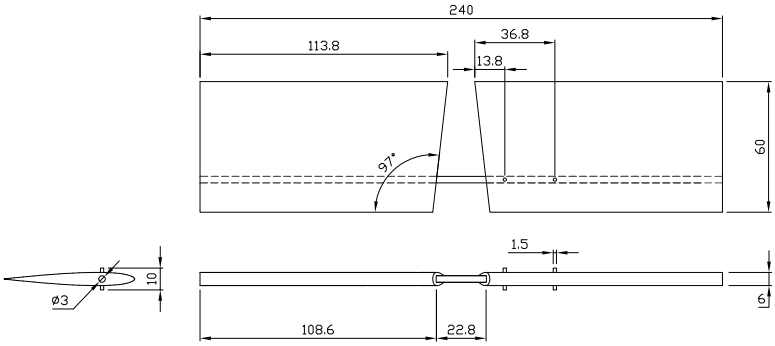

(b) Horizontal tail dimensions

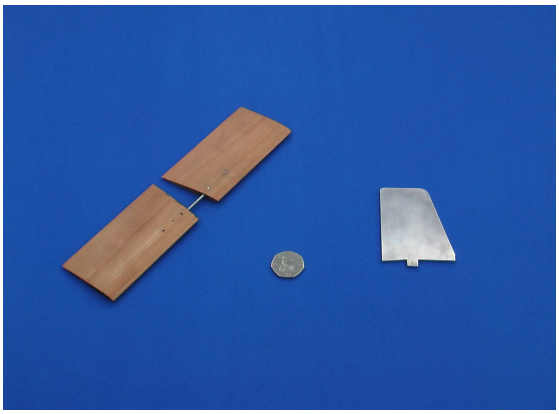

(c) The finished components

Figure 6.6: The empennage. All dimensions in mm.

The horizontal tail was kept similarly straightforward by adopting an all-moving stabilator design of rectangular planform, with no sweep or taper, that had an aspect ratio of $AR = 4$ and a chord of 60 mm (see Figure 6.6b and Table 6.1). A suitable aerofoil section for the tail was chosen by consulting existing experimental test data for low Reynolds number aerofoils.[263–265] This led to the selection of the SD8020, a symmetrical section with thickness-chord ratio of $t/c \approx 0.1$ and a popular choice in model aircraft manufacture, where it is often employed as a stabilator due to its good low-Re_c performance.

The tail was constructed out of wood and manufactured in two sections that were joined on a single steel shaft (of 3 mm diameter) running through the quarter-chord position. On the starboard side the tail section was glued on to the central shaft, whereas the port section was held in place using two small removable pins that passed through both wing and shaft. This enabled the tail to be repeatedly attached to, or removed from, the model with minimal difficulty. The tail setting angle, i_t, was set manually using a digital inclinometer,

with the chord line of the aerofoil (which was inscribed into the tip profile) used as a reference datum, and was defined as positive when the trailing edge moved down. A grub screw, located in the fuselage tailcone section, was used to lock the tail at the desired angle. The use of this particular mechanism made it slightly difficult to effect very small changes in i_t, which meant that the tail setting angle was typically set only to an accuracy of about $\pm 0.25^\circ$

Note that empennage sizing and design was influenced by a number of different factors but was primarily driven by the need to have structures that, given the low speed of the tests, were sufficiently large as to generate aerodynamic forces and moments of adequate magnitude that they could be reliably measured with the T2 balance (this was a particular concern for the pitching moment). A large size for the empennage was also intended to magnify the interactions between the tail, fin, and cylinders and make investigation and assessment of the changes due to interference effects easier. Manufacturing difficulties arising from the small dimensions involved were a concern too.

Consequently, whilst conventional guidelines on the size of the fin and tail, such as suggested values for the fin and tail volume coefficients or typical aspect ratios,[266] were consulted, they were not always implemented and the final sizes were somewhat larger (approximately three to four times so) than these suggestions. This decision reflects the lack of information regarding whether sizing guidelines for the volume coefficients, which are based on the ratio of tail or fin area to wing area, are applicable to this type of design where the cylinders produce much larger forces than their planform area would otherwise suggest. As a result, the design of the empennage contained a degree of arbitrariness.

The interest in examining the interactions between the cylinder, specifically its trailing vortex system as identified in §5, and the empennage primarily affected the design of the horizontal tail and led to its span being made large enough that the tips were aligned with the mid-spans of the cylinders. This was intended to see if there were any effects caused by the spanwise motion of the cylinder tip vortices as velocity ratio increased. The horizontal tail was also sized as to provide a chord Reynolds number close to $Re_c = 3 \times 10^4$, matching that of the existing available test data for the SD8020 and providing a basis for comparison.

6.1.5 Propulsion System

For some tests, the model was fitted with a tractor propeller so as to simulate powered flight and investigate the interference from the propeller slipstream on the cylinders'

aerodynamic performance. In these cases, the commercially available Grand Wing Servo (GWS) EDP-400C electric drive system for low-speed model aircraft, consisting of a two-bladed GWS EP7035 plastic microflight propeller (having diameter 178 mm and pitch 89 mm) and a GWS EM400 electric motor, was adapted for use in the tests (see Figure 6.7).

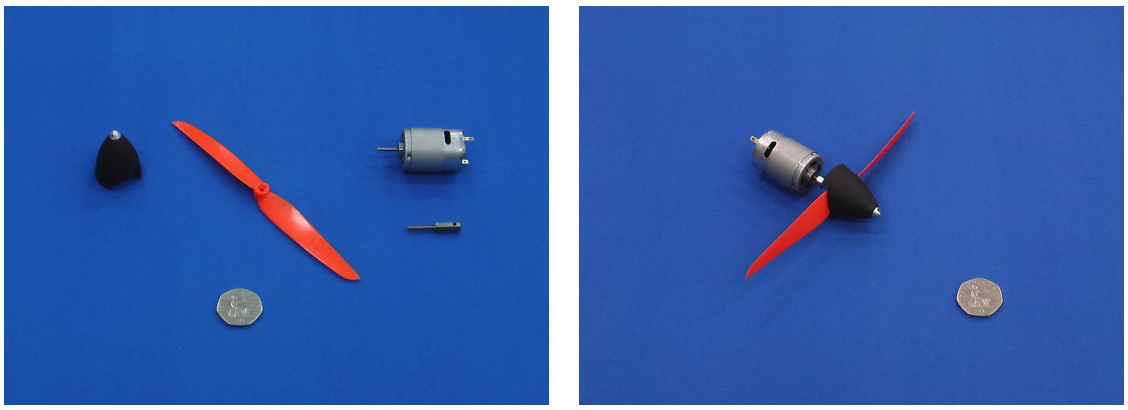

(a) The propeller, motor, adaptor, and nose fairing

(b) The assembled system

Figure 6.7: The propulsion system.

Connection between the propeller and motor drive shaft was made directly, without the use of a gearbox, through the recommended GW/DS002 hexagonal propeller adaptor. In addition, the nose fairing from the GWS EPS-400C electric power system, designed for use with the EM400 and of suitable dimensions to fit the fuselage nose section, was modified to accommodate the propeller adaptor. Testing of the model was always conducted with this nose fairing attached to the fuselage, even if the propeller itself was absent (see §6.2). This helped the model retain a more aerodynamic shape. Power was supplied to the EM400 using a Digimess HY3010 DC power supply and the propeller rpm was controlled simply by varying the voltage across the motor.

Note that the choice of drive system was made based on manufacturers performance data that suggested it would, given the final cylinder size and the tunnel speeds envisaged for the tests, be able to provide sufficient thrust as to simulate cruise conditions (defined as $T - D = 0$) across most of the desired velocity ratio range. This was confirmed through a brief series of preliminary wind tunnel tests using the EDP-400C system. The rather large size of the propeller thus reflects the large cylinder drag.

6.1.6 Support Structure

The model was attached to the T2 balance plate through a single cylindrical sting (having maximum diameter 32 mm but tapering to 9 mm at the model) that was connected to a

pivot point located on the fuselage and aligned with the axis of rotation of the cylinders (see Figure 6.5). The use of this arrangement left the cylinder ends free of interference from the support structure. A tail rod, connecting the fuselage tailcone to the pitch arm of the balance, allowed model incidence to be changed as desired. Together, this system was used to mount the model, in an upside down orientation, in the center of the T2 tunnel. The sting was also used to support and guide the wiring for all three motors into the model (see Figure 6.8).

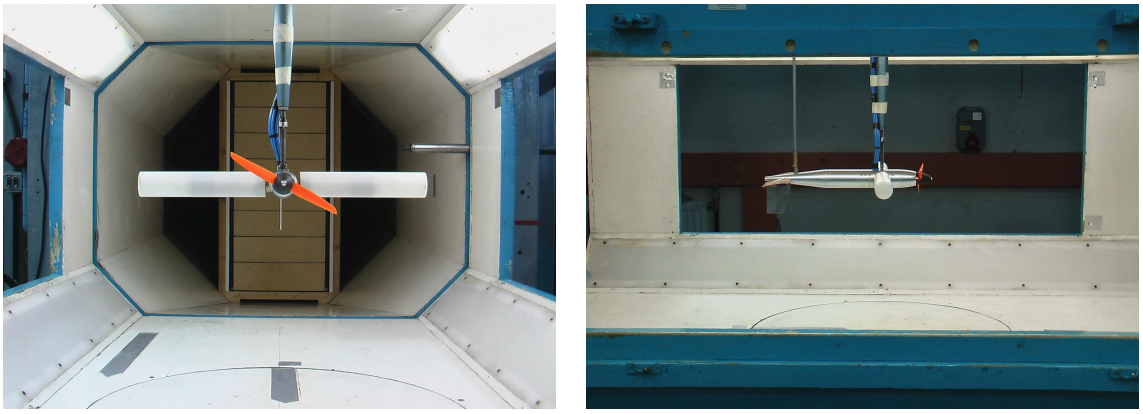

(a) Front view (b) Side view

Figure 6.8: Views of the model mounted in T2.

Note that the ratio of model frontal area, including the sting, to tunnel cross-sectional area was found to be $A/C \approx 0.013$ for all vehicle configurations without the cylinders attached, rising to $A/C \approx 0.032$ for those configurations with the cylinders attached (see Figure 6.9 for an overview of vehicle configurations). The ratio of cylinder diameter to tunnel height was $d/H \approx 0.05$.

6.2 Testing Regime and Procedures

All the tests were performed in the T2 wind tunnel at a single test speed of $V = 7$ m/s, this low speed being implemented by using the same louver door arrangements described in §5. As with the isolated cylinder experiments, the use of the louver door was again prompted by the high value of the minimum start-up speed (16 m/s) of the T2 tunnel and the ensuing detrimental consequences: At this higher test speed, obtaining the same Reynolds number as that expected of the full-scale operational MAV ($Re \approx 2 \times 10^4$) would have required a cylinder diameter of just 16 mm, resulting in the rotational rate necessary to produce a velocity ratio of $\Omega = 2$ being in excess of 35,000 rpm.

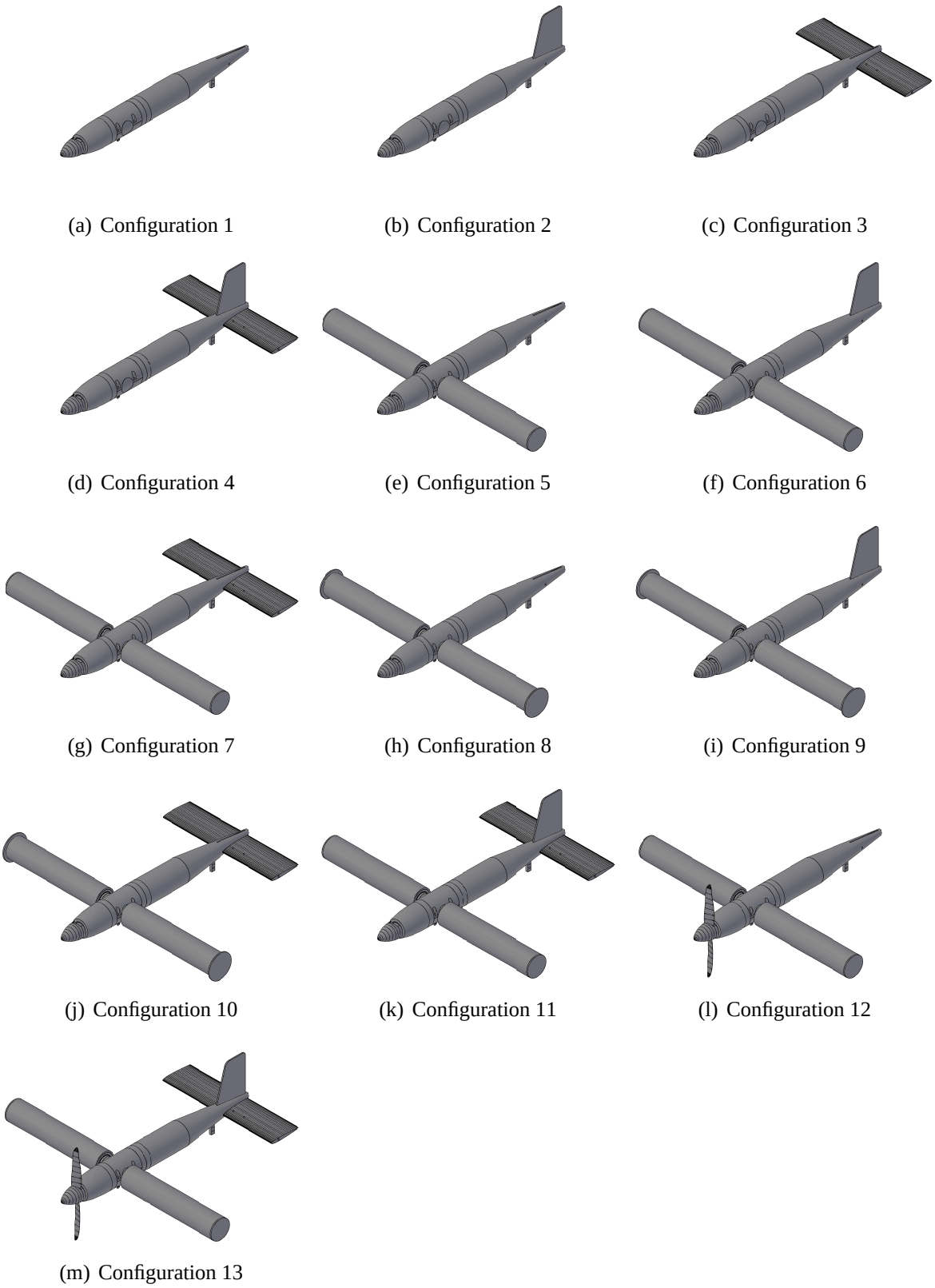

(a) Configuration 1 (b) Configuration 2 (c) Configuration 3

(d) Configuration 4 (e) Configuration 5 (f) Configuration 6

(g) Configuration 7 (h) Configuration 8 (i) Configuration 9

(j) Configuration 10 (k) Configuration 11 (l) Configuration 12

(m) Configuration 13

Figure 6.9: Model configurations used during wind tunnel testing.

The tests began by examining the aerodynamics of the fuselage by itself and then suc-

cessively adding or subtracting the different components of the model until all required combinations of fuselage, tail, fin, cylinders, and propeller had been investigated. This approach resulted in the examination of thirteen separate configurations during testing, the complete set of which are shown in Figure 6.9. Further details for each configuration are given in Table 6.3. Note that configurations 5 to 7 differ from configurations 8 to 10 only in regards to the size of the endplate at the outboard end of each cylinder.

Table 6.3: Model configuration weights and balance. All weights are rounded to the nearest 0.5 g. Center of gravity positions are given relative to the origin of reference axes $o_i x_i y_i z_i$ (see Figure 6.11a). Moment of inertia values are determined in system $o_i x_i y_i z_i$ and are given in units of gm^2.

Configuration	**Weight (g)**	**c.g. location (mm)**	$\mathbf{I}_{xx}$	$\mathbf{I}_{yy}$	$\mathbf{I}_{zz}$	$\mathbf{I}_{xz}$
1	811.5	-58.6, 0, 0	0.226	10.29	10.29	-0.013
2	834	-63.9, 0, -1.1	0.279	11.81	11.75	0.230
3	857.5	-68.6, 0, 0	0.465	13.05	13.29	-0.013
4	880	-73.3, 0, -1	0.517	14.56	14.75	0.230
5	2194	-21.7, 0, 0	13.65	10.53	23.71	-0.013
6	2216.5	-24, 0, -0.4	13.70	12.04	25.17	0.230
7	2240	-26.2, 0, 0	13.89	13.29	26.71	-0.013
8	2198	-21.6, 0, 0	13.84	10.53	23.90	-0.013
9	2220.5	-24, 0, -0.4	13.89	12.04	25.36	0.230
10	2244	-26.2, 0, 0	14.07	13.29	26.90	-0.013
11	2262.5	-28.5, 0, -0.4	13.94	14.80	28.17	0.230
12	2197	-21.5, 0, 0	13.65	10.55	23.74	-0.013
13	2265.5	-28.4, 0, -0.4	13.94	14.83	28.19	0.230

For those configurations without the cylinders attached (configurations 1 to 4), testing was limited to the collection of force and moment readings for angles of attack between $-10^\circ \leq \alpha \leq 25^\circ$ (in steps of $\Delta\alpha = 2.5^\circ$) and yaw angles of $-10^\circ \leq \Psi \leq 30^\circ$ (in ten nonuniform steps). With the horizontal tail attached (configurations 3 and 4), readings were taken across the same values of α and Ψ, but the tests were repeated for a range of tail setting angles ($-8^\circ \leq i_t \leq 8^\circ$, in steps of $\Delta i_t \approx 4^\circ$). Note that when the cylinders were not attached to the body, the resulting hole in the fuselage was filled with a plasticine plug that was shaped so that it conformed to the local contours of the fuselage.

The majority of the experiments were concerned with those configurations where the cylinders were attached but the propeller was not (configurations 5 to 11). For these cases, the measurements were designed to investigate different aspects of the cylinders' interaction with the other components of the model and assess any changes to the aerodynamic performance of the cylinders themselves due to their location about a central fuselage. Testing thus included repeating the force and moment measurements taken with

configurations 1 to 4, but with the cylinders rotating at fixed velocity ratios of $\Omega = 0$, 1, 2, and 2.5. In addition, a number of tests examining the effect of varying velocity ratio in the range $\Omega \leq 2.5$ (in steps of $\Delta\Omega \approx 0.2$) were carried out for selected values of α and Ψ. Note that velocity ratios in excess of $\Omega = 2.5$ could not be implemented due to a combination of factors relating to motor performance, the limitations of the bearings, and structural vibration. Alongside the force and moment readings the tests with configurations 5 and 9 also included measurements of the power required to spin the cylinders.

In addition, these two configurations were used to try and investigate the gyroscopic effects caused by the rotation of the cylinders. These were examined by taking measurements of the moments acting on the model in the range $\Omega \leq 2.5$, with steps of $\Delta\Omega = 0.5$, whilst the model was simultaneously being rotated through the entire range of yaw angles of interest. However, the available facilities were not well-suited to this type of investigation and the limitations of the T2 balance (for instance, the yaw rate at which the model rotated was fixed at a single value; it was not possible to examine moments induced by roll rate; and the balance lacked the necessary sensitivity to accurately measure the small magnitude of the induced moments) meant that the analysis did not provide any meaningful results.

Some of the tests with configurations 5 to 11 also examined the efficacy of using a differential rotation rate to effect vehicle roll control. These experiments were limited to tests with the model at zero yaw but examined two separate means of differential rotation. In the first, the speeds of both cylinders were changed by equal but opposite amounts, so that when the port cylinder had its rotation rate increased by an amount ΔN, the starboard cylinder had its rotation rate decreased by the same ΔN. In the second method, changes were only made to the starboard cylinder, which had its rotation rate continuously decreased. In all cases, a maximum difference between port and starboard cylinders of $\Delta\Omega = 1$ was implemented.

Since previous studies[152, 267] have indicated that cylinder wall temperature plays a significant role in the magnitude of the Magnus forces generated, and given the location of the motors within the cylinders, a small number of reference tests to monitor the temperature of the cylinder surface under operating conditions were carried out with configuration 5. These tests were performed using a Reed Instruments ST-880 infrared thermometer to measure the wall temperature at all velocity ratios of interest across a time period of a typical test run (approximately 15 to 20 minutes of continuous use). At each value of Ω tested, temperatures were measured at three spanwise locations on the cylinders: at the tips and at the mid-span. The total time elapsed (from the beginning of the test) when each measurement was taken was also monitored.

Tests with the propeller attached (configurations 12 and 13) were similar to those for configurations 5 to 11, except that there was no investigation of gyroscopic or temperature related effects and a smaller number of velocity ratios ($0.5 \leq \Omega \leq 2.5$, in steps of $\Delta\Omega \approx 0.5$) and angles of attack ($-10^\circ \leq \alpha \leq 25^\circ$, in steps of $\Delta\alpha = 5^\circ$) were examined. This was a consequence of having to keep the run time of each test as low as possible due to concerns about the propeller motor overheating. Note that for $\Omega > 2$, the drag for some combinations of Ψ and α was such that the propeller could not always provide enough thrust to produce a zero net horizontal force without exceeding the recommended maximum continuous safe operation voltage for the motor (7.2 V). In these cases, so as to preserve the motor, testing was halted at the highest velocity ratio at which a zero net force could be established. In all instances, power requirements for the propeller were always monitored throughout the test.

The procedures used during all the tests with the vehicle model were mostly similar or identical to those employed during testing of the isolated cylinder. For the basic pitch and yaw sweeps, the forces and moments were recorded through the T2 balance control programme over a period of 30 s and at a sampling frequency of 10 Hz. The average value of each channel was then determined for use in later analysis. Tests investigating the gyroscopic moments were performed over a 60 s period, again at a sampling frequency of 10 Hz. In these experiments, the time variation of the forces and moments during the test run was recorded alongside the average values. In all cases, the value of N for both cylinders was recorded manually throughout the testing period and later averaged. Motor voltage and current readings for the power measurement tests (for both the cylinders and the propeller) were also recorded manually.

For all the tests, but particularly those performed at a fixed velocity ratio, great care was taken to ensure that the desired velocity ratio was maintained throughout all angles of attack or yaw angles examined in that run. To this end, efforts were made to always keep the tunnel speed to within ± 0.1 m/s of the target speed of $V = 7$ m/s, whilst also ensuring that the cylinder rotation rate never drifted by more than ± 10 rpm from the target value for a given Ω. Similarly, to mitigate hysteresis effects, both angle of attack and yaw angle were always varied in a specific manner: Beginning with the model at zero incidence, α was increased from 0° up to 25° degrees, then reduced down to -12.5°, and finally increased back to zero. Yaw angle was increased from 0° to 30° degrees, reduced down to -12.5°, and then increased back to zero. The same approach was adopted for all wind-off zero reading tests too.

Testing with the propeller attached proceeded in the same manner as the other tests except that the propeller thrust was (for each combination of Ω, α, and Ψ) always adjusted so

that the net force in the horizontal direction, taking into account any strut or wind-off contributions, was zero before any measurements were taken. In practice, the unsteadiness associated with the cylinders meant that it was difficult to completely cancel out the drag, so the net force was always kept to ≤ 0.1 N instead. The time required to stabilise the drag at a near-zero value also contributed to the need to reduce the angles of attack and velocity ratios examined with these configurations so as to prevent the motor overheating.

6.3 Analysis of Data

Methods of analysis of the data collected with the vehicle test model were, with minor variations, identical to the procedures outlined in §5.3 for the analysis of the isolated cylinder test results. Similarly, the definitions and notation used in the analysis were largely the same as those described in §3.1. Where differences in the approach employed did occur, they arose primarily because of the use of two separate cylinders and the interest in examining the effects of changing angle of attack.

6.3.1 Analysis of Force and Moment Measurements

Force and moment data were reduced to coefficient form in the same manner as that employed for the isolated cylinder. However, the reference area was now taken as the total planform area of both cylinders, without any contribution from the fuselage section that separated them (see Figure 6.10). This area was used even for model configurations without the cylinders attached. Thus, the lift coefficient was always defined as

$$C_L = \frac{L}{\frac{1}{2}\rho V^2 sd} \tag{6.1}$$

where $s = 2b$. Equivalent equations were used for the drag and sideforce.

Similarly, whilst the reference length for the pitching moment coefficient was still taken to be the cylinder diameter, lateral moments were now always converted to coefficient form using the total span of both cylinders as the reference length (see Figure 6.10). For example, the yawing moment coefficient was defined as

$$C_n = \frac{n}{\frac{1}{2}\rho V^2 s^2 d} \tag{6.2}$$

As with the determination of the reference area, the width of the fuselage was not included in the length s.

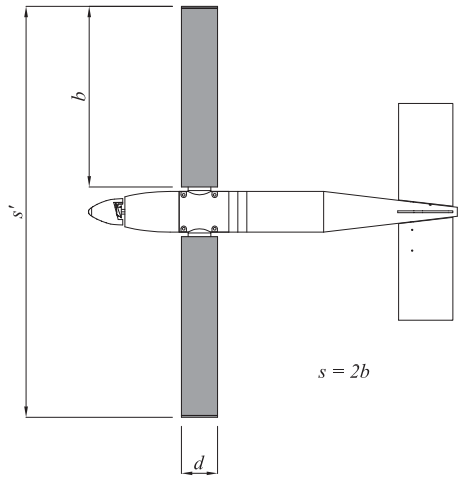

Figure 6.10: Definition of reference areas and lengths for analysis of vehicle model test data. Note that the shaded sections represent the reference area, sd.

Wind-on strut contributions to the measured forces and moments were investigated for all possible combinations of yaw angle and angle of attack in a similar manner as discussed for the isolated cylinder. The effects of flexing of the motor wires attached to the support sting due to changing angle of attack and yaw were incorporated into this assessment of the strut contribution by obtaining strut-only results with the wires arranged in all the orientations experienced throughout the range of α and Ψ examined. Such testing revealed a substantial strut contribution to the drag, sideforce, and rolling moment, but only a very small addition to the lift, yawing moment, and pitching moment.

Investigation of wind-off readings due to the variation of α and Ψ indicated that a change in α induced only a change in the pitching moment reading and had no effect on the other forces and moments, whereas a change in Ψ resulted in a wind-off contribution to all forces and moments other than the pitching moment. Furthermore, wind off readings arising from changing α were found to be wholly independent from the effects of changing Ψ, and vice versa. Thus, the changes in the pitching moment reading due to varying α were the same for all values of Ψ whilst changes due to varying Ψ were the same for all α. This behaviour greatly simplified the assessment and correction of the wind-off contributions to the measured data.

As a result, the calculation of the aerodynamic coefficients from the measured data was adjusted to correct for the strut and wind-off components. Thus, for the lift, the final corrected value of C_L was determined as follows:

$$C_L = \frac{L - L_0(\alpha, \Psi)}{\frac{1}{2}\rho V^2 sd} - C_{L_{strut}}(\alpha, \Psi) \tag{6.3}$$

Equivalent equations were used for the other forces and moments. As with the isolated cylinder tests, no attempt at assessing interference effects between the support structure and model was made. Nor were there any efforts to investigate contributions to the measured forces and moments from the tail rod.

6.3.2 Presentation and Correction of Data

Although the force and moment data obtained with the vehicle model were measured by the T2 wind tunnel balance in coordinate system $o_w x_w y_w z_w$, the results presented throughout this section are discussed with reference to coordinate axes $o_i x_i y_i z_i$ (see Figure 6.11a). This system is equivalent to the axes used with the isolated cylinder ($ox'y'z'$, as defined in Figure 3.2), but with the origin now positioned at the intersection of the fuselage's longitudinal axis and the cylinders' axis of rotation, rather than at the cylinder center of gravity. This location represents a more natural reference position than the actual point of attachment between the sting and the model.

However, this decision required that the pitching moment and rolling moment results, as measured by the balance, be corrected to account for changes to the contributions from the lift and drag (to pitching moment only) and the sideforce (to rolling moment only) due to the vertical offset between the model-to-sting attachment point and the origin of $o_i x_i y_i z_i$. For example, the measured pitching moment, m, for the general configuration shown in Figure 6.11b may be seen to require the following correction:

$$m_c = m + L\Delta x - D\Delta z \tag{6.4}$$

where m_c is the corrected pitching moment; L and D are, respectively, the measured lift and drag for the given vehicle configuration; and moment arms Δx and Δz are given by $l_1 \sin\alpha$ and $l_1 \cos\alpha$ respectively (with $l_1 = 29.5$ mm). The rolling moment was corrected in a similar fashion, though now only the effect of the measured sideforce, Y, needed to be considered (see Figure 6.11c). Hence,

$$l_c = l - Y\Delta z \tag{6.5}$$

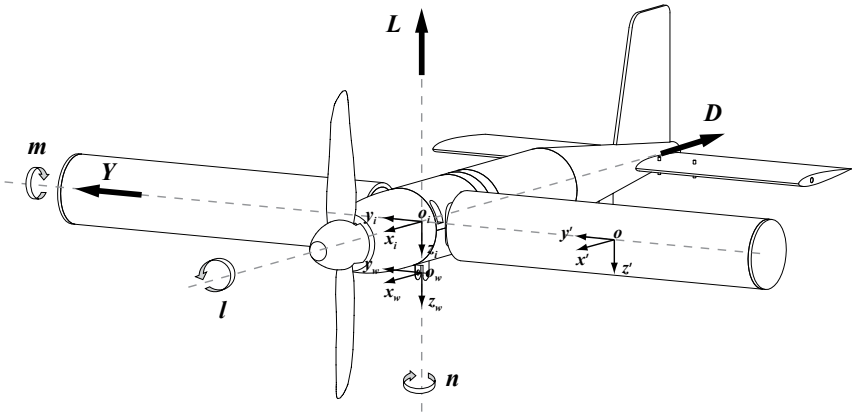

(a) Reference axes for vehicle model

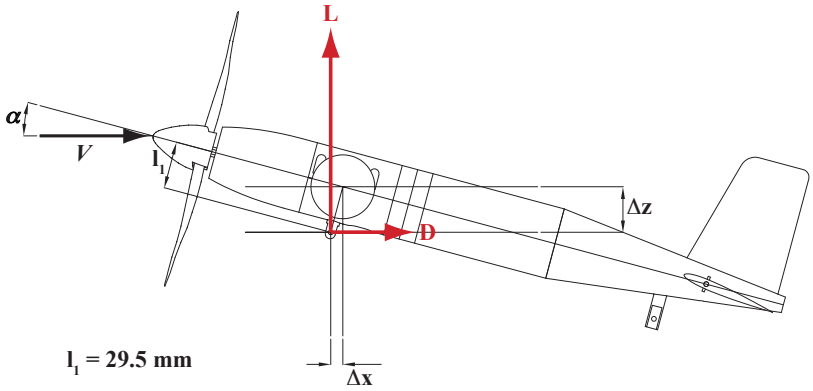

(b) Correction of pitching moment data

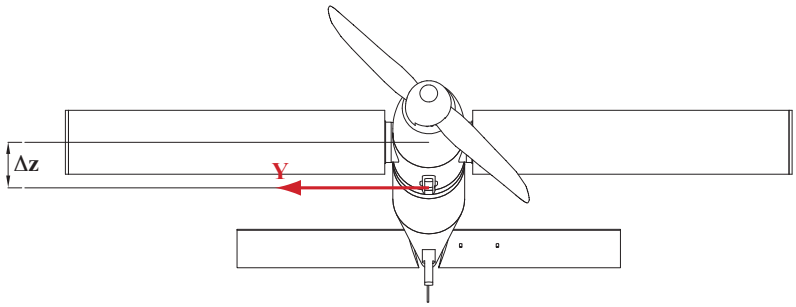

(c) Correction of rolling moment data

Figure 6.11: Axes for correction and presentation of vehicle model results. Arrows denote positive directions.

6.3.3 Analysis of Power Measurements

The reduction of power measurements for spinning the cylinders to coefficient form was performed in the same manner as for the isolated cylinder results. Thus,

$$C_P = \frac{\text{IV}}{\frac{1}{2}\rho V^3 sd}\ \eta(N) \tag{6.6}$$

Note that the efficiencies (as a function of motor speed) of the two Vortex outrunner motors were estimated from manufacturers performance data.

6.3.4 Analysis of Gyroscopic Effects

The importance of the gyroscopic moments arising from simultaneous rotation of the cylinders about both their spin and yaw or roll axes was assessed by comparing the gyroscopically-induced component of C_l and C_n, as predicted by theory for the given conditions, to the aerodynamically derived lateral moment coefficients, as measured by the T2 balance during testing at fixed yaw angles. Theoretical estimates for the gyroscopic contributions were determined by converting Equation 4.13 to coefficient form. Thus, the gyroscopic rolling moment coefficient induced by yawing the aircraft with the cylinders rotating, C_{l_g}, was estimated from

$$C_{l_g} = \frac{4 I_{yy} \Omega r}{\rho V s^2 d^2} \tag{6.7}$$

where I_{yy} is the moment of inertia of the cylinders and endplugs about their spin axis in $o_i x_i y_i z_i$ (the moment of inertia of the outer casing of the motors was ignored) and r is the yaw rate. A similar equation was formulated for the gyroscopic yawing moment coefficient induced by rolling the aircraft at rate p

6.3.5 Uncertainty Estimates

The uncertainty in the determination of the force and moment coefficients was found to vary between different configurations of the model and was also noted to be dependent on whether the cylinders were stationary or rotating. Typical results are shown in Table 6.4. The larger uncertainties for configurations 1 to 4 reflect the much smaller magnitudes of

the forces and moments for these arrangements, but are also partly due to increased unsteadiness in the results (particularly the lift). Data measured with the cylinders attached but stationary also showed higher uncertainty, which was probably a result of vortex shedding from the rotors. Changes in the angle of attack or yaw angle had a negligible effect on the uncertainties, but were generally beneficial as increasing the magnitude of either α or Ψ slightly reduced the uncertainty in all the forces and moments.

Table 6.4: Estimates of average uncertainty in the T2 force and moment data for different model configurations. Note that values in brackets correspond to the uncertainty with the cylinders rotating. All uncertainties are rounded up to nearest 0.5%.

Quantity	**1 to 4**	**5 to 11**	**12 to 13**
Lift coefficient	± 20.0	± 15.0 (± 5.0)	± 13.0 (± 5.0)
Drag coefficient	± 4.5	± 4.5 (± 4.5)	± 42.0 (± 12.0)
Pitching moment coefficient	± 4.5	± 4.0 (± 4.0)	± 4.5 (± 4.5)
Sideforce coefficient	± 8.0	± 8.0 (± 8.0)	± 8.0 (± 15.0)
Yawing moment coefficient	± 8.0	± 7.5 (± 7.0)	± 12.0 (± 10.0)
Rolling moment coefficient	± 10.0	± 10.5 (± 9.0)	± 8.5 (± 9.0)

For the velocity ratio, the average uncertainty in assessing Ω was estimated to be approximately $\pm 2\%$. A much larger uncertainty of approximately $\pm 10\%$ was noted in the determination of the power coefficient for spinning the cylinders. This was a result of a highly fluctuating current. Similarly large uncertainties, of average value $\pm 6.5\%$, also occurred in the calculation of the power coefficient for the propeller, although these were primarily a result of the precision of the readings for the motor voltage and current being limited (by the equipment) to one decimal place.

6.3.6 Wind Tunnel Boundary Corrections

No corrections for wall interference were made to any of the data obtained with the vehicle model, whether for those configurations with the cylinders attached or those without. With respect to the former, this decision seemed the most prudent given the discussions in §3.10 and §5.4 and the results of the attempted correction of the isolated cylinder data in §5.5.1. In addition, both the ratio of model frontal area to tunnel cross-section area ($A/C \approx 0.03$) and the ratio of cylinder diameter to tunnel height ($d/H \approx 0.05$) were less than the critical 6% limit quoted by West & Apelt[239] as being the point below which interference effects on stationary cylinders were effectively negligible. This suggests that any wall interference effects on the current results may be regarded as unimportant.

Similarly, although the results from the tests without the cylinders attached could have been corrected using conventional techniques, this would have prevented a like-for-like comparison with the data obtained with the cylinders attached. Furthermore, the small size of the model also meant that corrections for the fuselage, tail, and fin were effectively negligible: The total blockage correction factor for all three components was estimated to be of the order of 10^{-3}, with lift interference effects being of equally small size.

6.4 Results and Discussion

The corrected results of all the tests are presented below. Note that, in plotting the data and discussing the results, the different configurations of Figure 6.9 are referred to with the label 'C1' for configuration 1, 'C2' for configuration 2, and so on. Similarly, where comparison is required, data from the isolated cylinder tests are given the label 'IC'.

6.4.1 Cylinder Wall Temperature

The results of the investigation into the effects of the motor location on heating of the cylinders showed that wall temperatures rose gradually (from an initial ambient value of 22° C) at both the mid-span and inboard end as rotation rate increased, eventually reaching a maximum of about 40° C at the end of the testing period (see Figure 6.12). However, temperatures at the outboard tip remained largely unchanged regardless of motor speed or time. The tests also showed that, as long as there was a gap of a few minutes between individual test runs (during which the tunnel was operating, so as to provide additional cooling, but the cylinders did not spin), wall temperature did not rise significantly beyond 40° C even for multiple consecutive tests over a prolonged period of several hours.

It should be noted that the ST-880 thermometer used to monitor cylinder wall temperature had a resolution of only 1° C and that the readings at the inboard edge may well have been affected by reflections from the nearby aluminium fuselage. Consequently, the results may not be wholly accurate. Nevertheless, they do still give an indication of the heating experienced by the cylinder, although the exact effects of this change in temperature on the cylinders' aerodynamic performance remains somewhat unclear.

Peller's[151–153] discussion of the effects of surface heating was limited to analysis of the boundary layer profiles for wall temperatures of between 80° and 120°, where a favourable effect on separation was reported. Other mentions of an effect, such as that by Vaughn & Reis,[267] are more vague and no examination of the change in the force coefficients is

known to exist. However, whilst some impact on performance may be expected, comparison of the model force data with the results for the isolated cylinder (which did not undergo any heating) indicates that, at least for the temperature range currently in question, wall temperature is not of primary importance.

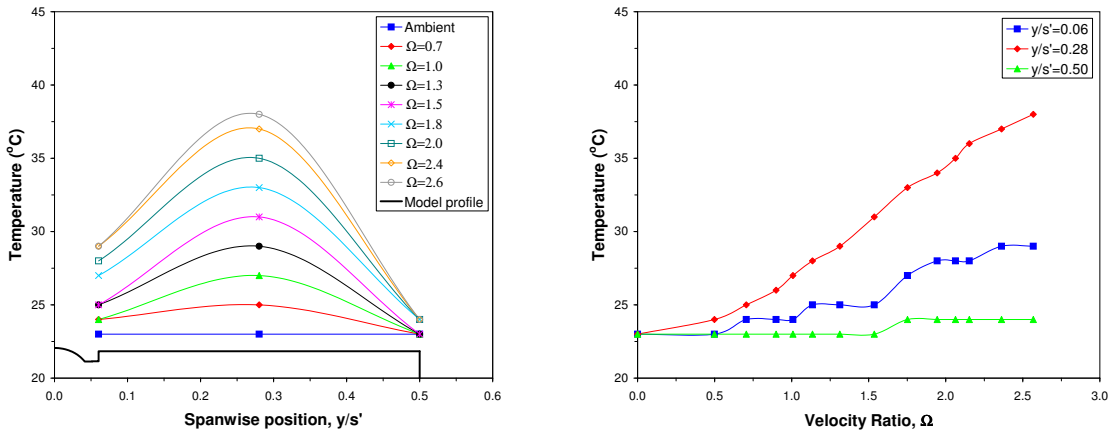

(a) Spanwise variation

(b) Variation with Ω

Figure 6.12: Changes in cylinder surface temperature during a typical test run.

6.4.2 Force Results

Comparison of the variation of lift with velocity ratio for the isolated cylinder (both with and without endplates) against the results obtained using the two cylinder-and-fuselage-only model configurations shows good agreement between the data, particularly when $\Omega \leq 1$ (see Figure 6.13a). At higher velocity ratios the lift for C5 and C8 is noticeably greater than for an isolated cylinder with equivalent end conditions. Since the results shown are for zero angle of attack, at which the fuselage by itself is seen to produce no significant lift (see Figure 6.13b), and given the similarity between the results for C5 and the isolated cylinder with one $d_e/d = 1.25$ endplate and those of C8 and the isolated cylinder with two $d_e/d = 1.25$ endplates, this suggests that the presence of the fuselage may be acting somewhat like an extra endplate on each rotor.

The results at varying angle of attack (Figure 6.13b) also show that for those configurations without the tail the lift curve slope $dC_L/d\alpha$ is unaffected by the presence of the cylinders, or the velocity ratio at which they operate (at least for $\Omega \leq 2.5$). For these cases the lift due to angle of attack was generated solely by the fuselage and the value of the lift curve slope was thus only $dC_L/d\alpha \approx 0.5$ per radian. Figure 6.13b also indicates an increase in the fluctuations in the data with rising Ω. This was possibly due to greater vibration of the model as the cylinder rotational rate was increased.

Figure 6.13c shows that vehicle angle of attack has no effect on the shape of the variation of C_L with Ω. Instead, an increase or decrease in α simply shifts the lift curve up or down by a small amount that is consistent with the shallow linear slope seen in the results for the variation of C_L with angle of attack. Figure 6.13c also reveals that Reynolds number effects at low Ω are still visible in the lift curve despite the low value of Re. Although there is no pronounced nonlinearity in the variation of C_L with Ω, as seen during Magnus effect inversion at high Re, the lift curve slope $dC_L/d\Omega$ at low velocity ratios is still reduced in comparison to that at higher velocity ratios, being approximately half the value ($dC_L/d\Omega \approx 1.1$ for $\Omega \leq 1$, $dC_L/d\Omega \approx 2.4$ for $\Omega > 1$).

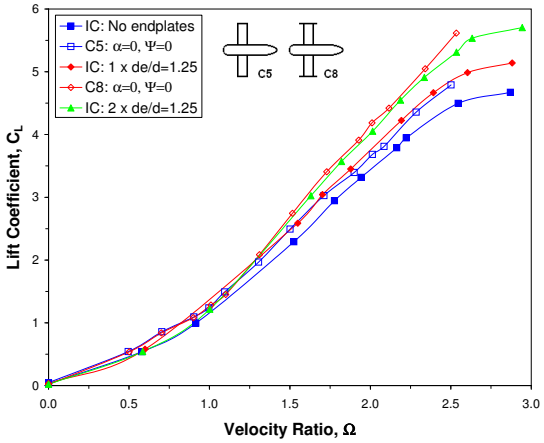

(a) Comparison with isolated cylinder ($\alpha = \Psi = 0°$)

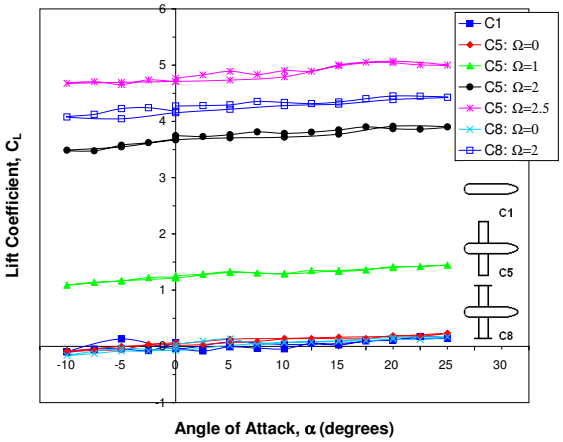

(b) Variation of C_L with angle of attack at $\Psi = 0°$

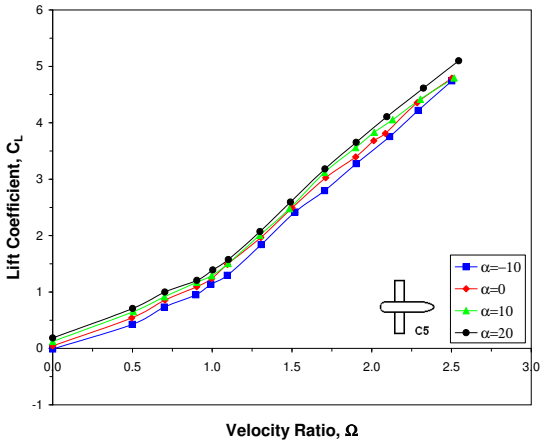

(c) Effect of α on C_L vs Ω for C5 at $\Psi = 0°$

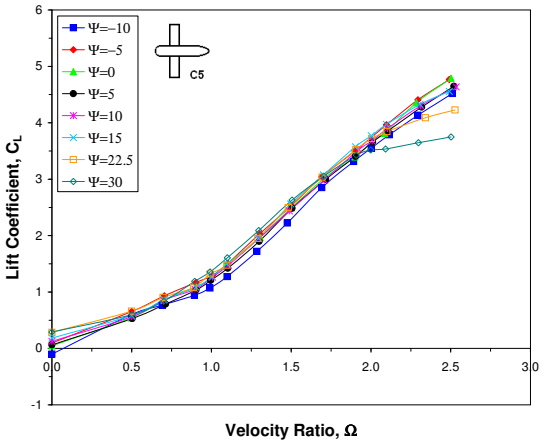

(d) Effect of Ψ on C_L vs Ω for C5 at $\alpha = 0°$

Figure 6.13: Lift coefficient results for the vehicle model without tail at $Re = 1.83 \times 10^4$.

The variation of lift with velocity ratio at different yaw angles (see Figure 6.13d) shows the same fall in C_L when $\Omega > 1.5$ and $\Psi \geq 15°$ as was noted with the isolated cylinder. The results indicate too that the unusual behaviour of the lift curve at low velocity ratios

($\Omega < 0.5$) and high yaw ($\Psi = 30°$) was also repeated. In general, the use of endplates were found to have no effect on the influence of either α or Ψ on C_L, though this may be because of the low endplate size ratio employed: §5 shows that for $d_e/d \leq 1.25$ the use of endplates produces characteristics much like those for the cylinder with no endplates. Larger d_e/d may well have an effect on the behaviour with changing α and Ψ.

The addition of the tail had a considerable effect on the variation of vehicle lift with angle of attack. Without the cylinders attached (see Figure 6.14a) the results for C3 showed the tail to stall at $\alpha \approx 5°$ when $i_t = 8°$ and at $\alpha \approx 17°$ and $\alpha \approx -5°$ when $i_t = -8°$. In addition, the maximum lift coefficient was determined to be $C_{L_{max}} \approx 0.7$ and the lift curve slope was $dC_L/d\alpha \approx 3.1$ per radian. These results agreed well with values obtained with the SD8020 aerofoil by previous studies[263–265] into low-Re_c aerofoils, which found that, when $Re_c = 3 \times 10^4$, $\alpha_s \approx 13°$, $C_{L_{max}} \approx 0.8$, and $dC_L/d\alpha \approx 4.6$ per radian.

With the cylinders added to the model but not rotating, the lift response to changing angle of attack was, relative to C3, much more linear and stall was delayed to at least $\alpha_s = 15°$ or greater, irrespective of tail setting angle (see Figure 6.14b). Furthermore, the maximum lift coefficient was increased to $C_{L_{max}} \approx 0.9$, and the lift curve slope was now $dC_L/d\alpha \approx 2.3$ per radian. Whilst this represents a 33% reduction from that obtained with the tail alone, it is a fourfold increase in the value of $dC_L/d\alpha$ for the tail-off configurations.

Rotation of the cylinders with the tail present did not appreciably change the form of the variation of lift with α from that when $\Omega = 0$, though the magnitude of C_L was, for all angles, now obviously much greater (see Figure 6.14b). Operation at $\Omega = 2$ further improved the stall angle (to $\alpha_s > 20°$) and also increased the lift curve slope slightly (to $dC_L/d\alpha \approx 2.7$ per radian), though this remained less than that for C3. The maximum benefit to the lift curve slope seemed to occur at $\Omega = 1$ where $dC_L/d\alpha$ for C7 had its greatest magnitude of $dC_L/d\alpha \approx 2.9$ per radian. However, this is only a small increase over the value noted at $\Omega = 2$ and may simply be a result of experimental variation or error. Larger velocity ratios ($\Omega > 3$) may have a greater effect on performance. The use of small endplates was found to have no significant effect on the performance of the tail.

The presence of the tail also did not alter the influence of angle of attack on the shape of the curve of C_L against Ω (see Figures 6.14c and d). Thus, it may be concluded that neither α nor i_t change the relationship between C_L and Ω, which is consistent with the independence of rotating cylinder flow from angle of attack. The addition of the tail did, however, enhance the degree to which the lift curve was offset as α changed, so that the tail acted as to cause a net increase in α. The effect of tail stall on the offsetting of C_L

against Ω is illustrated by the results for $\alpha = 20°$ of Figure 6.14d. Also, the tail had no effect on the response to yaw angle, which remained as before (see Figures 6.14e and f).

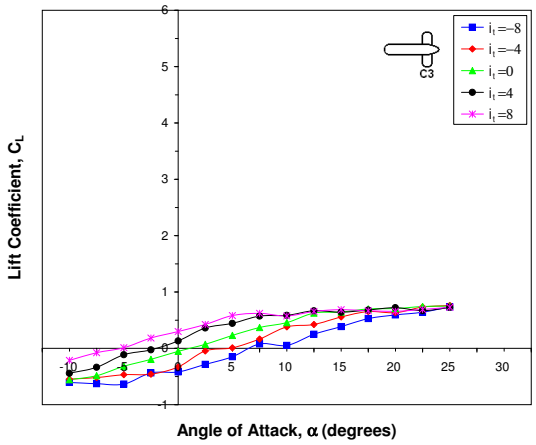

(a) Lift variation with α for C3 at $\Psi = 0°$

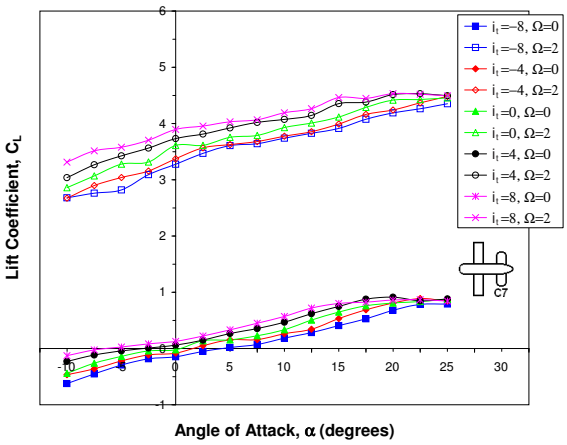

(b) Lift variation with α for C7 at $\Psi = 0°$

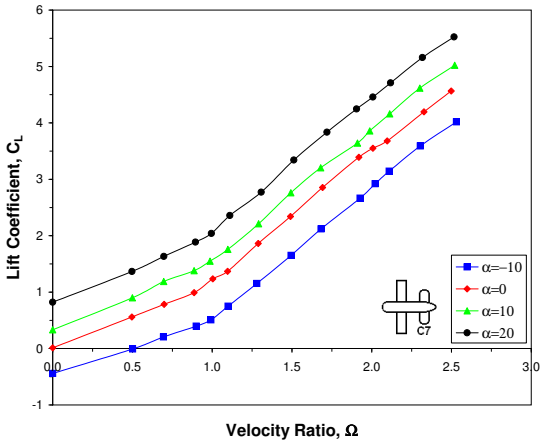

(c) Lift variation with Ω for C7 ($i_t = 0°$, $\Psi = 0°$)

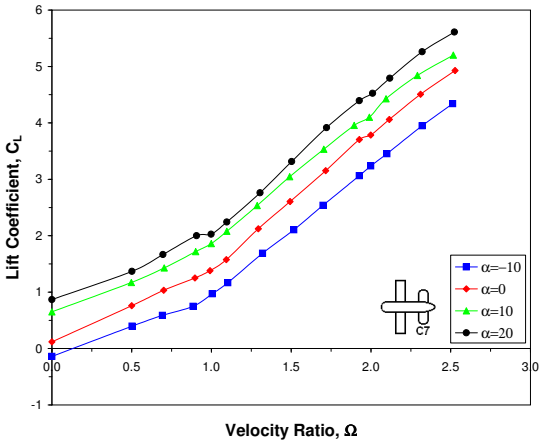

(d) Lift variation with Ω for C7 ($i_t = 8°$, $\Psi = 0°$)

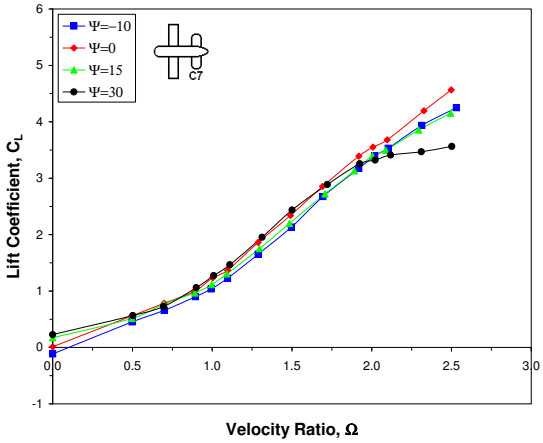

(e) Lift variation with Ω for C7 ($i_t = 0°$, $\alpha = 0°$)

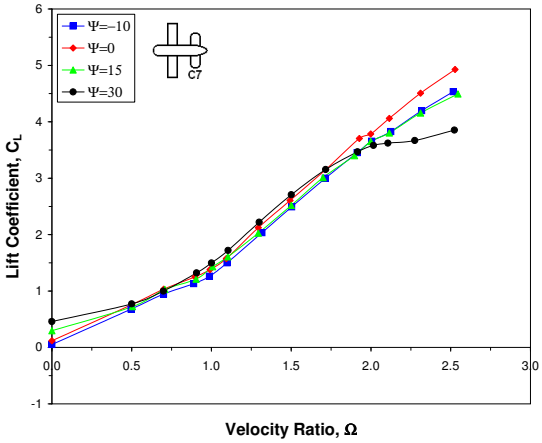

(f) Lift variation with Ω for C7 ($i_t = 8°$, $\alpha = 0°$)

Figure 6.14: Lift coefficient results for the vehicle model with tail at $Re = 1.83 \times 10^4$.

The variation of drag with velocity ratio for model configurations C5 and C8 at $\alpha = 0°$ and $\Psi = 0°$ showed general agreement with the results for the isolated cylinder, although the magnitude of C_D was almost always higher (see Figure 6.15a). This difference was most notable when $\Omega > 1.5$ and was quite substantial at the higher velocity ratio values. Such an increase in C_D is almost certainly due to the presence of the fuselage, which in this regard does not appear to behave like an extra endplate and brings no benefits to C_D. The substantial nature of the rise in drag over the isolated cylinder may be due to the lack of attention given to the design of the fuselage-cylinder junction, which was deliberately not shielded from the flow nor shaped to be particularly aerodynamic.

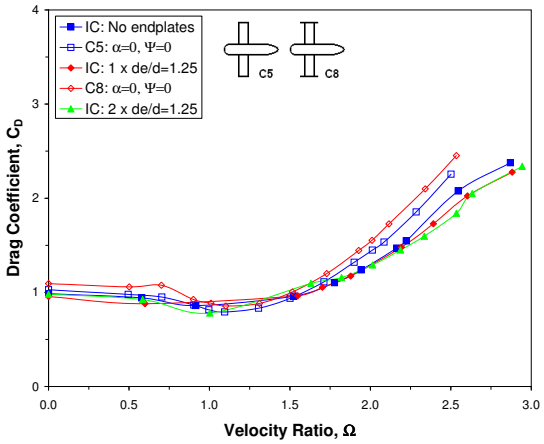

(a) Comparison with isolated cylinder ($\alpha = \Psi = 0°$)

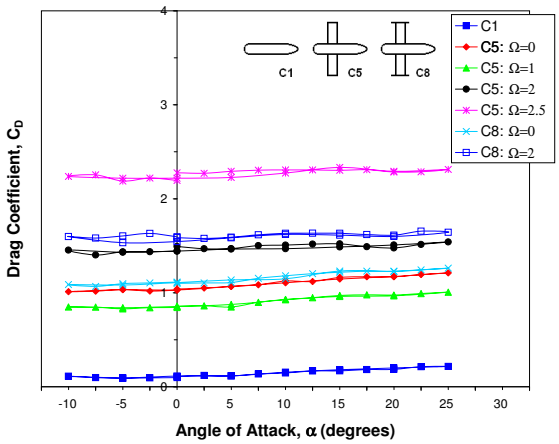

(b) Variation of C_D with angle of attack at $\Psi = 0°$

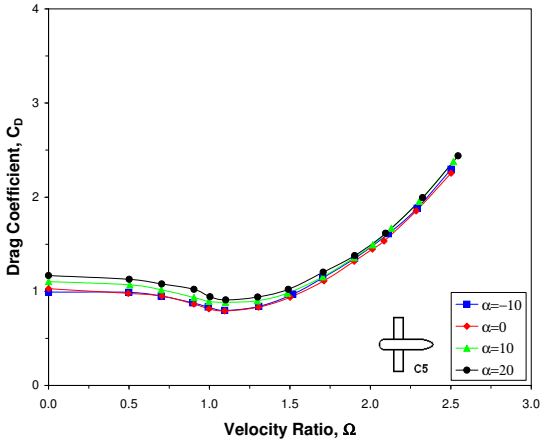

(c) Effect of α on C_D vs Ω for C5 at $\Psi = 0°$

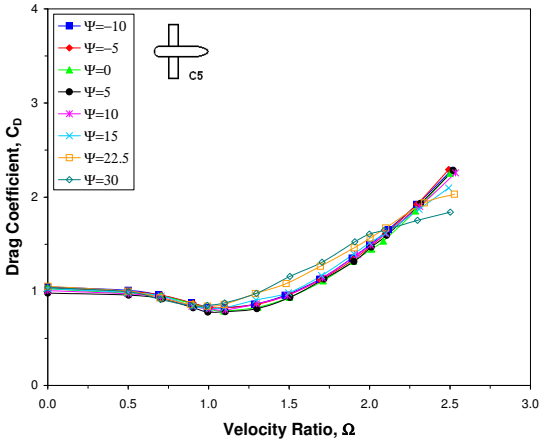

(d) Effect of Ψ on C_D vs Ω for C5 at $\alpha = 0°$

Figure 6.15: Drag coefficient results for the vehicle model without tail at $Re = 1.83 \times 10^4$.

As with the lift results, the drag coefficient for those configurations with just the rotors and fuselage was largely independent of angle of attack, so that the curve of C_D against α increases only very slightly with increasing angle (see Figure 6.15b). This increase is

primarily due to the fuselage and the drag is seen to become less responsive to angle of attack as the velocity ratio is increased, thus indicating that the influence of the cylinders comes to dominate the flow.

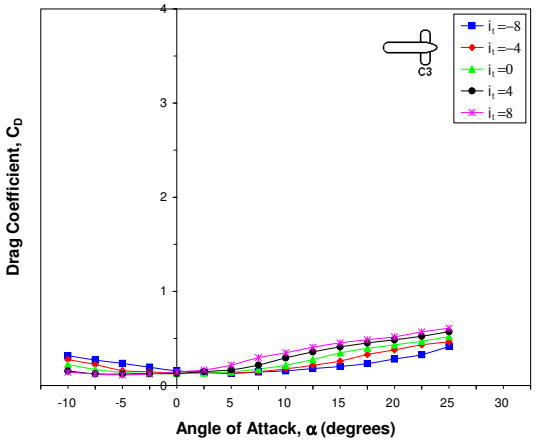

(a) Drag variation with α for C3 at $\Psi = 0°$

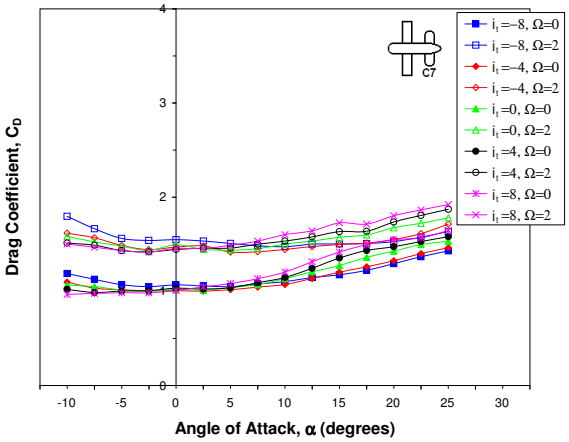

(b) Drag variation with α for C7 at $\Psi = 0°$

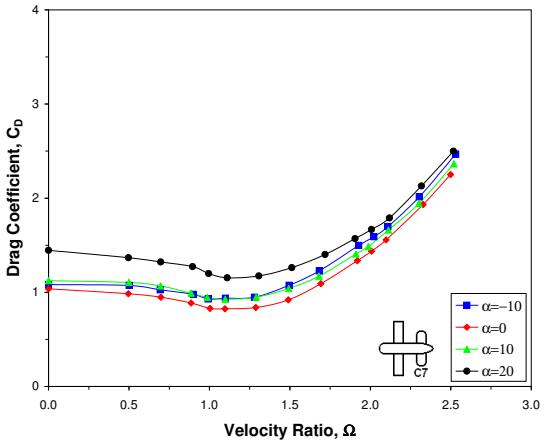

(c) Drag variation with Ω for C7 ($i_t = 0°$, $\Psi = 0°$)

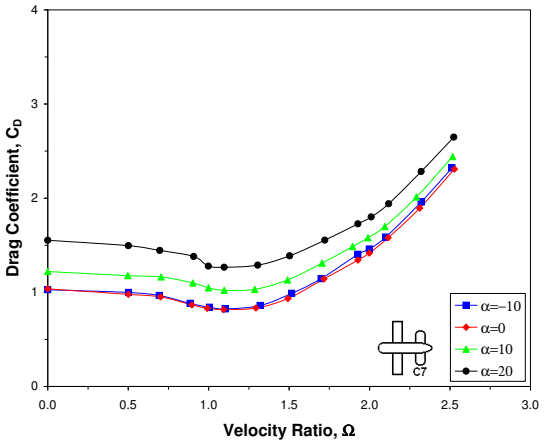

(d) Drag variation with Ω for C7 ($i_t = 8°$, $\Psi = 0°$)

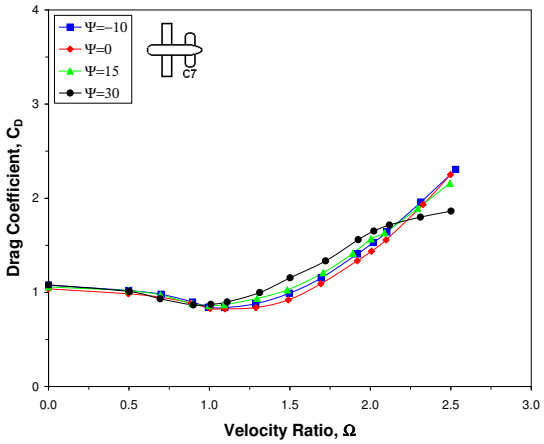

(e) Drag variation with Ω for C7 ($i_t = 0°$, $\alpha = 0°$)

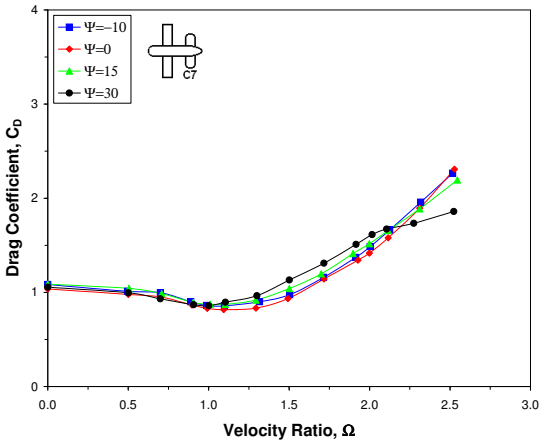

(f) Drag variation with Ω for C7 ($i_t = 8°$, $\alpha = 0°$)

Figure 6.16: Drag coefficient results for the vehicle model with tail at $Re = 1.83 \times 10^4$.

The influence of α on the variation of drag with Ω was also found to be the same as that noted for the lift (see Figure 6.15c). As before, a change in angle of attack did not alter the shape of the drag curve but merely offset it slightly so that increasing or decreasing α created more drag. This increase in C_D was, in accordance with the results of Figure 6.15b, most apparent for $\Omega < 1$, and the data for different values of α collapsed into a single curve when $\Omega > 1.5$. Such behaviour may be associated with the effects of rising Ω on the drag of the fuselage, this component being primarily responsible for any variation in C_D due to α for the model without tail. The effect of yaw angle on C_D was found to remain the same as that for the isolated cylinder (see Figure 6.15d), and neither the use of endplates nor the fin had any effect on the form of the drag curve, whether against changing α or Ω. The addition of these components changed only the magnitude of C_D.

The presence of the tail caused the variation of C_D with angle of attack to become significantly different from that with the tail off. Figures 6.16a and b show that the tail makes the drag more dependent on α, so that the shape of the drag curve for the vehicle more closely resembles that of a conventional aircraft, including a region of increased drag due to stall at high angles. Consequently, whilst the difference in drag due to the presence of the tail was, relative to the equivalent tail-off case, effectively zero at low angles, it increased to as much as $\Delta C_D \approx 0.45$ when $\Omega = 2$, $\alpha = 25°$, and $i_t = 8°$. That the graph of C_D against α with the tail attached is of the same form whether the cylinders are present or not indicates that the addition of the tail makes it the primary factor in determining the drag response to changing angle of attack for such an aircraft.

The effect of velocity ratio with the tail present was primarily to alter the magnitude of C_D (decreasing it for $\Omega < 1$ and increasing it for $\Omega > 1$), though changing the velocity ratio also affected the onset of stall. As with the lift, different tail setting angles did not alter the form of the curve of C_D against Ω (see Figures 6.16c and d), causing only an exaggeration of the shifting of the curve due to changing α. Also, the tail had no effect on the variation of drag with Ω at non-zero yaw angles (see Figures 6.16e and f).

Although the influence of the tail on C_L and C_D meant that it also affected the vehicle lift-to-drag ratio, no substantial benefit to C_L/C_D was obtained through use of the tail, whether with or without the cylinders (see Figure 6.17a). Without the tail the lift-to-drag ratio was constant with changing α and its value was fixed by the velocity ratio and end conditions of the cylinders. The addition of the tail reduced the range of angles for which the lift-to-drag ratio was constant to those values not associated with tail stall at a given i_t. Outside of this range there was a slight reduction in C_L/C_D with α, though this was not as dramatic as that observed for configuration C3. Results for configurations C1, C3, and C5 (at $\Omega = 0$) also illustrate the highly unsteady nature of the flow without the

cylinders and tail present on the model and highlight the poor aerodynamic performance of conventional wings at low Reynolds numbers.

For the tail-off configurations the angle of attack had little influence on the variation of lift-to-drag ratio with velocity ratio (see Figure 6.17b). With the tail present, negative values of α and i_t combined to cause a substantial downwards shift of the curve of C_L/C_D against Ω that considerably reduced the lift-to-drag ratio at all velocity ratios. Large positive angles of attack caused a modest increase in C_L/C_D for $\Omega \leq 1.5$ but had little influence at higher Ω. Neither α nor i_t affected the magnitude of the maximum lift-to-drag ratio achievable with the model, which was determined by the choice of rotor end conditions and found to be $(C_L/C_D)_{max} \approx 3$. The velocity ratio at which this maximum occurred was generally slightly lower than for an isolated cylinder, typically being at $\Omega \approx 1.75$, but could be displaced towards $\Omega \approx 2$ by changing α and i_t.

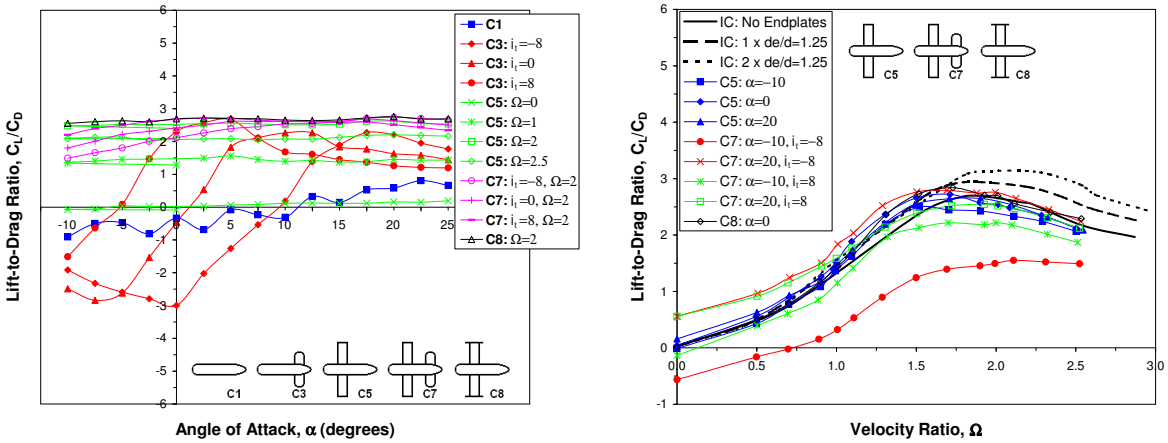

(a) Variation of C_L/C_D with angle of attack

(b) Variation of C_L/C_D with velocity ratio

Figure 6.17: Lift-to-drag ratio results for the vehicle model at $Re = 1.83 \times 10^4$.

A comparison of the variation of the sideforce coefficient with velocity ratio for the cylinders-plus-fuselage configurations against that of the isolated cylinder with similar end conditions reveals far less agreement than noted between the lift and drag results (see Figures 6.18a to d). Trends such as the tendency of C_Y towards zero magnitude when $1.5 \leq \Omega \leq 2.5$ and the change observed in the nature of the response of sideforce to velocity ratio when $\Psi \geq 30°$ are not apparent in the results of testing with the vehicle model. Furthermore, the data for configuration C8 showed that the use of endplates on the model produced quite different behaviour than the same size and arrangement of end-plate on the isolated cylinder. The addition of the fin was found to increase the magnitude of the sideforce but did not change the nature of the variation of C_Y with Ω (see Figures 6.18e and f).

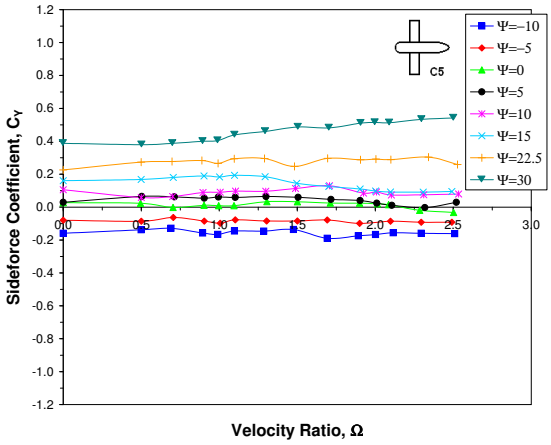

(a) Results for configuration C5 at $\alpha = 0°$

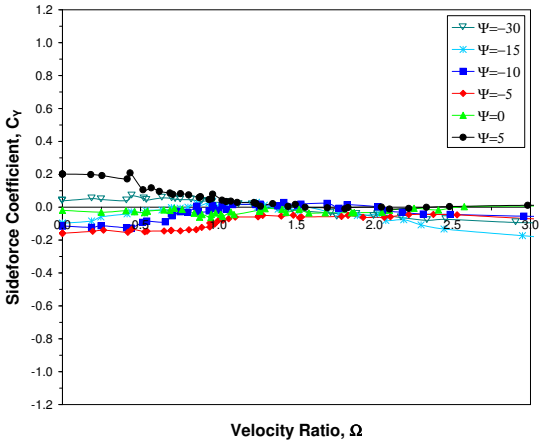

(b) Isolated cylinder results for $d_e/d = 1$

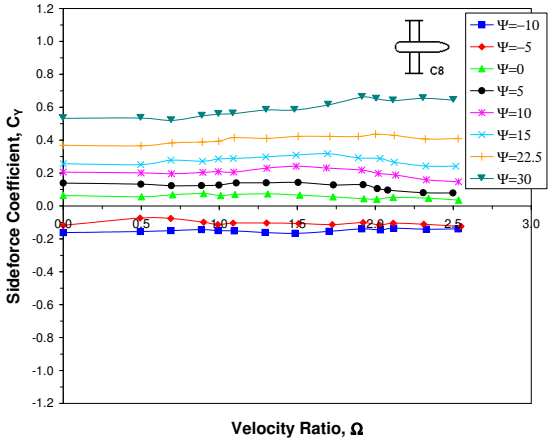

(c) Results for configuration C8 at $\alpha = 0°$

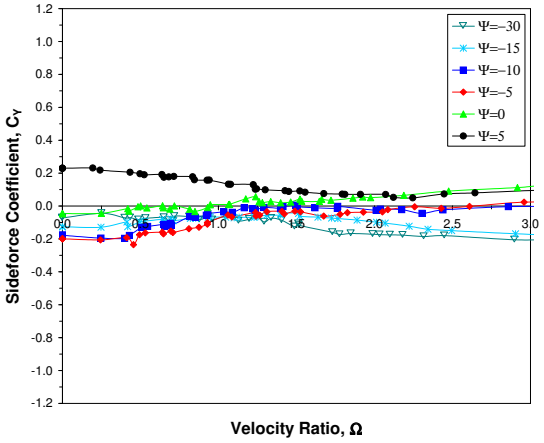

(d) Isolated cylinder results for 1 x $d_e/d = 1.25$

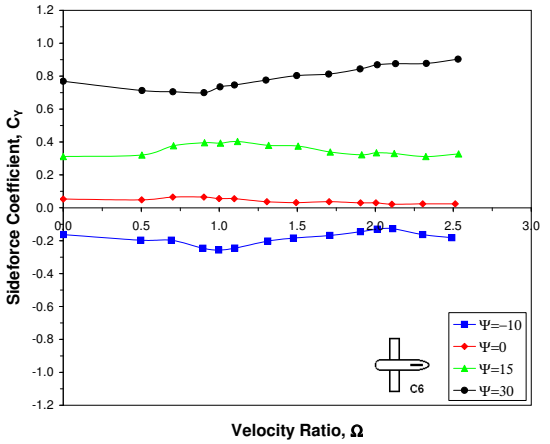

(e) Results for configuration C6 at $\alpha = 0°$

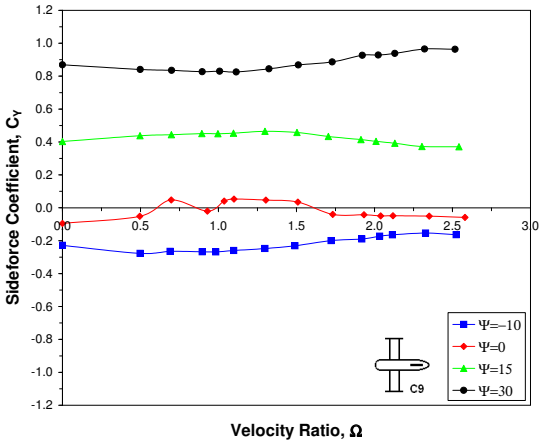

(f) Results for configuration C9 at $\alpha = 0°$

Figure 6.18: Variation of sideforce coefficient with velocity ratio for the vehicle model with and without vertical fin at $Re = 1.83 \times 10^4$.

The differences between the results with the cylinders as part of an aircraft and those of

§5.5.10 appear to be caused primarily by the presence of the fuselage, which was found to be much more influential in determining the magnitude of the sideforce, and its variation with both α and Ψ, than the cylinders, whether stationary or rotating (see Figures 6.19 and 6.20). Changes in the flow caused by the use of two separate rotating cylinders and the higher Re of some of the isolated cylinder data may also have contributed to the differences observed relative to the isolated cylinder.

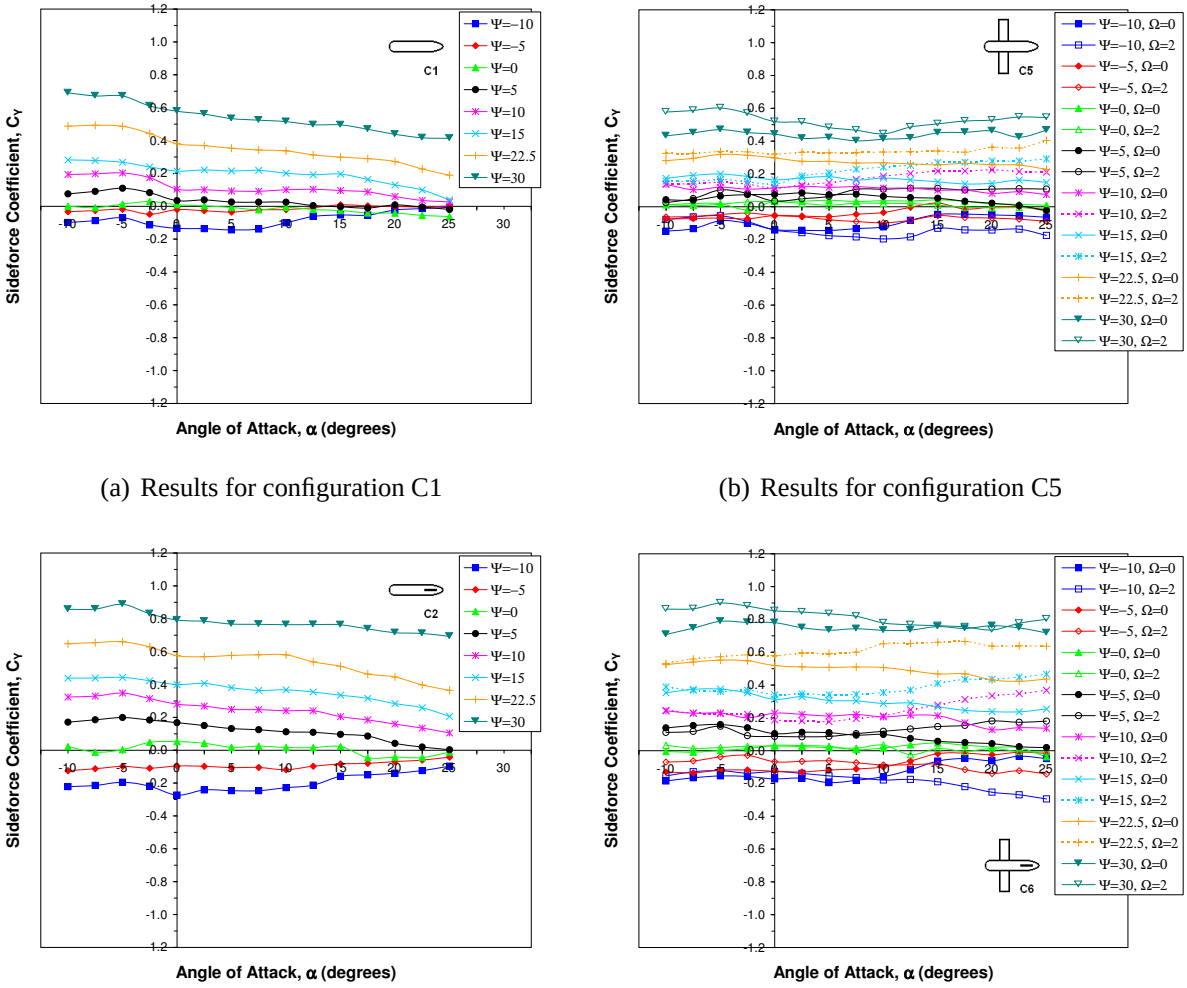

(a) Results for configuration C1

(b) Results for configuration C5

(c) Results for configuration C2

(d) Results for configuration C6

Figure 6.19: Variation of sideforce coefficient with angle of attack for the vehicle model with and without vertical fin at $Re = 1.83 \times 10^4$.

In general, the addition of stationary cylinders to the model acted to reduce the magnitude of C_Y and its dependence on α. Rotation of the cylinders tended to increase both these quantities. The presence of the rotors also made the variation of C_Y with Ψ more linear than with the fuselage and fin alone (particularly when $\Omega = 0$) but had little influence on the gradient $dC_Y/d\Psi$, which was always positive and underwent no change in sign with varying Ω (as was noted in §5.5.10). This indicates that the stability derivative $dC_Y/d\beta$ is

independent of the rotors and will, as for a conventional aircraft, generally be of negative sign, but may well be of greater magnitude ($-1 \leq dC_Y/d\beta \leq -1.5$ per radian for C6).

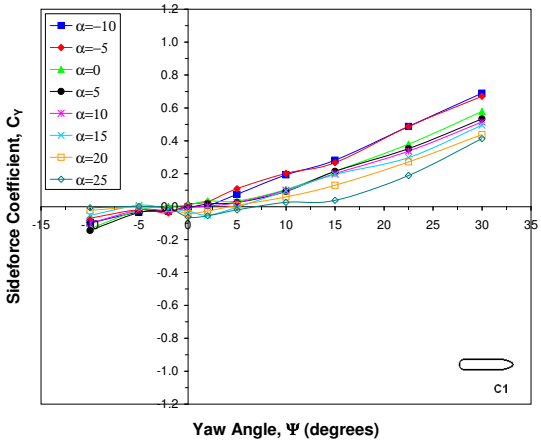

(a) Results for configuration C1

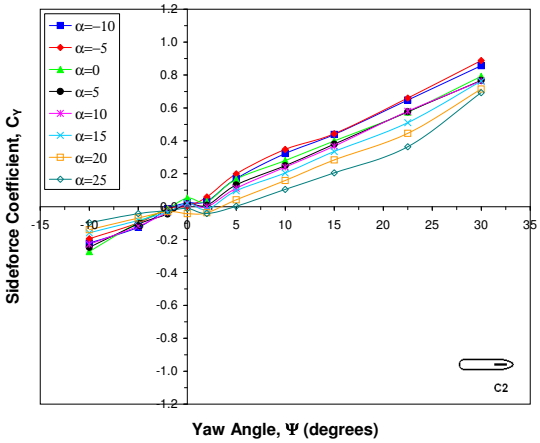

(b) Results for configuration C2

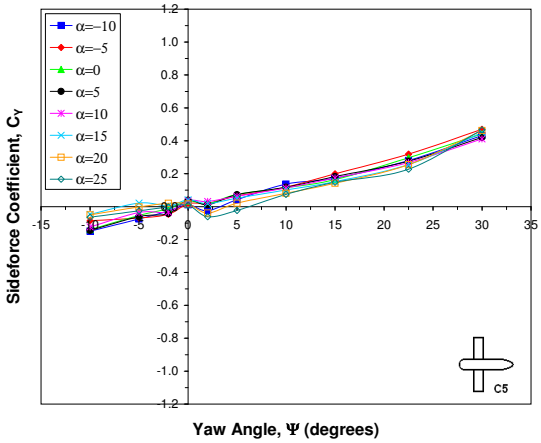

(c) Results for configuration C5 at $\Omega = 0$

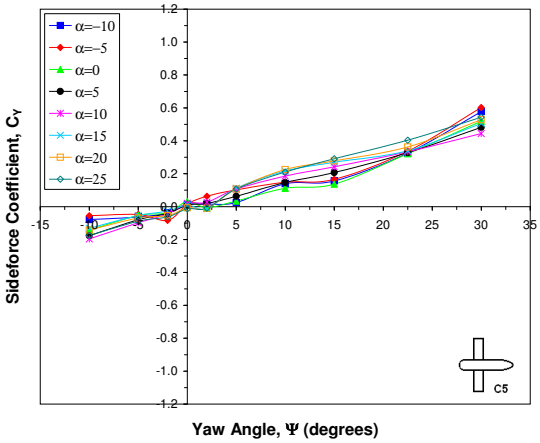

(d) Results for configuration C5 at $\Omega = 2$

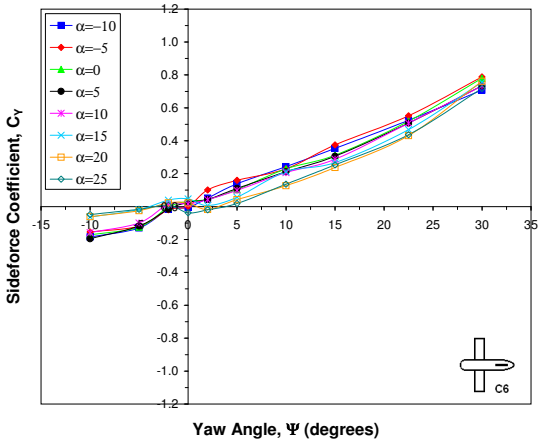

(e) Results for configuration C6 at $\Omega = 0$

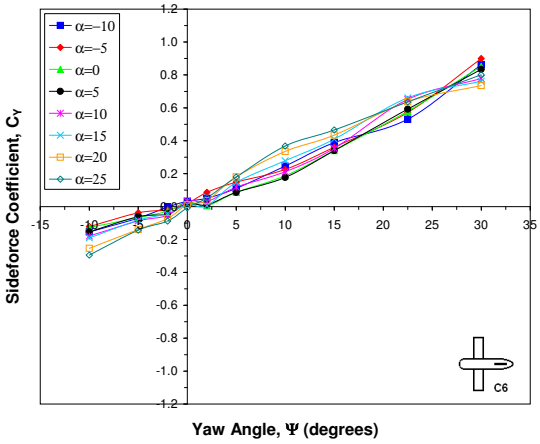

(f) Results for configuration C6 at $\Omega = 2$

Figure 6.20: Variation of sideforce coefficient with yaw angle for the vehicle model with and without vertical fin at $Re = 1.83 \times 10^4$.

6.4.3 Moment Results

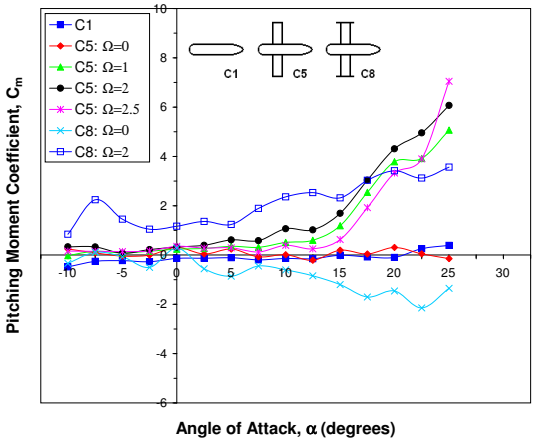

(a) Variation of C_m with angle of attack at $\Psi = 0°$

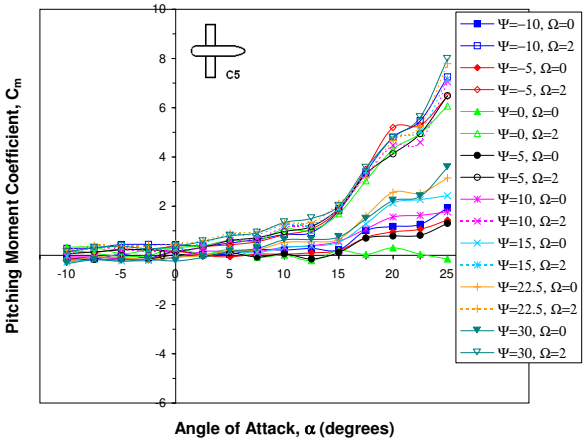

(b) Variation of C_m with angle of attack for C5

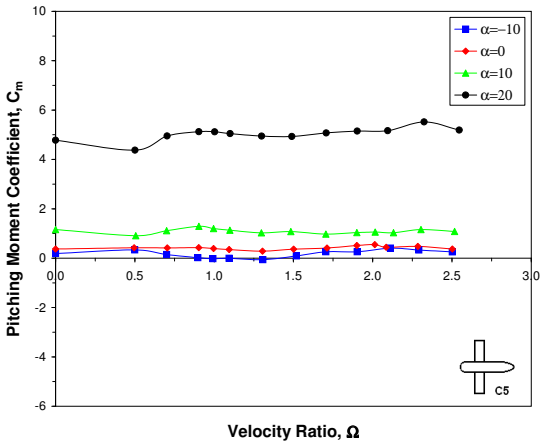

(c) Effect of α on C_m vs Ω for C5 at $\Psi = 0°$

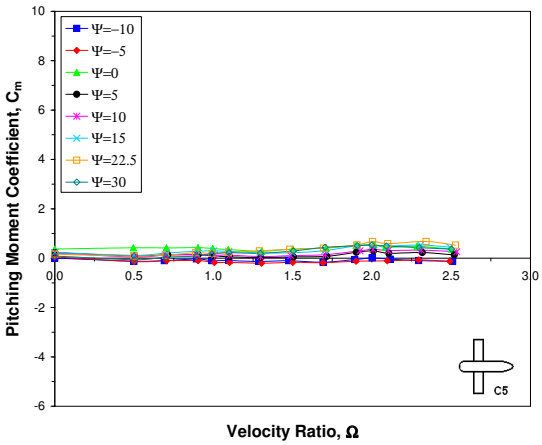

(d) Effect of Ψ on C_m vs Ω for C5 at $\alpha = 0°$

Figure 6.21: Pitching moment coefficient results for the model without tail at $Re = 1.83 \times 10^4$.

Figure 6.21a shows that for configuration C5 the curve of C_m against α, and hence the pitch stability of the model, was affected by both angle of attack and velocity ratio. For $\Omega = 0$ the model was found to be approximately neutrally stable or slightly unstable for all angles of attack examined. A comparison with the results for configuration C1 indicates that the presence of stationary cylinders may have had a slight stabilising effect as $dC_m/d\alpha$ was more positive with the fuselage alone.

Rotation of the cylinders, up to $\Omega = 2$, increased the magnitude of the pitching moment coefficients and caused the model to become progressively more unstable in pitch, with the value of $dC_m/d\alpha$ at low α becoming more positive with increasing Ω. This is somewhat inconsistent with the expected effects on the vehicle due to the reaction torque aris-

ing from spinning of the cylinders but may be a result of more influential aerodynamic effects and the location of the center of gravity. For $\Omega > 2$ the magnitude of C_m and $dC_m/d\alpha$ both decreased with increasing velocity ratio. Results at all nonzero Ω showed a significant increase in the magnitude of the pitching moment generated and the magnitude of $dC_m/d\alpha$, so that the vehicle became severely unstable, when $\alpha > 12°$. This behaviour may be a result of the simple design of the body, the highly three-dimensional nature of the flow, and the interactions between the rotors and fuselage.

The addition of endplates to the rotors appeared to significantly change the pitching moment characteristics of the model, generally increasing the magnitude of C_m and altering the stability of the model so that for $\Omega = 0$ configuration C8 was actually stable in pitch, even without a tailplane, and was, for $\Omega = 2$, less unstable than C5. However, there is considerable uncertainty over the accuracy of the findings, and the pitching moment results in general, due to difficulties in measuring the small magnitude moments generated by the model. The rather large magnitudes of the actual pitching moment coefficients appears to be a consequence of the design of the model and the choice of reference area and length used in reducing the data to coefficient form.

The results without the tail also revealed that, for $\Omega = 0$, the curve of pitching moment coefficient against angle of attack varied considerably with yaw angle when $\alpha > 15°$, but that this was substantially reduced when the cylinders were rotating (see Figure 6.21b). The relationship between pitching moment coefficient and velocity ratio generally showed only a slight variation of C_m with increasing Ω, and was not significantly altered by either angle of attack or non-zero yaw (see Figures 6.21c and d). Note that comparison of Figures 6.21a and c suggests an inconsistency between pitching moment results obtained by varying α at constant Ω and those from varying Ω at constant α, most prominently for $\alpha > 10°$ and $\Omega < 1$. This discrepancy remains unexplained but is thought to be a result of incorrect determination of the wind-off or strut contributions to C_m under the different testing procedures used for each type of test (with changes in the static friction at the point of contact between the model and the support sting being the most likely cause of error).

The effects of interaction between the tail and the cylinders on the pitching moment characteristics were similar to those noted for the lift and drag (see Figure 6.22). By itself the tail produced a negative value of $dC_m/d\alpha$ for all tail settings and all pre-tail-stall angles of attack (with average values of $dC_m/d\alpha \approx -18$ per radian and $dC_m/dC_L \approx -6$) so that configuration C3 was always stable. Post-stall angles showed a levelling-off of C_m. The addition of stationary cylinders to the model caused the pitching moment curve to become more linear and pushed stall effects to higher angles of attack but also slightly reduced vehicle stability ($dC_m/d\alpha \approx -13$ per radian and $dC_m/dC_L \approx -5.7$ for C7).

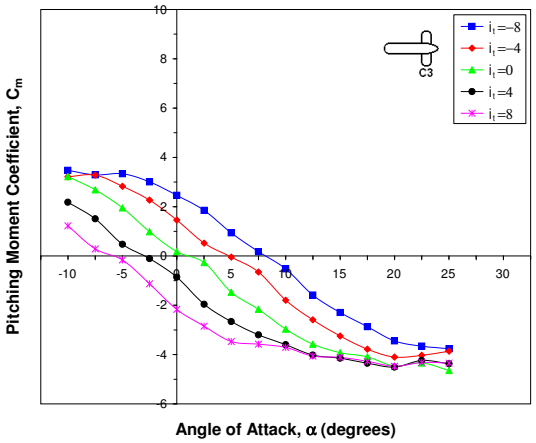

(a) Variation of C_m with α for C3 at $\Psi = 0°$

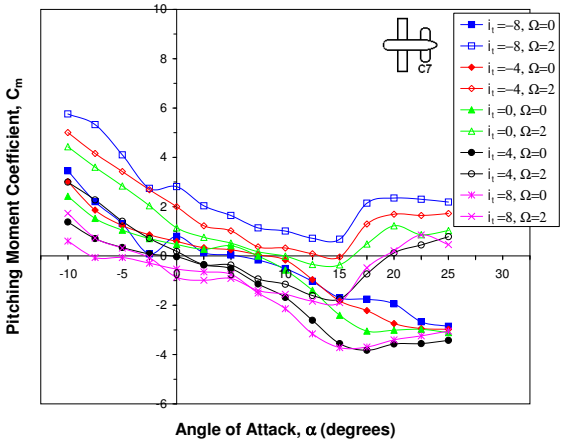

(b) Variation of C_m with α for C7 at $\Psi = 0°$

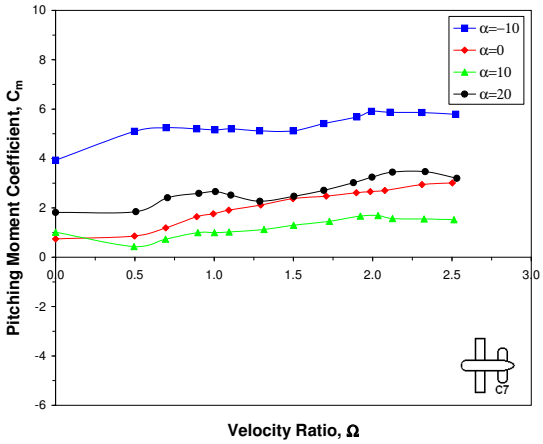

(c) C_m vs Ω for C7 ($i_t = -8°$, $\Psi = 0°$)

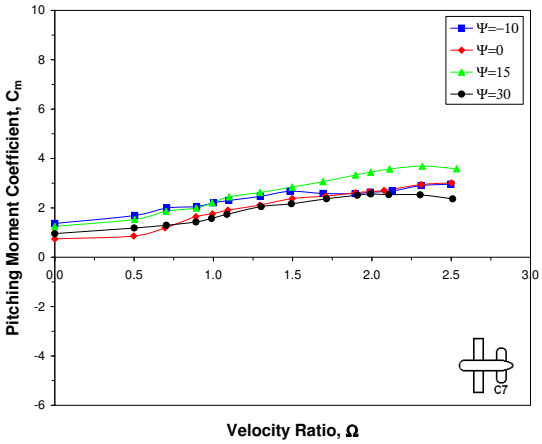

(d) C_m vs Ω for C7 ($i_t = -8°$, $\alpha = 0°$)

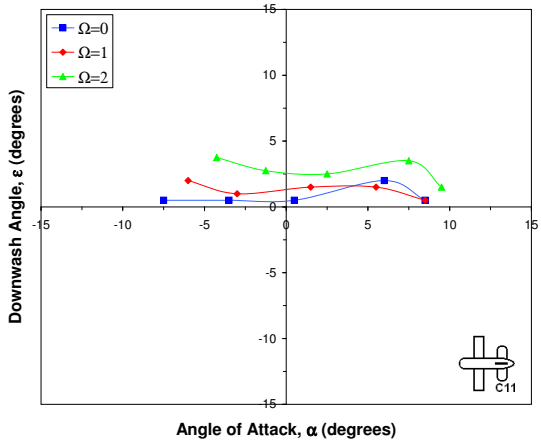

(e) Variation of downwash at tail with α for C11

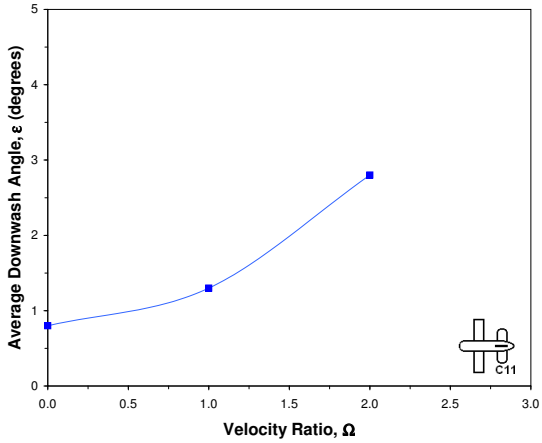

(f) Variation of downwash at tail with Ω for C11

Figure 6.22: Pitching moment coefficient results for the model with tail at $Re = 1.83 \times 10^4$.

With rotation of the cylinders the form of the pitch curve and the slope $dC_m/d\alpha$ remained largely the same except that a sudden shift towards large positive values of C_m and un-

stable pitch behaviour, as observed for C5 when $\Omega > 0$ and $\alpha > 15°$, was once again apparent (see Figure 6.22b). Such characteristics appear to be associated primarily with the rotors but were somewhat mitigated by the addition of the tail, which caused the increase in C_m for C7 to plateau when $\alpha > 20°$. Results for $\Omega = 2$ and $\alpha = 0°$ also show that a tail setting of $i_t = 4°$ was able to trim the pitching moment on the model. Unlike for a regular aircraft, which must have $C_m = 0$ for some $\alpha > 0°$, this situation is a possible configuration for flight for this type of design as the rotor lift is independent of α.

Figures 6.22c and d show the addition of the tail to change the relationship between the pitching moment and the velocity ratio so that the curve of C_m against Ω took on an obvious positive gradient (of magnitude $0.5 \leq dC_m/d\Omega \leq 1$, depending on α, Ψ, and i_t). A similar change was seen in the pitching moment response to nonzero yaw, although $dC_m/d\Omega$ was largely constant with changing Ψ. Different tail setting angles also had the effect of changing the magnitude of the pitching moment at a given velocity ratio by moving the curve of C_m against Ω up or down the y-axis. This was true for all α and Ψ.

Pitching moment results also enabled an estimation of the downwash at the tail due to the cylinders (see Figures 6.22e and f), which was assessed by determining the angle of attack for which the tail-on pitching moment at a given tail setting was equal to the tail-off pitching moment. The results for C11 show the downwash angle to be nearly constant with changing α, which is consistent with the insensitivity of the circulation due to the cylinders to angle of attack. The gradient $d\epsilon/d\alpha$ was found to be affected by velocity ratio, being $d\epsilon/d\alpha \approx 0$ when $\Omega = 0$ and slightly negative when $\Omega > 0$, but there is considerable uncertainty in the results. Similarly, the estimated average downwash angle was also dependent on Ω, with a nonlinear, slightly parabolic, variation being indicated.

The actual values of the downwash angle (e.g. $\epsilon \approx 3$ at $\Omega = 2$) were found to be somewhat smaller than might be expected given the high value of C_L associated with high velocity ratios. These low values may be indicative of inaccuracies in estimating downwash and, indeed, the results cannot be confirmed because of a lack of data for comparison. Alternatively, such results may be a consequence of the highly inclined nature of the cylinder's wake flow at high Ω and the large spacing between the tail and rotors, which was equivalent to six cylinder diameters.

Wake pressure data for the isolated cylinder (see §5.5.8) shows that for such a downstream distance the wake of the cylinders would, for $\Omega = 2$, be about two tail-chord lengths below the level of the tail. Hence, despite its body-mounted position, the tail may actually be well away from most of the effects of downwash, so that it is similar to a fin-mounted or T-tail arrangement but without the susceptibility to deep stall. Downwash angles may

thus be considerably greater, and tail performance significantly different, if the tail were closer to the rotors. Upwash from the fuselage may also play a role in the low values of ϵ.

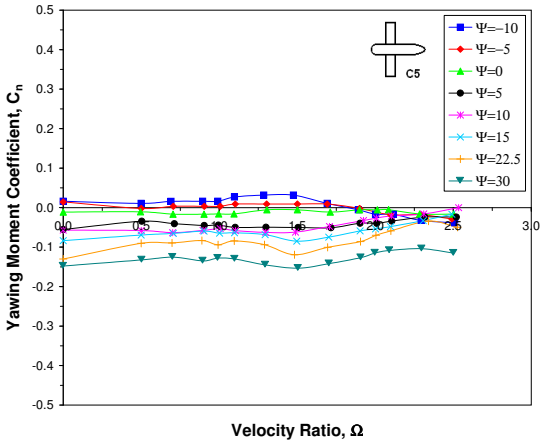

(a) Results for configuration C5 at $\alpha = 0°$

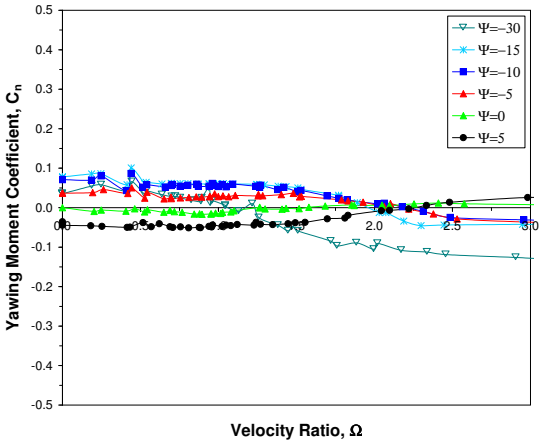

(b) Isolated cylinder results for $d_e/d = 1$

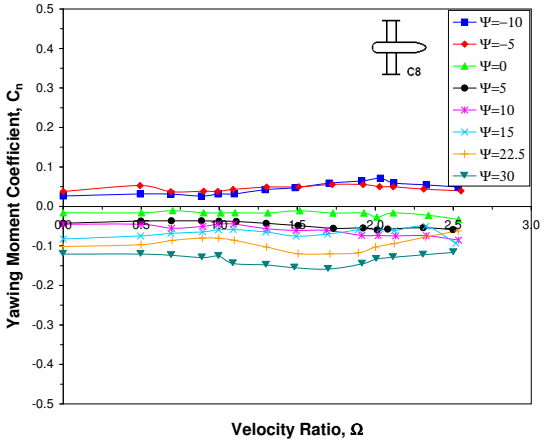

(c) Results for configuration C8 at $\alpha = 0°$

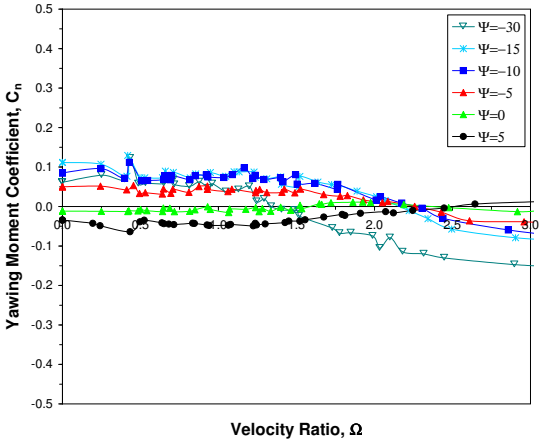

(d) Isolated cylinder results for 1 x $d_e/d = 1.25$

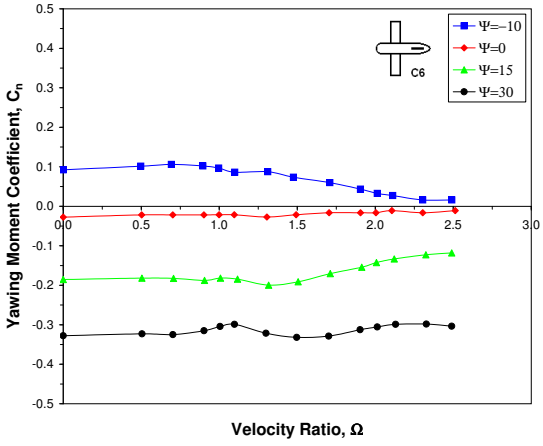

(e) Results for configuration C6 at $\alpha = 0°$

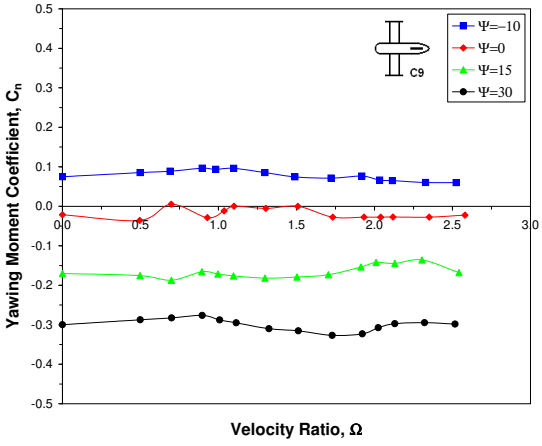

(f) Results for configuration C9 at $\alpha = 0°$

Figure 6.23: Variation of yawing moment coefficient with velocity ratio for the vehicle model with and without vertical fin at $Re = 1.83 \times 10^4$.

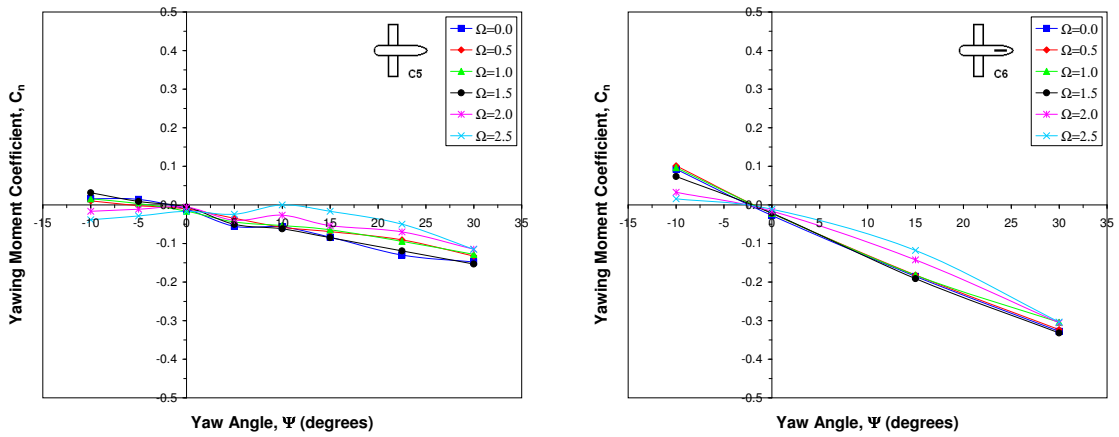

(a) Variation of C_n with Ψ for C5

(b) Variation of C_n with Ψ for C6

Figure 6.24: Effect of velocity ratio on $dC_n/d\Psi$ for the vehicle model with and without vertical fin at $Re = 1.83 \times 10^4$.

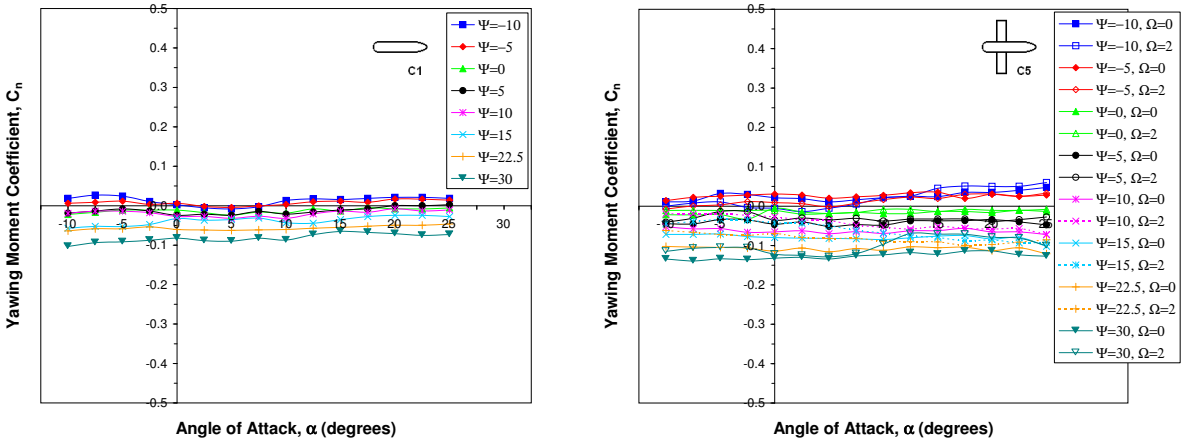

(a) Results for configuration C1

(b) Results for configuration C5

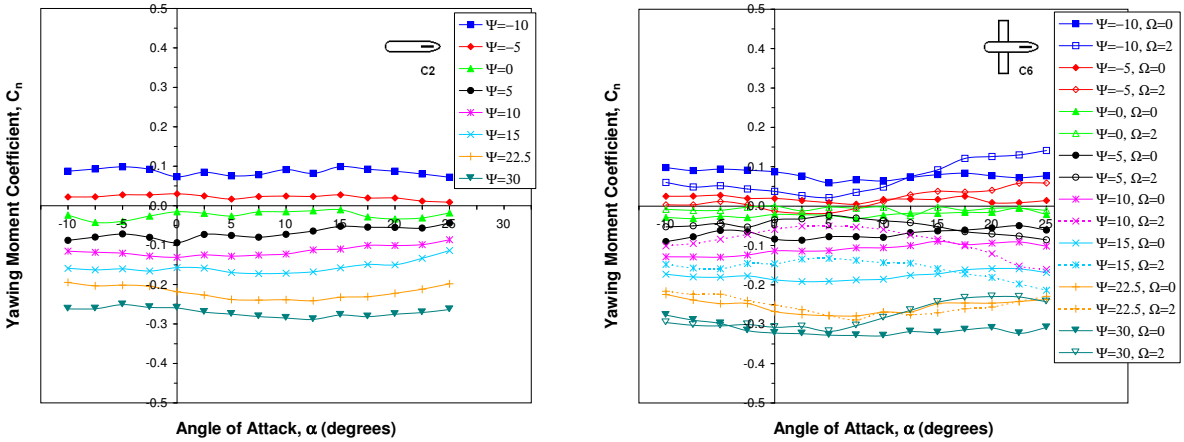

(c) Results for configuration C2

(d) Results for configuration C6

Figure 6.25: Variation of yawing moment coefficient with angle of attack for the vehicle model with and without vertical fin at $Re = 1.83 \times 10^4$.

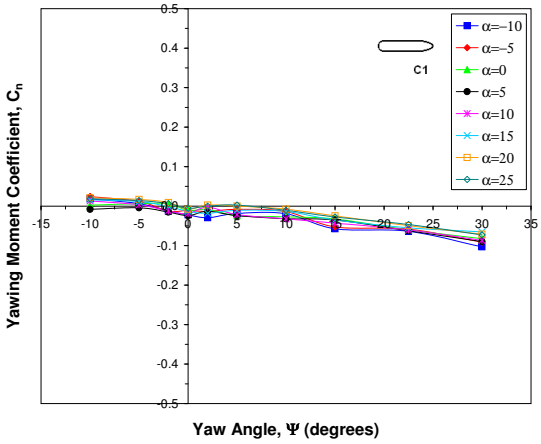

(a) Variation of C_n with Ψ for C1

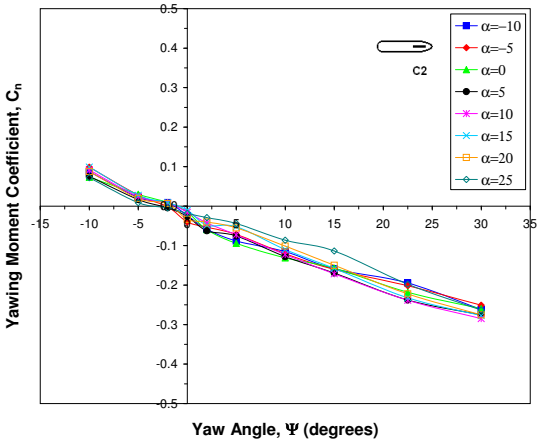

(b) Variation of C_n with Ψ for C2

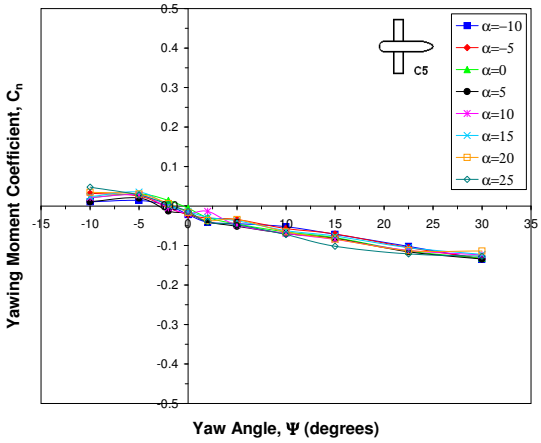

(c) Variation of C_n with Ψ for C5 at $\Omega = 0$

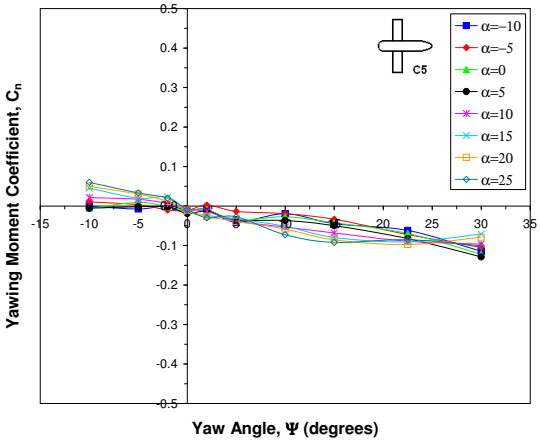

(d) Variation of C_n with Ψ for C5 at $\Omega = 2$

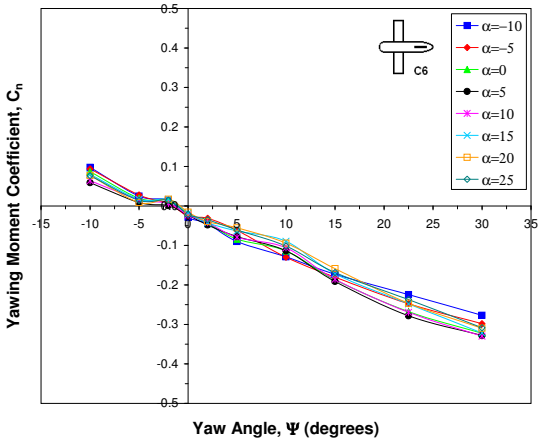

(e) Variation of C_n with Ψ for C6 at $\Omega = 0$

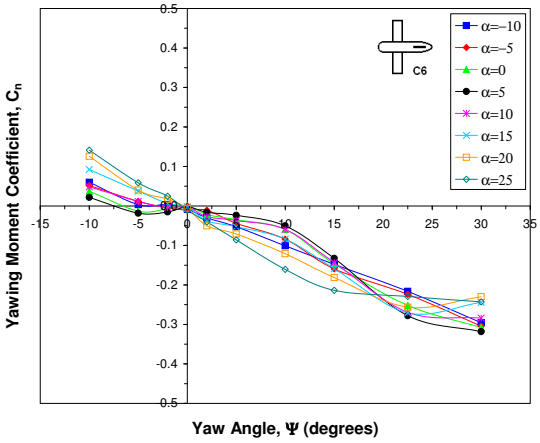

(f) Variation of C_n with Ψ for C6 at $\Omega = 2$

Figure 6.26: Variation of yawing moment coefficient with yaw angle for the vehicle model with and without vertical fin at $Re = 1.83 \times 10^4$.

Yawing moment results showed many similarities with the sideforce data, particularly in

regards to the differences relative to the isolated cylinder tests and the dominance of the influence of the fin and fuselage over that of the cylinders. However, the yawing moment data also showed greater agreement with the results of §5.5.10 than the sideforce, with C_n for C5 tending towards zero magnitude for $\Omega \approx 2$ and a change in the behaviour at high yaw, though less overt than with the isolated cylinder, being apparent (see Figures 6.23a and b). That being said, discrepancies with regards to the magnitude of C_n and the effect of the endplates remain visible in the results (see Figures 6.23c and d). Like the sideforce, these differences appear to be largely a result of the fuselage; the addition of the fin increased only the magnitude of the yawing moment and did not change the nature of the variation of C_n with Ω (see Figures 6.23e and f).

Unlike with the sideforce, the fuselage itself was found to be less important in determining the directional stability characteristics of the aircraft and so the ability of increasing Ω to change the sign of $dC_n/d\Psi$, as observed with the isolated rotating cylinder, remained visible in the results until the fin was added (see Figure 6.24). With the fin, Ω was less important and trends due to the cylinders were much reduced. Consequently, for these configurations, the sign of $dC_n/d\Psi$ remained negative for all Ω, the stability derivative $dC_n/d\beta$ was thus always positive, and the vehicle was always statically stable in yaw.

Spinning of the cylinders was found to have an effect on the variation of yawing moment with angle of attack, particularly for $\Psi > 10^\circ$ where quite significant changes in behaviour were introduced (see Figure 6.25). Rotation at $\Omega = 2$ tended to substantially reduce the magnitude of C_n at low α and then increase it slightly for high angles. This behaviour changed when $\Psi = 30^\circ$ so that the opposite trend was generally observed. Such effects on the curve of C_n against α were also seen to be magnified by the fin.

The variation of C_n with Ψ further confirmed the dominance of the fin over the cylinders in establishing the yawing moment characteristics of the vehicle. Comparison of the gradients of Figures 6.26a, b, and c showed that, whereas the fin increased the magnitude of $dC_n/d\Psi$ by a factor of four relative to the fuselage-alone case (for C1, $dC_n/d\Psi \approx -0.13$ per radian; for C2, $dC_n/d\Psi \approx -0.51$ per radian), the cylinders provided an increase of only 83% when $\Omega = 0$ and just 40% when $\Omega = 2$ (for C5 at $\Omega = 0$, $dC_n/d\Psi \approx -0.24$ per radian; for C5 at $\Omega = 2$, $dC_n/d\Psi \approx -0.18$ per radian). This reduction in $dC_n/d\Psi$ is associated with non-linearity of the relationship between yawing moment and yaw angle that is introduced by spinning of the cylinders, and which varies with both α and Ψ.

Rotation of the cylinders with the fin attached acted to enhance the effect of the fin and increased directional stability by a modest amount ($dC_n/d\Psi \approx -0.52$ per radian for C6 at $\Omega = 2$) but also increased the extent of the observed non-linear behaviour. However,

such nonlinear characteristics were substantially reduced by the use of endplates, which also tended to increase stability ($dC_n/d\Psi \approx -0.57$ per radian for C9 at $\Omega = 2$).

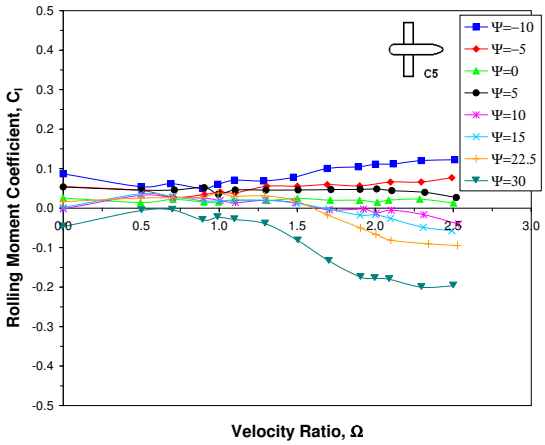

(a) Results for configuration C5 at $\alpha = 0°$

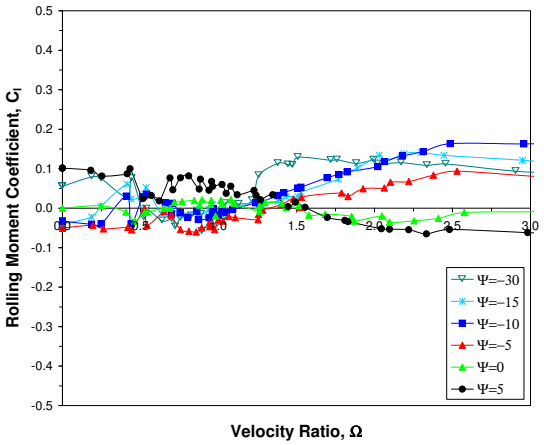

(b) Isolated cylinder results for $d_e/d = 1$

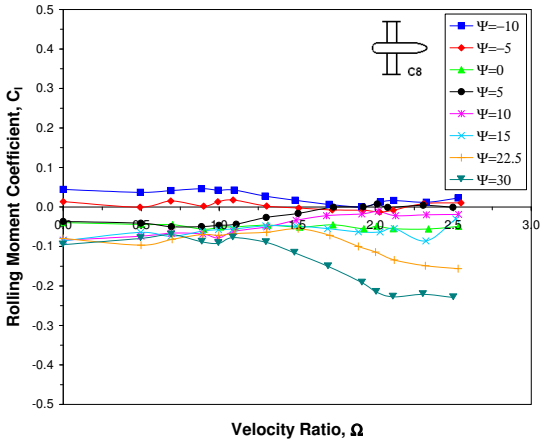

(c) Results for configuration C8 at $\alpha = 0°$

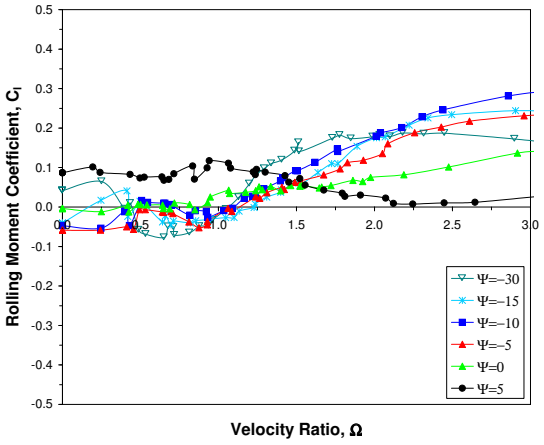

(d) Isolated cylinder results for 1 x $d_e/d = 1.25$

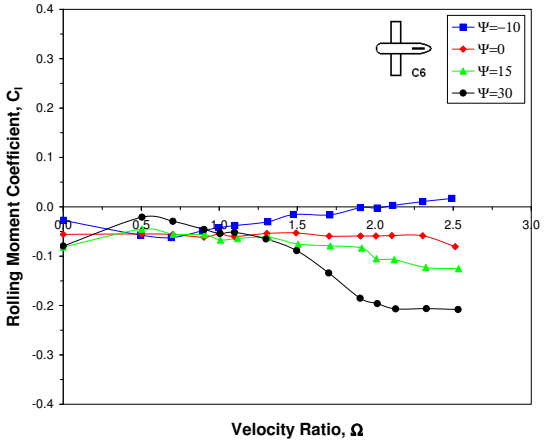

(e) Results for configuration C6 at $\alpha = 0°$

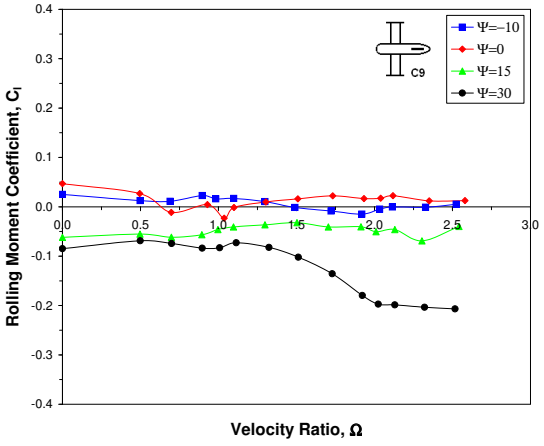

(f) Results for configuration C9 at $\alpha = 0°$

Figure 6.27: Variation of rolling moment coefficient with velocity ratio for the vehicle model with and without vertical fin at $Re = 1.83 \times 10^4$.

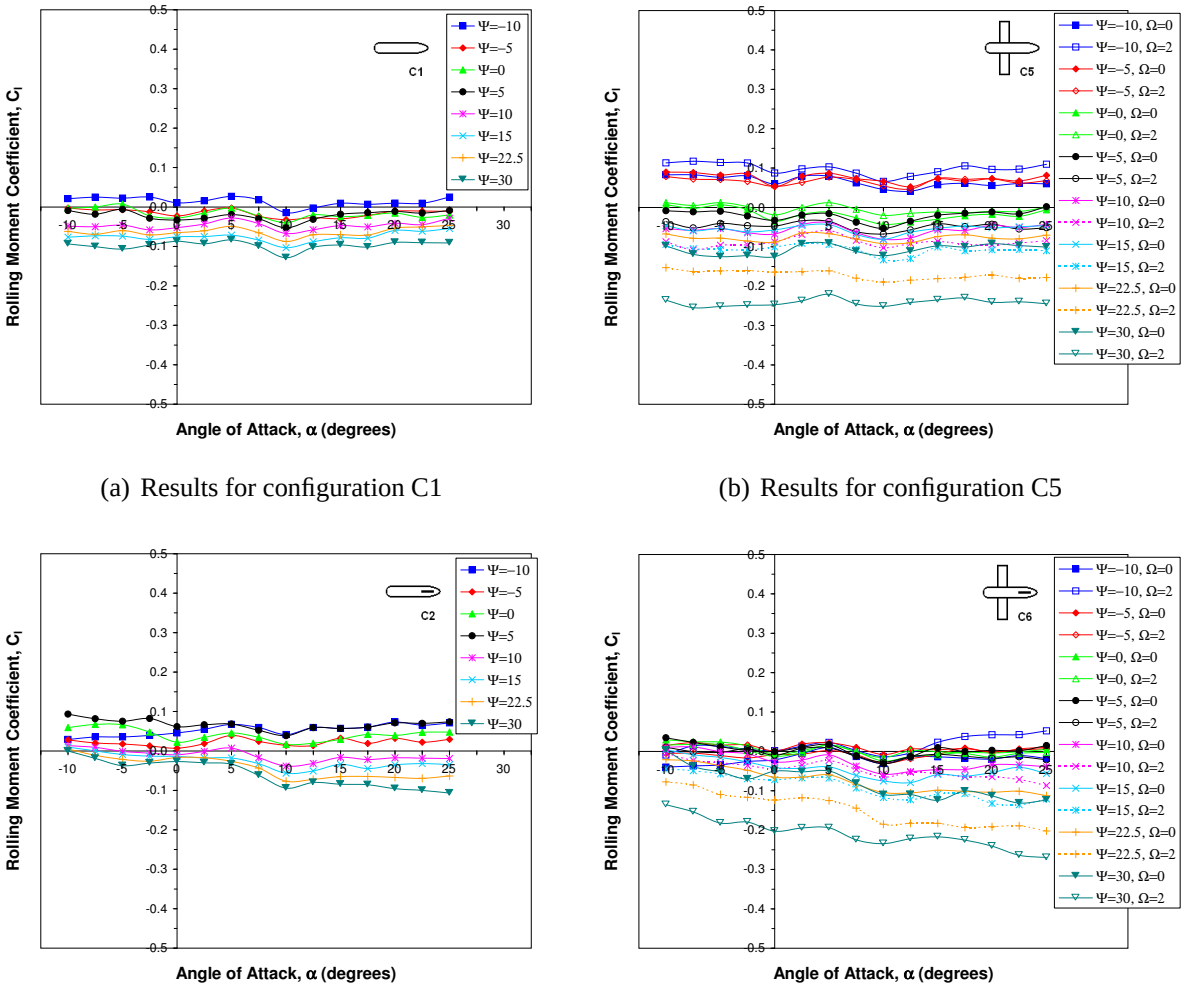

(a) Results for configuration C1

(b) Results for configuration C5

(c) Results for configuration C2

(d) Results for configuration C6

Figure 6.28: Variation of rolling moment coefficient with angle of attack for the vehicle model with and without vertical fin at $Re = 1.83 \times 10^4$.

Rolling moment trends (see Figures 6.27, 6.28, and 6.29) were similar to those observed in the sideforce and yawing moment results, although the cylinders, especially when fitted with endplates, were found to be more influential in determining stability characteristics than for the other lateral forces and moments. As with C_Y and C_n, a comparison with the isolated cylinder results (Figures 6.27a to d) showed similarities between the data, though the influence of the fuselage on the variation with Ω, whilst not as strong as for the sideforce and yawing moment, remained apparent. Furthermore, the effect of asymmetric end conditions on the rolling moment for the model was seen to differ from that on the isolated cylinder, this probably being a result of the model having two individual cylinders with endplates at opposing ends. Results for the variation of C_l with Ω also showed that the addition of the fin changed only the magnitude of the rolling moment at a given velocity ratio without altering the form of the curves in Figures 6.27e and f.

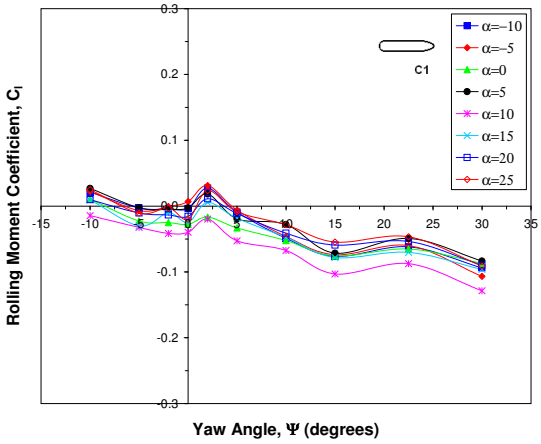

(a) Variation of C_l with Ψ for C1

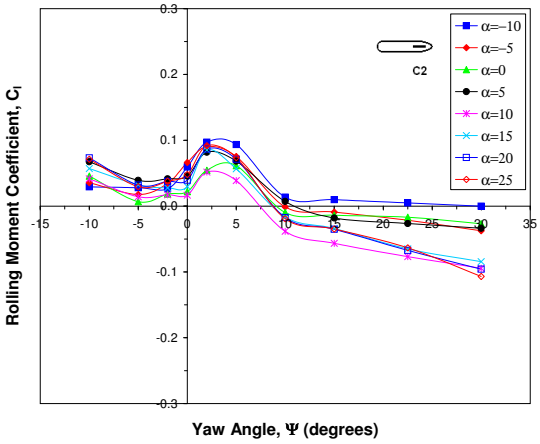

(b) Variation of C_l with Ψ for C2

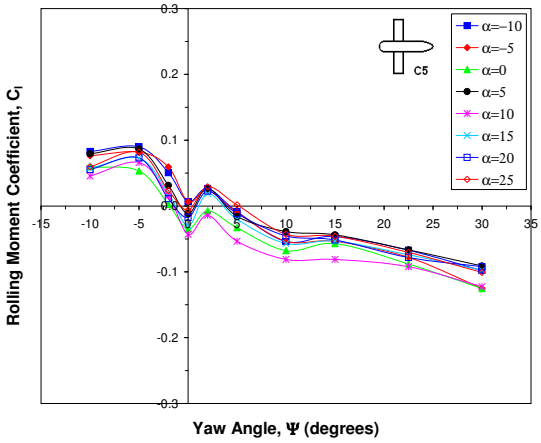

(c) Variation of C_l with Ψ for C5 at $\Omega = 0$

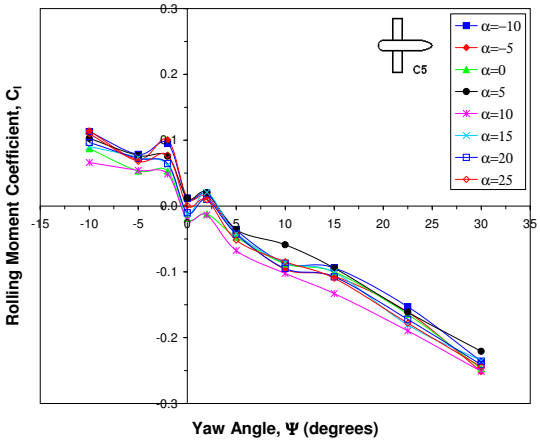

(d) Variation of C_l with Ψ for C5 at $\Omega = 2$

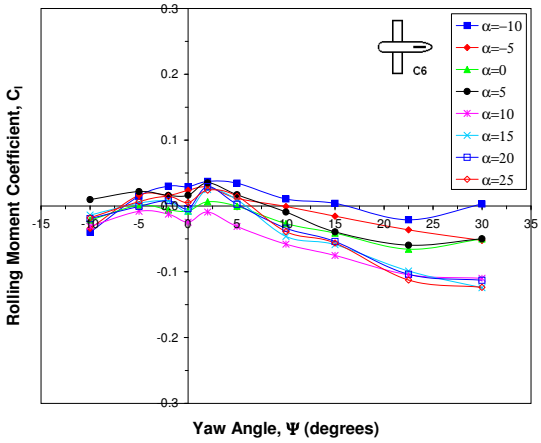

(e) Variation of C_l with Ψ for C6 at $\Omega = 0$

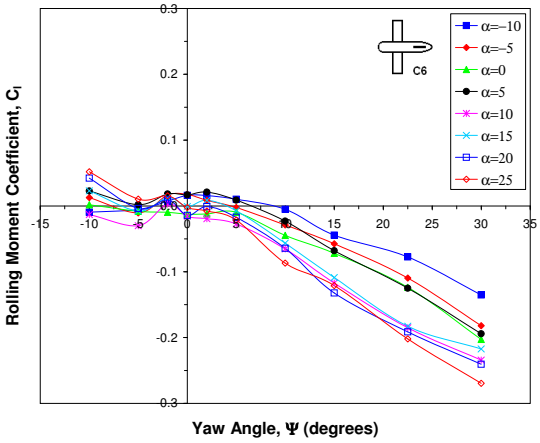

(f) Variation of C_l with Ψ for C6 at $\Omega = 2$

Figure 6.29: Variation of rolling moment coefficient with yaw angle for the vehicle model with and without vertical fin at $Re = 1.83 \times 10^4$.

Figure 6.28 shows the rolling moment to be generally constant with changing angle of

attack, although the addition of the fin caused a slight negative gradient when $\Psi > 15°$. Results at different angles of attack also suggest that the fuselage provided a substantial contribution to the magnitude of C_l. The addition of the cylinders increased the magnitude of the rolling moment at a given angle of attack, particularly when $\Psi > 15°$ and $\Omega > 1.5$, but did not appreciable alter the variation of C_l with α.

The variation of rolling moment with yaw angle showed that the relationship between C_l and Ψ was generally linear. Figure 6.29 also indicates that the sign of $dC_l/d\Psi$ for those configurations without the fin was always negative, and hence $dC_l/d\beta$ always positive, so that the model was unstable in roll for such configurations. The results for C5 show that the addition of stationary cylinders to the model had little effect on the curve of C_l against Ψ, but that rotation of the cylinders made the model more unstable, particularly when $\Omega > 1.5$. This behaviour is consistent with the results for the isolated rotating cylinder. The use of a single endplate on each rotor made the effects of rotation worse, indicating that asymmetric end conditions are particularly undesirable for stability in roll. Configurations with the fin showed the model to be laterally stable only for a small range of yaw angles around $\Psi = 0°$, this probably being a result of the simple design of the fin.

6.4.4 Effects of Differential Rotation of the Cylinders

The results of tests with the cylinders undergoing differential rotation are shown in Figure 6.30. Note that the x-axis in these graphs illustrates the total percentage difference between the port and starboard velocity ratios, relative to their initial values of $\Omega = 2$. For example, with the first method of differential rotation investigated, in which both rotors had their velocity ratios changed by an equal but opposite amount, a percentage difference of 50% indicates that the port velocity ratio was $\Omega = 2.5$ and the starboard one $\Omega = 1.5$. For the second method, where only the starboard cylinder had its velocity ratio altered whilst the port cylinder stayed at a constant $\Omega = 2$, a difference of 50% refers to a condition where the starboard rotor had a velocity ratio of $\Omega = 1$.

The results show that differential rotation produces a substantial rolling moment that changes linearly with increasing percentage difference between port and starboard velocity ratios. The magnitude of C_l and the nature of the response to differential rotation was the same for both methods of differential rotation implemented, though the starboard-only approach yielded slightly larger rolling moments when the difference between the rotors, relative to $\Omega = 2$, was greater than 35%. However, both methods of differential rotation also resulted in a substantial adverse yaw response, whereby large yawing moment coefficients of nearly equal magnitude to C_l but of opposing sign (and which thus work

against the desired roll direction) were generated alongside the induced rolling moment.

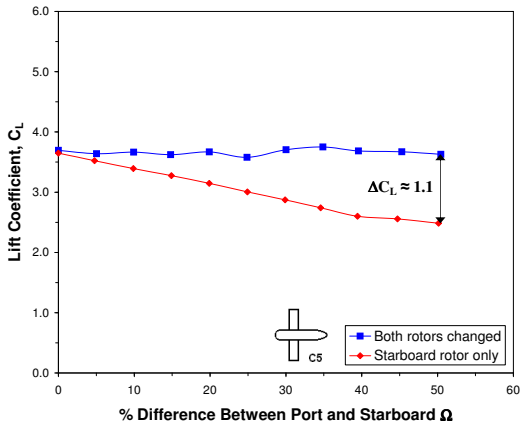

(a) Lift results

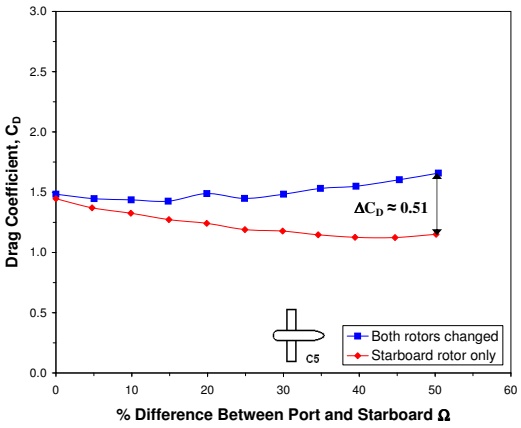

(b) Drag results

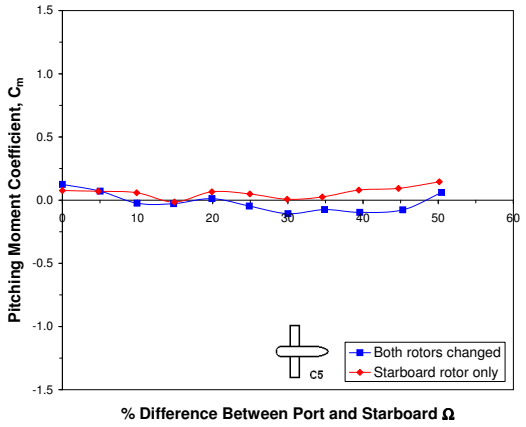

(c) Pitching moment results

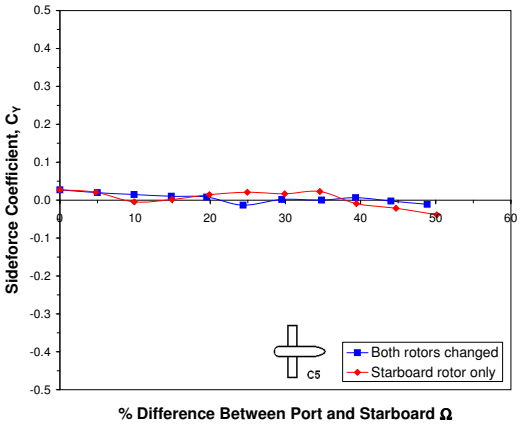

(d) Sideforce results

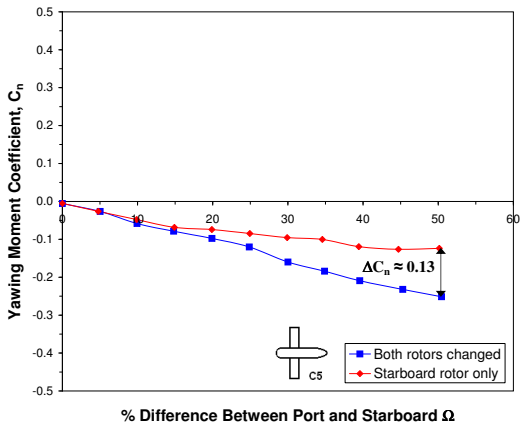

(e) Yawing moment results

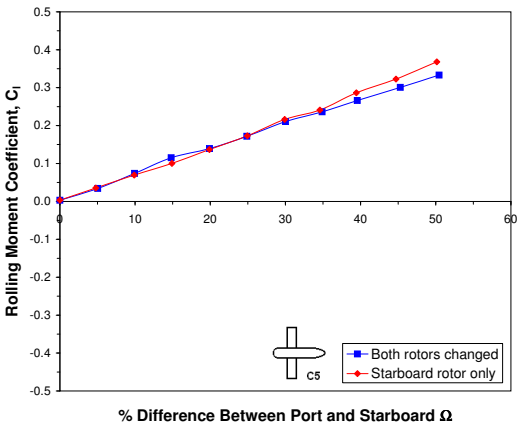

(f) Rolling moment results

Figure 6.30: The effects of differential rotation of the cylinders on the aerodynamic forces and moments for configuration 5 at $\alpha = 0°$, $\Psi = 0°$, and $Re = 1.83 \times 10^4$. Note that for both types of differential rotation the starboard cylinder always had its velocity ratio decreased.

For the case where only the starboard rotor had its rotation rate changed, the adverse yawing moment was found to be more modest and eventually reached a plateau once a large difference between the velocity ratios of the two cylinders was implemented. This occurred because this particular method of differential rotation also causes a fall and subsequent plateau in the drag coefficient, as well as the lift. Although this is beneficial to reducing the adverse yaw response it also has the undesirable consequence of coupling together the longitudinal and lateral motion. Changing both rotors in an equal but opposite manner introduced no such change in lift and drag. Neither method had any appreciable effect on the sideforce or pitching moment, with differences in the C_m data being primarily due to the large error associated with the determination of this component.

The basic nature of the response to differential rotation, as shown in Figure 6.30, was found to be unaffected by the presence of either the fin, tail, endplates, or propeller, although the actual magnitudes of the aerodynamic coefficients generated were changed. Endplates were found to substantially increase (by up to 50%) the rolling moment generated by both methods of differential rotation, whereas the tail and propeller were found to reduce it (by 25% each). When both the tail and endplates were used, the influence of the endplates was found to be dominant. The tail did not have any effect on the yawing moment but the effects of the propeller and endplates on C_n were the same as for C_l.

Note that, if the 'center of pressure' for each rotor is assumed to be located at its geometric center ($y/s \approx \pm 0.32$), then the measured values of the rolling moment and yawing moment generated by both methods of differential rotation are found to be wholly consistent with the differences in the lift and drag forces acting on the port and starboard rotors, as indicated by Figures 6.13c and 6.15c when $\alpha = \Psi = 0^\circ$ (taking into account that, from Equation 6.1, C_L and C_D for the individual rotors at a given Ω will be half the values when the cylinders rotate together at the same velocity ratio).

Thus, for example, the maximum generated rolling moment when the velocity ratios of both rotors were changed ($C_{l_{max}} \approx 0.33$) is approximately equal to the product of the difference in lift under these conditions (port rotor at $\Omega = 2.5$, $C_L \approx 2.4$; starboard rotor at $\Omega = 1.5$, $C_L \approx 1.25$; $\Delta C_L \approx 1.15$) and the moment arm y/s. Such correlation may also be shown for ΔC_D and C_n, including the fall in C_n for the 'starboard only' case.

6.4.5 Propeller Effects

The effects of the propeller on the forces and moments acting on the model are shown in Figures 6.31 and 6.32. The presence of the propeller had a significant beneficial effect

on the lift generated (see Figures 6.31a and b) and its variation with angle of attack, such that the lift curve slope for C12 was increased to $dC_L/d\alpha \approx 3$ per radian (representing a 400% rise over that for C5). The addition of the tail caused a further increase in lift curve slope, which for C13 now reached a maximum of $dC_L/d\alpha = 6.8$ per radian when $\Omega = 2$ and $i_t = -8°$ (a 100% increase over that for C11 at the same velocity ratio and tail setting angle).

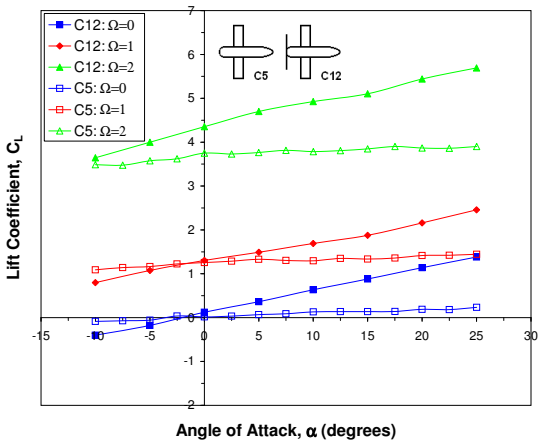

(a) C_L vs α for C12 at $\Psi = 0°$

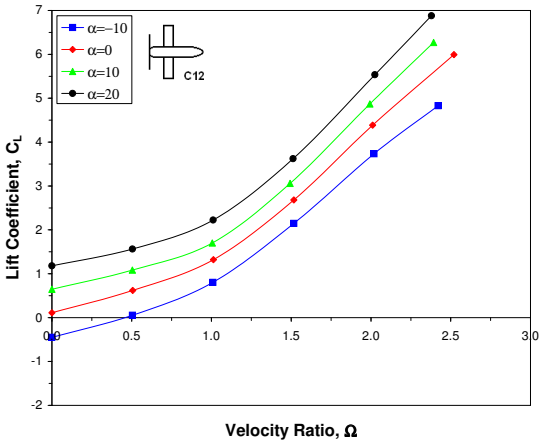

(b) C_L vs Ω for C12 at $\Psi = 0°$

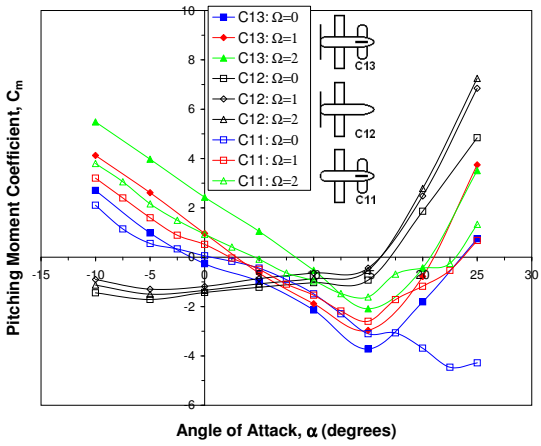

(c) C_m vs α for C12 and C13 at $\Psi = 0°$, $i_t = 0°$

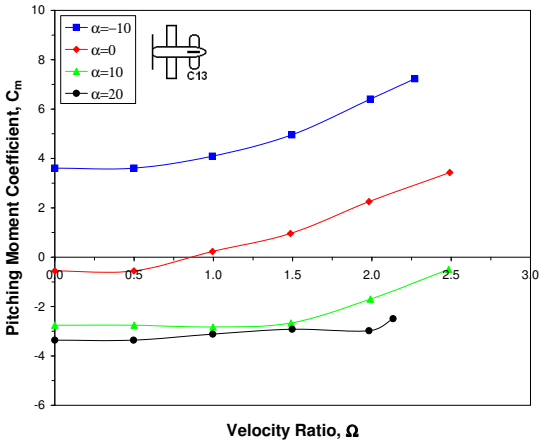

(d) C_m vs Ω for C13 at $\Psi = 0°$, $i_t = 0°$

Figure 6.31: Propeller effects on the longitudinal forces and moments at $Re = 1.83 \times 10^4$.

The influence of velocity ratio on the lift curve slope was also more obvious with the propeller and there was a substantial increase in $dC_L/d\alpha$ as velocity ratio increased from $\Omega = 0$ to $\Omega = 2$. The propeller had no influence on the variation of C_L with Ω and did not affect the response to high yaw angles. This is in keeping with the work of Weiberg & Gamse, who found their rotating cylinder flap to be insensitive to the propeller slipstream.[4]

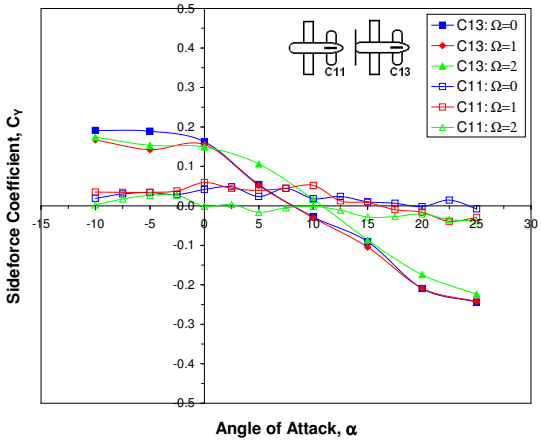

(a) C_Y vs α for C13 at $\Psi = 0°$, $i_t = 0°$

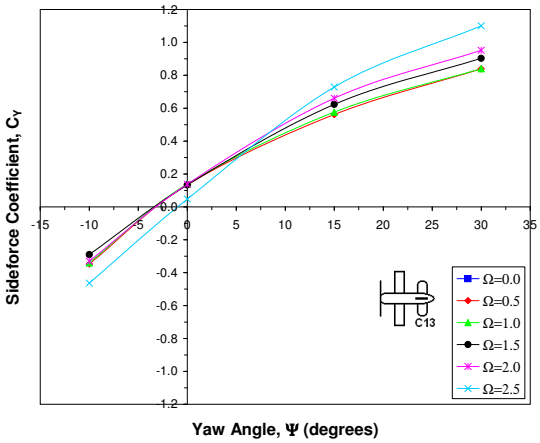

(b) C_Y vs Ψ for C13 at $\alpha = 0°$, $i_t = 0°$

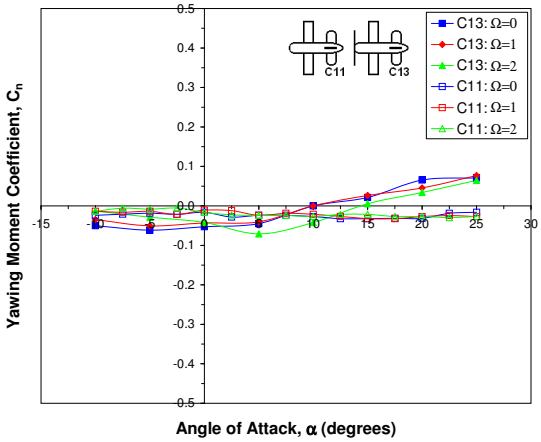

(c) C_n vs α for C13 at $\Psi = 0°$, $i_t = 0°$

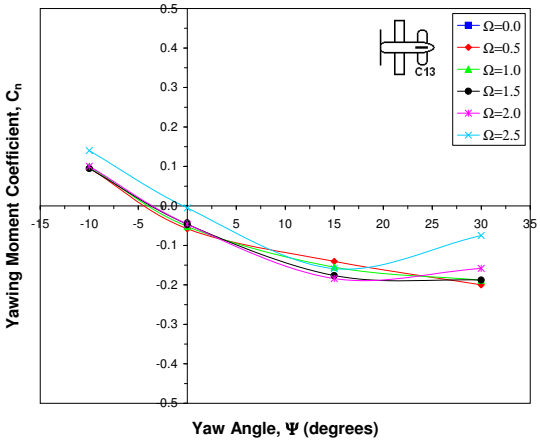

(d) C_n vs Ψ for C13 at $\alpha = 0°$, $i_t = 0°$

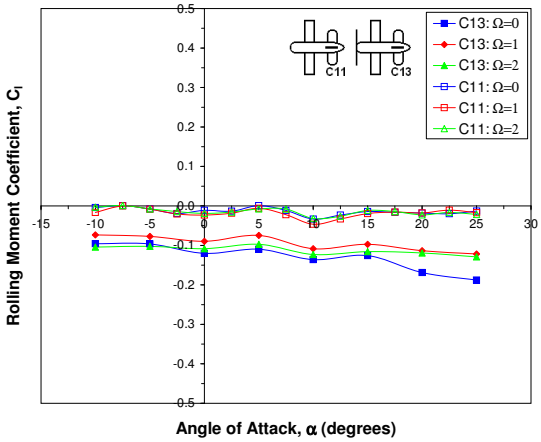

(e) C_l vs α for C13 at $\Psi = 0°$, $i_t = 0°$

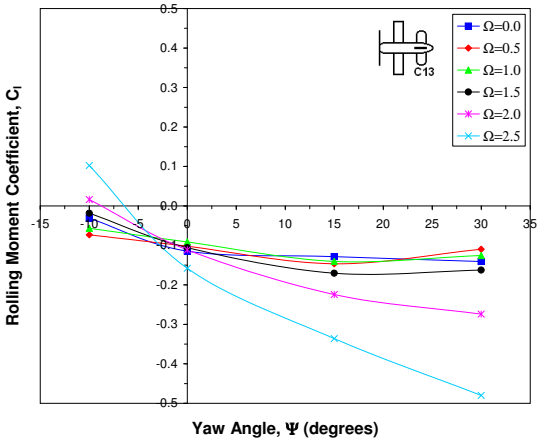

(f) C_l vs Ψ for C13 at $\alpha = 0°$, $i_t = 0°$

Figure 6.32: Propeller effects on the lateral forces and moments at $Re = 1.83 \times 10^4$.

Propeller effects on the pitching moment coefficient were dependent on the presence of the tail (see Figures 6.31c and d). Without the tail, the propeller made the slope $dC_m/d\alpha$

more positive at low angles of attack and exacerbated the change in the pitching moment characteristics that occurs for $\alpha > 15°$. This effect was independent of velocity ratio and is consistent with the contribution to pitching moment from an inclined propeller. The propeller also made the value of C_m at a given yaw angle more negative but did not change the variation of C_m with either Ψ (which was essentially constant) or Ω. With the tail, the propeller increased the magnitude of C_m at a given angle of attack, particularly for $\Omega > 1.5$, and again exacerbated the behaviour for $\alpha > 15°$. However, the propeller now also caused a small increase in the pitch stability of the model ($dC_m/d\alpha \approx -16$ for C13 when $\Omega > 0$). In addition, interactions between the propeller and the tail acted to change the variation of pitching moment coefficient with velocity ratio, causing a slight increase in the growth of the magnitude of C_m with Ω to occur when $\Omega > 1.5$.

The influence of the propeller on the lateral aerodynamic coefficients was found to be generally detrimental (see Figure 6.32). As well as the expected negative contributions to the rolling moment (due to propeller torque) and yawing moment (from the effects of propeller wash) the propeller also acted to increase the influence of angle of attack on C_Y and C_n. In addition, the propeller caused a change in the variation of all the lateral forces and moments with velocity ratio, so that the magnitudes of C_Y, C_n, and C_l increased much more rapidly with increasing velocity ratio when $\Omega > 1.5$. This also resulted in the occurrence of detrimental changes to $dC_n/d\Psi$ and $dC_l/d\Psi$, and hence the stability of the model, when $\Psi > 15°$ and $\Omega > 1.5$. These changes subsequently worsen for $\Omega > 2$.

6.4.6 Gyroscopic Effects

Figure 6.33 provides a comparison of the variation with Ω of the theoretical gyroscopically-induced yawing and rolling moment coefficients, due to rolling and yawing (respectively) of the model, against the experimentally measured, aerodynamically-generated values of C_n and C_l at different fixed angles of yaw. The results indicate that the applied rates of roll and yaw are more important in determining the magnitude of the induced gyroscopic moments than the velocity ratio at which the cylinders spin.

Thus, for motion such as a rate 1 turn ($r = 3$ deg/s), gyroscopic moments would be small and easily trimmed. However, given the manoeuvrability required of MAV-sized craft, much larger rates of roll and yaw may be required (a correctly banked turn at $\phi = 30°$ and $V \approx 7$ m/s requires a yaw rate of $r \approx 40$ deg/s). Figure 6.33 shows that, for the design investigated during testing, the gyroscopic moments induced by such rates of motion would, even at high yaw, be of an equal or greater magnitude than the aerodynamic moments generated by the model, and so may significantly effect its behaviour. In addi-

tion, the gyroscopic contributions to the yawing moment coefficient that are theoretically induced by rolling motion are seen to be such that they may help combat the adverse yaw generated by using differential rotation of the cylinders to initiate roll. However, in practice, the exact behaviour of the aircraft may be somewhat different from this predicted motion. More generally, the sign of the gyroscopically-induced rolling moments is such that they may contribute detrimentally to spiral mode characteristics.

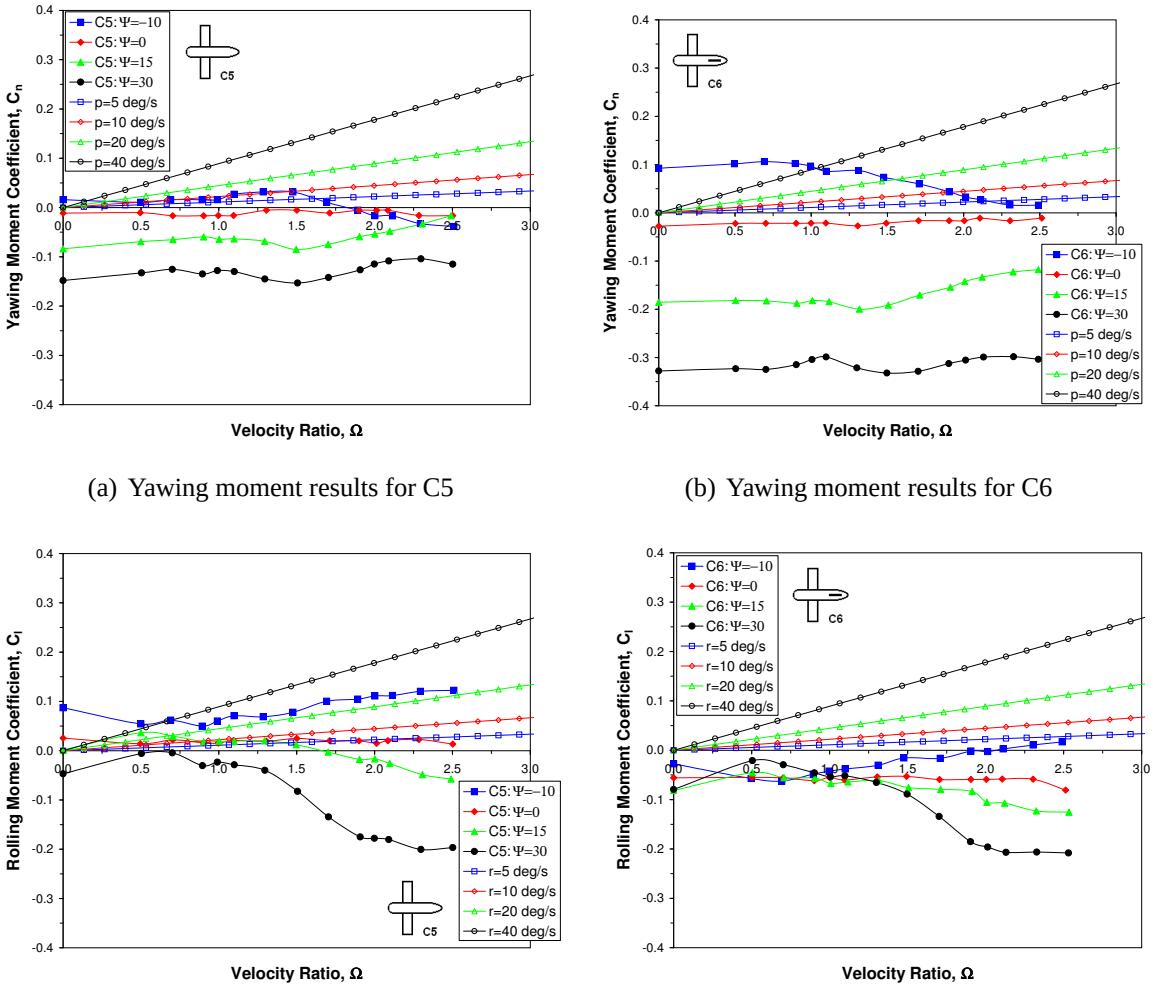

(a) Yawing moment results for C5

(b) Yawing moment results for C6

(c) Rolling moment results for C5

(d) Rolling moment results for C6

Figure 6.33: Comparison of the variation with Ω of the gyroscopic and aerodynamic lateral moment coefficients at $Re = 1.83 \times 10^4$ and various values of yaw angle, roll rate, and yaw rate.

6.4.7 Power Requirements

Power requirements for spinning the cylinders were found to be unaffected by vehicle configuration and, except for at the highest rotation rates implemented, were also largely independent of both angle of attack and yaw angle (see Figure 6.34a). For $N \geq 7000$

rpm, or $\Omega > 2.1$, a slight variation in C_P with changing α and Ψ was found to occur. The results for the variation of C_P with Ω also showed very good agreement with the data for the isolated cylinder (see Figure 6.34b) and reveal the power required to spin the cylinders to be quite low relative to the propeller; in fact, spinning the propeller generally required more power (≈ 40 W at $\Omega = 2$ and $\alpha = \Psi = 0°$) than both cylinders combined.

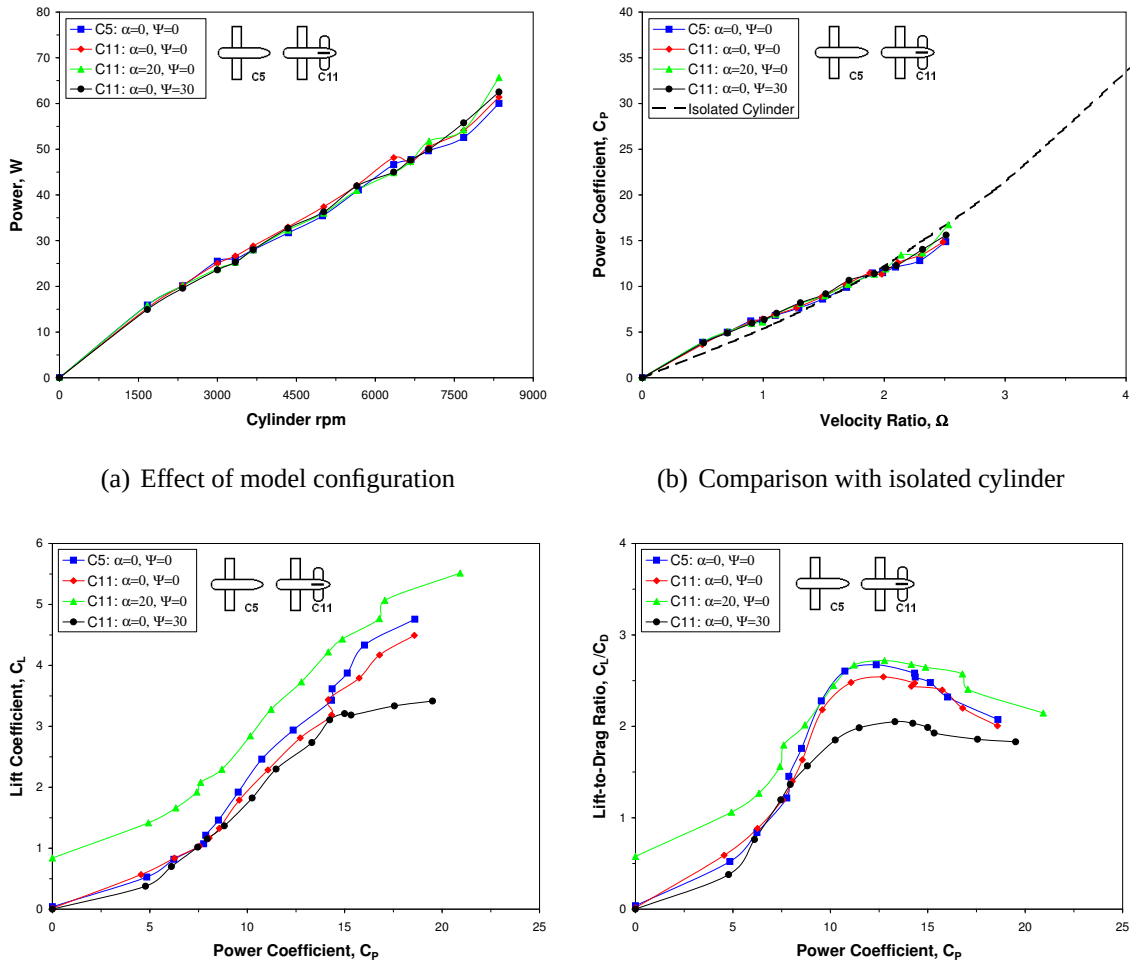

(a) Effect of model configuration

(b) Comparison with isolated cylinder

(c) Effect of power input on lift

(d) Effect of power input on lift-to-drag ratio

Figure 6.34: Power requirements for spinning the cylinders at $Re = 1.83 \times 10^4$.

Changes in the angle of attack, yaw angle, and tail setting angle were found to have an effect on the relationship between the power coefficient and the lift or lift-to-drag ratio (see Figure 6.34c and d). Large, positive α generally increased the performance at a given power input, whereas negative α and non-zero Ψ decreased it. A change in the tail setting angle was found to have a similar influence on C_P as was noted for C_L/C_D. However, the general trends in power performance remained the same as for the isolated cylinder, so that C_L still reached a maximum that was not improved with further increases in C_P and the most power efficient velocity ratio was still $\Omega \approx 2$, regardless of α, Ψ, or i_t.

7 Implications for MAV Design and Performance

The results of the experimental phase of the project have several implications for the design and operation of an MAV or mini-UAV based around rotating circular cylinders, most notably in the choice of operating velocity ratio, the geometry of the rotors, the design and layout of the aircraft, and its stability and control.

7.1 Vehicle Design

The results of tests with the full vehicle model suggest that the chosen design configuration of twin rotating cylinders about a central fuselage with a conventional empennage arrangement behaves like a modified fixed-wing aircraft and that the designs of the tail, fin, and fuselage are of considerable importance. As well as controlling the pitching moment response (with results showing it to successfully provide the required longitudinal static stability) the tail was also found to dictate the value of the lift curve slope $dC_L/d\alpha$ for the entire aircraft and alter the drag response of the vehicle to changing α. Similarly, the designs of the fin and fuselage were found to be very important to the lateral force and moment characteristics, particularly as the model was found to be statically unstable in roll even with the fin attached. This may have been due to the flat-plate nature of the fin and may be rectified through better design or a larger fin. Alternatively, such an aircraft may benefit from a high setting for the rotors, though this might then be detrimental to longitudinal stability.

The aerodynamic performance of the tail was found to be influenced by the wake of the cylinders, with their presence on the vehicle (whether spinning or stationary) leading to a delay of stall and a slight increase in the lift curve slope, so that the cylinders may be considered as high-lift devices that boost the performance of the tail. The results also suggest that an optimum separation between the tail and the cylinders may exist and should be investigated. The cylinders and velocity ratio were less influential in changing the performance of the fin, though this may only have been due to its basic design. Note that these findings may well differ if the fin and tail were of a different size relative to the rotors or if larger endplates were used.

The fundamental nature of the response of the vehicle forces and moments to changing velocity ratio was found to be altered, in comparison to the isolated rotating cylinder, by the addition of the tail (which altered C_m but not C_L, C_D, or C_L/C_D) and the fin and fuselage (which significantly altered C_Y, C_n, and C_l). Propeller effects on the variation with

velocity ratio were generally limited to $\Omega > 2$. However, many of the same characteristics of the isolated cylinder were also observed in the behaviour of the model and the cylinders dictated both the magnitudes of the lift and drag and the total power requirements. Thus, the design of the rotors is of equal importance as that of the fin, tail, and fuselage.

The performance assessments of §4.3 indicate that substantial benefits to the feasibility of this type of design can be achieved if the rotor's aerodynamic performance is equivalent to that of a cylinder of $AR \geq 10$, but that a physically small aspect ratio is preferable for reasons of keeping rotational rates low. As such, the use of endplates will likely have some role to play in the design of a rotating cylinder MAV. In this regard the experiments show that, in terms of endplate configuration, stationary plates are less effective than rotating ones and that symmetric end conditions are generally more favourable than asymmetric conditions, whether due to one free end or two endplates of different size. However, results also indicate that the exact choice of endplate size ratio, d_e/d, will be dependent on the mission profile and the operating velocity ratio range.

For operation at low velocity ratios ($\Omega \leq 1$) the impact of endplate size on cylinder lift performance is effectively zero, although smaller plates ($d_e/d \leq 1.25$) do generally produce slightly smaller drag coefficients and so may be preferred. For moderate velocity ratios ($1 < \Omega < 3$), larger endplates ($d_e/d \geq 2$) result in both more lift and less drag, the latter primarily due to a reduction in induced drag. For high velocity ratio applications ($\Omega > 3$), smaller plates are, in terms of C_D, again more desirable as the drag quickly approaches a limiting value. However, the exact opposite is true of the cylinder's lift at high velocity ratio: large endplates are necessary to delay the onset of a limiting C_L.

Thus, for a rotating cylinder MAV or mini-UAV design, large symmetric endplates that spin with the cylinders provide the best improvement to the lift and drag characteristics of the rotors. However, at non-zero yaw angles, the use of large endplates results in a substantial reduction in the lift at high yaw and detrimentally large lateral forces and moments that may be difficult to trim. The most favourable response to yaw was achieved when the cylinder had no endplates ($d_e/d = 1$), although any choice of symmetric endplates of size $d_e/d \leq 1.25$ generated lateral forces and moments that were largely the same for all Ψ and changed only slightly with velocity ratio. Such findings mean that investigation into whether large aspect ratio cylinders can provide the same benefits to lift and drag as experienced with large endplates, but without the adverse response under yaw, is recommended.

Interestingly, when employed in a vehicle configuration that places the cylinders about a central fuselage (as in model configurations C8, C9, and C10), the effects of asym-

metric end conditions appeared to differ considerably from those observed with the isolated cylinder, although a detrimental impact on rolling moment remained apparent. This change in behaviour may be a consequence of the symmetry of the endplates about the xz plane or may be associated with the presence and influence of the fuselage. In either case, an investigation into the effects of the size and shape of the junction between the cylinders and body, as discussed below, could be beneficial.

Although the results of §6.4.2 did not extend to sufficiently high Ω for explicit confirmation, it can be reasonably assumed that the lift and drag of the vehicle as a whole will exhibit a similar plateauing in the magnitude of C_L and C_D when $\Omega > 4$ as was noted with the isolated cylinder. The value of the maximum lift coefficient at this point will not be much increased by the influence of the tail; thus, the design of the rotors and the choice of end conditions also define the maximum weight for the aircraft at a given flight speed.

In addition, the design of the rotors should be such that the choice of diameter d avoids similarity between the shedding frequency (at the given flight speed) and the rotational frequency of the cylinder. This would prevent the possibility of lock-on phenomena occurring if the vehicle was operating at low velocity ratios where shedding has not yet been suppressed. Note that power requirements for spinning the cylinders were largely unaffected by the choice of end conditions, or Reynolds number, and were also not influenced by yaw angle. Thus, these are of lesser importance when considering the choice of rotor design.

The experiments also revealed that, through the influence of propeller wash on the flow past the cylinders, the use of a tractor propeller arrangement results in a substantial increase to the magnitude of the lift coefficient and the lift curve slope $dC_L/d\alpha$, but not $dC_L/d\Omega$. However, the propeller had a strong adverse effect on C_Y, C_n, and C_l that was apparently primarily due to its location, thus suggesting that this type of MAV may ultimately benefit from a pusher propeller arrangement. Alternatively, since the benefits to C_L appear to stem from the effects of propeller wash on the cylinders, it may be instructive to investigate a design with counter-rotating propellers positioned in front of each cylinder in such a way as to maximise the influence of the propeller slipstream on the lift. A possible configuration of interest is shown in Figure 7.1a.

Finally, the investigation into the use of differential rotation of the cylinders to provide roll control revealed that, whilst effective, this approach produces a considerable adverse yaw effect that could make control of the aircraft difficult, although the results of tests with model configuration C2 indicate that a large enough vertical fin, with a sufficient rudder deflection, should be able to trim such yawing moments. In any case, if they

prove transferrable, it may be useful to implement equivalent techniques to those used to combat adverse yaw on fixed-wing aircraft. Alternatively, more conventional means of roll control may be needed. For the configuration investigated this would mean using tailerons, as ailerons could not be integrated into such a design. However, ailerons could be implemented if an alternative configuration, such as the hybrid design illustrated in Figure 7.1b, were to be adopted.

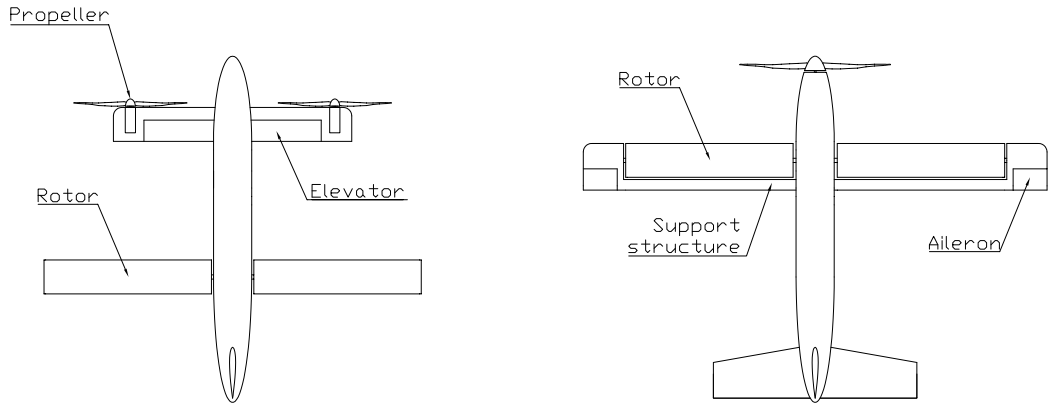

(a) Canard mounted engines (b) Aileron application

Figure 7.1: Possible configurations of interest for a rotating-cylinder-based small-UAV.

7.2 Operational Velocity Ratio Range

The results of experimental testing with both the isolated cylinder and the full vehicle model confirm that operation at $\Omega \approx 2$ remains the most appropriate choice of cruise velocity ratio. At this point, the lift curve (with respect to both α and Ω) is always linear, the lift-to-drag ratio is a maximum, and the cylinders achieve their best efficiency in terms of aerodynamic performance relative to power requirements for spinning. The only disadvantage to operation at $\Omega = 2$ was that lateral stability characteristics generally suffered when $\Omega > 1.5$, though this may be alterable by the design of the fin and fuselage. The actual location of the point of maximum C_L/C_D was also found to vary slightly with rotor end conditions, so that the final choice of cruise Ω would need to take into account the slight drift in the optimum velocity ratio with changing AR and d_e/d.

The experiments also confirmed that operation at $\Omega \leq 1$ would leave the vehicle susceptible to Reynolds number effects (of the sort reported by Swanson[12] and others) on the rotor lift and drag and revealed similar variation due to increasing Re to occur for the pitching moment and lateral forces and moments too, particularly at non-zero yaw. In addition, the

tests indicated that vortex shedding, though irregular, does occur for three-dimensional rotating cylinders at the typical Reynolds numbers associated with MAV-scale flight and velocity ratios below the critical value for suppression of shedding (found to be $\Omega_c \approx 2$ regardless of end configuration). Fluctuations in the forces and moments due to shedding were also found to be exacerbated by 'lock-on' phenomena arising from a similarity between the shedding frequency and the rotational frequency of the cylinder. Such behaviour further supports operation at $\Omega \approx 2$.

That being said, for low Reynolds numbers ($Re \leq 3 \times 10^4$), operation at higher velocity ratios ($\Omega \approx 3$) may actually be beneficial to performance as the results suggest a possible increase in the lift from a rotating cylinder with decreasing Re at such Ω. However, although a similar finding was also noted by Thom,[115] in both cases the effect has not been explicitly confirmed due to the lack of sensitivity of the equipment used in the experiments. Furthermore, the results of testing at high velocity ratio suggest that for $\Omega > 2.5$ there may be a return to some sort of periodicity of the flow due to the action of the trailing vortex system associated with a three-dimensional rotating cylinder, particularly one of low AR. Such phenomena may have structural ramifications and need to be considered both when selecting the cruise Ω and in defining the full range of operational velocity ratios of the aircraft.

For very high velocity ratios, the tendency towards flatness of the lift curve when $\Omega > 4$ makes operation at such high Ω generally inadvisable as, once the plateau region is reached, no further benefits to performance are obtained regardless of increasing power input. In fact, the power intensive and inefficient nature of the Magnus effect would seem to exclude operation beyond the velocity ratio for maximum lift-to-drag (i.e. $\Omega \approx 2$) as aerodynamic efficiency only worsens with increasing P. Operation at high velocity ratios is also subject to unfavourable yaw performance of the cylinders, with large force and moment coefficients being generated when employing some rotor endplate configurations.

7.3 Revised Performance Estimates

The results of the wind tunnel tests on the isolated cylinder showed that lift coefficient values were found to agree well with data from existing studies, although the limiting of the lift at high velocity ratios was much more prominent than previously noted. Drag coefficients at low velocity ratios ($\Omega \leq 3$) were generally found to be more favourable than indicated by previous research with the same aspect ratio cylinder, but the value of C_D at higher Ω was somewhat larger than expected. Similarly, power requirements for spinning the cylinders were found to be considerably greater than predicted in the

preliminary design phase using data from pre-existing studies, with current results being approximately twice as large.

The measurements of C_L, C_D, and C_P for the isolated cylinder were used to revise the performance estimates of §4.3. A comparison between the initial estimates and the actual level of performance as suggested by the wind tunnel tests is shown in Figure 7.2. The change in the general shape of the power contours reflects the fact that the power requirements for flight are now dominated by the power needed to spin the cylinders and not the drag coefficient, as had been indicated by the preliminary design study. The graphs also show that whilst a vehicle of mass $m = 250$ g that cruises at $V \approx 8$ m/s and $\Omega \approx 2$ is still possible, the increase in the power requirements are very detrimental to the overall performance of such a design.

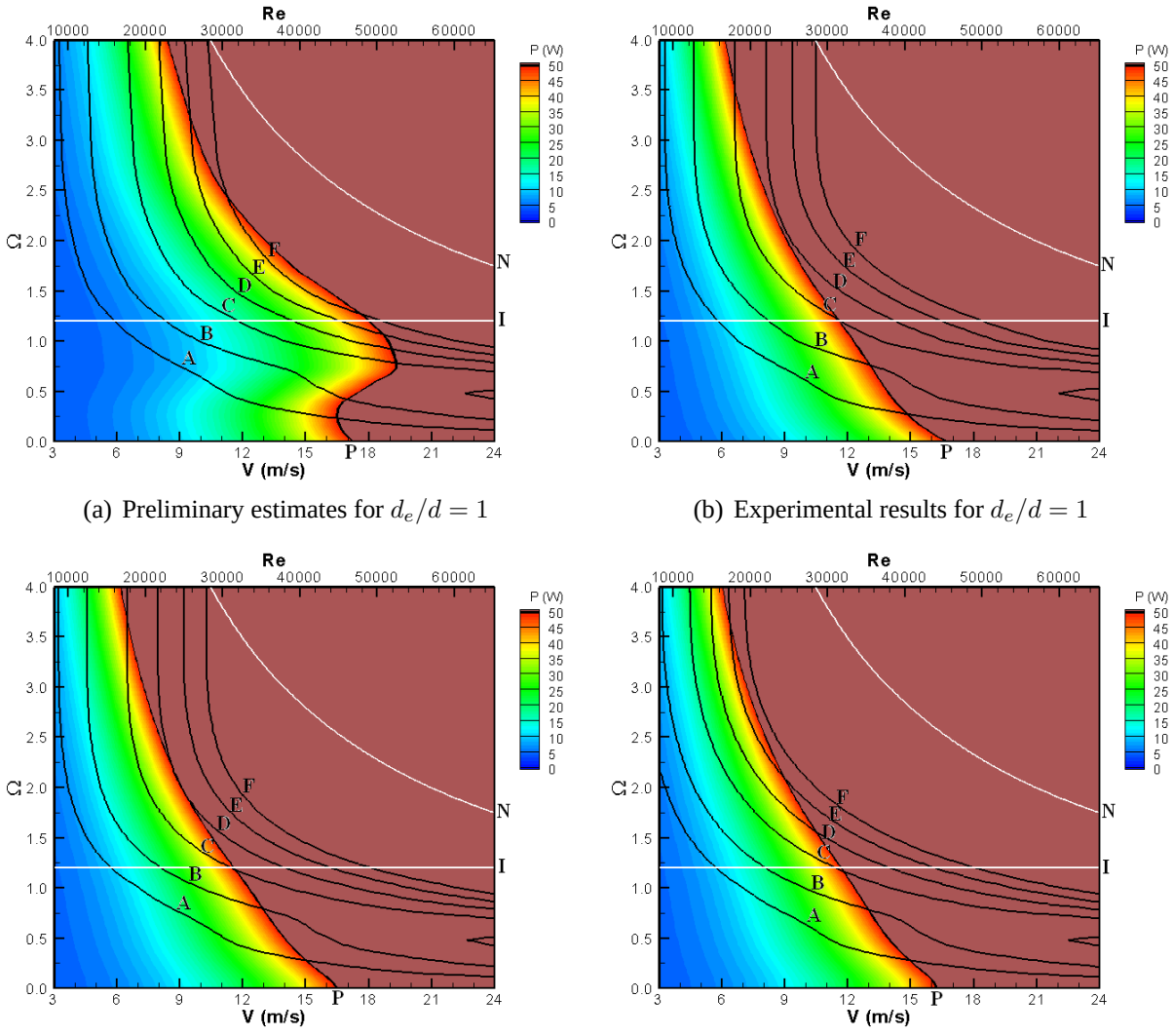

(a) Preliminary estimates for $d_e/d = 1$

(b) Experimental results for $d_e/d = 1$

(c) Experimental results for $d_e/d = 1.25$

(d) Experimental results for $d_e/d = 2$

Figure 7.2: Revised performance estimates for two rotors of size $d = 0.04$ m, $b = 0.2$ m, and $AR = 5$ at $\alpha = \Psi = 0°$.

Revised calculations suggest that a vehicle with a rotor configuration that did not employ endplates (see Figure 7.2b) would now require approximately twice the originally estimated battery capacity, thus making the construction of such a design so that it also provided a suitable payload capacity practically impossible. The use of small endplates ($d_e/d = 1.25$) is seen to have little effect on performance and an increase in battery capacity of 85% would still be required in such a case (see Figure 7.2c). Larger endplates (of size $d_e/d = 2$, see Figure 7.2d) are more successful at improving performance (a battery capacity increase of only 33% over that predicted in §4 is needed) but such end conditions come with adverse lateral forces and moments.

The disparity between the current C_P data and previous studies means that there remains some ambiguity about the accuracy of the power requirements for spinning the cylinders. If the present measurements are correct then some means of reducing power requirements will be necessary for the development of a useful aircraft. Increasing aspect ratio appears to have the same effect on performance as large endplates but without the associated adverse effects on forces and moments.

However, due to the constraints on rotor span, a high AR results in much increased values of the required rotational rates for the cylinders. Reducing overall vehicle weight would allow lower flight speeds to be implemented, thus reducing total power, but is detrimental to the large payload carrying capability that was originally sought. Drag reduction measures may provide some benefit, but alternative methods of increasing the lift at a given velocity ratio appear far more productive.

Changing the aerodynamic characteristics of a low AR rotating cylinder so that it provides as much lift at a velocity ratio of, say, $\Omega \approx 1.5$ as the unmodified cylinder does at $\Omega = 2$ would allow operation at this slightly lower velocity ratio, where both power requirements for spinning the cylinders and the drag coefficient are much reduced, yet many of the advantages associated with flight at $\Omega = 2$ still apply. This approach would not be possible without an increase in the lift curve slope ($dC_L/d\Omega$) of the cylinders as the value of C_L at $\Omega \approx 1.5$ would not otherwise provide sufficient lift for a vehicle of the required capability unless a faster flight velocity were implemented, which would cause power requirements to remain high.

Moulding of the rotor-fuselage junction to act as a shroud that shields the inboard end of each cylinder from the flow could provide such improvements to performance. Under these conditions, the two separate cylinders may act as a single entity of twice the aspect ratio, thus increasing C_L at a given Ω, whilst also benefitting C_D, without either the use of endplates or a change in the dimensions of the cylinders. The recent work of

Takayama & Aoki[194] suggests that substantial improvements to lift and drag performance could also be achieved through the use of distributed surface roughness. A combination of such techniques, together with the use of small endplates, may be able to reduce power requirements to acceptable levels for the construction of an operational small-UAV.

Note also that the results of §6 show that the tail, fuselage, and fin produced quite substantial contributions to the lift and drag at some angles of attack and were very important at non-zero yaw angles too. Thus, although the rotors remain the primary drivers of the performance with respect to velocity ratio and are key to the performance of the aircraft as a whole, it is unrealistic to estimate total vehicle performance solely from a consideration of the performance of the rotors, as was done for simplicity in the preliminary design process. Instead, in terms of performance with respect to changing angle of attack, a rotating cylinder MAV can be considered to behave largely like a fixed-wing aircraft.

The results of testing with the vehicle model indicate that the increased drag from the non-rotor components of the aircraft will result in a rise in the power requirements for forward flight that, particularly at high α and Ψ, will combine with the increase in the power needed to spin the cylinders to further inhibit the development of a useful design. However, the extra lift provided by the tail can be used to reduce the velocity ratio for flight, in the manner described above, so as to provide benefits to the total power requirements.

Furthermore, the exact performance characteristics will depend greatly on the specific design of the tail, fin, and fuselage, which for the experimental model were very basic and may have adversely impacted on performance. Consequently, as considerable benefits to performance may follow from an improved design, any further modelling and investigation of performance is best conducted with a more realistic vehicle geometry.

7.4 Stability and Control

The static stability characteristics of the isolated rotating cylinder were found to be very complicated and were altered by yaw angle, velocity ratio, and the choice of end conditions. For $\Psi \leq 15^\circ$ the cylinder was generally seen to be stable in yaw and roll for low velocity ratios ($\Omega \leq 1.5$); to possess neutral stability for $1.5 \leq \Omega \leq 2$ (and to also be trimmed in roll and yaw, so that $C_n = C_l = 0$, for some end configurations at $\Omega \approx 1.5$); and to be unstable in yaw and roll for $\Omega > 2$. The cylinder maintained neutral static stability in pitch for all conditions tested. Results showed that the lateral stability characteristics of the cylinder could also be significantly altered by changing the degree of

relative asymmetry between the inboard and outboard end conditions.

Results with vehicle model configurations involving only the cylinders and fuselage indicate that the natural stability of such designs was similar to that of the isolated cylinder, with these configurations being unstable in pitch and roll, but stable in yaw, when $\Omega \approx 2$. However, the characteristics of the aircraft as a whole were, at least when only small endplates are employed, governed primarily by the contributions from the horizontal tail, which controlled pitch stability, and the fuselage and vertical fin, which controlled the directional and lateral static stability of the aircraft. The velocity ratio and rotor end conditions were an important, but secondary, factor in the behaviour of the vehicle.

Consequently, an aircraft making use of rotating cylinders rather than wings, and that possesses the desired stability characteristics, is possible, irrespective of the stability characteristics of the cylinder's themselves, through careful design of the components of the aircraft. That being said, it should be noted that rotor designs with large endplates may have considerably more influence on the stability of such an aircraft.

In terms of the induced gyroscopic moments associated with the spinning of the cylinders, the data from §6 showed that gyroscopic contributions to the yawing and rolling moments of a quite substantial magnitude, rivalling that of the aerodynamically-generated lateral moments at non-zero yaw, could be generated by the experimental model under certain manoeuvering conditions. For an actual MAV or mini-UAV the mass of the rotors would need to be at least an order of magnitude lighter than those of the test model (say ≈ 20 g as opposed to ≈ 200 g) so that the moment of inertia of the cylinders, and hence (all other parameters remaining equal) the induced gyroscopic moments, would also be reduced by a similar degree.

In addition, the results seem to indicate that a suitably sized and well-designed fin and rudder, together with whatever means of roll control are employed, should be able to trim any gyroscopic rolling and yawing moments even at high rates of motion. However, due to the inability of the present experiments to accurately investigate gyroscopic effects, a fuller exploration of the consequences for dynamic stability and control remains necessary. Such an analysis may also have implications for vehicle design as well.

For instance, consideration of the form of the gyroscopic moment equation (Equation 4.13) suggests that a larger vehicle of greater dimensions could be more susceptible to the influence of gyroscopic effects. Although the required manoeuver rates p or r (which control term ω_3) would remain the same as size increases, and the angular velocity term ω_2 would (for a given Ω) reduce linearly with increasing d, the moment of inertia term, I_2, would scale to the fifth power of d. Since aerodynamic forces and moments scale only by

d^2, so gyroscopic moments may become much harder to trim. There is thus the possibility of an upper limit to how large such a vehicle can practically be made.

The results of testing with the isolated rotating cylinder and vehicle model also allow the continuation of the analysis of the linearised equations of motion, as begun in §4.4.4. The data indicate that the complex aerodynamic characteristics of the rotors, and the vehicle as a whole, are such that the simplification of the stability analysis through the separation of the equations of motion into longitudinal and lateral groups that can be considered independent of each other is only justifiable under restrictive conditions (symmetrical end conditions of $d_e/d \leq 1.25$, $\Psi \leq 10°$, $\alpha \leq 10°$, and $\Omega \leq 2$). It is likely that this range could be altered through improvement of the design of the vehicle as a whole.

Under the above-described circumstances the rate of change of C_Y, C_n, and C_l with both α and Ω is seen to be approximately zero and C_L, C_D, and C_m are unaffected by yaw. As a result the stability derivatives for asymmetric forces and moments due to perturbations in the symmetric velocities, and vice versa, may all be set to zero, as is the case in conventional analysis. Consequently, the aerodynamic forces and moments arising during a disturbance for an aircraft with rotating cylinders may now be assumed to be given by

$$\Delta X = X_u \Delta u^e + X_{\dot{u}} \Delta \dot{u}^e + X_w \Delta w^e + X_{\dot{w}} \Delta \dot{w}^e + X_q \Delta q + \Delta X_C \tag{7.1}$$

$$\Delta Y = Y_v \Delta v^e + Y_p \Delta p + Y_r \Delta r + \Delta Y_C \tag{7.2}$$

$$\Delta Z = Z_u \Delta u^e + Z_{\dot{u}} \Delta \dot{u}^e + Z_w \Delta w^e + Z_{\dot{w}} \Delta \dot{w}^e + Z_q \Delta q + \Delta Z_C \tag{7.3}$$

$$\Delta L = L_v \Delta v^e + L_p \Delta p + L_r \Delta r + \Delta L_C \tag{7.4}$$

$$\Delta M = M_u \Delta u^e + M_{\dot{u}} \Delta \dot{u}^e + M_w \Delta w^e + M_{\dot{w}} \Delta \dot{w}^e + M_q \Delta q + \Delta M_C \tag{7.5}$$

$$\Delta N = N_v \Delta v^e + N_p \Delta p + N_r \Delta r + \Delta N_C \tag{7.6}$$

Note that, in reference to the discussion in §4.4.4, derivatives due to both $\Delta \dot{u}^e$ and $\Delta \dot{w}^e$ have been retained in the X, Z, and M equations since any downwash effects at the tail due to the rotating cylinders would now be primarily a function of the time-history of the velocity ratio, Ω, which is itself dependent on u^e and w^e, so that the flow field at the tail may be expected to be a function of the quantities $\Delta \dot{u}^e$ and $\Delta \dot{w}^e$.

If Equations 7.1 to 7.6 are now substituted into the linearised equations of motion (Equations 4.37 to 4.48) and the results are separated into longitudinal and lateral groups, then the simplified longitudinal and lateral linearised equations of motion, as written in matrix form, may be seen to be as follows:

$$
\begin{bmatrix} \Delta\dot{u}^e \\ \Delta\dot{w}^e \\ \Delta\dot{q} \\ \Delta\dot{\theta} \end{bmatrix} = \begin{bmatrix} \frac{X_u+X_{\dot{w}}K_1}{m-X_{\dot{u}}} & \frac{X_w+X_{\dot{w}}K_2}{m-X_{\dot{u}}} & \frac{X_q-mw_0^e+X_{\dot{w}}K_3}{m-X_{\dot{u}}} & \frac{-(mg\cos\theta_0+X_{\dot{w}}K_4)}{m-X_{\dot{u}}} \\ \frac{Z_u(m-X_{\dot{u}})+Z_{\dot{u}}X_u}{(m-X_{\dot{u}})(m-Z_{\dot{w}})-Z_{\dot{u}}X_{\dot{w}}} & \frac{Z_w(m-X_{\dot{u}})+Z_{\dot{u}}X_w}{(m-X_{\dot{u}})(m-Z_{\dot{w}})-Z_{\dot{u}}X_{\dot{w}}} & \frac{(Z_q+mu_0^e)(m-X_{\dot{u}})+Z_{\dot{u}}(X_q-mw_0^e)}{(m-X_{\dot{u}})(m-Z_{\dot{w}})-Z_{\dot{u}}X_{\dot{w}}} & \frac{-mg[(m-X_{\dot{u}})\sin\theta_0+Z_{\dot{u}}\cos\theta_0]}{(m-X_{\dot{u}})(m-Z_{\dot{w}})-Z_{\dot{u}}X_{\dot{w}}} \\ \frac{M_u+M_{\dot{u}}\left(\frac{X_u+X_{\dot{w}}K_1}{m-X_{\dot{u}}}\right)+M_{\dot{w}}K_1}{I_{yy}} & \frac{M_w+M_{\dot{u}}\left(\frac{X_w+X_{\dot{w}}K_2}{m-X_{\dot{u}}}\right)+M_{\dot{w}}K_2}{I_{yy}} & \frac{M_q+M_{\dot{u}}\left(\frac{X_q-mw_0^e+X_{\dot{w}}K_3}{m-X_{\dot{u}}}\right)+M_{\dot{w}}K_3}{I_{yy}} & -\frac{M_{\dot{u}}\left(\frac{mg\cos\theta_0+X_{\dot{w}}K_4}{m-X_{\dot{u}}}\right)+M_{\dot{w}}K_4}{I_{yy}} \\ 0 & 0 & 1 & 0 \end{bmatrix} \begin{bmatrix} \Delta u^e \\ \Delta w^e \\ \Delta q \\ \Delta\theta \end{bmatrix}
$$

$$
+ \begin{bmatrix} \frac{\Delta X_C+X_{\dot{w}}K_5}{m-X_{\dot{u}}} \\ \frac{\Delta Z_C(m-X_{\dot{u}})+Z_{\dot{u}}\Delta X_C}{(m-X_{\dot{u}})(m-Z_{\dot{w}})-Z_{\dot{u}}X_{\dot{w}}} \\ \frac{\Delta M_C+M_{\dot{u}}\left(\frac{\Delta X_C+X_{\dot{w}}K_5}{m-X_{\dot{u}}}\right)+M_{\dot{w}}K_5}{I_{yy}} \\ 0 \end{bmatrix} \tag{7.7}
$$

$$
\begin{bmatrix} \Delta\dot{v}^e \\ \Delta\dot{p} \\ \Delta\dot{r} \\ \Delta\dot{\phi} \end{bmatrix} = \begin{bmatrix} \frac{Y_v}{m} & \frac{Y_p}{m}+w_0^e & \frac{Y_r}{m}-u_0^e & g\cos\theta_0 \\ I_1L_v+I_3N_v & I_1L_p+I_3N_p-2I_3J_{yy}\Gamma_0 & I_1L_r+I_3N_r+2I_1J_{yy}\Gamma_0 & 0 \\ I_3L_v+I_2N_v & I_3L_p+I_2N_p-2I_2J_{yy}\Gamma_0 & I_3L_r+I_2N_r+2I_3J_{yy}\Gamma_0 & 0 \\ 0 & 1 & \tan\theta_0 & 0 \end{bmatrix} \begin{bmatrix} \Delta v^e \\ \Delta p \\ \Delta r \\ \Delta\phi \end{bmatrix} + \begin{bmatrix} \frac{\Delta Y_C}{m} \\ I_1\Delta L_C+I_3\Delta N_C \\ I_3\Delta L_C+I_2\Delta N_C \\ 0 \end{bmatrix} \tag{7.8}
$$

where

$$K_1 = \frac{Z_u(m - X_{\dot{u}}) + Z_{\dot{u}}X_u}{(m - X_{\dot{u}})(m - Z_{\dot{w}}) - Z_{\dot{u}}X_{\dot{w}}} \tag{7.9}$$

$$K_2 = \frac{Z_w(m - X_{\dot{u}}) + Z_{\dot{u}}X_w}{(m - X_{\dot{u}})(m - Z_{\dot{w}}) - Z_{\dot{u}}X_{\dot{w}}} \tag{7.10}$$

$$K_3 = \frac{(Z_q + mu_0^e)(m - X_{\dot{u}}) + Z_{\dot{u}}(X_q - mw_0^e)}{(m - X_{\dot{u}})(m - Z_{\dot{w}}) - Z_{\dot{u}}X_{\dot{w}}} \tag{7.11}$$

$$K_4 = \frac{mg[(m - X_{\dot{u}})\sin\theta_0 + Z_{\dot{u}}\cos\theta_0]}{(m - X_{\dot{u}})(m - Z_{\dot{w}}) - Z_{\dot{u}}X_{\dot{w}}} \tag{7.12}$$

$$K_5 = \frac{\Delta Z_C(m - X_{\dot{u}}) + Z_{\dot{u}}\Delta X_C}{(m - X_{\dot{u}})(m - Z_{\dot{w}}) - Z_{\dot{u}}X_{\dot{w}}} \tag{7.13}$$

and

$$I_1 = \frac{I_{zz}}{I_{xx}I_{zz} - I_{xz}^2} \tag{7.14}$$

$$I_2 = \frac{I_{xx}}{I_{xx}I_{zz} - I_{xz}^2} \tag{7.15}$$

$$I_3 = \frac{I_{xz}}{I_{xx}I_{zz} - I_{xz}^2} \tag{7.16}$$

Equations 7.7 to 7.16 could now be used to examine the stability of uncontrolled motion of this type of aircraft under the specific set of conditions, as outlined above, for which the longitudinal and lateral forces and moments are decoupled. Analysis of controlled motion will also depend on the specific arrangement of the aircraft and the control elements employed. However, although such investigations with the linearised equations may provide further information on the stability of this type of design, a full analysis of the nonlinear equations of motion is ultimately required.

Preliminary attempts at further investigation of the stability of rotating-cylinder-based aircraft centered around obtaining solutions to the linearised equations by first establishing, and then finding the roots to, the characteristic polynomials for quasi-steady longitudinal and lateral free motion (i.e. the homogenous case). In this analysis the simplified vehicle

geometry described in §6 was assumed. Due to the limitations of the T2 tunnel and balance, an experimental determination of all the stability derivatives was not possible, nor was such information available anywhere in the pre-existing literature. Instead, analytical expressions for the stability derivatives were derived using a modified version of strip theory (in which small changes in velocity rather than angle were considered) and the assumption, based on Thom's[116] pressure measurements, of an elliptic lift distribution.

However, the results of the above described efforts were generally unsatisfactory and are thus not presented here or pursued further at this time. In general, the analysis was hampered by the lack of experimental results in key areas, as detailed in §4.4.4, that could be used to corroborate the assumptions made, guide the analysis, and validate the results. Further investigation along these lines would thus benefit from a combined analytical and experimental programme of study.

8 Concluding Remarks

The aim of this study was to determine the feasibility of using rotating circular cylinders as the primary means of generating lift for flight at the small scales associated with miniature unmanned aircraft known as Micro Air Vehicles (MAV). Successful application of rotating cylinders to MAV design could provide benefits by taking advantage of the large lift force generated by the rotating cylinder to increase the payload carrying capacity of these small craft, this typically being severely limited for conventional designs. Alternatively, a high C_L may instead be used to improve vehicle compactness.

The research involved a design study to investigate possible configurations, estimate the likely performance, and determine the practical feasibility of developing such a craft. Wind tunnel experiments with an isolated rotating cylinder were performed to extend understanding of aerodynamic behaviour and investigate means for improving performance. Experiments with a prototype MAV design using two cylinders about a central fuselage were carried out to determine its aerodynamic characteristics and investigate interactions between the cylinders and the rest of the aircraft.

Experimental investigation of the flow past an isolated rotating cylinder revealed several important items of interest:

- The lift and drag of a rotating cylinder tend to approach a limiting value when $\Omega > 4$. The magnitude of the limiting values, the point of onset (in terms of Ω) of this plateau, and its severity are all dependent on cylinder end conditions.
- The static stability characteristics of an isolated rotating cylinder were found to change with increasing velocity ratio and were also altered by the choice of end conditions. In addition, for yaw angles greater than $|\Psi| = 15^\circ$ there was a change in both lateral and longitudinal force and moment characteristics.
- For velocity ratios greater than $\Omega = 2$, the aerodynamic characteristics of a three-dimensional rotating circular cylinder were found to be governed by the formation and evolution (with changing Ω) of a large trailing vortex system. Endplates were found to be able to control the evolution (in terms of strength and spanwise position) of the vortices, providing an effective means of controlling the aerodynamics of the cylinder in a manner that seems equivalent to an increase in aspect ratio.
- The best improvement in lift performance was achieved with two plates of equal size that spin with the cylinder. For these cases, increasing endplate size caused the value of $C_{L_{max}}$ at high velocity ratios to be augmented by an amount that was

directly proportional to the endplate size ratio d_e/d (a minimum ratio of $d_e/d = 1.5$ was found necessary to significantly change the lift). Within the limits of the tests, no upper ceiling to the value of the maximum lift that could be generated by increasing d_e/d was found. It is unclear whether this would continue indefinitely with further increases in plate size, or if some optimum value of d_e/d exists. Endplate influence on drag differed at high and low Ω, but was most beneficial when $d_e/d \geq 1.5$ and $\Omega \approx 2$. Having one free end, mismatched plates, or stationary plates generally provided a much smaller improvement in lift and drag performance.

- The use of large endplates results in undesirable lateral force and moment characteristics at non-zero yaw angles that ultimately make this means of controlling the performance of a rotating cylinder unattractive. A study of the literature indicates that influencing tip vortex strength and position with varying velocity ratio through a combination of aspect ratio, small endplates, and surface roughness seems likely to provide the required aerodynamic characteristics for a successful MAV.

The key findings from the investigation into the design and performance of a rotating cylinder MAV/mini-UAV were as follows:

- A 50 g, 0.15 m vehicle with a general configuration of twin cylinders about a central fuselage and a suitable level of performance that also provided benefits to payload capability was found to be theoretically possible but practically very difficult. A larger vehicle of 250 g weight and 0.4 m dimension was more feasible but still challenging. The primary obstruction to successful development was the high performance demands placed on the power and propulsion systems. These were a result of both the high drag of the cylinders and the power required to spin them.

- A viable design was found to require a suitable selection of rotor geometry, in particular the choice of end conditions. Given the constraints on cylinder span required for an MAV or mini-UAV scale craft, augmenting the aerodynamic characteristics of a low aspect ratio cylinder to simulate the improved performance of a high aspect ratio cylinder was deemed highly important to the development of a successful design based around the rotating cylinder.

- A velocity ratio of $\Omega \approx 2$ was found to be the preferred cruise Ω for such a vehicle as it is the location of the maximum lift-to-drag and it also offers advantages to power requirements, stability and control, and vortex shedding suppression.

- The aerodynamic characteristics of the chosen configuration were found to be governed primarily by the tail, which dictated the response of the aircraft to changes

in α, and the fin and fuselage, which were found to dominate the lateral characteristics, so that the vehicle behaved much like a modified fixed-wing aircraft. The influence of the tail, fin, and fuselage also altered the response to changing velocity ratio so that, except for C_L and C_D, the variation of the forces and moments with Ω for the entire aircraft was often significantly different from that of the isolated cylinder. Vehicle lift-to-drag ratio was dependent primarily on the rotor design and operating velocity ratio.

- The stability characteristics of the model were also found to be driven by the characteristics of the tail, fin, and fuselage, with the cylinders generally providing only a secondary effect. With careful design it should thus be possible to develop an aircraft with the desired stability characteristics irrespective of the behaviour of an isolated rotating cylinder. Gyroscopic moments induced by spinning the cylinders may be problematic given the maneuverability required of MAVs, but the experiments indicate that a sufficiently large fin and a suitable method of roll control should be able to counter their influence.

- The interaction between the cylinders' wake and the tail were found to improve the performance of the tail, delaying stall by several degrees and increasing the lift curve slope, $dC_L/d\alpha$, of the aircraft as a whole. The rotors were less influential in augmenting the characteristics of the fin. Interactions between the propeller slipstream and the cylinders, tail, and fin were also highly influential, being greatly beneficial to lift ($dC_L/d\alpha$ was more than doubled to approximately 6.8 per radian) but generally detrimental to stability and control.

- That the design of the tail, fin, and fuselage are of primary importance to this type of design is probably due to the greater influence of low Re on these components than on a rotating cylinder. However, the relative influence of the rotors may be increased with larger endplates or a smaller fin and tail.

Overall, a successful rotating cylinder MAV or mini-UAV capable of providing the level of performance expressed in this study is not precluded by the aerodynamic properties of the rotating cylinder but is dependent on more sophisticated technologies than are currently commercially available, particularly with regards to the power and propulsion systems. Clearly, such advances in technology would also be of benefit to the capabilities of conventional MAV designs, possibly rendering the idea of using rotating cylinders moot. That being said, the greater lift generating capability of the rotating cylinder design would remain an advantage, but it would seem that more investigation is required so as to determine how to fully exploit its potential.

9 Recommendations for Future Work

Although the current study indicates that the application of the rotating cylinder concept to small unmanned aircraft is both feasible and beneficial, further investigation is required to fully explore the potential of such designs. A number of extensions to the present work, both in terms of the fundamental aerodynamics of a rotating cylinder and the configuration and design of a small-UAV incorporating rotating cylinders, are thus suggested:

- Extension of the tests with the isolated cylinder to explicitly examine the characteristics of high AR cylinders, particularly the motion of the tip vortices and the lateral forces and moments, for comparison against behaviour with low AR and large d_e/d.
- Investigation of any correlation of the wake structure with the lateral forces and moments at non-zero yaw angles, with a view to improving aerodynamic performance through the control of vortex formation.
- Examination of the effects of distributed surface roughness on the aerodynamic forces and moments for a rotating cylinder, its effects on power requirements for spinning the cylinder, and any consequences for the vortex shedding process.
- Investigation into the effects of using a combination of endplates, aspect ratio, and surface roughness to improve the aerodynamic performance of the cylinders. Such a unified approach has the potential to provide superior benefits than individual application of each technique.
- Clarification of the possible beneficial influence of low Re on the lift at high Ω and the power requirements for spinning the cylinders.
- Further refinement of vehicle performance modelling using data from present and future tests together with a more realistic vehicle geometry.
- Further investigation into the optimum vehicle configuration for this type of design, with particular focus on the rotor-fuselage junction, the interaction between the cylinders and other components, and the beneficial effects of propeller wash.
- Determination of the effects of aeroelasticity and structural vibration on the aerodynamics of both an isolated cylinder and the vehicle as a whole.
- A full assessment of the static and dynamic stability of the preferred vehicle configuration, including the response to gusts, with a view towards the development of a control system that takes into account the specific behaviour of this type of design.

References

[1] T. Coffey and J. A. Montgomery, The Emergence of Mini UAVs for Military Applications, *Defense Horizons*, Vol. 22, 2002, Available at http://www.ndu.edu/inss/DefHor/DH22/DH22.pdf.

[2] S. J. Morris and M. Holden, Design of Micro Air Vehicles and Flight Test Validation, In *Proceedings of the Conference on Fixed, Flapping, and Rotary Wing Vehicles at Very Low Reynolds Numbers*, Notre Dame University, IN, 2000.

[3] F. Rizzo, The Flettner Rotor Ship in Light of the Kutta–Joukowski Theory and of Experimental Results, Technical Report TN-228, NACA, 1925.

[4] J. A. Weiberg and B. Gamse, Large-Scale Wind-Tunnel Tests of an Airplane Model with Two Propellers and Rotating Cylinder Flaps, Technical Report TN-D-4489, NASA, 1968.

[5] W. S. Johnson, J. S. Tennant and R. E. Stamps, Leading-Edge Rotating Cylinder for Boundary-Layer Control on Lifting Surfaces, *Journal of Hydronautics*, Vol. 9, 1975, pp. 76–78.

[6] V. J. Modi, J. L. C. Sun, T. Akutsu, P. Lake, K. McMillan, P. G. Swinton and D. Mullins, Moving Surface Boundary-Layer Control for Aircraft Operation at High Incidence, *Journal of Aircraft*, Vol. 18, 1981, pp. 963–968.

[7] A. Flettner, The Flettner Rotorship, *Journal of Engineering*, Vol. 19, 1925, pp. 117–120.

[8] A. Betz, The Magnus Effect: The Principle of the Flettner Rotor, Technical Report TM-310, NACA, 1925.

[9] L. Prandtl, Application of the Magnus Effect to the Wind Propulsion of Ships, Technical Report TM-367, NACA, 1926.

[10] J. Ackeret, Recent Experiments at the Göttingen Aerodynamic Institute, Technical Report TM-323, NACA, 1925.

[11] S. R. H. Rogers, *Freak Ships*, John Lane, The Bodley Head, London, UK, 1936.

[12] W. M. Swanson, The Magnus Effect: A Summary of Investigations to Date, *Journal of Basic Engineering*, Vol. 83, 1961, pp. 461–470.

[13] A. Klemin, A Rotor Airplane, *Scientific American*, Vol. 146, 1932, pp. 362.

[14] Department of Defense Dictionary of Military Terms, Available at http://www.dtic.mil/doctrine/jel/doddict/.

[15] Directorate of Airspace Policy, CAP 722 Unmanned Aerial Vehicle Operations in UK Airspace, Technical report, Civil Aviation Authority, 2004, Available at http://www.caa.co.uk/docs/33/CAP722.pdf.

[16] P. La Franchi, Directory: Unmanned Air Vehicles, *Flight International*, Vol. 166, 27 July–2 August 2004, pp. 42–64.

[17] Office of the Secretary of Defence, Unmanned Aircraft Systems Roadmap 2005–2030, Technical report, United States Department of Defense, August 2005.

[18] A Strategic Outlook on New International UAV Technology and Procurement Developments, Concepts, and Challenges, 2004, Available at http://www.uavworld.com/reportspec.htm.

[19] J. Wilson, UAV Worldwide Roundup 2009, *Aerospace America*, Vol. 47, April 2009, pp. 30–36.

[20] SAAB eyes UCAV, *Flight International*, Vol. 166, 27 July–2 August 2004, pp. 16.

[21] A. Chuter, SUAV(E) Could Have Big Impact on UK UAVs, 2006, Available at http://isrjournal.com/story.php?F=2112461.

[22] Office of the Secretary of Defence, Unmanned Aerial Vehicles Roadmap 2002–2027, Technical report, United States Department of Defense, December 2002.

[23] M. S. Pardesi, UAVS/UCAVs - Missions, Challenges, and Strategic Implications for Small and Medium Powers, Working Paper Series No. 66, Institute of Defence and Strategic Studies, Singapore, 2004.

[24] P. Bowes, High Hopes for Drone in LA Skies, 2006, Available at http://news.bbc.co.uk/1/hi/world/americas/5051142.stm.

[25] Unmanned Plane Finds Child Sex Abuse Suspect, 2007, Available at http://www.cnn.com/2007/US/03/22/plane.border/index.html.

[26] J. Karp and A. Pasztor, Drones in Domestic Skies? *Wall Street Journal*, 7 August 2006.

[27] FAA Authorizes Predators to Seek Survivors, 2006, Available at http://www.af.mil/news/story.asp?storyID=123024467.

[28] R. O. Hundley and E. C. Gritton, Future Technology-Driven Revolutions in Military Operations, Document Number DB-110-ARPA, RAND Corporation, 1994.

[29] W. R. Davis, Micro UAV, In *23rd AUVSI Symposium (AUVSI '96) – 'Innovations for the Future'*, Orlando, FL, 1996.

[30] Micro Air Vehicles for Optical Surveillance, *Lincoln Laboratory Journal*, Vol. 9, 1996, pp. 197–213.

[31] A. H. Epstein, K. S. Breuer, J. H. Lang, M. A. Schmidt, S. D. Senturia, S. M. Spearing, C. S. Tan and I. A. Waitz, Micro Gas Turbine Generators, Technical report, Massachusetts Institute of Technology, 2000, Available at http://handle.dtic.mil/100.2/ADA385644.

[32] N. Pornsin-Sisirak, S. W. Lee, H. Nassef, J. Grasmeyer, Y. C. Tai, C. M. Ho and M. Keennon, MEMS Wing Technology for a Battery-Powered Ornithopter, In *13th IEEE International Conference on Micro Electro Mechanical Systems*, Miyazaki, Japan, 2000.

[33] K. D. Frampton and M. Goldfarb, Passive Aeroelastic Tailoring for Optimal Flapping Wings, In *Conference on Fixed, Flapping, and Rotary Winged Vehicles for Very Low Reynolds Numbers*, Notre Dame, IN, 2000.

[34] K. D. Jones, C. J. Bradshaw, J. Papadopoulos and M. F. Platzer, Bio-Inspired Design of Flapping-Wing Micro Air Vehicles, *Aeronautical Journal*, Vol. 109, 2005, pp. 385–393.

[35] J. M. Grasmeyer and M. T. Keennon, Development of the Black Widow Micro Air Vehicle, In *39th AIAA Aerospace Sciences Meeting and Exhibit*, Reno, NV, 2001.

[36] J. M. McMichael and M. S. Francis, Micro Air Vehicles - Towards a New Dimension in Flight, *Unmanned Systems*, Summer, 1997, Also available at http://www.casde.iitb.ac.in/IMSL/MAVDOCS/www.darpa.mil/tto/MAV/mav_auvs%i.html.

[37] C. Boller and H. Hönlinger, Workshop Summary Report, In *Micro Aerial Vehicles - Unmet Technological Requirements*, Elmau Castle, Germany, 2003.

[38] S. C. Weed, The Quality of Quantity: Mini-UAVs as an Alternative UAV Acquisition Strategy at the Army Brigade Level, Technical report, School of Advanced Military Studies, United States Army Command and General Staff College, Fort Leavenworth, KS, 2002.

[39] M. Buschmann, J. Bange and P. Vörsmann, MMAV - A Miniature Unmanned Aerial Vehicle (Mini-UAV) for Meteorological Purposes, In *16th Symposium on Boundary Layers and Turbulence, American Meteorological Society*, Portland, ME, 2004.

[40] S. Winkler, M. Buschmann, L. Kruger, H. W. Schulz and P. Vörsmann, AutoMAV - Micro Aerial Vehicles for Airport Surveillance, In *TENCON 2005 - IEEE Region 10 Annual International Conference*, Melbourne, Australia, 2005.

[41] Miami-Dade Hoping to Use Unmanned Aircraft to Fight Crime, 2008, Available at http://www.palmbeachpost.com/state/content/state/epaper/2008/03/27/m1a_%drones_0327.html.

[42] R. C. Michelson, Novel Approaches to Miniature Flight Platforms, *Proceedings of the Institution of Mechanical Engineers, Part G: Journal of Aerospace Engineering*, Vol. 218, 2004, pp. 363–373.

[43] MAV - Combat Lessons Learned, 2004, Available at http://www.defense-update.com/features/du-2-04/mav-oif.htm.

[44] T. J. Mueller and J. D. DeLaurier, An Overview of Micro Air Vehicle Aerodynamics, In *Fixed and Flapping Wing Aerodynamics for Micro Air Vehicle Applications*, edited by T. J. Mueller, AIAA Publishing, Reston, VA, 2001, pp. 1–9.

[45] Y. Hu and Z. Y. Zhou, Micro Air Vehicles - A Survey of Recent Developments, In *Proceedings of the International Symposium on Test and Measurement*, Shenzen, China, 2003, pp. 117–120.

[46] I. Kroo and P. Kunz, Mesoscale Flight and Miniature Rotorcraft Development, In *Fixed and Flapping Wing Aerodynamics for Micro Air Vehicle Applications*, edited by T. J. Mueller, AIAA Publishing, Reston, VA, 2001, pp. 503–517.

[47] A. Ananthaswamy, March of the Motes, *New Scientist*, Vol. 2409, 23 August 2003, pp. 27–31.

[48] W. Ren and Y. Q. Chen, Leaderless Formation Control for Multiple Autonomous Vehicles, In *AIAA Guidance, Navigation, and Control Conference and Exhibit*, Keystone, CO, 2006.

[49] R. W. Deming and L. I. Perlovsky, Concurrent Multi-Target Localization, Data Association and Navigation for a Swarm of Flying Sensors. *Information Fusion*, Vol. 8, 2007, pp. 316–330.

[50] S. J. Morris, Miniature Spy Planes: The Next Generation of Flying Robots, In *7th Annual Symposium On Frontiers Of Engineering*, Irvine, CA, 2002.

[51] Bluetooth Flying Bot Creates Buzz, 2004, Available at http://news.bbc.co.uk/go/pr/fr/-/1/hi/technology/3579232.stm.

[52] T. T. H. Ng and G. S. B. Leng, Application of Genetic Algorithms to Conceptual Design of a Micro-Air Vehicle, *Engineering Applications of Artificial Intelligence*, Vol. 15, 2002, pp. 439–445.

[53] D. Lundström and P. Krus, Micro Aerial Vehicle Design Optimization Using Mixed Discrete and Continuous Variables, In *11th AIAA/ISSMO Multidisciplinary Analysis and Optimization Conference*, Portsmouth, VA, 2006.

[54] J. Bartron, T. Simpson and H. Thompson, Lehigh University Micro Air Vehicle Design, Technical report, Lehigh University, Bethlehem, PA, 2003, Note: unpublished.

[55] P. Boyle, S. Giffin, R. Kurz and H. Thompson, Lehigh University Micro Air Vehicle Design, Technical report, Lehigh University, Bethlehem, PA, 2004, Note: unpublished.

[56] G. Torres and T. J. Mueller, Micro Aerial Vehicle Development: Design, Components, Fabrication, and Flight-Testing, In *AUVSI Unmanned Systems 2000 Symposium and Exhibition*, Orlando, FL, 2000.

[57] F. Bohorquez, P. Samuel, J. Sirohi, L. Rudd, D. Pines and R. Perel, Design, Analysis and Performance of a Rotary Wing MAV, *Journal of the American Helicopter Society*, Vol. 48, 2003, pp. 80–90.

[58] B. Peterson, B. Erath, K. Henry, M. Lyon, B. Walker, N. Powell, K. Fowkes and W. J. Bowman, Development of a Micro Air Vehicle for Maximum Endurance and Minimum Size, In *41st AIAA Aerospace Sciences Meeting and Exhibit*, Reno, NV, 2003.

[59] M. Gad-el-Hak, Micro-Air-Vehicles: Can They be Controlled Better? *Journal of Aircraft*, Vol. 38, 2001, pp. 419–428.

[60] G. E. Torres and T. J. Mueller, Aerodynamic Characteristics of Low Aspect Ratio Wings at Low Reynolds Numbers, In *Fixed and Flapping Wing Aerodynamics for Micro Air Vehicle Applications*, edited by T. J. Mueller, AIAA Publishing, Reston, VA, 2001, pp. 115–141.

[61] I. Gursul, G. Taylor and C. L. Wooding, Vortex Flows over Fixed-Wing Micro Air Vehicles, In *40th AIAA Aerospace Sciences Meeting and Exhibit*, Reno, NV, 2002.

[62] E. J. Schroeder and J. D. Baeder, Using Computational Fluid Dynamics for Micro-Air Vehicle Airfoil Validation and Prediction, In *23rd AIAA Applied Aerodynamics Conference*, Toronto, Canada, 2005.

[63] P. Cosyn and J. Vierendeels, Numerical Investigation of Low-Aspect-Ratio Wings at Low Reynolds Numbers, *Journal of Aircraft*, Vol. 43, 2006, pp. 713–722.

[64] X. Q. Zhang and L. Tian, Three-Dimensional Simulation of Micro Air Vehicles with Low-Aspect-Ratio Wings, *Key Engineering Materials*, Vol. 339, 2007, pp. 377–381.

[65] D. L. Raney and M. R. Waszak, Biologically Inspired Micro-Flight Research, Technical Report SAE 2003-01-3042, Society of Automotive Engineers, 2003.

[66] P. G. Ifju, D. A. Jenkins, S. Ettinger, Y. Lian, W. Shyy and M. R. Waszak, Flexible-Wing-Based Micro Air Vehicles, In *40th AIAA Aerospace Sciences Meeting and Exhibit*, Reno, NV, 2002.

[67] C. Galinski, Gust Resistant Fixed Wing Micro Air Vehicle, *Journal of Aircraft*, Vol. 43, 2006, pp. 1586–1588.

[68] L. A. Young, E. W. Aiken, J. L. Johnson, R. Demblewski, J. Andrews and J. Klem, New Concepts and Perspectives on Micro-Rotorcraft and Small Autonomous Rotary-Wing Vehicles, In *20th AIAA Applied Aerodynamics Conference*, St. Louis, MO, 2002.

[69] S. D. Hanford, L. N. Long and J. F. Horn, A Small Semi-Autonomous Rotary-Wing Unmanned Air Vehicle (UAV), In *Infotech@Aerospace*, Arlington, VA, 2005.

[70] Project MARVEL, Micro Air Vehicles for Multi-Purpose Remote Monitoring and Sensing, Technical Report IST-1999-29043, Centro Ricerche FIAT, Department of Optics and Photonics, 2004.

[71] R. K. Arning and S. Sassen, Flight Control of Micro Aerial Vehicles, In *AIAA Guidance, Navigation, and Control Conference and Exhibit*, Providence, RI, 2004.

[72] D. Page, The UCLA MAV Feasibility Study, Available at http://www.hightechcareers.com/doc198e/uclamav198e.html, 1998.

[73] T. T. H. Ng and G. S. B. Leng, Design Optimization of Rotary-Wing Micro Air Vehicles, *Journal of Mechanical Engineering Science*, Vol. 220, 2006, pp. 865–873.

[74] K. D. Jones and M. F. Platzer, Experimental Investigation of the Aerodynamic Characteristics of Flapping-Wing Micro Air Vehicles, In *41st AIAA Aerospace Sciences Meeting and Exhibit*, Reno, NV, 2003.

[75] C. Galinski and R. Zbikowski, Some Problems of Micro Air Vehicles Development, *Bulletin of the Polish Academy of Sciences: Technical Sciences*, Vol. 55, 2007, pp. 91–98.

[76] L. Schenato, X. Deng and S. Sastry, Hovering Flight for a Micromechanical Flying Insect: Modeling and Robust Control Synthesis, In *15th IFAC World Congress on Automatic Control*, Barcelona, Spain, 2002.

[77] L. Schenato, X. Deng and S. Sastry, Flight Control System for a Micromechanical Flying Insect: Architecture and Implementation, In *IEEE International Conference on Robotics and Automation*, Seoul, South Korea, 2001.

[78] R. C. Michelson and S. Reece, Update On Flapping Wing Micro Air Vehicle Research: Ongoing Work to Develop a Flapping Wing, Crawling "Entomopter", In *13th Bristol International RPV/UAV Systems Conference*, Bristol, UK, 1998.

[79] R. C. Michelson and M. A. Naqvi, Beyond Biologically-Inspired Insect Flight, In *Low RE Aerodynamics on Aircraft Including Applications in Emerging UAV Technology*, RTO-AVT von Kármán Institute for Fluid Dynamics, 2003, Note: lecture series.

[80] M. I. Woods, J. F. Henderson and G. D. Lock, Energy Requirements for the Flight of Micro Air Vehicles, *Aeronautical Journal*, Vol. 105, 2001, pp. 135–149.

[81] M. P. Merchant and L. S. Miller, Propeller Performance Measurement for Low Reynolds Number UAV Applications, In *44th AIAA Aerospace Sciences Meeting and Exhibit*, Reno, NV, 2006.

[82] W. S. Cheung and J. R. Tilston, Hydrogen Peroxide Based Propulsion System for Micro Air Vehicle Applications, Technical report, DERA, UK, September 1999.

[83] N. Naimer, B. Koretz and R. Putt, Zinc-Air Batteries for UAVs and MAVs, Available at http://www.electric-fuel.com/defense/UVS02.pdf, 2002.

[84] Miniature Aerial Vehicles: Design Considerations, 2005, Available at http://www.defense-update.com/features/du-2-04/mav-design.htm.

[85] D. A. Lawrence and K. Mohseni, Efficiency Analysis for Long-Duration Electric MAVs, In *Infotech@Aerospace*, Arlington, VA, 2005.

[86] AeroVironment's "WASP" Micro Air Vehicle Sets World Record, Available at http://www.aerovironment.com/news/news-archive/wasp62.html.

[87] AeroVironment's "Hornet" Micro Air Vehicle Completes First Fuel Cell Powered Flight, Available at http://www.aerovironment.com/news/news-archive/hornet62.html.

[88] A. Hooper and E. O' Keefe, Micro-Aerial Vehicles Materials & Structures, In *Micro Aerial Vehicles - Unmet Technological Requirements*, Elmau Castle, Germany, 2003.

[89] Army "Future": Fewer Drones, 2006, Available at http://www.defensetech.org/archives/003069.html.

[90] S. Li, Z. Zhou, G. Wang, H. Wu, S. Xiong, X. Wang and J. Xiong, Research on Computer Control System of MAV, In *Proceedings of the International Symposium on Test and Measurement*, Shanghai, China, 2001, pp. 1629–1632.

[91] Z. S. Kuo, C. Y. Soong and Y. S. Chang, Longitudinal Dynamic Stability Analysis and Design of Micro Air Vehicles, *Transactions of the Aeronautical and Astronautical Society of the Republic of China*, Vol. 32, 2002, pp. 297–308.

[92] M. W. Orr, S. J. Rasmussen, E. T. Karni and W. B. Blake, Framework for Developing and Evaluating MAV Control Algorithms in a Realistic Urban Setting, In *Proceedings of the American Control Conference*, Portland, OR, 2005, pp. 4096–4101.

[93] J. K. Conroy, P. D. Samuel and D. J. Pines, Development of an MAV Control and Navigation System, In *Infotech@Aerospace*, Arlington, VA, 2005.

[94] Y. S. Chang, C. Y. Soong and Z. S. Kuo, Lateral Dynamic Stability Analysis and Design of Micro Air Vehicles, *Journal of Aeronautics, Astronautics, and Aviation*, Vol. 38, 2006, pp. 37–48.

[95] D. B. Kingston and R. W. Beard, Real-Time Attitude and Position Estimation for Small UAVs Using Low-Cost Sensors, In *3rd AIAA "Unmanned Unlimited" Technical Conference, Workshop and Exhibit*, Chicago, IL, 2004.

[96] S. M. Ettinger, M. C. Nechyba, P. G. Ifju and M. R. Waszak, Vision-Guided Flight Stability and Control for Micro Air Vehicles, In *Proceedings of the IEEE International Conference on Intelligent Robots and Systems*, Lausanne, Switzerland, 2002, pp. 2134–2140.

[97] S. Todorovic, M. C. Nechyba and P. G. Ifju, Sky/Ground Modeling for Autonomous MAV Flight, In *Proceedings of the IEEE International Conference on Robotics and Automation*, Taipei, Taiwan, 2003, pp. 1422–1427.

[98] A. Kurdila, M. Nechyba, R. Prazenica, W. Dahmen, P. Binev, R. Devore and R. Sharpley, Vision-Based Control of Micro-Air-Vehicles: Progress and Problems in Estimation, In *Proceedings of the IEEE Conference on Decision and Control*, Nassau, Bahamas, 2004, pp. 1635–1642.

[99] J. J. Kehoe, R. S. Causey, M. Abdulrahim and R. Lind, Waypoint Navigation for a Micro Air Vehicle Using Vision-Based Attitude Estimation, *Aeronautical Journal*, Vol. 110, 2006, pp. 821–829.

[100] G. B. Bao, S. S. Xiong and Z. Y. Zhou, Vision-Based Horizon Extraction for Micro Air Vehicle Flight Control, *IEEE Transactions on Instrumentation and Measurement*, Vol. 54, 2005, pp. 1067–1072.

[101] F. Ruffier, S. Viollet, S. Amic and N. Franceschini, Bio-Inspired Optical Flow Circuits for the Visual Guidance of Micro-Air Vehicles, In *Proceedings of the 2003 IEEE International Symposium on Circuits and Systems*, Bangkok, Thailand, 2003, pp. 846–849.

[102] G. Magnus, On the Deflection of a Projectile, *Poggendorf's Annalen der Physik und Chemie*, Vol. 88, 1853, pp. 804–810.

[103] B. Robins, *New Principles of Gunnery*, London, UK, 1742.

[104] J. Gleick, *Isaac Newton*, Harper Perennial, London, UK, 2004.

[105] G. T. Walker, Spiel und Sport, *Encyklopädie der mathematischen Wissenschaft*, Vol. IV, 1900, pp. 136 ff.

[106] H. Bateman, Rotating Cylinders and Rectilinear Vortices, *Bulletin of the American Mathematical Society*, Vol. 25, 1919, pp. 358–374.

[107] Lord Rayleigh, On the Irregular Flight of a Tennis Ball, *Scientific Papers*, Vol. 1, 1857, pp. 344–346.

[108] L. Prandtl and O. Tietjens, *Applied Hydro- and Aeromechanics*, MacGraw-Hill Book Company, Inc., New York, NY, 1961, pp. 80–85.

[109] M. A. Lafay, Sur l'Inversion du Phénomène de Magnus, *Comptes–Rendus*, Vol. 151, 1910, pp. 867.

[110] M. A. Lafay, Contribution Expérimentale a l'Aerodynamique du Cylindre, *Revues Mécanique*, Vol. 30, 1912, pp. 417–442.

[111] F. Ahlborn, The Magnus Effect in Theory and Practice, Technical Report TM-567, NACA, 1929.

[112] G. A. Tokaty, *A History and Philosophy of Fluid Mechanics*, G. T. Foulis & Co. Ltd., Henley-on-Thames, Oxfordshire, UK, 1971.

[113] E. G. Reid, Tests of Rotating Cylinders, Technical Report TN-209, NACA, 1924.

[114] A. Thom, *The Aerodynamics of a Rotating Cylinder*, Ph.D. thesis, University of Glasgow, UK, 1926.

[115] A. Thom, Experiments on the Air Forces on Rotating Cylinders, Technical Report R&M No. 1018, Aeronautical Research Council, 1925.

[116] A. Thom, The Pressures Round a Cylinder Rotating in an Air Current, Technical Report R&M No. 1082, Aeronautical Research Council, 1926.

[117] A. Thom, Experiments on the Flow Past a Rotating Cylinder, Technical Report R&M No. 1410, Aeronautical Research Council, 1931.

[118] A. Thom and S. R. Sengupta, Air Torque on a Cylinder Rotating in an Air Stream, Technical Report R&M No. 1520, Aeronautical Research Council, 1932.

[119] A. Thom, Effects of Discs on the Air Forces on a Rotating Cylinder, Technical Report R&M No. 1623, Aeronautical Research Council, 1934.

[120] M. M. Zdravkovich, *Flow Around Circular Cylinders, Volume 2: Applications*, Oxford University Press Inc., New York, NY, 2003.

[121] F. O. Wilhofft, Industrial Applications of the Flettner Rotor, *Mechanical Engineering*, Vol. 49, 1927, pp. 249–255.

[122] A. Flettner, Application of Aerodynamic Knowledge to Wind–Driven Ships, *Zeit. für Flugtechnik und Motorluft–Schiffahrt*, Vol. 16, 1925, pp. 52–65.

[123] G. L. Johnson, *Wind Energy Systems*, Prentice Hall, Englewood Cliffs, NJ, 1985, pp. 16–20.

[124] D. H. Whitford and J. E. Minardi, The Madaras Rotor Power Plant – An Alternate Method for Extracting Large Amounts of Power from the Wind, In *17th AIAA Aerospace Sciences Meeting*, New Orleans, LA, 1979.

[125] E. B. Wolff, Preliminary Investigation of the Effect of a Rotating Cylinder in a Wing, Technical Report TM-307, NACA, 1925.

[126] E. B. Wolff and C. Koning, Tests for Determining the Effect of a Rotating Cylinder Fitted into the Leading Edge of an Airplane Wing, Technical Report TM-354, NACA, 1925.

[127] A. Busemann, Messungen an Rotierenden Zylindern, In *Ergebnisse der Aerodynamik Versuchsanstalt zu Göttingen*, No. IV. Lieferung, 1931, p. 101 ff.

[128] E. v. Holst, Der rotierende Flügel als Littel zur Hochauftriebserzeugung, Technical Report FB 1308, Aerodynamische Versuchsanstalt Göttingen, 1940.

[129] D. Küchemann, Auftrieb und Widerstand eines rotierenden Flügels, Technical Report FB 1651, Aerodynamische Versuchsanstalt Göttingen, 1942.

[130] D. Küchemann, Dreikomponentmessungen an einem Flügel mit rotierenden Hilfsflügel, Technical Report FB 1513, Aerodynamische Versuchsanstalt Göttingen, 1941.

[131] R. N. Liptrot, Rotating Wing Activities in Germany During the Period 1939–1945, BIOS Overall Report No. 8, Her Majesty's Stationary Office, London, UK, 1948.

[132] L. F. Crabtree, The Rotating Flap as a High-Lift Device, Technical Report CP No. 480, Aeronautical Research Council, 1960.

[133] V. J. Modi, Moving Surface Boundary-Layer Control: A Review, *Journal of Fluids and Structures*, Vol. 11, 1997, pp. 627–663.

[134] J. D. Brooks, Effect of a Rotating Cylinder Flap at the Leading and Trailing Edges of a Hydrofoil, NAVWEPS Report No. 8042, U.S. Naval Ordnance Test Station, Department of the Navy, 1963.

[135] B. N. Steele and M. H. Harding, The Application of Rotating Cylinders to Ship Maneuvering, Report No. 148, National Physics Laboratory, London, UK, 1970.

[136] A. Alverez-Calderon and F. R. Arnold, A Study of the Aerodynamic Characteristics of a High-Lift Device Based on Rotating Cylinder Flap, Technical Report RCF-1, Stanford University, 1961.

[137] J. S. Tennant, A Subsonic Diffuser with Moving Walls for Boundary Layer Control, *AIAA Journal*, Vol. 11, 1973, pp. 240–242.

[138] R. P. Holland, *Self-Adjusting Wind Power Machine*, Patent No. 4,582,013, United States Patent Office, 1986.

[139] V. J. Modi, M. S. U. K. Fernando and T. Yokomizo, Moving Surface Boundary-Layer Control: Studies with Bluff Bodies and Application, *AIAA Journal*, Vol. 29, 1991, pp. 1400–1406.

[140] F. Moktarian and V. J. Modi, Fluid Dynamics of Airfoils with Moving Surface Boundary-Layer Control, *Journal of Aircraft*, Vol. 25, 1988, pp. 163–167.

[141] V. J. Modi, F. Mokhtarian and T. Yokomizo, Effect of Moving Surfaces on the Airfoil Boundary Layer Control, *Journal of Aircraft*, Vol. 27, 1990, pp. 42–50.

[142] J. A. Weiberg, D. Giulianetti, B. Gambucci and R. C. Innis, Takeoff and Landing Performance and Noise Characteristics of a Deflected Slipstream STOL Airplane with Interconnected Propellers and Rotating Cylinder Flaps, Technical Report TM-X-62320, NASA, 1973.

[143] D. R. Cichy, J. W. Harris and J. K. MacKay, Flight Tests of a Rotating Cylinder Flap on a North American Rockwell YOV-10A Aircraft, Technical Report CR-2135, NASA, 1972.

[144] W. L. Cook, D. H. Hickey and H. C. Quigley, Aerodynamics of Jet Flap and Rotating Cylinder Flap STOL Concepts, In *AGARD Fluid Dynamics Panel. Symposium on V/STOL Aerodynamics*, Delft, The Netherlands, 1974.

[145] History of NASA: Boundary Layer Control, STOL, V/STOL Aircraft Research, Available at http://history.nasa.gov/SP-3300/ch8.htm.

[146] H. R. Kelly and R. W. Van Aken, The Magnus Effect at High Reynolds Numbers, *Journal of the Aeronautical Sciences*, Vol. 23, 1956, pp. 1053–1054.

[147] J. F. Jaminet and C. W. Van Atta, Experiments on Vortex Shedding from Rotating Circular Cylinders, *AIAA Journal*, Vol. 7, 1969, pp. 1817–1819.

[148] J. M. Davies, The Aerodynamics of Golf Balls, *Journal of Applied Physics*, Vol. 20, 1949, pp. 821–828.

[149] E. Krahn, Negative Magnus Force, *Journal of the Aeronautical Sciences*, Vol. 23, 1956, pp. 377–378.

[150] T. K. Aldoss and T. W. Abou-Arab, Experimental Study of the Flow Around a Rotating Cylinder in Crossflow, *Experimental Thermal and Fluid Science*, Vol. 3, 1990, pp. 316–322.

[151] H. Peller, V. Lippig, D. Straub and R. Waibel, Thermofluiddynamic Experiments with a Heated and Rotating Circular Cylinder in Cross-Flow. Part 1: Sub-critical Heat Transfer Measurements, *Experiments in Fluids*, Vol. 2, 1984, pp. 113–120.

[152] H. Peller, Thermofluiddynamic Experiments with a Heated and Rotating Circular Cylinder in Cross-Flow. Part 2.1: Boundary Layer Profiles and Locations of Separation Points, *Experiments in Fluids*, Vol. 4, 1986, pp. 223–231.

[153] H. Peller and D. Straub, Thermofluiddynamic Experiments with a Heated and Rotating Circular Cylinder in Cross-Flow. Part 2.2:, *Experiments in Fluids*, Vol. 6, 1988, pp. 111–114.

[154] Y. T. Chew, Flow Past a Rotating Cylinder, In *Proceedings of the International Conference on Fluid Mechanics*, Beijing, China, 1987, pp. 556–560.

[155] T. E. McLaughlin, E. J. Stephen and M. C. Robinson, Pressure Measurements on a Rotating Cylinder, In *9th AIAA Applied Aerodynamics Conference*, Baltimore, MD, 1991.

[156] M. C. Miller, Surface Pressure Measurements on a Spinning Wind Tunnel Model, *AIAA Journal*, Vol. 14, 1976, pp. 1669–1670.

[157] M. C. Miller, Wind-Tunnel Measurements of the Surface Pressure on a Spinning Magnus Rotor, *Journal of Aircraft*, Vol. 16, 1979, pp. 815–822.

[158] F. Díaz, J. Gavaldà, J. G. Kawall, J. F. Keffer and F. Giralt, Vortex Shedding from a Spinning Cylinder, *Physics of Fluids*, Vol. 26, 1983, pp. 3454–3460.

[159] F. Díaz, J. Gavaldà, J. G. Kawall, J. F. Keffer and F. Giralt, Asymmetrical Wake Generated by a Spinning Cylinder, *AIAA Journal*, Vol. 23, 1985, pp. 49–54.

[160] J. Massons, J. Gavaldà, F. Díaz and L. Solé, Image Processing of Cylinder Wake Generation, *Physics of Fluids A: Fluid Dynamics*, Vol. 1, 1989, pp. 1415–1423.

[161] D. C. Thoman and A. A. Szewczyk, Numerical Solutions of Time-Dependent Two-Dimensional Flow of a Viscous Incompressible Fluid Over Stationary and Rotating Cylinders, Technical Report 66–14, University of Notre Dame, 1966.

[162] P. L. Ta, Étude Numerique de l'Écoulement d'un Fluide Visqueux Incompressible Autor d'un Cylindre Fixe ou en Rotation. Effet Magnus. *Journal de Mécanique*, Vol. 14, 1975, pp. 109–134.

[163] V. A. Lyul'ka, Numerical Solution of the Problem of the Rotation of a Cylinder in a Flow of a Viscous Incompressible Fluid, *USSR Computational Mathematics and Mathematical Physics*, Vol. 17, 1977, pp. 178–188.

[164] P. Townsend, A Numerical Simulation of Newtonian and Viscoelastic Flow Past Stationary and Rotating Cylinders, *Journal of Non-Newtonian Fluid Mechanics*, Vol. 6, 1980, pp. 219–243.

[165] D. B. Ingham, Steady Flow Past a Rotating Cylinder, *Computers and Fluids*, Vol. 11, 1983, pp. 351–366.

[166] H. M. Badr, M. Coutanceau, S. C. R. Dennis and C. Ménard, Unsteady Flow Past a Rotating Circular Cylinder at Reynolds Numbers 10^3 to 10^4, *Journal of Fluid Mechanics*, Vol. 220, 1990, pp. 459–484.

[167] H. M. Badr and S. C. R. Dennis, Time-Dependent Viscous Flow Past an Impulsively Started Rotating and Translating Circular Cylinder, *Journal of Fluid Mechanics*, Vol. 158, 1985, pp. 447–488.

[168] G. E. Karniadakis and G. S. Triantifyllou, Three-Dimensional Dynamics and Transition to Turbulence in the Wake of Bluff Bodies, *Journal of Fluid Mechanics*, Vol. 238, 1992, pp. 1–31.

[169] M. Cheng, Y. T. Chew and S. C. Luo, Discrete Vortex Simulation of the Separated Flow Around a Rotating Circular Cylinder at High Reynolds Number, *Finite Elements in Analysis and Design*, Vol. 18, 1994, pp. 225–236.

[170] S. M. Belotserkovskii, V. N. Kotovskii, M. I. Nisht and R. M. Fedorov, Computer Modeling of the Stalled Flow of a Rotating Cylinder and the Reverse Magnus Effect, *Journal of Engineering Physics and Thermophysics*, Vol. 48, 1985, pp. 175–180.

[171] T. Kimura and M. Tsutahara, Flows About a Rotating Circular Cylinder by the Discrete-Vortex Method, *AIAA Journal*, Vol. 25, 1987, pp. 182–184.

[172] T. Kimura, M. Tsutahara and Z. Y. Wang, Wake of a Rotating Circular Cylinder, *AIAA Journal*, Vol. 30, 1991, pp. 555–556.

[173] C. C. Chang and R. L. Chern, Vortex Shedding from an Impulsively Started Rotating and Translating Circular Cylinder, *Journal of Fluid Mechanics*, Vol. 233, 1991, pp. 265–298.

[174] G. P. Ling and T. M. Shih, Numerical Study of the Vortex Motion Patterns Around a Rotating Circular Cylinder and Their Critical Characters, *International Journal for Numerical Methods in Fluids*, Vol. 29, 1999, pp. 229–248.

[175] Y. T. Chew, M. Cheng and S. C. Luo, A Numerical Study of Flow Past a Rotating Circular Cylinder Using a Hybrid Vortex Scheme, *Journal of Fluid Mechanics*, Vol. 299, 1995, pp. 35–71.

[176] A. Elmiligui, K. S. Abdol-Hamid, S. J. Massey and S. P. Pao, Numerical Study of Flow Past a Circular Cylinder Using RANS, Hybrid RANS/LES and PANS Formulations, In *22nd Applied Aerodynamics Conference and Exhibit*, Providence, RI, 2004.

[177] W. G. Bickley, The Influence of Vortices Upon the Resistance Experienced by Solids Moving Through a Liquid, *Proceedings of the Royal Society of London. Series A. Mathematical and Physical Sciences*, Vol. 119, 1928, pp. 146–156.

[178] M. B. Glauert, A Boundary Layer Theorem, With Application to Rotating Cylinders Whose Streamlines are Closed, *Journal of Fluid Mechanics*, Vol. 2, 1957, pp. 89–99.

[179] M. B. Glauert, The Flow Past a Rapidly Rotating Circular Cylinder, *Proceedings of the Royal Society of London. Series A, Mathematical and Physical Sciences*, Vol. 242, 1957, pp. 108–115.

[180] D. W. Moore, The Flow Past a Rapidly Rotating Circular Cylinder in a Uniform Stream, *Journal of Fluid Mechanics*, Vol. 2, 1957, pp. 541–550.

[181] W. W. Wood, Boundary Layers Whose Streamlines are Closed, *Journal of Fluid Mechanics*, Vol. 2, 1957, pp. 77–87.

[182] M. C. Ece, J. D. A. Walker and T. L. Doligalski, The Boundary Layer on an Impulsively Started Rotating and Translating Cylinder, *Physics of Fluids*, Vol. 27, 1984, pp. 1077–1089.

[183] E. H. Smith, Autorotating Wings: An Experimental Investigation, *Journal of Fluid Mechanics*, Vol. 50, 1971, pp. 513–534.

[184] F. N. M. Brown, The Organized Boundary Layer, In *Proceedings of the Sixth Midwestern Conference on Fluid Mechanics*, Austin, TX, 1959, pp. 331–349.

[185] F. N. M. Brown, Some Characteristics of the Periodic Vortical Elements Within the Transitioning Boundary Layer, Technical report, University of Notre Dame, 1960.

[186] M. Coutanceau and C. Ménard, Influence of Rotation on the Near-Wake Development Behind an Impulsively Started Circular Cylinder, *Journal of Fluid Mechanics*, Vol. 158, 1985, pp. 399–446.

[187] J. W. Maccoll, Aerodynamics of a Spinning Sphere, *Journal of the Royal Aeronautical Society*, Vol. 32, 1928, pp. 777–798.

[188] H. Tanaka and S. Nagano, Study of Flow Around a Rotating Circular Cylinder, *Bulletins of the Japanese Society of Mechanical Engineers*, Vol. 16, 1973, pp. 234–243.

[189] R. T. Griffiths and C. Y. Ma, Differential Boundary-Layer Separation Effects in the Flow over a Rotating Cylinder, *Aeronautical Journal*, Vol. 73, 1969, pp. 524–526.

[190] L. E. Ericsson, Moving Wall Effects in Unsteady Flow, *Journal of Aircraft*, Vol. 25, 1988, pp. 977–990.

[191] P. T. Tokumaru and P. E. Dimotakis, The Lift of a Cylinder Executing Rotary Motions in a Uniform Flow, *Journal of Fluid Mechanics*, Vol. 255, 1993, pp. 1–10.

[192] T. K. Sengupta, A. Kasliwal, S. De and M. T. Nair, Temporal Flow Instability for Magnus-Robins Effect at High Rotation Rates, *Journal of Fluids and Structures*, Vol. 17, 2003, pp. 941–953.

[193] M. M. Zdravkovich, V. P. Brand, G. Mathew and A. Weston, Flow Past Short Circular Cylinders with Two Free Ends, *Journal of Fluid Mechanics*, Vol. 203, 1989, pp. 557–575.

[194] S. Takayama and K. Aoki, Flow Characteristics around a Rotating Grooved Circular Cylinder with Grooves of Different Depths, *Journal of Visualization*, Vol. 8, 2005, pp. 295–303.

[195] E. Achenbach, Influence of Surface Roughness on the Cross-Flow Around a Circular Cylinder, *Journal of Fluid Mechanics*, Vol. 46, 1971, pp. 321–335.

[196] A. Fage and J. H. Warsap, The Effects of Turbulence and Surface Roughness on the Drag of a Circular Cylinder, Technical Report R&M No. 1283, Aeronautical Research Council, 1929.

[197] D. Stojković, M. Breuer and F. Durst, Effect of High Rotation Rates on the Laminar Flow Around a Circular Cylinder, *Physics of Fluids*, Vol. 14, 2002, pp. 3160–3178.

[198] S. Mittal, Three Dimensional Instabilities in Flow Past a Rotating Cylinder, *Journal of Applied Mechanics*, Vol. 71, 2004, pp. 89–95.

[199] S. Kang, H. Choi and S. Lee, Laminar Flow Past a Rotating Cylinder, *Physics of Fluids*, Vol. 11, 1999, pp. 3312–3320.

[200] J. C. Padrino and D. D. Joseph, Numerical Study of the Steady State Uniform Flow Past a Rotating Cylinder, *Journal of Fluid Mechanics*, Vol. 557, 2006, pp. 191–223.

[201] W. Tollmien, Ph.D. thesis, Göttingen University, Germany, 1924.

[202] G. R. Ludwig, An Experimental Investigation of Laminar Separation from a Moving Wall, In *2nd AIAA Aerospace Sciences Meeting*, New York, NY, 1964.

[203] S. Mittal and B. Kumar, Flow Past a Rotating Cylinder, *Journal of Fluid Mechanics*, Vol. 476, 2003, pp. 303–334.

[204] P. K. Stansby and R. C. T. Rainey, On the Orbital Response of a Rotating Cylinder in a Current, *Journal of Fluid Mechanics*, Vol. 439, 2001, pp. 87–108.

[205] T. K. Aldoss and A. Mansour, Theoretical Calculations of the Flow Around a Rotating Cylinder Placed in a Uniform Flow, *Journal of Fluids Engineering*, Vol. 110, 1988, pp. 96–98.

[206] H. M. Badr, S. C. R. Dennis and P. J. S. Young, Steady and Unsteady Flow Past a Rotating Circular Cylinder at Low Reynolds Numbers, *Computers and Fluids*, Vol. 17, 1989, pp. 579–609.

[207] M. T. Nair, T. K. Sengupta and U. S. Chauhan, Flow Past Rotating Cylinders at High Reynolds Numbers Using Higher Order Upwind Scheme, *Computers and Fluids*, Vol. 27, 1998, pp. 47–70.

[208] G. Polidori, G. Pineau, K. A. Meriam and M. Coutanceau, Shedding Processes of the Initial Vortices from Impulsively Started Cylinders at Re = 1000: End and Body Geometry Effects, In *Proceedings of the IUTAM Symposium on Bluff-Body Wakes, Dynamics and Instabilities*, Göttingen, Germany, 1993.

[209] T. Tang and D. B. Ingham, On Steady Flow Past a Rotating Circular Cylinder at Reynolds Numbers 60 and 100, *Computers and Fluids*, Vol. 19, 1991, pp. 217–230.

[210] S. Taneda, Visual Study of Unsteady Separated Flows Around Bodies, *Progress in Aerospace Sciences*, Vol. 17, 1976, pp. 287–348.

[211] T. Matsui, Flow Visualisation Studies of Vortices, In *Proceedings of the Indian Academy of Sciences*, 1982, pp. 239–257.

[212] J. Massons, X. Ruiz and F. Díaz, Image Processing of the Near Wakes of Stationary and Rotating Cylinders, *Journal of Fluid Mechanics*, Vol. 204, 1989, pp. 167–184.

[213] Y. M. Chen, Y. R. Ou and A. J. Pearlstein, Development of the Wake Behind a Circular Cylinder Impulsively Started into Rotatory and Rectilinear Motion, *Journal of Fluid Mechanics*, Vol. 253, 1993, pp. 449–484.

[214] Y. R. Ou and J. A. Burns, Optimal Control of Lift/Drag Ratio on a Rotating Cylinder, ICASE Report No. 91-49, Institute for Computer Applications in Science and Engineering, 1991.

[215] M. B. Glauert, The Laminar Boundary Layer on Oscillating Plates and Cylinders, *Journal of Fluid Mechanics*, Vol. 1, 1956, pp. 97–110.

[216] J. Calamote, Effets de la Rotation Sur le Sillage de Cylindres Tournants, Thèse de 3ème cycle de l'Université Aix-Marseille II, 1984.

[217] M. H. Chou, Numerical Study of Vortex Shedding from a Rotating Cylinder Immersed in a Uniform Flow Field, *International Journal for Numerical Methods in Fluids*, Vol. 32, 2000, pp. 545–567.

[218] C. W. Van Atta, Comments on "Hopf Bifurcation in Wakes Behind a Rotating and Translating Circular Cylinder", *Physics of Fluids*, Vol. 9, 1997, pp. 3105–3106.

[219] G. H. Hu, D. J. Sun, X. Y. Yin and B. G. Tong, Hopf Bifurcation In Wakes Behind a Rotating and Translating Circular Cylinder, *Physics of Fluids*, Vol. 8, 1996, pp. 1972–1974.

[220] T. Matsui, The Flow Near the Surface of a Cylinder Rotating in a Uniform Flow, In *Euromech 90 Colloquium*, Nancy, France, 1977.

[221] T. Matsui, Flow Behind a Rotating Cylinder, *The Physics of Fluids Supplement*, Vol. 10, 1967, pp. S305.

[222] M. M. Zdravkovich, *Flow Around Circular Cylinders, Volume 1: Fundamentals*, Oxford University Press Inc., New York, NY, 1997.

[223] D. Stojković, P. Schön, M. Breuer and F. Durst, On the New Vortex Shedding Mode Past a Rotating Circular Cylinder, *Physics of Fluids*, Vol. 15, 2003, pp. 1257–1260.

[224] G. H. Koopmann, The Vortex Wake of Vibrating Cylinders at Low Reynolds Numbers, *Journal of Fluid Mechanics*, Vol. 28, 1967, pp. 501–512.

[225] P. K. Stansby, The Locking-On of Vortex Shedding Due to Cross-Stream Vibration of Circular Cylinders in Uniform and Shear Flows, *Journal of Fluid Mechanics*, Vol. 74, 1976, pp. 641–665.

[226] J. C. Cincotta, G. W. Jones Jr. and R. W. Walker, Experimental Investigation of Wind-Induced Oscillation Effects on Cylinders in Two-Dimensional Flow at High Reynolds Numbers, In *Meeting on Ground Wind Load Problems in Relation to Launch Vehicles*, Langley Research Center, US, 1966.

[227] W. C. Howerton, *Experimental Investigation of the Aerodynamics of Independently Rotating Cylindrical Shells*, Master's thesis, Air Force Institute of Technology, Wright Patterson AFB, School of Engineering, 1992.

[228] M. M. Zdravkovich, Review of Flow Interference Between Two Circular Cylinders in Various Arrangements, *Journal of Fluids Engineering*, Vol. 99, 1977, pp. 618–633.

[229] E. J. Watson, The Rotation of Two Circular Cylinders in a Viscous Fluid, *Mathematika*, Vol. 42, 1995, pp. 105–126.

[230] Y. Ueda, A. Sellier, T. Kida and M. Nakanishi, On the Low-Reynolds-Number Flow About Two Rotating Circular Cylinders, *Journal of Fluid Mechanics*, Vol. 495, 2003, pp. 255–281.

[231] A. Pope and J. J. Harper, *Low Speed Wind Tunnel Testing*, John Wiley & Sons, Inc., New York, NY, 1966.

[232] B. F. R. Ewald *et al.*, Wind Tunnel Wall Correction, AGARDograph AG-336, AGARD, 1998.

[233] H. C. Garner, E. W. E. Rogers, W. E. C. Acum and E. C. Maskell, Subsonic Wind Tunnel Wall Corrections, AGARDograph AG-109, AGARD, 1966.

[234] Blockage Corrections for Bluff Bodies in Confined Flows, Engineering Sciences Data Item No. 80024, ESDU, London, UK, 1980.

[235] E. C. Maskell, A Theory of the Blockage Effects on Bluff Bodies and Stalled Wings in a Closed Wind Tunnel, Technical Report R & M No. 3400, Aeronautical Research Council, 1963.

[236] R. Fail, J. A. Lawford and R. C. W. Eyre, Low-Speed Experiments on the Wake Characteristics of Flat Plates Normal to an Air Stream, Technical Report R&M No. 3120, Aeronautical Research Council, 1957.

[237] F. Cowdrey, Two Topics of Interest in Experimental Industrial Aerodynamics - Part 1: Application of Maskells Theory of Wind-Tunnel Blockage to Some Large Models, Part 2: Design of Velocity-Profile Grids, NPL Aero Report 1268, National Physics Laboratory, 1968.

[238] J. E. Hackett, Tunnel-Induced Gradients and Their Effect on Drag, *AIAA Journal*, Vol. 34, 1996, pp. 2575–2581.

[239] G. S. West and C. J. Apelt, The Effects of Tunnel Blockage Ratio and Aspect Ratio on the Mean Flow Past a Circular Cylinder with Reynolds Numbers Between 10^4 and 10^5, *Journal of Fluid Mechanics*, Vol. 114, 1982, pp. 361–377.

[240] C. Farell, S. Carrasquel, O. Guven and V. C. Patel, Effect of Wind-Tunnel Walls on the Flow Past Circular Cylinders and Cooling Tower Models, *Journal of Fluids Engineering*, Vol. 99, 1977, pp. 470–479.

[241] J. E. Fackrell, Blockage Effects on Two-Dimensional Bluff Body Flow, *Aeronautical Quarterly*, Vol. 26, 1975, pp. 243–253.

[242] V. J. Modi and S. El-Sherbiny, On the Wall Confinement Effects in the Industrial Aerodynamic Studies, In *Symposium on Vibration Problems in Industry*, Paper No. 116, Keswick, UK, 1973.

[243] H. J. Allen and W. G. Vincenti, Wall Interference in a Two-Dimensional-Flow Wind Tunnel, with Consideration of the Effect of Compressibility, Technical Report TR-782, NACA, 1944.

[244] R. C. Pankhurst and D. W. Holder, *Wind Tunnel Technique*, Sir Isaac Pitman & Sons, London, UK, 1952.

[245] C. Homescu, I. M. Navon and Z. Li, Suppression of Vortex Shedding for Flow Around a Circular Cylinder Using Optimal Control, *International Journal for Numerical Methods in Fluids*, Vol. 38, 2002, pp. 43–69.

[246] J. Xiong, G. Ling and K. Zhu, Numerical Estimate of the Stability Curve for the Flow Past a Rotating Cylinder, *Physics of Fluids*, Vol. 16, 2004, pp. 2697–2699.

[247] F. H. Barnes, Vortex Shedding in the Wake of a Rotating Circular Cylinder at Low Reynolds Numbers, *Journal of Physics D: Applied Physics*, Vol. 33, 2000, pp. L141–L144.

[248] A. Klemin, The Savenius Wing Rotor, *Mechanical Engineering*, Vol. 47, 1925, pp. 911–912.

[249] J. Gavaldà, J. Massons and F. Díaz, Drag and Lift Coefficients of the Savonius Wind Machine, *Wind Engineering*, Vol. 15, 1991, pp. 240–246.

[250] Y. Oshima, N. Izutsu, K. Oshima and K. Kuwahara, Autorotation of an Elliptic Airfoil, In *21st AIAA Aerospace Sciences Meeting*, Reno, NV, 1983.

[251] J. D. Iversen, Autorotating Flat-Plate Wings: The Effect of the Moment of Inertia, Geometry, and Reynolds Number, *Journal of Fluid Mechanics*, Vol. 92, 1979, pp. 327–348.

[252] J. S. Tennant, W. S. Johnson and A. Krothapalli, Rotating Cylinder for Circulation Control on an Airfoil, *Journal of Hydronautics*, Vol. 10, 1976, pp. 102–105.

[253] E. B. Wolff, Preliminary Study of the Influence of a Rotating Cylinder on a Wing, *Flight*, 15 January 1925.

[254] E. L. Houghton and P. W. Carpenter, *Aerodynamics for Engineering Students*, Edward Arnold, London, UK, 4th ed., 1993.

[255] C. N. H. Lock, The Interference of a Wind Tunnel on a Symmetrical Body, Technical Report R&M No. 1275, Aeronautical Research Council, 1929.

[256] J. B. Barlow, Jr. W. H. Rae and A. Pope, *Low Speed Wind Tunnel Testing*, John Wiley & Sons, Inc., New York, NY, 3rd ed., 1999.

[257] J. E. Hackett, Tunnel-Induced Gradients and Their Effect on Drag, Technical Report LG83ERO108, Lockheed Corporation, Smyrna, GA, 1994.

[258] E. Achenbach, Distribution of Local Pressure and Skin Friction Around a Circular Cylinder in Cross-flow up to Re = 5 x 10^6, *Journal of Fluid Mechanics*, Vol. 34, 1968, pp. 625–639.

[259] C. Norberg, An Experimental Investigation of the Flow Around a Circular Cylinder: Influence of Aspect Ratio, *Journal of Fluid Mechanics*, Vol. 258, 1994, pp. 287–316.

[260] K. Stewart, J. Wagener and G. Abate, Design of the Air Force Research Laboratory Micro Aerial Vehicle Research Configuration, In *45th AIAA Aerospace Sciences Meeting and Exhibit*, Reno, NV, 2007.

[261] S. F. Hoerner, *Fluid Dynamic Drag*, Hoerner Fluid Dynamics, Brick Town, NJ, 1975.

[262] F. G. Howard and W. L. Goodman, Axisymmetric Bluff-Body Drag Reduction Through Geometrical Modification, *Journal of Aircraft*, Vol. 22, 1985, pp. 516–522.

[263] M. S. Selig, J. Guglielmo, A. P. Broeren and P. Giguère, *Summary of Low-Speed Airfoil Data*, Vol. 1, Soartech Publications, Virginia Beach, VA, 1995.

[264] M. S. Selig, C. A. Lyon, P. Giguère, C. Ninham and J. Guglielmo, *Summary of Low-Speed Airfoil Data*, Vol. 2, Soartech Publications, Virginia Beach, VA, 1996.

[265] C. A. Lyon, A. P. Broeren, P. Giguère, A. Gopalarathnam and M. S. Selig, *Summary of Low-Speed Airfoil Data*, Vol. 3, Soartech Publications, Virginia Beach, VA, 1997.

[266] D. Stinton, *The Design of the Aeroplane*, Blackwell Scientific Publications Ltd., Oxford, UK, 1993.

[267] H. R. Vaughn and G. E. Reis, A Magnus Theory, *AIAA Journal*, Vol. 11, 1973, pp. 1396–1403.